Conference Proceedings of the Society for Experimental Mechanics Series

Marco Rossi · Marco Sasso · Nathanael Connesson · Raman Singh
Adrian DeWald · David Backman · Paul Gloeckner *Editors*

Residual Stress, Thermomechanics & Infrared Imaging, Hybrid Techniques and Inverse Problems, Volume 8

Proceedings of the 2013 Annual Conference on Experimental and Applied Mechanics

Springer

Conference Proceedings of the Society for Experimental Mechanics Series

Series Editor
Tom Proulx
Society for Experimental Mechanics, Inc.,
Bethel, CT, USA

For further volumes:
http://www.springer.com/series/8922

Marco Rossi • Marco Sasso • Nathanael Connesson • Raman Singh
Adrian DeWald • David Backman • Paul Gloeckner
Editors

Residual Stress, Thermomechanics & Infrared Imaging, Hybrid Techniques and Inverse Problems, Volume 8

Proceedings of the 2013 Annual Conference on Experimental and Applied Mechanics

Springer

Editors
Marco Rossi
Università Politecnica delle Marche
Ancona, PA
Italy

Marco Sasso
Università Politecnica delle Marche
Ancona, PA
Italy

Nathanael Connesson
University of Joseph Fourier
Grenoble
France

Raman Singh
Oklahoma State University
Tulsa, OK
USA

Adrian DeWald
Hill Engineering, LLC
Rancho Cordova, CA
USA

David Backman
National Research Council Canada
Ottawa, ON
Canada

Paul Gloeckner
Cummins, Inc.
Columbus, IN
USA

ISSN 2191-5644 ISSN 2191-5652 (electronic)
ISBN 978-3-319-00875-2 ISBN 978-3-319-00876-9 (eBook)
DOI 10.1007/978-3-319-00876-9
Springer Cham Heidelberg New York Dordrecht London

Library of Congress Control Number: 2011922268

Printed on acid-free paper

Springer is part of Springer Science+Business Media (www.springer.com)

Preface

Residual Stress, Thermomechanics & Infrared Imaging, Hybrid Techniques and Inverse Problems, Volume 8: Proceedings of the 2013 Annual Conference on Experimental and Applied Mechanics represents one of eight volumes of technical papers presented at the SEM 2013 Annual Conference & Exposition on Experimental and Applied Mechanics organized by the Society for Experimental Mechanics and held in Lombard, IL, June 3–5, 2013. The complete Proceedings also includes volumes on: *Dynamic Behavior of Materials; Challenges in Mechanics of Time-Dependent Materials and Processes in Conventional and Multifunctional Materials; Advancement of Optical Methods in Experimental Mechanics; Mechanics of Biological Systems and Materials; MEMS and Nanotechnology; Experimental Mechanics of Composite, Hybrid, and Multifunctional Materials; Fracture and Fatigue*.

Each collection presents early findings from experimental and computational investigations on an important area within Experimental Mechanics, Residual Stress, Thermomechanics & Infrared Imaging, Hybrid Techniques and Inverse Problems being three of these areas.

Residual stresses have a great deal of importance in engineering systems and design. The hidden character of residual stresses often causes them to be underrated or overlooked. However, they profoundly influence structural design and substantially affect strength, fatigue life, and dimensional stability. Since residual stresses are induced during almost all materials processing procedures, for example, welding/joining, casting, thermal conditioning, and forming, they must be taken seriously and included in practical applications.

In recent years, the application of infrared imaging techniques to the mechanics of materials and structures has grown considerably. The expansion is marked by the increased spatial and temporal resolution of the infrared detectors, faster processing times, and much greater temperature resolution. The improved sensitivity and more reliable temperature calibrations of the devices have meant that more accurate data can be obtained than were previously available.

Advances in inverse identification have been coupled with optical methods that provide surface deformation measurements and volumetric measurements of materials. In particular, inverse methodology was developed to more fully use the dense spatial data provided by optical methods to identify mechanical constitutive parameters of materials. Since its beginnings during the 1980s, creativity in inverse methods has led to applications in a wide range of materials, with many different constitutive relationships, across material heterogeneous interfaces. Complex test fixtures have been implemented to produce the necessary strain fields for identification. Force reconstruction has been developed for high strain rate testing. As developments in optical methods improve for both very large and very small length scales, applications of inverse identification expand to include geological and atomistic events.

Ancona, PA, Italy — Marco Rossi
Ancona, PA, Italy — Marco Sasso
Grenoble, France — Nathanael Connesson
Tulsa, OK, USA — Raman Singh
Rancho Cordova, CA, USA — Adrian DeWald
Ottawa, ON, Canada — David Backman
Columbus, IN, USA — Paul Gloeckner

Contents

Chapter 1
Analysis of Thrust Production in Small Synthetic Flapping Wings

Kelvin Chang, Jason Rue, Peter Ifju, Raphael Haftka, Tony Schmitz, Chris Tyler, Anirban Chaudhuri, and Vasishta Ganguly

Abstract For flapping micro air vehicles, geometrical parameters such as size, aspect ratio as well as structural topology can affect thrust production in hover mode. Synthetic wings similar in size to that of a humming bird's were manufactured with the hope of understanding these affects. The experimental method for measuring thrust and the manufacturing process used to make the wings have seen improvement from previous work such that there is less scatter and uncertainty; this allows for smaller variations in thrust to be detected. With confidence in the fabrication and testing procedure, an optimization problem was attempted where three design parameters were chosen as variables and the objective was to maximize thrust. These efforts were coupled with noncontact imaging techniques like digital image correlation and laser doppler velocimetry to help extract the characteristics that are consistent with wings that produce considerable thrust. The results of these tests will help to obtain the relationships between the consciously selected geometric parameters and the thrust produced. It was found that by machining the synthetic wings from acetal resin sheet and pairing that skeleton with a carbon fiber rod less variation was present. This wing construction was found to have a quick production time, making an experimental optimization feasible.

Keywords MAV • Flapping • Thrust • DIC • LDV

1.1 Introduction

Small flapping wing micro air vehicles (MAV) are continuously filling new roles and are presenting extraordinary functions. Theoretically, the possibilities for flapping wing MAVs stretch much further than previous aerial vehicles since they may have accumulative advantages of both rotary wing and fixed wing designs. These include efficiencies, noise level, and maneuverability although research is still being conducted to learn the physics behind flapping flight. In a study comparing flapping wing MAVs and conventional fixed wing MAVs, Hu et al. found definitive benefits in flapping flight below an advance ratio of 1.0 (forward flight speed to wingtip velocity) [1]. For this study, an unsteady state regime is investigated with advance ratio closer to 0 (hovering flight) with focus on the thrust produced by wings possessing wingspans no longer than 230 mm (~9 in.) at the highest aspect ratio. The purpose of this experiment was to take an enhanced manufacturing process along with digital image correlation, vibrational analysis, thrust testing, and optimization techniques to correlate certain variables to thrust production [2]. With in-site into the parameters that correlate well with thrust, new knowledge of desirable design features and reinforcement can be developed.

K. Chang (✉) • J. Rue • P. Ifju • R. Haftka • A. Chaudhuri
Mechanical and Aerospace Engineering Department, University of Florida, Florida, USA
e-mail: kc3635@ufl.edu

T. Schmitz • C. Tyler • V. Ganguly
Mechanical and Aerospace Engineering Department, University of North Carolina in Charlotte, Florida, USA

M. Rossi et al. (eds.), *Residual Stress, Thermomechanics & Infrared Imaging, Hybrid Techniques and Inverse Problems, Volume 8*, Conference Proceedings of the Society for Experimental Mechanics Series, DOI 10.1007/978-3-319-00876-9_1,

1.2 Advances in Manufacturing Process

The wings take advantage of passive wing deformation, much like hummingbirds or insects, as described by Wu [3]. The wing compliance and leading edge stiffness have positive aerodynamic effects and, while using passive deformation, can simplify kinematic actuation while reducing parts and weight. Having wings that are repeatable and robust are essential to any further developments in this area. The first step to creating a high-fidelity experimental process was to improve a commonly used method for wing assembly, as Nguyen performed [4]. A hand lay-up technique where carbon fiber strips are delicately laid on a flat plate in a certain pattern and cured under pressure in an oven is typical but holds many uncertainties and concerns. Details of how the hand lay-up method can lead to frequent problems and inconsistencies are described by Rue [5] along with an iteration using a CNC milled Teflon mold.

Figure 1.1 below shows an apparent difference, even visually, amongst a wing created with the original hand lay-up process and one with the CNC milled Teflon mold.

Several mold options had progressed to fix arising problems such as uneven pressure distributions, warping, or thermal expansion, although, ultimately, cost and precision needs drove the study to the current method. As seen in Fig. 1.2, a CNC milled Delrin (Acetal Resin) [6] frame is constructed and a pre-cured commercially available carbon fiber circular rod is

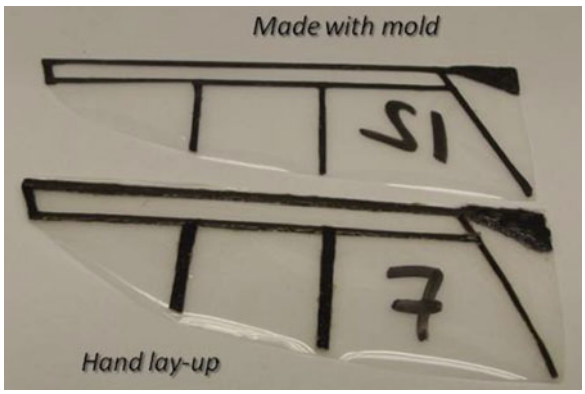

Fig. 1.1 Comparison of the original hand lay-up process with the CNC milled carbon fiber wing showing a clear distinction between the two in terms of precision and repeatability. (These wings are 75 mm in length)

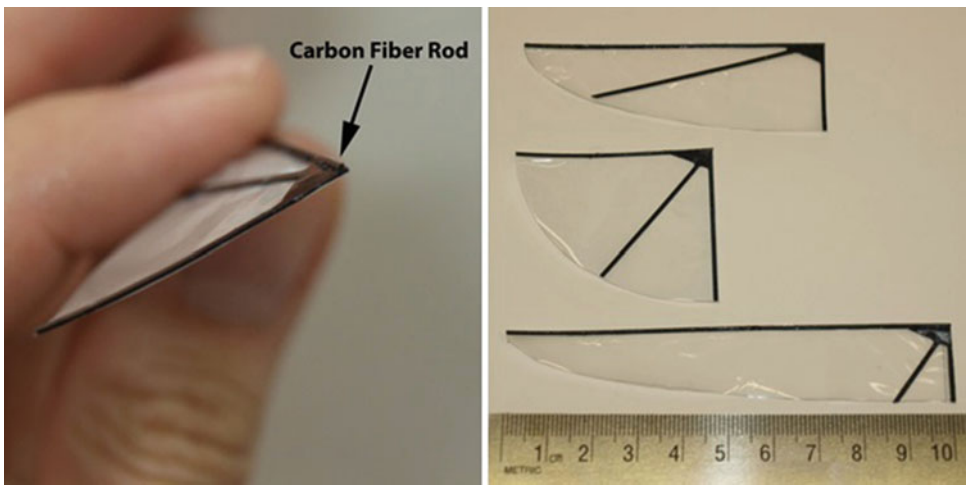

Fig. 1.2 Pictured on the *left* is a CNC milled plastic wing with a circular carbon fiber rod attached along the length of the leading edge. On the *right* is an image that depicts three of the six different aspect ratios tested with each wing possessing various batten angle degrees and leading edge rod lengths

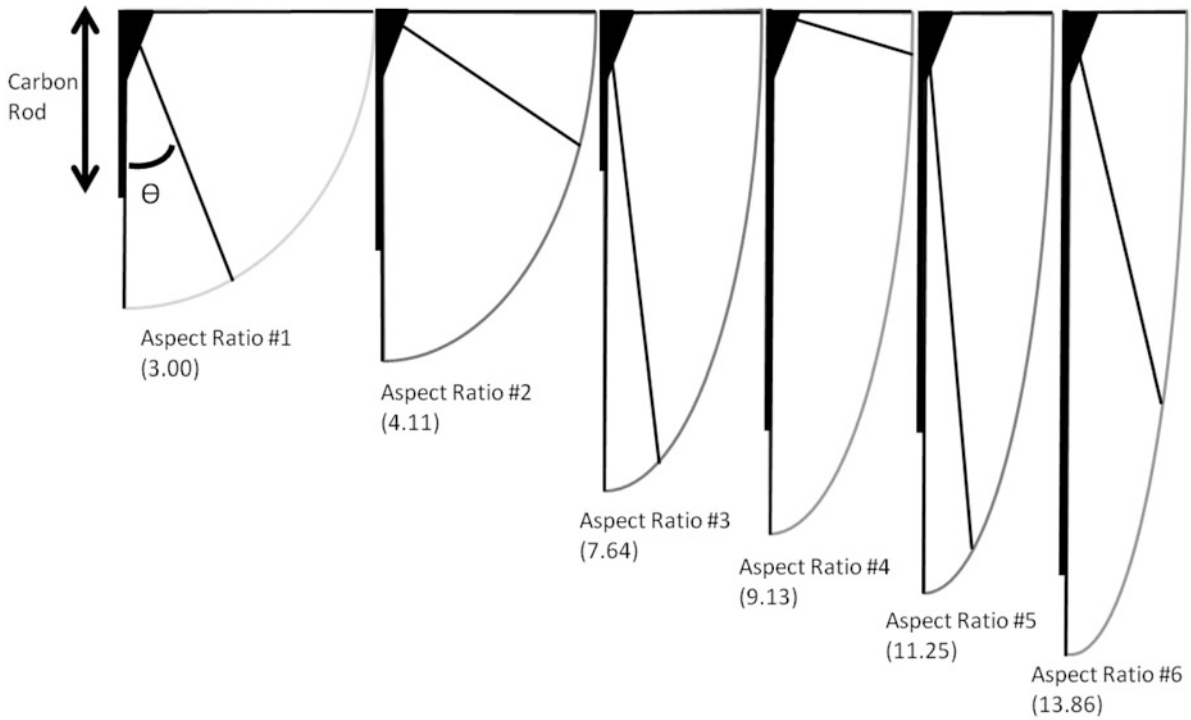

Fig. 1.3 Three chosen variables that could be manufactured and tested within the first round of optimization. Each of the six aspect ratios has the same quarter-elliptical area and three main components: a Delrin plastic frame, a 0.02 in. circular diameter carbon fiber rod, and a nylon based membrane called Capran. Each has a leading edge, a root batten, a triangular attachment point, and a batten elongating at a certain angle, θ, from the leading edge

attached in a trough on the leading edge. This process does not require any curing cycle for the carbon fiber and adds the precision and repeatability capability of a CNC to the wing. The weight of the wings remains compare well with the previous carbon fiber wings as well, ranging from approximately 0.1 to 0.25 g per wing. To keep a solid bond between the frame and rod, a rubber toughened cyanoacrylate glue was applied. Identical to the all carbon construct wing, the completed frame is glued down to a nylon based, 14 μm thick, membrane created by Honeywell, called Capran [7]. The wing area has an affect on the thrust output, so to maximize repeatability and to further development; thin marks are printed onto the Capran as cutting guides. An ink jet printer is utilized so that heat does not affect the material properties of the membrane.

Once the manufacturing was acceptable in terms of how repeatable the thrust measurements became, three variables were chosen for the initial optimization period (Fig. 1.3). These consist of varying the carbon fiber rod length on the leading edge, the angle of the one batten, and the aspect ratio. The aerodynamic definition for aspect ratio $\left(\frac{b^2}{S} \equiv \frac{span^2}{wing\ area}\right)$ was used for this term. These three variables are the bases of the optimization approach used, allowing for a consistent manufacturing process that is characterized by little minimal human error.

1.3 Vibration Analysis

Given the various actuation frequencies that the wings are exposed to, an investigation of the mode shapes and natural frequencies of the wings were put in place to assist in developing a better understanding of the wing's dynamics. The added benefit of this experiment includes the possibility of finding a correlation between these vibration parameters and the thrust produced.

A Polytec scanning vibrometer is used in the experimental setup for testing the wings which includes a PSV-I-400 scanning head, a PSV-400 junction box, and a OFV-500 controller module. These components work alongside a Low Dynamic Stiffness (LDS) V201 permanent magnet shaker that possesses a useful frequency range between 5 Hz and 12 kHz and is mounted on a trunnion for stability [8]. The shaker assembly was placed on a Newport RS1000 Research grade optical table Fig. 1.4.

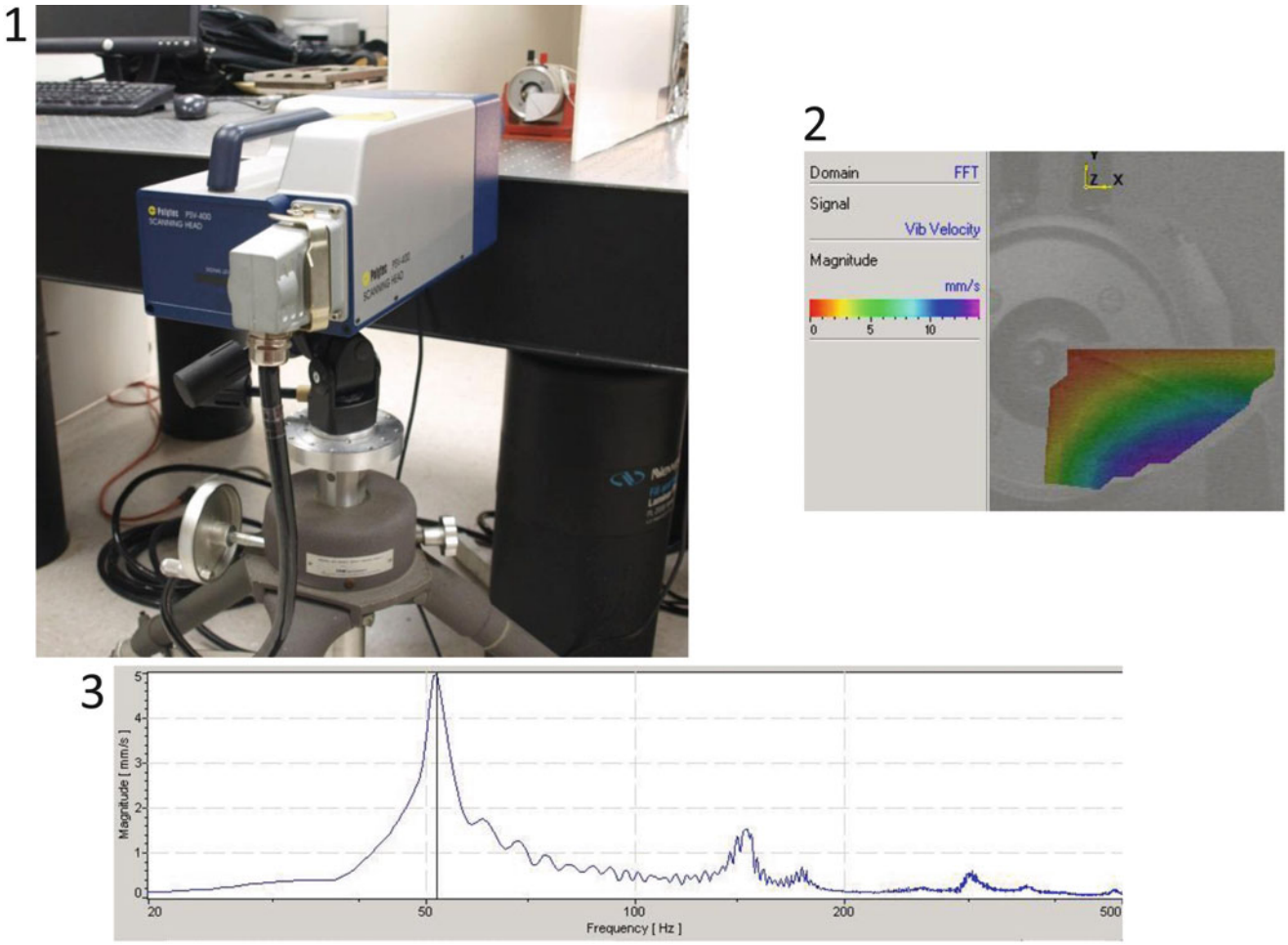

Fig. 1.4 (**1**) The Polytec scanning head, mounted on a tripod, is pictured with a shaker that linearly actuates the attached wing. (**2**) A typical instantaneous velocity color plot. (**3**) FFT graph showing the first three natural frequencies

Each wing is attached to the shaker assembly with a rigid bolt system and is lightly painted to increase the opacity of the surface. Ideally, the exposed surface would be physically flat and matte in finish. The experiment was performed in a dim external light setting to reduce any possible noise. Along with that, an enclosure was developed to shield it from excess wind created by the room's air conditioner unit. For each study, a grid of sampling points was populated on the wing. The shaker was commanded to sweep between 1 Hz and 500 Hz in a 1.6 s time period. Each point over the wing was tested five times to conclude in an averaged result. Data collected in this manner automatically generates an FFT graph, showing the modal frequencies for each wing (Fig. 1.4).

1.4 Preliminary Power Investigation

The controller software used with the flapping mechanism (Fig. 1.5) serves to obtain a commanded motor velocity for the wings by taking information from an encoder mounted on the back of the motor and devising a response in the form of an output current. For each of the wings, it becomes apparent that unequal quantities of power are being consumed by each trial, including discrepancies between different wing designs. Preliminary studies suggest that power consumed by a wing flapping at 10 hz, in a 5 s window, can vary by as much as 45 %, depending on controller response.

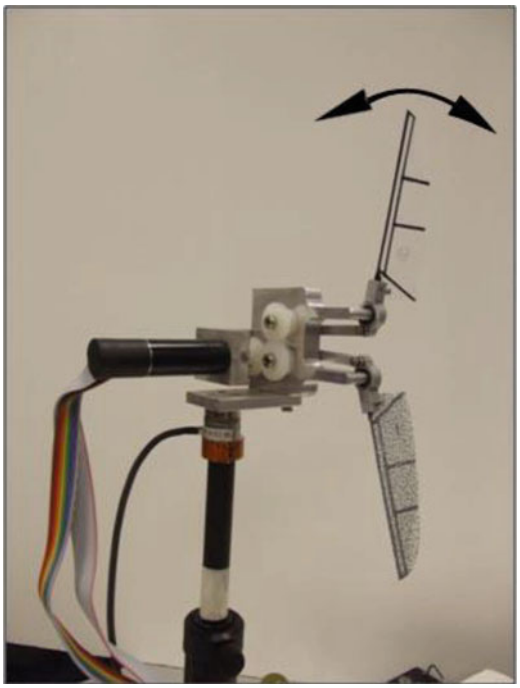

Fig. 1.5 A figure containing the flapping mechanism which entails an aluminum stand, an ATI Nano17 6 axis sensor (with *black cord* extending to the left), Maxon motor, and aluminum mechanism with nylon gearing system. This coupled with dual LabVIEW programs allows for the generated thrust and lift to be read and processed through MATLAB

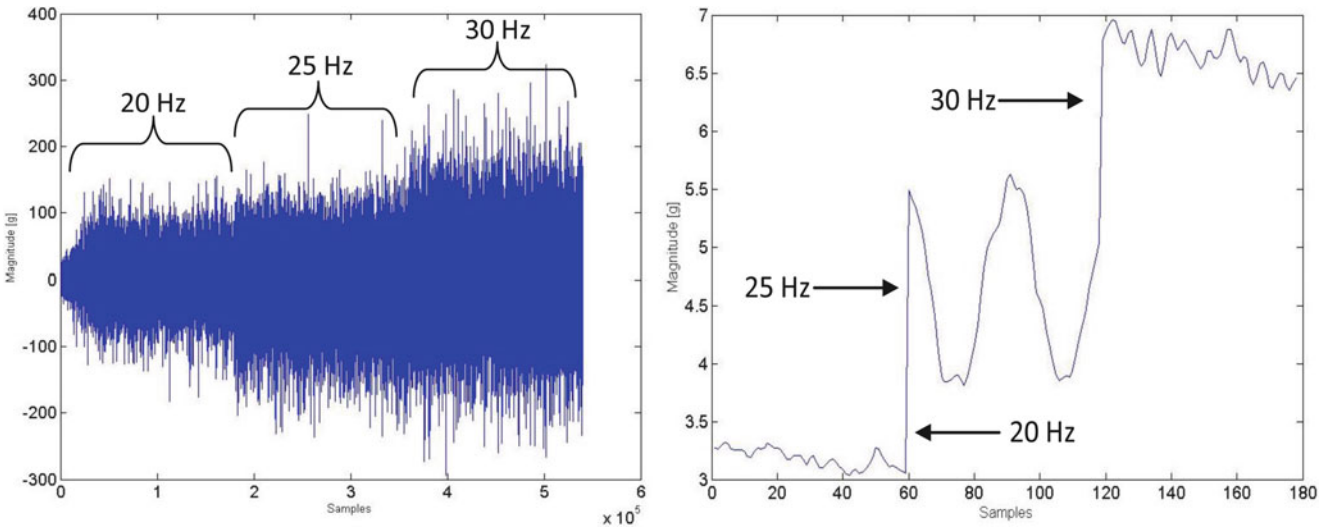

Fig. 1.6 Shows a view of two thrust data output examples, unfiltered on the *left* and low pass filtered on the *right*. Calculations done on the same wing give the same averaged thrust values for each frequency, though clearer distinctions between the three different frequency regimes are observed. Note that these are not of the same wing

1.5 Thrust Acquisition

Thrust measurements acquired within this experiment are gathered through two LabVIEW programs. Each wing outputs raw data at a sampling rate of 30,000 samples per second for several flapping frequencies-controlled by the Maxon motor and LabVIEW-for both thrust and lift. The raw data is then averaged over the specific run time for a single averaged thrust/lift value for each frequency. The flapping mechanism is pictured in Fig. 1.5.

The output signal from the load cell possesses a considerable amount of noise; making is very difficult to interpret. Therefore, a filter to extract a more manageable signal was required (Fig. 1.6). A point by point low pass Butterworth filter

was used real time in the LabVIEW software code to process the noisy signal to present the low frequency thrust offset data that is desired for each frequency. This filter provides the operator of the experiment real time performance that is easy to interpret, serving as a check to assure consistency and create a warning sign for possible delamination or damage to the wing between trials.

1.6 Digital Image Correlation

Based on previous studies, the leading edge stiffness of a wing has been proven to correlate with thrust production. Unique to this study, only a percentage of the leading edge length is fortified by the stiffness of a circular cross section carbon fiber rod. For each of the wings tested for thrust, digital image correlation (DIC) was utilized to extract deflections resulting from standardized weights (0.3 g, 0.5 g, 1.0 g) attached to the wing by a Kevlar string. The intent of this is find correlation between these deflections and the thrust output.

For the setup, each wing is misted with black paint and thin Kevlar strings are attached at the root and leading edge with thin cyanoacrylate glue, allowing for the application of the loads. The experimental setup includes two Point Grey Research Flea2 cameras that are aimed at the matte side of the Capran wing skin. Correlated Solution's VIC 2010 picture capturing software is used to take stills that are processed in VIC-3d. Two pictures at every load state are taken and the deflection results from these are averaged to reduce error (Fig. 1.7).

The resulting tip deflection due to a 0.5 g weight plotted against the percentage of the plastic leading edge that is fortified provides insight into the behavior of the wings. The bubble plot, Fig. 1.8, follows an exponential curvature with an

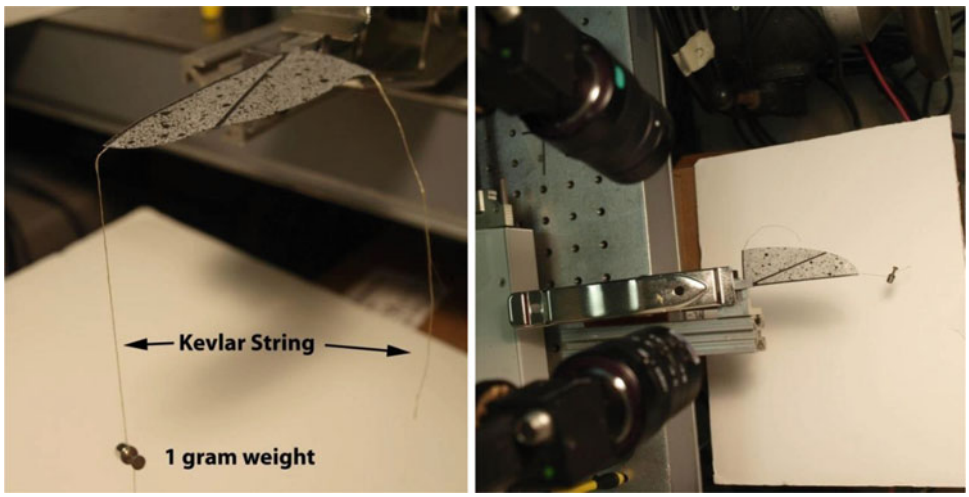

Fig. 1.7 On the *left*, a wing clamped in place and tested using DIC. On the *right* is an image of the DIC setup used to test for deflections. Speckled with enamel paint, the wing is subjected to a 1 g load at the tip of its leading edge via a Kevlar string

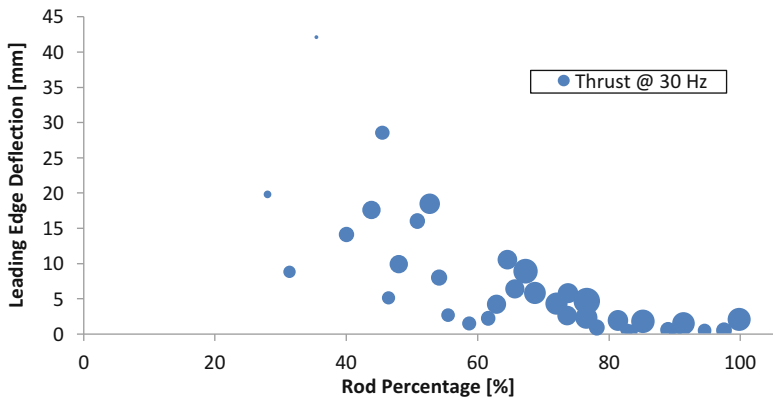

Fig. 1.8 A bubble plot presents the deflection data with a 0.5 g load obtained for different carbon rod percentages that occupy the plastic leading edge. The sizes of the bubbles illustrate the amount of thrust obtained for the wings

asymptote at zero deflection, indicating little deflection for wings with close to 100 % fortification. This expected result brings validation to the procedure used to gather the deflection. Another interesting behavior of this plot is how some of the data points have drifted to the left of the densely populated curve. This suggests that variables not considered in this plot have reduced the deflection. There are reasons to believe that the batten angle variable played a role in reducing the deflection of some of the points described in the plot.

1.7 Optimization

There is a multitude of variables that lend to the resulting thrust produced by a specific wing design. This complexity has encouraged efforts to optimize in a three variable space, seen in Fig. 1.9, focusing on variables that have proven to be strongly correlated with thrust output. The advantage of this is in the ease of populating the design space in a reasonable amount of time, and that the results of this smaller study could lend to larger ones where previously constrained variables could be allowed to vary. A technique called Efficient Global Optimization (EGO) is used to determine a set of wing designs that are good candidates for producing more thrust than the best designs found in previous tests. In batches of 20 new designs, the wings were tested for thrust production and a host of other parameters explained previously. EGO is able to conjure designs by considering previous tests. Therefore, the optimization is guided, pivoting off of results obtained from previous batches.

Table 1.1 explains the initial design space for the first 20 wings. After extensive testing, the space was altered slightly to exclude unreasonable regions for wings 21–40. For example, the leading edge stiffness percentage range was reduced to 40–100 % since. Even though the prior range was feasible to manufacture, the excess deformation and poor results in flapping led to concerns. Also, the angle of the batten was changed to a minimum of 10° to address structural support along the trailing edge.

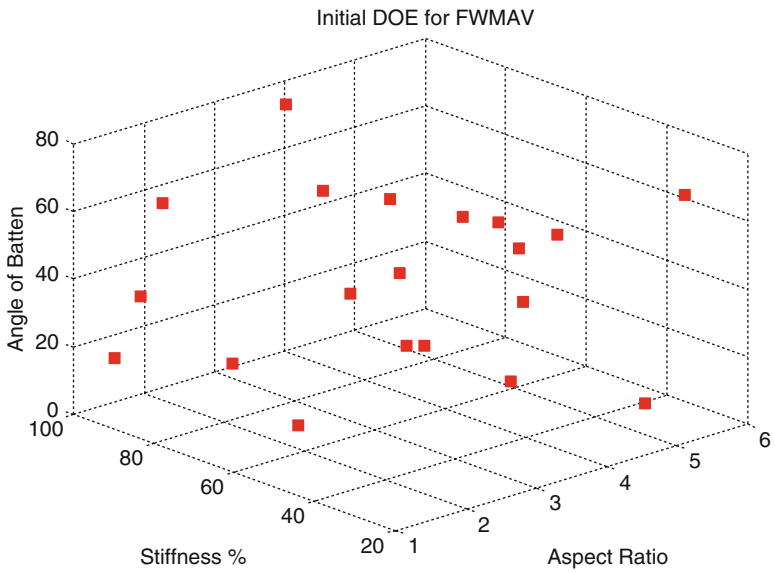

Fig. 1.9 Three dimensional design space with equally spaced specimens. Variables include aspect ratio, the percentage of the leading edge that the carbon fiber rod extends (commercially available), and the angle of the one batten, measured from the leading edge. For a detailed illustration, refer to Fig. 1.3

Table 1.1 The table below details the three variables that dictate the design of each wing in the single objective, multi-variable optimization

Design space		
Variable	Range	Description
Aspect ratio	[0.55, 6.45]	Contains six options of aspect ratio, rounded to the nearest one
Stiffness percentage	[25, 100]	Percentage of the leading edge that a commercially available carbon fiber rod extends
Angle of batten	[0.55, 80.45]	Angle of the one batten, measured from the leading edge

1.8 Future Work

The optimization process is continuing and will hopefully create new knowledge for the design of wing reinforcement. This study will continue to explore other variables that correlate with thrust production, expanding the optimization space in areas such as larger aspect ratios. Along with that, future advances in the flapping mechanism are planned, hoping to increase the reliability, control, and function of the device. One feature in particular that is of interest is the capability of commanding wing position in the axis perpendicular to the flapping axis which is much in the same capability of natural fliers. In regard to the optimization, the guide algorithm suggests higher thrust production in wings with aspect ratios beyond those chosen for our study, so investigation of that is expected. Ultimately, this study hopes to create wings for usage on flapping micro air vehicles.

References

1. Hu H, Kumar AG, Abate G, Albertani R (2010) An experimental investigation on the aerodynamic performances of flexible membrane wings in flapping flight. Aerosp Sci Technol 14:575–586
2. Ifju P, Schmitz T, Haftka R (2010) Expanding the design space of synthetic flexible flapping wings by advancing fabrication and optimization methodologies. University of Florida, AFOSR/RSA Proposal
3. Wu P (2010) Experimental characterization, design, analysis and optimization of flexible flapping wings for micro air vehicles. Dissertation, University of Florida, Gainesville
4. Nguyen Q, Park H, Goo N, Byun D (2010) Characteristics of a Beetle's free flight and a flapping-wing system that mimics beetle flight. J Bionic Eng 7(1):77–86
5. Rue J, Chang K (2012) Fabrication and analysis of small flapping wings. In: 2012 annual conference on experimental and applied mechanics, Costa Mesa
6. McMaster-Carr (2012) More about plastics [Online]. Available http://www.mcmaster.com/#8574kac/=lnff8t. Accessed 26 Feb 2013
7. Honeywell International Inc (2010) CAPRAN 1200 Matte [Online]. Available http://www51.honeywell.com/sm/capran/common/documents/PP_Capran_1200_matte_Specification_sheet.pdf. Accessed 26 Feb 2013
8. Bruel & Kjaer (2012) Bruel & Kjaer LDS v201 product data [Online]. Available (by request). Accessed Feb 2013

Chapter 2
Coarse-Resolution Cone-Beam Scanning of Logs Using Eulerian CT Reconstruction. Part I: Discretization and Algorithm

Yuntao An and Gary S. Schajer

Abstract Computed Tomography (CT) is extensively used as a medical diagnostic tool, and increasingly for scientific and industrial research. In the wood industry, there is a growing interest in using the CT technique to assess the quality of logs entering a sawmill. Internal features of interest include knots, heartwood/sapwood boundary, rot and splits. Most commercially available CT scanning systems are modeled on medical designs and provide high spatial and density resolution. However, they are very complex and delicate devices and their cost is correspondingly high. So far, there is no commercially available CT scanner that can meet the extreme scanning speed requirement, moderate affordability and severe working environment in a sawmill. To address these challenges for using CT technology for industrial log scanning, a novel coarse-resolution cone-beam CT scanning system has been developed. To accommodate the modestly accurate log transport systems in sawmills and hence address the substantial associated lateral motions, an Eulerian approach is taken whereby the CT reconstruction is based on the moving log rather than on the fixed space traversed by the log. This paper, the first of a two-part report, describes a novel cone beam scanning concept, geometry-based coarse-resolution log models, customized CT data processing, normalization and efficient cone beam reconstruction algorithms. The second part of this report will describe the construction details and practical performance of a prototype device.

Keywords Log sorting • Log scanning • Cone-beam CT • Coarse-resolution CT • Log feature identification

2.1 Introduction

Wood is a highly variable natural material that requires an individual decision for each wood piece to identify the most advantageous processing method. In this way the most appropriate and highest value products can be produced from the available raw material. At present, log inspection is based on visual observation of surface defects and optical measurement of external features [1]. The logs are then cut according to their observed characteristics. However, many quality-controlling features are not visible on the surface, causing the resulting cutting to be far from optimal. Studies indicate that only half of inspected logs are classified correctly by a human inspector [2]. Consequently, many logs are placed at the wrong breakdown position, dramatically reducing the amount of high-value products obtained [3, 4]. It is estimated that the value of sawn timber could increase by 7–15 % if the internal defects in logs were accurately known [5, 6]. This is a massive value increase and urgently points to the need for an effective log scanning tool.

Computed Tomography (CT) is powerful technique to create 2-dimensional cross-sectional views of an object from multiple 1-dimensional X-ray measurements called "projections". These 2-D views reveal the internal features within the object. Traditionally, CT has mainly been used as a medical diagnostic tool, but now is increasingly applied in industry. There is a growing interest in using the CT technique to assess log quality in sawmills, both on the measurement side [6, 7] and on the data analysis side [8–11]. CT is a powerful tool to identify quality-defining features such as knots, heartwood/sapwood extent, rot and splits, and it provides rich information to guide subsequent manufacturing of high-value products.

CT scanning systems applied to log-scanning applications are modeled on medical designs and have very high spatial and density resolution. Consequently, the equipment is complex, requires high-precision motions of sensors and

Y. An • G.S. Schajer (✉)
Department of Mechanical Engineering, University of British Columbia, Vancouver, BC, Canada
e-mail: schajer@mech.ubc.ca

M. Rossi et al. (eds.), *Residual Stress, Thermomechanics & Infrared Imaging, Hybrid Techniques and Inverse Problems, Volume 8*, Conference Proceedings of the Society for Experimental Mechanics Series, DOI 10.1007/978-3-319-00876-9_2,

specimen, and is very costly. In addition, the associated CT reconstruction is very computationally intensive. It requires massive data collection, processing and data analysis to identify features of interest within the CT images. These requirements do not fit well within a sawmill environment where the needs are for straightforward operation, tolerance of inaccurate motions, and moderate affordability. The logs must be scanned, analyzed and have sawing decisions made in real-time, often just 5–10 s per log. To address the challenges in applying CT technology to log scanning, a novel coarse-resolution cone-beam CT system has been designed and prototyped here. The proposed system uses straightforward and modest cost equipment, and uses advance ("a-priori") knowledge of the specific geometry of saw logs to reduce dramatically the quantity and quality of data required, the required precision of the relative motion of the X-ray sensors and measured logs, and the scale of the CT image reconstruction computation. To accommodate the relative motion challenge, an Eulerian approach is taken whereby the CT reconstruction is based on the moving log rather than on the fixed space traversed by it. This paper is the first of a two-part series. It introduces the proposed cone-beam log scanning concept, the geometric log models, the associated algorithms and computation procedures.

2.2 Conventional CT Versus Cone-Beam Coarse-Resolution CT

Conventional CT scanning functions by making X-ray measurements from multiple directions and mathematically combining them to generate a 3-dimensional model of the scanned object [12]. Figure 2.1a, b respectively show a typical medical-style third generation fan-beam CT scanner and a typical cone-beam CT scanner. For both scanning geometries, the object of the measurement, commonly a patient in a hospital but here a log, stays at the center and an X-ray source and a line or area detector rotates around the outside to gather the multi-directional series of radiographs required for the CT reconstruction. These designs both require that the X-ray source and detector accurately rotate around the measured object so as to maintain accurate spatial registration among the radiographs measured from the various directions. The single-slice CT arrangement using a line-detector shown in Fig. 2.1a has to scan each cross-section individually and thus operates relatively slowly. It also uses only a small area-fraction of the emitted X-rays, and so forces the use of a much higher X-ray flux than required solely for the detectors. Use of an area detector such as in Fig. 2.1b with a cone-beam X-ray source allows a large volume of an object to be measured simultaneously while gaining data from a much greater fraction of the available X-rays. However, such systems are complex both in construction and in mathematical processing of the X-ray measurement. In addition, commercial cone-beam detectors rarely are larger than 12″ (30 cm) across [12], and thus are not sufficient in size for saw-log scanning. The low end of the range for saw-logs is 10–18″ (25–45 cm), so allowing for the cone angle and some free space at the edges, a minimum detector size of 24″ (60 cm) across is required.

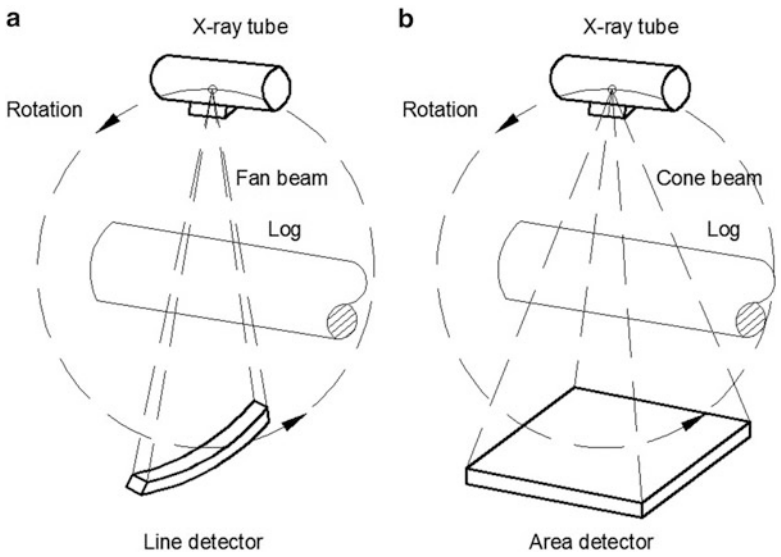

Fig. 2.1 CT scanning geometry: (**a**) third generation single-slice CT, (**b**) cone-beam CT

2.3 Cone-Beam Log Scanning Concept

Log CT scanning can be a much more tolerant process than medical CT scanning. Logs are inanimate, so they can be moved and maneuvered conveniently. The features of interest (knots, heartwood/sapwood boundary, rot and holes) are fairly large, mostly in the centimeter range, so that they can be identified using measurements with relatively coarse spatial resolution. Very significantly, logs have specific geometry, which is known in advance ("a-priori"). If used effectively, knowledge of that geometry can greatly simplify and stabilize the CT reconstruction. In addition, the circular symmetry of logs allows easy compensations for lateral rigid-body motions of the logs as they pass through the scanner. This is a very important feature because the handling of the rough logs in sawmills cannot be done with the high precision that is required when doing conventional medical style CT scanning. The practical saw-log CT scanning system described here incorporates these features.

Figure 2.2 shows a schematic of the proposed log CT scanner. The scanner uses a cone-beam collimated X-ray source, a lab-made large area X-ray detector and a log transport and rotation mechanism. The log to be inspected is rotated within the cone-shape illumination space between the X-ray source and detector. During log rotation, X-ray images are taken at a series of incremental angles, from which the log cross-sections within the illumination cone are reconstructed. The arrangement in Fig. 2.2 has two key features: the log rotation mechanism and the large area detector. The log rotation mechanism allows the use of a stationary source and detector, which avoids the difficulty of generating high speed, complex and meticulously controlled rotation of X-ray source and detector needed in medical style equipment. This greatly simplifies the required scanner hardware and makes the design much more practical and robust. The large-area detector dramatically increases the scanned volume, and so makes possible the reconstruction of many slices simultaneously, thereby enabling a much higher scanning speed. Mechanical details of the proposed log CT scanner hardware design and construction will be described in Part II of this paper.

2.4 Geometry-Based Log Models

The a-priori information provided by knowledge of the specific geometry of logs allows substantial computation economy through the use of geometry-based CT models. For most medical and industrial CT scanners, the typical CT geometry is the square-grid pattern shown in Fig. 2.3d, which divides each cross-section into fine-meshed squares. The material density at each square, called a "voxel", is determined ("reconstructed") from the X-ray measurements. This generalized geometry is chosen because it accommodates internal structures of any geometry and maximizes the resolution to identify fine features of interest.

In contrast, log scanning doesn't require very high spatial and density resolution. In particular, logs have specific geometrical shapes: in areas away from knots, they are generally circular with axi-symmetric cross-sectional features and,

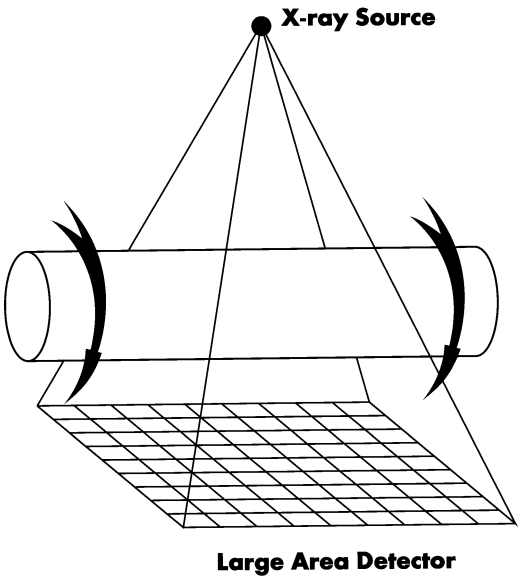

Fig. 2.2 Proposed cone-beam log CT scanning

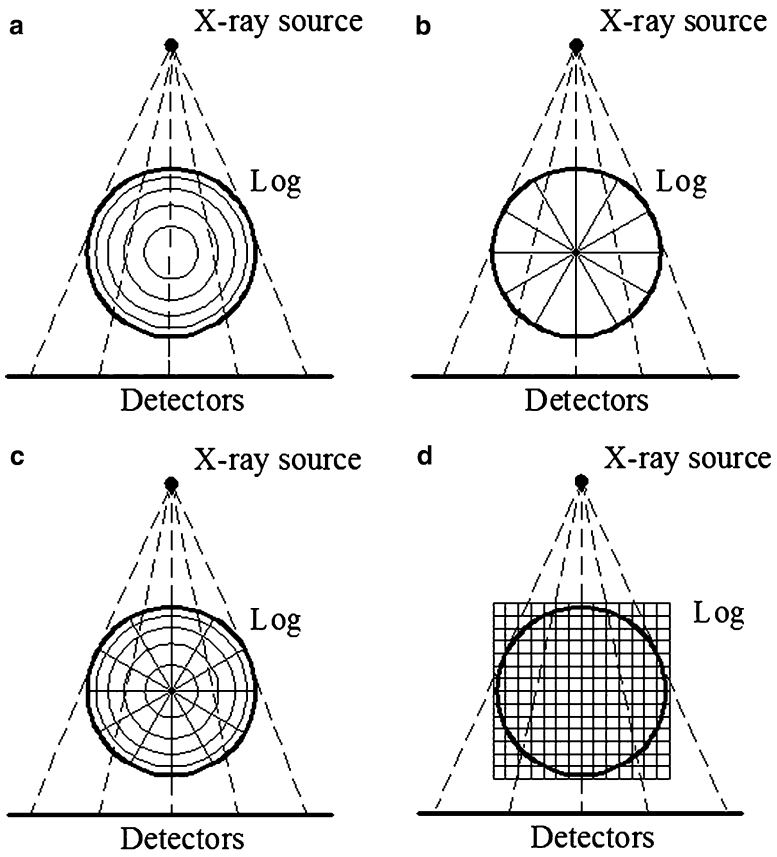

Fig. 2.3 Log geometric CT models: (**a**) annular model, (**b**) sector model, (**c**) combined model, (**d**) conventional model

where present, the knots start from the center and grow approximately in a sector shape through the perimeter. This a-priori information makes possible the use of much simpler feature-specific log cross-section models instead of the commonly used fine-meshed square pattern. Three coarse-resolution, geometry-based CT log models are proposed here. These three geometric models target different internal features. The first model shown in Fig. 2.3a comprises annular regions. This arrangement is suited for the clear wood regions between knots, where heartwood/sapwood, rings and rot tend to be axi-symmetric. The second model shown in Fig. 2.3b comprises sector-shaped regions. This arrangement is suited to the knot regions where the features are sector-shaped. Figure 2.3c shows a combined model, which is suitable when multiple features are present simultaneously. All three log models divide the cross-section into feature-specific regions and tend to guide the resulting cross-sectional reconstructions towards physically realistic solutions. The smaller number of unknown voxels compared with the generic square grid shown in Fig. 2.3d dramatically reduces the quantity of X-ray measurements and the size of the computation.

Two very important features of the geometry-based CT models Fig. 2.3a, b, c are their circular symmetry and their containment of all the voxels within the log boundary. These features enable some pragmatic approximations to be made when processing the measured data to compensate for the lateral rigid-body motions that occur when rough saw-logs are moved within sawmills. This compensation is done by reversing the conventional arrangement where the voxels in Fig. 2.3d are fixed in space and the specimen moves within that space. This arrangement requires very accurate motion of the scanner and specimen. In contrast, the voxels in Fig. 2.3a, b, c are fixed to the log. In the subsequent discussions, it will be shown how this arrangement substantially compensates for lateral rigid-body motions and log non-circularity.

2.5 General CT Computation Description

In each proposed CT model, X-rays fan out from the source, pass through the log and reach the large-area detector. The part of the log within a given X-ray path attenuates the radiation according to the line integral of the density along that path [8]. The relationship between X-ray attenuation and log densities can be expressed using Beer's Law as Eq. 2.1, where I is the

attenuated X-ray intensity, I_0 is the unattenuated intensity, $\rho(x)$ is the log density along the path length at position x, and β is the basis weight coefficient [13, 14].

$$\frac{I}{I_0} = \exp\left(-\int \frac{\rho(x)dx}{\beta}\right) \tag{2.1}$$

Equation 2.1 can be linearized by taking logarithms on both sides:

$$\int \rho(x)dx = -\beta \ln\left(\frac{I}{I_0}\right) \tag{2.2}$$

where the left side of Eq. 2.2 represents the line integral of the material density along the X-ray path. This quantity corresponds to the local basis weight (= density per unit area). After discretization, Eq. 2.2 can be written for the given ray as:

$$\sum g_j \rho_j = d_j \tag{2.3}$$

where g_j is a set of discrete lengths corresponding to material densities ρ_j within a sequence of voxels along the overall ray path. The quantity d_j is the basis weight observed for the given ray according to the measured X-ray attenuation. For the combination of all the rays within the X-ray cone, Eq. 2.3 can be generalized as:

$$\sum G_{ij} \rho_j = d_j \tag{2.4}$$

where G_{ij} is a matrix whose entries represent the path length within ray "*i*" as it passes through voxel "*j*". This equation can be expressed in vector–matrix format as:

$$[G]\{\rho\} = \{d\} \tag{2.5}$$

where brackets and braces respectively indicate matrix and vector quantities.

2.6 Basis Weight Data Alignment

The cone-beam reconstruction in Eq. 2.5 requires the assembly of data vector {d} from the measured basis weight data. If done with some care, this assembly can mostly eliminate the effects of any lateral rigid-body motions of the log within the X-ray beam. Such motions are very damaging in conventional CT scanning and require very accurate control of the scanner or specimen motion. The use of the geometrical CT models in Fig. 2.3a, b, c allow the effects of lateral rigid-body motions to be accommodated mathematically by adjusting the arrangement of the data vector {d}. The following paragraphs describe the proposed procedure.

2.6.1 Cylindrical Adjustment

For ease of manufacture, the large-area detector used here has a flat detection surface. However, mathematically, it would be more convenient instead to use a curved detection surface in the form of a cylinder whose axis passes through the X-ray source parallel to the longitudinal motion of the log. The measurement points ("pixels") on the detection surface would then be equally spaced in an angular sense. This gives the detector panel a circular symmetry to complement the circular symmetry of the log model. The log and the detection cylinder have different centers.

Measurements X_i, which are linearly spaced on a flat panel detector, can be mathematically adjusted so that they appear to be angularly spaced θ_i on an equivalent cylindrical detector. This is a fixed geometrical relationship:

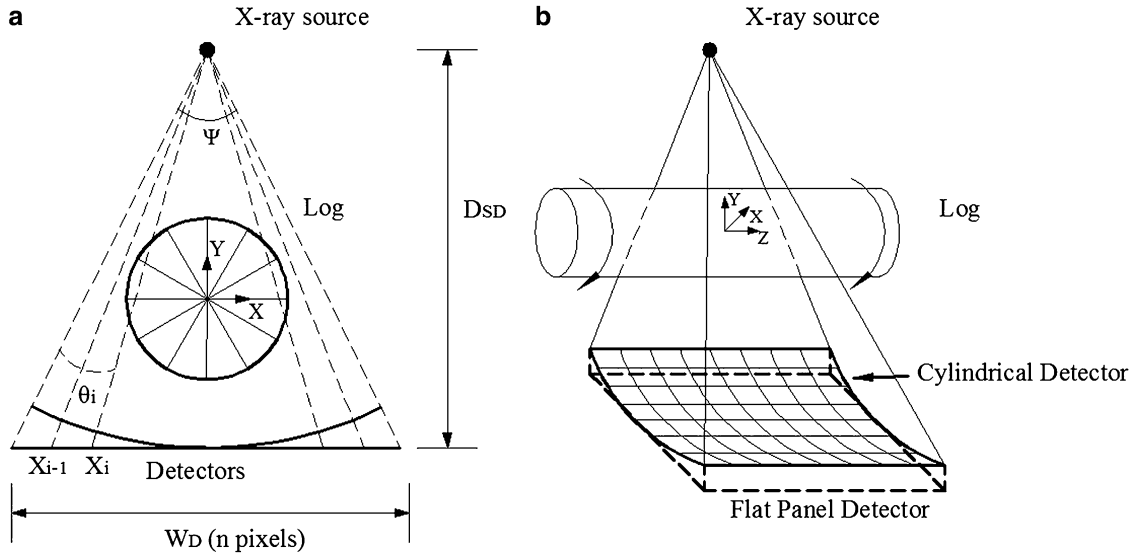

Fig. 2.4 Flat and cylindrical X-ray detectors: (**a**) axial view, (**b**) side view

$$X_i = \frac{D_{SD}\tan\left(\theta_i - \frac{\psi}{2}\right)}{\frac{W_D}{n}} + \frac{n}{2} \tag{2.6}$$

where D_{SD} is the distance between source and detector, W_D is the detector width, n is the number of detectors within the detector width, and ψ is the X-ray cone illumination angle subtended by the detector width. The corresponding basis weight $b_a[i]$ at angular pixel "*i*" is evaluated from the integral of the linear basis weights b(x) bounded by the given angular pixel

$$b_a[i] = \frac{\int_{X_{i-1}}^{X_i} b(x)dx}{X_i - X_{i-1}} \tag{2.7}$$

This arrangement is applied column-by-column to all pixels to create the arrangement shown in Fig. 2.4b.

2.6.2 *Rigid-Body Motion and Log Ellipticity Correction*

The circular symmetry of the cylindrical panel detector shown in Fig. 2.4, together with the log-based CT models in Fig. 2.3, can be exploited to enable corrections of rigid-body motions and non-circular log geometry. For example, consider a small circumferential rigid-body motion of a log relative to the center of the X-ray fan shown in Fig. 2.5a. The effect is to shift the measured radiograph along the arc of the X-ray detector from A-B to A′-B′. The radiograph image seen between A′-B′ is the same as would have been seen between A-B had the rigid-body motion not occurred. Thus, a circumferential rigid-body motion can simply be corrected by shifting the radiograph image between pixels A′-B′ back to the pixels A-B, which for convenience is assumed to be in the center of the cylindrical panel detector.

Similarly, for radial rigid-body motions such as in Fig. 2.5b, the effect of the motion is to expand the radiograph image A-B to A′-B′ (or contract it for an outward radial motion). Thus, a radial rigid-body motion can be corrected by scaling the radiograph image circumferentially between pixels A′-B′ to the pixels A-B, and reciprocally scaling the basis weight data so that the same amount of mass is represented within the resulting scaled radiograph image. This scaling concept can be taken a step further to accommodate logs that are slightly elliptical. The arc length A′-B′ of the radiograph image in Fig. 2.5c caused by a non-constant log diameter can similarly be scaled to fit the arc length A-B. Thus, this shifting and scaling of the radiograph data around the cylindrical measurement surface can substantially eliminate the effects of rigid-body motions

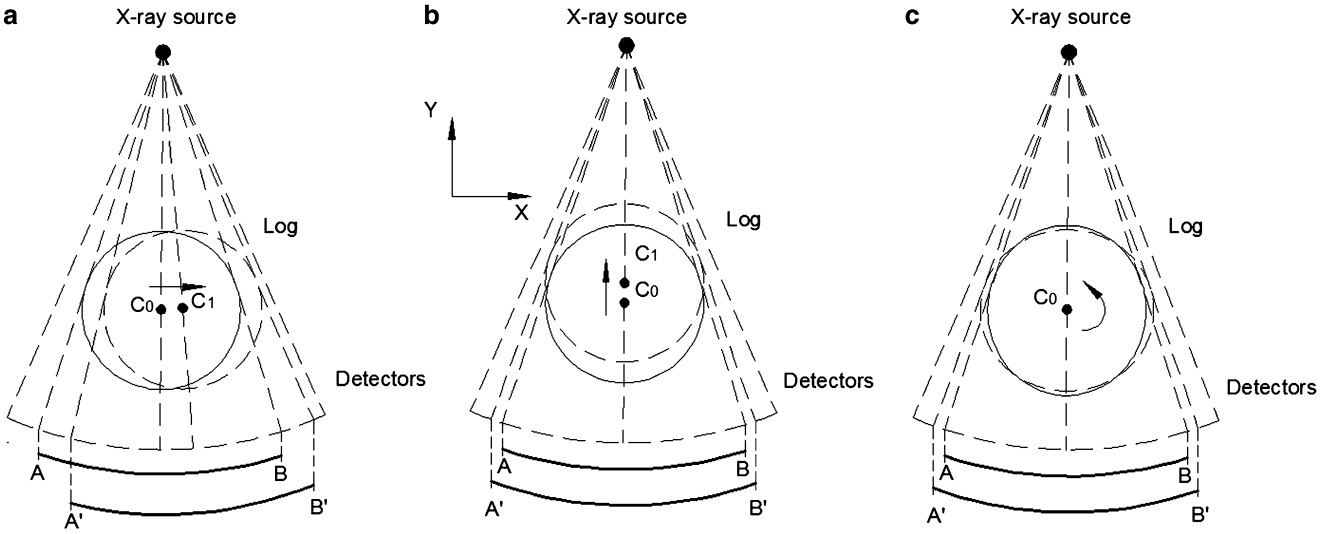

Fig. 2.5 Measurement re-centering and uniform scaling: (**a**) circumferential motion, (**b**) radial motion, (**c**) ellipticity effect

and log non-circularity. The adjustment is not perfect because of small angle changes within the X-ray fan, but for modest rigid-body motions and log diameter variations, the process is quite effective.

2.6.3 Geometry Normalization

The data shifting and scaling shown in Fig. 2.5 opens the opportunity to pursue to concept of arranging Eq. 2.5 in a standardized form, where matrix [G] is the same for all sizes and positions of logs. The idea is to shift the radiograph data so that the log appears as if it were in the center of the field, and to scale the data so that the log appears as if it had a "standard" diameter. The actual diameter of the log ultimately needs to be used to scale the material densities computed for the "standard" log to those of the actual log. Examination of the path lengths shown in Fig. 2.3 shows that the diameter of the log relative to the X-ray source to detector distance does have some influence on relative path lengths, beyond just a simple multiplier based on log diameter. However, for the small ray angles that occur when the X-ray source to detector distance is much greater than the log diameter, this effect is modest.

2.6.4 Log Center and Radius Estimation

The ability to do the rigid-body motion and log ellipticity corrections shown in Fig. 2.5 depends on an ability to identify the log position and diameter within the measured radiograph image. Doing this through image edge detection is unreliable because the image edge information depends on just a small number of local pixels. These may be subject to noise, especially if some local irregularity exists at that point on the log, say due to a branch. A more robust approach is to estimate the log diameter from the entire radiograph image. This can be done by assuming that the log is circular and of uniform density (physically not exactly true, but appears to be good computational approximation). The radiograph profile then has a semi-elliptical shape. Its area is proportional to radius × axial height, while its centroidal height is proportional to axial height only. Dividing the area by the centroidal height gives a remarkably robust estimate of the log radius:

$$r = D_{SL} \sin\left(\frac{16\ d\psi}{3\pi^2}\ \frac{(\sum b)^2}{\sum (b^2)}\right) \tag{2.8}$$

where r is the estimated log radius, D_S is the distance between X-ray source to log center, b are the basis weight data, dψ is the angular spacing between detectors after cylindrical correction, and i is the angular pixel index. The circumferential position of the centroid of the radiograph gives the log center position:

$$c = \frac{\sum ib}{\sum b} \tag{2.9}$$

2.7 Path Length Computation in Cone-Beam CT

Alignment of the data vector {d} provides the right side of Eq. 2.5. The next step towards completing the CT reconstruction is to assemble the path length matrix [G].

2.7.1 Single-Slice Path Length Computation

Figure 2.6 illustrates the single-slice path length computation for the three geometry-based CT models in Fig. 2.3. The sequence of annulus radii in Fig. 2.6a, c is in equal increments of the square root of radius. In this way, the areas of the annuli are equal, thereby approximately equalizing the subsequent computational accuracy of the material densities within the annuli. The matrix [G] in Eq. 2.5 has elements G_{ij}, which represent the path length of ray *i* as it passes through voxel *j*. Matrix [G] is sparse, with much fewer than half of the elements having non-zero values. The path lengths within the voxels for the annular and sector models in Fig. 2.6a, b can be computed geometrically. The path lengths in the combined model Fig. 2.7c can be computed by evaluating the path lengths using the sector model in Fig. 2.6b with an "log radius" equal to each of the annulus radii in Fig. 2.6c. The path lengths in Fig. 2.6c are equal to the difference of the path lengths of the inner and outer radius sector model path lengths corresponding to each annulus.

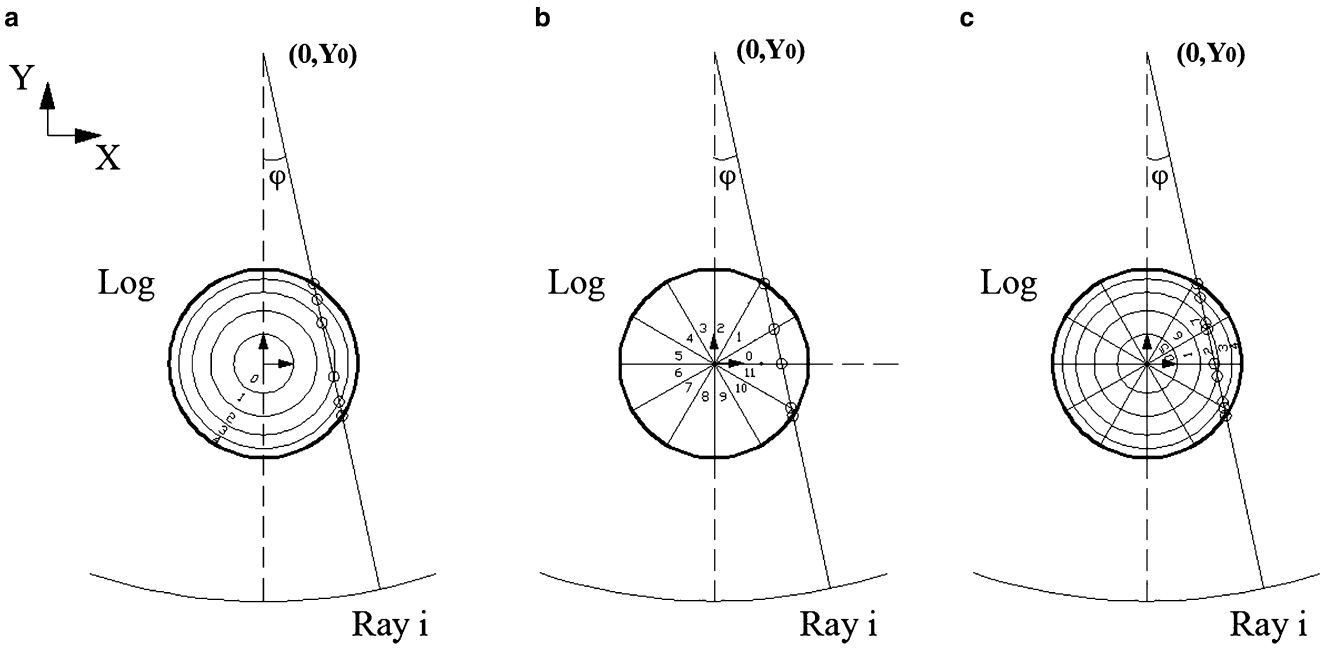

Fig. 2.6 Voxel X-ray path computation: (**a**) annular model (**b**) sector model (**c**) combined model

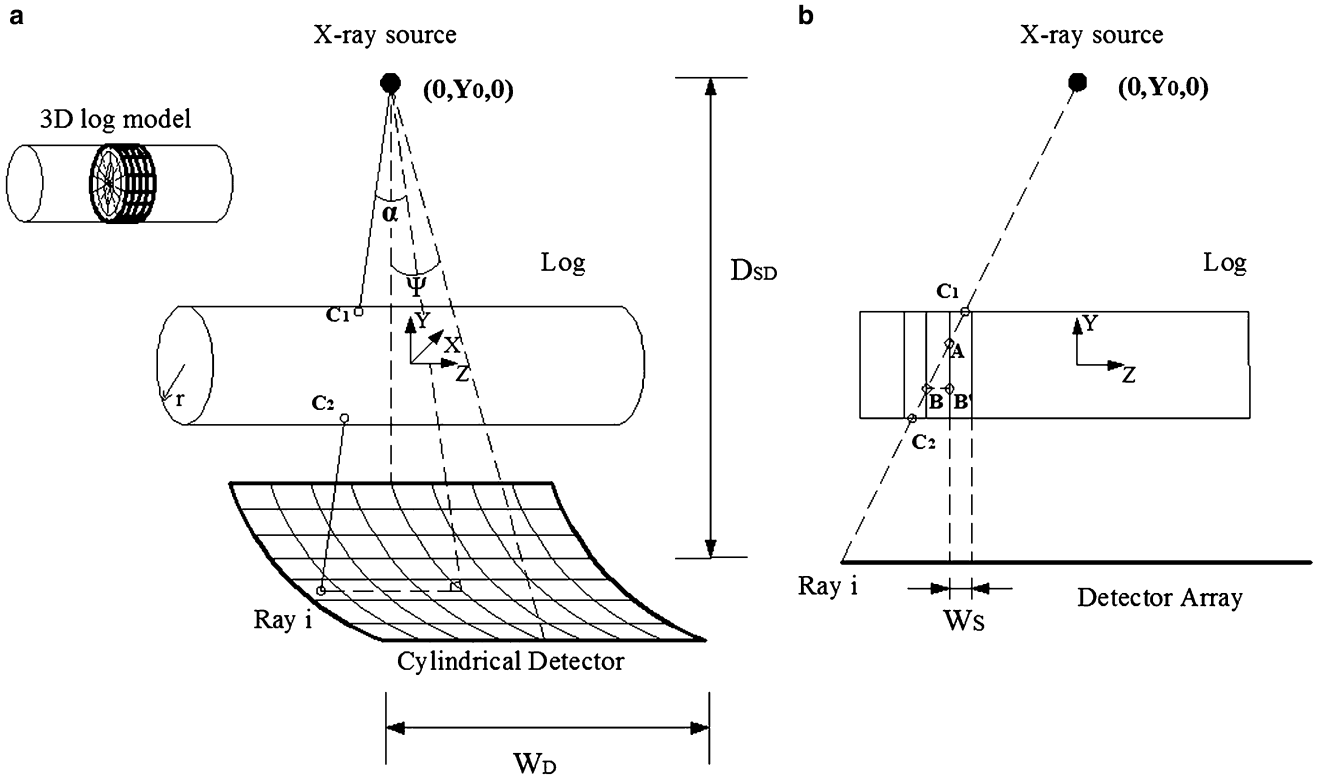

Fig. 2.7 X-ray paths through the log specimen: (**a**) perspective view, (**b**) side view

2.7.2 Multiple-Slice Path Length Computation

The geometry shown in Fig. 2.6 is appropriate for CT measurements within single cross-sectional slices. This single-slice approach is used where X-ray measurements are made use line detectors such as in Fig. 2.1a, and is quite common in medical applications. Here, to make fuller use of the X-ray data, the cone-beam arrangement shown in Fig. 2.1b is used. This arrangement creates no conceptual change to the measurement, and the CT reconstruction Eq. 2.5 still applies. However, the path length matrix becomes considerably larger and more computationally intensive to evaluate.

Figure 2.7 illustrates the geometry of the cone-beam scanning configuration. This cone-beam arrangement is very challenging compared with the single-slice arrangement in Fig. 2.6 because the paths of the inclined rays in Fig. 2.7b pass through multiple adjacent slices. This circumstance couples the calculations between adjacent slices so that they no longer can be reconstructed separately; the voxel densities in all slices must be computed simultaneously. This feature greatly multiplies the size of the matrix Eq. 2.5, but fortunately, with the coarse-resolution models used here, the resulting size is still tractable. The resulting path length matrix is very sparse, and if care is taken to accommodate this feature, significant computational economy can be achieved.

Path length computation for cone-beam model in Fig. 2.7 follows the same concept as the computation for the combined model in Fig. 2.6c. First, the inclination of each ray on the cylindrical detector surface is determined geometrically. Then, the radii at which the ray passes through each slice are determined. The path lengths for combined models of the type in Fig. 2.6 are computed, with the path lengths within each slice evaluated by subtraction of the path lengths in adjacent slices.

Computation of the path length matrix [G] is a computationally intensive process, taking some minutes to complete. However, the process is much simplified by the data alignment process described above because the aligned data are placed symmetrically within the scanner geometry, so only one quarter of the path lengths need be computed, and the others assigned by reflections across the two symmetry axes. In addition, for a practical scanner arrangement where the cone-beam angles are small, the data normalization previously described to form a "standard" log geometry means that the path length matrix need be computed only once, stored, and recalled for use with all subsequent logs. Thus, the computation time of matrix [G] is not an issue for real-time use.

2.8 Density Inverse Computation

The path length computations and X-ray data normalization described above provide [G] and {d} in Eq. 2.5 for a single X-ray measurement, a "projection". In general, [G] is not square. For a single projection using the single slice arrangement in Fig. 2.6, the number of rows equals the number of pixel measurements within the cylindrical detector, and the number of columns equals the number of voxels within the geometrical model used. For multiple projections, the number of rows is correspondingly multiplied, but the number of columns remains the same. Substantial computational economy can be achieved by arranging the number of projections to correspond to the number of sectors used in Fig. 2.6b, c. That way the path alignments relative to the sector pattern are the same for each projection, just rotated by an integer number of sectors. Thus, the new rows required for the path length matrix [G] can be simply added by rotating the columns from the path lengths computed for the first projection.

For the multiple-slice arrangement shown in Fig. 2.7, path length matrix [G] expands greatly to have a number of columns equal to the total number of voxels in all slices within the log. The number of rows is much larger, equalling the number of pixels within each panel detector image times the number of images used for the measurement. In conventional CT practice, the resulting massive size of [G] requires the use of inverse solution methods such as filtered back-projection. Here, the number of voxels is much smaller because of their feature-specific shapes, and so a direct solution of Eq. 2.5 is feasible. The resulting highly over-determined Eq. 2.5 can be solved in a least-squares sense as:

$$[G]^T[G]\{\rho\} = [G]^T\{d\} \tag{2.10}$$

where matrix $[G]^T[G]$ is square with row/column size equal to the number of voxels, which is a moderate size number compared with the number of pixels used in all the projections. If care is taken with the sequence of doing the operations $[G]^T[G]$, it is possible to form the result without explicitly storing the very large matrix [G]. Actually, it is necessary only to store the part of the matrix for a single projection and then to rotate the columns as required to correspond to the alignment of the subsequent projections. Matrix $[G]^T[G]$ is symmetric positive-definite and can be solved efficiently using a Cholesky solver [15].

2.9 Discussion

The use of the feature-specific geometrical models in Fig. 2.3 for CT reconstructions substantially and fundamentally influences the associated CT inversion. On one level, the geometric resemblance of the models to the physical features of the logs being scanned has the effect of guiding the inversion towards physically realistic results. This important feature will be seen in the experimental results shown in Part II of this paper. On a further and deeper level, the proposed approach is very unusual in that the CT inversion is referenced to the log and not to a fixed volume in space, as is done in conventional practice. By analogy to finite element modeling, the proposed approach may be described as "Eulerian", while the conventional practice is "Lagrangian". One consequence is that the thrust of the CT calculation is focused entirely on the volume of the scanned log; the three feature-specific models in Fig. 3a, b, c do not contain any of the external voxels seen in Fig. 2.3d. A further consequence is that the CT inversion becomes fairly tolerant to small rigid-body motions of the log relative to the X-ray source and detector. The measured data from the X-ray detector can be shifted and scaled to transform the data to a "standardized" configuration, for which the path length matrix [G] is predetermined. This scaling is not perfect because change in log diameter changes the angles within the scanned volume in a slightly non-linear way. However, for the small angles used here (16° X-ray cone angle), the non-linearities are modest. This feature will have to be tested in practice. At worst, predetermined path length matrices [G] will be needed for a compact sequence of different log diameters to accommodate large changes in log size.

The shifting and scaling of the X-ray data to a standardized format enable the CT inversion to be done in a normalized form. This is a great mathematical convenience. However, the results ultimately need to be referenced to the actual log diameter to identify true physical dimensions. The X-ray measurements do provide an indication of the physical dimensions, but the presence of radial rigid-body motions within a cone-beam geometry change the size of the scanned log image and therefore impedes precise identification of dimensions. Multiple X-ray systems from different angles could be used to resolve the ambiguity, but this would be a rather complex and expensive solution. A more practical approach is to use an added optical scanner to identify log size and position. Such optical scanners are widely used in the wood industry and are rugged and relatively inexpensive. Ultimately, the tolerance of small rigid-body motions is significant because it greatly

simplifies the required mechanical arrangement for the needed X-ray scanner. In conventional CT practice, the measured object stays stationary while the X-ray scanner system rotates around it. For medical applications, this approach is essential because the objective of the measurement is a human patient, which cannot be conveniently rotated! But even in non-medical applications, the same approach is used because the X-ray system can be rotated with much higher precision than then measured object. This is certainly the case with logs in a sawmill. The logs are large and rough and cannot be moved with great precision. The tolerance of rigid-body motions by the proposed CT arrangement makes acceptable the imprecision of the log motions available in a sawmill and very greatly reduces the complexity, fragility and cost of the required X-ray scanner.

2.10 Conclusion

This paper, the first of a two-part series, introduces the novel cone-beam log scanning concept, the coarse-resolution, geometry-based log models, the associated algorithms and computation procedures. This proposed Eulerian approach has several advantages over conventional medical style CT scanning:

1. It reduces scanner mechanical complexity by using a stationary X-ray source and detector while rotating the measured object.
2. It uses feature-specific voxel geometries to guide and stabilize the CT reconstruction.
3. It is tolerant of rigid-body-motions and log ellipticity.
4. It reduces the number of features that need to be determined, thus reducing the scale of computation and effort for data processing.
5. It used all data available within the X-ray cone beam, thus increasing the data content and stability of the CT inversion.

The practical demonstration of proposed log CT system will be introduced as the second part of this serial paper.

Acknowledgments The authors gratefully thank the Natural Science and Engineering Research Council of Canada (NSERC) for their financial support of this project through the ForValueNet network, the Centre for Hip Health and Mobility, Vancouver General Hospital, for use of facilities, and the Institute for Computing, Information and Cognitive Systems (ICICS).

References

1. Oja J, Grundberg S, Fredriksson J, Berg P (2004) Automatic grading of sawlogs: a comparison between X-ray scanning optical three-dimensional scanning and combinations of both methods. Scand J Forest Res 19:89–95
2. Pietkäininen M (1996) Detection of knots in logs using X-ray imaging. Dissertation, Technical Research Centre of Finland, Espoo, VTT Publications 266
3. Usenius A (2003). Optimization of sawing operation based on internal characterization of the logs. In: Proceedings ScanTech 2003, Wood Machining Institute, Seattle, pp 11–18
4. Rinnhofer A, Petutschnig A, Andreu JP (2003) Internal log scanning for optimizing breakdown. Comput Electron Agric 41:7–21
5. Chiorescu S, Grönlund A (2000) Validation of a CT-based simulator against a sawmill yield. Forest Prod J 50:69–76
6. Oja J, Wallbacks L, Grundberg S, Hagerdal E, Grönlund A (2003) Automatic grading of Scots pine (*Pinus sylvestris* L.) sawlogs using an industrial X-ray log scanner. Comput Electron Agric 41:63–75
7. Seger MM, Danielson PE (2003) Scanning of logs with linear cone-beam tomography. Comput Electron Agric 41:45–62
8. Lindgren LO (1991) Medical CAT-scanning X-ray absorption coefficients, CT-number and their relation to wood density. Wood Sci Technol 25:341–349
9. Som S, Wells P, Davis J (1992) Automated feature extraction of wood from tomographic images. In: Proceeding of international conference on automation, robotics and computer vision, Singapore, 15–18 Sept 1992, pp CV-14.4.1–CV-14.4.5
10. Krahenbuhl A, Kerautret B, Longuetaud F (2011) Knots detection in X-ray CT images of wood. Scand J Forest Res 12:80–90
11. Longuetaud F, Mothe F, Kerautret B (2012) Automatic knots detection and measurements from X-ray CT images of wood: a review and validation of an improved algorithm on softwood samples. Comput Electron Agric 85:77–89
12. Wang G, Yu H (2008) An outlook on X-ray CT research and development. Med Phys 35(3):1051–1064
13. Kak AC, Slaney M (1987) Principles of computerized tomography. IEEE Press, New York
14. ASTM (1993) Standard guide for computed tomography (CT) imaging. American Society for Testing and Materials, West Conshohocken. ASTM Standard E-1441-11, 33pp
15. Galassi M et al (2009) GNU scientific library reference manual, 3rd edn. http://www.gnu.org/software/gsl/. Accessed 25 June 2011

Chapter 3
Coarse-Resolution Cone-Beam Scanning of Logs Using Eulerian CT Reconstruction. Part II: Hardware Design and Demonstration

Yuntao An and Gary S. Schajer

Abstract Computed Tomography (CT) provides an attractive opportunity in the wood industry for quality assessment of logs entering a sawmill to enable the material to be appropriately processed into maximum value products. A CT scanner suitable for this task must be simple and economical, considerably more so than the complex and costly scanners typically used for medical applications. Part I of this paper presented the design concept and the theory of operation of a specially designed coarse-resolution cone-beam CT scanner. This second part focuses on the CT system hardware design, construction and performance. Key components are a large-format custom-designed X-ray detector panel, a log spiral-motion mechanism and a real-time data acquisition system. These are described in detail. The coarse-resolution reconstruction results for an example log using feature-specific models and algorithms introduced in Part I of this paper are demonstrated and they compare well with CT reconstructions for same log using the same measurement with conventional filter back projection algorithm. The good comparison gives confidence in the usefulness and applicability of the proposed CT scanner design for industrial use in sawmills for log quality assessment.

Keywords Log CT scanner • Large area X-ray detector • Cone-beam CT • Coarse-resolution CT • Log feature identification

3.1 Introduction

Wood is a natural material and has highly variable structure. To process it efficiently in sawmills, it is essential to be able to identify internal features such as knots, heartwood/sapwood boundary, rot and holes, so that appropriate cutting decisions can be made. The highest value products can then be made from the given raw material. Some interesting log scanning systems have appeared on the market, among which are some that use X-ray imaging by one or more line detectors viewing the log from various angles [1, 2]. X-ray images only provide 2-D information, so the features in the third direction are not well identified [3]. Although using multiple X-ray sources and detectors at different angles allows better perception of internal features, this approach greatly increases the scanner system cost. In addition, the limited number of measurements provides only limited capacity to identify log internal features. Several researchers have indicated that successful application of CT log scanning in sawmill can greatly improve productivity and profit [4, 5]. However directly applying existing CT technology to saw-log scanning is not an easy task to accomplish [6].

Commercial CT systems modeled on medical designs and don't fit well with sawmill operation environment. They are very expensive, beyond the budget of most sawmills. They are also mechanically complex and delicate, require high-precision motions of sensors and specimen and thus won't tolerate the severe working environment in a sawmill. They also require massive data collection, processing and intensive CT reconstruction computations, thus are challenged by the extreme scanning speed required for real-time operation.

In Part I of this paper [7], the use of X-ray CT scanning is explored and the particular challenges of using this technique in sawmills are identified. These challenges include the need of the CT system to be mechanically robust and straightforward, to be tolerant of material handling inaccuracies, and to be of modest cost. All these needs do not align well with the characteristics of conventional CT scanners designed for medical use, which tend to be complex, highly precise and very costly devices.

Y. An • G.S. Schajer (✉)
Department of Mechanical Engineering, University of British Columbia, Vancouver, BC, Canada
e-mail: schajer@mech.ubc.ca

M. Rossi et al. (eds.), *Residual Stress, Thermomechanics & Infrared Imaging, Hybrid Techniques and Inverse Problems, Volume 8*, Conference Proceedings of the Society for Experimental Mechanics Series, DOI 10.1007/978-3-319-00876-9_3,

To address these challenges, a novel cone-beam CT scanning concept involving geometry-based coarse-resolution log models is introduced, together with associated reconstruction algorithms. An Eulerian approach is taken to allow effective CT reconstructions to be carried out even in the presence of significant lateral motions of the measured log during the scanning process. In this paper, the hardware design of a prototype CT log scanner is described, example measurements are illustrated, and CT inversion results are presented and assessed.

3.2 Cone-Beam CT Log Scanner

Figure 3.1 illustrates the major components of the prototype log scanner that was built. An industrial cone-beam X-ray source (Comet MXR 160 kVp, 10 mA) illuminates an example log (amabilis fir, typically 40 cm diameter) secured within a mechanical transport mechanism. The X-rays go on to be detected by a large-area X-ray detector, with the setup surrounded by lead-lined X-ray shielding panels for personnel radiation safety [8]. Behind the shielding panels, not visible in the photo, are supporting control and data acquisition electronics, and a CT inversion computer system. Except for the X-ray source, all items were lab-built to meet the overall measurement needs, and were assembled at the Centre for Hip Health and Mobility (CHHM) at the Vancouver General Hospital (VGH).

3.2.1 Large Area X-ray Detector

Medical X-ray detectors are designed to fit a human scale, so they tend to be too small for measuring saw-logs. The low end of the diameter range for saw-logs is 25–45 cm, so allowing for the enlargement caused by the cone shape of the X-ray illumination and adding some free space at the edges, a minimum detector size needed is 60 cm across. Commercial area-type detectors are very costly and rarely larger than 30 cm across [9], so they are not appropriate for saw-log scanning. Some researchers have proposed using many line detectors placed together to form an area detector for log scanning [10], but this approach gives quite sparse data in the longitudinal direction.

Figure 3.2 illustrates the X-ray measurement system used here. It consists of a large-area (60 × 60 cm) X-ray scintillator screen (Gd_2O_2S, Kyokko DRZ) [11], a reflection mirror and an EMCCD camera (Andor iXon 897). The scintillator absorbs the X-rays that passed through the log and proportionally converts them into visible light. The mirror reflects the light and allows placement of the camera outside the primary X-ray radiation path. The EMCCD (Electron Multiplying Charge Coupled Device) camera detects the low-level light from the scintillator and forms a 2-D measurement set. The EMCCD camera works like a conventional CCD camera but with internal features that allow it to provide detection of extremely low light levels [12]. Pixel binning further increases effective light sensitivity and enables image processing at high frame rates. The detector system design in Fig. 3.2 was chosen because it provides 2-D data and can be conveniently scaled up as needed for sawmill use.

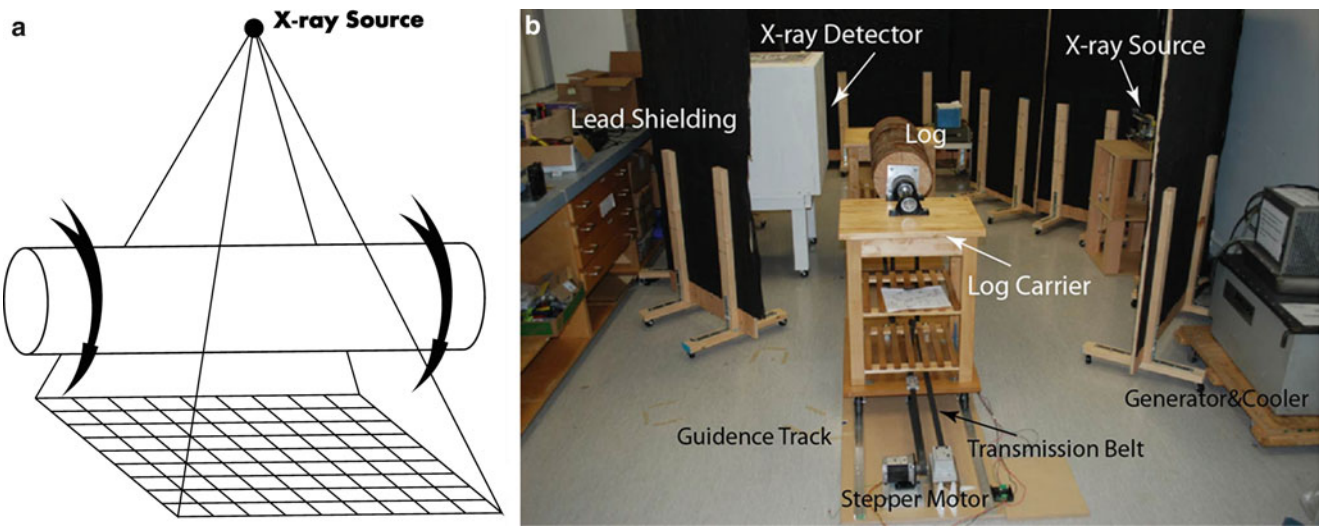

Fig. 3.1 CT log scanner: (**a**) schematic design, (**b**) prototype assembly

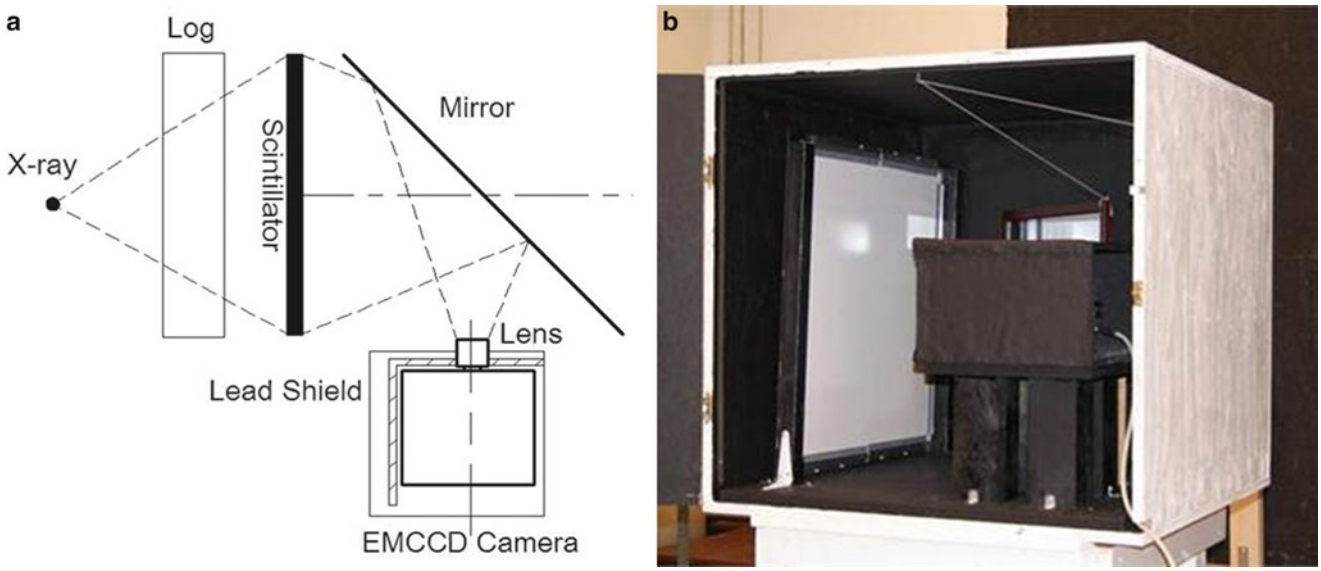

Fig. 3.2 Scintillator-EMCCD X-ray detector: (**a**) schematic design, (**b**) detector assembly

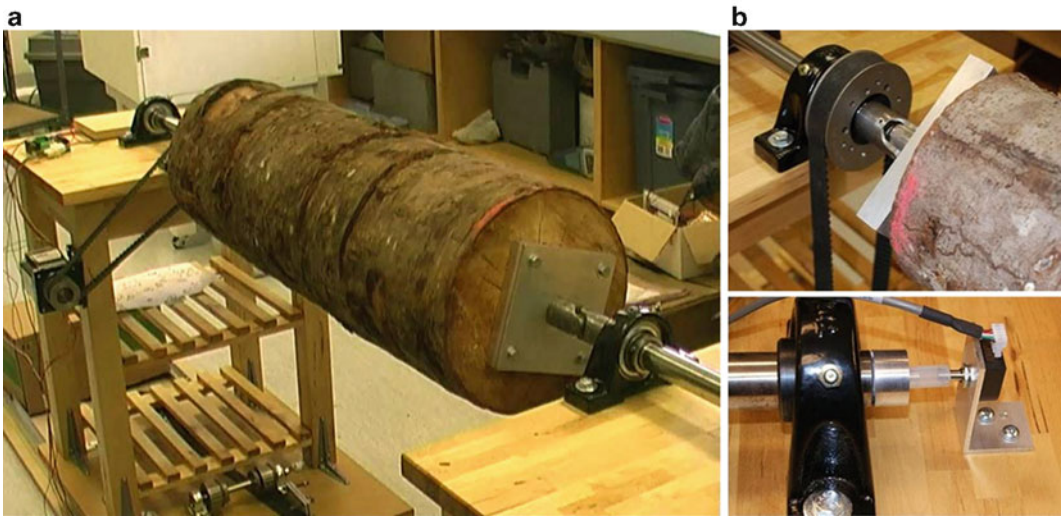

Fig. 3.3 Log rotation carrier: (**a**) overall view, (**b**) shaft encoder

3.2.2 Log Carrier System and Scanner Control

Figure 3.3 shows the log rotation mechanism used here. The log sample is mounted using end plates on the rotation shaft of the log carrier. (This is not a practical design in a sawmill, but is expedient in a compact lab). A stepper motor-pulley-belt assembly (PowerPac 1.8° NEMA 34) drives the log rotation, with an incremental speed-control scheme providing controlled rotation speed with appropriate accelerations and decelerations [13].

Figure 3.3b shows the shaft encoder (US Digital S1) used to monitor the log rotation. This log rotation monitoring is key feature of the CT reconstruction scheme proposed in Part I of this paper. The objective is to make X-ray measurements at angular intervals equal to the number of sectors in the chosen geometrical CT reconstruction model (see Fig. 3.3 of Part I [7]). In this way, the scanning geometry at each measurement is the same relative to the CT reconstruction model, except for an

integer rotation of the sectors. The path lengths of the X-rays are then the same within the CT reconstruction model, apart from a rotation of the sector numbering. This measurement procedure supports the Eulerian approach chosen for the CT reconstruction of the log structure [7]. The shaft encoder is used to trigger frame acquisition from the EMCCD camera at the angular intervals chosen for the sector CT model. This angle-based procedure has the further advantage of rendering the data acquisition insensitive to log rotation speed so that accurately placed data can be acquired even during the acceleration/deceleration phases of the log motion.

3.3 Sample Log Scanning Results

Log scanning tests were conducted to demonstrate the proposed cone-beam coarse-resolution CT scanning approach. The example log is of amabilis fir, approximately 40 cm in diameter and 90 cm in length. Thirty-six X-ray images were taken at 10° rotational intervals of the log using the EMCCD camera, each with 1 s exposure time. CT reconstructions were then done using the voxel models corresponding to Fig. 3.3 in Part I [7] with (a) 16 annuli, (b) 36 sectors, and (c) 36 sectors with 18 annuli. The same set of X-ray images was used for each of the CT reconstruction choices.

3.3.1 Cone-Beam X-ray Images

Figure 3.4 a shows a raw X-ray image, presented in the format of a photographic negative. In this image, the bright areas indicate high material density (high X-ray absorption) and the dark areas indicate low material density (low X-ray absorption). The vertical bright regions near the center indicate some knots within the log cross-section and the horizontal dark streak shows a large radial crack. The curved outer boundaries of Fig. 3.4a show that the image is contains barrel distortion from the wide-angle lens used to view the X-ray scintillator. A spline function based interpolation method [14] is used to correct this distortion to produce the rectilinear image in Fig. 3.4b. This image is further adjusted to make the flat panel detector appear as having a cylindrical surface and the image to have a normalized vertical size.

Figure 3.5 shows a series of normalized X-ray measurements at rotation positions of 60°, 120°, 180°. The vertical bright areas in the center correspond to the high density of a cluster of four approximately equally spaced knots. Smaller nearby knots appear as smaller light areas on each side. The horizontal dark line in Fig. 3.5a corresponds to a deep radial crack (the log had substantially dried in the lab environment). View (a) is taken looking directly into the crack, so the crack appears very prominently, while views (b) and (c) are oblique views and therefore do not clearly show the crack.

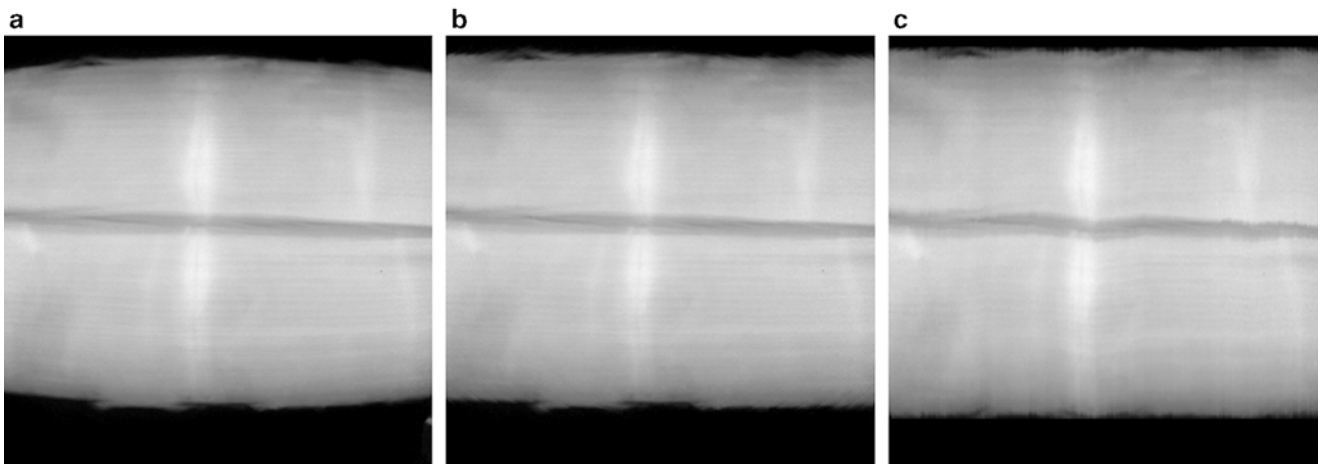

Fig. 3.4 Log X-ray images: (**a**) raw image, (**b**) barrel distortion correction, (**c**) cylindrical adjustment and geometry normalization

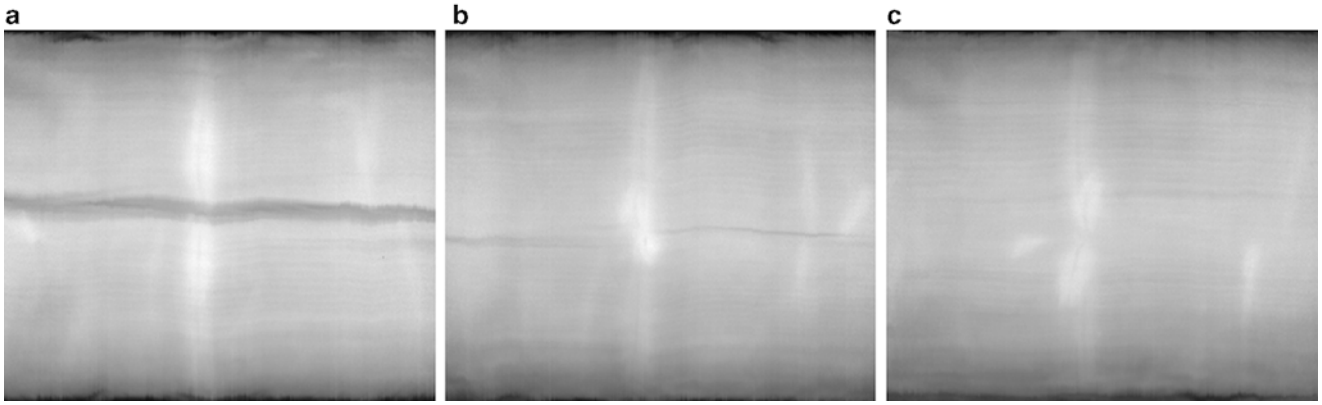

Fig. 3.5 Imaging log rotation: (**a**) 60° position, (**b**) 120° position, (**c**) 180° position

3.3.2 Single-Slice Reconstruction

A single-slice inversion study was done an initial step to investigate the CT reconstruction characteristics of the prototype X-ray scanner system with the three geometry-based voxel models. A single column of pixels was extracted from the center of each of the set of 36 X-ray images exemplified in Fig. 3.5. These single columns of pixels simulate the data that would be measured from a conventional line-detector system. This cross-section contains four knots approximately spaced at 90° intervals and a deep radial crack.

Figure 3.6a shows the CT reconstruction created using a purely annular model. There are 16 annular voxels with radial boundaries at regular intervals of the square root of log radius. This sequence is chosen so that all annuli have the same cross-sectional area and thus have approximately equal measurement accuracy. This annular arrangement can effectively model axisymmetric features; the bright periphery in Fig. 3.6a clearly indicates the higher material density of the sapwood just below the bark of the log. Angularly arranged features such as knots are not displayed in this view. The sector-shaped reconstruction shown in Fig. 3.6b, computed using the same X-ray image data, has the opposite characteristics. It clearly indicates the cluster of four knots as bright sectors, and the deep crack as a dark sector. However, the sapwood presence is not indicated. The combined model shown in Fig. 3.6c, using 18 annuli and 36 sectors, shows the sapwood and the knot/crack features, but at the expense of greater reconstruction noise.

For comparison, Fig. 3.6d shows the filtered back-projection result using the same X-ray data as the previous three geometrical models [15]. The sapwood, knot and crack features are also visible in the reconstruction, but with substantial noise, causing the contrast to become quite low. In addition, substantial artifacts are created in the area around the outside of the log where no material density exists.

The character of the results in Fig. 3.6 can be explored in more detail by representing the results in graphical form. Figure 3.7a shows a plot of the reconstructed density profile along a log radius for the annular results shown in Fig. 3.6a. A steadily increasing density trend can be observed, which is typical because most logs have a low-density pith, slightly higher density heartwood region and much higher density sapwood. In this particular log, the sapwood density reduced to a narrow ring close to the perimeter because the log had dried for a long time in the laboratory. A similar narrow ring of sapwood can also be observed in Fig. 3.6c, d. Figure 3.7b shows a plot of the reconstructed density profile around the log circumference for a sector results in Fig. 3.6b. In this graph, the knots observed in Fig. 3.6b appear as four sharp peaks and the crack appears as a sharp valley. This graph has circular continuity so that the right side joins back to the left. The graph shows the average density of the log is about 0.38 g/cm^3, with the knot area density 0.45 g/cm^3 about 20 % higher than the average.

A very important characteristic of the geometrical CT models used here is that they produce reconstructions that are much more robust and noise immune than those from conventional procedures. To illustrate this characteristic, a second scanning of the same sample log was done using different measurement parameters (36 projections, 100 ms exposure time). This change substantially reduces the X-ray measurement quality by the presence of substantial shot noise. Figure 3.8 compares the results of the second measurements with those of the higher quality measurements in Fig. 3.6. Figure 3.8a, b respectively show the conventional filtered back-projection results using the higher and lower quality data. The much-increased noise within the log and the artifacts outside the log are very evident. The corresponding results in Fig. 3.8c, d for the sector model show a much more stable response and a much greater tolerance for the lower-quality data.

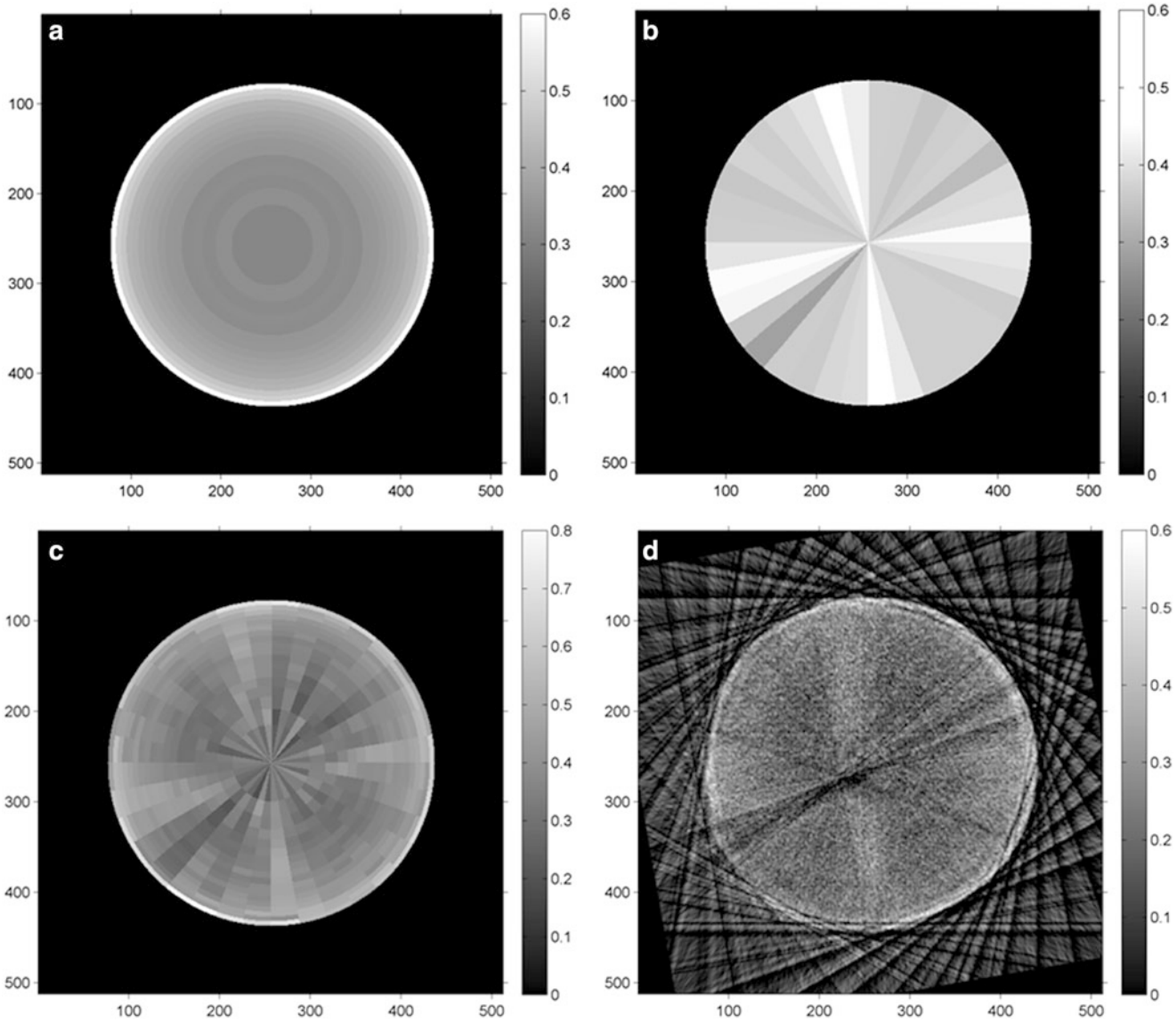

Fig. 3.6 Log CT reconstruction results: (**a**) reconstruction using 16 annuli, (**b**) reconstruction using 36 sectors, (**c**) reconstruction using 18 annuli × 36 sectors, (**d**) reconstruction using 36 filtered back projections

3.3.3 Multi-slice Reconstruction

The single-slice reconstruction results are interesting because they provide useful comparisons with conventional practice using line-detector measurements. It is further of interest to explore the capabilities of the cone-beam measurements to reconstruct multiple parallel cross-sectional slices simultaneously. This is challenging mathematically because the off-axis X-rays are inclined longitudinally as well as laterally, and so pass through multiple slices of the log. The mathematical formulations described in Part I of this paper [7] take these features into account and allow the simultaneous evaluation of multiple parallel slices from cone-beam data. Figure 3.9 shows the multi-slice sector results derived from the same data as used for Figs. 3.6 and 3.7, but using the entire X-ray images, not just the central column. The diagram illustrates the computed variation of log density along the length (56 slices horizontally) and around the circumference of the log (36 sectors vertically). Figure 3.9a is named a "veneer" plot because it corresponds to the pattern that would be seen if a veneer sheet were cut from the outside of the log. (Rotary veneer cutting is done using a large knife that peels the outside of a log in much the same way that a pencil sharpener cuts a pencil. The cut is parallel to the outside cylindrical surface rather than conical, thus producing a rectangular veneer sheet.)

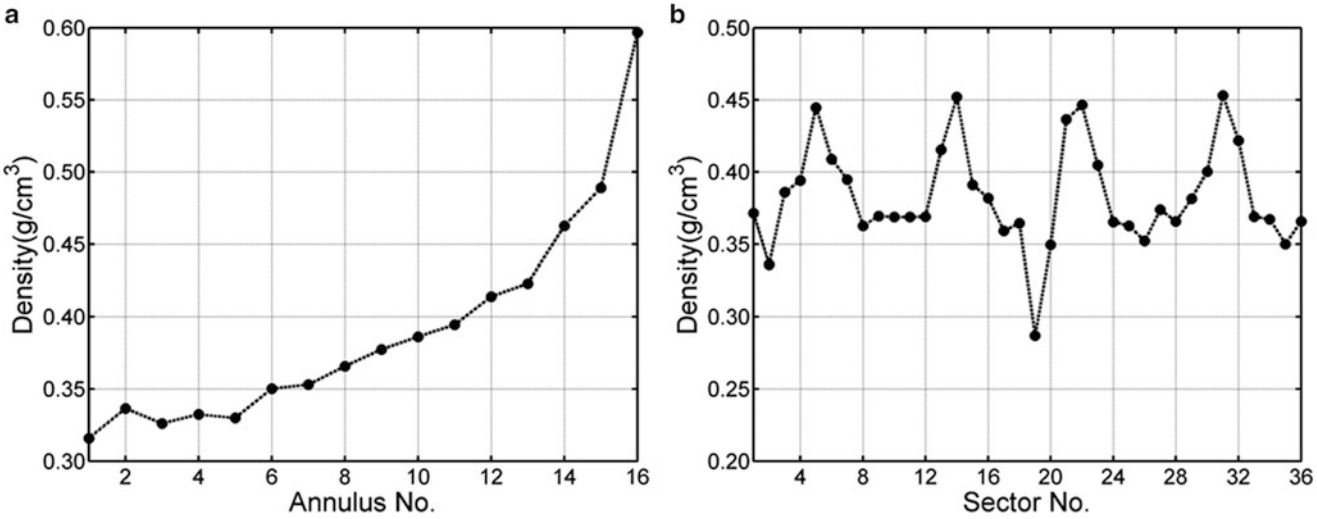

Fig. 3.7 Log cross-section density plot: (**a**) annular density distribution, (**b**) sector density distribution

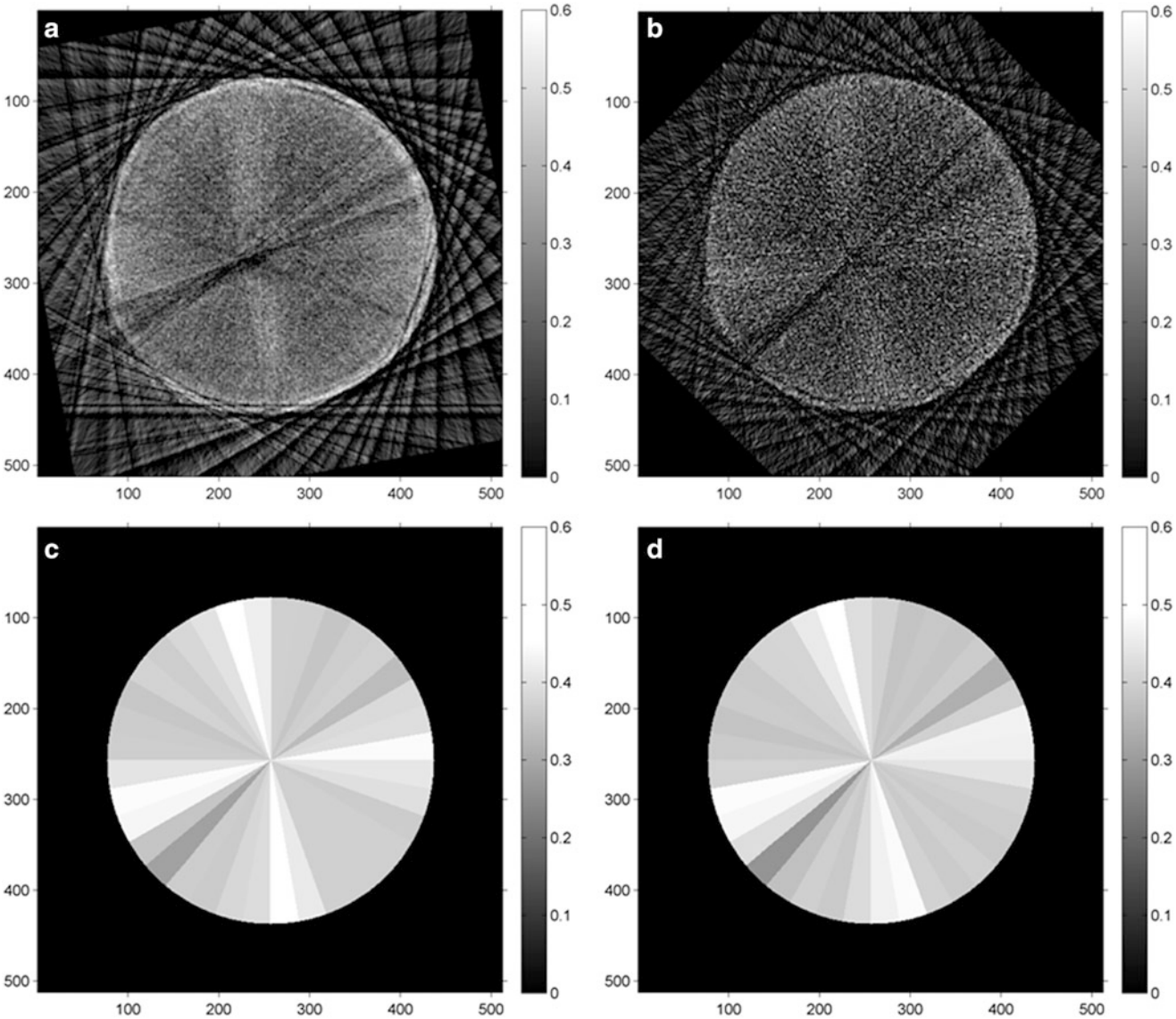

Fig. 3.8 Comparison between filtered back projection (FBP) and sector reconstruction: (**a**) FBP reference, (**b**) FBP with noisy data, (**c**) sector reconstruction, (**d**) sector reconstruction with noisy data

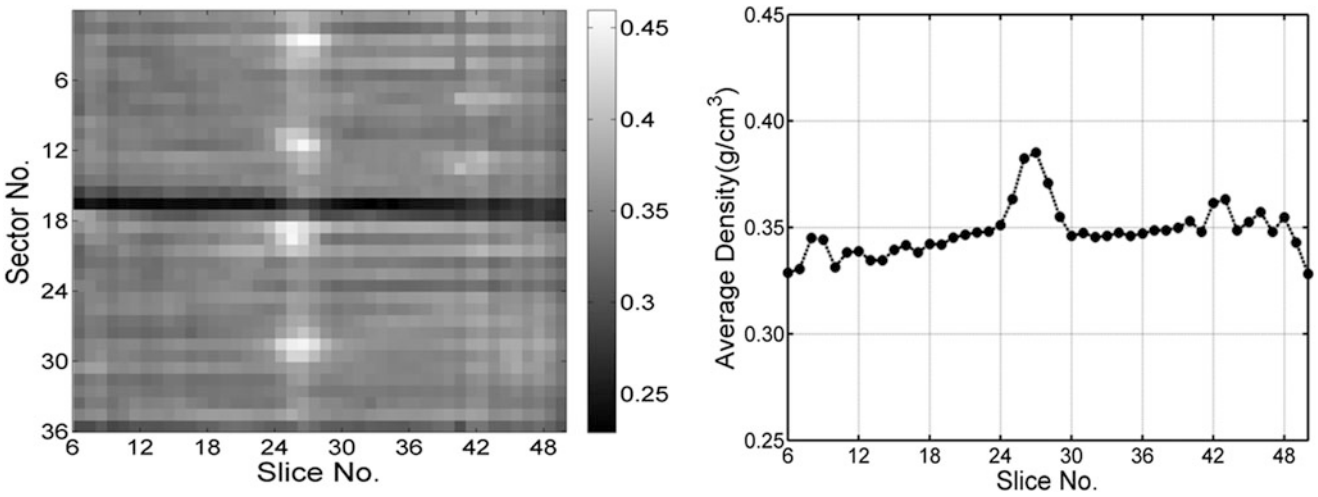

Fig. 3.9 Log longitudinal density profile: (**a**) sector veneer plot, (**b**) average sector density plot

The veneer plot in Fig. 3.9a clearly shows the four prominent knots vertically at the center, with two much smaller knots appearing on the right side. Such knot patterns are very typically seen in rotary cut veneers. The horizontal dark line corresponds to the radial crack. This is deliberately not a feature of commercial veneers because a crack in the log would produce frequent cuts in the veneer sheet, causing it to break up into small pieces instead of forming into a long continuous ribbon. (Veneer is cut from fresh logs that are still wet inside ("green"); they are deliberately kept wet to prevent them from drying out and cracking like the log used here.) Figure 3.9b shows the average density within the parallel slices. The graph prominently shows the locally elevated wood density caused by the presence of the central knot cluster. The two small knots on the right produce a much smaller average density peak. These average density peaks provide a simple method for identifying the location of knot clusters.

3.4 Discussion

The preliminary results presented here indicate a great practical potential for the proposed geometry-based Eulerian approach to CT reconstruction. It is an approach highly tailored to a specific application: the scanning of logs in a sawmill. This rough industrial environment differs greatly from the controlled laboratory environment that is the typical location of CT equipment. The measurement needs in terms of spatial and density resolutions are much less demanding than for conventional medical and scientific applications. Thus, the measurement equipment need not be so complex and costly. For practical use, ruggedness, straightforward operation and moderate cost are essential to make the equipment a practical proposition for use in an ordinary sawmill.

The X-ray equipment described here is homemade by generalists, and so it lacks the sophistication of specialized design. Yet, even with the present design, the prototype equipment clearly shows the promise and capabilities of the proposed geometry-based CT reconstruction approach. The feature-specific models are strongly tailored to the known geometrical characteristics of logs. This a-priori information guides the CT inversions towards physically realistic results and stabilizes the solutions against the noise in the X-ray data, which have relatively low quality compared with those from medical CT equipment. In addition, the Eulerian approach that is taken, whereby the CT inversion is based on the log rather than on the fixed space through which the log moves, provides substantial tolerance to the presence of rigid-body translations within the log motions. Such motions are very damaging in conventional CT reconstructions and so highly accurate mechanical systems are required, usually involving motion of the X-ray source and detector system, which is a complex challenge. The proposed CT system design overcomes this challenge by keeping the X-ray source and detector system fixed, moving the logs through the scanner using conventional sawmill style transport mechanisms, and allowing the geometrical CT models to compensate for the resulting rigid-body motions.

The initial results presented here illustrate the noise tolerance of the geometry-based CT reconstructions and they also suggest significant tolerance of rigid-body motions. No special care was taken to mount the log specimen exactly along the rotation axis of the transport system, and an eccentricity of about 1 cm is present. Errors of this scale would be catastrophic in medical CT scanning, but are not greatly problematic here. Further tests are planned whereby larger eccentricities will be investigated to assess tolerance to rigid-body motion effects.

The present work has also explored the ability to use cone-beam X-ray data. This practice greatly expands the use of the available data from the X-ray source. Traditional CT systems use a collimated X-ray beam to illuminate a line detector. However, collimation is a subtraction process, where the majority of the available beam is discarded to leave remaining the desired narrow X-ray line. In contrast, a cone-beam has little or no collimation and the entire X-ray beam is actively used. However, the use of a cone beam creates a more complex 3-dimensional geometry within the X-ray fan, causing off-axis rays to pass through multiple adjacent CT slices. Thus, all slices must be reconstructed simultaneously. Fortunately, the coarseness and symmetry of the proposed CT reconstruction arrangement keeps the size of the calculation moderate. In addition, the dimensional normalization that is possible with the geometry-based CT models allows some calculations to be done in advance, so that the final reconstruction can be completed rapidly to meet the "real-time" requirements of a sawmill. The present explorations into cone-beam use have started using a purely rotational log motion. Future work is planned whereby the log will rotate and advance axially through the X-ray scanner in a spiral motion.

3.5 Conclusion

This paper, the second of a two-part series, explores the geometry-based CT concept proposed in Part I, describes the prototype cone-beam CT log scanner and presents some example results. The prototype system realizes efficient cone-beam X-ray scanning and uses the X-ray data with the coarse-resolution log models and algorithms. Effective single-slice and multi-slice log density reconstructions are successfully achieved. The proposed geometry-based coarse-resolution log reconstructions compare well with results from conventional CT reconstruction. The proposed CT approach is genetic and can be also adapted into cone-beam and spiral-motion CT scanning. This research is currently in progress. The availability of the location and size of internal features provide rich information to determine the grade of input logs and to optimize the subsequent processing to improve the yield of high-quality products in sawmills. The promising scanning results obtained give confidence in the usefulness and applicability of the proposed approach to practical log scanning in sawmills.

Acknowledgement The authors gratefully thank the Natural Science and Engineering Research Council of Canada (NSERC) for their financial support of this project through the ForValueNet network, the Centre for Hip Health and Mobility, Vancouver General Hospital, for use of facilities, and the Institute for Computing, Information and Cognitive Systems (ICICS).

References

1. Oja J, Grundberg S, Grönlund A (1998) Measuring the outer shape of Pinus sylvestris saw logs with an X-ray LogScanner. Scand J Forest Res 13:340–347
2. Holtec X-ray Log Scanner. http://www.holtec.de/en/2015/ct_roentgen_rundholzscanner.html. Accessed 15 Sep 2011
3. Wang G, Yu H (2008) An outlook on X-ray CT research and development. Med Phys 35(3):1051–1064
4. Rinnhofer A, Petutschnig A, Andreu JP (2003) Internal log scanning for optimizing breakdown. Comput Electron Agr 41:7–21
5. Chiorescu S, Grönlund A (2000) Validation of a CT-based simulator against a sawmill yield. Forest Prod J 50:69–76
6. Oja J, Grundberg S, Fredriksson J, Berg P (2004) Automatic grading of sawlogs: a comparison between X-ray scanning, optical three-dimensional scanning and combinations of both methods. Scand J For Res 19:89–95
7. An Y, Schajer GS (2013) Coarse-resolution cone-beam CT scanning of logs: part I: discretization and algorithm. In: Proceeding of 2013 SEM Annual conference, Lombard, 3–5 June
8. Chilton AB, Shultis JK, Faw RE (1984) Principles of radiation shielding. Prentice Hall, Englewood Cliffs
9. Chotas HG, Dobbins JT, Ravin CE (1999) Principles of digital radiography with large-area, electronically readable detectors: a review of the basics. Radiology 3:595–599
10. Seger MM, Danielson PE (2003) Scanning of logs with linear cone-beam tomography. Comput Electron Agr 41:45–62
11. Kyokko DRZ X-ray Screen. http://www.mcio.com/Products/drz-screens.aspx. Accessed 20 Jan 2011
12. Andor iXon 897 EMCCD Camera. http://www.andor.com/scientific-cameras/ixon-emccd-camera-series/ixon-ultra-897. Accessed 15 Oct 2010
13. Zribi M, Chiasson J (1991) Position control of a PM stepper motor by exact linearization. IEEE Trans Autom Control 36(5):620–625
14. Wang ZB, Zhao H, Tao W, Tang Y (2008) Barrel distortion correction of wide-angle lens based on spline function. Opto-Electron Eng 4:20–30
15. Zeng GL, Gullberg GT (2004) Cone-beam and fan-beam image reconstruction algorithms based on spherical and circular harmonics. Phys Med Biol 49(11):2239–2256
16. Kak AC, Slaney M (1987) Principles of computerized tomography. IEEE Press, New York

Chapter 4
Crack Nucleation Threshold Under Fretting Loading by a Thermal Method

B. Berthel and S. Fouvry

Abstract The aim of this study is to develop a new experimental method to measure temperature field during a fretting test in a cylinder on flat contact configuration. Analyze of temperature evolution during a fretting test with constant loading shows that this latter can be decompose on a global warming and a sum on two periodic signal at f_L and $2f_L$, where f_L is the loading frequency. Analyze of the thermal signal during a fretting test with step by step increasing of tangential force unable us to develop an empirical method to determine crack nucleation conditions.

Keywords Fretting • Infrared measurement • Dissipation • Crack nucleation • Fatigue

4.1 Introduction

Fretting damage has been recognized as a problem in several industrial applications for years ago. Fretting is a small amplitude oscillatory movement, which may occur between contacting surfaces subjected to vibration or cyclic stress. Fretting is therefore encountered in assemblies of components and thus concerns a wide range of industries (e.g., helicopters, aircraft, trains, ships, trucks, electrical connectors. . .). Fretting damage on the contacting surface is critically controlled by the amplitude of slip displacement [1] and two sliding regimes can be defined: gross slip and partial slip regimes. Fretting is characterized by sliding amplitudes always lower than the contact size. Under partial slip conditions the contact area is split in a sticking and two sliding zones (cf. Fig. 4.1b) and the main damaging process is crack nucleation. Determination of crack nucleation conditions requires time-consuming and expensive destructive methods giving dispersive results [2]. Locally, fretting is a complex cyclic multiaxial loading and the aim of this study is to develop a new method based on previous works on the field of fatigue to determine crack nucleation conditions. Indeed, assuming that the temperature evolution of a specimen during a fatigue test is an indicator of plasticity at the microscopic scale, alternative method based on analysis of self-heating during stepwise loading tests have been developed to rapidly provide fatigue limits in the case of uniaxial [3] or multiaxial [4] loadings.

The paper is composed as follows: a rapid description of our experimental device is first made. A brief review of computed temperature evolution method is then given. After that, an analysis of temperature variation during fretting test is done. Finally, the developed method to determine crack thresholds is presented.

B. Berthel (✉) • S. Fouvry
LTDS UMR5513, Ecole Centrale de Lyon, 36, Avenue Guy de Collongue, 69134 Ecully Cedex, France
e-mail: bruno.berthel@ec-lyon.fr; siegfried.fouvry@ec-lyon.fr

M. Rossi et al. (eds.), *Residual Stress, Thermomechanics & Infrared Imaging, Hybrid Techniques and Inverse Problems, Volume 8*, Conference Proceedings of the Society for Experimental Mechanics Series, DOI 10.1007/978-3-319-00876-9_4,

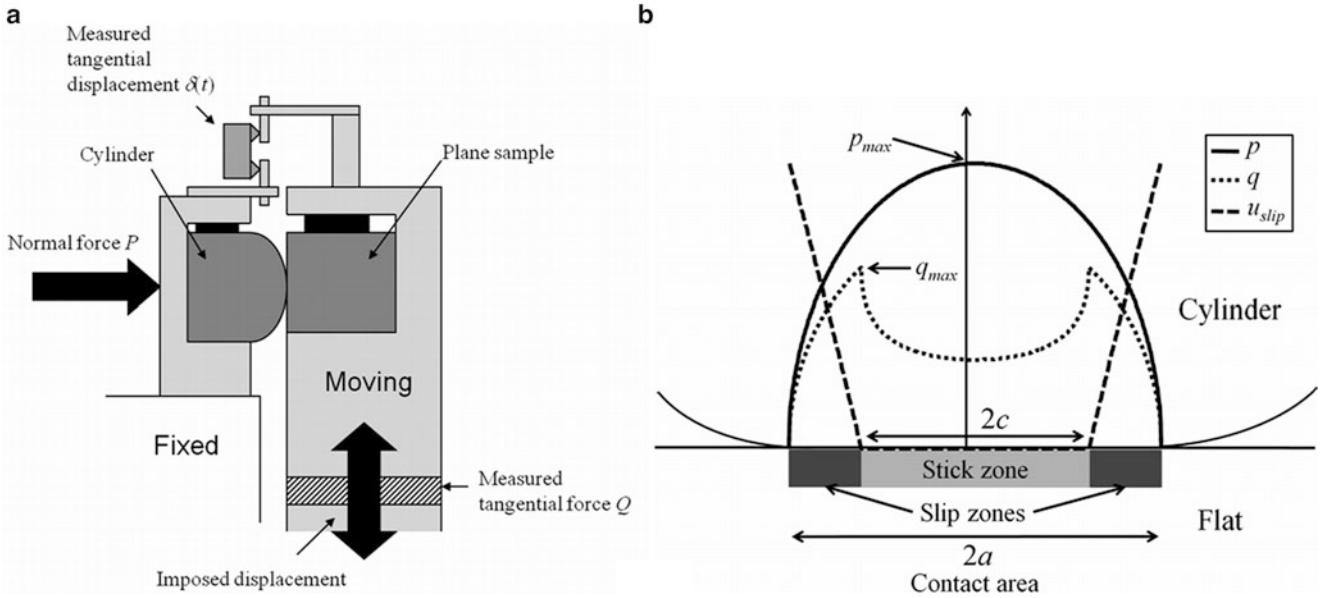

Fig. 4.1 (**a**) Fretting device (**b**) shear stress and pressure distributions over the contact

4.2 Material and Experimental Device

4.2.1 Fretting Device

Cylinder on flat configuration and two steel alloys with specified heat treatments were chosen for this study. Tests have been carried out using an experimental layout specially designed at LTDS (cf. Fig. 4.1a) [5]. A constant normal force P is applied on the counter body causing an elliptic pressure over the contact zone with a maximal value p_{max} (cf. Fig. 4.1b). A cyclic relative displacement δ is imposed leading to a macroscopic tangential force Q and a classical shear stress over the surface witch exhibits its maximum q_{max} at the stick zone limit (cf. Fig. 4.1b). During tests, P, Q and δ are recorded. p_{max}, q_{max} and the loading frequency f_L were chosen to characterize our tests.

4.2.2 Destructive Experimental Procedure

Previous tests were performed to determine crack nucleation threshold by conventional method and this latter is describe in this part. For each normal load P, several tangential load amplitudes Q_a are tested to locate the crack initiation threshold. All of the tests are investigated with respect to the following methodology. For all fretting tests, the sample is cut in the middle of the scar perpendicular to the fretting loading. Then, the new surface created is polished and observed with an optical microscope. The crack length and crack depth are measured. Note that the polishing and observation phase is repeated triple in order to evaluate the homogeneity of the crack data. Only maximal cracks lengths were considered. Therefore a threshold regarding the crack depth is defined to consider if crack initiated or not. This threshold is set at 10 µm.

4.2.3 Thermal Measurement

The camera used in this work was a FLIR SC7600 MWIR 2.5–5 µm. The focal length of the optical lens is 25 mm. This camera is equipped with an InSb 640 × 512 element detector. The maximal frame rate f_a is 380 Hz and the noise-equivalent temperature (NET) is lower than 25 mK. In this study the size of a pixel is about 0.16 × 0.16 mm^2. The lens axis of the camera

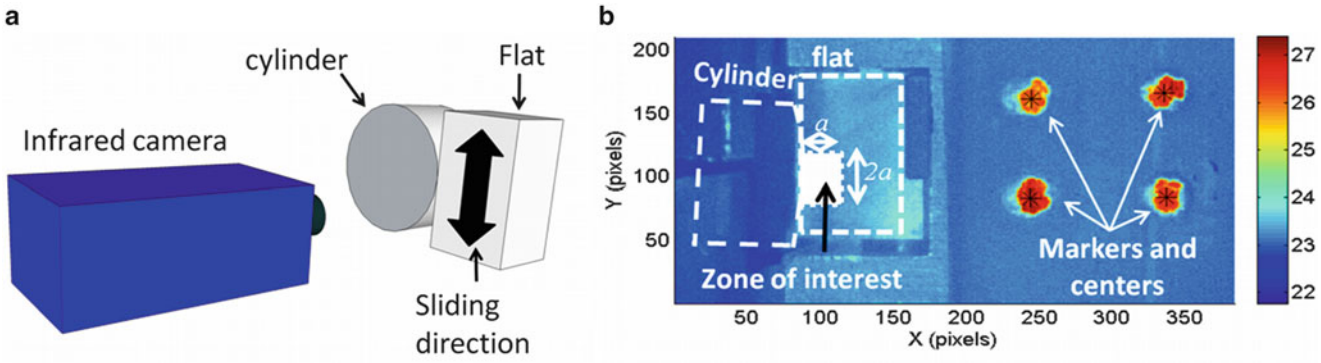

Fig. 4.2 (**a**) Basic sketch of the camera position (**b**) temperature field

was kept fixed and held perpendicular to the lateral surface of the specimen during the mechanical tests (cf. Fig. 4.2a). According to the high conductivity factor of steel alloys, it is assuming that the thermal image is very close to the temperature below the contact. Observed faces of specimen and cylinder are coating with a black matt paint to increase its emissivity.

For these first tests, a macroscopic scale was chosen. At this scale, specimen deformations can be neglected. Temperature is average over a Zone Of Interest (ZOI – cf. Fig. 4.2b). The size of this zone is characterized by the Hertzian contact size a. Vibrations and flexibility of the experimental device impose rigid movement body (rotation and translation) on the flat specimen. A marker tracking method was chosen to eliminate these displacements (cf. Fig 4.2b).

4.3 Thermal Method

4.3.1 Computes Temperature Evolutions

To estimate the dissipative effect induced by microplasticity in measured temperature evolutions, temperature evolutions were computed assuming that the material behavior remains elastic during the fretting tests (i.e. no intrinsic dissipation). So only dissipative effects induced by friction in sliding zones were taking into account. Under partial slip conditions, fretting loading is a non-propotionnal multiaxial fatigue loadind with small temperature variation and under classical hypotheses formulated for fatigue tests the local heat equation can be written in the following simplified form [6, 7]:

$$\rho C \frac{\partial \theta}{\partial t} - k\Delta\theta = d_1 + s_{\text{the}} \tag{4.1}$$

where k is the heat conduction coefficient, ρ the density, C the specific heat, θ the temperature variation defined by $\theta = T - T_0$, T the temperature, T_0 is the equilibirum temperature at the beginning of the test, d_1 the intrinsic dissipation and s_{the} the thermoelastic source.

Thermoelastic sources were computed via the classical linear thermoelastic model applied to non-proportional multiaxial loadings:

$$s_{\text{the}} = -T_0.\alpha.\text{tr}(\dot{\sigma}) \tag{4.2}$$

where α is the thermal expansion coefficient and $\boldsymbol{\sigma}$ the stress tensor.

The knowledge of time evolution of surface traction distributions q [8] and constant Hertz contact pressure distribution p allows computing the subsurface stress fields using elastic hypothesis [9] and time derivation of the stress tensors were obtained by a finite difference method.

To estimate heat flux in slip zone of the contact induced by friction, tangential slip velocity v_{slip} was derived from analytical solution of tangential slip u_{slip} [10, 11] (cf. Fig. 4.1b) and heat flux is given by:

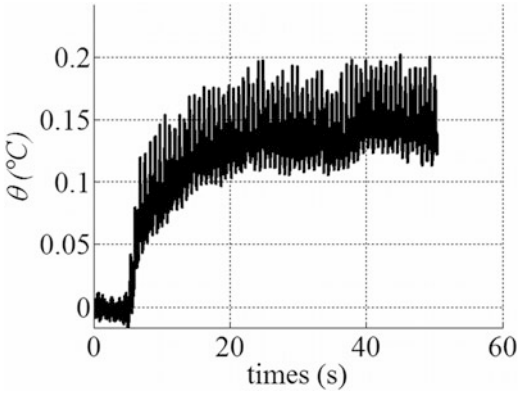

Fig. 4.3 Temperature variation evolution

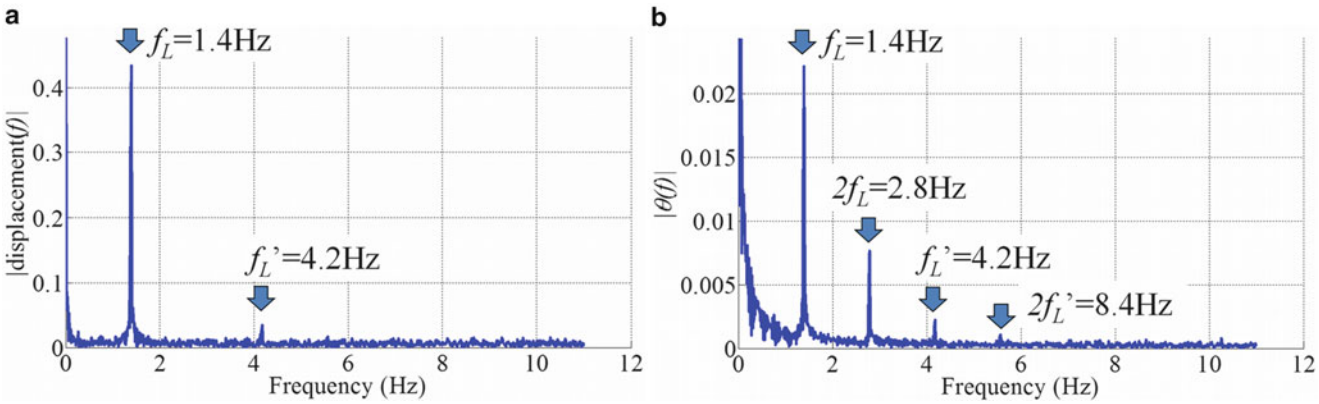

Fig. 4.4 (**a**) Single-sided amplitude spectrum of the displacement; (**b**) single-sided amplitude spectrum of the temperature variation

$$\phi_{slip} = \left| q v_{slip} \right| \tag{4.3}$$

This heat flux is split in equal part between cylinder and flat [12]. Somewhere else linear boundaries conditions were chosen:

$$\frac{\partial \theta}{\partial \vec{n}} . \vec{n} = -\lambda_{A/B} \theta \tag{4.4}$$

where λ is the thermal exchange coefficient between A and B (air or steel) while $\vec{n}$ is the normal of the surface.

To compute three dimensional temperature field evolutions for a cylinder/plane contact under partial slip an explicit finite difference method was implemented using the Matlab programming language to resolve Eq. 4.1. Results are shown in Fig. 4.7.

4.3.2 Temperature Evolution During a Fretting Test at Constant Loading

Figure 4.3 shows the variation of average temperature θ over the ZOI during a fretting test with following parameters: $p_{max} = 800$ MPa, $q_{max} = 520$ MPa, $f_L = 1$ Hz and $f_a = 100$ Hz. On these latter, it can be observed a global warming of about 0.15 °C, superimposed to oscillatory variation of temperature with maximal amplitude of about 0.02 °C. Temperature stabilization is reached after several numbers of cycles. To identify frequency spectrum of the thermal response of the specimen, discrete Fourier transformations were performed on the measured displacement by the marker tracking method and temperature evolutions. Results are shown in Fig. 4.4a, b. It can be observed that displacement is not monochromatic,

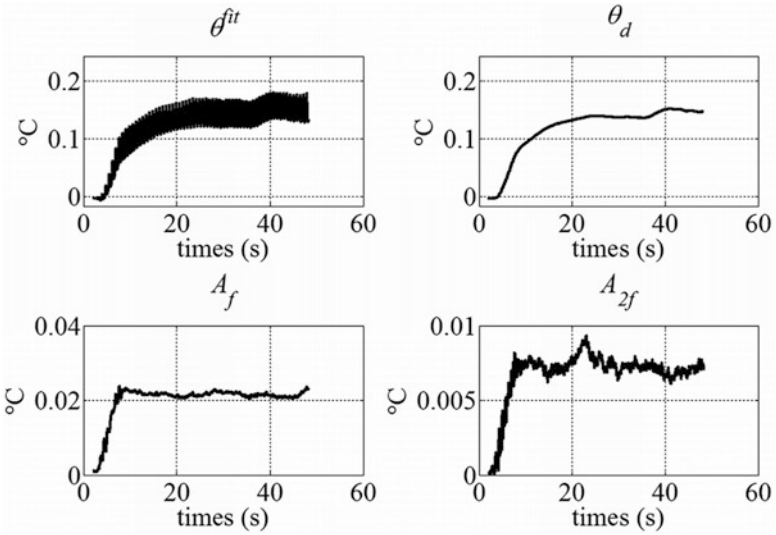

Fig. 4.5 Evolutions of: θ^{fit}, θ_d, A_f and A_{2f}

two amplitudes levels can be determined: high level amplitude at $f_L = 1.4$ Hz and a lower amplitude at $f_L' = 4.2$ Hz. A sinusoidal loading was imposed by the actuator but near the contact zone, loading shape was probably distorted by the experimental device and the contact rigidity. Analysis of the temperature variation spectrum at Fig. 4.4b exhibits a high level amplitude and a lower amplitude level respectively at f_L and $2f_L$. We can assume that the high amplitude at f_L is induced by thermoelastic effect then amplitude at $2f_L$ and global warming are induced by several dissipative effects like plasticity and friction in the sliding zone of the contact.

To analyse the thermal signal, among several possible methods, a local least-squares fitting of the thermal signal was considered in this work like in [6] and [7]. The temperature approximation functions account for the spectral properties underlying previously. The local fitting function θ^{fit} of the temperature variation charts is chosen like this:

$$\theta^{fit}(t) = \underbrace{p_1 + p_2 t}_{\text{linear drift}} + \underbrace{p_3 \cos(2\pi f_L t) + p_4 \sin(2\pi f_L t)}_{\text{perdiodic signal at } f_L} + \underbrace{p_5 \cos(4\pi f_L t) + p_6 \sin(4\pi f_L t)}_{\text{perdiodic signal at } 2f_L} \tag{4.5}$$

where the trigonometric time functions at f_L describe the periodic part of the thermoelastic effects while the linear time function and the periodic part at $2f_L$ takes transient effects due to heat losses, dissipative heating and possible drifts in the equilibrium temperature into account.

Thermal drift θ_d, amplitudes of periodic signals at f_L and $2f_L$, respectably A_f and A_{2f}, can be defined by:

$$\begin{cases} \theta_d = p_1 \\ A_f = \sqrt{{p_3}^2 + {p_4}^2} \\ A_{2f} = \sqrt{{p_5}^2 + {p_6}^2}. \end{cases} \tag{4.6}$$

Figure 4.5 shows that evolutions of thermal drift θ_d, A_f and A_{2f} reach a stabilized value after a few number of cycles and remain constant.

4.3.3 Temperature Evolution During a Fretting Test at P Constant

For several values of p_{max}, variable displacement tests were made [5]: the normal load was kept constant whereas the relative displacement amplitude (δ_a) starts from a very low value, imposing a clear partial slip condition (with $Q_a < \mu P$, where μ is the coefficient of friction). When stabilized mechanical and thermal conditions were reached, δ_a was increased and then

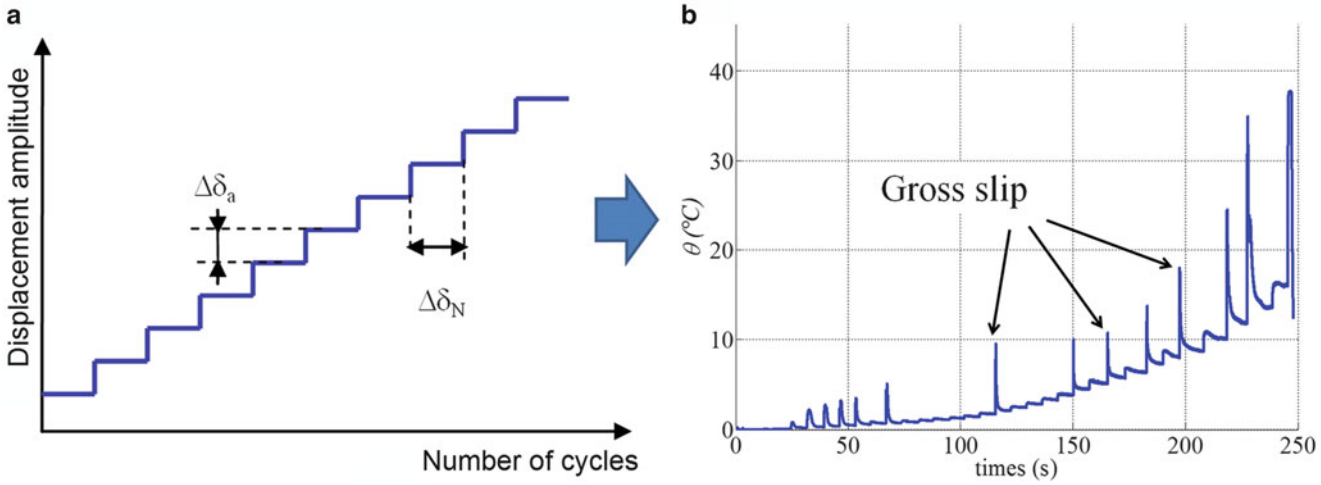

Fig. 4.6 (**a**) Principle of a variable displacement test; (**b**) evolution of the variation of temperature during a variable displacement test for $p_{\max} = 1{,}000$ MPa

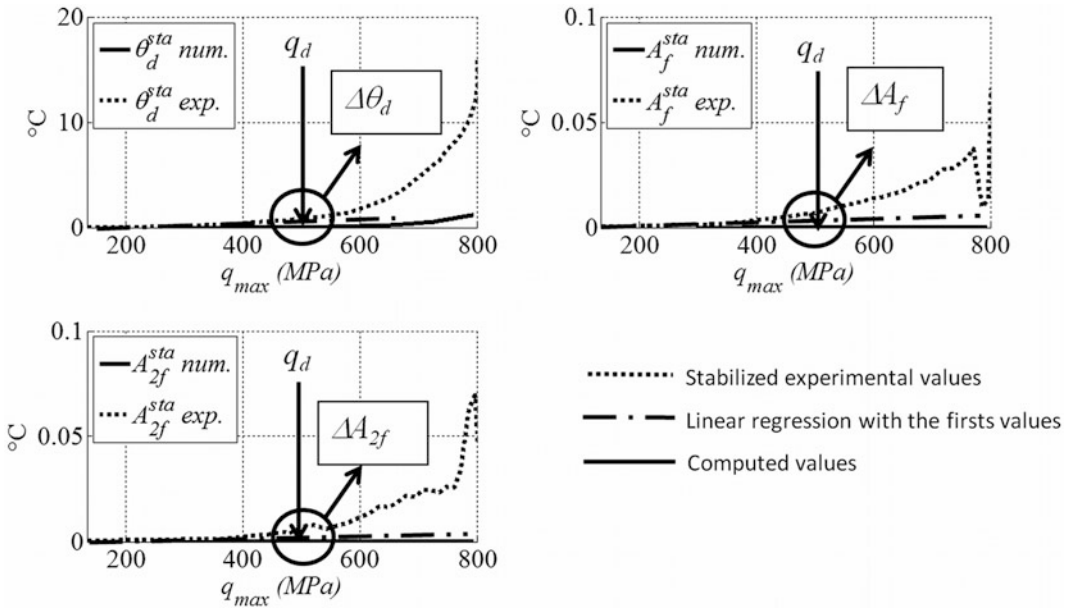

Fig. 4.7 Stabilised values of θ_d, A_f and A_{2f} versus q_{max}

maintained constant until a new stable situation was reached (cf. Fig. 4.6a). The imposed displacement, δ_a, was increased in this way, step by step, until the contact makes the transition to sliding ($Q_a = \mu P$). During each step, evolution of the temperature field on the surface of the flat was record by the infrared camera. The variation of average temperature over the ZOI θ is shown in Fig. 4.6b for $p_{max} = 1000$ MPa. At the begenning of some steps, a very small number of cycles in gross slip can be induced by contact instability. These latters indroduce short but higth increase of the variation of temperature that can be observed in Fig. 4.6 b.

For each step, stabilized values of θ_d, A_f and A_{2f} (respectively θ_d^{sta}, A_f^{sta} and A_{2f}^{sta}) were estimated and results are shown in Fig. 4.7. Comparaison of order of magnitude between experimental data and numerical results show that for each stabilized value, experimetal data are higher when q_{max} exceeds a therhold value (cf. Fig. 4.7). This difference of behavior can be connect to the plasticity in the material because computed temperature were obtained with a thermoelastic behaviour. So, evolutions of θ_d, A_f and A_{2f} can be considered as indicators of the microplastic behevior of the material and then indicators of crack initiation contitions. The slope change in evolution of these stabilized values in Fig. 4.7 can be empiricaly connected with a critical maximal contact shear stress q_{TH} ginving rise to a fretting crack by the method describe in the next paragraph.

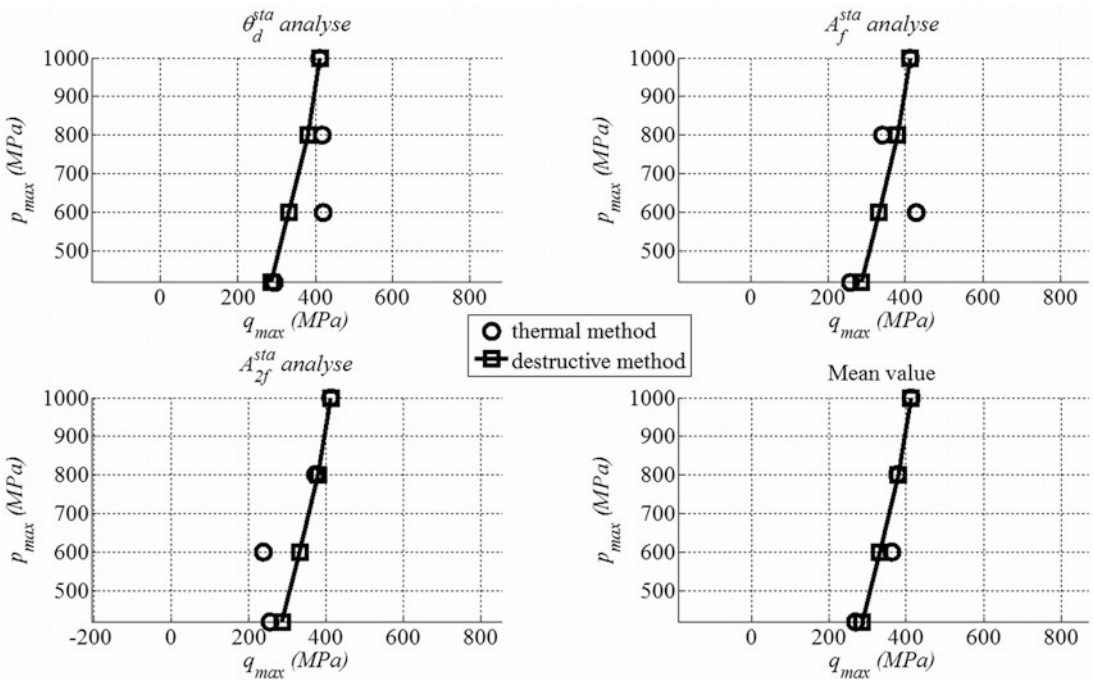

Fig. 4.8 Results obtained by destructive and thermal methods

For each p_{max}, linear regressions of θ_d, A_f and A_{2f} for $Q_a < 0.6P$ are made to determine the difference between these linear regressions and experimental data for all q_{max} (cf. Fig. 4.7). To adjust the method, at $p_{max} = 1000$ MPa yield values $\Delta\theta_d$, ΔA_f and ΔA_{2f} were set. These latter correspond to the diffecence between experimantal data and linear regression at the crack threshold q_d obtained by the destructive method. Finally, for all other test at different values of p_{max}, q_{max} corresponding to these yield values was chosen as the crack threshold q_{TH} obtained by the thermal method. Figure 4.8 shows the comparaison between results obtained with destructive method resulting of severals days of expertise and thermal method developed in this paper for four levels of p_{max}. Relative difference remains lower than 10 % fior the mean value.

4.4 Concluding Comment

In this paper, an experimental device using an infrared camera that enables estimation thermal effects accompanying fretting loading on steel in a cylinder on flat contact configuration was presented. Thermal measurement was coupled to a markers tracking method to eliminate rigid body movements induced by vibrations and rigidity of the fretting device.

During a fretting test with constant loading, results show that the temperature evolution averaged over a zone of interest can be decompose on a global warming and a sum of two periodic signals at f_L and $2f_L$, where f_L is the loading frequency. A local least-square fitting was proposer to approximate the temperature evolution. Results show that global warming and amplitudes of periodic signals reaches stabilized value after several cycles.

During a fretting test with constant normal force but increasing tangential force step by step, results show that stabilized value of drift and amplitudes of periodic signals of temperature can be empirically connected with crack threshold determined by destructive method. Differences between thermal method and destructive method on the crack thresholds were less than 10 %.

References

1. Vincent L, Berthier Y, Godet M (1992) Testing methods in fretting fatigue: a critical appraisal. ASTM 1159:33–48
2. Proudhon H, Fouvry S, Yantio G (2006) Determination and prediction of the fretting crack initiation: introduction of the (P, Q, N) representation and definition of a variable process volume. Int J Fatigue 28(7):707–713

3. Luong MP (1998) Fatigue limit evaluation of metals using an infrared thermographic technique. Mech Mater 28(1–4):155–163
4. Doudard C, Poncelet M, Calloch S, Boue C, Hild F, Galtier A (2007) Determination of an HCF criterion by thermal measurements under biaxial cyclic loading. Int J Fatigue 29(4):748–757
5. Proudhon H, Fouvry S, Buffière J-Y (2005) A fretting crack initiation prediction taking into account the surface roughness and the crack nucleation process volume. Int J Fatigue 27(5):569–579
6. Boulanger T, Chrysochoos A, Mabru C, Galtier A (2003) Analysis of heat sources induced by fatigue loading. Fatigue Damage Mater(40)
7. Berthel B, Chrysochoos A, Wattrisse B, Galtier A (2008) Infrared image processing for the calorimetric analysis of fatigue phenomena. Exp Mech 48(1):79–90
8. Hills DA (1994) Mechanics of fretting fatigue. Wear 175(1–2):107–113
9. Johnson KL (1985) Contact mechanics, 1st ed. Cambridge University Press, Cambridge
10. Ciavarella M (1998) The generalized Cattaneo partial slip plane contact problem. II – examples. Int J Solids Struct 35(18):2363–2378
11. Ciavarella M, Demelio G (2001) A review of analytical aspects of fretting fatigue, with extension to damage parameters, and application to dovetail joints. Int J Solid Struct 38(10–13):1791–1811, Jan 1999
12. Denape J, Laraqi N (2000) Aspect thermique du frottement: mise en évidence expérimentale et éléments de modélisation. Mécanique Industries 1(6):563–579

Chapter 5
Crack Growth Study of Fibre Metal Laminates Using Thermoelastic Stress Analysis

Rachel A. Tomlinson, Khurram Amjad, and Gonzalo Genovart Urra

Abstract The behaviour of crack growth in fibre metal laminates (FML) was investigated using Thermoelastic Stress Analysis (TSA). Fatigue tests were performed on Single Edge Notch Tension (SENT) specimens and thermoelastic data recorded. A Newton–Raphson iteration combined with a least-squares approach was used to fit equations describing the stress field around the fatigue crack tip to the thermoelastic data. The stress intensity factor range was thus determined at intervals of fatigue crack growth. By correlating the experimental results with a phenomenological crack growth prediction model, it was shown that our thermoelastic methodology which had been used previously for crack studies in monolithic metal specimens is capable of determining accurately fracture parameters in hybrid materials. The thermoelastic technique also allows identification of the crack tip in the metal layer, thus fatigue crack growth rate was determined easily. The experimental results agreed with the general trend reported elsewhere, of decreasing crack growth rate in FMLs. Delamination between the metal and fibre layers in the crack wake was investigated by comparing thermoelastic data with ultrasound measurements. It was found that the out-of-phase thermoelastic signal gave an accurate representation of the delamination in the crack wake. TSA, therefore, shows great potential for several aspects of fracture study in FMLs.

Keywords Thermoelastic stress analysis • Crack • Fatigue • Fibre metal laminate • GLARE

5.1 Introduction

Glass Laminate Aluminium Reinforced Epoxy (GLARE) is a fibre metal laminate (FML) which has started to be used extensively in aerospace applications due to its better damage tolerance and improved fatigue performance as compared to the aluminium alloy. It consists of thin layers of 2024-T3 aluminium alloy and pre-preg. The aluminium layer is nominally 0.3–0.5 mm thick and the pre-preg layer is 0.13 mm thick, consisting of unidirectional S-glass fibres embedded with FM94 adhesive and has a nominal fibre volume fraction of 59 % [1]. Currently there are six standard grades of GLARE which result from the different orientation and stacking order of pre-preg layers within the aluminium alloy layers [1]. In this study, fatigue behaviour of GLARE 3–3/2 [AL/0°/90°/AL/90°/0°/AL] was investigated using the technique of Thermoelastic Stress Analysis (TSA), also known as lock-in thermography.

In recent years Thermoelastic Stress Analysis (TSA) has been found to be an ideal method to study crack tip strain fields, due to its non-contacting, full-field, data collection capabilities. The method is based on the principle that under adiabatic and reversible conditions, a cyclically loaded structure experiences temperature variations that are proportional to the sum of the principal stresses. These temperature variations may be measured using a sensitive infra-red detector and thus the cyclic sum of the principal stresses on the surface of the structure may be obtained. An expression for the first stress invariant in the region of the crack-tip can be derived from stress field equations and used to determine the fracture parameters, such as the stress intensity factor [2, 3] and T stress [4]. The advantage of using TSA for such measurements is that the technique provides a direct measure of fracture behaviour which has been invaluable in studies of crack closure [5], cracks in welds [6] and crack-tip plasticity [7]. All these fracture studies have been on monolithic metal specimens but it is hypothesized that the same methodology could be used to quantify the fatigue behaviour of FML materials. It has been demonstrated [8, 9] that

R.A. Tomlinson (✉) • K. Amjad • G.G. Urra
Department of Mechanical Engineering, The University of Sheffield, S1 3JD Sheffield, UK
e-mail: r.a.tomlinson@sheffield.ac.uk

M. Rossi et al. (eds.), *Residual Stress, Thermomechanics & Infrared Imaging, Hybrid Techniques and Inverse Problems, Volume 8*, Conference Proceedings of the Society for Experimental Mechanics Series, DOI 10.1007/978-3-319-00876-9_5,

TSA has significant potential for investigating damage and fatigue behaviour in FMLs but is believed that there are no published literature on determining fracture parameters of FMLs using TSA. Therefore the aim of this work was use TSA to investigate fatigue behaviour of a fibre metal laminate material in such a quantitative manner.

5.2 Test Specimen and Experimental Procedure

A GLARE 3–3/2 Single Edge Notch Tension (SENT) specimen was manufactured to the dimensions shown in Fig. 5.1, and prepared by spraying one of its faces with matt black paint in order to increase the emissivity of the surface. The edge notch was 2 mm long and 0.3 mm wide. For the purpose of calibration, an orthogonal strain gauge rosette was also bonded to the back face of the specimen far away from the edge notch to ensure uniform stresses at that point. The strain gauge location is given in Fig. 5.1. The specimen was loaded in a 100 kN load range MAND servo hydraulic test machine using two pin jointed grips. The experimental arrangement is shown in Fig. 5.2.

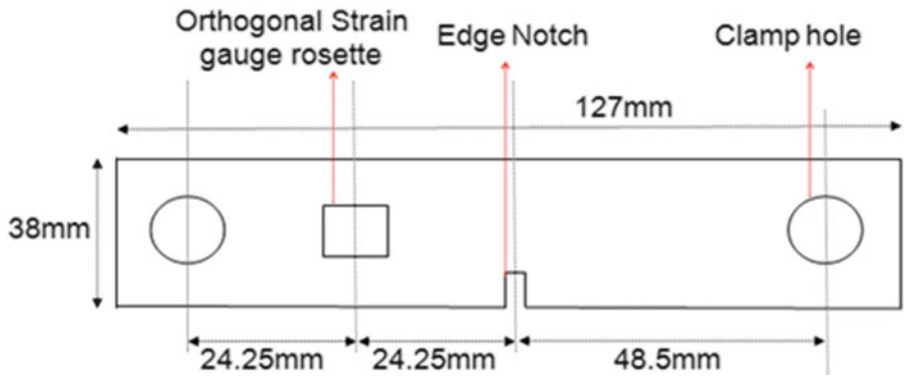

Fig. 5.1 Dimension of GLARE 3–3/2 SENT specimen

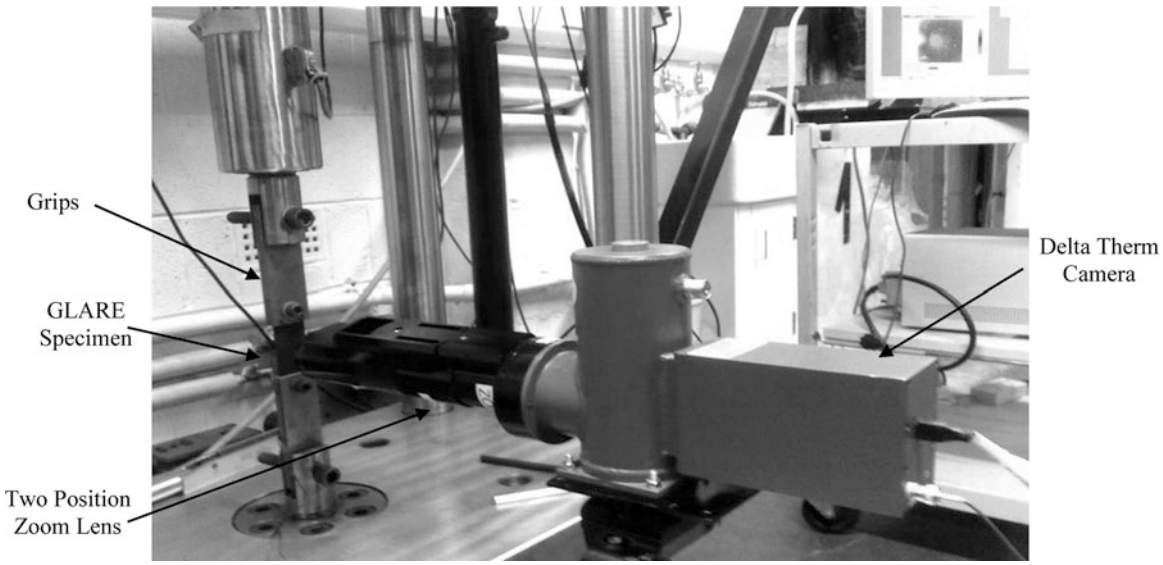

Fig. 5.2 Experimental arrangement

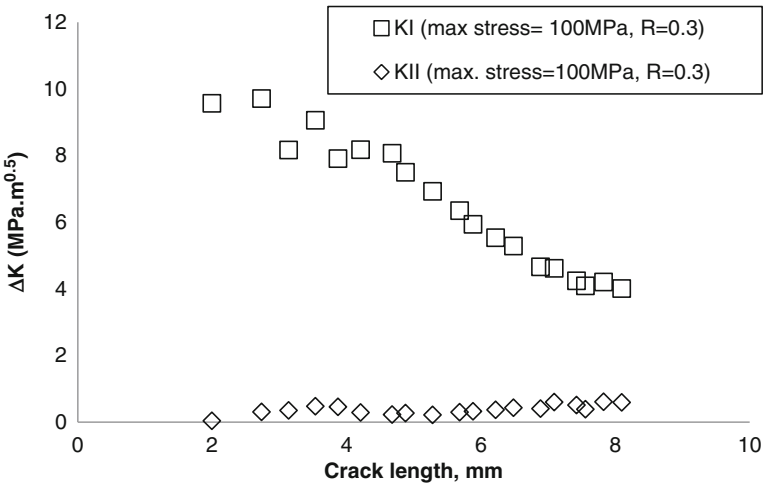

Fig. 5.3 Experimental stress intensity factor range with increasing crack length for the first set of fatigue tests

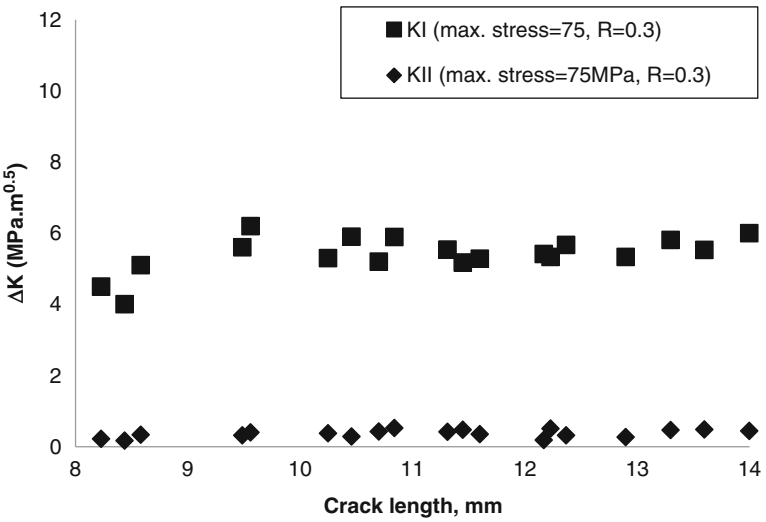

Fig. 5.4 Experimental stress intensity factor range with increasing crack length for the second set of fatigue tests

A constant amplitude tensile cyclic load with a maximum applied stress, σ_{max} of 100 MPa and the stress ratio, R of 0.3 was applied at a frequency of 10 Hz for 450 $\times$ 10^3 cycles. Thermoelastic images of the crack tip region were recorded at regular intervals during the fatigue crack growth using a Deltatherm 1410 Thermoelastic Stress Measurement System.[1] A Newton–Raphson iteration combined with a least-squares approach was used to fit equations describing the stress field around the fatigue crack tip to the thermoelastic data [2] and the mode I and mode II stress intensity factor (SIF) ranges, ΔK_I and ΔK_{II}, were determined as shown in Fig. 5.3. As the specimen was loaded perpendicular to the crack, negligible values of ΔK_{II} were expected.

In a second set of fatigue tests, the same GLARE 3–3/2 SENT specimen was cyclically loaded with a maximum applied stress of 65 MPa and the stress ratio of 0.5 for further 50 $\times$ 10^3 cycles at a frequency of 10 Hz and no crack growth was observed. The maximum load was then increased to a maximum applied stress, σ_{max} of 75 MPa and the stress ratio, R of 0.3 and the near steady state crack growth was observed for the test duration of further 250 $\times$ 10^3 cycles at a frequency of 10 Hz. The stress intensity factors and the monitored crack growth for the second set of fatigue tests are given in Figs. 5.4 and 5.5.

[1] Stress Photonics Inc., WI, USA

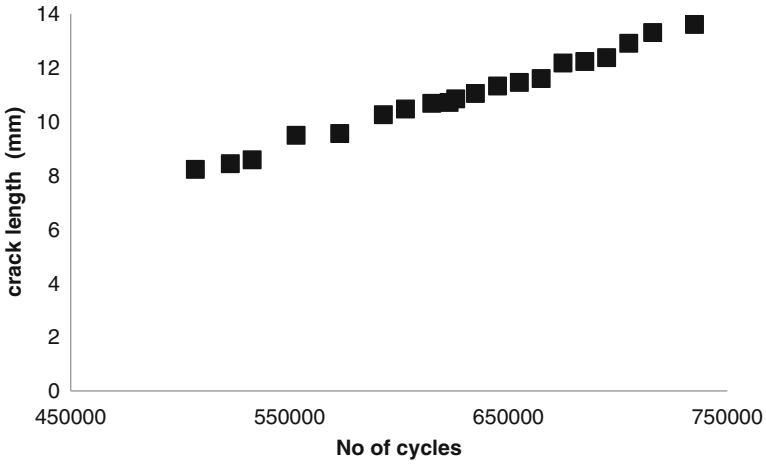

Fig. 5.5 Monitored crack length versus number of cycles for the second of fatigue tests

5.3 Fatigue Crack Growth Mechanism in Glare

The general trend of decreasing SIF and steady crack growth rate were observed from the fatigue test results (see Figs. 5.3, 5.4, and 5.5). Many authors [10–12] have reported the general trend of approximately constant crack growth rate in fibre metal laminates over a significant period of crack growth life. The reason for the decrease in SIF can be explained by the analysis of the crack growth mechanism in FMLs. The fatigue crack propagation in GLARE involves crack growth in the aluminium layers only, as the glass fibres are insensitive to fatigue [10]. The intact fibre layers in the wake of the crack act as a second load path which significantly reduces the load transferred around crack in the aluminium layers. This effect of crack bridging results in a decrease in SIF at the crack tip (as shown in Fig. 5.3) and thus a decrease in the crack growth rate. Once the fibre bridging becomes effective, balance is established between the crack propagation in the aluminium layers and the delamination growth at the interface, which results in a constant SIF (as shown in Fig. 5.4) at the crack tip and thus, a constant crack growth rate (as shown in Fig. 5.5).

The intact fibre layers also induce cyclic shear stresses at the prepreg/aluminium interface, which causes delamination at the interface. Delamination plays an important role in the GLARE fatigue mechanism as it decreases the bridging stresses in the fibres, by allowing an increase in length over which fibres are elongated [10]. Delamination at the interface is the reason why fibres don‘t break in the crack wake during the crack growth in the aluminium layers. Takamatsu et al. [11] and Toi [13] in their study on FMLs reported almost no fibre breakage in the wake of the crack during the crack propagation in the aluminium layers. Takamatsu et al. [11] investigated the crack length in the inner aluminium layers of GLARE 3–5/4, by machining the specimen in the vicinity of the crack tip, and reported the difference between the crack lengths of the top and inner layers to be about 8 % for the short cracks and 2 % for the long cracks.

5.4 Sub-surface Damage Detection in Glare

In order to investigate the delamination at the prepreg-aluminium interface further the phase images from the TSA data were observed. In TSA the thermal signal recorded by the camera is correlated with a reference signal from the loading device in order to filter out any background IR radiation and extract the TSA signal from the specimen. Each point in the data field may be represented as a vector where the magnitude is the TSA signal and the angle is the phase shift between the thermoelastic and reference signals. If adiabatic and reversible conditions apply, then the phase shift will be uniform over the whole specimen. However if heat is generated, there will be a relative phase difference due to non-adiabatic effects. Figure 5.6 shows the TSA signal and phase difference from the SENT specimen when the crack length was 14 mm. The phase in Fig. 5.6b has been shifted so that the far field is zero, so the map is really the phase *difference* relative to the far field.

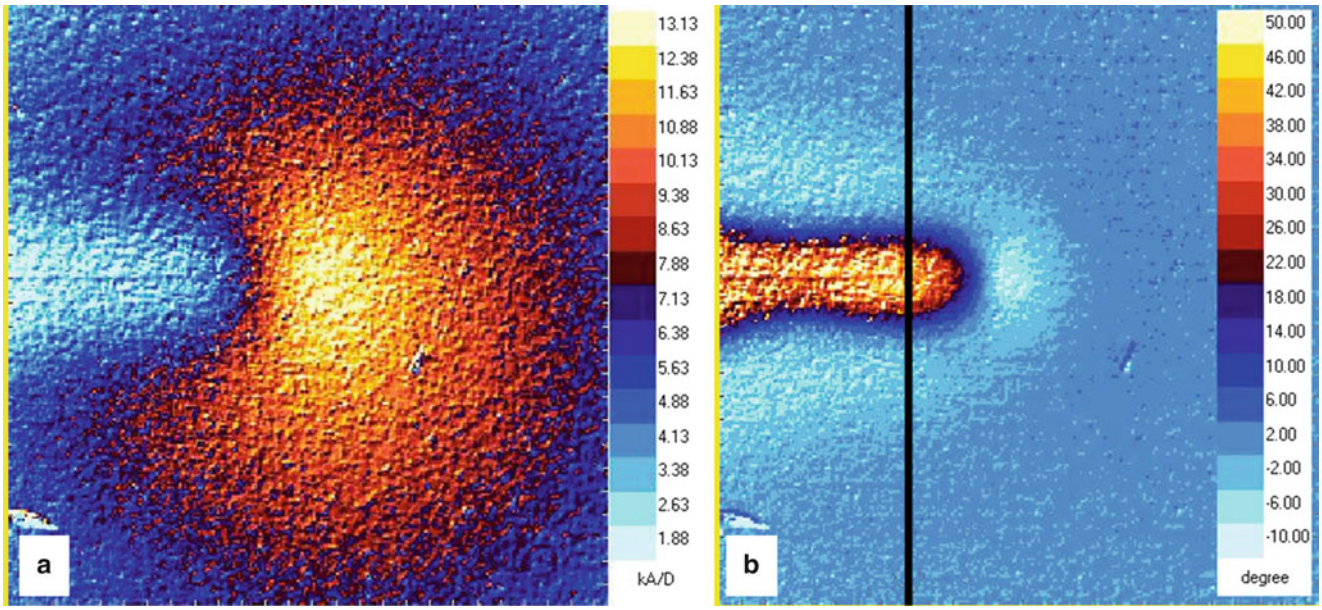

Fig. 5.6 (**a**) TSA signal and (**b**) phase difference around a 14 mm long crack in a GLARE 3–3/2 SENT specimen

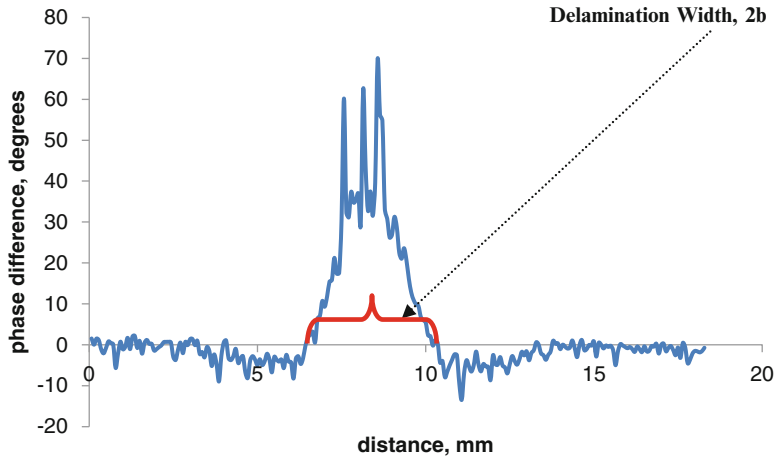

Fig. 5.7 Phase difference through the delamination zone as indicated in Fig. 5.6b

Meola et al. [9] observed that the phase map gives an indication of the delamination at the prepreg/aluminium interface but did not seek to use the data to quantify its extent. It is hypothesised that the phase difference of the thermoelastic image (Fig. 5.6b) gives an accurate representation of the delamination size in the crack wake. A phase shift can be seen at both sides of the crack wake, indicating some heat generation due to delamination. In order to obtain a measure of this out-of-phase region and thus the delamination zone, a line plot of the phase difference as indicated in Fig. 5.6b was plotted in Fig. 5.7, and the delamination width was measured as shown to be $2b = 3.8$ mm.

Ultrasonic scanning of the GLARE 3–3/2 SENT specimen was performed in order to compare the actual delamination size with the one proposed from the map of phase difference in Fig. 5.6b. The delamination width, $2b$ measured from the region near the crack tip from the ultrasound C-scan (see Fig. 5.8) was found to be approximately 4 mm, which is similar in magnitude to the delamination width measured from the phase map of the thermoelastic image i.e. 3.8 mm. The delamination zones measured using TSA (Fig. 5.6) and Ultrasound (Fig. 5.8) are a very similar shape as well as size. Therefore it is proposed that the phase difference method is an effective way to quantify the delamination zone since it has the advantages over ultrasound of being fast and non-contacting.

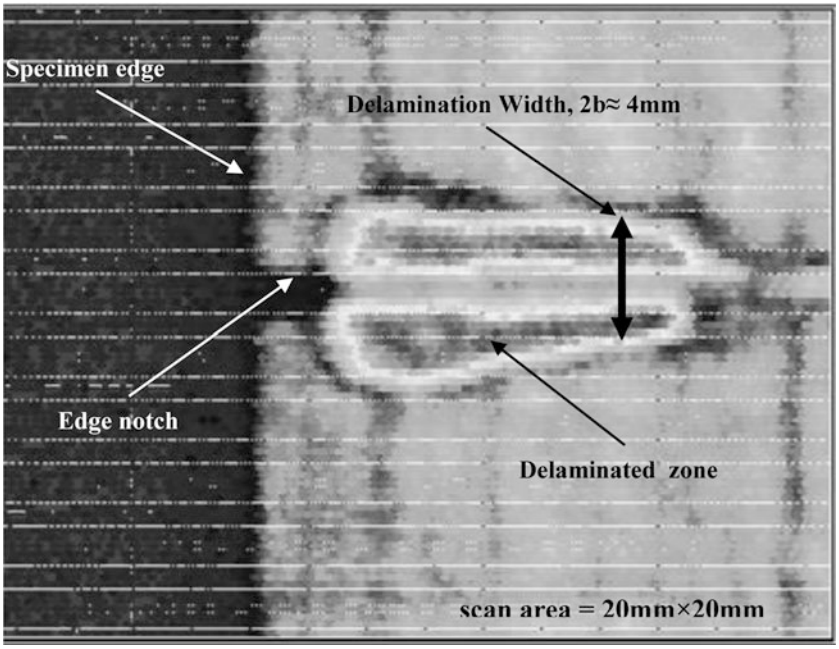

Fig. 5.8 Ultrasonic C-scan of the crack region of a of 14 mm crack in GLARE 3–3/2 SENT specimen

5.5 Comarision of Experimental Results with the Phenomenological Crack Growth Prediction Model

The experimentally determined SIF values for the steady state crack growth in GLARE were compared with the ones determined from phenomenological prediction model proposed by Wu and Guo [12]. The prediction model is based on the experimental observation of decreasing crack growth rate in GLARE which tends to a constant value, once the fibre bridging becomes fully effective. According to the prediction model, the stress intensity factor equation for the steady state crack growth in GLARE is as follows:

$$\Delta K_{eff} = \Delta S\sqrt{\pi l_o} \tag{5.1}$$

where ΔS is the stress range and l_o is the equivalent length, which is being defined as a material parameter. The crack growth rate in GLARE can be determined from the Walker's crack growth rate equation for the monolithic aluminium [14].

$$\frac{da}{dN} = C[(1 - R_c)^{m-1}\Delta K_{eff}]^n \tag{5.2}$$

where C, m and n are the coefficients of Walker's equation for 2024-T3 aluminium alloy. R_c is the effective stress ratio considering the effect of residual stress in the aluminium layers. In order to determine the effective stress ratio, the tensile residual stress, $R_c = 19$ MPa was calculated by applying the classical laminate theory.

The value of equivalent length, l_o which according to Wu and Guo [12] is a material parameter was not available for GLARE 3–3/2 in the literature. Hence, the mean crack growth rate of 2×10^{-5} mm/cycle determined from the crack growth plot in Fig. 5.5 was substituted in Walker's equation (5.2) to determine the effective SIF for the steady state crack growth in GLARE 3–3/2 SENT specimen. These values were compared with those determined using TSA as shown in Fig. 5.9.

In order to determine the validity of this phenomenological model, the predicted values of crack growth rate were compared with the crack growth rate curves for other GLARE grades found elsewhere in the literature. It was concluded that the model is able to predict the crack growth rate in GLARE fairly well but it is limited in its range of applicability because the equivalent length, l_o doesn't appear to be a material parameter, as it depends on other parameters as well such as specimen width and the specimen type i.e. CCT or SENT. In their work on crack closure, Diaz et al. [5] noted that TSA gave a direct measure of the effective ΔK, as is the case in this current work. This is a distinct advantage in such cases where the material behaviour is not predicted easily.

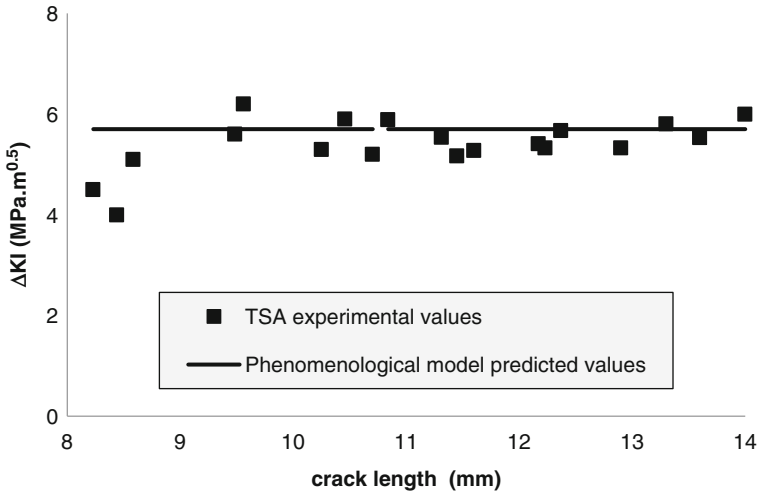

Fig. 5.9 Comparison of experimental and predicted values of Mode I SIF values versus crack length

5.6 Conclusions

The aim of the current work was to investigate the fatigue behaviour of GLARE using TSA. By correlating the experimental results with a phenomenological crack growth prediction model, it was shown that our thermoelastic methodology which had been used previously for crack studies in monolithic metal specimens is capable of determining accurately fracture parameters in FMLs. It was also found out that the phase map of the thermoelastic image gives an accurate representation of the delamination size in the crack wake. The delamination size determined from the phase map correlated well with the one determined from the ultrasonic scan of crack wake region. Based on these encouraging results, it was concluded that TSA can be further developed into a novel technique for simultaneously assessing fracture parameters, monitoring the fatigue crack growth and quantifying the sub-surface damage in FMLs with the aim of developing a technique which may be used on not only laboratory specimens but also real engineering structures.

Acknowledgements The authors would like to thank the UK Engineering Physical Science Research Council Instrument Loan Pool for the use of the TSA equipment used in this study.

References

1. Volt AD, Gunnink JW (2001) Fibre metal laminates-an introduction. Kluwer Academic, Dordrecht
2. Tomlinson RA, Nurse AD, Patterson EA (1997) On determining stress intensity factors for mixed-mode cracks from thermoelastic data. Fatigue Fract Eng Mater Struct 20:217–226
3. Tomlinson RA, Olden EJ (1999) Thermoelasticity for the analysis of crack tip stress fields – a review. Strain 35(2):49–55
4. Zanganeh M, Tomlinson RA, Yates JR (2008) T-stress determination using thermoelastic stress analysis. J Strain Anal Eng Des 43:529–537
5. Diaz FA, Patterson EA, Yates JR (2004) Some improvements in the analysis of fatigue cracks using thermoelasticity. Int J Fatigue 26:365–376
6. Diaz FA, Patterson EA, Tomlinson RA, Yates JR (2004) Measuring stress intensity factors during fatigue crack growth using thermoelasticity. Fatigue Fract Eng Mater Struct 27:571–583
7. Patki AS, Patterson EA (2010) Thermoelastic stress analysis of fatigue cracks subject to overloads. Fatigue Fract Eng Mater Struct 33 (12):809–821
8. Backman D, Patterson EA (2012) Effect of cold working on crack growth from holes in fiber metal laminates. Exp Mech 52:1033–1045
9. Meola C, Squillace A, Giorleo G, Nele L (2003) Experimental characterization of an innovative Glare (R) fiber reinforced metal laminate in pin bearing. J Compos Mater 37(17):1543–1552
10. Alderliesten RC (2007) Analytical prediction model for fatigue crack propagation and delimitation growth in GLARE. Int J Fatigue 29:628–646
11. Takamatsu T, Matsumura T, Ogura N, Shimokawa T, Kakuta Y (1999) Fatigue crack growth properties of a GLARE3-5/4 fiber/metal laminate. Eng Fract Mech 63:253–272
12. Wu X-R, Guo Y-J (1999) A phenomenological model for predicting crack growth in fiber-reinforced metal laminates under constant-amplitude loading. Compos Sci Technol 59:1825–1831
13. Toi Y (1995) An experimental crack growth model for fiber/metal laminates. In: proceedings of the eighteenth symposium of ICAF, Melbourne, pp 899–999
14. Walker K (1970) The effect of stress ratio during crack propagation and fatigue for 2024-T3 and 7075-T6 aluminium, effects of environment and complex load history on fatigue life. ASTM STP(462)

Chapter 6
Crack Detection in Large Welded Components Under Fatigue Using TSA

Andrew Robinson, Janice Dulieu-Barton, Simon Quinn, and David Howarth

Abstract Thermoelastic stress analysis (TSA) is used to investigate the initiation and growth of cracks in large welded specimens under fatigue loading. The dimensions and weld geometries investigated are characteristic of those found in the ship building industry, and specimens that have different weld geometries and have undergone different peening treatments are examined. The application of such a technique in industrial situations is explored further by subjecting the specimen to conditions that are representative of those found in service or those that could be realistically applied during construction and assembly.

Keywords TSA • Non-destructive testing • Fatigue • Welded structures • Crack growth

6.1 Introduction

The fatigue of welded structures is a common problem, and research is on-going to further understand the mechanisms and effects of various peening treatments, fatigue life extension, crack formation and crack detection [1]. It is known that design limits based on small scale test coupons are not necessarily representative of larger scale problems. Moreover, when coupled with the difficulty in incorporating variations in residual stress and variable loads that can be present in reality this often leads to overly conservative design approaches being taken. This is especially true in the ship building industry where tensile limits are often applied to the design of components that experience predominantly compressive stresses in service. In the presence of reduced tensile residual stress such compressive stresses should be somewhat non-damaging, which would allow an increase in allowable stress levels or reduced fatigue damage index.

With the quality of materials and processes being greatly improved in recent years, there is an opportunity to reassess these structures and the design regulations [2]; in addition, new techniques are also available that may provide new means of non-destructively evaluating these components. The primary specimens tested in the present work (Fig. 6.1) represent part of a typical longitudinal stiffener to transverse web connection in a ship's hull. The specimens incorporate the fillet weld detail from large panels at which fatigue cracks are known to initiate and enabled a detailed investigation of the fatigue performance of the fillet welded joint.

Thermoelastic stress analysis (TSA) is a quick, portable and robust non-contacting analysis technique that provides full-field stress data over the surface of a cyclically loaded component [3]. It is shown to provide a wealth of data around the welded joint, enabling full-field information about the stress distribution and crack evolution to be obtained. Use of such a technique may help to provide valuable information about the presence of cracks or defects within a structure, and help understand the mechanisms driving the growth of fatigue cracks; furthermore it may be possible to inspect large areas of structural components in a quick and efficient way, using relatively inexpensive equipment and in real industrial situations. TSA is based on the small temperature changes that occur when a material is subject to a change in elastic strain, generally referred to as the 'thermoelastic effect'. When a material is subjected to a cyclic load, the induced strain

A. Robinson (✉) • J. Dulieu-Barton • S. Quinn
University of Southampton, SO17 1BJ Southampton, UK
e-mail: A.Robinson@soton.ac.uk

D. Howarth
Lloyd's Register EMEA, 71, Fenchurch Street, EC3M 4BS London, UK

M. Rossi et al. (eds.), *Residual Stress, Thermomechanics & Infrared Imaging, Hybrid Techniques and Inverse Problems, Volume 8*, Conference Proceedings of the Society for Experimental Mechanics Series, DOI 10.1007/978-3-319-00876-9_6,

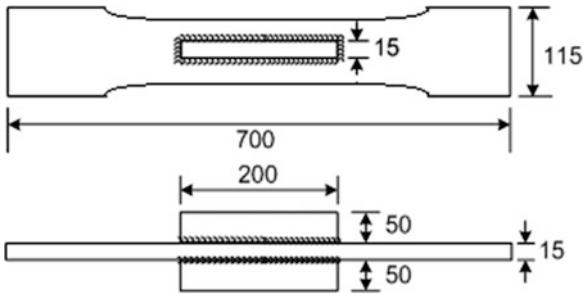

Fig. 6.1 Longitudinal fillet weld specimen

produces a cyclic variation in temperature. An infra-red detector is used to measure the small temperature change, ΔT, and a direct relationship between ΔT and the change in the 'first stressinvariant', $\Delta(\sigma_1 + \sigma_2)$, or the sum of the principal stressescan be established.

6.2 Experimental Procedure, Results and Discussion

When using TSA, the necessity for the cyclic load that is required to generate the temperature changeis often considered an experimental disadvantage. In the case of fatigue testing, the fatigue loading itself can be used to provide the key element required for this non-destructive technique. However, for the thermoelastic equation to be valid, there is a requirement that the temperature change occurs adiabatically, which typically leads to relatively high loading frequencies and dictates that the theory is invalid for areas experiencing heating [4]. It is also the case that the theory is invalid for regions experiencing cyclic plasticity such as experienced at a crack tip. Furthermore the plasticity leads to heating and subsequent diffusion (i.e. non adiabatic behaviour) and dissipation in the region of the neighbourhood of the crack. Therefore direct stress information cannot be obtained from the measured temperature change in this region, however it is clearly shown that analysis of temperature and phase data in these areas can still offer significant insight albeit qualitatively and further processing may enable quantitative information to be obtained regarding the condition of the material and crack growth.

Steel specimens were subjected to a range of fatigue conditions including: tension-tension, compression-compression, and variable mean stress and amplitude loading. The loading conditions (unless otherwise stated) were equivalent to a stress amplitude of 200 MPa, and were cyclically loaded at a frequency of 10 Hz in a Schenck 630 kN servo-hydraulic test machine. Steel butt welded specimens (Fig. 6.2) that had been subjected to laser and shot peening treatments were also investigated under similar conditions. A Cedip Silver 480 M infra-red detector was used to obtain the thermoelastic data.

Figure 6.3 shows the temperature and phase data around the toe of the fillet welded joint, throughout various stages of the fatigue life of the specimen. The specimen was loaded at 10 Hz in compression with a stress range of 200 MPa, R = 0.1; thermoelastic data was recorded at 5,000 cycle intervals and the plots shown are after (a) 10,000, (b) 150,000 and (c) 315,000 cycles. The displacement data was also monitored throughout the test. As the loading was compressive, failure was defined to be when the fatigue crack has initiated on one face, and propagated through the entire thickness emerging on the opposite side, as opposed to total failure into two pieces; this was monitored using visual inspection and a solution of soap and water.

The temperature data in Fig. 6.3a clearly shows the full field stress distribution around the weld toe. Often the stress concentration factor around such joints are obtained using strain gauges; the benefit of thermoelastic stress analysis is that the technique is full field, and the such stress information can be readily obtained from the temperature change through a straightforward calibration process. It is also possible to identify a small difference on the right side of the weld toe (marked with an arrow) in both the phase and temperature data. This correlates with a small lip in the weld profile suggesting a change in the stress distribution and the likely initiation point of a crack. Obtaining thermoelastic data takes a matter of seconds, and TSA may provide the ability to quickly inspect large areas or welded structures for potential surface defects and initiation points.

The location of the crack is confirmed in Fig. 6.3b, where the temperature, and therefore stress distribution around the weld toe has changed significantly. A small change indicating the start of a crack was first noted in the TSA data after approximately 40,000 cycles; this was prior to any indication from strain gauge or displacement data. It is also noteworthy that there is a significant change in the phase data; this change is indicative of non-linear behaviour which can include non-adiabaticity, specimen heating, regions of plasticity, or large stress gradients. Figure 6.3c shows the crack after 315,000 cycles just prior to the failure criteria being met, and it can be seen that the crack has propagated across the entire toe and has now grown laterally into the main body of parent material. It is also possible to identify the approximate location of the crack

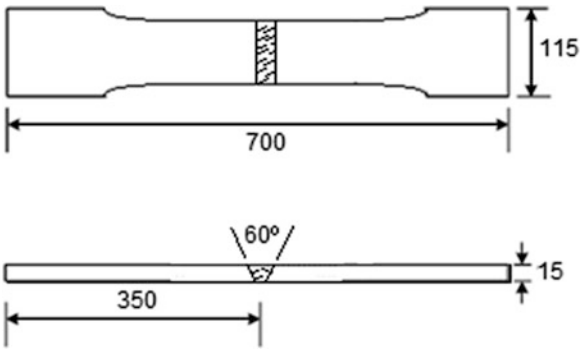

Fig. 6.2 Butt weld specimen geometry

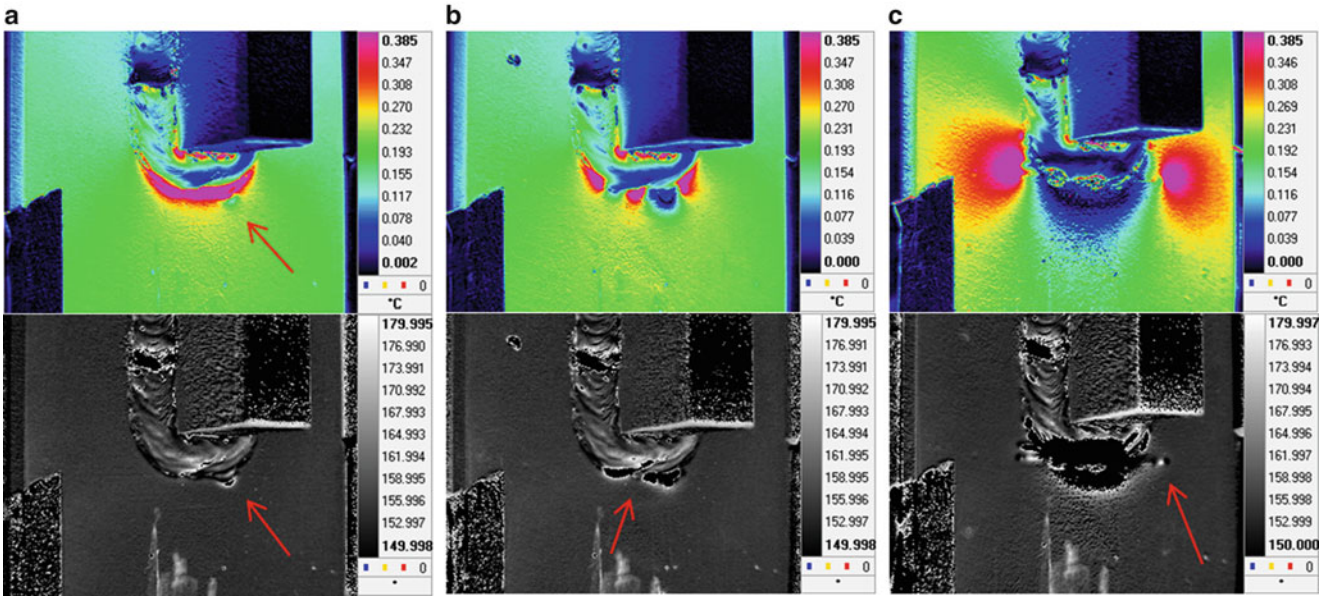

Fig. 6.3 Temperature (*upper*) and phase (*lower*) data throughout fatigue test, (**a**) 10,000 cycles, (**b**) 150,000 cycles, (**c**) 315,000 cycles

tips from both the temperature and phase data and additional processing may elicit further information such as the extent of the heat affected zone and crack growth rates. While it can clearly be seen that TSA is an excellent technique for providing stress and crack growth information throughout the life of a component in a laboratory environment, it is not practical to apply high cyclic loads to real structures in-service. The requirement for a relatively high cyclic frequency to achieve adiabatic conditions is a further hindrance; it may not be possible to locally load a ship structure at 10 Hz and/or develop such high stresses to provide a strong thermoelastic response.

The potential of applying TSA in the field has been explored further by subjecting the specimens to very low loading amplitudes and low cyclic frequencies. A range of tests were performed, whereby the longitudinal fillet welded specimen was subjected tocompressive stress ranges equivalent to 200, 100, and 20 MPa, and at loading frequencies of 10, 1, and 0.1 Hz. While the temperature data obtained is not fully thermoelastic, and therefore quantitative stress information cannot be directly calculated, qualitatively it can be seen from Fig. 6.4 that the stress distribution, and therefore presence of cracks, can still be inferred at the lower frequencies and loads.

Data was again recorded at 5,000 cycle intervals, and the primary difference between data taken at different loads and frequencies is the change in magnitude of temperature recorded. Nevertheless, a clear evolution of the temperature change around the weld toe can be seen from comparison of data sets throughout the test. Likewise, similar conclusions could be drawn from the phase information.

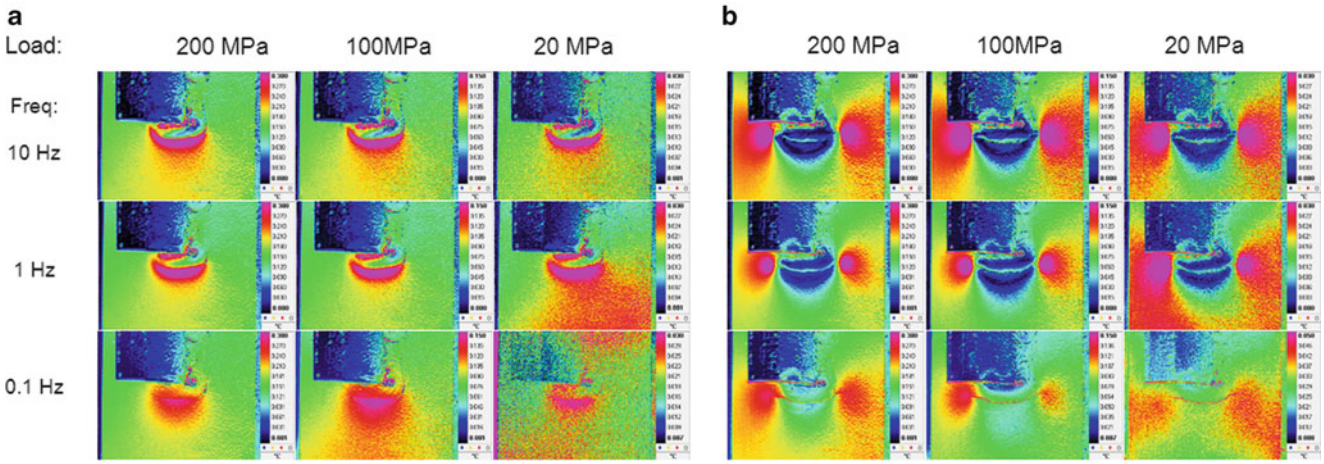

Fig. 6.4 Temperature data from around a crack in a longitudinal fillet welded specimen loaded over a range of stress amplitudes and frequencies. Data taken after (**a**) 100 cycles, (**b**) 200,000 cycles

6.3 Conclusions and Further Work

TSA has been shown to have the potential to be a non-contact technique for assessing the stress distributions around cracks in welded structures. It is possible to obtain full-field stress information over large areas and obtain information about the characteristic features of fatigue cracks. Furthermore, it has shown potential for application with in-service structures through the possibility of obtaining data rich thermoelastic information at lower frequencies and loads that are more realistically achievable in industrial settings. The data presented in this paper was obtained using a relatively high-tech and expensive infra-red detector. Further work will be conducted using a more inexpensive bolometer.

References

1. Gurney TR (1979) Fatigue of welded structures, 2nd edn. Cambridge University Press, London
2. Hobbacher A (2009) The new IIW recommendations for fatigue assessment of welded joints and components – a comprehensive code recently updated. Int J Fatigue 31(1):50–58
3. Dulieu-Barton J, Stanley P (1998) Development and applications of thermoelastic stress analysis. J Strain Anal Eng Des 33(2):93–104
4. Offerman S, Beaudoin JL, Bissieux C, Frick H (1997) Thermoelastic stress analysis under non-adiabatic conditions. J Exp mech 37:409–413

Chapter 7
Hybrid Thermoelastic Analysis of an Unsymmetrically-Loaded Structure containing an Arbitrarily-Shaped Cutout

W.A. Samad and R.E. Rowlands

Abstract The most critical stresses frequently occur at holes or notches, thereby influencing structural integrity. The prevalence of arbitrarily-shaped cutouts in engineering structures makes it necessary to be able to determine the state of stress reliably at and near these discontinuities. The fact that external boundary conditions are often not well known in practice complicates such situations. Unfortunately, theoretical solutions are seldom available for perforated finite geometries, and like numerical methods, they require accurate knowledge of external boundary conditions. On the other hand, traditional purely experimental methods typically do not readily provide the individual components of stress or reliable results close to the edge of a cutout. Acknowledging the above, this paper describes the ability to evaluate the full-field state of stress in an unsymmetrical-loaded finite structure containing an arbitrarily-shaped hole by processing the recorded load induced temperature information with an Airy stress function and imposing the local traction-free conditions discretely. As well as satisfying load equilibrium, the present hybrid-thermoelastic stress analysis (TSA) results agree with those from measured strains and a finite element analysis.

Keywords Thermoelasticity • Arbitrarily-shaped cutouts • Hybrid

7.1 Introduction

Stresses have been determined in a symmetrically loaded tensile plate having an arbitrarily-shaped hole [1]. Since loading and boundary conditions are rarely symmetrical in practice, this paper extends the approach presented earlier such that it is applicable to more general and practical situations. The present hybrid-TSA approach combines measured temperature data with an Airy stress function in polar coordinates, and imposes the local traction-free boundary conditions in order to determine the full-field individual components of stress at and in the neighborhood of an arbitrarily-shaped hole in a finite unsymmetrically loaded tensile plate, Fig. 7.1. Lacking an analytical coordinate system aligned with the boundary of the cutout in Fig. 7.1, the local traction-free conditions are imposed discretely by determining the directions normal and tangent to the edge at multiple locations on the boundary of the hole. The present lack of symmetry greatly increases the amount of recorded temperature data required, the number of edge locations at which one must impose the traction-free conditions and the number of Airy coefficients involved. These increased conditions aggravate the accompanying least-squares computation. The hybrid-TSA results agree with those from measured strains and finite element analysis (FEA).

W.A. Samad (✉)
Mechanical Engineering, Rochester Institute of Technology - Dubai, Dubai Silicon Oasis, Dubai, UAE
e-mail: wascad@rit.edu

R.E. Rowlands
Department of Mechanical Engineering, University of Wisconsin, 53706 Madison, WI, USA
e-mail: rowlands@engr.wisc.edu

M. Rossi et al. (eds.), *Residual Stress, Thermomechanics & Infrared Imaging, Hybrid Techniques and Inverse Problems, Volume 8*, Conference Proceedings of the Society for Experimental Mechanics Series, DOI 10.1007/978-3-319-00876-9_7,

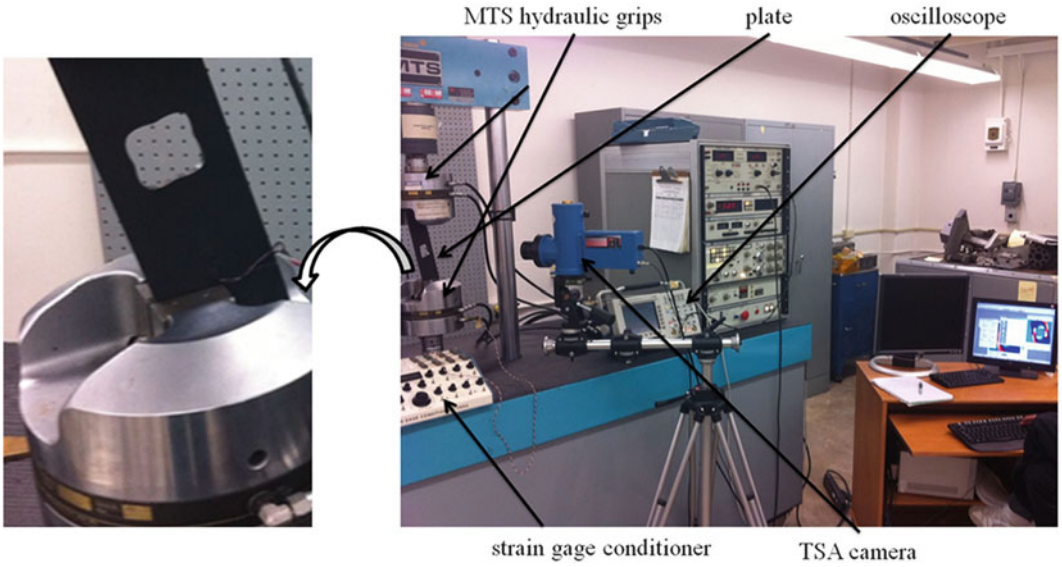

Fig. 7.1 Experimental setup and loading condition

7.2 Experimental Details

A 6061 T-6 aluminum structure, Fig. 7.1, was used to assess the viability of the proposed approach. The structure is 27.94 cm long, 7.62 cm wide, and 0.63 cm thick and at its center is an irregularly-shaped cutout whose exact geometry is unknown. The profile of this arbitrarily-shaped hole was created by passing a B-spline through three defined points. The plate was tilted at 13° from the horizontal axis and then loaded through the hydraulic grips of the MTS hydraulic machine, Fig. 7.1. The lower hydraulic grip applied a cyclic loading varying from 500 lbs to 1,500 lbs (1,000 lbs +/− 500 lbs) at a rate of 20 Hz while the top hydraulic grip held the specimen fixed. Prior to testing, the plate was polished using sand paper and degreased to provide a clean smooth surface, after which the specimen was spray covered with Krylon Ultra-Flat black paint in order to increase the thermal emissivity of the structure. Only two uniform passes were applied to the surface of the structure such that any attenuation effects due to the paint thickness are minimized.

The load-induced temperature data, S^*, were recorded by a liquid nitrogen cooled DeltaTherm model DT1400 camera. The camera used here has a sensor array of 256 horizontal × 256 vertical pixels.

Under adiabatic and reversible conditions associated with the applied cyclic loading, the recorded TSA image, S^*, in Fig. 7.2 is proportional to the summation of stresses as follows [2]:

$$S^* = K\Delta S = K\Delta\left[\sigma_1 + \sigma_2 = \sigma_r + \sigma_\theta = \sigma_x + \sigma_y = \sigma_\xi + \sigma_\eta\right] \tag{7.1}$$

K in Eq. 7.1 is a calibration factor related to the relevant physical properties of the material, surface condition and TSA system parameters [3] and σ_1, σ_2, σ_r, σ_θ, σ_x, σ_y, σ_ξ and σ_η are the normal stresses in the principal, polar, Cartesian rectangular coordinates, and normal and tangential to the edge of the hole, respectively. The calibration factor was obtained using a similar TSA test but on a different non-perforated specimen since there is no region in Fig. 7.2 where the stresses are known.

7.3 Airy's Stress Function

The hybrid approach combines analytical expressions for the stresses from derivatives of the Airy stress function, ϕ, with measured data in Eq. 7.1. In the absence of body forces, a relevant Airy stress function satisfying the biharmonic equation, $\nabla^4\phi = 0$, can be expressed as [4]

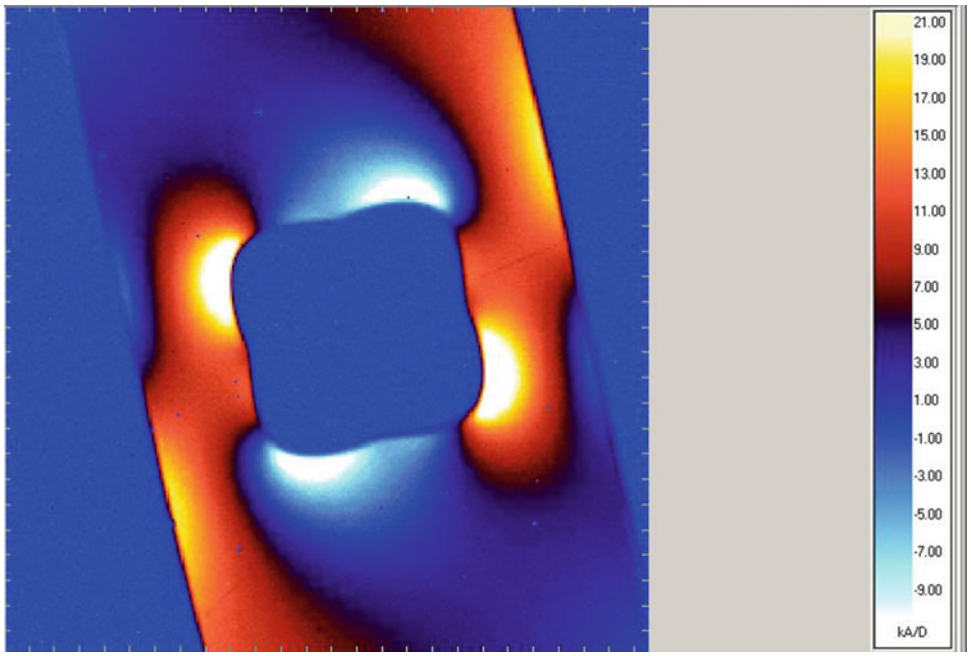

Fig. 7.2 TSA image of perforated plate of Fig. 7.1

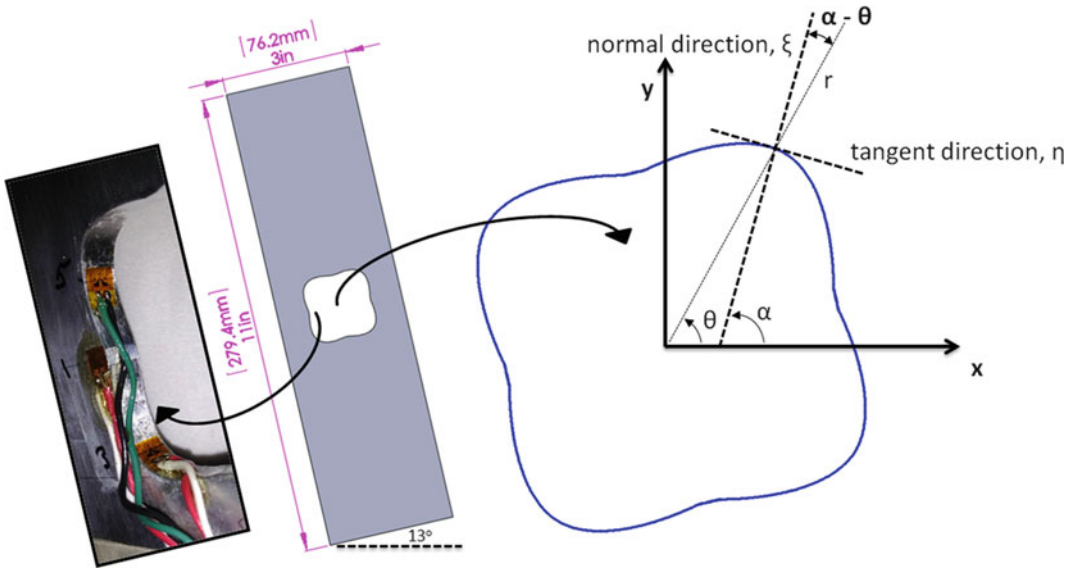

Fig. 7.3 Test specimen dimension, coordinate systems and strain gage locations

$$\begin{aligned}\phi = {} & a_0 + b_0 lnr + c_0 r^2 + A_0\theta + \left(a_1 r + \frac{c_1}{r} + d_1 r^3\right)\sin\theta + \left(a'_1 r + \frac{c'_1}{r} + d'_1 r^3\right)\cos\theta \\ & + \sum_{n=2,3,4\ldots}^{\infty}\left(a_n r^n + b_n r^{(n+2)} + c_n r^{-n} + d_n r^{-(n-2)}\right)\sin(n\theta) \\ & + \sum_{n=2,3,4\ldots}^{\infty}\left(a'_n r^n + b'_n r^{(n+2)} + c'_n r^{-n} + d'_n r^{-(n-2)}\right)\cos(n\theta)\end{aligned} \tag{7.2}$$

where radius r is measured from the center of the hole, angle θ is measured counterclockwise from the horizontal x-axis, Fig. 7.3 and N is the terminating index value of the series and can be any positive even integer.

Upon differentiating equation (7.2), the individual polar components of stress are as expressed as follows:

$$\sigma_r = \frac{1}{r}\frac{\partial \phi}{\partial r} + \frac{1}{r^2}\frac{\partial^2 \phi}{\partial \theta^2} = \begin{array}{l} \frac{1}{r^2}b_0 + 2c_0 + \left(\frac{-2c_1}{r^3} + 2rd_1\right)\sin\theta + \left(\frac{-2c'_1}{r^3} + 2rd'_1\right)\cos\theta - \\ \sum_{n=2,3,4,\ldots}^{N} \begin{bmatrix} a_n n(n-1)r^{n-2} + b_n(n+1)(n-2)r^n \\ +c_n n(n+1)r^{-(n+2)} + d_n(n-1)(n+2)r^{-n} \end{bmatrix} \sin(n\theta) \\ -\sum_{n=2,3,4,\ldots}^{N} \begin{bmatrix} a'_n\, n(n-1)r^{n-2} + b'_n\,(n+1)(n-2)r^n \\ +c'_n\, n(n+1)r^{-(n+2)} + d'_n\,(n-1)(n+2)r^{-n} \end{bmatrix} \sin(n\theta) \end{array} \tag{7.3}$$

$$\sigma_\theta = \frac{\partial^2 \phi}{\partial r^2} = \begin{array}{l} \frac{-1}{r^2}b_0 + 2c_0 + \left(\frac{-2c_1}{r^3} + 6rd_1\right)\sin\theta + \left(\frac{2c'_1}{r^3} + 6rd'_1\right)\cos\theta + \\ \sum_{n=2,3,4,\ldots}^{N} \begin{bmatrix} a_n n(n-1)r^{n-2} + b_n(n+1)(n-2)r^n \\ +c_n n(n+1)r^{-(n+2)} + d_n(n-2)(n-1)r^{-n} \end{bmatrix} \sin(n\theta) \\ +\sum_{n=2,3,4,\ldots}^{N} \begin{bmatrix} a'_n\, n(n-1)r^{n-2} + b'_n\,(n+1)(n+2)r^n \\ +c'_n\, n(n+1)r^{-(n+2)} + d'_n\,(n-2)(n-1)r^{-n} \end{bmatrix} \sin(n\theta) \end{array} \tag{7.4}$$

$$\sigma_{r\theta} = -\frac{\partial}{\partial r}\left(\frac{1}{r}\frac{\partial \phi}{\partial \theta}\right) = \begin{array}{l} \frac{1}{r^2}A_0 + \left(\frac{2c_1}{r^3} + 2rd'_1\right)\cos\theta - \left(\frac{-2c'_1}{r^3} - 2rd_1\right)\sin\theta - \\ \sum_{n=2,3,4,\ldots}^{N} \begin{bmatrix} a_n n(n-1)r^{n-2} + b_n n(n+1)r^n \\ -c_n n(n+1)r^{-(n+2)} - d_n n(n-1)r^{-n} \end{bmatrix} \cos(n\theta) \\ +\sum_{n=2,3,4,\ldots}^{N} \begin{bmatrix} a'_n n(n-1)r^{n-2} + b'_n\, n(n+1)r^n \\ -c'_n n(n+1)r^{-(n+2)} + d'_n\, n(n-1)r^{-n} \end{bmatrix} \sin(n\theta) \end{array} \tag{7.5}$$

With the separate stresses expressed analytically in terms of the various Airy coefficients, Eqs. 7.3 and 7.4 can now be added together and substituted into the right hand side of Eq. 7.1 which relates the experimentally determined values of S with an analytical expression for the quantity $\sigma_r + \sigma_\theta$.

$$S = \sigma_r + \sigma_\theta = \begin{array}{l} 4\,c_0 + 8r\sin\theta d_1 + 8r\cos\theta\, d'_1 \\ +\sum_{n=2,3,4,\ldots}^{N} [4(n+1)r^n b_n - 4(n-1)r^{-n}d_n]\sin(n\theta) \\ +\sum_{n=2,3,4,\ldots}^{N} [4(n+1)r^n b'_n - 4(n-1)r^{-n}d'_n]\cos(n\theta) \end{array} \tag{7.6}$$

Note that the separate expressions for the stresses in Eqs. 7.3, 7.4, and 7.5 necessitate knowing the Airy coefficients A_0, c_1, c'_1, a_n, a'_n, c_n *and* c'_n which do not appear in Eq. 7.6, and hence the need for additional conditions by which to evaluate all of the necessary coefficients and consequently the separate stresses.

7.4 Traction-Free Conditions

The additional conditions are those from imposing the traction-free boundary conditions on the edge of the hole. A normal-tangential coordinate system is employed here to impose the traction-free conditions at the edge of the cutout, Fig. 7.2. Equation 7.7 is used to convert the stresses from polar (r, θ) to normal-tangential (ξ, η) coordinates on the edge of the hole such that σ_ξ and $\sigma_{\xi\eta}$ can be imposed to zero.

$$\begin{Bmatrix} \sigma_\xi \\ \sigma_\eta \\ \sigma_{\xi\eta} \end{Bmatrix} = \begin{bmatrix} \cos^2\psi & \sin^2\psi & 2\sin\psi\cos\psi \\ \sin^2\psi & \cos^2\psi & -2\sin\psi\cos\psi \\ -\sin\psi\cos\psi & \sin\psi\cos\psi & \cos^2\psi - \sin^2\psi \end{bmatrix} \begin{Bmatrix} \sigma_r \\ \sigma_\theta \\ \sigma_{r\theta} \end{Bmatrix} \tag{7.7}$$

The angle ψ used in the transformation matrix of Eq. 7.7 is the angle between the normal direction, ξ, and the polar radial direction, r, Fig. 7.3. In order to determine the angle ψ along the boundary of the hole, 1,272 discrete points on the edge of the hole were first imported from a CAD model of the hole of Fig. 7.1. After which, a second order polynomial was

fitted to a set of three neighboring boundary points. Differentiating the polynomial analytically provides the slope, hence the tangential and normal directions and ultimately the angle ψ, at the midpoint of the polynomial. Repeating this process incrementally at overlapping sets of neighboring points along the edge of the hole gives ψ at the 1,272 discrete positions on the boundary.

7.5 Results

Once the TSA image has been recorded and calibrated, a set of linear isopachic expressions of the form of Eq. 7.6, as well as the set of linear equations from imposing the local traction-free boundary conditions ($\sigma_\xi = \sigma_{\xi\eta} = 0$) at the hole, can be written in matrix form as follows:

$$[A]_{(m+2h)\ \mathrm{x}\ k}\ \{c\}_{k\ \mathrm{x}\ 1} = \{d\}_{(m+2h)\ \mathrm{x}\ 1} \tag{7.8}$$

where [A] is the $m + 2h$ by k Airy matrix composed of m isopachic Airy expressions of the form of Eq. 7.6 in terms of r and θ associated with the m selected source locations of the input values of S as well as $2h = 2{,}554$ traction-free boundary conditions of the form $\sigma_\xi = \sigma_{\xi\eta} = 0$, {c} is the set of k unknown Airy coefficients and vector {d} includes the set of m data values for S at the same set of image data locations used in [A] as well as the $\sigma_\xi = \sigma_{\xi\eta}$ consequences on the edge of the hole.

The locations of the measured input TSA data were selected such that pixels were equally separated and distributed across the component's area of interest. Only recorded temperature values which originated at least two pixels away from the edge of the hole were used. Based on that, the number of data points used here is $m = 19{,}600$ while the number of Airy coefficients used is $k = 90$.

Figure 7.4 compares the isopachic stress contours of the reconstructed TSA image from the hybrid technique versus the original TSA information. The good agreement between the two contour plots validates the choice of the number of Airy

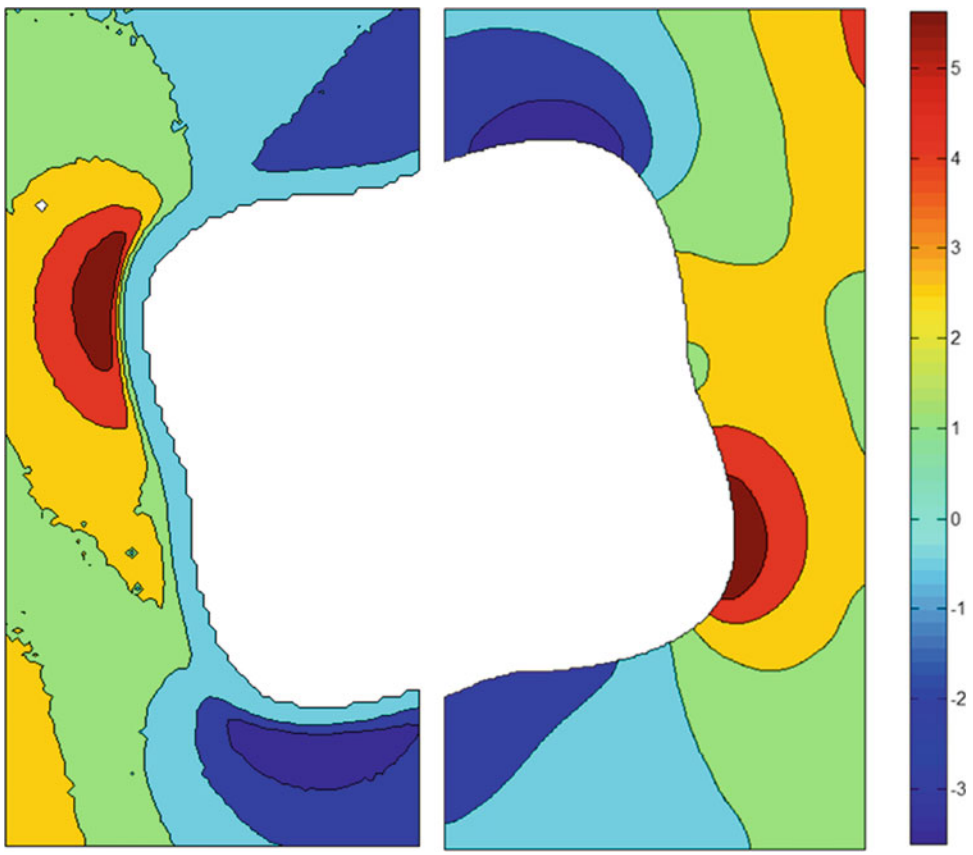

Fig. 7.4 Contour plots of S from measured TSA (*left*) and reconstructed based on the determined Airy coefficients (*right*)

Fig. 7.5 Stress contour plots of σ_θ/σ_0 from FEA (*left*) and hybrid (TSA + Airy's stress function) (*right*)

Table 7.1 Strain comparison from gage measurements, FEA and hybrid TSA method

ε_θ for a static load of 4,448 N (1,000 lbs)				
Location on curved surface	Strains from gages	Average strain from gages	Hybrid TSA	FEA
$\theta = 232^\circ$	0.93×10^{-3}	0.91×10^{-3}	0.89×10^{-3}	0.87×10^{-3}
$\theta = 52^\circ$	0.89×10^{-3}			
$\theta = 338^\circ$	-0.42×10^{-3}	-0.41×10^{-3}	-0.48×10^{-3}	-0.44×10^{-3}
$\theta = 158^\circ$	-0.40×10^{-3}			

coefficients and data points used ($m = 19{,}600$ and $k = 90$). Moreover, the advantage of hybridizing TSA data over solely using TSA results is evident from Fig. 7.4 as the stress contours are cleaned of any noise or dead pixels and most importantly, the of results right at the edge of the irregularly-shaped cutout are now available reliably.

For comparative purposes, an ANSYS finite element model was generated using Plane-82 isoparamteric elements to model the unsymmetrically loaded tensile plate of Fig. 7.3. The boundary conditions at the ends of the specimen, Fig. 7.1, were replicated numerically using different ways. Figure 7.5 compares the normalized hoop stresses from the hybridized TSA data and finite element prediction.

Table 7.1 compares the hybrid TSA obtained normalized strains at a static load of 5,337.6 N with those from commercial foil strain gages mounted on the transverse curved edge of the hole at each of $\theta = 52^\circ$, 158°, 232° and 338°, Fig. 7.3 (left). Angle θ is measured from the global horizontal axis as identified in Fig. 7.3.

7.6 Conclusion

The present paper demonstrates the ability to determine the independent components of stress on and near the edge of an arbitrarily-shaped hole in an unsymmetrically loaded tensile structure by combining TSA data with an Airy stress function. The traction-free conditions were imposed discretely on the edge of the hole using a different tangential-normal coordinate system at each boundary location. Unlike purely analytical or numerical techniques, the present hybrid method enjoys the

advantages of not having to know the material properties or external loading conditions. Particularly the latter are often unknown in practice. Utilizing a stress function in real (rather than complex) variables for other than a circular cut-out is highly convenient. The approach smoothes the measured data and provides the full-field separate stresses. Moreover, and unlike displacement-based techniques, these are accomplished without having to differentiate any measured data.

References

1. Samad WA, Rowlands RE (2012) Hybrid full-field stress analysis of finite structures containing arbitrarily-shaped cutouts. In: International symposium on experimental mechanics ISEM'12, Taipei, 8–11 Nov2012
2. Greene RJ, Patterson EA, Rowlands RE (2008) Thermoelastic stress analysis, Ch. 26. In: Sharpe WE (ed) Handbook of experimental solid mechanics. Springer, New York
3. Dulieu-Barton JM, Stanley P (1998) Development and applications of thermoelastic stress analysis. Strain Anal 33:93–104
4. Soutas-Little RW (1998) Elasticity. Dover Publications, New York

Chapter 8
Quantitative Themographic Characterization of Composites

Steven M. Shepard

Abstract Thermography has become a widely accepted method for NDT of composite structures. The low thermal effusivity of polymer and ceramic matrix components makes the time scale and signal strength of their response to thermal excitation nearly ideal for thermographic inspection methods. At present, composite NDT applications are primarily qualitative, based on identification of discrete flaws such as delaminations, voids, inclusions or unbonds. Quantification is limited to flaw sizing, and to a lesser extent, measurement of flaw depth or thermal diffusivity. Using the Thermographic Signal Reconstruction (TSR) method to interrogate each pixel time history individually, it is possible to accurately measure flaw size and depth, and also to characterize the thermophysical properties of the constituent layers of a multilayer sample. This type of material characterization task can be performed by quantitative analysis of the logarithmic time derivatives and their attributes, obtained from the TSR analysis. However, a significant amount of information can be inferred from the basic shape characteristics of the derivatives. As an example, we present a set of primitives that represent 2nd derivative responses for various one and two layer material configurations.

Keywords Thermography • Nondestructive • Thermographic signal reconstruction • Primitives

8.1 Introduction

Active thermography has become a widely used method for Nondestructive Testing (NDT) of composite materials. In the most basic configuration, the surface of a test article is subjected to a thermal stimulus, and observed with an infrared camera as it responds to that stimulus [1]. The subsurface state of the sample is then inferred from the dynamic response of the surface temperature, based on the assumption that subsurface variations in thermophysical properties, whether intentional or anomalous, affect the flow of heat from the sample surface to the interior of the sample and result in transient surface temperature changes. The stimulus is usually a transient heat source, although cooling excitation may also be employed. This approach can be applied qualitatively, to identify subsurface anomalies, or quantitatively, to measure thermal diffusivity or thickness of a sample. However, the accuracy of the measurement depends on several factors associated with the 3 primary operations that comprise the method:

Thermal excitation – The type, duration and amplitude of the excitation method are selected to match the characteristics of the test piece.

Surface temperature measurement – The sampling rate, wavelength, sensitivity and spatial resolution of the IR camera, and the degree to which surface-emitted IR radiation is successfully measured, (as opposed to reflected background radiation).

Data analysis and processing – In simple cases, large, severe flaws can be detected by viewing the unprocessed image data from the IR camera. However, most modern implementations of thermography employ some degree of signal processing to improve sensitivity and accuracy.

S.M. Shepard (✉)
Thermal Wave Imaging, Inc, 845 Livernois, Ferndale MI 48220, USA
e-mail: sshepard@thermalwave.com

M. Rossi et al. (eds.), *Residual Stress, Thermomechanics & Infrared Imaging, Hybrid Techniques and Inverse Problems, Volume 8*, Conference Proceedings of the Society for Experimental Mechanics Series, DOI 10.1007/978-3-319-00876-9_8,

8.1.1 Thermographic Flaw Detection and Materials Characterization

Thermography has been most widely used for flaw detection based on feature contrast, i.e. visual evaluation of the contrast between an indication of a subsurface feature and the flaw-free sample background in the IR image. Effectively, the operator identifies either "hot spots" associated with internal flaws that obstruct the flow of heat (e.g. a composite delamination), or "cold spots", indicating a subsurface inclusion that absorbs incident heat (e.g. water trapped in composite honeycomb core). This approach is often employed for simple applications where the indication is obvious in the image sequence. While relatively inexpensive and easy to implement, it requires subjective interpretation by the operator and is highly susceptible to excitation nonuniformity. More significantly, it presupposes that a flaw-free background can be identified, or that it even exists in a particular sample. For many applications, e.g. quality control, a discrete flaw may not exist, and the "flaw" may be extended and larger than the field of view of the thermography system. In such cases, a seriously flawed and flaw-free sample may not be distinguishable using contrast based analysis.

8.1.2 Single Point Analysis

Modern methods tend to eschew contrast analysis, and instead, employ approaches that treat each pixel as an independent time history [2]. The most basic example of thermographic signal response is that of a defect-free, infinitely-thick slab heated by an instantaneous, uniform source [3]. The solution for surface temperature relative to the pre-flash temperature in this case is

$$\Delta T(t) = \frac{Q}{e\sqrt{\pi t}} \tag{8.1}$$

where Q is the energy absorbed by the sample per unit area, and e is the thermal effusivity, given by

$$e = \sqrt{k\rho C} \tag{8.2}$$

where k, ρ and C are the thermal conductivity, density and heat capacity, respectively.

Taking the logarithm of both sides of Eq. 8.1, we observe that the logarithmic surface temperature decreases with a linear dependence on the log of time, with slope −0.5.

$$\log(\Delta T) = \log\left(\frac{Q}{e}\right) - 0.5\log(\pi t) \tag{8.3}$$

For the more realistic configuration of a slab with finite thickness L, we obtain a more complex series solution for surface temperature (Fig. 8.1)

$$T(x,t) = \frac{Q}{\rho C L}\left[1 + 2\sum_{n=1}^{\infty} e^{\frac{\alpha n^2 \pi^2 t}{L^2}} \cos\left(\frac{n\pi x}{L}\right)\cos\left(\frac{n\pi x'}{L}\right)\right] \tag{8.4}$$

where x and x′ indicate the depth of the heat source and field point, respectively. For front surface heating and measurement, both x and $x' = 0$.

Comparing the log of Eqs. 8.3 and 8.4, we find that they behave identically immediately after excitation, but Eq. 8.4 deviates from straight-line behavior at time t^*, depending on slab thickness (L) and thermal diffusivity (α) according to the relationship

$$t^* = \frac{L^2}{\pi\alpha} \tag{8.5}$$

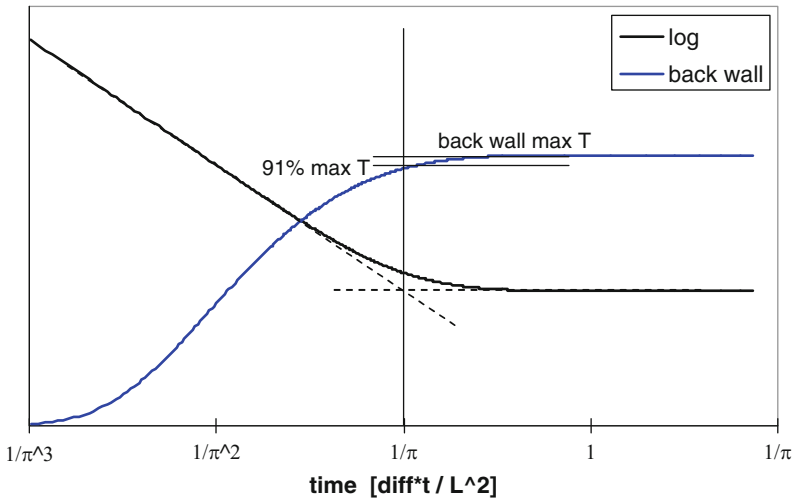

Fig. 8.1 Rear wall (*blue*) and logarithmic front surface (*black*) temperatures. The break from linearity in the front surface temperature occurs at the intersection of asymptotes at time at time 1/π, expressed in dimensionless units of αt/L^2

It is often useful to express t^* in dimensionless coordinates, where

$$\tau = \frac{\alpha t}{\pi L^2} \tag{8.6}$$

$$\tau^* = \frac{1}{\pi} \tag{8.7}$$

The physical significance of t^* can be understood by considering Eq. 8.4 in the case where heating occurs at the front surface ($x' = 0$) and temperature is measured at the back wall ($x = L$). We find that at time t^* the back wall reaches 91 % of its maximum temperature.

8.1.3 Thermographic Signal Reconstruction

The Thermographic Signal Reconstruction (TSR) method is a widely used processing approach in composite NDT applications [4–7]. It is particularly useful in situations where high sensitivity or automation is required, and has been adapted to pulsed, step and modulated excitation. The method builds on the simplicity of the behavior of the logarithmic temperature vs. time plot, and amplifies anomalous deviations from linearity. In TSR, the logarithmic temperature response of each pixel is fit to a simple function (e.g. a low order polynomial), using a least squares fit algorithm. The resulting equation is a replica of the original data that is free of temporal noise, enabling further processing without generation of additional noise.

The derivatives of the logarithmic signal, calculated with respect to logarithmic time are extremely useful in identifying and amplifying deviations from normal thermal diffusion [8]. Figure 8.2 shows the logarithmic surface temperature and derivatives for a flaw-free slab. For an infinitely thick, flaw-free sample, the 1st and 2nd derivatives begin with constant values of −0.5 and 0, respectively, and independently of the sample material or the amount of energy applied to the sample surface. However, as time evolves, the presence of a subsurface interface perturbs normal 1-dimensional diffusion and causes the derivatives to change in a predictable way.

8.1.4 Logarithmic Derivative Characteristics

The logarithmic derivatives calculated in TSR provide a useful means for non-imaging material characterization, so that some information about the local subsurface state of a sample can be obtained from a single pixel time history, without reference to an image or other pixels in the image. The derivative plots shown in Fig. 8.2 represent the ideal, limiting case of a slab with adiabatic boundary conditions at the back wall, i.e. no heat passes through the back wall. While the scale of the

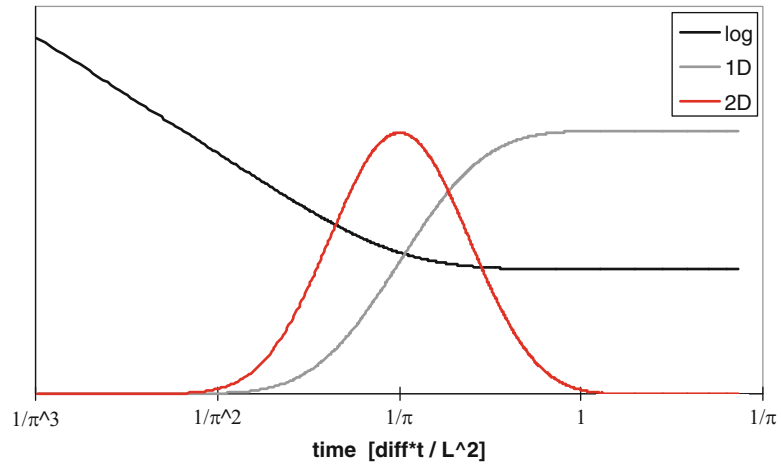

Fig. 8.2 Time evolution of the logarithmic front surface temperature and its 1st and 2nd derivatives, shown in dimensionless time units

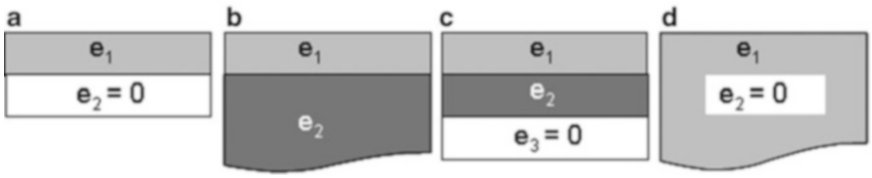

Fig. 8.3 Basic sample configurations (**a**) adiabatic slab, (**b**) infinitely thick second layer, (**c**) second layer with finite thickness and adiabatic back wall, (**d**) infinitely thick with laterally discrete adiabatic discontinuity

log plot may change with the composition of the slab or the amount of energy absorbed at the surface, the 1st and 2nd derivatives of the adiabatic slab are invariant, maintaining their shape, but translating along the x axis as thickness or thermal diffusivity of the slab changes. The logarithmic 2nd derivative can be approximated by a Gaussian function with amplitude 0.47 and standard deviation 0.5941. The 1st derivative, by definition, is the integral of the Gaussian, i.e. the error function erf(), ranging between −0.5 and 0 [8]. The amplitude zero expresses a physical upper limit of the 1st derivative, since an amplitude greater than zero would indicated a sample that is generating heat, rather than one that is cooling.

8.1.5 Logarithmic Derivative Primitives

It is possible to characterize several multi-layer situations beyond the adiabatic case using logarithmic derivative primitives, which may be based on either 1st or 2nd derivative characteristics. In the multilayer case, overall derivative response can be characterized according to the ratio of thermal effusivities (e_n) of the n layers (Fig. 8.3).

The 2nd derivative signals for cases a–c can be generated using inverse Laplace transform (quadrupole) modeling (Fig. 8.4) [10]. It is useful to present these in dimensionless time coordinates so that varying geometries and material properties can be compared. The response for case d is generated using finite difference modeling Fig. 8.5. We present select 2nd derivative primitives below:

(a) Adiabatic slab ($e_2 = 0$): The 2nd derivative is a positive Gaussian function, as described above (Fig. 8.2).
(b) 2-layer sample with infinitely thick second layer:

1. e2 < e1: The 2nd derivative is a positive Gaussian function with amplitude is less than that of the adiabatic case. After the positive peak the derivative crosses zero and remains negative, approaching zero asymptotically (Fig. 8.4).
2. e2 > e1: The 2nd derivative is a negative function that reaches a minimum at a time later than t^* and then crosses zero and reaches a maximum, after which, it asymptotically approaches zero.

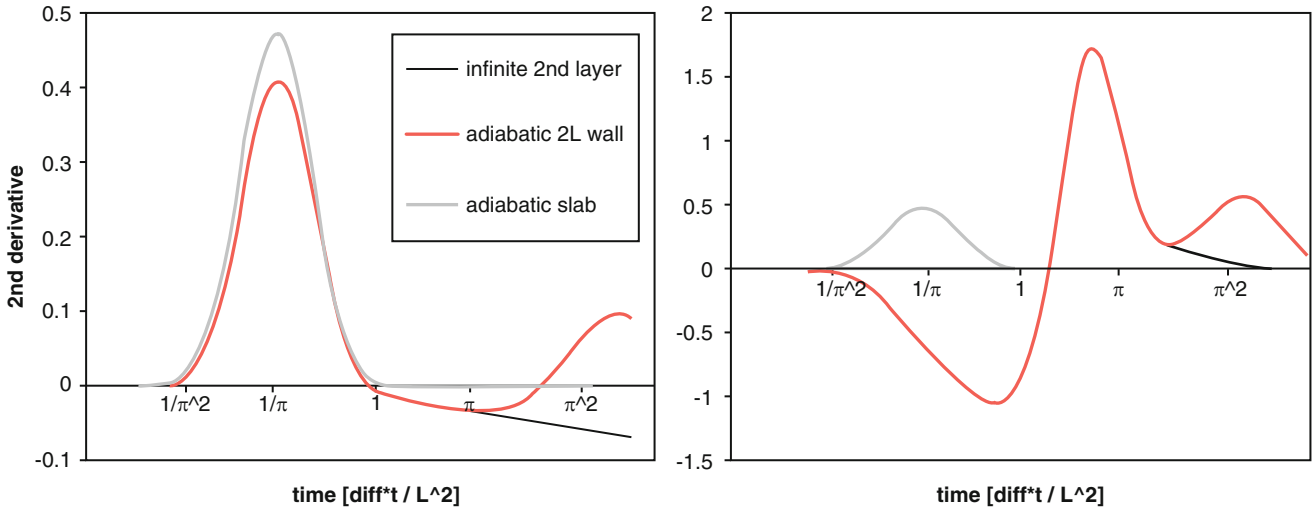

Fig. 8.4 2nd derivative for two-layer sample configurations with e2 < e1 (*left*) and e2 > e1 (*right*). The adiabatic slab is shown (*gray*) for reference

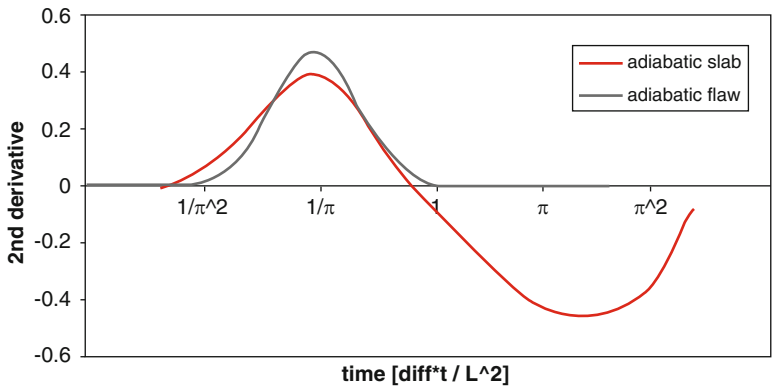

Fig. 8.5 2nd derivative for an infinitely thick sample with a laterally finite adiabatic discontinuity. The adiabatic slab with thickness equal to the flaw depth is shown in gray for comparison

(c) 2-layer sample with finite second layer and adiabatic back wall:

1. e2 < e1: Behavior is identical to infinitely thick 2nd layer e2 < e1 case, except that the negative derivative crosses zero and displays a positive peak.
2. e2 > e1: Behavior is identical to infinitely thick 2nd layer e2 > e1 case, except that the signal displays a 2nd positive peak associated with the back wall.

(d) Spatially discrete adiabatic flaw in an infinitely thick sample

1. The 2nd derivative reaches a positive peak at the time t^* associated with flaw depth L, based on Eq. 8.5, where the peak amplitude is less than or equal to that of the adiabatic slab. The signal then crosses zero and remains negative. Approaching zero asymptotically (Fig. 8.5).

8.2 Experiment

A composite laminate sample was examined using flash thermography to demonstrate the behavior of logarithmic derivative signals and compare image contrast and single pixel-based analysis methods for detection of embedded flaws. The flaws represent varying degrees of difficulty of detection, and illustrate the issues involved in performing thermographic NDT on

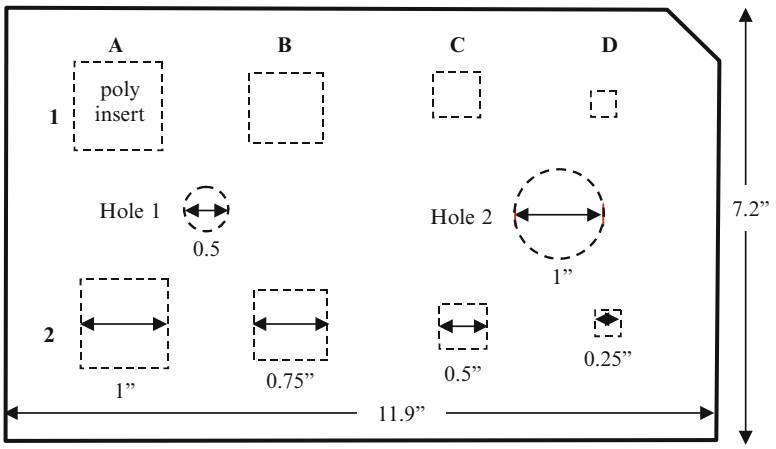

Fig. 8.6 12-ply graphite epoxy test sample with polymer inserts embedded mid-depth, and back-drilled flat bottom holes

composite samples. Experiments were performed on a 12-ply graphite epoxy test sample with plies orientation 0, ±45, ±90 and dimensions 11.9″ × 7.2″ × 0.12″. Eight polymer inserts with nominal thickness 0.1″ were embedded in two identical rows between plies 6 and 7, the approximate mid-depth of the panel. The inserts were square shaped with respective dimensions of 1″, 0.75″, 0.5″ and 0.25″ per side. Flat bottom holes were also machined in a center row, with diameters 1″ and 0.5″, and depths 0.70″ and 0.66″, respectively (Fig. 8.6).

The samples were tested using a commercial flash thermography system with two quartz-xenon linear flash lamps, housed in a reflective hood [9]. Each lamp is mounted in a reflector and driven by a 6 kJ power supply that provides a truncated rectangular optical pulse with variable duration ranging from 10 msec to 200 microseconds. The system employs a 640 × 480 pixel InSb camera operating in the 2–5 μm spectral range at a maximum full frame rate of 130 Hz (higher frame rates are attained by reducing the frame size). Digital data from the camera is transferred to a PC in real-time, and the temperature-time sequence immediately before, during and after flash heating is processed using TSR on each pixel in a dedicated software program that displays the reconstructed signal, as well as its 1st and 2nd logarithmic derivatives and various attributes of the derivatives.

The sample was placed 12″ from the camera lens and lamps and heated with a 3 msec duration rectangular flash pulse. Data was acquired for 33 msec prior to the flash pulse and for 30 s after, at a frame rate of 30 Hz. The sample was inspected in “as is” condition, i.e. no surface preparation was applied.

8.3 Results

8.3.1 Contrast Analysis

The unprocessed data sequence was compared to the processed TSR 2nd derivative sequence, so that they could be viewed simultaneously in a running movie display. The flat bottom holes were readily detected in both sequences, although the shape and size of each hole was more clearly defined in the derivative sequence. The inserts were only visible in the derivative sequence. The “best” image of each sequence in terms of detection of the inserts was determined by evaluating signal to background contrast for a square region covering 75 % of the actual insert size for the insert upper left corner of the sample (Fig. 8.7).

8.4 Observations

The back wall and flat-bottom hole in the composite laminate correspond to the adiabatic slab and spatially finite adiabatic flaw cases described by 2nd derivative primitives a and d described in Sect. 8.5 (Fig. 8.8). Both derivative signals display the peak and zero crossing behavior predicted by the primitives. The peak associated with the flat bottom hole occurs earlier than that of the back wall signal, consistent with the relative depth of the features.

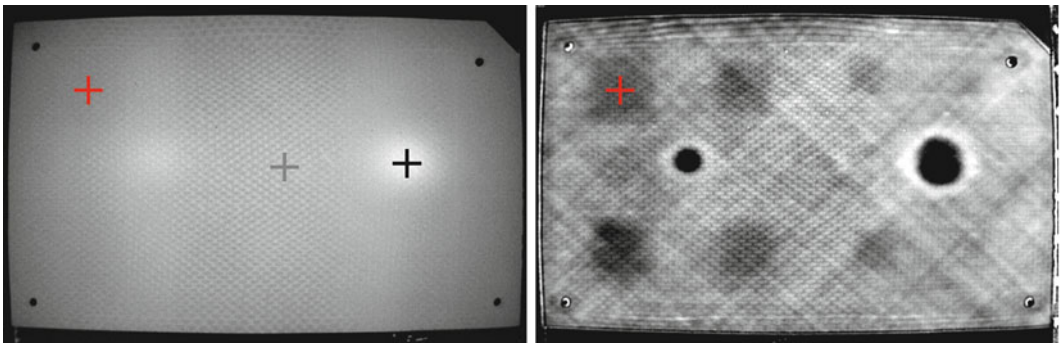

Fig. 8.7 Highest signal to background images from the cooling time sequence for the unprocessed IR image and the TSR 2nd derivative, based on evaluation of the 1″ insert in the upper left of the sample

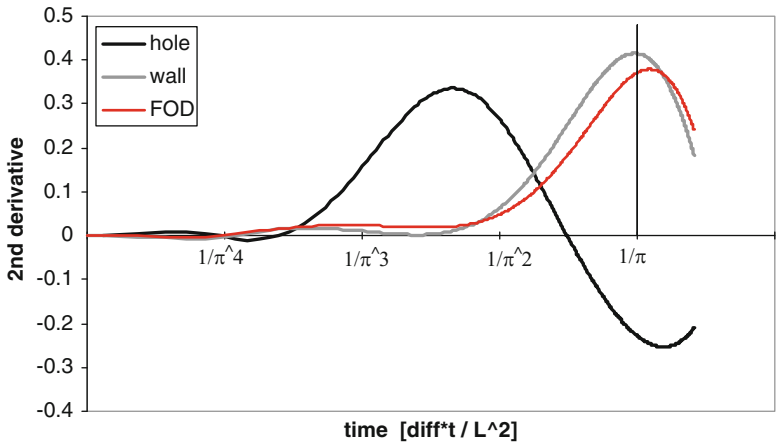

Fig. 8.8 2nd derivative of points corresponding to the back wall (*gray*), flat bottom hole (*black*) and a Teflon insert

Table 8.1 Typical thermal effusivities

Material	Typical thermal effusivity [J/(m^2 C $\sqrt{s}$)]
Graphite epoxy (perpendicular orientation)	1,240
Polymer film	750
Air (273 K)	5

The polymer insert has the characteristics of the adiabatic slab primitive. It is quite similar to the back wall signal, except for the fact that it has slightly lower amplitude and its peak is delayed in time. Intuitively, this might seem curious, since the inserts are at the same depth plane as the flat-bottom hole, and it is reasonable to expect their derivative peaks to occur simultaneously. However, the amplitude of the derivative signal for a particular interface is determined by the ratio of thermal effusivities of the constituent layers. As e2/e1 approaches unity, the interface becomes undetectable. Typical effusivity ratios of graphite epoxy to air are on the order of hundreds, producing a strong derivative signal, based on Table 8.1. However, the graphite epoxy to polymer ratio is <5, which accounts for the fact that the expected derivative signal does not appear. However, the presence of the insert is observed later in the signal, in the retardation of the back wall signal. Unlike the flat-bottom hole, the insert does not substantially block the flow of heat, but it does delay its arrival at the back wall.

8.5 Conclusions

The 2nd derivative primitives presented here are by no means comprehensive. Actual samples are likely to be some combination of the primitive cases described here, subject to the usual limitations imposed by thermal diffusion, e.g. the necessity for diameter to depth ratio >1 for discrete flaws. The primitives are intended to serve as broad classifiers, which allow some qualitative assessment of local subsurface conditions to be made based on the behavior a single pixel. Using the primitives, it is relatively easy to discriminate between the sample types discussed. Similar primitives can be created using the logarithmic first derivative, or for samples with more layers. As demonstrated in the experiment on the composite panel, features such as the polymer inserts, can occur that are not uniquely represented by a primitive. Cases such as these may manifest themselves as perturbations of one, or more, of the primitives, exemplified by the delayed peak and reduced amplitude of the insert relative to the back wall primitive.

References

1. Xavier PVM (2001) Theory and practice of infrared technology for nondestructive testing, 1st edn. Wiley-Interscience, New York
2. Genest M (2009) Image processing for automated flaw detection in pulsed thermography. In: 6th international workshop-NDT signal processing, London, Ontario, Canada, Nov 2009, pp 1–9
3. Carslaw HS, Jaeger JC (1986) Conduction of heat in solids, 2nd edn. Oxford University Press, New York
4. Balageas DL (2011) Defense and illustration of time-resolved pulsed thermography for NDE.In: Proceedings of SPIE 8013, thermosense: thermal infrared applications XXXIII, Vol 80130, 2011. doi:10.1117/12.882967
5. Shepard SM,(2004) System for generating thermographic images using thermographic signal reconstruction. US Patent 6,751,342, 15 June 2004
6. Shepard SM, (2003) Temporal noise reduction, compression and analysis of thermographic image data sequences. US Patent 6,516,084, 4 Feb 2003
7. Shepard SM,(2010) Automated binary processing of thermographic sequence data. US Patent 7,699,521, 20 April 2010
8. Shepard SM, Hou YL, Lhota JR, Golden JM (2007) Automated processing of thermographic derivatives for quality assurance. Opt Eng 46(5):051008
9. Echotherm®, Thermal Wave Imaging, Inc., Ferndale, MI, USA
10. Maillet D, André S, Batsale JC, Degiovanni A, Moyne C (2000) Thermal quadrupoles: solving the heat equation through integral transforms. Wiley, New york

Chapter 9
Thermal Deformation of Micro-structure Diffuser Plate in LED Backlight Unit

Chun-Cheng Chen, Chi-Hui Chien, Bo-Syun Chen, Ting-Hsuan Su, Jyun-Jie Li, Jia-Wei Che, Jie-Lin Yu, and Zhi-Yan Wang

Abstract In this research, the thermal deformations and thermal warpages of micro-structure diffuser plate in LED backlight unit subjected to long lighting state were studied. The thermal deformations and warpages were obtained by adopting finite element method. In order to obtain more accurate finite element solutions, instead of using the data collected from the existed literatures, the Young's modulus, Poisson's ratio, and thermal expansion coefficient of the micro-structure diffuser plate were proposed to be measured by using micro tensile test and thermomechanical analyzer, respectively, in advance. Then the measured mechanical properties were be used as the input data for finite element simulations. By comparing the finite element results with the experimental results measured by using strain gauges, it can be seen that the differences were within in 3 %. In this research, the thermal warpage phenomena of micro-structure diffuser plate corresponding to different temperature were discussed. Also, the difference of the thermal deformation between conventional diffuser plate and micro-structure diffuser plate were compared.

Keywords Conventional Diffuser Plate • LED Backlight Unit • Micro-Structure Diffuser Plate • Thermal Deformation • Thermal Warpage

9.1 Introduction

Liquid crystal displays (LCDs) have been widely used in the information technology such as LCD-TV, LCD monitor, laptop computer and mobile phones. Direct-type LED BLU answers LCD TV characters required to have wide vision, high illumination, and high contract. An important element of most direct-type LED BLU is diffuser plate that diffuses and/or refracts light directly from the LED and supports the other films and panel called Conventional Diffuser Plate. Lately, a new and innovative product, Micro-structure Diffuser Plate (MDP), has been developed. MDP is used to refract light for the purpose of collimating the light to the viewer, increase luminance and decrease number of LED at the same time as an average power reduction of 30 % instead of conventional diffuser plate. MDP is optical device with one side covered by a linear array of micro-structure. The direct-type LED BLU utilizes a lot of LEDs directly under the diffuser plate so as to provide enough luminance to liquid crystal panel. However, it comes after that the high heat energy originated from the LEDs in the LED BLU caused thermal problem, emitted heat results in a high thermal strain on compound material diffuser plate. Common issues with MDP include plate distortion, which causes optical defects after long-term environmental exposure, and scratching or flaking of the micro-structure surface. Due to the temperature increase, thermal deformations will occur in the MDP and result mura, which will generate danger to the liquid crystal panel.

Using LED as a light source for backlights has a lot of benefits, as discussed in previous papers [1, 2], The direct-lit BLU is comprised of several kinds of optical materials, such as a reflective film, diffusing plate, diffusing sheet, and reflective film, etc [3, 4]. The diffuser plate is one of important components in LCDs and it is made from the Polymethyl Methacrylate (PMMA) or PolyCarbonate (PC) or Polystyrene (PS). The diffuser plate is used to homogenize the distribution of the output light resulting in the Lambertian distribution on it, which means equal luminance irrespective of the viewing angle.

C.-C. Chen • C.-H. Chien (✉) • B.-S. Chen • T.-H. Su • J.-J. Li • J.-W. Che • J.-L. Yu • Z.-Y. Wang
Department of Mechanical and Electro-Mechanical Engineering, National Sun Yat-Sen University, No. 70, Lien-Hai Road, Kaohsiung 80424, Taiwan ROC
e-mail: chchien@faculty.nsysu.edu.tw

M. Rossi et al. (eds.), *Residual Stress, Thermomechanics & Infrared Imaging, Hybrid Techniques and Inverse Problems, Volume 8*, Conference Proceedings of the Society for Experimental Mechanics Series, DOI 10.1007/978-3-319-00876-9_9,

Kim et al. studied diffusion plate with PET/PC/PBT copolymer and PMMA diffusion plate modified with glass fibers in a direct-backlight of a LCD, and both of them have better thermo-physical properties and water absorption compared with conventional PMMA [5, 6]. Due to price of PS is lower than the others; PS material is used widely in conventional diffuser plate and MDP. It is well known that the common disadvantage of Polystyrene is that its mechanical properties are quite unstable. The environments in which LCDs may be operated are elevated temperature from LED. Chu et al. set up a systematic analysis by using finite element analysis (FEA), computational fluid dynamics (CFD), and structure-heat transfer, to simulate warpage due to heat source from CCFLs in the backlight module of a TFT-LCD TV [7]. Although MDP can decrease effectively the number of LED and concentrate light to increase luminance in order to get out diffuser sheet or BEF, yet structure of the top is different from bottom side that will lead to large deformation. Therefore, the considerable thermal deformation of the MDP could possibly lead to poor display quality of LCDs but attention has not been paid on this issue no matter in industrial or academic research. Moreover, Young's modulus, Poisson's ratio and Coefficient of thermal expansion are the most fundamental properties in mechanics investigation. The micro tensile test was first employed to directly measure Young's modulus [8, 9]. The other hand, strain gauges were used to measure strain of the conventional diffuser plate and the MDP in order to acquire really thermal deformation under BLU operating high temperature. The large deformation from diffuser plate can cause quality issues on panel. C. Yi. Chu, et al. studied Thermal Analysis and Experimental Validation on TFT-LCD Panels for Image Quality Concerns [10]. Park et al. analyzed the thermal deformation of the sheet inside using FEM. The results of temperature distribution were shown in the finite element analysis comparing with experimentation [11]. In the published literature, the investigation on the mechanical properties and thermal deformation of the diffuser plate is very limited, much less MDP. The purpose of this research is to study the effects of heat source from LEDs to MDP using the 10 in. direct-type commercial LED BLU in compliance with mechanical properties from experiment. On the other hand, the characteristics of the conventional diffuser plate and MDP can be compared with each other. In this paper, we first proposed a methodology combining the micro tensile test, strain gauges and thermomechanical Analyzer (TMA Q-400) to characterize Young's modulus, Poisson's ratio and Coefficient of thermal expansion of the conventional diffuser plate and MDP from 10 in. direct-type commercial LED BLU. Simultaneously, the finite element analysis (FEA), which was imported some above mechanical parameters, was utilized to simulate thermal deformation of the conventional diffuser plate and MDP in order to verify the precision compared with our experiment data by strain gauges. This paper verified the accuracy of the measurement parameters were, respectively, substituted into a numerical model based on the finite element analysis (FEA) to simulate thermal deformation and verified their difference of with those of the experimental results using strain gauges, simultaneously, to realize influence of micro-structures on the surface of the MDP compared with the conventional diffuser plate.

9.2 Experiment

The 10 in. direct-type commercial LED BLU was used in this study as shown in Fig. 9.1. The BLU was comprised of several kinds of optical materials such as one conventional diffuser plate (237.5 × 137.5 × 1.5 mm) or MDP (237.5 × 137.5 × 1.5 mm with microstructure), one reflective film and two diffuser sheets. The operating temperature distributions to the surface of diffuser plates were measured by thermal couple. Then the temperature impacts on diffuser plates can be studied. Besides, the Young's modulus, Poisson's ratio, and thermal expansion coefficient of diffuser plates were proposed to be measured by using micro tensile test, strain gauges and thermomechanical analyzer, respectively.

The temperature histories of LED and two sides of the conventional diffuser plate or MDP were measured and recorded. The data were taken every 5 min for 60 min continuously in order to study the temperature variation of the LED BLU corresponded to thermal deformation of the conventional diffuser plate and MDP during operating status. Figure 9.2 shows the temperature versus lighting time curves of each material of the 10 in. LED BLU, respectively. It can be seen that the temperature variation will become stable after the LED BLU was on for 60 min. The raise of temperature was after 60 min of the LED BLU, the diffuser plate is about $41°C$ on both surface-sides.

On the other hand, prepared in the dimensions following the suggestion in the ASTM D-638-03 [12], and its geometrical configuration is shown in Fig. 9.3. After the preparation of the conventional diffuser plate and MDP according to the prescribed geometry, it was gripped by the jigs of the micro tensile testing machine (Instron 5564).

Then the tensile force was applied, and the displacement and the applied load were simultaneously recorded by the micro tensile testing machine. For the experimental setting, the acquisition frequency of experimental data is 10 times/s, and the maximum load and speed are 5N and 5 mm/min, respectively. The relation between the stress and strain had been addressed in the theoretical description of the micro tensile test [13]. Finally, Young's modulus and Poisson's ratio of the conventional diffuser plate and MDP can be calculated from the slope of the fitting curve for stress versus strain relation

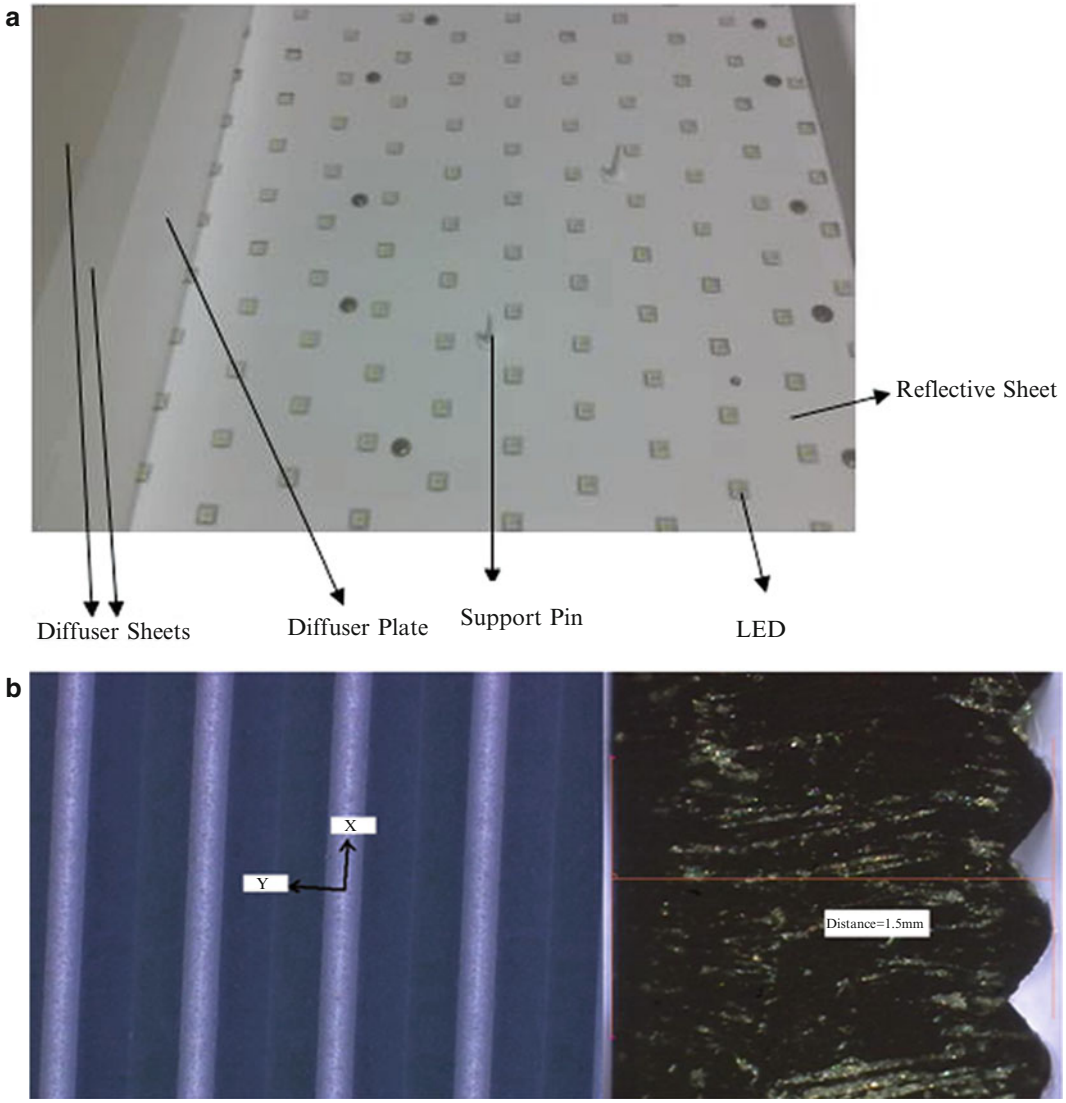

Fig. 9.1 (**a**) The structure of LED BLU comprised of a diffuser plate, two diffuser sheets, a reflective film and a lot of light source LED (**b**) Figure of the Microstructure Diffuser Plate (MDP)

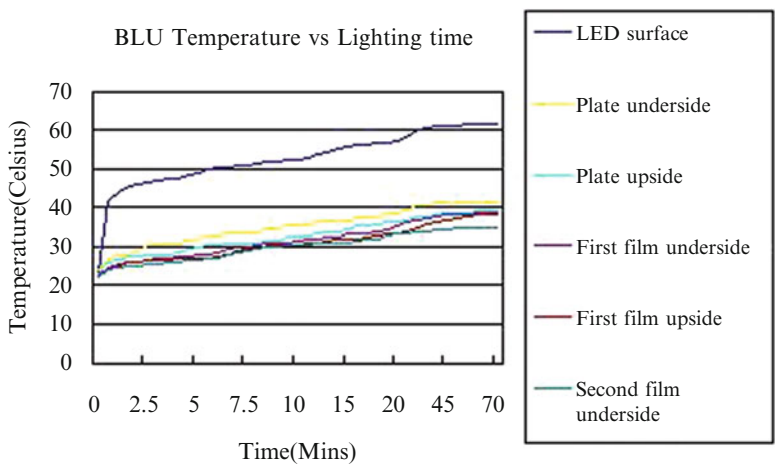

Fig. 9.2 The temperatures of BLU lighted status

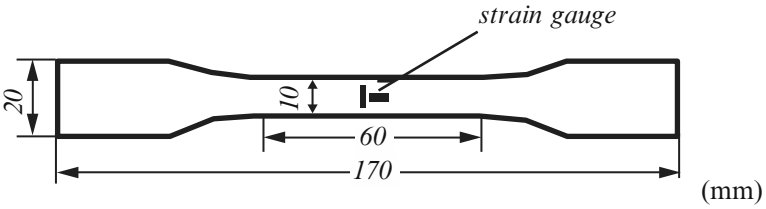

Fig. 9.3 Specimen geometry

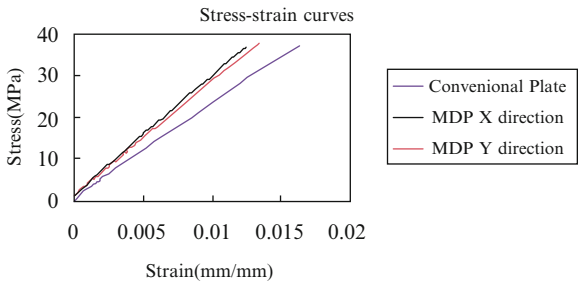

Fig. 9.4 The experimental results of stress–strain relation of the conventional diffuser plate and MDP

Table 9.1 Young's modului and Poisson's ratios

	Modulus(GPa)	Poisson's ratio
Conventional diffuser plate	Ex = Ey	νyx = νxy
Smaple1	2.596	0.367
Smaple2	2.621	0.361
Smaple3	2.649	0.342
Smaple4	2.586	0.356
Smaple5	2.618	0.331
Average	2.611	0.350
Standard deviation	0.024	0.015
MDP	Ex	νyx
Smaple1(X direction)	3.404	0.327
Smaple2(X direction)	3.329	0.331
Smaple3(X direction)	3.259	0.358
Smaple4(X direction)	3.513	0.334
Smaple5(X direction)	3.375	0.329
Average	3.376	0.336
Standard deviation	0.094	0.013
MDP	Ey	νxy
Smaple1(Y direction)	3.418	0.350
Smaple2(Y direction)	3.276	0.366
Smaple3(Y direction)	3.165	0.364
Smaple4(Y direction)	3.375	0.365
Smaple5(Y direction)	3.424	0.346
Average(Y direction)	3.332	0.358
Standard deviation	0.110	0.009

and perpendicular strain gauges. Five specimens were tested and their results are averaged to represent Young's modulus and Poisson's ratio. The experimental results of stress–strain relation of the conventional diffuser plate and MDP obtained from micro tensile test in which the curve between the stress and strain is quite linear as Fig. 9.4 shown.

The measurement results of Young's modulus of the conventional diffuser plate and MDP are listed in Table 9.1. Simultaneously, the strain gauges were used herein to characterize Poisson's ratio of the conventional diffuser plate and the MDP. Since Poisson's ratio of the conventional diffuser plate and MDP will be recorded by datalogger with computer. The experimental results of the average value of five specimens are also listed in Table 9.1. The thermal effects on the mechanical properties of the conventional diffuser plate and the MDP were also investigated by Thermomechanical

Table 9.2 Coefficient of thermal expansion

	Thermal expansion(1/°C)
Conventional diffuser plate	
Smaple1	6.68E-05
Smaple2	6.45E-05
Smaple3	6.34E-05
Average	6.49E-05
Standard deviation	1.75E-06
MDP	
Smaple1(X direction)	7.39E-05
Smaple2(X direction)	7.66E-05
Smaple3(X direction)	7.50E-05
Average	7.51E-05
Standard deviation	1.38E-06
MDP	
Smaple1(Y direction)	6.70E-05
Smaple2(Y direction)	6.46E-05
Smaple3(Y direction)	6.65E-05
Average	6.60E-05
Standard deviation	1.29E-06

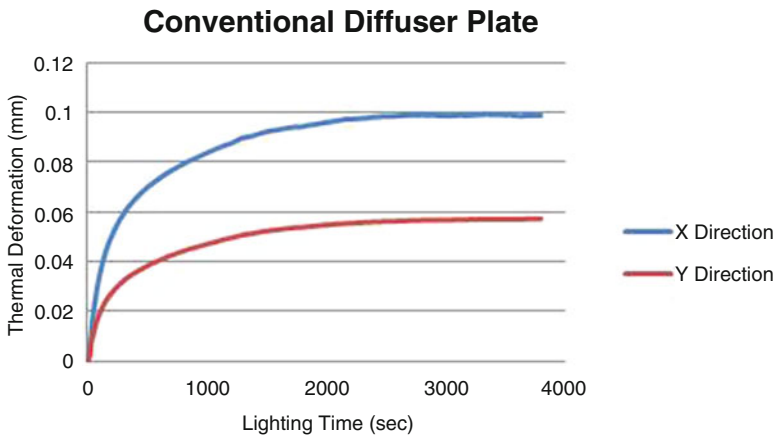

Fig. 9.5 The thermal deformation of the conventional diffuser plate by strain gauges

Analyzer (TMA Q-400) to measure Coefficient of Thermal Expansion of the conventional diffuser plate and MDP in the X and Y direction following the suggestion in the ISO 11359–2. Thus, Coefficient of Thermal Expansion of the conventional diffuser plate and MDP were collected from the tested results of three specimens in the X and Y direction. The experimental results of thermal expansion are listed in Table 9.2.

The 10 in. direct LED BLU was used in this study. The strain gauges were set on the surface of the conventional diffuser plate or MDP with datalogger to record the thermal deformations at long-lighted temperature. Figure 9.5 shows the thermal deformation of the conventional diffuser plate versus BLU lighting time, whose environment temperature was from 28.5°C to 41°C, obtained from strain gauges with computer. Figure 9.6 shows the thermal deformation of the MDP versus BLU lighting time, whose environment temperature was from 28.5°C to 41°C, obtained from strain gauges with computer. The experimental results of the conventional diffuser plate and MDP obtained from datalogger and the measurement results were compared to simulation by ANSYS software.

9.3 Numerical Approach

In order to analyze the distribution of thermal deformation in the conventional diffuser plate and MDP, The numerical approach based on FEA was employed to construct the simulation model. The commercially available software, ANSYS, was utilized. The procedure comprises four steps such as geometrical modeling, mesh design, boundary conditions and

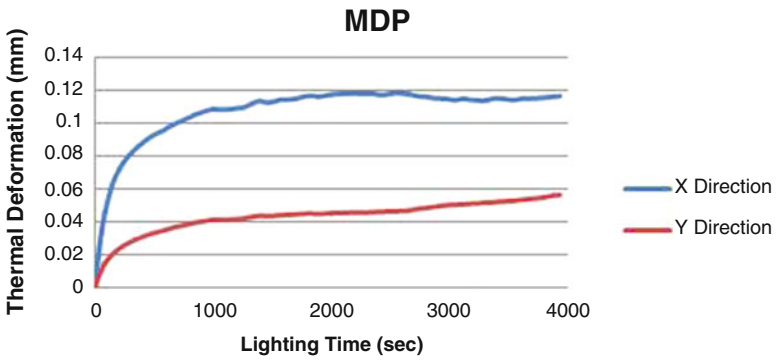

Fig. 9.6 The thermal deformation of the MDP by strain gauges

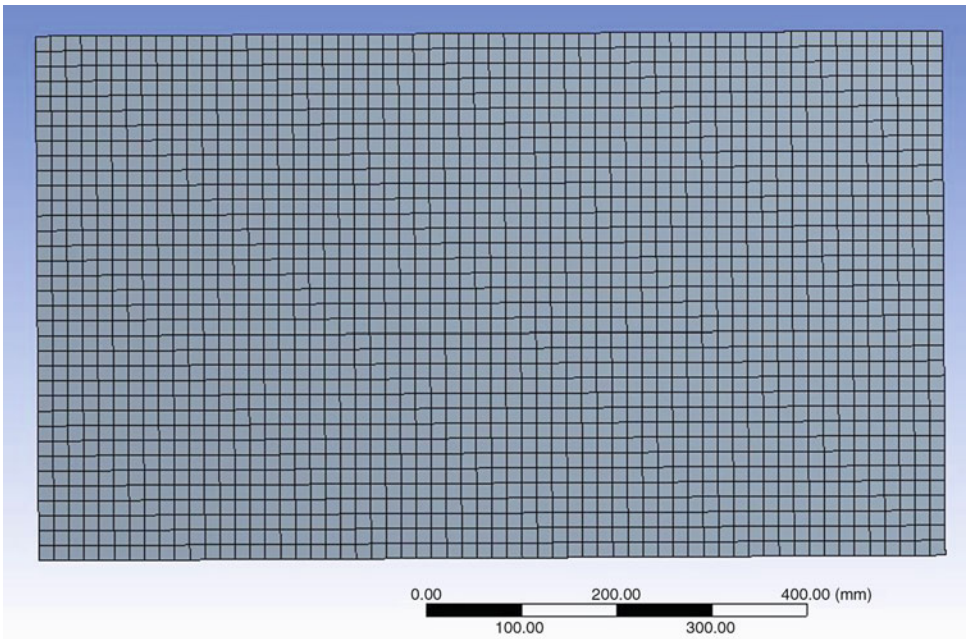

Fig. 9.7 The meshed diagram of the conventional diffuser

thermal deformation analysis. The geometrical modeling generates the input data for the analysis. Auto-mesh was used to mesh the numerical model due to the shape of diffuser plates is a rectangular figure. Four sides of the modeling were free, which was used as boundary condition for the initial thermal deformation analysis. From the results of initial thermal deformation compares with experiment strain gauges in order to verify FMA simulation accuracy. Finally, using the modeling, material properties, boundary conditions and thermal deformations to realize different diffuser plates and boundary conditions lead to different results by FMA.

The size of the diffuser plate of the 10 in. BLU is 237.5 × 137.5 × 1.5 mm that is symmetric figure. Combining the advantage of 3D design software Pro/E in modeling with the ability of finite element analysis (FEA) software ANSYS in analysis and calculation, this paper built 3D solid model with Pro/E, then imported the model into ANSYS through interface technology, finally established the FEA mechanical model of the conventional diffuser plate and MDP. The thermal deformation distribution of the conventional diffuser plate and MDP under environment temperature is achieved by using ANSYS to analyze and calculate. The meshed diagram of the conventional diffuser plate and the MDP respectively are shown in Figs. 9.7 and 9.8, and the number of the elements is respectively 2,100 and 215,109.

The mechanical properties listed in Tables 9.1 and 9.2 and environment temperature from 28.5°C to 41°C were substituted into the numerical model. Initial boundary condition was free at four sides. It was used to verify the accuracy of FMA compared with strain gauges. Following above, FMA can be used to simulate thermal deformations using different boundary conditions such as different temperature distributions or fixed at four sides at the conventional diffuser plate and MDP.

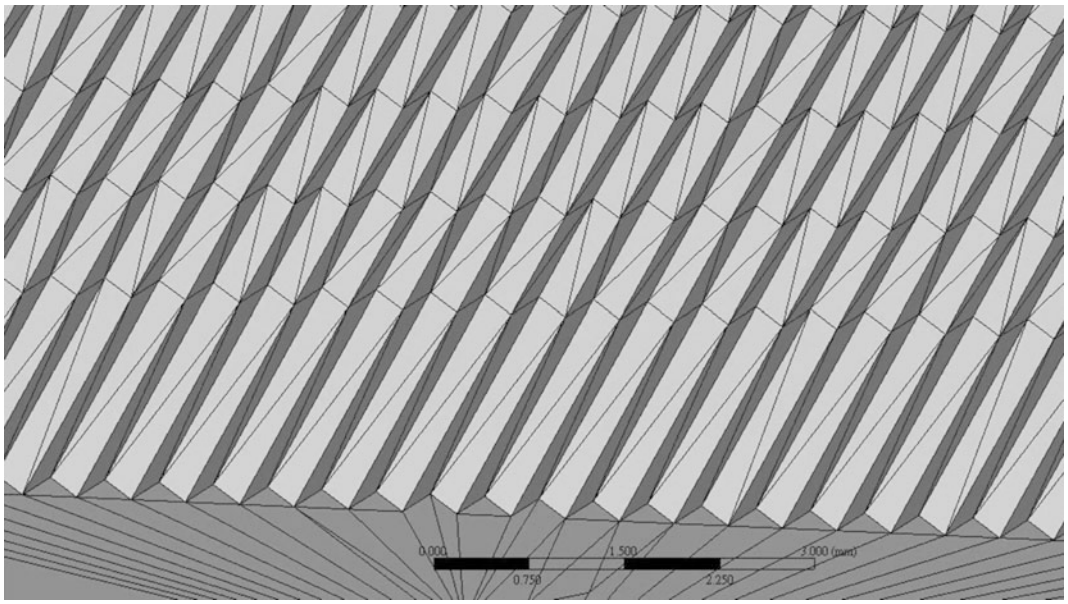

Fig. 9.8 The meshed diagram of the MDP

9.4 Result and Discussion

It can also be seen in Table 9.1 that Young's modulus of the conventional diffuser plate is lower than the MDP because of micro-structure on surface of the MDP. The micro-structure can enhance the strength of substrate. So in the X direction Young's modulus of the MDP is much bigger than in the Y direction. In Table 9.2 simultaneously shows Thermal Expansion of the conventional diffuser plate is isotropic, but Thermal Expansion of the MDP is anisotropic due to micro-structure is covered on surface of the MDP, yet conventional diffuser plate is a flat plate. Therefore, the structure will cause obviously degree of expansion different in the X direction and the Y direction. Figure 9.5 shows the thermal deformations of the conventional diffuser plate versus BLU lighting time, whose environment temperature was from 28.5°C to 41°C, when the LED BLU subjected to long lighting state, obtained from strain gauges with datalogger. The final thermal deformations of the conventional diffuser plate are 0.0987 mm and 0.0573 mm in the X direction and the Y direction respectively. Furthermore, Fig. 9.6 shows the final thermal deformations of the MDP are 0.1162 and 0.0563 mm in the X direction and the Y direction respectively at the same environment condition. The thermal deformation of the MDP is bigger than the conventional diffuser plate.

The same phenomenon also occurs for FEM to simulate by using ANSYS. Figures 9.9 and 9.10 show the thermal deformations of the conventional diffuser plate obtained from FEA in the X direction and the Y direction at the same environment temperature as above mentioned separately. The FEM shows the biggest thermal deformations of the conventional diffuser plate in the X direction and the Y direction are 0.0965 and 0.0559 mm respectively, when its boundary condition the Z direction was constrained, the X and Y direction were free. Figures 9.12 and 9.13 show the thermal deformations of the MDP obtained from FEA in the X direction and the Y direction separately. The FEM shows the biggest thermal deformations of the MDP in the X direction and the Y direction are 0.1123 and 0.0582 mm respectively, when its boundary condition the Z direction was constrained, the X and Y direction were free.

Comparing Fig. 9.5 with Fig. 9.9, the thermal deformation of the conventional diffuser plate obtained from FMA that has a deviation 2.23 % in the X direction at environment temperature 41°C. Comparing Fig. 9.5 with Fig. 9.10, the thermal deformation of the conventional diffuser plate obtained from FMA that has a deviation 2.44 % in the Y direction at environment temperature 41°C. The Thermal deformation obtained from FEM shows the results that are precise well comparing with experiments by strain gauges. The results certify the properties of the conventional diffuser plate. The results of FMA match the experiment results come from strain gauges. In the same way comparing Fig. 9.6 with Fig. 9.11, the thermal deformation of the MDP obtained from FMA that has a deviation 3.36 % in the X direction. Comparing Fig. 9.6 with Fig. 9.12, the thermal deformation of the MDP obtained from FMA that has a deviation 3.37 % in the Y direction. The Thermal deformation obtained from FEM shows the results that are precise well comparing with experiments by strain gauges. In addition, it should be noticed that the results certify the properties of the MDP. According to above, when the four

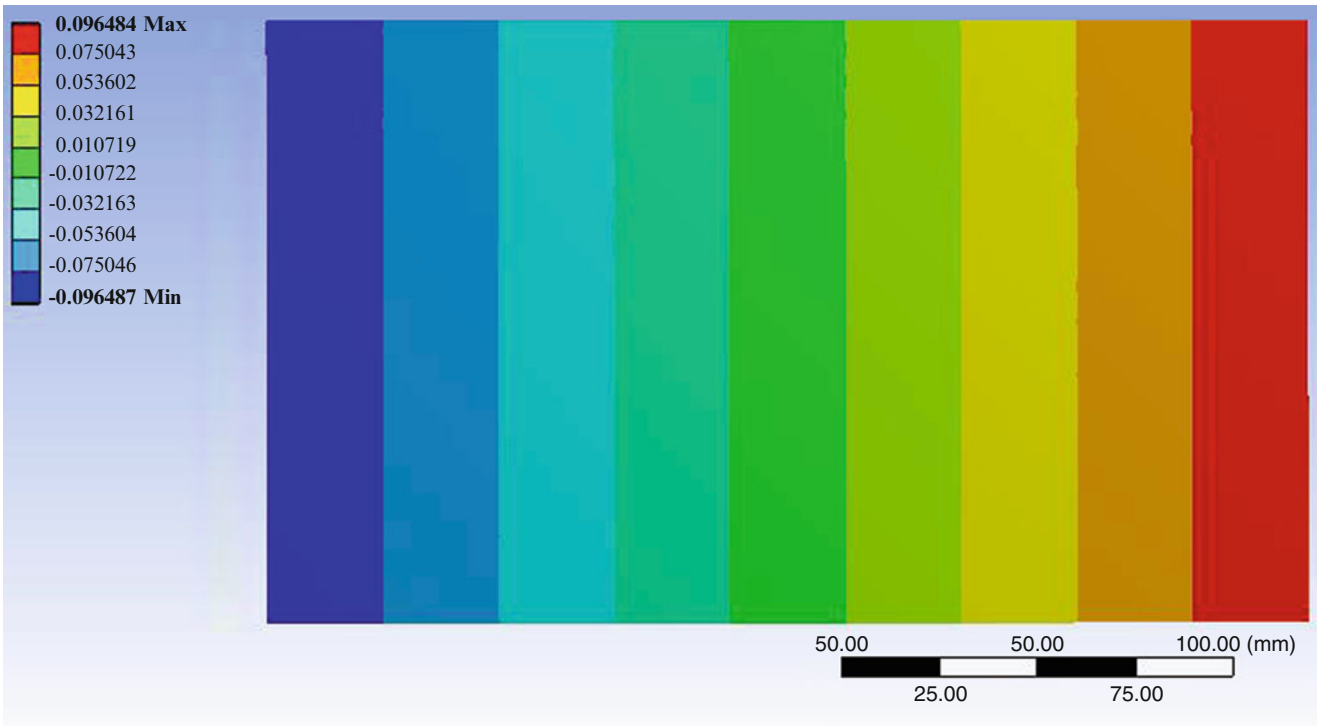

Fig. 9.9 The thermal deformation of the conventional diffuser plate in the X direction by FEM

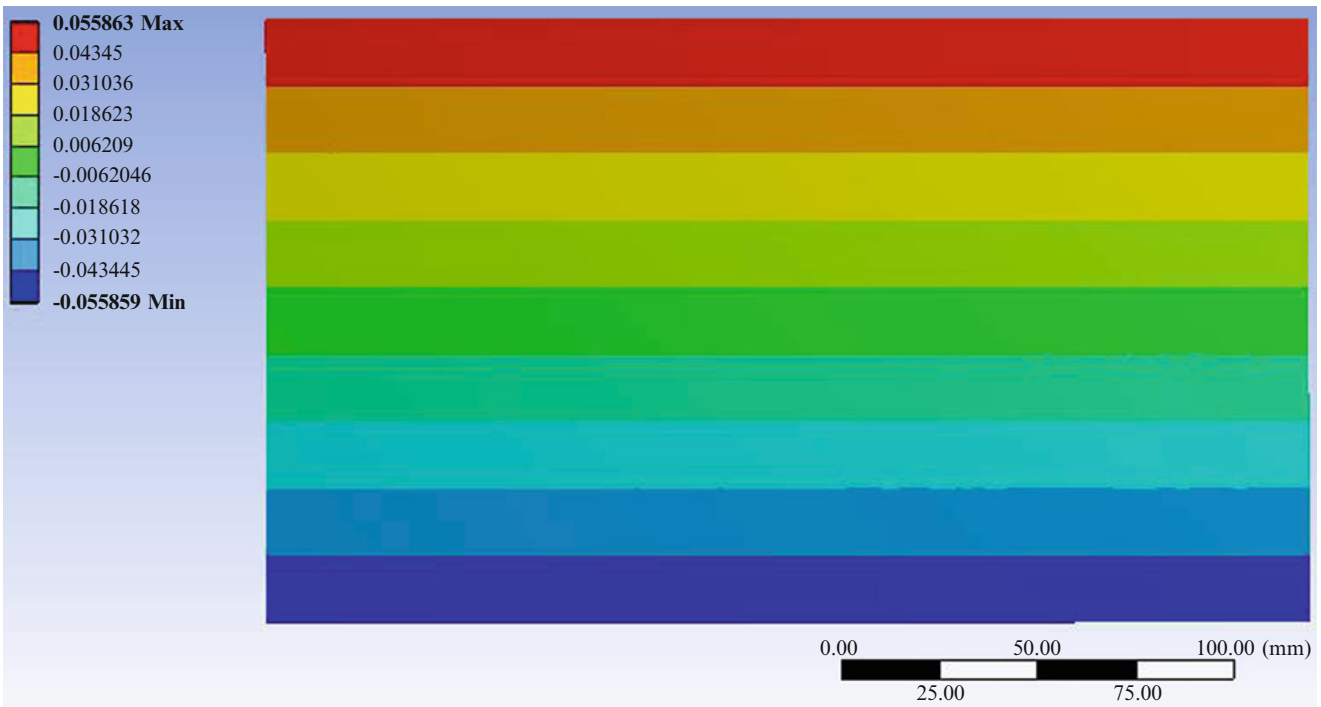

Fig. 9.10 The thermal deformation of the conventional diffuser plate in the Y direction by FEM

sides of the conventional diffuser plate and MDP were fixed, the bending of the thermal deformation come from LED high temperature can be simulated by FEM. Those results can be utilized to analyze different boundary conditions, when bezel of LED BLU constricts on four sides of conventional diffuser plate or MDP. Figure 9.13 shows the thermal deformation of the conventional diffuser plate, whose environment temperature was at $41°C$, obtained from FEA. The FEM shows the biggest

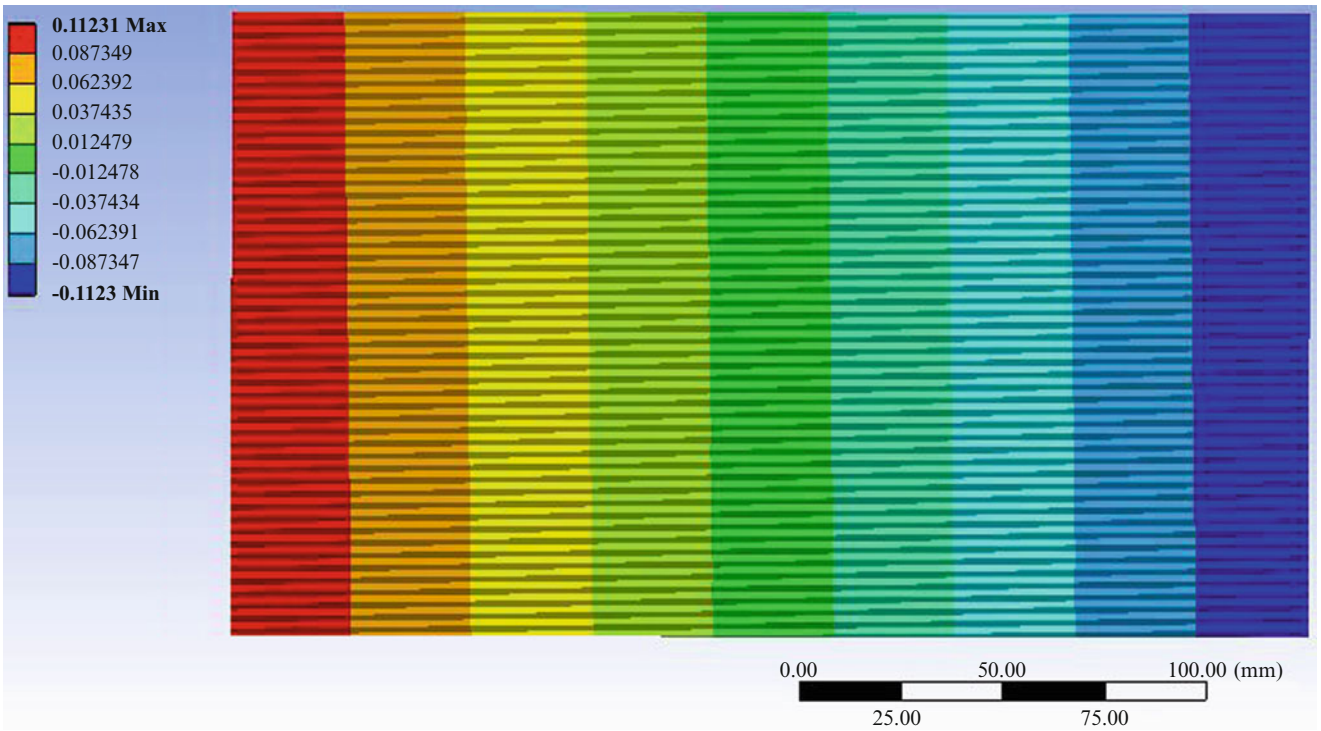

Fig. 9.11 The thermal deformation of the MDP in the X direction by FEM

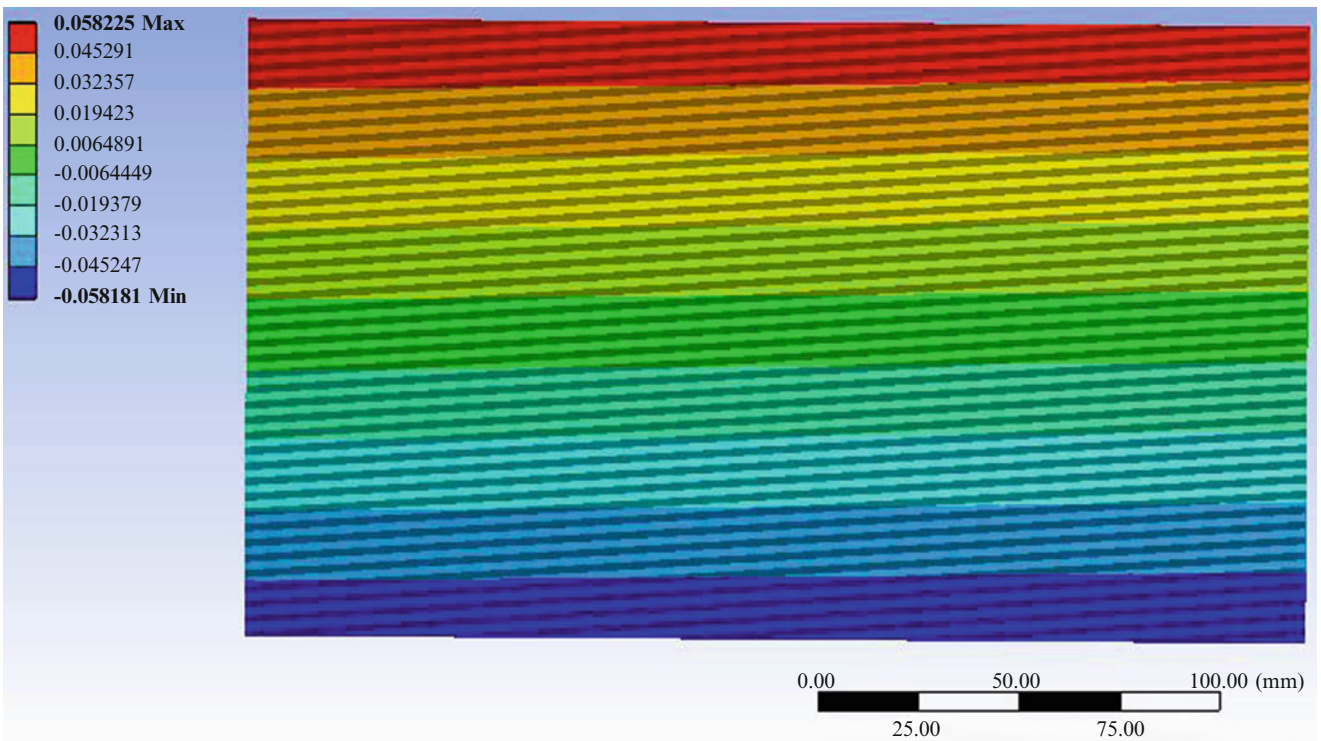

Fig. 9.12 The thermal deformation of the MDP in the Y direction by FEM

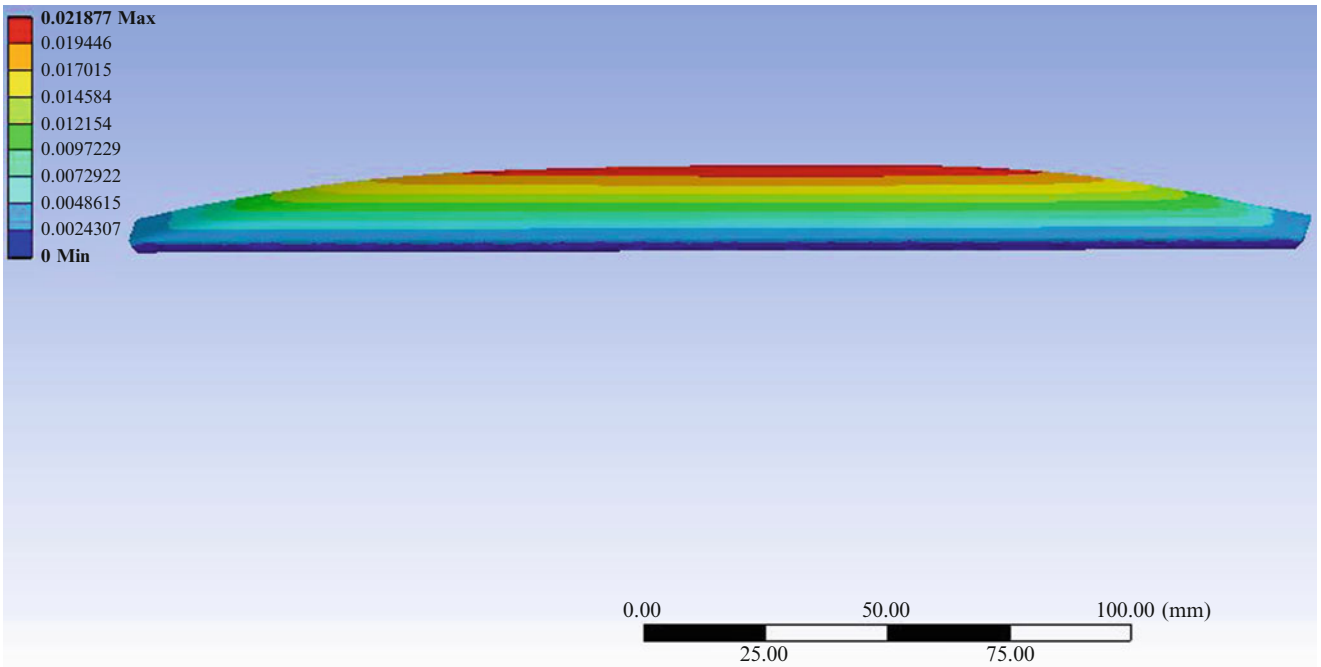

Fig. 9.13 The bending of the conventional diffuser plate in the Z direction at 41°*C* by FEM

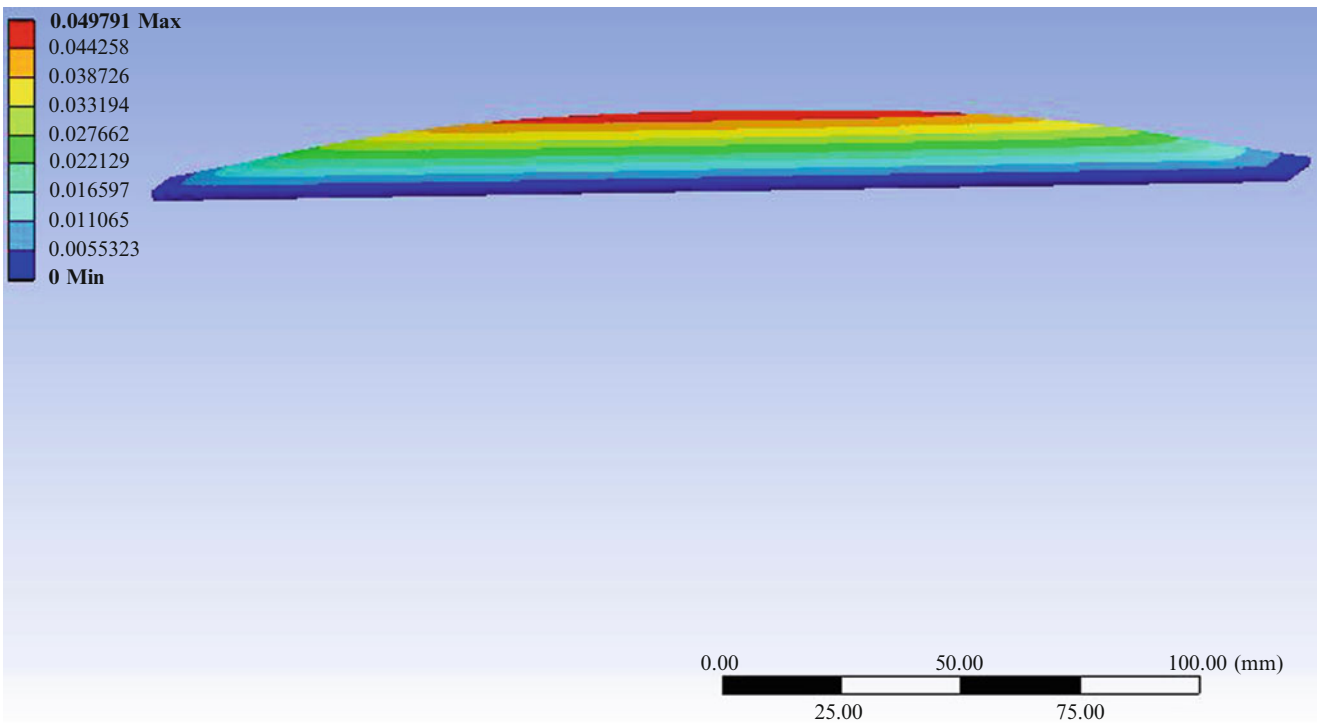

Fig. 9.14 The bending of the MDP in the Z direction at 41°*C* by FEM

thermal deformation of the conventional diffuser plate in the Z direction is 0.0219 mm when the four sides were fixed. Figure 9.14 shows the thermal deformation of the MDP, whose environment temperature was at 41°*C*, obtained from FEA. The FEM shows the biggest thermal deformation of the MDP in the Z direction is 0.0498 mm when four sides of the MDP were fixed.

9.5 Conclusion

In this paper, the characters of the conventional diffuser plate and MDP were researched by using experimental technique, measuring temperature and thermal deformations. The results show good compatibility to demonstrate that the simulation process successfully predicts the warpage phenomenon. The methodology can be further utilized to understand the difference of characteristics between the conventional diffuser plate and MDP within the LED BLU such that the display quality of the LED BLU could probably be improved or controlled through methodology above.

References

1. Harbers G, Timmers W, Sillevis-Smitt W (2002) LED backlighting for LCD HDTV.. In: Proceedings 2nd internation display manufacturing conference. Seoul, Korea, pp 181–184
2. Harbers G and Holen CGA (2001) High performance LCD backlighting using high intensity red, green, and blue light emitting diodes. In: SID international symposium digest of technical papers. San Jose, California, pp 702–706
3. Anandan M (2002) SID'02 Seminar Lecture Notes, society for information display. San Jose, pp 169
4. Ko JH (2005) Asian J Phys 14:231
5. Kim GH, Kim WJ, Kim SM, Son JG (2005) Analysis of thermo-physical and optical properties of a diffuser using PET/PC/PBT copolymer in LCD backlight units. Displays 26(1):37–43
6. Kim GH (2005) A PMMA composite as an optical diffuser in a liquid crystal display backlighting unit (BLU). Eur Polym J 41(8):1729–1737
7. Chu CY, Pan MC, Ho J (2005) Thermal analysis and experimental validation on TFT-LCD panels forimage quality concerns. In: IEEE 2005 electronics packaging technology conference. Singapore, vol. 2. pp 543–548
8. Ishiyama C, Higo Y (2002) Effects of humidity on Young's modulus in poly(methyl methacrylate). J Polym Sci, Part B: Polym Phys 40:460–465
9. Chao LP, Hsu JS, Tsai WC, Chen MC (2009) Measurement of the mechanical properties of brightness enhancement films (BEFs) for LCDs by optical interferometry. Elsevier Displays 30:140–146
10. Chu CY, Pan MC, Ho J (2005) Thermal analysis and experimental validation on TFT-LCD panels for image quality concerns.In: IEEE 2005 electronics packaging technology conference. Singapore
11. Park SK, Kim J, Chang YC, Kang BS (2001) Analysis of the deformation of perforated sheet under thermal and tension using finite element method. J Mater Process Technol 113:761–765
12. Annuual Book of ASTM Standards, American society for testing and materials (2005)
13. Ugural AC (1999) Stresses in plates and shells. McGraw-Hill, Boston

Chapter 10
Polariscopy Measurement of Residual Stress in Thin Silicon Wafers

K. Skenes, R.G.R. Prasath, and S. Danyluk

Abstract Near-infrared (NIR) Polariscopy has been used to find residual stresses in thin silicon wafers using phase shifting techniques. This paper describes the usage of the ten-step phase shifting method to measure the in-plane residual stresses in single- and multi-crystalline silicon wafers. We show how this technique can be applied to wafers without the application of external loading. The system is calibrated with a beam of monocrystalline CZ silicon loaded in an in-plane four-point bending fixture. The residual maximum shear stresses of the unloaded wafers are then determined. The shear difference technique is used for obtaining the normal stress values. Results are compared before and after smoothing of the isoclinic parameter, and its impact on the separated stress values is explained.

Keywords Phase stepping • Photoelasticity • Residual stress • Silicon wafers • Smoothing • Stress separation

10.1 Introduction

Residual stresses are of major concern in thin silicon wafers, and may negatively affect performance when the wafers are involved in applications such as photovoltaic cells and electronic devices. These residual stresses may be introduced by the temperature gradients present in crystal growth and other processing techniques or by the wafering process. Photoelasticity is an optical non-contact technique which provides information on principal stress differences (isochromatics) and principal stress directions (isoclinics) [1]. Several alternate techniques exist for measuring residual stresses, including Moiré interferometry, x-ray diffraction, transmission electron microscopy and micro-Raman spectroscopy [2, 3]. Among all these techniques Near-infrared (NIR) polariscopy is promising as a residual stress measurement tool for thin silicon wafers due to its non-contact nature and balance between accuracy, spatial resolution, and computational efficiency. This paper describes the usage of the ten-step phase shifting technique to measure the in plane residual stress in single and multi-crystalline silicon wafers which are predominantly used in the fabrication of photovoltaic cells.

Digital transmission photoelasticity is regaining popularity as a residual stress measurement tool. Improvements in digital cameras, computers, and image processing techniques allow for increased accuracy and precision. The use of phase shifting is considered superior to load stepping or wavelength shifting due to its increased accuracy and sensitivity to stress measurement. Danyluk's group has shown that phase shifting can be used to measure stresses in PV silicon wafers [1, 4]. Brito et al. also used phase shifting to measure residual stresses in EFG ribbons [5]. The quality of the resulting photoelastic parameters depends on various factors, including wavelength mismatch, inherent error in the optical elements, and optical misalignments.

In the six-step phase shifting technique, lower levels of modulation in the retardation increase the noise level in the measured isoclinic parameters (though the isochromatic data is quite accurate). High accuracy of isoclinic and isochromatic data is required if stress separation into normal components is desired. Ramji and Ramesh [6] reported the "streak" formation in stress separation is mainly due to the presence of noise in isoclinic parameter. Ramji and Prasath [7] have

K. Skenes • R.G.R. Prasath • S. Danyluk (✉)
The George W. Woodruff School of Mechanical Engineering, Georgia Institute of Technology, Atlanta, GA 30332, USA
e-mail: steven.danyluk@marc.gatech.edu

M. Rossi et al. (eds.), *Residual Stress, Thermomechanics & Infrared Imaging, Hybrid Techniques and Inverse Problems, Volume 8*, Conference Proceedings of the Society for Experimental Mechanics Series, DOI 10.1007/978-3-319-00876-9_10,

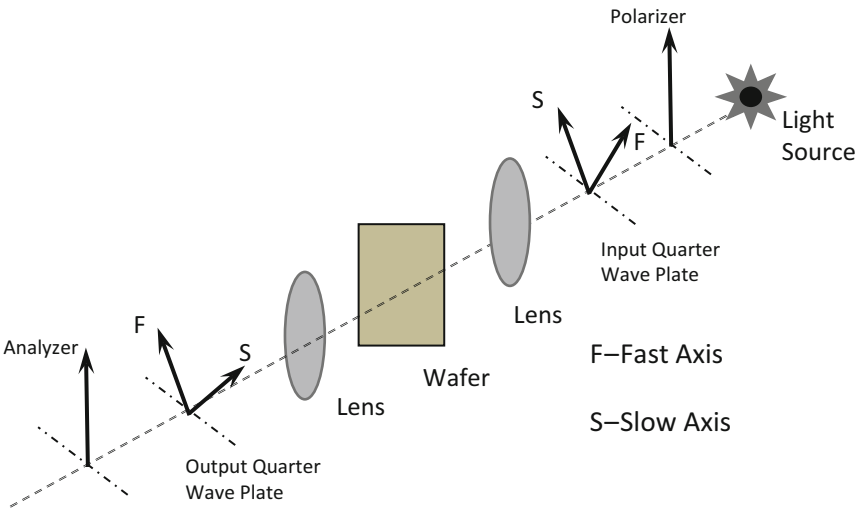

Fig. 10.1 Schematic of the circular polariscope setup

performed an error analysis using Jones calculus to quantify the efficacy of ten-step methodology in photoelastic parameter estimation. Recently Prasath, Skenes and Danyluk [8] further investigated the effectiveness of the ten-step phase shifting technique and performed a comparative study between phase shifting techniques. They recommended the ten-step method over others for accurate photoelastic parameter estimation. In order to extract the normal stress components, there are many auxiliary methods which may be used in tandem with photoelasticity. Among these, the shear difference technique is recommended for its accuracy and simplicity.

10.2 Methodology

Photoelasticity is based on the stress-induced birefringence phenomenon. A schematic of the experimental setup is shown in Fig. 10.1. It consists of a broadband light source, polarizer and NIR filter, input quarter wave plate, collimating lens pair, output quarter wave plate, analyser and camera. A modified Canon EOS 50D digital camera with a resolution of 4752 × 3168 pixels and equipped with a 750 nm low-pass filter is used for recording images. The transmitted intensity depends on the physical characteristics of the wafer and the wavelength of the light. Retardation of transmitted light occurs when the material contains stresses. The relative retardation varies from point to point depending on the amount of residual stress in the sample. Maxwell's stress optic law can then be used to find the absolute magnitude of the differences in normal principal stresses:

$$\delta = \frac{|\sigma_1 - \sigma_2| 2\pi t C}{\lambda} \tag{10.1}$$

Where δ – Relative retardation
λ – Wavelength of light used
C – Relative stress-optic coefficient
t – Thickness of the sample

10.3 Ten-Step Method

Table 10.1 shows the orientation of optical elements with the corresponding intensity equations of the ten-step phase shifting technique. The first four steps match the optical arrangements of the plane polariscope-based algorithm of Brown & Sullivan [9]. The next six arrangements are identical to those of another six-step phase shifting technique based on a circular polariscope arrangement. From the intensity data the isoclinic parameter is obtained as

Table 10.1 Orientation of optical elements for ten-step phase shifting technique

Polarizer	Input QWP	Output QWP	Analyzer	Intensity equations
$\pi/2$	–	–	0	$I_1 = I_b + I_a \sin^2\frac{\delta}{2}\sin^2 2\theta$
$5\pi/8$	–	–	$\pi/8$	$I_2 = I_b + \frac{I_a}{2}\sin^2\frac{\delta}{2}(1 - \sin 4\theta)$
$3\pi/4$	–	–	$\pi/4$	$I_3 = I_b + I_a \sin^2\frac{\delta}{2}\cos^2 2\theta$
$7\pi/8$	–	–	$3\pi/8$	$I_4 = I_b + \frac{I_a}{2}\sin^2\frac{\delta}{2}(1 + \sin 4\theta)$
$\pi/2$	$3\pi/4$	$\pi/4$	$\pi/2$	$I_5 = I_b + \frac{I_a}{2}(1 + \cos\delta)$
$\pi/2$	$3\pi/4$	$\pi/4$	0	$I_6 = I_b + \frac{I_a}{2}(1 - \cos\delta)$
$\pi/2$	$3\pi/4$	0	0	$I_7 = I_b + \frac{I_a}{2}(1 - \sin 2\theta \sin\delta)$
$\pi/2$	$3\pi/4$	$\pi/4$	$\pi/4$	$I_8 = I_b + \frac{I_a}{2}(1 + \cos 2\theta \sin\delta)$
$\pi/2$	$\pi/4$	0	0	$I_9 = I_b + \frac{I_a}{2}(1 + \sin 2\theta \sin\delta)$
$\pi/2$	$\pi/4$	$3\pi/4$	$\pi/4$	$I_{10} = I_b + \frac{I_a}{2}(1 - \cos 2\theta \sin\delta)$

$$\theta_c = \frac{1}{4}\tan^{-1}\left(\frac{I_4 - I_2}{I_3 - I_1}\right) \tag{10.2}$$

In Eq. 10.2, the subscript c indicates that the principal value of the inverse trigonometric function is used, and Ramesh [6] recommends that θ_c be evaluated with the *atan2* function. The isoclinic values obtained by Eq. 10.2 are within the range $-\pi/4$ to $\pi/4$. This must be unwrapped further to a range of $-\pi/2$ to $\pi/2$ before use for isochromatic evaluation through Eq. 10.3. The relative retardation is obtained as

$$\delta_c = \tan^{-1}\left(\frac{(I_9 - I_7)\sin 2\theta + (I_8 - I_{10})\cos 2\theta}{(I_5 - I_6)}\right) \tag{10.3}$$

The stress optic coefficient C is calibrated by using a four point bending method [10]. The usage of the ten-step method is demonstrated for the problems of two beams, one single crystal and one multi-crystalline, subjected to four point bending.

10.4 Stress Separation and Smoothing Algorithm

The shear difference method uses the equilibrium equations of a free body as a mechanism to separate the stresses. This allows for an integration scheme along lines parallel to the x-axis and y-axis [6] starting from a free boundary. The integral is represented by the finite difference approximations

$$(\sigma_x)_j = (\sigma_x)_i - \sum_i^j \frac{\Delta\tau_{yx}}{\Delta y}\Delta x \qquad (\sigma_y)_j = (\sigma_x)_j - \frac{\delta\lambda}{2\pi Ch}\cos 2\theta \tag{10.4}$$

where Δx is the increment along x-axis, Δy is the increment along y-axis, and $\Delta\tau_{yx}$ is the increment in shear stress over Δy. In-plane shear stress is then obtained by

$$\tau_{xy} = \frac{|\sigma_1 - \sigma_2|}{2}\sin 2\theta \tag{10.5}$$

The major issue this stress separation technique is the accumulation of streaks in separated stress components due to the presence of noise in isoclinic parameter. To counter this problem, we have performed smoothing operations using spatial averaging. Equivalently, this averaging operation in the spatial domain corresponds to low-pass filtering in the frequency domain.

10.5 Four Point Bend Specimen (MONO)

Four point bending was used as a calibration tool to obtain the stress optic coefficient [1, 10]. In this case, a silicon 'bar' sample was prepared by dicing a (111) semiconductor-grade single crystal wafer into an 8 mm-wide 'bar' and subjecting the 'bar' to a known load at the sample edge. The silicon bar had dimensions as shown in Fig. 10.2a and a thickness of 450 μm. The dark field isochromatics are shown in Fig. 10.2b. The corresponding fringe order, raw isoclinic and smoothed isoclinic data are shown in Fig. 10.2c, d, e respectively. The individual stress components obtained by the shear difference technique are shown in Fig. 10.3. Upon closer observation of the σ_y plot in 3c, numerous streaks are generated due to the noise in isoclinic data, driving the stress value up to a maximum of 25 MPa. After smoothing the isoclinic data the streaks are completely removed and its value is reduced to 3 MPa as shown in Fig. 10.3d. The in plane shear stress plots obtained by using raw and smoothed isoclinic data are shown in Fig 10.3e, f. Maximum shear stress is shown in Fig. 10.3g.

10.6 Four Point Bend Specimen (Multi Crystalline)

Figure 10.4 shows the experimental results obtained for a multi-crystalline wafer subjected to four point bending. The silicon bar had dimensions as shown in Fig. 10.2a and a thickness of 280 μm. The dark field isochromatics are shown in Fig. 10.4a. The corresponding fringe order, raw isoclinic and smoothed isoclinic data are shown in Figs. 10.4c, 10.2d, e respectively. To show the influence of isoclinic noise in integration scheme, results obtained for both raw isoclinic data and smoothed isoclinic data are shown. Note that in Fig. 10.4f, h, the σ_x and σ_y plot each contain many streaks due to the noise in isoclinic data. After smoothing the isoclinic data the streaks decrease significantly in magnitude as shown in Fig. 10.4g, i. Maximum shear stress is shown in Fig. 10.4b.

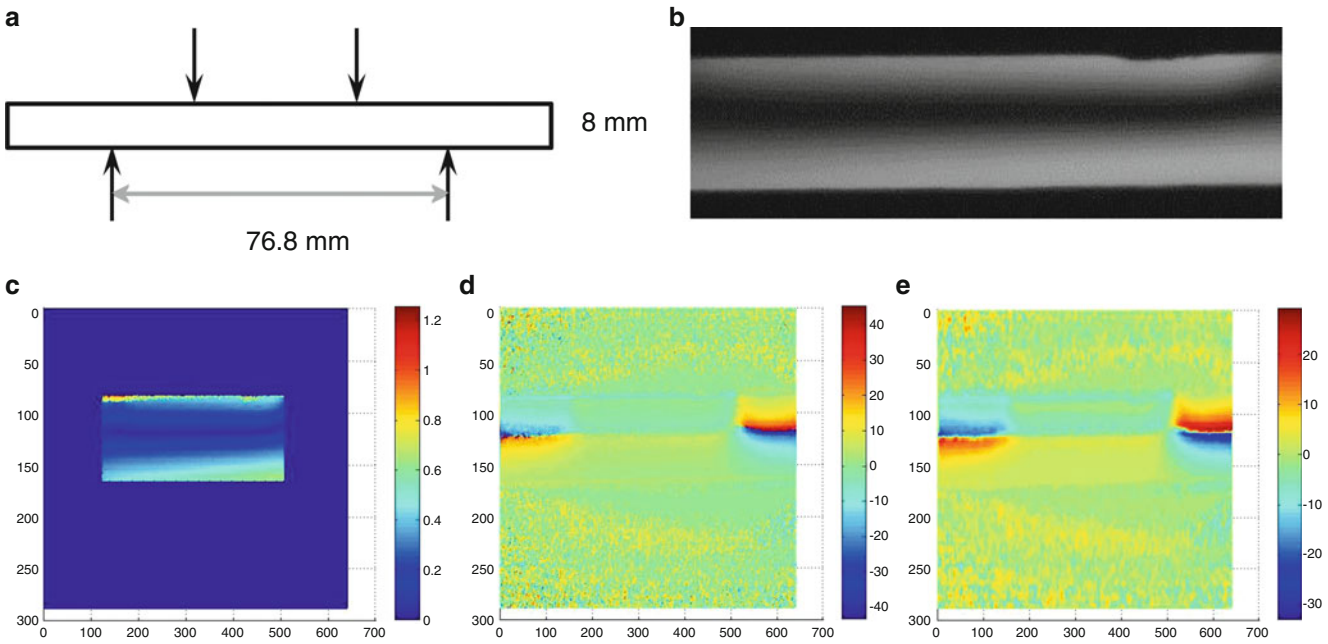

Fig. 10.2 Four point bending (**a**) schematic of loaded specimen (**b**) dark field image (**c**) fringe order (**d**) raw isoclinic (**e**) smoothed isoclinic

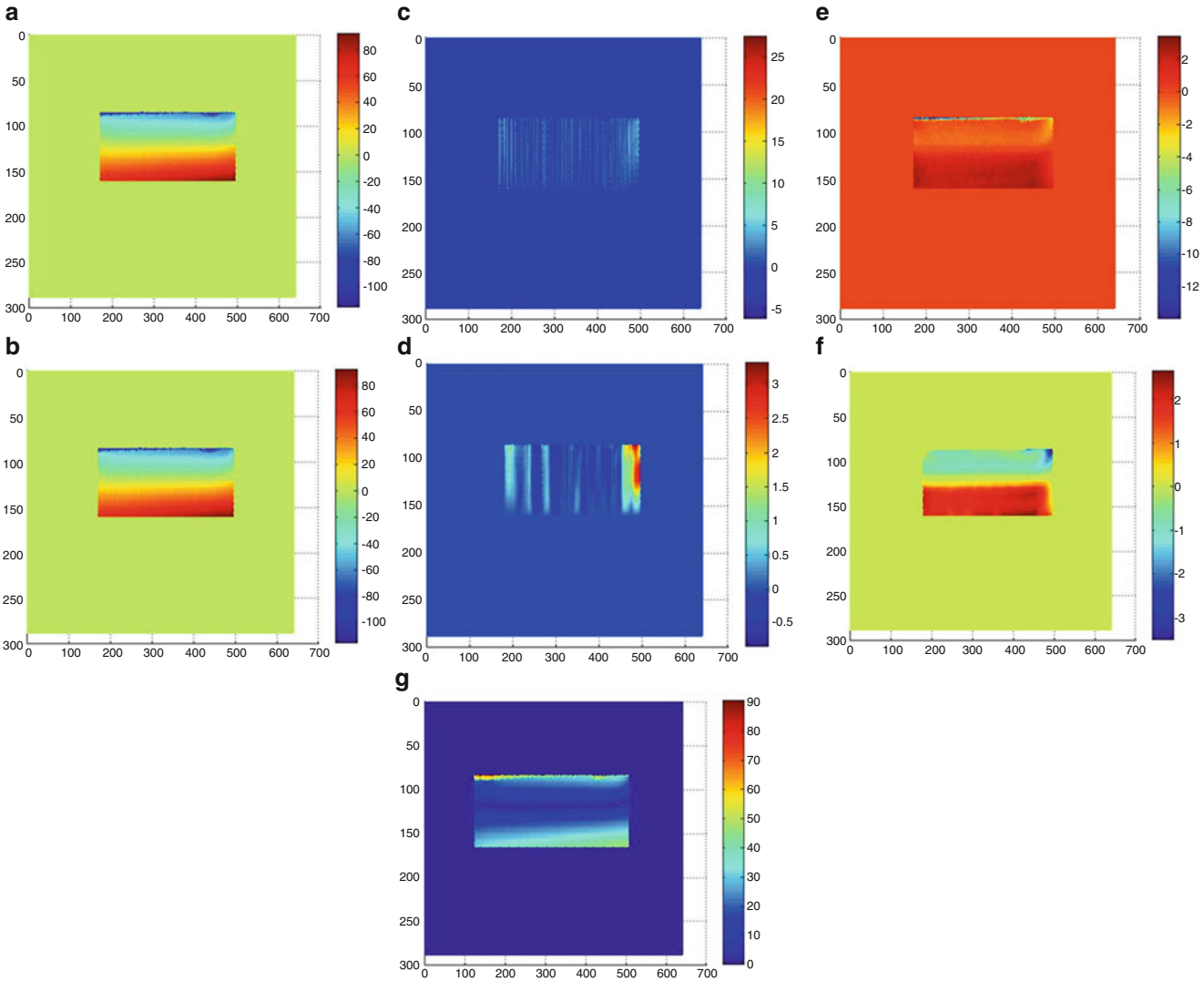

Fig. 10.3 Four point bending (**a**) σ_x using raw isoclinic data (**b**) σ_x using smoothed isoclinic data (**c**) σ_y using raw isoclinic data (**d**) σ_y using smoothed isoclinic data (**c**) τ_{xy} using raw isoclinic data (**d**) τ_{xy} using smoothed isoclinic data (**e**) max. shear stress

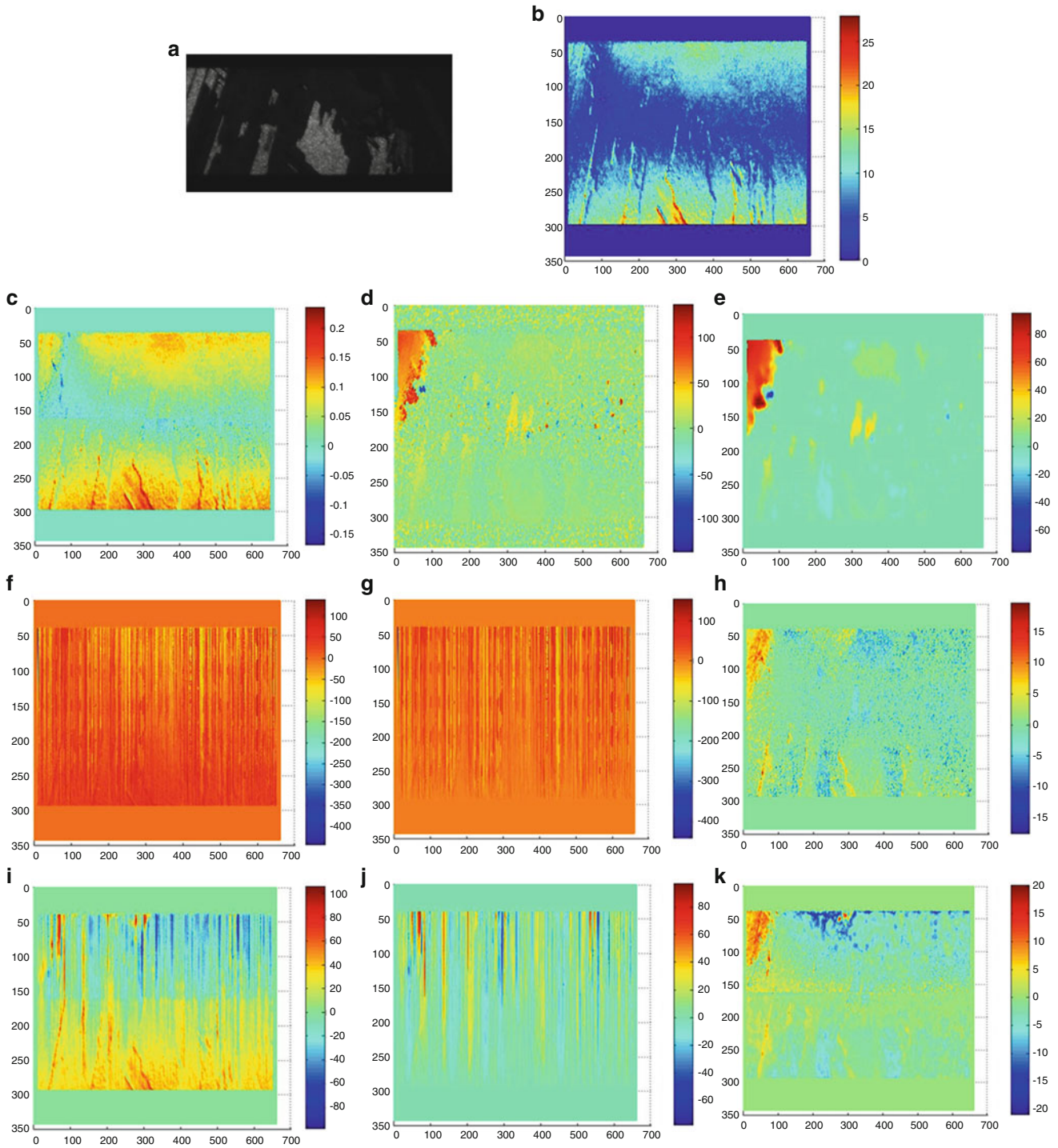

Fig. 10.4 Four point bending multi crystalline wafer (**a**) dark field isochromatics (**b**) max. shear stress (**c**) fringe order (**d**) raw isoclinic data (**e**) smoothed isoclinic data (**f**) σ_x using raw isoclinic data (**g**) σ_x using smoothed isoclinic data (**h**) σ_y using raw isoclinic data (**i**) σ_y using smoothed isoclinic data (**j**) τ_{xy} using raw isoclinic data (**k**) τ_{xy} using smoothed isoclinic data

10.7 Conclusion

Stress separation into normal components remains a challenge at low residual stress magnitudes due to lower levels of modulation in the measurement and the occurrence of noise in the isoclinic parameter. To overcome this, smoothing of the isoclinic parameter using spatial averaging is implemented for this study. Smoothing reduces the noise levels present in stress separation by a significant amount, allowing features which were previously masked to be seen. This paper describes the usage of ten-step phase shifting technique to measure the in plane residual stress in single, and multi-crystalline silicon wafers which are predominantly used in the fabrication of cells in the photovoltaic industries.

Acknowledgement The authors acknowledge the support of the Morris M. Bryan Jr. chair funds and Dr. Shreyes Melkote, Dr. Frank Mess, and Dr. Juris Kalejs for providing samples and illuminating discussions.

References

1. Zheng T, Danyluk S (2001) Nondestructive measurement of in plane residual stress in thin silicon substrates by infrared transmission. Mater Eval 50(10):1227–1233
2. Li F, Garcia V, Danyluk S (2006) IEEE 4th world conference on photovoltaic energy conversion, p 1245–1248
3. He S, Danyluk S, Tarasov I, Ostapenko S (2006) Residual stresses in polycrystalline silicon sheet and their relation to electron–hole lifetime. Appl Phys Lett 89:111909
4. Zheng T, Danyluk S (2002) Study of stresses in thin silicon wafers with near-infrared phase stepping photoelasticity. J Mater Res 17(1):36–42
5. Brito MC, Maia Alvesa J, Serraa JM, Gamboab RM, Pintoa C, Vallera AM (2005) Measurement of residual stress in EFG ribbons using a phase-shifting IR photoelastic method. Sol Energy Mater Sol Cells 87(1–4):311–316
6. Ramji M, Ramesh K (2008) Whole field evaluation of stress components in digital photoelasticity: issues, implementation and application. Opt Lasers Eng 46(3):257–271
7. Ramji M, Prasath RGR (2007) Sensitivity of isoclinic data using various phase shifting techniques in digital photoelasticity towards generalized error sources. Opt Lasers Eng, 49 (9–10):1153–1167
8. Prasath RGR, Skenes K, Danyluk S (2011) Comparison of phase shifting techniques for measuring in-plane residual stress in thin, flat silicon wafers. J Electron Mater (Accepted)
9. Brown GM, Sullivan JL (1990) The computer aided holophotoelastic method. Exp Mech 30(2):135–144
10. He S, Zheng T, Danyluk S (2004) Analysis and determination of stress optic coefficients of thin single crystal silicon samples. J Appl Phys 96(6):3103–3109

Chapter 11
Curvature from Residual Stress in Rapidly Quenched Amorphous Metals Using Abrasive Layer Removal

Balaji Jayakumar and Jay C. Hanan

Abstract Due to the need for rapid quenching, residual stresses have been expected in amorphous metals. Early predictions were high, but the measured stresses in cast and quenched alloys were significantly below predictions. Layer removal methods to measure residual stress typically employ etchants or polishing to remove upper layers. Recently, significant residual stresses were observed in a rapidly quenched (10^{-5} K/s) amorphous metal alloy using an abrasive layer removal method blasting glass beads. While the prediction of a tempering state would imply a residual compressive surface stress, this layer removal shows an opposite response. A significant curvature was obtained using an impact treatment method, suggesting a change in the residual stress state. The ribbon thickness and resulting surface effects were characterized using SEM. Bulk tension testing was performed on the treated ribbon to study the influence of the impact treatment on the mechanical properties of the ribbon.

Keywords Amorphous metal • Curvature • Layer removal • Microstructure • Residual stress

11.1 Introduction

Amorphous Metal Ribbons (AMR) are rapidly quenched metals produced at a freezing rate of 10^{-5}–10^{-6} K/s. The cooling characteristics of the alloys require such high rates to retain an amorphous structure, limiting thickness. Due to the lack of magneto-crystalline anisotropy and defects, they have found applications as soft magnetic materials. Their unique mechanical properties have promise for structural applications, especially in the bulk form. The rapid solidification required for manufacturing however limits the length scale.

Residual stresses, also referred as quenched-in stresses, are imparted on the ribbon during the rapid solidification process. Applied stresses are a result of external loading on the ribbon while in operation, for example, a ribbon wound on a transformer core [1]. Residual stresses are expected in rapidly solidified ribbons, from surface chilling that causes temperature gradients as the ribbon cools through the glass transition [2, 3]. Depending on the nozzle shape and nozzle-substrate distance, two processes are used. In Chilled block Melt Spinning (CBMS), a jet of liquid metal is ejected from a circular nozzle several mm away from the spinning wheel and in Planar Flow Casting (PFC), rectangular nozzles with a smaller gap are used [3]. AMR widths of 1–20 mm are manufactured using the CBMS; while greater widths in the order of 50–200 mm are manufactured using a PFC. In both the processes, non-uniform temperature distribution along the ribbon thickness are predicted to cause high compressive stresses ($\sigma < 0$) near the surface facing the drum and tensile stresses ($\sigma > 0$) are formed in the free surface [4]. Using layer removal methods, an analytical instant-freezing model has been demonstrated to predict residual stresses in metallic glasses due to thermal tempering [2]. For Bulk Metallic Glasses (BMGs), their visco-elastic nature, poor thermal conductivity and the high freezing rates lead to compressive residual stresses on the surface and tensile stress on the interior. Substantial surface residual stresses (upto 900 MPa) have been shown through analytical and Finite Element models [5].

In AMR manufacturing, due to the processing parameters such as the nozzle distance, orientation, shape, and platen temperature, different quenched-in stress anisotropy and surface tension can be expected. These process variables influence

B. Jayakumar (✉) • J.C. Hanan (✉)
Mechanical and Aerospace Engineering, Oklahoma State University, Tulsa, OK 74106, USA
e-mail: jay.hanan@gmail.com

M. Rossi et al. (eds.), *Residual Stress, Thermomechanics & Infrared Imaging, Hybrid Techniques and Inverse Problems, Volume 8*, Conference Proceedings of the Society for Experimental Mechanics Series, DOI 10.1007/978-3-319-00876-9_11,

the structure and physical properties [6, 7]. Like any production process, the quenched-in stresses depend on both the macroscopic and the microscopic length scales. Controlling properties depend on the production process [6]. Surface or bulk defects on ribbons from different processes may also vary for the same reason. This is also evident from the in-homogeneities of rapid quenching demonstrated using experimental procedures [8]. As a result, sizeable curvatures have been demonstrated with concavity towards the free surface. This is due to different solidification time taken by each successive layer in the ribbon. Homogeneous models have been developed to predict the curvature in as-quenched ribbons. Major curvatures have been postulated to result also from early solidification of edges due to a high cooling rate that adds compressive stresses in narrow ribbons using CBMS. Wider ribbons manufactured using PFC maintains the ribbon flat owing to the weight of the puddle [9]. Measuring and understanding the magnitude and direction of these residual stresses is crucial in explaining their response to certain subsequent processing treatments.

With an interest in increasing the general plasticity of Bulk Metallic Glasses (BMGs), Shot Peening as a surface treatment process has been widely studied [10–14]. Peening of a Zr -based BMG (Vitreloy 1) has shown a decrease in surface hardness, which was also correlated to the compressive residual stresses on the surface. Also, a convex curvature was observed on the peened surface of the BMG plate [10]. DSC measurements on shot peened Pd-based BMG show a reduced high temperature peak, suggesting a uniform distribution and a partial relaxation of the glassy structure [12]. In the same work, peening has shown to increase atomic mobility in annealed and subsequently peened samples. Studies on Zr-based metallic glass plate [11] show that the maximum sub-surface compressive stresses caused due to shot peening is close to the uniaxial yield stress of undeformed BMG. A change in bond orientation ordering is also observed due to plastic flow. Similar studies have indicated that the flexion of the shot peened surface and microstructural deformation were observed with increase in peening time or pressure. Interestingly, increasing shot-peening time or pressure did not increase the residual stresses [13]. Compressive residual stresses have also shown to increase the fatigue cycles for crack initiation [13]. In the work referenced here, there was no evidence of crystallization induced by the peening. In certain BMG alloys, peening has been employed as a method to induce useful residual stresses as a method to improve plasticity and the fatigue limits.

In this work, an abrasive layer removal method (referred hereon as impact treatment) on amorphous ribbons and the resulting curvature due to a change in residual stress state is discussed. Different ribbon widths were tested using similar conditions. The effect of impact treatment, on the ribbon thickness, curvature and their mechanical properties are discussed here.

11.2 Materials and Methods

Amorphous $Fe_{45}Ni_{45}Mo_7B_3$ ribbons of 30 μm thickness and two different widths, 8 mm and 50.8 mm were used. Impact treatment on the amorphous ribbon was performed using custom plates made of A316 steel, with 8 mm wide window slits, held together using clamps (Fig. 11.1).

Impact treatment was performed using a sandblaster[1] equipped with an enclosure, reclaimer and a dust bag. Glass beads of the type BT-8 were used as the abrasive impact media (0.15–0.2 mm in diameter). The treatment was performed on the ribbons while holding them between the custom plates. Bulk tension tests were performed on the 8 mm wide ribbon samples using a hydraulic driven Instron UTM. ASTM E345 – 93(2008) "Standard Test Methods of Tension Testing of Metallic Foil" was followed. Aluminum tabs were glued to the ribbon test specimen ends to avoid slippage from the grips (Fig. 11.2).

Applied strain was computed using a Laser Extensometer[2] along with a datalogger suitable for recording compliance free strain measurements. Micrographs on the ribbon surface and thickness measurements were taken using a field emission

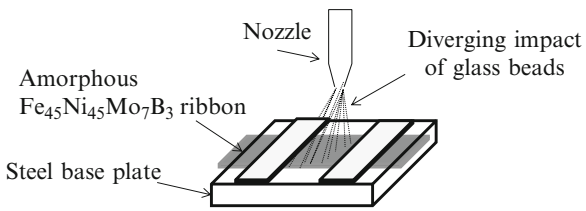

Fig. 11.1 Schematic of the "impact treatment" process of metallic glass ribbon

[1] Zero INEX 3048R.

[2] Model LE-05.

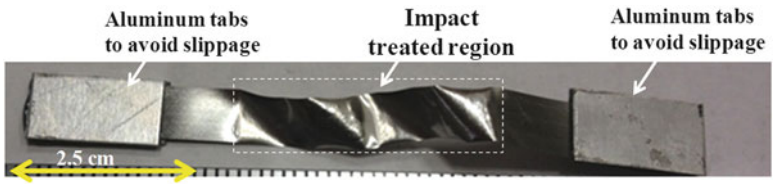

Fig. 11.2 Tension testing sample, with impact treated regions

scanning electron microscope (FESEM)[3] equipped with a back scatter detector and EDAX system. X-ray diffraction[4] was performed with Cu-Kα radiation at tube parameters of 40 kV/40 mA. The detector distance to the center of diffraction was kept at 30 cm which covers approximately the area of 20° in 2θ and 20° in χ with 0.02° resolution. A motorized five axis (X, Y, Z (translation), χ (tilt), φ (rotation)) stage was used to move the measurement spot to the instrument center within 12.5 μm position accuracy. Sample positioning was controlled by a video-laser positioning system before each exposure to ensure diffraction patterns come from the impact treated regions of the ribbon. Ribbon widths of 25.4 mm, 12.5 mm, 8 mm were cut from the 50.8 mm precursor roll and subjected to impact treatment. Samples from the 8 mm precursor roll were used for comparison. The mass of the ribbon to 0.01 g accuracy was measured before and after impact treatment. Both 8 mm wide ribbons and 50.8 mm wide ribbons were subjected to impact treatment under a similar pressure.

11.3 Results

By varying the pressure of impact, time and distance several conditions of impact treatment were performed. Different curvature responses of the ribbon were observed. Response of the ribbon for a blasting pressure of 0.5 MPa (75 Psi) from a distance of 50 mm was chosen for further examination, as the curvature in the ribbon in this condition was significant enough to curl and close it onto itself. Results from tension testing of the 8 mm wide impact treated ribbons were compared to untreated ribbons. Yield strength and the Young's modulus were calculated from the resulting stress- strain data (Fig. 11.3).

The 8 mm wide ribbons and the 50.8 mm wide ribbons showed different curvature responses for the same pressure and time of impact. The wider ribbons showed a significant curvature, enough to curl and close onto itself (Fig. 11.7), while the narrow ribbon did not close, but showed slightly greater curvature. Different ribbon samples were cut from 8 mm wide and 50.8 mm wide precursor rolls and the mass of the samples were measured before and after impact treatment (Table 11.1).

The surface of the ribbon after impact was examined through SEM. Micrographs of the treated ribbon show a loss of material. A 10–14 % decrease in the thickness of the ribbon was measured, while the edges of the ribbon were non-uniformly distorted due to impact (Fig. 11.4).

11.4 Discussion

Bulk tension testing of impact treated ribbons show a 10 % increase in the modulus and a 11 % decrease in the yield strength. However, the results from the tension tests are not statistically significant to show a difference in these properties due to impact treatment. Unlike shot peened BMGs [10, 11, 14], there was no plasticity in the treated ribbon samples.

Each of the impact regions on Fig. 11.5 was 164 mm^2 in exposure area. In tensile loading, the failure occurred in the treated-untreated transition region of the ribbon, where edge distortions and thickness reduction were observed from SEM measurements.

SEM micrographs on the treated ribbon surface show regions of damage like micro-cracks, emanating from the surface of impact, as seen in Fig. 11.6. A non-uniform stress distribution and a brittle response are seen. Hardness of the base plate (A316 steel) may also influence the ribbon behavior. The process of impact potentially changes the residual stress state of the ribbon. This was evident from a change in curvature (Fig. 11.7). There was evidence of layer removal from the thickness

[3] Hitachi S4800-high resolution.

[4] Bruker D8 Discover XRD^2 micro-diffractometer equipped with the General Area Diffraction Detection System (GADDS) and Hi-Star 2D area detector.

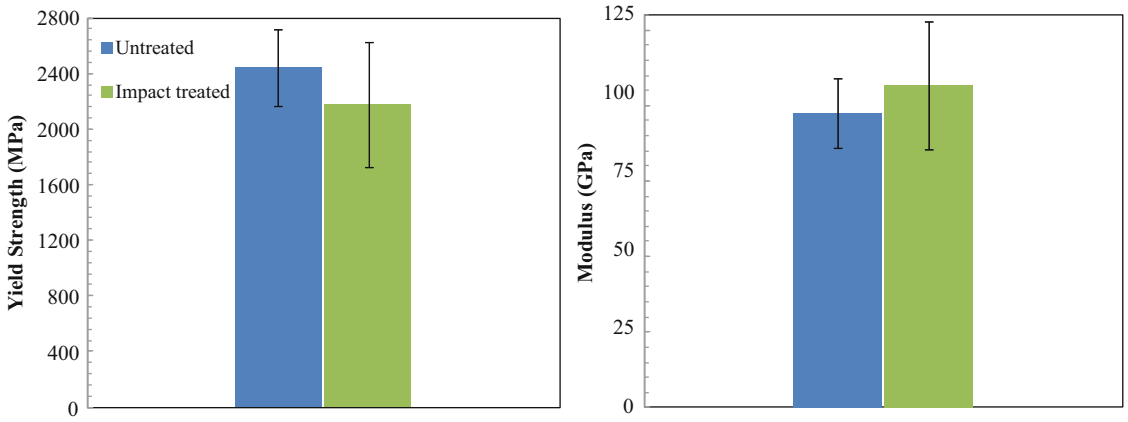

Fig. 11.3 Comparison of yield strength and Young's modulus for untreated and impact treated ribbons

Table 11.1 Mass of the precursor before and after impact

Precursor roll width (mm)	Sample width (mm)	Mass (g) before impact	Mass (g) after impact
50.8	50.8	2.48	2.50
50.8	25.4	1.27	1.27
50.8	12.7	0.61	0.62
50.8	8	0.42	0.42
8	8	0.50	0.48

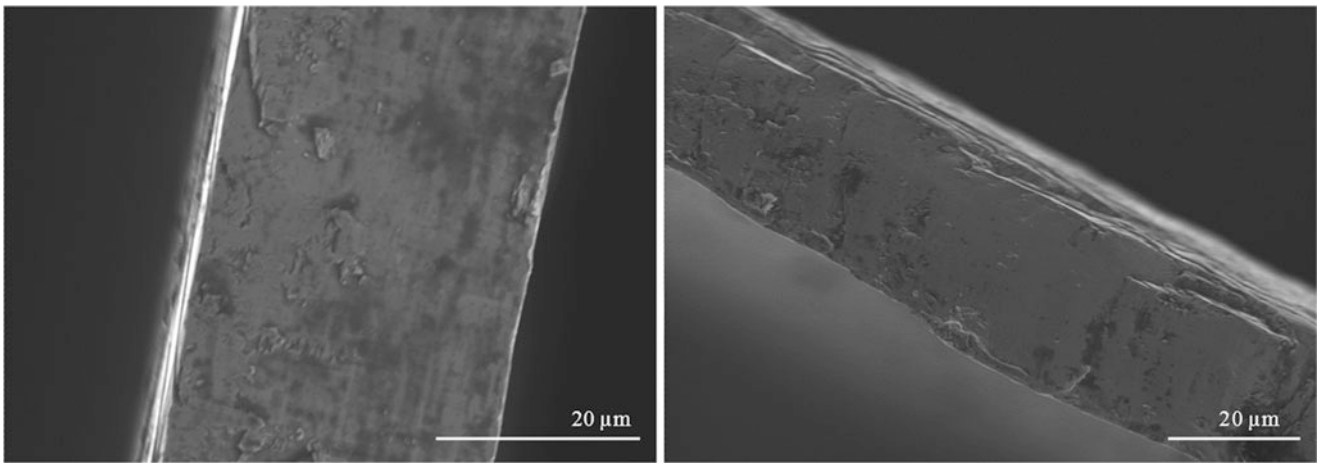

Fig. 11.4 SEM micrographs of untreated (*left*) and impact blasted (*right*) amorphous $Fe_{45}Ni_{45}Mo_7B_3$ ribbons; Note the reduction of thickness after impact, and the distorted edges

measurements. While the prediction of a tempering state would imply a residual compressive surface stress, the layer removal shows an opposite response. Tempering of conventional glasses stifle the cracks at the surface level around impact and have shown to increase the bending strength [10]. BMGs benefit from compressive residual stresses for increasing both plasticity [10, 11] and fatigue limits [13], MGs (this work) may also benefit from residual stresses. The slight increase in the Young's modulus of the impact treated ribbon may have resulted from a possible change in the bond length and the equilibrium bond distance of the atoms, as peening has shown to atomic mobility in BMGs [11]. Further experimentation is needed.

XRD measurements on impact treated ribbons show no signs of crystallization. This behavior is consistent with shot peened BMGs [12]. The formation of significant curvature upon impact is interesting. Ribbons manufactured both using CBMS and PFC has shown residual stresses due to manufacturing conditions [3, 4, 8]. External processing such as the impact treatment changes the residual stress state on the ribbon, causing a change in curvature. As opposed to chemical

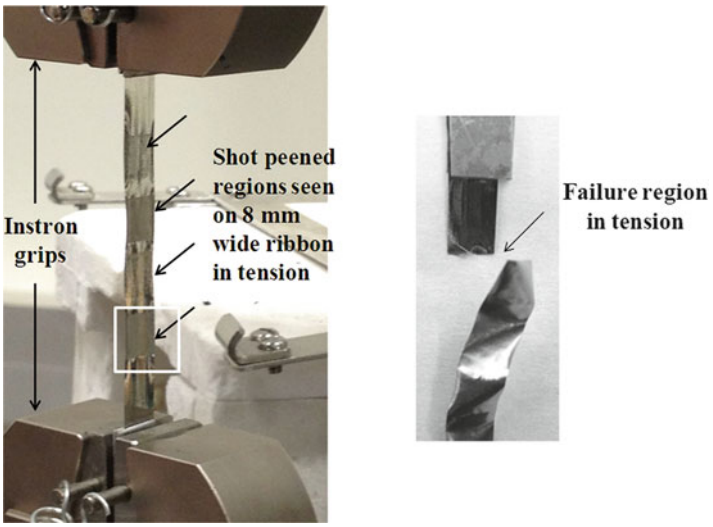

Fig. 11.5 Impact treated tension testing sample under tension (*left*); Failure region in the treated-untreated interface

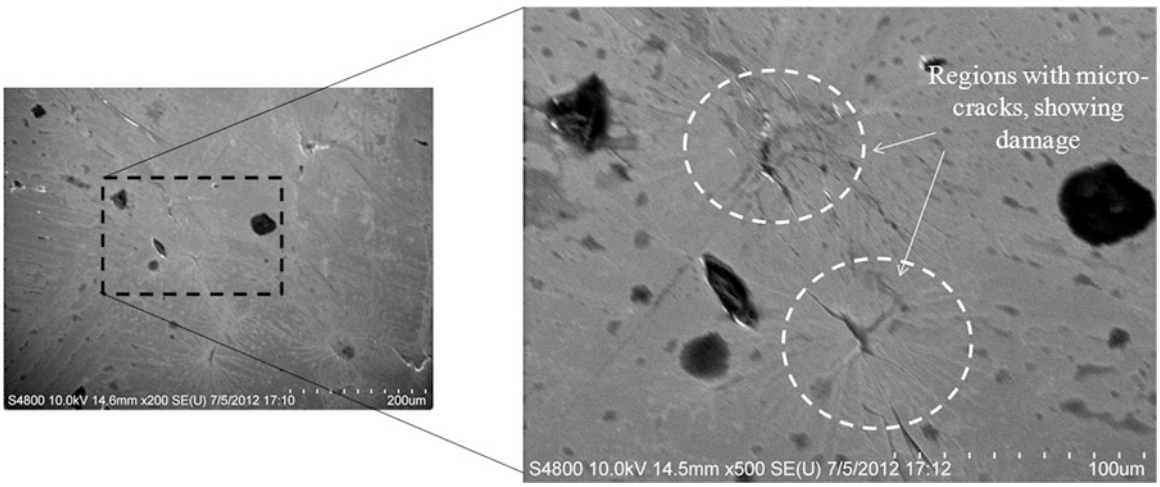

Fig. 11.6 SEM micrographs showing damage area and cracks due to impact treatment

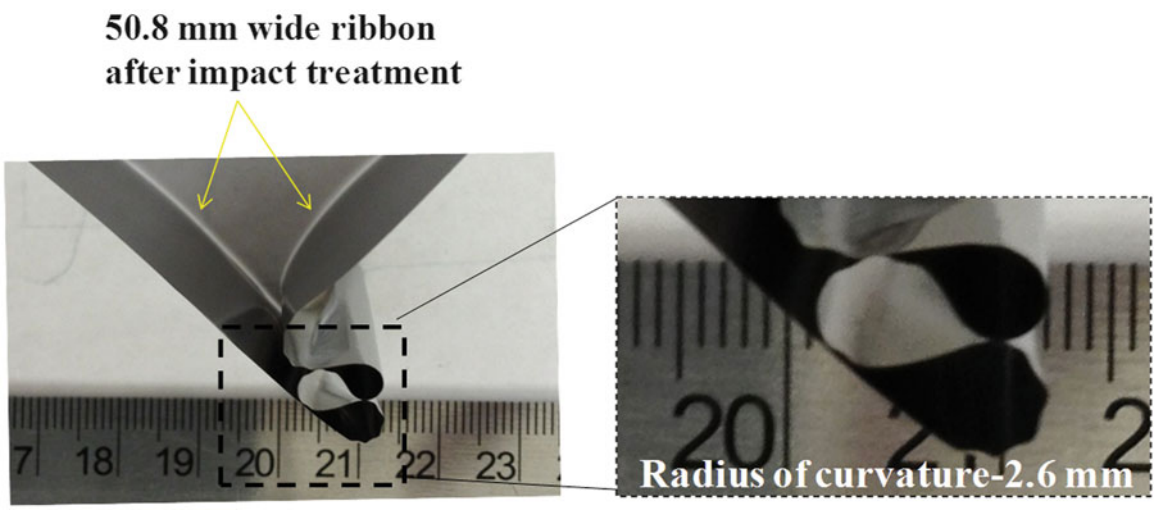

Fig. 11.7 Radius of curvature on the impact treated ribbons from the 50.8 mm precursor roll

etching processes, that relieve the compressive residual stress, impact forming apparently imparts tensile residual stresses on the ribbon surface. The stress states on the free surface, contact surface, and ribbon edges also contribute to the observed curvature. Ongoing work focuses on further reasoning behind AMR's response to impact treatment. Quantification of residual stresses imparted in this process and the influence of ribbon widths and resulting responses are under further investigation.

11.5 Conclusions

Significant residual stresses were observed in a rapidly quenched (10^{-5} K/s) amorphous metal alloy using an abrasive layer removal method. While the prediction of a tempering state would imply a residual compressive surface stress upon layer removal, the abrasive layer removal showed an opposite response. Different ribbon widths show consistently different responses, with possible reasons due to the difference in the residual stress states from the slip casting manufacturing processes. Distorted ribbon edges with 10–14 % reduction in ribbon thickness were observed with SEM micrographs on 8 mm wide impact treated ribbons. Defects in the form of micro-cracks were seen to emanate from the impact treated surface. Results from bulk tension testing show an insignificant decrease in the yield strength and a slight increase in the Young's modulus. The modulus difference is suggestive of a change in the average atomic bond lengths, and ongoing investigations continue.

Acknowledgements MetCel LLC for impact forming processes and tooling. Related research at MetCel was partially sponsored by NSF award number 1214985 and the Oklahoma Center for the Advancement of Science and Technology award AR12-041.

References

1. Taub AI (1984) Dynamic annealing method for optimizing the magnetic properties of amorphous metals. US Patent, 1984
2. Aydiner CC, Üstündag E, Hanan JC (2001) Thermal-tempering analysis of bulk metallic glass plates using an instant-freezing model. Metall Mater Trans A 32:2709–2715
3. Tkatch VI, Limanovskii AI, Denisenko SN, Rassolov SG (2002) The effect of the melt-spinning processing parameters on the rate of cooling. Mater Sci Eng A 323:91–96
4. Pozdnyakov VA, Borisov OV, Filippova1 VP (2010) Simulating residual stresses in ribbons of amorphous metallic alloys. J ASTM Int, pp 1–7
5. Aydıner CC, Üstündag E, Clausen B, Hanan JC, Winholtz RA, Bourke MAM, Peker A (2005) Residual stresses in a bulk metallic glass–stainless steel composite. Mater Sci Eng A 399:107–113
6. Calvo-Dahlborg M (1997) Structure and embrittlement of metallic glasses. Mater Sci Eng A 226–228:833–845
7. Lovas A, Kisdi-Koszó E, Potocký L, Novák L (1987) Effect of processing conditions on physical properties of transition metal-metalloid metallic glasses. J Mater Sci 22:1535–1546
8. Huang S-C, Fiedler H (1981) Effects of wheel surface conditions on the casting of amorphous metal ribbons. Metall Trans A 12:1107–1112
9. Varret F, Gal G, Henry M (1989) The curvature of amorphous metallic ribbons interpreted with a homogeneous quenching model. J Mater Sci 24:3399–3402
10. Zhang Y, Wang WH, Greer AL (2006) Making metallic glasses plastic by control of residual stress. Nat Mater 5:857–860
11. Méar FO, Vaughan G, Yavari AR, Greer AL (2008) Residual-stress distribution in shot-peened metallic-glass plate. Philos Mag Lett 88:757–766
12. Méar FO, Lenk B, Zhang Y, Greer AL (2008) Structural relaxation in a heavily cold-worked metallic glass. Scr Mater 59:1243–1246
13. Jeon C, Son C, Kim C, Lee S (2012) Effects of shot peening on fatigue properties of Zr-based amorphous alloys containing ductile crystalline particles. Metall Mater Trans A 43:471–478
14. Concustell A, Méar FO, Suriñach S, Baró MD, Greer AL (2009) Structural relaxation and rejuvenation in a metallic glass induced by shot-peening. Philos Mag Lett 89:831–840

Chapter 12
Slitting Method Measurement of Residual Stress Profiles, Including Stress Discontinuities, in Layered Specimens

Michael B. Prime and David L. Crane

Abstract Layered specimens can, and often do, have discontinuities in residual stress across the material interfaces. Stress discontinuities internal to specimens are notoriously difficult to measure, yet they can have profound impact on debonding and other failures. The incremental slitting method, also known as crack compliance, is generally excellent at resolving stress profiles even when there are high gradients. However, the data reduction for slitting usually involves some smoothing, which makes it hard to resolve discontinuities. In this work, we start with a recent technique to analyze slitting data using Tikhonov regularization, and extend that technique to allow stress discontinuities at material interfaces. The new method is then demonstrated experimentally on several specimens, including metals and ceramics.

Keywords Residual stress • Slitting • Regularization • Layers • Inverse solution

12.1 Introduction

Residual stresses play a significant role in many material failure processes like fatigue, fracture, and stress corrosion cracking [1, 2]. Residual stresses are the stresses present in a part free from external load, and they are generated by virtually any manufacturing process. The subject of this study is the measurement of residual stresses in layered specimens using the incremental slitting method [3, 4].

Incremental slitting generally provides excellent spatial resolution of residual stress profiles [5–8], but accurate resolution of the discontinuous stress profile across layers is more challenging. Analyzing slitting data requires the solution of an elastic inverse problem to calculate the original residual stresses based on strains measured during the incremental deepening of a slit. Because the inverse solution tends to amplify noise in the strain data into larger noise in the stress profile, some type of smoothing is usually used. However, such smoothing makes it difficult to resolve discontinuities. In fact, the most common method for solving the inverse problem is to expand the stresses in terms of a continuous polynomial series [3, 9], which does not allow for discontinuities at all. More sophisticated implementations of the series expansion method use piece-wise polynomials [10] which can resolve discontinuous stress profiles [11–13]. However, using piecewise polynomials is computationally intensive and numerically awkward.

In this work, we start with an inverse methodology that uses pulse functions and Tikhonov regularization [14] and has proven to be superior to the series expansion method for resolving stress profiles with high gradients [5, 15]. A simple modification of the pulse-regularization approach allows one to resolve discontinuities while still retaining the regularization benefits of smoothing other portions of the stress profile. The method is demonstrated on several examples.

M.B. Prime (✉) • D.L. Crane
Los Alamos National Laboratory, 1663 Los Alamos, NM 87545, USA
e-mail: prime@lanl.gov

M. Rossi et al. (eds.), *Residual Stress, Thermomechanics & Infrared Imaging, Hybrid Techniques and Inverse Problems, Volume 8*, Conference Proceedings of the Society for Experimental Mechanics Series, DOI 10.1007/978-3-319-00876-9_12,

12.2 Theory

12.2.1 Standard Pulse-Regularization

We first review the derivation of the traditional pulse-regularization method, for which the reader is referred to [14] for greater details, before moving onto the formulation that allows for discontinuities. Before adding regularization, the pulse method is equivalent to the "integral method," long used for hole drilling [16]. Prior to inverting the equation to solve for stress, the pulse method is given in equation form by

$$\mathbf{G}\ \sigma = \mathbf{d} \tag{12.1}$$

Where **d** is a column vector of the strains measured at each slit depth and **σ** is a column vector of the stresses originally present over each increment of slit depth. **G** is a lower triangular matrix of the coefficients relating those stresses to the measured strains, as illustrated in Fig. 12.1. The coefficients are usually determined using an elastic finite element analysis.

For an equal number of stresses and strains, inverting Eq. 12.1 returns a stress vector that exactly reproduces the measured strains but generally results in a noisy solution and the undesired behavior that taking more data (meaning more depth increments) results in a noisier solution. For solutions using pulse functions without regularization, the noise amplification is usually kept small by using only a few unevenly spaced material removal increments. This approach is effective, but it diminishes the data content of the calculation, and decreases the spatial resolution of the stress solution.

Tikhonov regularization applies a penalty function to some measure of noise in the calculated stress profile. This procedure effectively smooths the stress solution. It diminishes the adverse effect of the noise without significantly distorting the part of the stress solution corresponding to the "true data". When implementing Tikhonov regularization, Eq. 12.1 is pre-multiplied by $\mathbf{G^T}$ and augmented by an extra term. The result is:

$$\left(\mathbf{G^T G} + \beta\ \mathbf{C^T}\ \mathbf{S^T}\ \mathbf{H}\ \mathbf{S}\ \mathbf{C}\right)\sigma = \mathbf{G^T d} \tag{12.2}$$

where the regularization comes from the matrix **C** which numerically approximates the second derivative of the stress profile. For evenly spaced data, **C** contains rows (−1,2,−1) centered along its main diagonal. For uniformly spaced data,[1] the matrix product **H S C** has the following structure (for simplicity, illustrated for four cut increments)

$$\mathbf{H\ S\ C} \quad = \quad \begin{bmatrix} (h_1 - h_0)/W & & & \\ & (h_2 - h_1)/W & & \\ & & (h_3 - h_2)/W & \\ & & & (h_4 - h_3)/W \end{bmatrix} \begin{bmatrix} s_1 & & & \\ & s_2 & & \\ & & s_3 & \\ & & & s_4 \end{bmatrix} \begin{bmatrix} 0 & 0 & 0 & 0 \\ -1 & 2 & -1 & 0 \\ 0 & -1 & 2 & -1 \\ 0 & 0 & 0 & 0 \end{bmatrix} \tag{12.3}$$

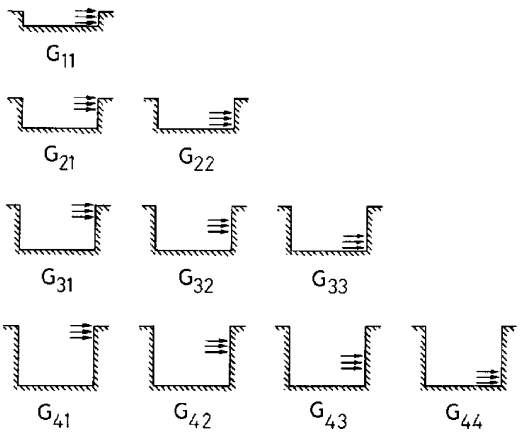

Fig. 12.1 The coefficients G_{ij} correspond to the contribution of the stress over depth increment *j* to the strains measured at slit depth *i*. From [14]

[1] See [14] for general formulas for unevenly spaced intervals.

where the first and last rows of **C** are set to zero to eliminate the degenerate regularization that an "incomplete" $(-1\ 2\ -1)$ pattern would produce at the end points. W is the part thickness in the cutting direction, h_i is the slit depth at increment i and matrix **S** in Eqs. 12.2 and 12.3 contains along its main diagonal the standard errors s_i in the deformation data d_i.

In Eq. 12.2, β is a weighting factor called the regularization parameter. $\beta = 0$ indicates no regularization, and $\beta > 0$ indicates an increasing amount of regularization. The Morozov Discrepancy Principle [17] can be used to determine the value of β that gives the optimal regularization that substantially reduces noise without significantly distorting the true solution. Equation 12.2 can be solved for stress using basic matrix algebra operations.

12.2.2 Pulse-Regularization for Layers and Discontinuous Stresses

Adapting the regularization approach to allow for discontinuities at known locations is as simple as removing select rows in the **C** matrix. For any given discontinuity that is directly at the interface between two depth increments, there are two rows in **C** that act to smooth across the interface that should be removed. An example of such a modified matrix for an example with eight cut increments and the material interface between the 4th and 5th slit depth is given by

$$\mathbf{C} = \left[\begin{array}{cccc|cccc} 0 & 0 & 0 & 0 & 0 & 0 & 0 & 0 \\ -1 & 2 & -1 & 0 & 0 & 0 & 0 & 0 \\ 0 & -1 & 2 & -1 & 0 & 0 & 0 & 0 \\ 0 & 0 & 0 & 0 & 0 & 0 & 0 & 0 \\ 0 & 0 & 0 & 0 & 0 & 0 & 0 & 0 \\ 0 & 0 & 0 & 0 & -1 & 2 & -1 & 0 \\ 0 & 0 & 0 & 0 & 0 & -1 & 2 & -1 \\ 0 & 0 & 0 & 0 & 0 & 0 & 0 & 0 \end{array}\right], \quad \sigma = \left\{\begin{array}{c} \sigma_1^A \\ \sigma_2^A \\ \sigma_3^A \\ \sigma_4^A \\ \hline \sigma_5^B \\ \sigma_6^B \\ \sigma_7^B \\ \sigma_8^B \end{array}\right\} \tag{12.4}$$

where σ_i^A, refers to the stress over depth increment i where that increment is in material A as compared to material B. For visual illustration, lines are shown in Eq. 12.4 to indicate the material interface where a stress discontinuity is allowed. Note that none of the $(-1\ 2\ -1)$ patterns in **C** cross the interface.

Further pairs of rows can be removed for additional interfaces. If the location of an interface is not known with sufficient precision, more than two rows may need to be removed to ensure the discontinuity is resolved.

12.2.3 Calibration Coefficients

The calibration coefficients (**G** in Eqs. 12.1 and 12.2) are calculated using a finite element model, which is standard practice for the slitting method [18, 19]. The calculation must model all n slit depths, and the ith slit depth must calculate a coefficient for i pulse loads, making for $n^*(n-1)/2$ calculations. In this work, the Abaqus software [20] was used along with the Python scripting interface, which allows for automation of the multiple calculations.

12.3 Experimental

12.3.1 Aluminum Clad Depleted-Uranium Fuel Plates

The purpose of the Department of Energy- National Nuclear Security Administration's Global Threat Reduction Initiative's (GTRI) Reactor Conversion program, formerly known as the Reduced Enrichment for Research and Test Reactors (RERTR) program, is to work with research reactor operators worldwide in an effort to convert reactors from the use of highly enriched uranium (HEU) fuel to the use of low enriched uranium (LEU). In support of this effort, the Reactor Conversion program is

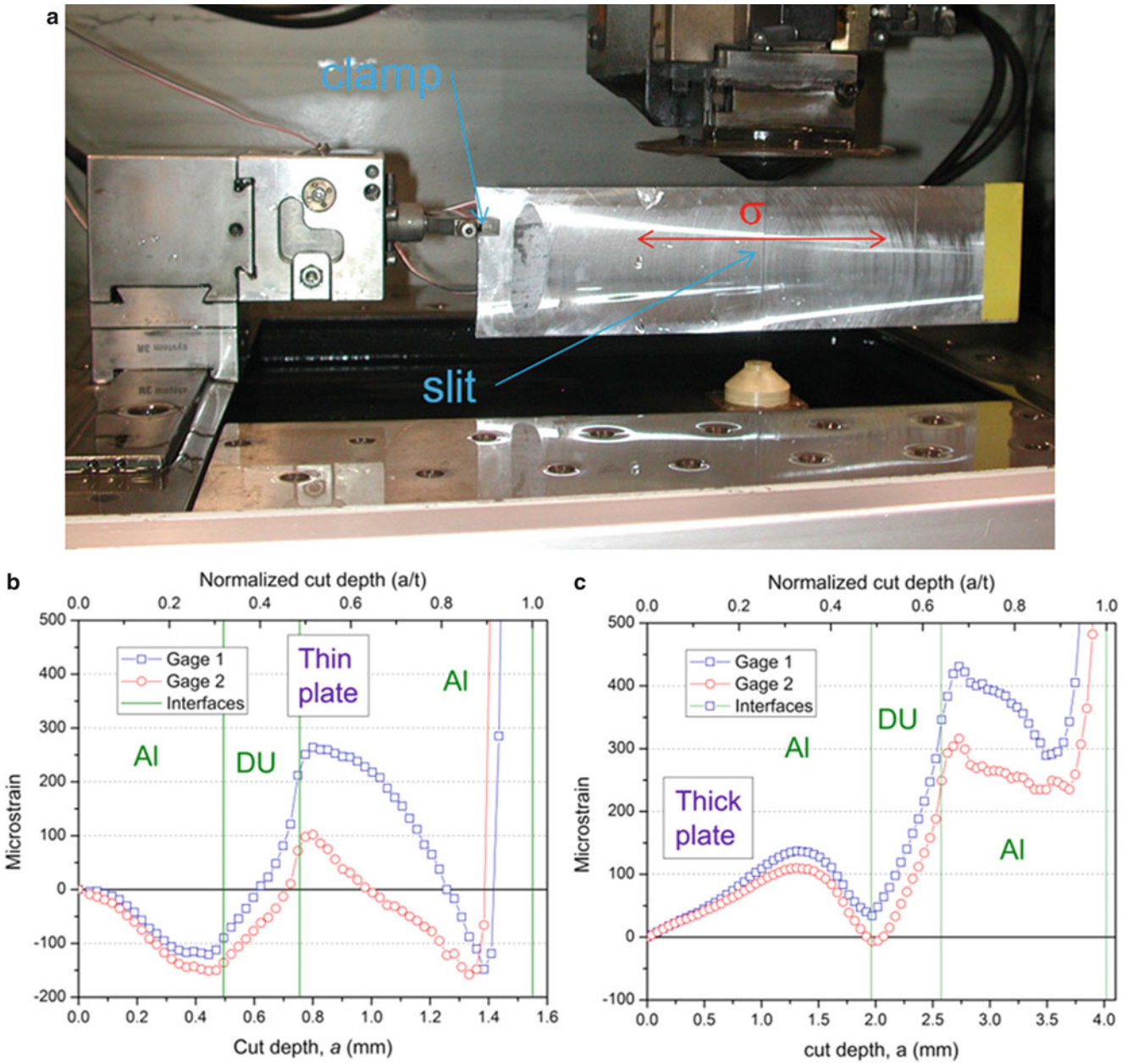

Fig. 12.2 (**a**) One of the plates in the EDM machine after slitting was completed. The strain gauges are on the opposite face. (**b**) strain data on the thin plate and (**c**) on the thick plate

working to develop new fuels to allow for the conversion of high performance research reactors worldwide. A significant goal for GTRI's Reactor Conversion program is converting high performance research reactors from highly enriched uranium (HEU) dispersion fuel plates to low enriched uranium (LEU) monolithic fuel plates. This requires development, qualification, and production of high-density, monolithic LEU-10Mo (wt. pct.) foils [21]. The monolithic fuel foils are to be co-rolled with Zr and clad with 6061Al using hot isostatic pressing (HIP) [22].

For testing purposes, samples were prepared using Depleted Uranium (DU) instead of LEU. Through-thickness profiles of the longitudinal residual stress were measured in two clad fuel plates with DU-10Mo elements, coated with a 20 μm zirconium layer, sandwiched between layers of Al 6061. Both samples were slit using wire Electric Discharge Machining (wire EDM) with a 100 μm diameter brass wire, and strain gages (two for redundancy) on the back face opposite the cut. One plate had 0.61 mm thick DU off-center in a 4.6 mm total plate thickness and was slit in increments of 50.8 μm. The other plate had 0.28 mm thick DU off-center in a 1.5 mm thick plate and was cut in increments of 25.4 μm. Figure 12.2 shows the test setup and the strain data.

Table 12.1 Material properties used to calculate calibration coefficients in finite element model

Material	E	ν	α
Alumina	350 GPa	0.23	8.1×10^{-6}/C
Zirconia	200 GPa	0.3	10.3×10^{-6}/C
50/50	265 GPa	0.267	9.07×10^{-6}/C

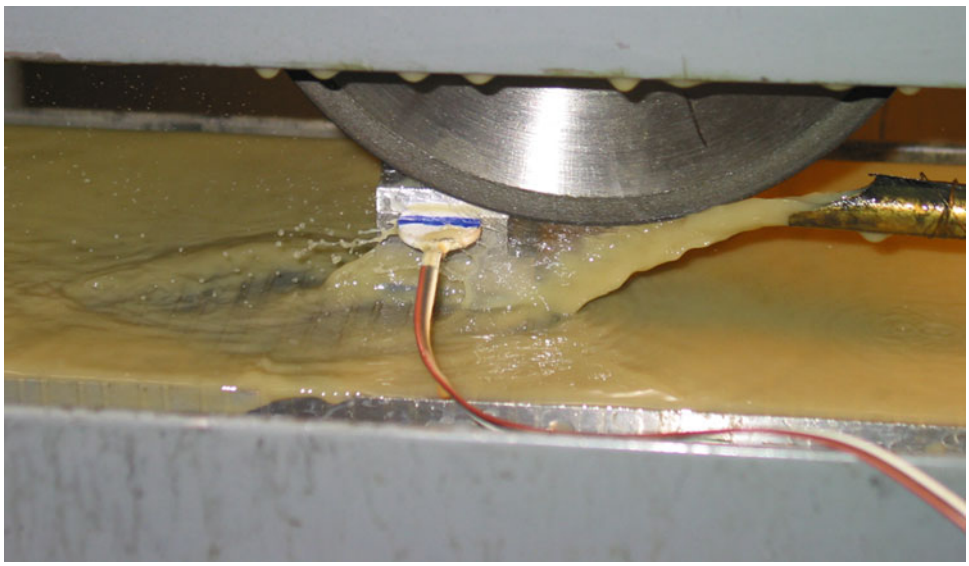

Fig. 12.3 The test specimen during the slitting process

12.3.2 Multi-Layered Ceramic

As part of an effort to manufacture functionally graded ceramics and mesoscale heat exchangers [23–25], 18 mm diameter multi-layered disk were fabricated using novel powder processing and sintering technology. A slitting measurement was performed on a disk with a 0.875 mm thick alumina layer, a 0.835 mm thick mixed alumina-zirconia layer, and then a 0.943 mm thick layer of zirconia [26]. Here we present a re-analysis of the old data. Table 12.1 shows the elastic and thermal expansion properties of the materials.

Figure 12.3 shows the experimental setup. A grinding wheel was used to initially make a diametrical slit 25 μm deep. The diamond grinding wheel was 1.07 mm thick and 152.9 mm in diameter. The wheel was spinning at 3,600 RPM, and approximately 1 μm was removed in each pass of the wheel while bathing the cut in coolant. A strain gage had been mounted on the circular face of the specimen opposite the cut to measure the strain in the direction normal to the slit face. A strain reading was taken after the cut. The slit was then deepened in increments of 25 μm, with a strain reading taken after each increment.

The specimen was cut from the Alumina side to about 89 % of the specimen thickness. Figure 12.4 shows the data. Because the specimen is curved from the same cooling deformations that cause the residual stresses, the strains are plotted versus an average slit depth

12.4 Results

12.4.1 Aluminum Clad Depleted-Uranium Fuel Plates

The calibration coefficients (**G** in Eqs. 12.1 and 12.2) were calculated using a 2-D, plane strain finite element model that included all the materials. The data was analyzed separately using the strain data from each gage as a check of repeatability. Figure 12.5 shows the resulting stress profiles. Although the locations of the thin zirconium layers are indicated, they were

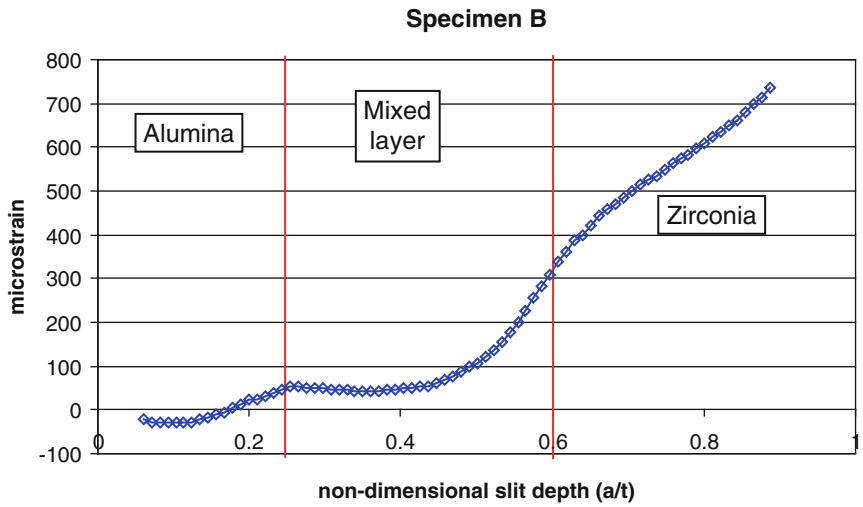

Fig. 12.4 Data from second slitting test

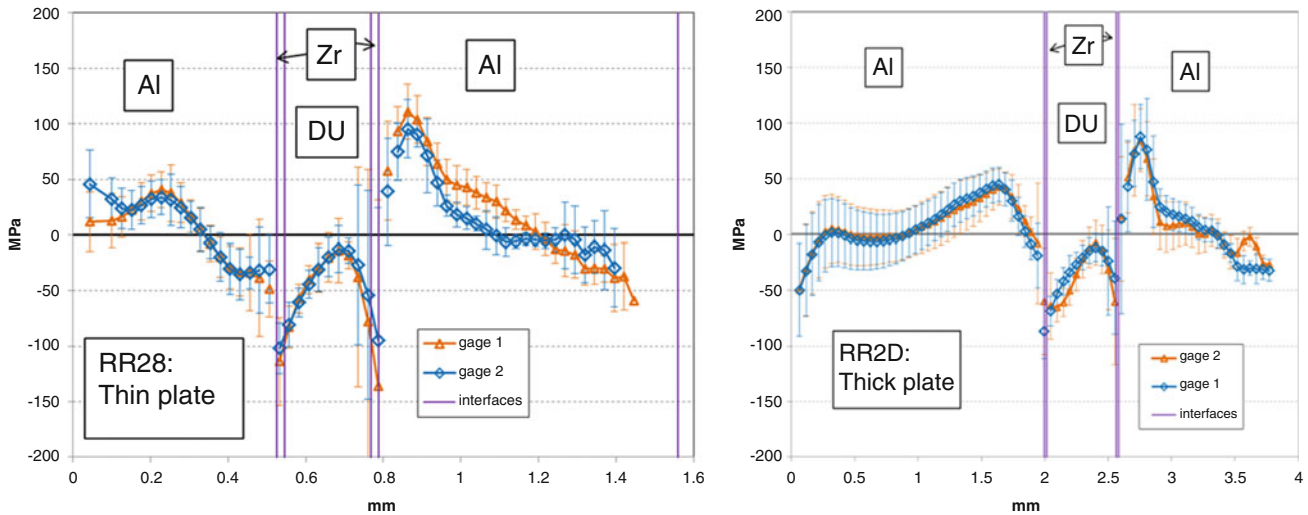

Fig. 12.5 Through-thickness stress profiles in layered plates

too small for their stresses to be independently identified by the measurements. The stress profiles show modest stress levels with significant discontinuities across the material interfaces. The stress magnitudes are generally limited by the yield strength of the 6061 Al which is reduced significantly because of the thermal history during the HIP process [27]. To aid interpreting the stresses, Fig. 12.6 shows a model of the stress profile in the thinner plate based on thermal expansion mismatch and elasticity. Because the model was meant to be explanatory rather than predictive, the temperature change was adjusted down to 200 °C (compared to HIP ΔT of ~ 530 °C) in order to get similar stress magnitudes. The basic nature and slopes of the stress profiles in Fig. 12.5 are well predicted by the thermal mismatch and the requirements of force and moment balance. The more complicated stress profile in the DU layer may come from residual stresses existing prior to the bonding process or from localized plasticity at the material interface.

Figure 12.7 shows how well the inverse solution that gave the stresses in Fig. 12.5 fits the data. The root-mean-square error for the fits ranges from about 1.5 to 2.5 με. Other inverse solutions, such as polynomial series, would not fit the data nearly so well.

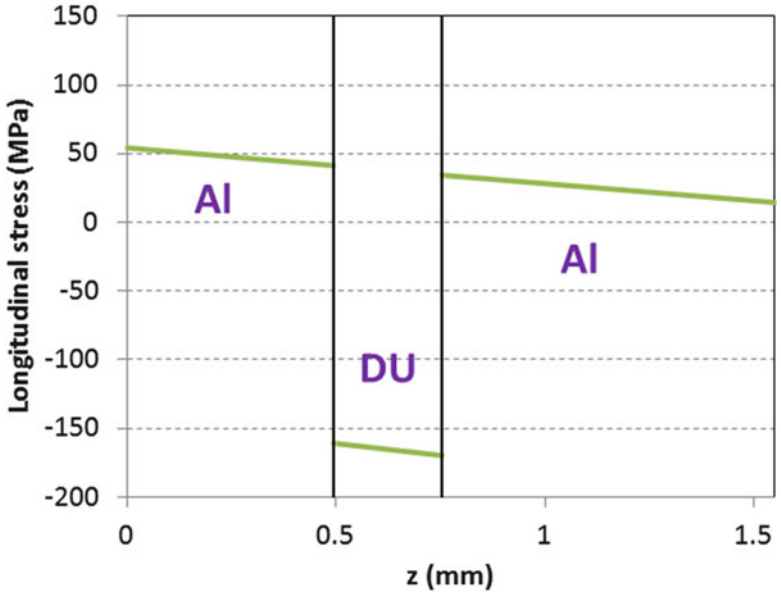

Fig. 12.6 Prediction of stress profile in thinner plate based on thermal expansion mismatch and elasticity

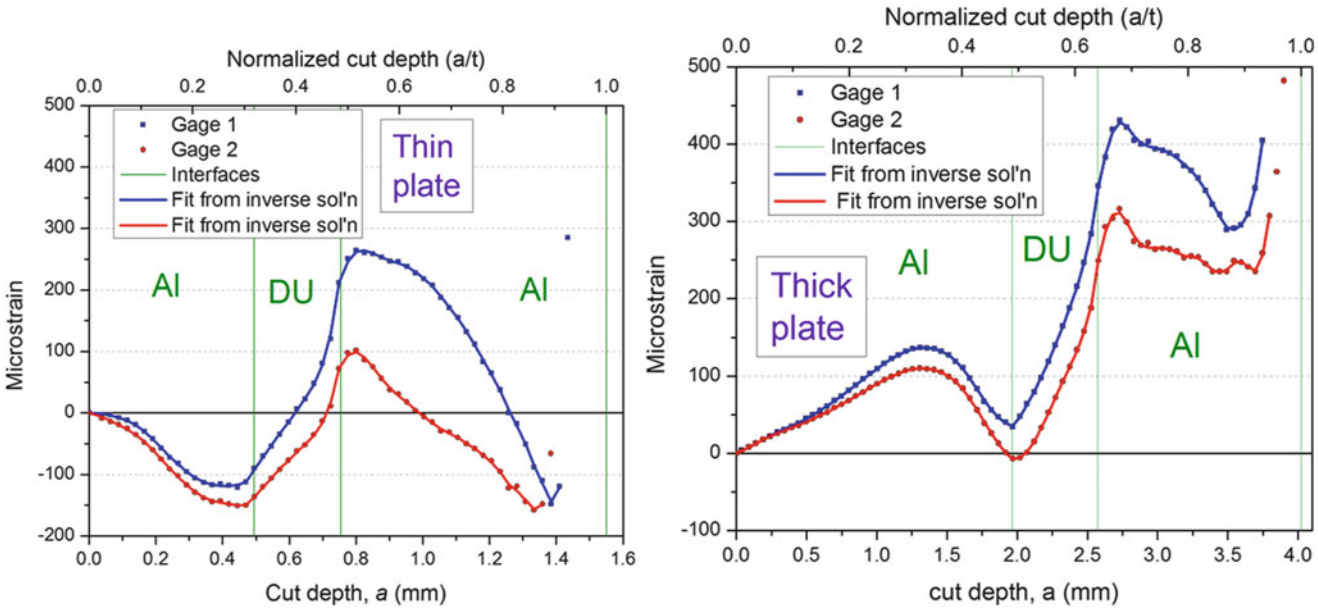

Fig. 12.7 The strain fit given by the inverse solution matched the data much better than other inverse solutions

12.4.2 Multi-Layered Ceramic

The calibration coefficients (**G** in Eqs. 12.1 and 12.2) were calculated using a 3-D, finite element model that included all the materials. Figure 12.8 shows the mesh. The mesh does not include the curvature of the actual specimen because of the difficulty of meshing the curved multi-layered part with the straight slits from the measurement.

The finite element model used coarser slit increments than the experiment. For simplicity of analysis, the strain data was interpolated to the depth increments from the model and analyzed. Because of the part curvature, the experimental slit did not simultaneously cross a material interface along the whole length of the slit. Rather, the crossing took several slit depth

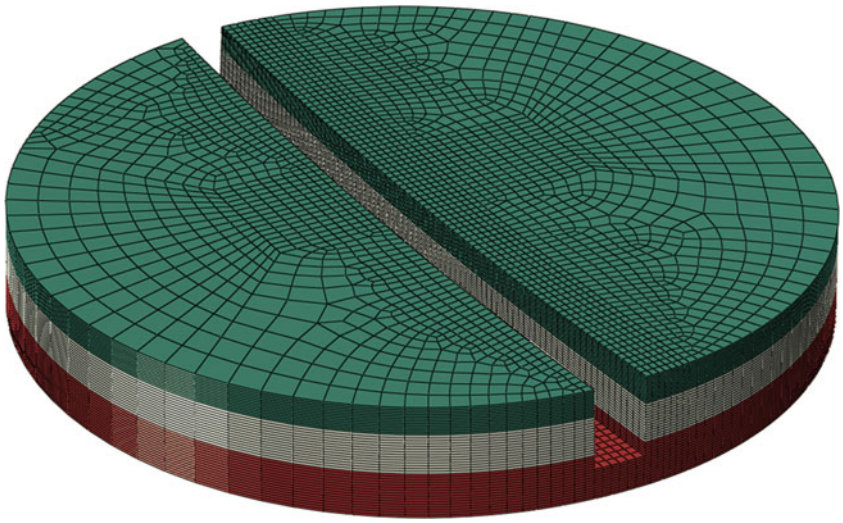

Fig. 12.8 The finite element model used to calculate the calibration coefficients for the data reduction procedure. The model is shown in an intermediate step with the slit at partial depth

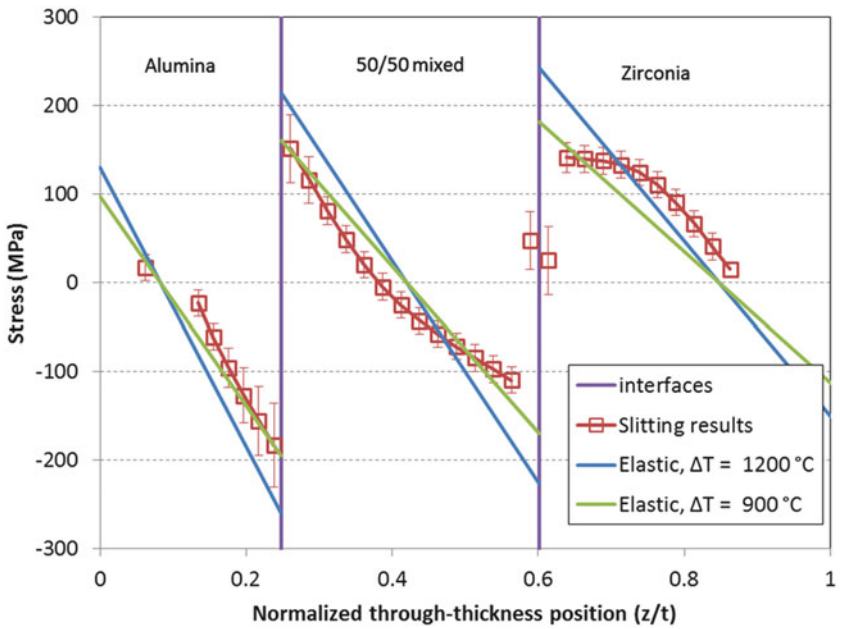

Fig. 12.9 Through-thickness stresses measured in multi-layered ceramic, compared to elastic analysis of thermal mismatch stresses

increments. This issue made the resolution of the stress discontinuities across the interfaces more difficult, and extra rows in the **C** matrix Eq. 12.4 were zeroed to allow the "discontinuity" to occur over two depth increments.

Figure 12.9 shows the through-thickness stress profile as determined by slitting measurements and the pulse-regularization method allowing for discontinuities. The stresses are significant and vary approximately linearly within each layer, with very large discontinuities across layers. A couple of stresses near the second interface appear as intermediate values, in the region were discontinuities were allowed. These points probably reflect the inability to resolve the discontinuity because of the non-uniform slit depth with respect to the interface boundary. For reference, Fig. 12.9 also plots the results of a simple prediction of elastic, thermal-mismatch stresses using the properties from Table 12.1. The results agree quite well with the trends in the results, with the results for a temperature change of 900 °C agreeing somewhat better than the results for the actual temperature change of about 1,200 °C.

Figure 12.10 shows how well the inverse solution that gave the stresses in Fig. 12.9 fits the data. The root-mean-square error for the fits ranges from about 4.8 με, with most of the misfit being evident for the data at shallow cut depths. A fairly large β Eq. 12.2 was used to force the results to stress profiles with less curvature in the regions away from the interfaces. The data for shallow slit depths is the most affected by the issue with part curvature, which is why more regularization was needed in order to reconcile the data with a smoother stress profile.

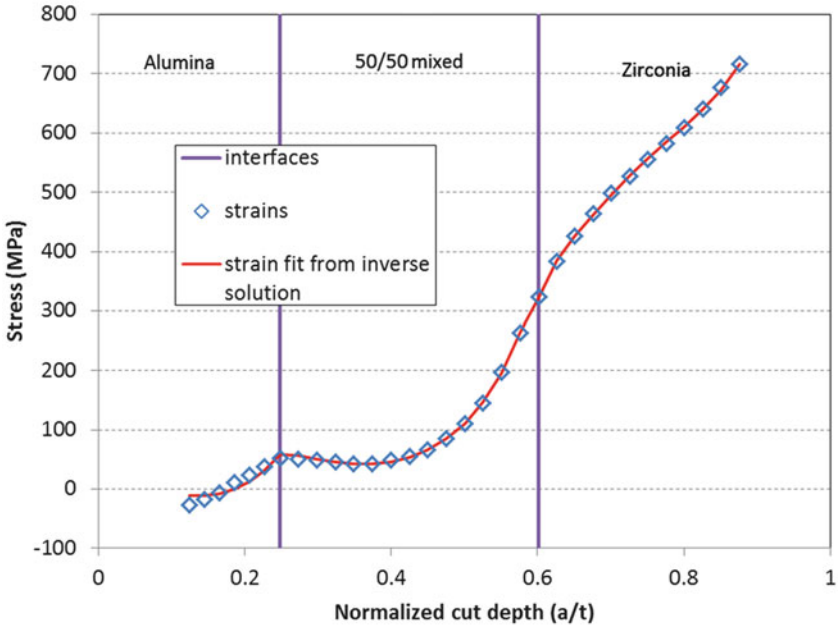

Fig. 12.10 The strain fit given by the inverse solution matched the data quite well

12.5 Conclusion

Residual stress profiles in layered samples were measured using the incremental slitting method. Using a modified pulse-regularization inverse solution approved to be superior to other approaches for solving the inverse problem because simultaneously:

1. It was able to resolve gradients in the residual stress profiles
2. It allowed for smoothing of the solution where appropriate while at the same time allowing for stress discontinuities across the layers
3. The resulting stress profiles were able to reproduce (i.e. fit) the measured strain data to within experimental accuracy.

With the power and flexibility of the modified pulse-regularization method, the ability to resolve discontinuous stress profiles for the tests in this paper was limited by experimental issues. In the aluminum clad depleted-uranium fuel plates, the plates were very wide and the layers were not of uniform thickness. In the multi-layered ceramic, the specimen was curved, but the slits were straight. So in each case, it was difficult to precisely know the slit depth relative to the interface location. For the fuel plates, it would have been possible to cut out a test specimen of thinner width without changing the longitudinal stresses, and then get a better controlled slit depth relative to the interface location. For the ceramic, we plan to test a new specimen with a symmetric layer arrangement and, therefore, no curvature.

Acknowledgments This work was performed at Los Alamos National Laboratory, operated by the Los Alamos National Security, LLC for the National Nuclear Security Administration of the U.S. Department of Energy under contract DE-AC52-06NA25396. By acceptance of this article, the publisher recognizes that the U.S. Government retains a nonexclusive, royalty-free license to publish or reproduce the published form of this contribution, or to allow others to do so, for U.S. Government purposes. The authors would like to acknowledge the financial support of the US Department of Energy- National Nuclear Security Administration's Global Threat Reduction Initiative's Reactor Conversion program.

References

1. Withers PJ (2007) Residual stress and its role in failure. Rep Prog Phys 70(12):2211–2264
2. James MN (2011) Residual stress influences on structural reliability. Eng Fail Anal 18(8):1909–1920
3. Cheng W, Finnie I (2007) Residual stress measurement and the slitting method, Mechanical engineering series. Springer Science + Business Media/LLC, New York
4. Hill MR (2013) The slitting method. In: Schajer GS (ed) Practical residual stress measurement methods. Wiley, Chichester
5. Wong W, Hill MR (2012) Superposition and destructive residual stress measurements. Exp Mech 53(3):339–344. doi:10.1007/s11340-012-9636-y

6. Aydiner CC, Ustundag E, Prime MB, Peker A (2003) Modeling and measurement of residual stresses in a bulk metallic glass plate. J Non-Cryst Solids 316(1):82–95
7. Prime MB, Hill MR (2004) Measurement of fiber-scale residual stress variation in a metal-matrix composite. J Compos Mater 38(23):2079–2095
8. Rankin JE, Hill MR (2003) Measurement of thickness-average residual stress near the edge of a thin laser peened strip. J Eng Mater Technol 125(3):283–293
9. Cheng W, Finnie I (1985) A method for measurement of axisymmetric axial residual stresses in circumferentially welded thin-walled cylinders. J Eng Mater Technol 107(3):181–185
10. Gremaud M, Cheng W, Finnie I, Prime MB (1994) The compliance method for measurement of near surface residual stresses-analytical background. J Eng Mater Technol 116(4):550–555
11. Cheng W, Finnie I, Gremaud M, Rosselet A, Streit RD (1994) The compliance method for measurement of near surface residual stresses-application and validation for surface treatment by laser and shot-peening. J Eng Mater Technol 116(4):556–560
12. Finnie S, Cheng W, Finnie I, Drezet JM, Gremaud M (2003) The computation and measurement of residual stresses in laser deposited layers. J Eng Mater Technol 125(3):302–308
13. Ersoy N, Vardar O (2000) Measurement of residual stresses in layered composites by compliance method. J Compos Mater 34(7):575–598
14. Schajer GS, Prime MB (2006) Use of inverse solutions for residual stress measurements. J Eng Mater Technol 128:375–382
15. Hill MR, Van Dalen JE, Prime MB (2011) Assessment of residual stress in fracture mechanics coupons. In: Proceedings of the 2011 Pressure Vessels and Piping Conference, Baltimore, Maryland, USA, July 17–21, 2011, ASME inc., doi:10.1115/PVP2011-57768
16. Schajer GS (1988) Measurement of non-uniform residual-stresses using the hole-drilling method 1. Stress calculation procedures. J Eng Mater Technol 110(4):338–343
17. Tikhonov AN, Goncharsky A, Stepanov V, Yagola AG (1995) Numerical methods for the solution of ill-posed problems. In: Hazewinkel M (ed) Mathematics and its applications. Vol. 328. Springer Netherlands
18. Lee MJ, Hill MR (2007) Effect of strain gage length when determining residual stress by slitting. J Eng Mater Technol 129(1):143–150
19. Rankin JE, Hill MR, Hackel LA (2003) The effects of process variations on residual stress in laser peened 7049 T73 aluminum alloy. Mater Sci Eng A A349(1/2):279–291
20. Simulia Abaqus 5.12-1 (2012) Dassualt systems
21. Wachs DM, Clark CR, Dunavant RJ (2008) Conceptual process description for the manufacture of low-enriched uranium-molybdenum fuel. *Idaho National Laboratory report INLIEXT-08-13840*
22. Crapps J, Clarke K, Katz J, Alexander DJ, Aikin B, Vargas VD, Montalvo JD, Dombrowski DE, Mihaila B (2013) Development of the hot isostatic press manufacturing process for monolithic nuclear fuel. Nucl Eng Des 254:43–52
23. Shin H, Case E, Kwon P (2003) Fabrication of internal channels in ceramics and ceramic composites. J Adv Mater 35(2):28–35
24. Case ED, Ren F, Kwon P, Kok CK, Rachedi R, Klenow B (2005) Machining and ceramic/ceramic joining to form internal mesoscale channels. Int J Appl Ceram Technol 1(1):95–103
25. Sun L, Kwon P (2010) ZrW2O8–ZrO2 continuous functionally graded materials fabricated by in situ reaction of ZrO2 and WO3. J Am Ceram Soc 93(3):703–708
26. Ekbote B, Kwon P, Prime MB (2006) Micromechanics-based design and processing of efficient meso-scale heat exchanger. In: Mallick PK (ed) Proceedings of the American society for composites – 21st technical conference, Dearborn, 2006
27. Alexander DJ, Clarke KD, Liu C, Lovato ML (2011) Tensile properties of 6061 aluminum alloy materials. Los Alamos National LAboratory report LA-UR-11-06707

Chapter 13
Repeatability of the Contour Method for Residual Stress Measurement

Michael R. Hill and Mitchell D. Olson

Abstract This paper describes the results of a residual stress measurement repeatability study using the contour method. The test specimen is an aluminum bar (cut from plate), with cross sectional dimensions of 50.8 × 76.2 mm (2″ × 3″) with a length of 609.6 mm (24″). There are two bars, one bar with high residual stresses and one bar with low residual stresses. The high residual stress configuration (±150 MPa) is in a quenched and over-aged condition (Al 7050-T74) and the low residual stress configuration (±20 MPa) is stress relieved by stretching (Al 7050-T7451). Five contour measurements were performed on each aluminum bar at the mid-length of successively smaller pieces. Typical contour method procedures are employed with careful clamping of the specimen, wire electric discharge machining (EDM) for the cut, laser surface profiling of the cut faces, surface profile fitting, and linear elastic stress analysis. The measurement results provide repeatability data for the contour method, and the difference in repeatability when measuring high or low magnitude stresses. The results show similar repeatability standard deviation for both samples, being less than 10 MPa over most of the cross section and somewhat larger, around 20 MPa, near the cross section edges. A comparison with published repeatability data for other residual stress measurement techniques (x-ray diffraction, incremental hole drilling, and slitting) shows that the contour method has a level of repeatability that is similar to, or better than, other techniques.

Keywords Residual stress • Repeatability • Uncertainty • Contour method • Aluminum

13.1 Introduction

Residual stresses exist in a component in the absence of external load, and while there is no obvious evidence of their existence, they have potentially significant effects on part performance [1, 2]. There are many options for residual stress measurement, each with advantages and limitations [3]. Thus, when choosing a residual stress measurement technique, it is important to understand first what the measurement should provide (e.g., what components of the stress tensor, over how many spatial dimensions), and secondly, the required precision expected from the measurement. While the contour method has recently emerged as a useful technique for measuring residual stress [4], there is currently no published information on its precision. This study develops data to quantify the repeatability of the contour method.

Repeatability is the precision provided by a measurement technique under repeatability conditions and is generally quantified by the *repeatability standard deviation*. The repeatability standard deviation is the standard deviation of a given measurand obtained under repeatability conditions [5], where repeatability conditions are defined as the conditions where independent test results are obtained with the same method on identical test items, in the same laboratory, by the same operator, using the same equipment, in short intervals of time. Since this paper regards a destructive residual stress measurement method, it should be noted that identical test items cannot be used, so multiple measurements are made on the same article, where the measurements are expected to be nearly identical. Also of interest is the *repeatability limit*, defined as an expected maximum absolute difference between two individual test results obtained under repeatability conditions, with a probability of approximately 95 %. Practically, the repeatability limit is 2.77 times the repeatability standard deviation. Both the repeatability standard deviation and repeatability limit will be reported later.

M.R. Hill (✉) • M.D. Olson
Department of Mechanical and Aerospace Engineering, University of California, One Shields Avenue, Davis, CA 95616, USA
e-mail: mrhill@ucdavis.edu; molson@ucdavis.edu

M. Rossi et al. (eds.), *Residual Stress, Thermomechanics & Infrared Imaging, Hybrid Techniques and Inverse Problems, Volume 8*, Conference Proceedings of the Society for Experimental Mechanics Series, DOI 10.1007/978-3-319-00876-9_13,

Measurements are made in two long aluminum bars of rectangular cross section, one bar that contains residual stress from quenching and a second bar that is stress relieved by stretching. A carefully processed long bar is well suited to assess repeatability of the contour method because, except near its ends, the bar is expected to have the same stress field at all planes along the length. The rectangular cross section eases several practicalities associated with the contour method, including issues arising from the "bulge error", described in [6], that are mitigated with good clamping on the flat edges of the bar. A second practicality made easier in a long bar relates to cutting artifacts that can arise during wire EDM when there is a change in the thickness being cut; this issue is mitigated by cutting across the width of a bar of uniform thickness. Thus, this specimen provides a good environment to study the repeatability of the contour method under best-case conditions. As with any repeatability study, the data developed to not address the accuracy of the technique.

13.2 Methods

Measurements were done on two aluminum bars that were cut from 50.8 mm (2 in) thick rolled 7,050 aluminum plate. The original plate was long, and in the T7451 condition, being over-aged and stress relieved by stretching. One bar, referred to as the stress relieved bar, had no additional heat treatment; the second bar, referred to as the quenched bar, had an additional heat treatment performed to introduce a higher stress. The quenched bar heat treatment was representative of that used for the T74 temper [7], and consisted of solution heat treatment at 477 °C for 3 h, immersion quenching in room temperature water with 16 % polyalkylene glycol (Aqua-Quench 260), and a dual artificial age at 121 °C for 8 h then 177 °C for 8 h. The bar cross section is 50.8 mm (2 in.) thick, by 76.2 mm (3 in.) wide. The length of the stress relived bar is 610 mm (24 in.) and the length of the quenched bar is 914 mm (36 in.), the latter being cut to 610 mm before making measurements, as described below (Fig. 13.1). Material orientation was different in the two bars, with the rolling direction (L) along the 76.2 mm width of the quenched bar and along the 610 mm length of the stress relieved bar. We adopt a coordinate system for residual stress measurement having an origin at the bottom left hand side of the bar cross section, with positive x along the 76.2 mm width, to the right, and positive y along the 50.8 mm thickness, upward.

Contour measurements, which involve cutting the sample through a given measurement plane, were performed at five locations along the length of the bar (Fig. 13.1). The first contour measurement was at the center of the bar length (plane 1), followed by contour measurements at the center of the remaining half bars (planes 2A, 2B), followed by two contour measurements at the center of two of the quarter bars (planes 3A, 3B). In general, anytime a specimen is cut, the stress in the body is altered, with the change being large at points close to the cut and negligible far from the cut. Therefore, it is generally important to account for the effects of a cut on subsequent stress measurements [8]. In the present study, the original bar has length L that is long compared to the width and thickness, and the measurements are far enough apart so that the contour cuts are not expected to significantly alter the stress at the locations of subsequent measurements. Preliminary finite element modeling suggests that if additional cuts were performed, stress measured in the smallest remaining piece, having length $L/8$ before cutting, would be about 5 % smaller than measured in the pieces with initial lengths L, $L/2$, and $L/4$.

To reduce end effects from quenching, 152 mm (6 in.) was removed from each end of the quenched bar (Fig. 13.2, planes 0A, 0B) before making contour measurements. Prior to cutting, four biaxial strain gages were attached to the top of the bar at the two contour planes closest to the end planes, with two gages on each plane, as shown in Fig. 13.2. Biaxial strain was recorded during the end removal process and stresses computed using plane stress Hooke's law showed a negligible change of stress (less than 5 MPa).

Detailed theoretical background for the contour method was provided earlier by Prime [4]. Detailed experimental steps for the contour method have been provided by DeWald and Hill [9], with a brief summary given here. At each contour plane, the specimen was cut in two using wire EDM. Cutting was performed with the specimen rigidly clamped to the EDM frame. Following cutting, the profile of each of the two opposing cut faces was measured with a laser scanning profilometer to determine the surface height normal to the cut plane as a function of in-plane position. For all measurements, surface height data was taken on a grid of points with spacing of 200 × 200 μm, so that there were roughly 96,000 data points for each surface. The two surface profiles were then averaged on a common grid, and the average was fit to a smooth bivariate Fourier series. A level of smoothing is determined by choosing fitting orders during data reduction.

The residual stress on the contour plane was found with a linear elastic finite element analysis that applied the negative of the smoothed surface profile as a set of boundary conditions on the cut plane. The finite element mesh used eight-node, linear displacement brick elements with node spacing of 1 mm on the cut face, along both x and y, and node spacing normal to the cut face that increased with distance away from the cut, being 1 mm at the cut face and 5 mm at the end of the bar. The mesh was sufficiently refined such that when the node spacing is halved there is negligible change in stress. The model used an elastic modulus of 71.0 GPa and a Poisson's ratio of 0.33 [10].

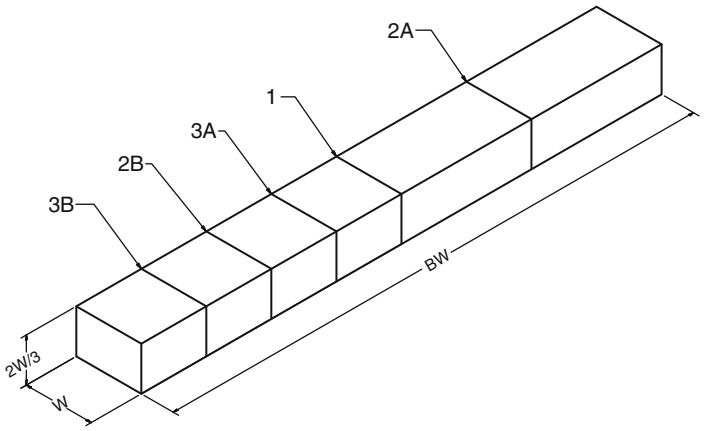

Fig. 13.1 Dimensioned aluminum bar with contour planes. Normalized dimension shown, where W = 76.2 mm

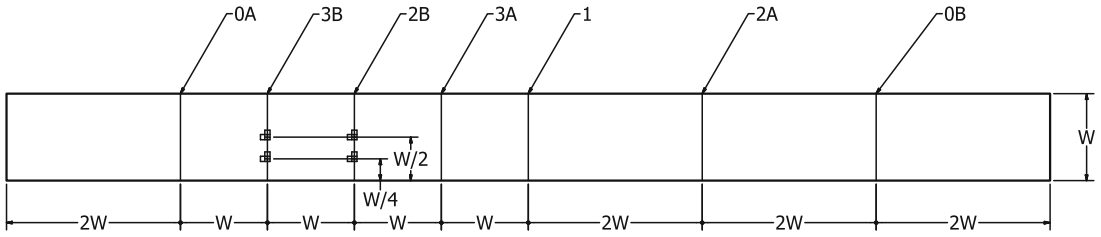

Fig. 13.2 Dimensioned aluminum bar with contour planes and locations of four biaxial strain gages used to measure strain during end removal (planes 0A and 0B) for the quenched bar. Normalized dimension shown, where W = 76.2 mm

The average, repeatability standard deviation, and repeatability limit, were found for each measurement as a function of in-plane position. The repeatability standard deviation was calculated as

$$s(x,y) = \sqrt{\frac{1}{N-1}\sum_{i=1}^{N}\left(\sigma_i(x,y) - \overline{\sigma}(x,y)\right)^2} \tag{13.1}$$

where, $s(x, y)$ is the repeatability standard deviation at a given in-plane position (x, y), N is the number of measurements (5), $\sigma_i(x, y)$ is the measured stress at (x, y) in the *ith* measurement, and $\overline{\sigma}(x, y)$ is the mean measured stress at (x, y) [11].

13.3 Results

Measured residual stress for the stress relieved bar can be seen in Fig. 13.3, and used a fitting orders $k_x = 1$ and $k_y = 2$ (15 terms in the bivariate Fourier series). The results show low magnitude residual stresses around ±20 MPa. The stress has a banded structure with tensile stress at the top, bottom, and center of the bar with compressive regions between; a similar banded residual stress field was seen in earlier measurements of residual stress in 7050-T7451 stress relieved plate [12]. Results for all planes are somewhat asymmetric about the mid-width (x = 38.1 mm), with the right hand side showing larger magnitude residual stress. This asymmetry is not expected in rolled aluminum plate, and may be a result of cutting irregularities, as the cutting direction for all measurements proceeded along the +x direction (left to right in Fig. 13.3). Results for planes 1, 2A, and 2B are nearly symmetric about the mid-thickness (y = 25.4 mm) but results for planes 3A and 3B have some asymmetry about the mid-thickness, with the top having somewhat higher magnitude stress. This asymmetry is also unexpected, as plate rolling, quenching, and stretching are typically symmetric processes.

The mean and repeatability standard deviation for the stress relieved bar can be seen in Fig. 13.4. The repeatability standard deviation is small in the interior, under 5 MPa, and somewhat larger within about 2 mm of the upper and lower

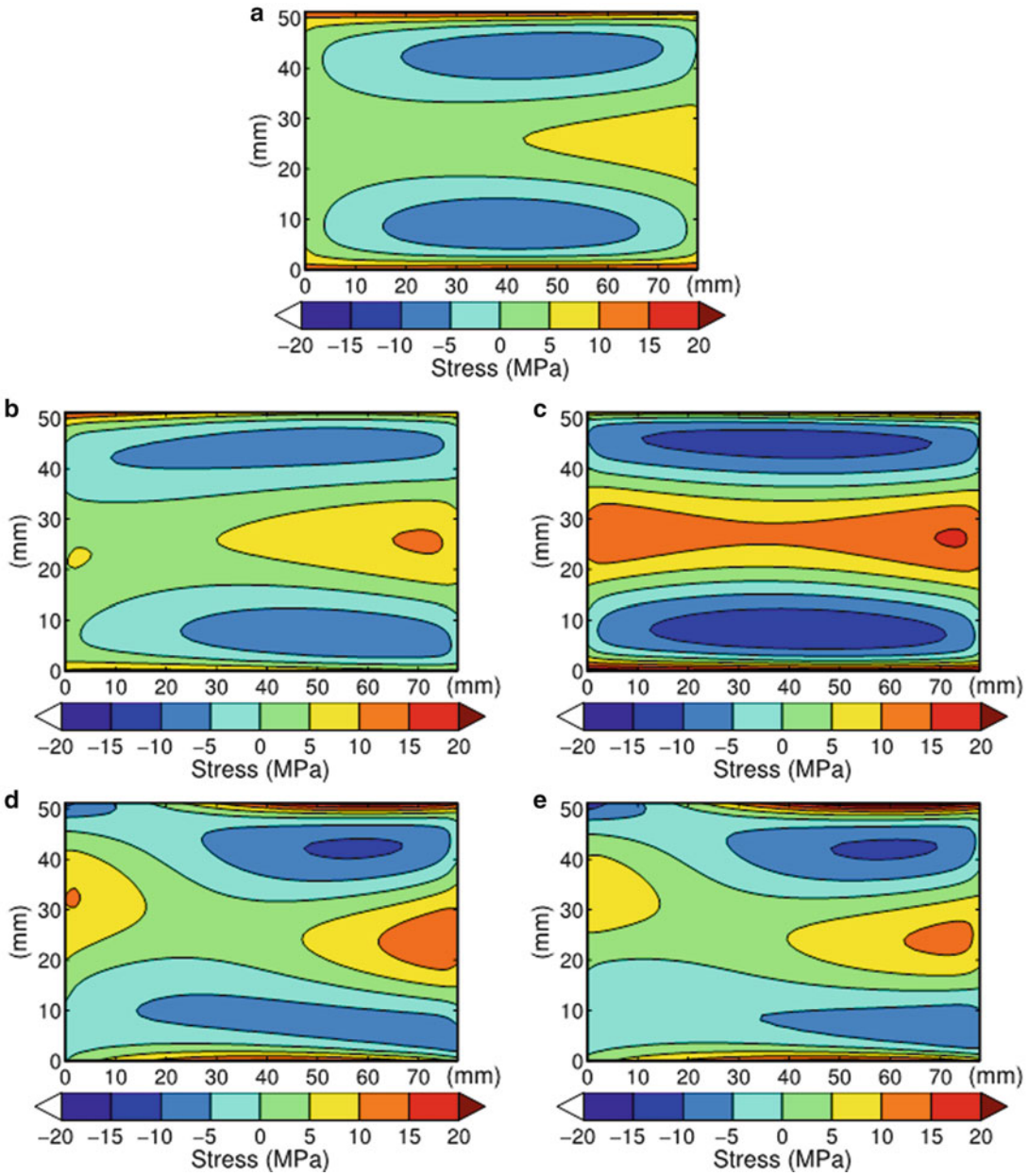

Fig. 13.3 Stress in the stress relieved bar for (**a**) plane 1, (**b**) plane 2A, (**c**) plane 2B, (**d**) plane 3A, and (**e**) plane 3B

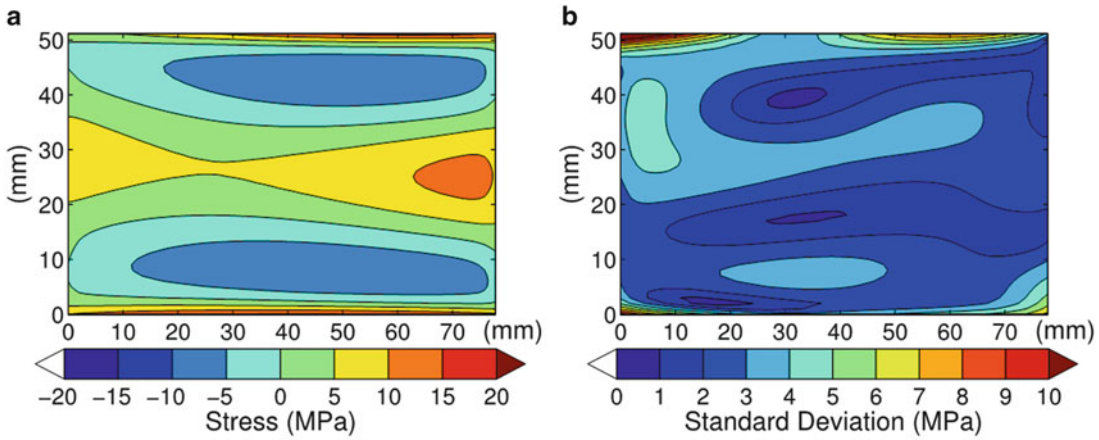

Fig. 13.4 Mean (**a**) and repeatability standard deviation (**b**) of stresses for the stress relieved bar

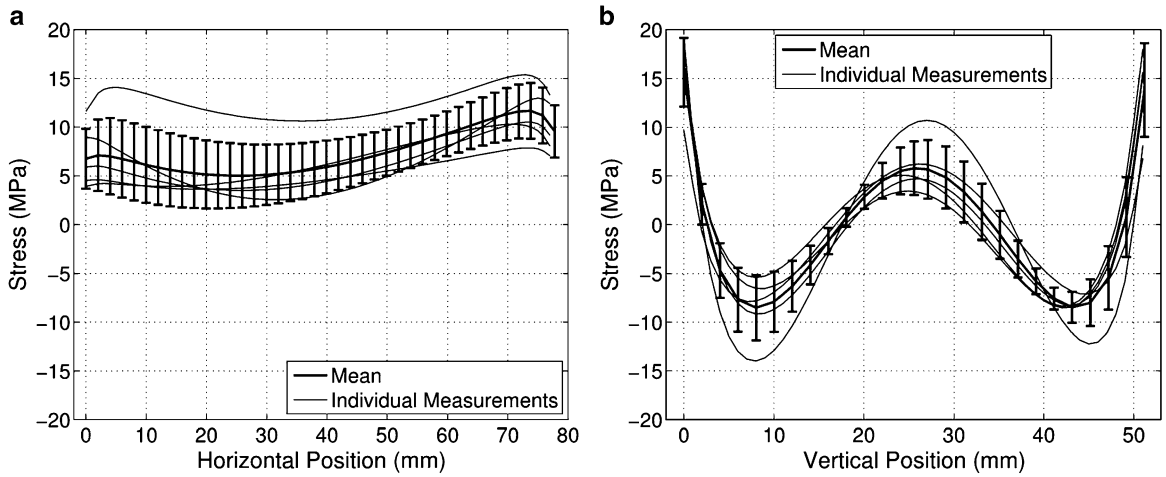

Fig. 13.5 Line plots for the stress relived bar (**a**) horizontal along the vertical mid-thickness and (**b**) vertical along the horizontal mid-thickness, where the error bars are the repeatability standard deviation. The outlier is plane 2B

boundaries of the contour plane, reaching a maximum of 14 MPa at the left side of the upper edge. The repeatability limit is proportional to the repeatability standard deviation, and therefore follows the trends seen in Fig. 13.4b, being less than 14 MPa in the interior and being larger near the upper and lower edges and having a maximum of 39 MPa. The absolute maximum deviation of stress from the mean is 16 MPa, which occurs at the same location as the maximum standard deviation.

Line plots of the stress along two orthogonal lines for the stress relieved bar, one horizontal along x at y = 25.4 mm and one vertical along y at x = 38.1 mm can be seen in Fig. 13.5. The mean stress shows the banded or W profile along the vertical, which was discussed above. Error bars show the repeatability standard deviation, which is a relatively large percentage of the measured stress (around 30 % of the stress range). The line plots underscore the difference between most measurements and a single outlier, plane 2B, that has a larger residual stress magnitude; this outlier significantly affects the standard deviation.

The stress results for the quenched bar can be seen in Fig. 13.6, and used a fitting orders $k_x = 1$ and $k_y = 1$ (9 terms). The results show much larger residual stresses than for the stress relieved bar, with magnitudes of about 150 MPa. The shape of the stress distribution is roughly paraboloid, with tensile stress at the center of the bar and compressive stress at the outside. These features agree with previous measurements of stress in quenched aluminum bar performed by Robinson et al. [13, 14]. The stress measurements appear to be very consistent, with results for plane 1 deviating from the other measurements to some degree

The mean and repeatability standard deviation for the quenched bar can be seen in Fig. 13.7. The repeatability standard deviation is small in the interior, around 5–10 MPa, and somewhat larger within 5 mm of the edges, having a maximum of 20 MPa at the upper left corner. The repeatability limit follows the same trend seen in the repeatability standard deviation (Fig. 13.7b), being 14–28 MPa in the interior with a maximum of 55 MPa. The absolute maximum deviation of stress from the mean is 31 MPa in the quenched bar, which occurs at the edges of the 76.2 mm width.

Line plots of stress along two orthogonal lines through the sample center can be seen in Fig. 13.8 for the quenched bar. The mean stress shows the paraboloid profile. Error bars show repeatability standard deviation, which is a small fraction of the stress (maximum around 5 % of the stress range). Results for plane 1 are a slight outlier.

13.4 Discussion

The repeatability data for the two measurement sets suggest a similar level of precision for measurements in the stress relieved and quenched bars. This indicates that the repeatability of the contour method may remain constant over the range of stress magnitude addressed in this study. When measuring low magnitude residual stresses, as in the stress relieved bar, the repeatability standard deviation is large relative to the resulting stress. This may or may not be acceptable, but there is not

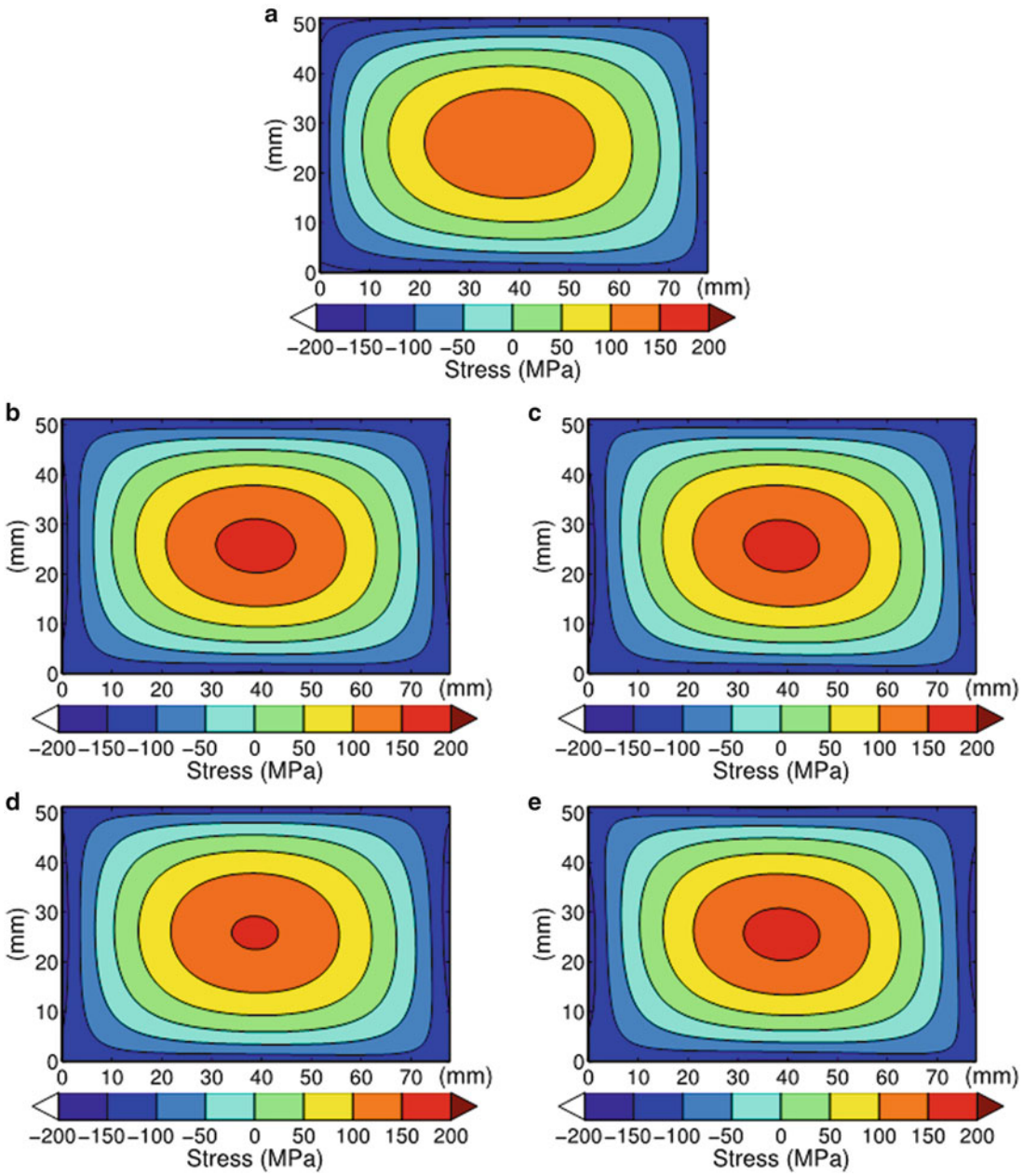

Fig. 13.6 Stress in the quenched bar for (**a**) plane 1, (**b**) plane 2A, (**c**) plane 2B, (**d**) plane 3A, and (**e**) plane 3B

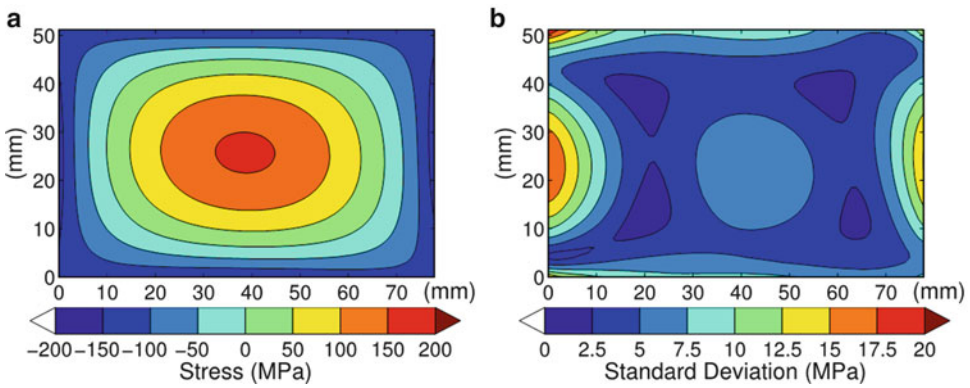

Fig. 13.7 Mean (**a**) and repeatability standard deviation (**b**) of stresses for the quenched bar

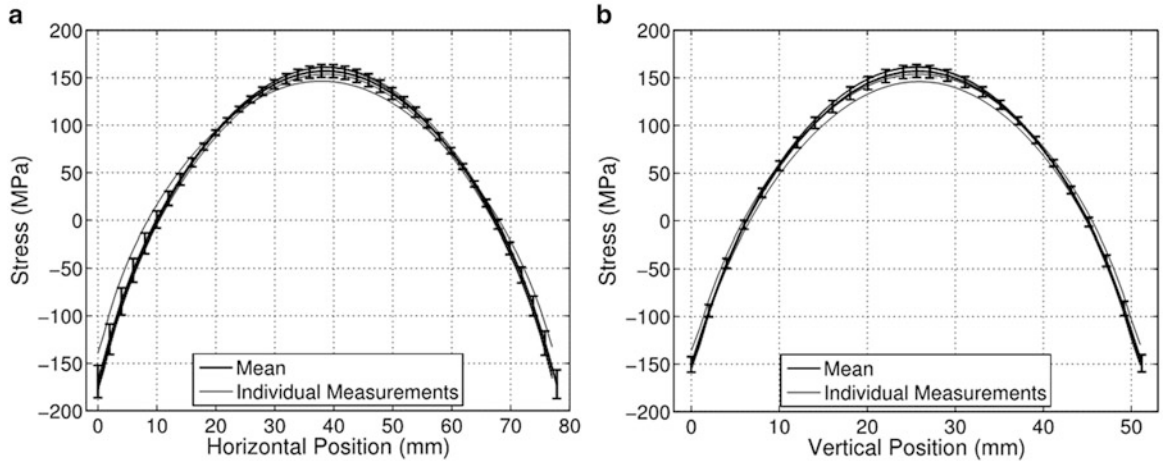

Fig. 13.8 Line plots for the quenched bar (**a**) horizontal along the vertical mid-thickness and (**b**) vertical along the horizontal mid-thickness, where the error bars are the repeatability standard deviation. The slight outlier is plane 1

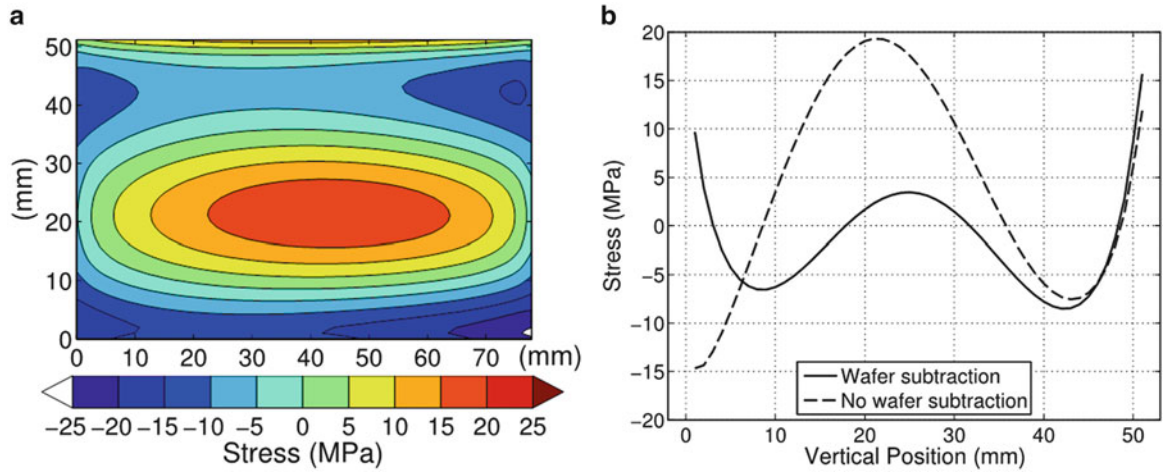

Fig. 13.9 Stress in the stress relived bar (**a**) without stress-free cut correction and (**b**) *vertical line*-out at the mid-width showing the stress with and without the stress-free cut correction

likely to be a more precise alternative for two-dimensional mapping of such residual stress fields. For high magnitude residual stresses, as in the quenched bar, the repeatability standard deviation found here is small relative to the stress magnitude.

The results here depend on using a stress-free cut correction, suggested earlier by Prime [4], to account for variation of the EDM cut from an ideal flat plane. This was accomplished by making a cut on a spare piece of the same material and cross-sectional dimension, where the cut removed a small thickness (1.27 mm) of material and left behind a larger piece. Because the cut was adjacent to a stress-free surface, the surface profile on the cut face is assumed a result of the EDM cutting process and not stress release. The cut profile on the face of the larger piece, called the stress-free profile, was measured using the same procedure as used during the contour experiments. The measured stress-free profile was then subtracted from the profile measured during each contour measurement to correct for the non-flat EDM cut. The differences due to the stress-free cut correction are nearly negligible in the quenched bar, but large in the stress relieved bar, with differences in residual stress less than 20 MPa for both bars. The contour results for the stress relieved bar at plane 3A without the stress-free cut correction in Fig. 13.9a can be compared with the corrected results in Fig. 13.3c, and the comparison shown as a line plot in Fig. 13.9b show the significant effect for the stress relieved bar.

Previous studies of residual stress measurement repeatability give useful context to the results presented above. Published repeatability studies were available for x-ray diffraction, incremental hole drilling, and slitting.

An x-ray diffraction repeatability study by Fry [15] made x-ray diffraction measurements for three different materials (a shot peened CCr3 spring steel block, a quenched 7,010 aluminum block, and a ground piece of titanium alloy) using a tabletop x-ray diffractometer to assess the instrument-operator repeatability. In each case, ten repeat measurements were conducted, where the specimen was removed and replaced in the x-ray diffractometer between each measurement. In this manner, the standard deviation of the measurement sets was established to be 8 MPa for the spring steel block, 3 MPa for the quenched 7,010 aluminum block, and 18 MPa for the ground piece of aluminum. The good repeatability is consistent with the minimal interaction between the test equipment and the test specimen in these measurements; one should expect significantly larger repeatability bounds when performing stress versus depth profiling using x-ray diffraction with layer removal on account of the greater interaction with the sample.

The study by Lee and Hill [16] made five measurements of residual stress versus depth from the surface using the slitting method in thick blocks removed from a single plate of 316L stainless steel. The plate had been uniformly laser peened to induce a deep residual stress field after which the plate was cut into blocks. Typical slitting method techniques were employed with a single back face strain gage and incremental cutting by wire EDM. Residual stress profiles were found as a function of depth from the surface using a polynomial basis. The maximum standard deviation of the five measurements occurred at the surface, and was 15 MPa, but the standard deviation away from the surface was less than 7 MPa; the absolute maximum deviation also occurred at the surface, and was 26 MPa.

Three incremental hole drilling interlaboratory reproducibility exercises have been performed [17, 18]. Two studies are reported by ASTM on specimens nominally free of residual stress, where one study used stress relieved AISI 1018 carbon-steel and the other used stress relieved 304 stainless steel, and where the hole drilling data reduction procedure assumed constant residual stress as a function of depth [17]. The repeatability standard deviation in these two sets of nominally stress free specimens was 14 and 12 MPa, respectively. A cautionary note [17] states that measurements on samples with non-zero residual stress should be expected to exhibit larger variability than found for unstressed samples. A second note states that additional variability should be expected when determining residual stress as a function of depth, a capability that was recently added to the ASTM standard. A third study by National Physical Laboratory (NPL) in the United Kingdom addressed reproducibility when determining residual stress as a function of depth with hole drilling. The NPL reported results for a shot peened steel sample and a friction stir welded aluminum sample. Unfortunately, there is not a direct reporting of the reproducibility standard deviation of the measurements, but rather stress versus depth for some of the participating laboratories at some cut depths. The standard deviation was not reported, but was approximated by the present authors, and ranged significantly depending on the material and underlying residual stress state, being lower for friction stir welded aluminum (about 40 MPa) and higher for shot peened steel (several hundred MPa), with data dispersion being higher near the surface and lower at 1 mm depth. There are three general cases that the repeatability studies fall into: surface measurements with little mechanical interaction with the sample (e.g., x-ray without layer removal), mechanical interaction with the sample but stress assumed constant with position (hole drilling), and mechanical interaction with the sample with spatially varying stress fields (incremental hole drilling, slitting, and contour). These classes should be expected to show increasing repeatability limits in the order listed for practical reasons. The contour method repeatability data developed here suggest that the method has good precision relative to other residual stress measurement techniques, especially considering that the measurement provides a two-dimensional map of a spatially varying stress field.

13.5 Summary

The present work has established repeatability data for the contour method in two long aluminum bars, one containing a low level of stress, of about ± 20 MPa, and the second containing a high level of stress, of about ± 150 MPa. Five repeated measurements in each part show repeatability standard deviation between 5 and 10 MPa over most of the measurement plane and about 20 MPa near the plane boundaries. The repeatability results for the low and high stress bars were nearly identical even while the stress in each bar was significantly different. The level of repeatability found here is in reasonable agreement with that found in other residual stress measurement repeatability studies. However, the repeatability data were gathered in a relatively straightforward measurement configuration having a simple geometry and opportunity for secure clamping; more complicated measurement configurations may lead to increased repeatability limits.

Acknowledgments With gratitude, the authors acknowledge Adrian DeWald (Hill Engineering, LLC) for his contributions to the contour measurements in the stress relieved bar at planes 1, 2A, and 2B, and Mike Prime for useful discussions regarding the contour method. Financial support was provided to University of California, Davis by the Electric Power Research Institute, Materials Reliability Program (Paul Crooker, Senior Project Manager).

References

1. James MN, Hughes DJ, Chen Z, Lombard H, Hattingh DG, Asquith D, Yates JR, Webster PJ (2006) Residual stresses and fatigue performance. Eng Fail Anal 14(2):384–395
2. Withers PJ, Bhadeshia HKDH (2001) Residual stress part 1 – measurement techniques. Mater Sci Technol 17(4):355–365
3. Kandil FA, Lord JD, Fry AT, Grant PV (2001) A review of residual stress measurement methods -a guide to technique selection, NPL Report MATC(A)04
4. Prime MB (2001) Cross-sectional mapping of residual stresses by measuring the surface contour after a cut. J Eng Mater Technol 123:162
5. ASTM Standard E177-10 (2010) Standard practice for use of the terms precision and bias in ASTM test methods
6. Prime MB, Kastengren AL (2010) The contour method cutting assumption. In: Error minimization and correction, proceedings of the SEM annual conference and exposition on experimental and applied mechanics, Society for Experimental Mechanics Inc., Indianapolis, 7–9 June 2010, paper # 507
7. AMS Standard 2770 (2006) Heat treatment of wrought aluminum alloy parts
8. Wong W, Hill MR (2012) Superposition and destructive residual stress measurements. Exp Mech 53:339–344
9. DeWald AT, Hill MR (2001) Residual stress in a thick steel weld determined using the contour method, Report on LANL contract 32390-001-01 49
10. United States Department of Defense (1998) Metallic materials and elements for aerospace vehicle structures, MIL-HDBK-5H
11. Coleman HW, Steele WG (2009) Experimentation, validation, and uncertainty analysis for engineers, 3rd edn. Wiley, Hoboken, Chapter 2
12. Prime MB, Hill MR (2002) Residual stress, stress relief, and inhomogeneity in aluminum plate, Acta Mater 46:77–82
13. Robinson JS, Tanner DA, Truman CE, Paradowska CM, Wimpory RC (2012) The influence of quench sensitivity on residual stresses in the aluminium alloys 7010 and 7075. Mater Character 65:73–85
14. Robinson JS, Tanner DA, van Petegem S, Evans A (2012) Influence of quenching and aging on residual stress in Al–Zn–Mg–Cu alloy 7449. Mater Sci Technol 28:420–430
15. Fry AT (2002) Evaluation of the repeatability of residual stress measurements using X-ray diffraction, NPL report MATC(MN)19
16. Lee MJ, Hill MR (2007) Intralaboratory repeatability of residual stress determined by the slitting method. Exp Mech 47:745–752
17. ASTM Standard E837-08e1 (2009) Standard test method for determining residual stresses by the hole-drilling strain-gage method
18. Lord JD, Fry AT, Grant PV (2002) A UK residual stress intercomparison exercise - an examination of the XRD and hole drilling techniques, NPL report MATC(A)98

Chapter 14
Repeatability of Incremental Hole Drilling and Slitting Method Residual Stress Measurements

Adrian T. DeWald and Michael R. Hill

Abstract Residual stresses are of interest from an engineering perspective because they can have a significant influence on material performance. For example, fatigue initiation, fatigue crack growth rate, stress corrosion cracking, and fracture are all influenced by the presence of residual stress. The commonly used methods for residual stress measurement include incremental hole drilling and slitting. This paper establishes the repeatability of these techniques through replicate measurements on nominally similar specimens. Each technique was used to measure the residual stress in peened aluminum plates at multiple locations. A statistical analysis of the data was performed to compare the level of repeatability obtained using the two techniques. The standard deviation of the slitting method data was about 2 % of the peak stress magnitude, compared with 5 % for the hole drilling measurements.

Keywords Residual stress • Incremental hole drilling • Incremental slitting • Repeatability • Aluminum

14.1 Introduction

Residual stresses are known to play a significant role in many material failure processes (e.g., fatigue, fracture, and stress corrosion cracking). Tensile residual stresses are of concern because they accelerate fatigue crack initiation and fatigue crack growth relative to what would occur in the absence of residual stress. Compressive residual stresses, on the other hand, have the opposite effect and can be used to improve performance (hence life improvement processes like cold working of fastener holes and shot peening). To effectively understand and predict residual stress effects on performance requires accurate and reliable residual stress measurement data. An understanding of the measurement uncertainty is important.

Many methods exist for the measurement of residual stress including: hole drilling, slitting, contour, neutron diffraction, and x-ray diffraction with layer removal. Each of these methods has particular advantages (e.g., repeatability, precision, and measurement depth) and trade-offs (e.g., accuracy versus throughput, measurement depth versus sensitivity). Selection of appropriate measurement methods is critical to obtaining residual stress data that suit an intended purpose. Only a limited amount of data are available to quantify measurement repeatability for any of the commonly applied residual stress measurement methods.

The objectives of this work are to quantify the repeatability of residual stress measurement for incremental slitting and incremental hole drilling methods on peened aluminum test specimens. A description of the test specimens is given followed by descriptions of the measurement methods and results obtained using each.

A.T. DeWald (✉)
Hill Engineering, LLC, Rancho Cordova, CA, USA
e-mail: atdewald@hill-engineering.com

M.R. Hill
University of California, Davis, CA, USA

M. Rossi et al. (eds.), *Residual Stress, Thermomechanics & Infrared Imaging, Hybrid Techniques and Inverse Problems, Volume 8*, Conference Proceedings of the Society for Experimental Mechanics Series, DOI 10.1007/978-3-319-00876-9_14,

14.2 Methods

Specimen description. Two test specimens were used for this study. Specimen A was a 7055-T7751 aluminum alloy plate nominally 0.65 in. thick, with in-plane dimensions of 3.0 by 8.0 in. The material yield strength is 88 ksi. This specimen was processed with a nominal shot peening treatment over the entirety of one 8 by 3 in. surface.

Specimen B was a 2324-T39 aluminum alloy plate nominally 0.35 in. thick with in-plane dimensions of 3 by 15 in. The handbook yield strength for this material is 54 ksi. This specimen was processed using an intense peening treatment over the entirety of one 15 by 3 in. surface.

Residual stress measurements. Residual stresses were measured in the test specimens using incremental hole drilling on Specimen A and incremental slitting on Specimen B. While it would have been useful to study repeatability of both measurement methods on a single specimen, the data reported here were developed at different times and to support different programs of work.

Hole drilling. Hole drilling is a mechanical release technique for measuring near-surface residual stress [1]. Hole drilling provides a measure of the residual stress in the plane of the surface, including the two normal stress components and the in-plane shear component, over a shallow region (typically 0.020–0.080 in. depending on the experimental set-up employed). The method involves drilling a small hole in the center of a strain gage rosette, which is specially designed for the method. The measured strain change due to drilling of the hole is a function of the residual stress that was originally present in the material. The coefficients relating measured strain to residual stress are determined though analysis (finite element method). Using the coefficients, the residual stress is calculated based upon the measured strain data.

The hole drilling measurements performed here follow the basic ASTM procedure for non-uniform stress in "thick" material [2]. A strain gage was attached to the material surface (0.062 in. gage size). The hole was drilled using a high-speed air turbine with an inverted-cone carbide cutter. A 0.080 in. diameter hole was drilled to a depth of 0.040 in. in 0.002 in. increments (20 increments). Residual stress was computed according to the ASTM standard, using coefficients for non-uniform stress and Tikhonov regularization for smoothing.

Incremental hole drilling measurements were performed on Specimen A at locations 1.0 in. from each end of the specimen ends. A spacing of 0.75 in. between adjacent measurement sites ensured negligible interaction between measurements. Three measurements were performed near each end of the specimen, for a total of six measurements. It is expected that the residual stress is similar at each location.

Slitting. The slitting method is a technique for measuring through-thickness residual stress [3]. Slitting determines a single stress component over a depth range that typically spans about 90 % of the material thickness. In the slitting method, a slit is cut in increments of depth into a body containing an unknown residual stress field. The strain released with each slit depth increment is measured near the slit with metallic foil strain gages. Gages are typically placed directly below the slit, on the back surface of the specimen. The measured strain versus slit depth data are used to calculate the residual stress that was initially in the part through an elastic inverse solution.

The elastic inverse solution for the slitting method assumes that the unknown stress field can be expressed as a series expansion

$$\sigma_{xx}(y) = \sum_{j=1}^{n} A_j P_j(y) \tag{14.1}$$

where $P_j(y)$ are given polynomial basis functions and A_j are coefficients to be determined. Assuming elastic deformation during slitting, and employing the principle of elastic superposition, the strain through the depth of the part can also be expressed as a series expansion

$$\varepsilon_{xx}(a_i) = \sum_{j=1}^{n} A_j C_{ij} = [C]\{A\} \tag{14.2}$$

where $\varepsilon_{xx}(a_i)$ is strain at the gage location for slit depth a_i, C_{ij} is a compliance coefficient, $[C]$ is a matrix having members C_{ij} (called the compliance matrix), and $\{A\}$ is a vector of the unknown coefficients A_j, of the series expansion. If the residual stress were given exactly by a single polynomial term $P_j(y)$, the strain that would occur at slit depth a_i is C_{ij}. Therefore,

C_{ij} can be found by solving a usual elasticity problem, either exactly or using finite element analysis. Repeatedly solving the elasticity problem for all basis polynomials and all slit depths provides all members of $[C]$. The polynomial coefficients of the stress expansion $\{A\}$ are then determined by inverting Eq. 14.2, in a least squares sense, using the measured strains versus depth data.

$$\{A\} = \left([C]^T[C]\right)^{-1}[C]^T\{\varepsilon_{measured}\} \tag{14.3}$$

The unknown residual stress profile is then computed from Eq. 14.1.

Incremental slitting measurements were performed on Specimen B. Due to physical limitations of the method, five small blocks were extracted from Specimen B prior to the slitting measurements. The removed blocks were nominally 0.7 by 0.8 in., and 0.35 in. thick. Since the original plate was processed uniformly and the blocks each have the same size, they are expected to contain identical residual stress.

The slitting method was used to measure the residual stress as a function of the depth through the middle of each block. A single strain gage with a grid length of 0.032 in. was applied to the back surface of each block directly below the center of the slit. Slitting was performed on a wire EDM. Released strain was measured after each slit depth increment.

Repeatability calculations. Statistical analysis was performed on each stress versus depth data set to quantify measurement repeatability. First, the arithmetic average of each data set was computed as a function of measurement depth. Next, the standard deviation of the data from the mean was computed as a function of measurement depth. A relative standard deviation was computed as the standard deviation divided by the maximum absolute value of the mean residual stress profile (peak stress level over the depth of measurement).

14.3 Results

Hole drilling. A line plot of residual stress versus distance from the surface for the hole drilling measurements is shown in Fig. 14.1. As expected for shot peened material, there is a thin layer of compressive residual stress near the surface. The peak stress magnitude is near 40 ksi (45 % of yield strength). The compressive stress layer persists over a depth of nominally 0.010 in. There is slight compression beyond this depth, nominally −8 ksi at 0.010 in. depth trending towards zero over the remaining measurement depth, which may be due to pre-existing residual stress in the material prior to shot peening (e.g., as may arise from plate rolling).

Slitting. A line plot of the measured residual stress versus distance from the surface for the slitting measurements in shown in Fig. 14.2. As expected for an intense peening treatment, there is a layer of compressive residual stress near the surface, with high peak magnitude, near 55 ksi (85 % of yield strength). The compressive stress layer persists over a depth of nominally 0.035 in. There is significant tensile stress below the compressive stress layer. The tensile stress is required to maintain equilibrium in the material.

Measurement repeatability. The computed average value for each data set is shown in Fig. 14.3 (hole drilling) and Fig. 14.4 (slitting). For hole drilling, the standard deviation ranges from 0.8 to 4.4 ksi over the depth range with the highest standard deviation near the surface and near the final measurement depth. For slitting, the standard deviation ranges from 0.2 to 6.2 ksi over the depth range with the highest standard deviation near the surface. The plots include lines representing one standard deviation from the mean for each data set. The relative standard deviation is plotted in Fig. 14.5 (hole drilling) and Fig. 14.6 (slitting). The relative standard deviation in the hole drilling measurements ranges from about 12 % to about 2 % over the depth range, with an average of 5 %. The relative standard deviation in the slitting measurements ranges from 11 % to 1 %, with an average of 2 %. Overall, slitting results have better repeatability than hole drilling results.

For hole drilling, the relatively high variability near the surface is likely due to the high near-surface stress gradient, so that measurements are especially sensitive to errors in incremental hole depth. The relatively high variability at deeper depths is likely due to the reduction in measurement signal as the hole progresses deeper into the material and farther from the surface-mounted strain gages.

For slitting, the relatively high variability near the surface is likely due to similar effects (high stress gradient and sensitivity to slit depth). The slitting configuration used here does not suffer from the same loss in signal found for hole

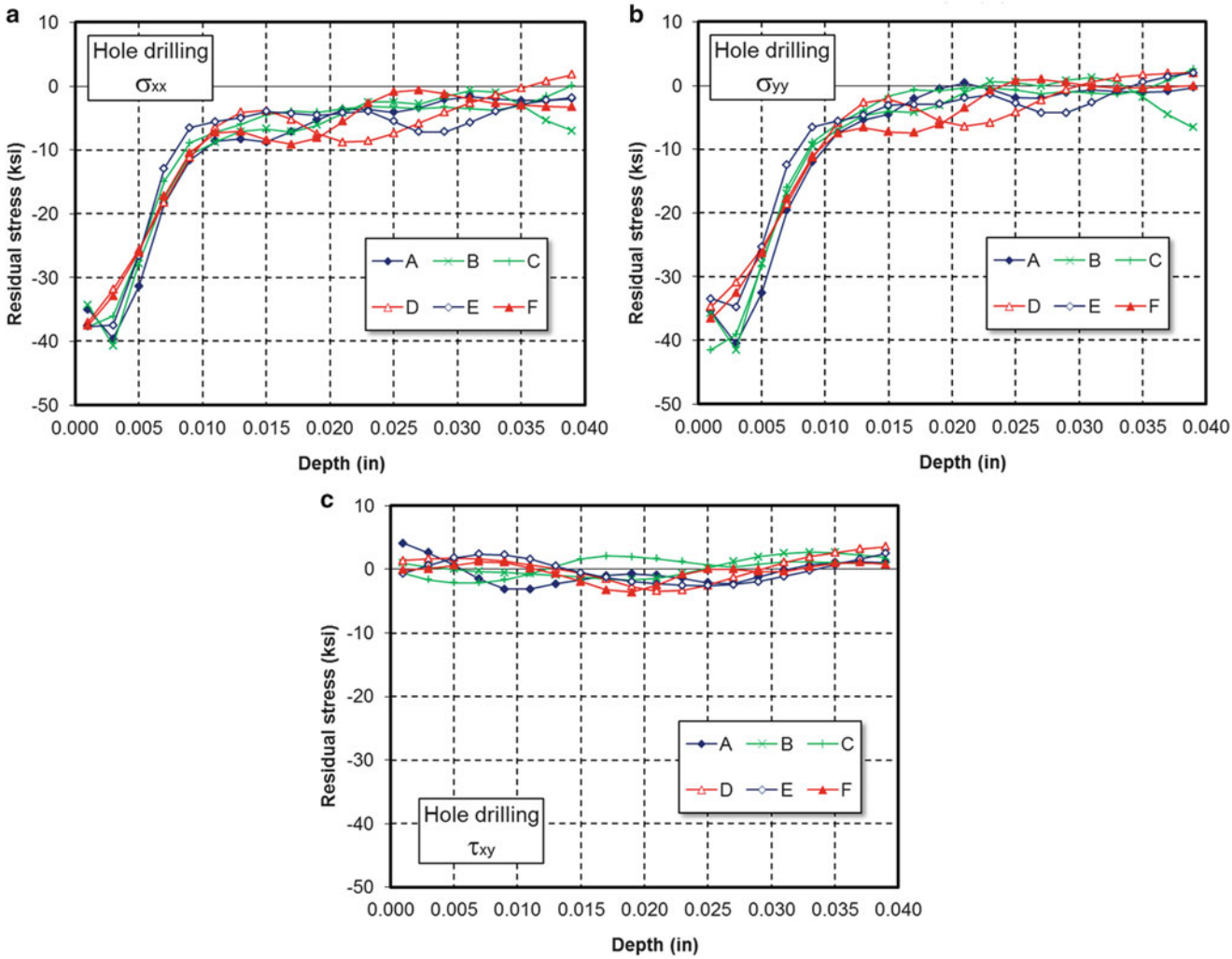

Fig. 14.1 Line plot of residual stress versus depth from the surface for the hole drilling measurements (**a**) σ_{xx}, (**b**) σ_{yy}, and (**c**) τ_{xy}

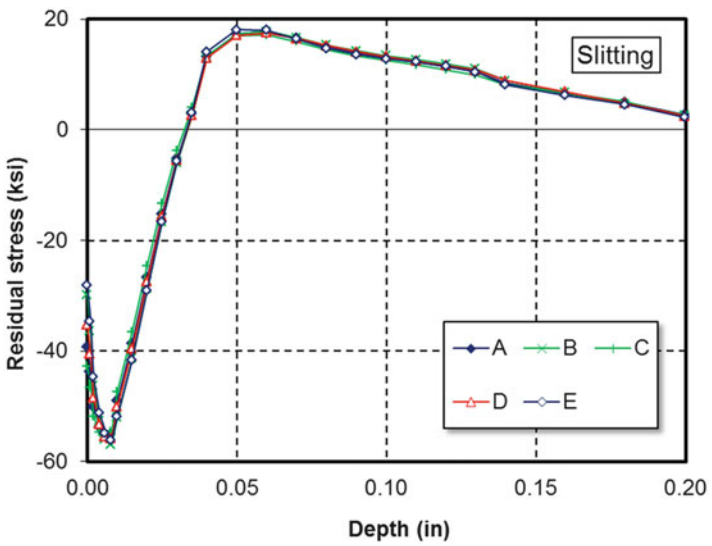

Fig. 14.2 Line plot of residual stress versus depth from the surface for the slitting measurements showing raw data from individual measurements

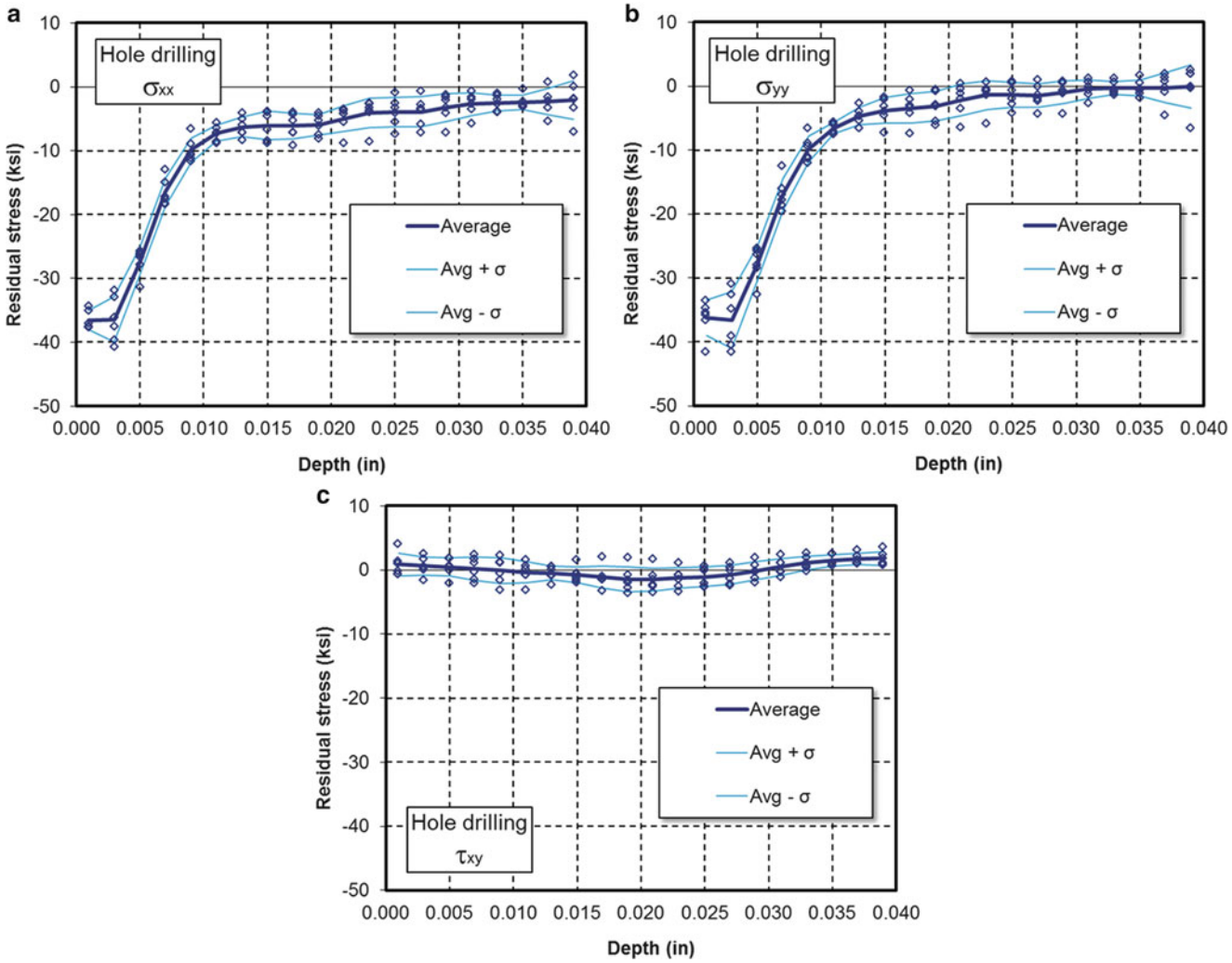

Fig. 14.3 Line plot of residual stress versus depth from the surface for the hole drilling measurements showing raw data, average, and average plus and minus one standard deviation (**a**) σ_{xx}, (**b**) σ_{yy}, and (**c**) τ_{xy}

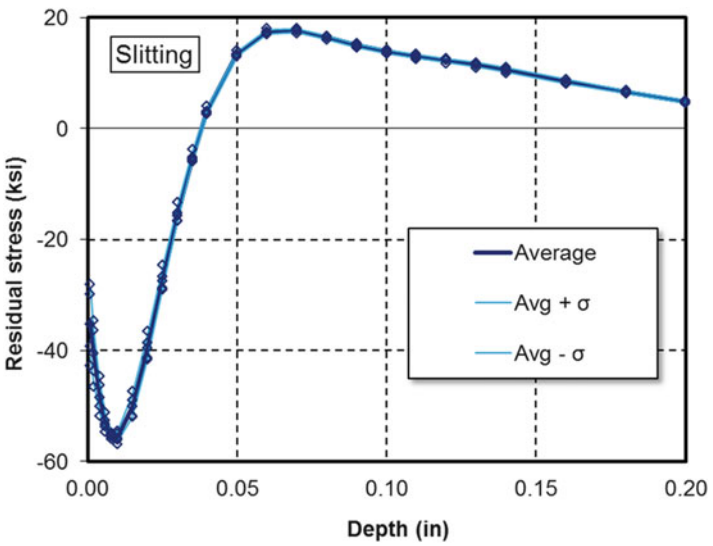

Fig. 14.4 Line plot of residual stress versus depth from the surface for the slitting measurements showing raw data, average, and average plus and minus one standard deviation

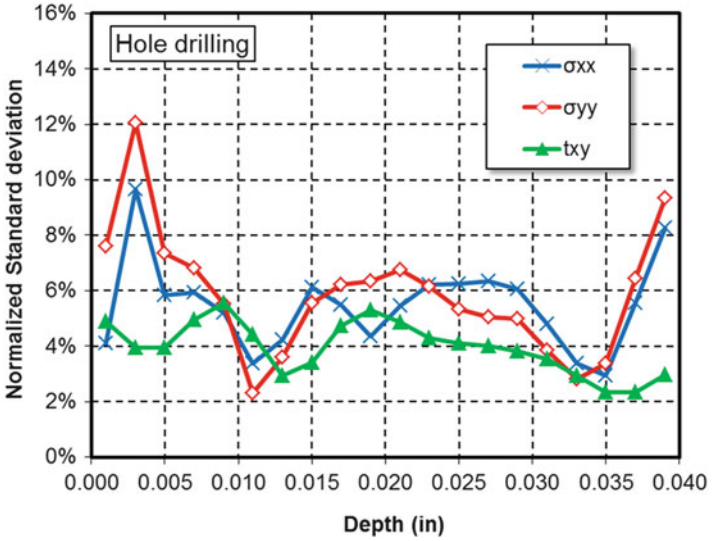

Fig. 14.5 Line plot of the standard deviation normalized by the maximum residual stress versus depth from the surface for the hole drilling measurements

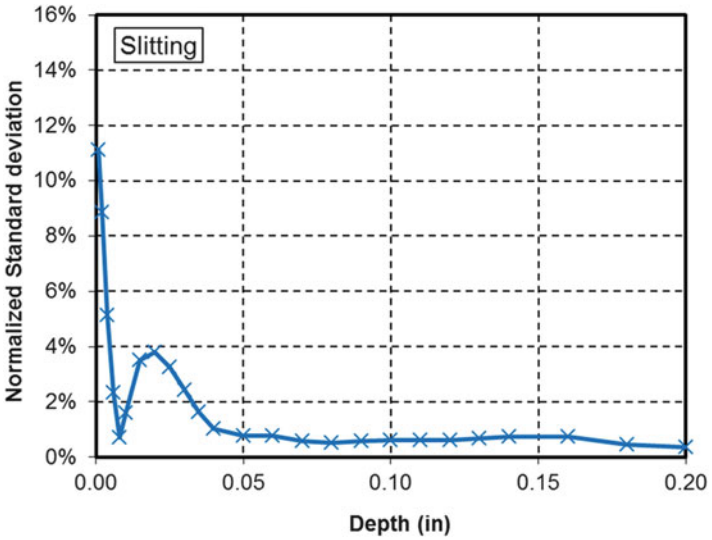

Fig. 14.6 Line plot of the standard deviation normalized by the maximum residual stress versus depth from the surface for the slitting measurements

drilling as the measurement depth increases. For a bottom gage configuration the signal is relatively good throughout the depth range. The slitting repeatability reported here is consistent with the results found earlier by Lee and Hill [4].

References

1. Schajer GS (2010) Hole-drilling residual stress measurements at 75: origins, advances, and opportunities. Exp Mech 50(2):245–253
2. ASTM Standard E 837–08 (2008) Standard test method for determining residual stress by the hole-drilling strain gage method. ASTM International
3. Prime MB (1999) Residual stress measurement by successive extension of a slot: the crack compliance method. Appl Mech Rev 52(2):75–96
4. Lee MJ, Hill MR (2007) Intralaboratory repeatability of residual stress determined by the slitting method. Exp Mech 47(6):745–752

Chapter 15
Drilling Speed Effects on Accuracy of HD Residual Stress Measurements

C. Barile, C. Casavola, G. Pappalettera, C. Pappalettere, and F. Tursi

Abstract The effect, on the residual stress measurement accuracy, of the drilling speed of the end-mill during the hole-drilling measurements was evaluated in Ti6Al4V. In spite of the well-known consideration that the highest achievable speed should be used during hole drilling, very few experimental works exist analyzing the effects of using lower velocities. Hole-drilling experiments were performed in this study by measuring the released strain by electronic speckle pattern interferometry. A known stress state was generated by loading the sample in a four point bending frame up to 50 % of the yield strength. Drilling speed ranging in 5,000 ÷ 50,000 rpm was investigated by using an electronically controlled mill. The expected stress field, evaluated by a numerical model in ANSYS®, was compared with the measured one at different drilling speeds.

Keywords Drilling speed • Electronic speckle pattern interferometry • Hole drilling • Residual stress • Titanium

15.1 Introduction

Residual stresses (RS) can remain in a sample as the final result of the chain of manufacturing processes which are necessary to produce the final part. An accurate knowledge of the entity of RS is a challenging but, at the same time, very important task. Their presence, in fact, can strongly affect the performance and the fatigue life of the component itself [1]. Due to the relevance of the topic a lot of experimental techniques have been developed ranging from X-Ray diffractometry [2], to Magnetic Barkhausen Noise [3], to contour methods [4]. However the most widespread method for measuring RS is the Hole Drilling Method [5] and it is actually the only one which is ruled by a standard [6]. HDM technique has undergone a lot of developments both in terms of measurement procedures and computation techniques [7]. Despite of the huge amount of work carried out on this topic only a few papers investigate what are the effects of the drilling speed on the accuracy of stress measurements by HDM [8, 9]. In [8] it is suggested to use the maximum achievable speed while in [9] results for Al 6061-T6 and 304 stainless steel are presented; however much work is necessary to better defining the dependency of the accuracy on the drilling speed and to enlarge the range of investigated materials. In this work, the effects of the rotation speed on the accuracy of residual stress measurement on Ti grade 5 are investigated. A known stress field is induced in a pre-annealed sample by a simple four-point bending frame. An electronic controlled drilling machine is then used to drill the hole up to a depth of $d = 0.4$ mm. Holes are drilled at three different velocities: 5,000 rpm, 35,000 rpm, 50,000 rpm. The first and the last values represent the minimum and the maximum rotation speed attainable by the drilling system. Electronic Speckle Pattern Interferometry (ESPI) [10] was used to detect the displacement map in correspondence of each drilling step. Residual stresses are calculated through integral method.

C. Barile (✉) • C. Casavola (✉) • G. Pappalettera • C. Pappalettere • F. Tursi
Dipartimento di Meccanica, Matematica e Management, Politecnico di Bari, Viale Japigia 182, 70126 Bari, Italy
e-mail: casavola@poliba.it

M. Rossi et al. (eds.), *Residual Stress, Thermomechanics & Infrared Imaging, Hybrid Techniques and Inverse Problems, Volume 8*, Conference Proceedings of the Society for Experimental Mechanics Series, DOI 10.1007/978-3-319-00876-9_15,

15.2 Materials and Methods

15.2.1 Experimental Set-up

A four-point-bending test was executed on a Titanium (Ti-6Al-4V) grade 5 specimen. The stress field, induced by the load applied, was measured by the hole drilling method combined with Electronic Speckle Pattern Interferometry (ESPI). The ESPI hole-drilling measurement system used in this experiment is schematically reported in Fig. 15.1.

A beam from a DPSS laser source is split into two beams and focused into two monomode optical fibers. One beam is collimated and illuminates the sample, while the second beam passes through a phase shifting piezoelectric system and then it goes to the CCD camera where it interferes with the light diffused by the optically rough surface of the specimen. Initial phase and final phase are evaluated by the four-step phase shifting technique, which allows to detect deformations released at each step of the hole-drilling process.

The hole is drilled by means of a high speed turbine which is mounted on a precision travel stage. Turbine rotation ranges from 5,000 to 50,000 rpm and is electronically controlled. The cutter is made by tungsten coated by TiCN and it has a nominal diameter d = 1.59 mm.

Experimental measurements were performed on a Titanium grade 5 (Ti-6Al-4V) specimen (248.5 × 42.5 × 3.0 mm). Three rotation speeds were investigated in this work, respectively 5,000, 35,000 and 50,000 rpm. The aim of the work was to evaluate the drilling speed effects on the accuracy of residual stress measurements. To this scope it was important to guarantee that the measured stress only refers to the applied external reference load by avoiding to include any initial residual stress field. To this purpose preliminary X-ray residual stress (XRD) measurements were performed in order to asses if the *as received* material can be considered free from stress or it has to undergo to annealing process. XRD technique was selected because it is a non-destructive technique that allows quantitative evaluation of residual stress. This data are essential to define the proper heat relieving treatment. Initial residual stress measurements were executed on both the surfaces of the specimen and in several points chosen in a random way.

The proper cycle was defined based on the specific material alloy and on the desired final value of residual stresses. Figure 15.2 illustrates the effects of stress relieving on Ti-6Al-4V at five temperatures ranging from 260 °C to 620 °C for periods of time ranging from 5 min to 50 h.

Specimen was heated up to 620 °C for 1 h and then cooled by air up to room temperature for 50 h according to [11].

The rate of cooling from the stress-relieving temperature is not critical. Uniformity of cooling is critical particularly in the temperature range from 480 °C to 315 °C.

In order to test the efficacy of the heat relieving process several RS measurements were performed on the sample by HDM. This technique was preferred to XRD at this stage because the presence of an oxide layer can influence the diffractometric measurements and at the same time to ensure that the relieving process attained the desired results up to the wanted depth. Finally, the HDM+ESPI method was utilized to evaluate the external four-point bending applied load (Fig. 15.3). The distance between the inner supports was 133 mm, the distance between the external supports was 208 mm.

The hole was drilled up to 0.40 mm depth, each step was 0.05 mm. The holes were drilled along two lines on the 248.5 × 42.5 mm face of each specimen (Fig. 15.4). The distance between the centers of the holes of each line was set to

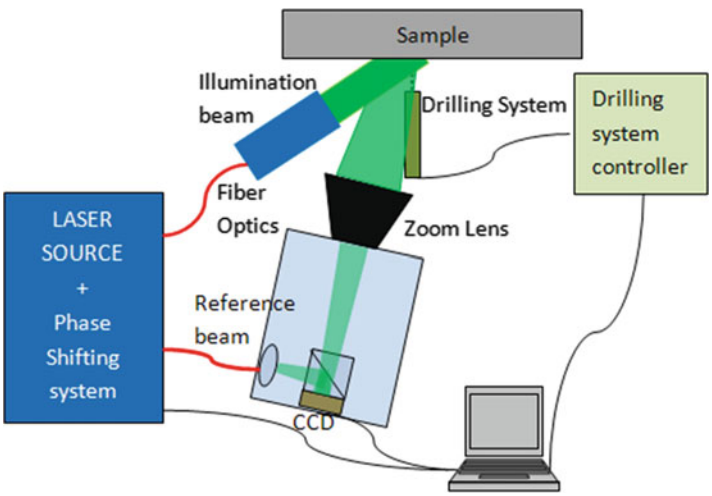

Fig. 15.1 Experimental set-up for ESPI measurements of strains relaxed by HDM

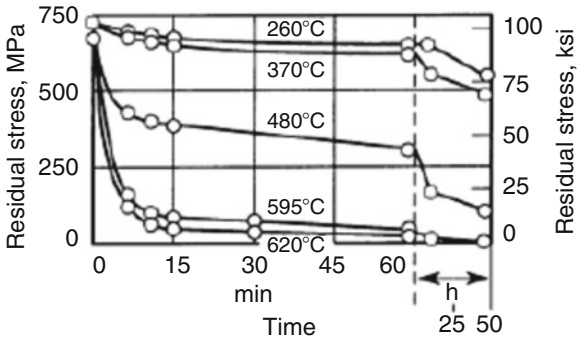

Fig. 15.2 Plot of the residual stress relaxation in Ti grade 5 at different heating temperatures [11]

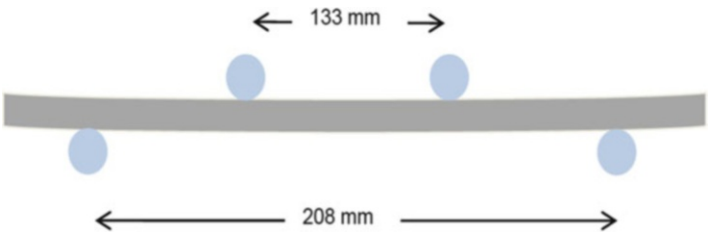

Fig. 15.3 Schematic of the four-point bending frame

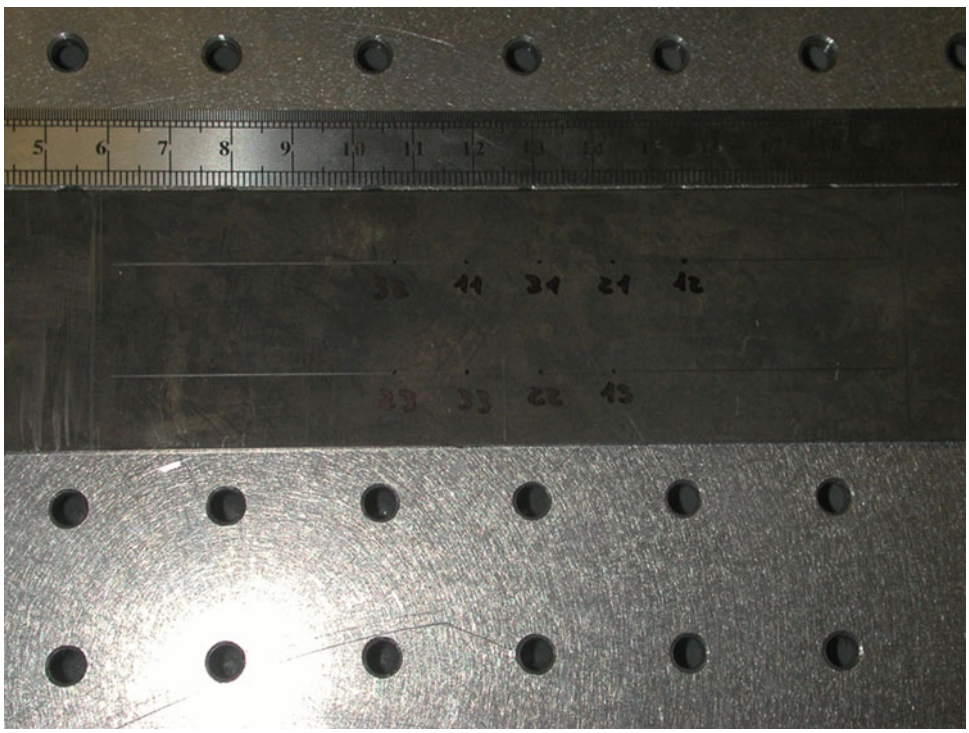

Fig. 15.4 Titanium grade 5 specimen

12 mm to minimize the interaction between the holes. The two lines were located at 12.0 mm from each edge in order to minimize edge effects and have sufficient distance between the center of the holes on opposite lines. The central holes were 6 mm from the centerline of the specimen in order to have a symmetrical distribution of the holes and enough distance from the inner supports of the loading system.

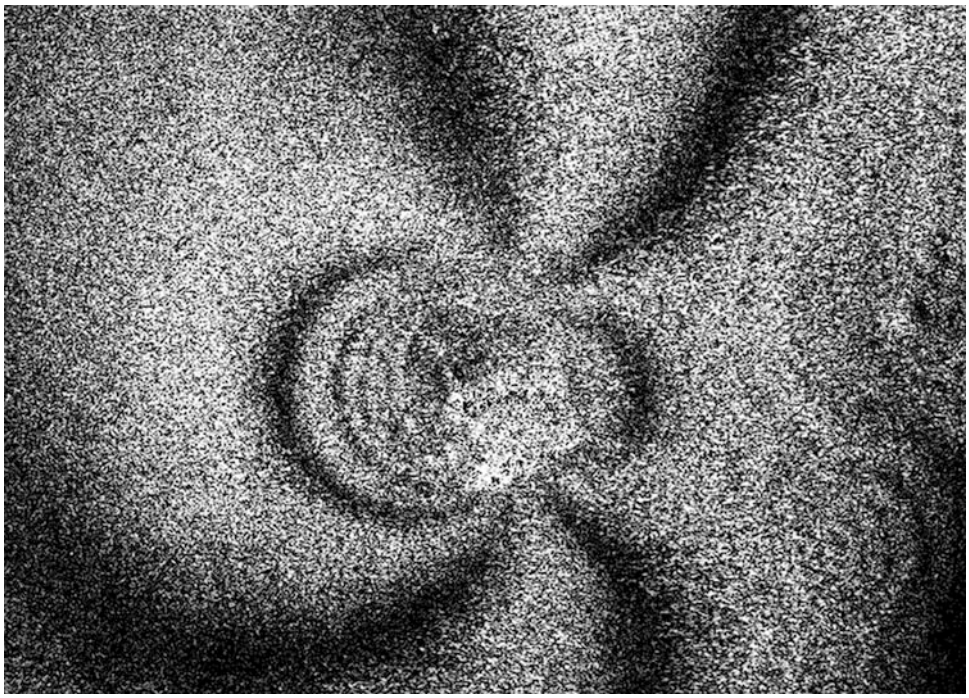

Fig. 15.5 ESPI fringe pattern recorded at the end of the drilling process

For each drill increment the corresponding speckle pattern was recorded at four different positions of the piezoelectric translator. These intensity maps were subtracted from the reference intensity pattern recorded on the sample before starting the drilling procedure. This operation allows obtaining fringe pattern (Fig. 15.5) encoding the information about the displacement experienced by the sample along the sensitivity vector. Accurate definition of the sensitivity vector, that is to say of the angles of illumination and observation was performed by projecting a 5 lines/mm grating on the sample and by measuring the projected pitch. Once displacement maps were obtained a derivative filter was used to get strain maps and then integral method was used to calculate stresses.

15.2.2 Numerical Validation

A finite element model was developed in order to simulate the four-point-bending test. The specimen is long 248.5 mm, tall 42.5 mm and thick 3.0 mm. Kinematic constraints were imposed in order to obtain an isostatic model and to reproduce correctly the mechanism with which the load is transferred to the specimen. FE analysis was carried out with the ANSYS 13.0 commercial software [12]. The specimen was modeled with three-dimensional elements SOLID185 for solid structures. It is defined by eight nodes having three degrees of freedom at each node: translations in the nodal x, y, and z directions. Although specimen thickness is small compared to length, the bar under four-point-bending was however modeled as a 3D specimen in order to account for asymmetries eventually occurring in the loading process or related with constraint conditions.

The mesh included 256452 elements and 303282 nodes. All finite element analyses were run on a standard PC equipped by an Intel® Core i7 processor and 8GB RAM memory. The structural analysis was completed in about 5 min.

Finite element model was realized in order to confirm the effectiveness of load apparatus. The convergence of stress field experimentally induced and the one numerically evaluated was obtained by comparing strains in four different locations. In these four locations, in fact, strain gages were previously applied on the back surface of specimen: two stayed along the longitudinal axes (10 mm far from the inner supports and symmetrically with respect to the transverse axis) the other two lied in correspondence of the transverse axis of specimen (5 mm far from the edges and symmetrically with respect to the longitudinal axis). This comparison confirmed a good agreement between theoretical and experimental results and provide a mean value of longitudinal stress (σ_x) of about 140 MPa.

15.3 Results and Discussion

The map of longitudinal stress of the four-point bended specimen, numerically evaluated, is reported in Fig. 15.6.

Results obtained from XRD measurements on the *as received* sample are listed in Table 15.1, they differ for direction of measurement and refer to longitudinal x axis of specimen and the transverse y axis.

Results show the presence of a not negligible level of residual stress both in the longitudinal and transverse direction of the specimen underlining the necessity to apply a heat treatment for relieving stresses. As it was mentioned in the previous section several HD measurements on the post annealed sample were performed. Measurements were executed on several points up to 0.4 mm depth, that corresponded to the depth that will be used during four-point bending test, with step of 0.05 mm. The mean value of the measured stress was $\sigma_x = -11.0$ MPa. This value resulted very low and in any case it was subtracted to the stress values measured during the four-point bending test. In this way only the external stress was evaluated.

Figure 15.7 shows the results obtained by measuring the longitudinal stress on the four point bent specimen at three different velocities on nine different points. Plotted results refer to the stress measured up to a depth of 0.4 mm. In the plot the theoretical expected value is also shown.

As it can be inferred from Fig. 15.7 the average value of the measured stress state is coherent with the expected theoretical value and almost independent from the drilling speed. However data corresponding to lower speed appear more scattered than data recorded at the maximum speed. In fact the standard deviation for the measurement at 5K rpm is $\sigma_{5K} = 26.6$ MPa

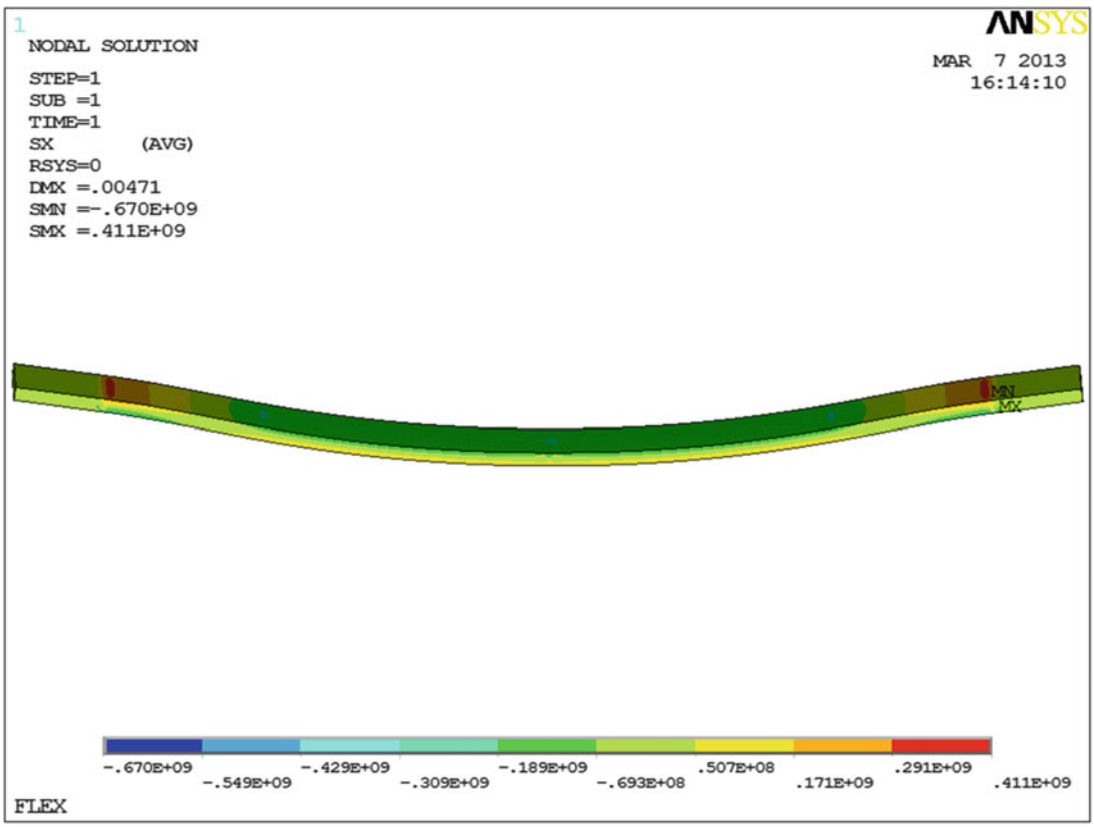

Fig. 15.6 Longitudinal stress map evaluated via FEM

Table 15.1 Residual stress measured on the sample before annealing treatment

	Point 1	Point 2	Point 3	Point 4	Point 5	Point 6	Point 7	Point 8	Point 9
Longitudinal stress [MPa]	−82.1	−50.6	−85.7	−52.9	−79.4	14.6	−39.3	−57.2	26.9
Standard deviation [MPa]	18.5	12.8	19.3	13.3	17.0	5.3	12.8	6.4	21.8
Transversal stress [MPa]	−52.6	−36.2	−59.6	−78.4	−45.6	−50.2	−39.1	−89.3	−42.3
Standard deviation [MPa]	11.9	9.3	8.2	14.8	9.4	7.8	11.7	12.4	5.1

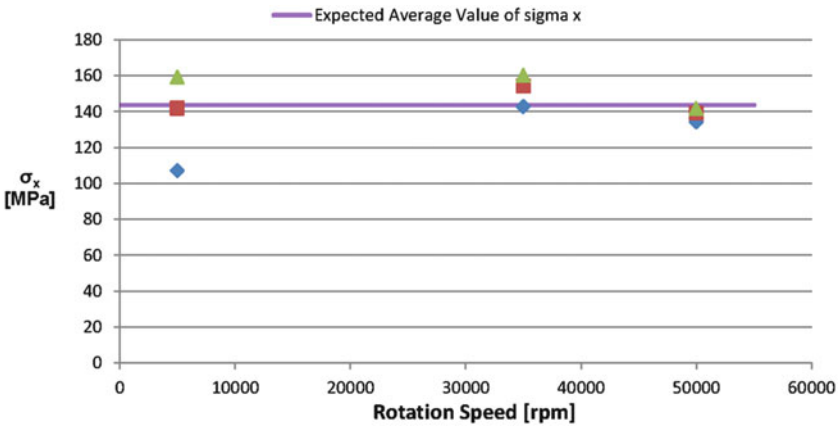

Fig. 15.7 Plot of the measured stress at the different rotations speed of the cutter

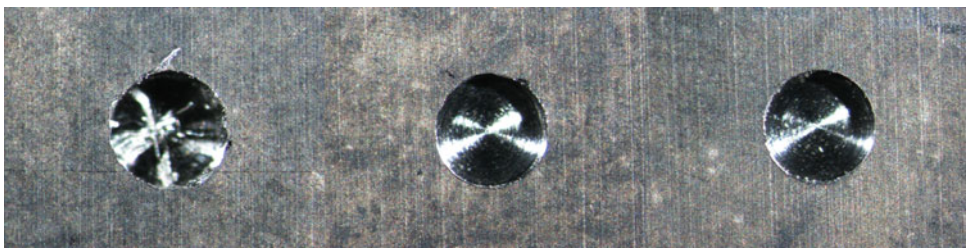

Fig. 15.8 Image of the drilled holes obtained at the optical microscope 20×. Left image refers to a hole drilled at 5,000 rpm, middle image refers to a hole drilled at 35,000 rpm and right image refers to a hole drilled at 50,000 rpm

that is to say about 20 % of the nominal expected value. This value decreases at 35K rpm being $\sigma_{35K} = 8.8$ MPa that is to say about 6 % of the nominal expected value and it reaches the minimum at 50K rpm where it is $\sigma_{50K} = 3.9$ MPa that is to say less than 3 % of the expected theoretical value. In other words the accuracy and the repeatability of the measurement diminishes by decreasing the rotation speed. This occurrence can be tracked back to the quality of the drilled hole (Fig. 15.8) which appears to be compromised at lower speed.

15.4 Conclusions

In this paper the effects of the rotation speed on the accuracy of residual stress measurements by Hole drilling method and ESPI was evaluated in Titanium grade 5 alloy. After an annealing process performed on the sample in order to relieve initial residual stresses the specimen was loaded into a four-point bending frame in order to introduce a known field of stress. Nine holes were drilled on the sample at three different rotation speeds of the cutting mill. Holes were drilled up to 0.4 mm and subsequent displacement field was measured by ESPI. Deformation maps allowed to obtain, by the integral method, the value of the relaxed stress. A comparison of the measured stress with the expected theoretical one showed a good agreement in terms of mean value. However data obtained at lower speed appeared less accurate than those obtained at higher speed. In fact the standard deviation found for the measurements increases up to 20 % of the expected value at 5,000 rpm while it stays at less than 3 % at the highest speed attainable by the system that is to say at 50,000 rpm.

References

1. Withers PJ, Bhadeshia HKDH (2001) Residual stress. Part 1 – measurement techniques. Mater Sci Technol 17(4):355–365
2. Fitzpatrick ME, Fry AT, Holdway P, Kandil FA, Shackleton J, Suominen L (2005) Determination of residual stresses by X-ray diffraction, vol 52, 2nd edn, A national measurement good practice guide. NPL, National Physical Laboratory, Teddington, UK, pp 8–10

3. Casavola C, Pappalettere C, Tursi F (2013) Calibration of Barkhausen noise for residual stress measurem. In: Experimental and applied mechanics IV. Conference proceedings of the society for experimental mechanics series, New York, vol 34, pp 255–266
4. Pagliaro P, Prime MB, Robinson JS, Clausen B, Swenson H, Steinzig M, Zuccarello B (2011) Measuring inaccessible residual stresses using multiple methods and superposition. Exp Mech 51:1123–1134
5. Schajer GS (2008) Advances in hole-drilling residual stress measurements. Exp Mech 50:159–168
6. ASTM E837 (2008) Standard method for determining residual stresses by the hole-drilling strain gage method, Annual Book of ASTM Standards
7. Casavola C, Pappalettera G, Pappalettere C, Tursi F (2013) Effects of strain's error on residual stresses calculated by HDM. In: Experimental and applied mechanics IV. Conference proceedings of the society for experimental mechanics series, New York, vol 34, pp 395–402
8. Flaman MT (1982) Brief investigation of induced drilling stresses in the center-hole method of residual-stress measurement. Exp Mech 22:26–30
9. Upshaw D, Steinzig M, Rasty J (2011) Influence of drilling parameters on the accuracy of hole-drilling residual stress measurements. In: Engineering applications of residual stress. Conference proceedings of the society for experimental mechanics series, New York, vol 8, pp 95–109
10. Barile C, Casavola C, Pappalettera G, Pappalettere C (2011) Residual stress measurement by electronic speckle pattern interferometry: a study of the influence of geometrical parameters. Struct Integrity Life 17(3):177–182
11. ASM Handbook Committee (1991) ASM handbook. Heat treating, vol 4. ASM International, Materials Park, OH
12. Analysis System Inc. Swanson (2010) The ANSYS© 13.0 user's manual

Chapter 16
Ultrasonic Nonlinear Guided Waves and Applications to Structural Health Monitoring

Claudio Nucera and Francesco Lanza di Scalea

Abstract Research efforts on nonlinear guided wave propagation have increased dramatically in the last few decades because of the large sensitivity of nonlinear waves to structural condition (defects, quasi-static loads, instability conditions, etc.. . .). However, the mathematical framework governing the nonlinear guided wave phenomena becomes extremely challenging in the case of waveguides that are complex in either materials (damping, anisotropy, heterogeneous, etc.. . .) or geometry (multilayers, geometric periodicity, etc.. . .). The present work develops predictions of nonlinear second-harmonic generation in complex waveguides by extending the classical Semi-Analytical Finite Element formulation to the nonlinear regime, and implementing it into a highly flexible, yet very powerful, commercial Finite Element code. Results are presented for the following cases: a railroad track, a viscoelastic plate, a composite quasi-isotropic laminate, and a reinforced concrete slab. In these cases, favorable combinations of primary wave modes and resonant double-harmonic nonlinear wave modes are identified. Knowledge of such combinations is important to the implementation of structural monitoring systems for these structures based on higher-harmonic wave generation. The presentation will also present a specific application of nonlinear guided waves for the monitoring of thermal stresses in rail tracks to prevent buckling.

Keywords Nonlinear ultrasonic guided waves • Higher-harmonics • Semi-analytical finite element • Internal resonance • Dispersion

16.1 Introduction

Traditionally the structural monitoring via ultrasounds has been accomplished measuring "linear" parameters of the waves (amplitude, speed, phase shifts) to infer salient features of the inspected structure. However, it is well documented [6] that "nonlinear" parameters are, in general, much more sensitive to structural conditions than their linear counterparts. Furthermore the use of nonlinear guided waves is extremely attractive because guided waves combine the mentioned high sensitivity typical of nonlinear parameters with large inspection ranges [3, 5, 14]. The aforementioned complexity of the mathematical framework governing nonlinear guided wave propagation limited most of the previous works on elastic waves to the linear elastic regime with the assumption of infinitesimal deformations.

However, different mechanisms (increase in wave amplitude, finite deformations, nonlinear strain energy potentials) can give rise to nonlinear effects that eventually become of primary importance. Hence the governing equations need to be modified accordingly: cubic (and possibly higher-order) terms must be included in the elastic energy density expression [9, 16]. Among the manifestations of the nonlinear behavior, higher harmonic generation is considered in particular. In this scenario, an initially sinusoidal stress wave of a given frequency distorts as it propagates, and energy is transferred from the fundamental frequency, ω, to the higher harmonics, 2ω, 3ω and so on. For a practical use, this nonlinearity can be quantified via an ultrasonic nonlinear parameter, β, well documented in literature [3].

While several investigations pertaining to nonlinear effect in solids and second harmonic generation were reported in the past [7, 8], most of them were limited in their applicability to structures with simple geometries (plates, rods, shells) where analytical solutions for the primary (linear) wave field are available in literature. In the present work the propagation of

C. Nucera (✉) • F.L. di Scalea
Department of Structural Engineering, University of California, San Diego, 9500 Gilman Drive, M.C. 0085, La Jolla, CA 92093-0085, USA
e-mail: cnucera@ucsd.edu; flanza@ucsd.edu

M. Rossi et al. (eds.), *Residual Stress, Thermomechanics & Infrared Imaging, Hybrid Techniques and Inverse Problems, Volume 8*, Conference Proceedings of the Society for Experimental Mechanics Series, DOI 10.1007/978-3-319-00876-9_16,

waves in nonlinear solid waveguides with complex geometrical and material properties is investigated theoretically and numerically. For the solution of the nonlinear boundary value problem, perturbation theory and modal expansion are used [7].

A numerical algorithm is introduced in order to efficiently predict and explore the nonlinear wave propagation phenomena in structural waveguides of different complexity. After a brief description of the theoretical background, three case-studies have been analyzed, namely a railroad track, a composite quasi-isotropic laminate, and a reinforced concrete slab. Favorable combinations of primary and resonant secondary modes (nonlinear resonance conditions) were successfully identified for these complex waveguides. The knowledge of these nonlinear resonance conditions is of primary importance for the actual implementation of structural diagnostic systems based on nonlinear ultrasonic guided waves features.

16.2 Waves in Nonlinear Elastic Regime: Internal Resonance

In presence of finite deformations, large amplitude waves, nonlinear strain energy potentials and similar nonlinear mechanisms, the generalized Hooke's Law no longer applies and must be replaced by a proper nonlinear constitutive law. Assuming that the body is homogeneous, isotropic and hyperelastic, it possesses a strain energy density $\boldsymbol{\varepsilon}$ that is an analytic function of the Green-Lagrange Strain Tensor $\boldsymbol{E}$ such that the Second Piola-Kirchoff Stress Tensor $\boldsymbol{S}$ can be expressed as:

$$S_{ij} = \rho_0 \frac{\partial \varepsilon}{\partial E_{ij}} \tag{16.1}$$

where $\boldsymbol{\rho_0}$ is the initial density. It is known that in this scenario the strain energy can be expressed as:

$$\varepsilon = \frac{1}{2}\lambda {I_1}^2 + \mu I_2 + \frac{1}{3} C {I_1}^3 + B I_1 I_2 + \frac{1}{3} A I_3 + O\left({E_{ij}}^4\right) \tag{16.2}$$

where $\boldsymbol{I_1} = \boldsymbol{E_{ii}}$, $\boldsymbol{I_2} = \boldsymbol{E_{ij}E_{ji}}$, $\boldsymbol{I_3} = \boldsymbol{E_{ij}E_{jk}E_{ki}}$, $\boldsymbol{\lambda}$ and $\boldsymbol{\mu}$ are the Lamé elastic constants and $\boldsymbol{A}$, $\boldsymbol{B}$ and $\boldsymbol{C}$ are the Landau-Lifshitz third-order elastic constants [10]. In Eq. 16.2 first order material nonlinearity was introduced. By substituting Eq. 16.2 into Eq. 16.1 and keeping up to second-order terms in $\boldsymbol{E_{ij}}$ we obtain the nonlinear stress–strain relation

$$S_{ij} = \lambda E_{kk}\delta_{ij} + 2\mu E_{ij} + \delta_{ij}(C E_{kk} E_{ll} + B E_{kl} E_{lk}) + 2B E_{kk} E_{ij} + A E_{jk} E_{ki} \tag{16.3}$$

Using Eq. 16.3 inside the general momentum equation the Nonlinear Boundary Value Problem governing the propagation of nonlinear elastic waves in isotropic, homogeneous and hyperelastic waveguides can be formulated in vector form as:

$$(\lambda + 2\mu)\nabla(\nabla \cdot u) - \mu \nabla \times (\nabla \times u) + f = \rho_0 \frac{\partial^2 u}{\partial t^2} \tag{16.4}$$

$$S^L(u) \cdot n_r = -\bar{S}(u) \cdot n_r \qquad \text{on} \qquad \Gamma \tag{16.5}$$

where $\boldsymbol{u}$ is the particle displacement vector, $\boldsymbol{\rho_0}$, $\boldsymbol{\lambda}$ and $\boldsymbol{\mu}$ are the defined above, $\boldsymbol{f}$ is the nonlinear term acting as a body force, $\boldsymbol{n_r}$ is the unit vector normal to the surface of the waveguide $\boldsymbol{\Gamma}$ and $\boldsymbol{S_L}$ and $\bar{S}$ are the linear and nonlinear parts of the second Piola-Kirchoff stress tensor, respectively. The nonlinear boundary value problem in Eqs. 16.4 and 16.5 is solved in the following using perturbation theory, which is based on writing the solution as sum of two terms, namely $\boldsymbol{u} = \boldsymbol{u^{(1)}} + \boldsymbol{u^{(2)}}$, where $\boldsymbol{u^{(1)}}$ is the primary solution and $\boldsymbol{u^{(2)}}$ is the secondary solution due to nonlinearity, this assumed to be small compared to $\boldsymbol{u^{(1)}}$ (*perturbation condition*). Using this condition the original nonlinear boundary value problem is divided into two linear boundary value problems, namely the first-order and second-order approximations. Following [1] and [7], if $\boldsymbol{\omega}$ is the primary frequency that we suppose to convey into the system via a monochromatic wave, the first order nonlinear solution is calculated through modal expansion using the existing propagating guided modes $2\boldsymbol{\omega}$ as:

$$v(x, y, z, t) = \frac{1}{2} \sum_{m=1}^{\infty} A_m(z) v_m(x, y) e^{-i2\omega t} + c.c. \tag{16.6}$$

where ***c.c.*** denotes complex conjugates, $\boldsymbol{v_m}$ is the particle velocity vector referred to the mth mode at $2\boldsymbol{\omega}$ and $\boldsymbol{A_m}$ is the higher order modal amplitude given by

$$A_m(z) = \bar{A}_m(z)e^{i(2kz)} - \bar{A}_m(0)e^{ik_n{}^*z} \tag{16.7}$$

All the details regarding the calculation of the modal amplitudes can be found in [7]. At this stage it is important to emphasize how the internal resonance mechanism, which in turn produces a cumulative nonlinear response, relies on the simultaneous occurrence of two conditions, namely:

1. Phase Matching: $k_n{}^* = 2k$
2. Non-zero power transfer from primary to secondary wave: $f_n{}^{surf} + f_n{}^{vol} \neq 0$

16.3 CO.NO.SAFE Algorithm

The Semi-Analytical Finite Element formulation (*S.A.F.E.*) in its linear fashion has been extensively discussed in the past highlighting its great potential in efficiently calculating the dispersion properties of waveguide-like structures. These properties are crucial for the implementation of any SHM system based on the use of ultrasonic guided waves. Concerning the detail of the classical *SAFE* formulation, the interested reader is referred to [2]. In the present work the classical linear formulation is extended to the nonlinear regime according to the theory discussed in the previous section. The resultant **No**nlinear **S.A.F.E.** formulation is implemented into **CO**MSOL commercial code (***CO.NO.SAFE***). In this way the full power of existing libraries and routines of the commercial code is exploited and the internal resonance conditions of several structural waveguides of different complexity can be studied in a straightforward manner via user-friendly interfaces.

Furthermore, since all the nonlinear parameters involve gradients of the displacement field up to the third order [7], high-order finite elements (at least cubic) need to be used in order to obtain meaningful results; this implement is not always trivial for general non-commercial SAFE algorithm. Starting from the nonlinear boundary value problem described in Eqs. 16.4 and 16.5, the displacement field is approximated in the cross-section of the waveguide and is enforced to be harmonic in time and along the direction of wave propagation. For the generic eth element this reads:

$$u^e = N^e U^e e^{i(kz-\omega t)} \tag{16.8}$$

where $\boldsymbol{N^e} = \boldsymbol{N^e(x,y)}$ is the matrix of shape functions and $\boldsymbol{U^e}$ is the nodal displacement vector for the eth element. Assuming this displacement field in (4–5) is the only trivial modification that needs to be done in the original FEM formulation. The original quadratic eigenvalue problem is linearized doubling the space dimension [2]. The nonlinear boundary value problem has been implemented in COMSOL using the general PDE solver engine. The COMSOL formalism for the boundary value problem with Neumann B.C. (which corresponds to the guided wave propagation since a stress-free B.C. needs to be applied) is:

$$\nabla \cdot (c\nabla U + \alpha U - \gamma) - \beta \cdot \nabla U - aU + \lambda d_a U = 0 \tag{16.9}$$

$$n \cdot (c\nabla U + \alpha U) + qU = 0 \tag{16.10}$$

where $\boldsymbol{U}$ represents the set of dependent variables to be determined and all the remaining quantities are matrix coefficients admitting complex values, which is essential for viscoelastic materials. The nonlinear part of the algorithm has been coded in MATLAB and connected to COMSOL using the *LiveLink* package.

In this way, once the dispersion properties are obtained, several possible combinations of potential resonant modes are selected and analyzed. Resonant modes are identified making use of the phase-matching and non–zero power transfer conditions discussed before. The possibility to assess internal resonance conditions for complex solid waveguides is crucial for the efficiency of a given SHM inspection approach. In fact, once a resonant combination of modes is identified, nonlinear response becomes cumulative, namely the amplitude of the second harmonic grows with distance [7]. In this way the efficiency of the given nonlinear technique is dramatically maximized.

16.4 Applications

16.4.1 Railroad Track

The widely used 136 lb RE railroad track was considered as first case-study. Due to the complex geometry of the cross section, dispersion curves and, consequently, higher harmonic generation conditions cannot be calculated analytically. The material properties considered are given in Table 16.1. The Landau-Lifshitz third-order elastic constants are detailed in [15].

The complexity of the guided wave propagation for this particular waveguide is evident considering the abundance of possible propagative modes present (Fig. 16.1a) and the complexity of the phase-velocity dispersion curves (Fig. 16.1b), especially at higher frequencies.

A flexural vertical mode was selected as primary excitation at 80 kHz. The results of the CO.NO.SAFE analysis disclosed the presence of some synchronous secondary modes at 160 kHz with one in particular (slightly different flexural vertical type) able to produce internal resonance. Figure 16.2a, b display the selected modes, while Fig. 16.2c spotlights the very high value of modal amplitude related to the only secondary resonant mode; small amplitude values associated to the other

Table 16.1 Material properties assumed for the railroad track analysis

ρ [kg/m^3]	λ [GPa]	μ [GPa]	A [GPa]	B [GPa]	C [GPa]
7,932	116.25	82.754	−340	−646.667	−16.667

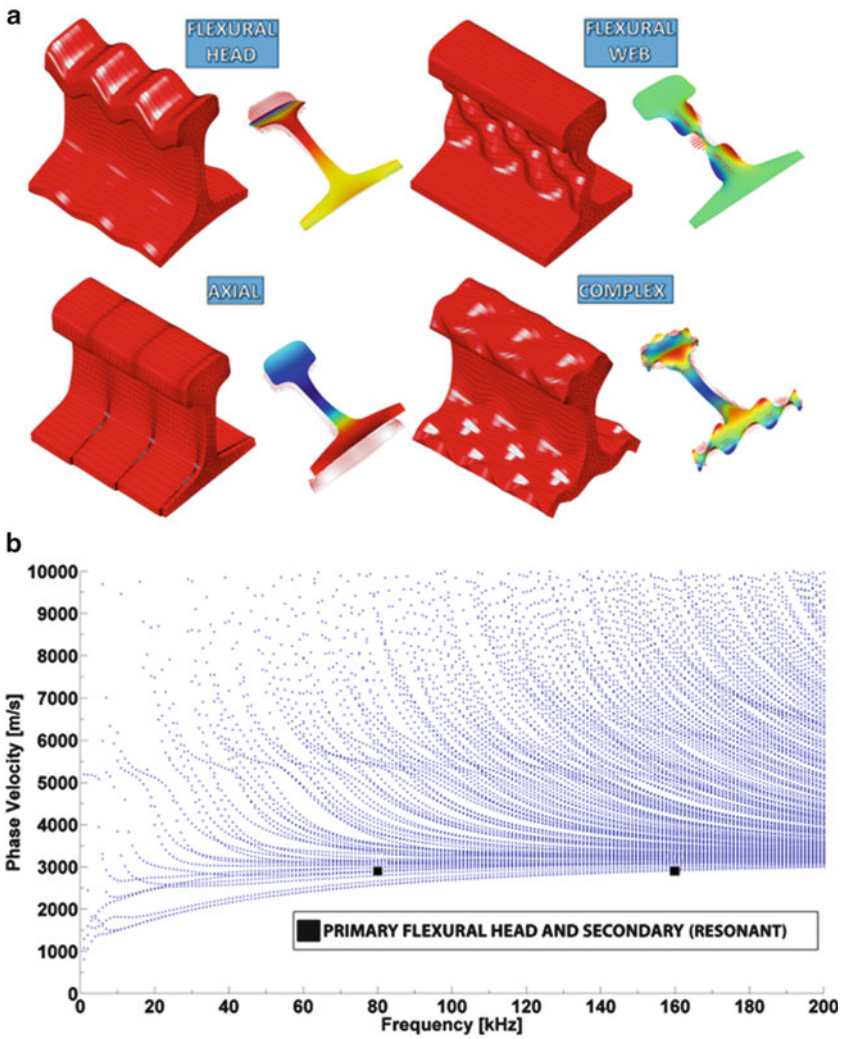

Fig. 16.1 (**a**) Exemplary propagative modes in the rail. (**b**) Phase-velocity dispersion curves in the (0–200) kHz frequency range with primary and secondary modes highlighted

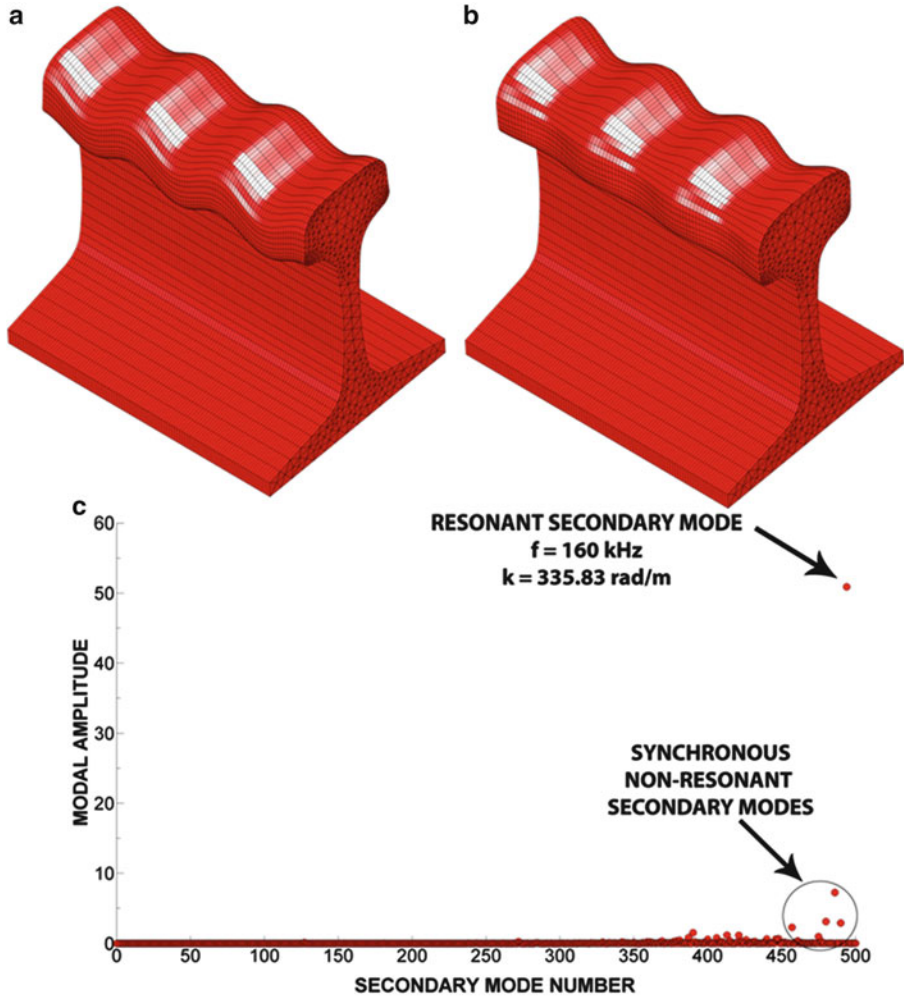

Fig. 16.2 (**a**) Selected primary mode at 80 kHz. (**b**) Resonant secondary mode at 160 kHz. (**c**) Modal amplitude plot for secondary propagative modes

synchronous modes, for which power transfer is absent, are also shown in the same figure. The previous results point up a favorable combination of primary and secondary wave fields able to maximize the nonlinear response of the waveguide.

16.4.2 Anisotropic Elastic Composite Laminate

A multi-layered composite laminate with unidirectional laminae in a quasi-isotropic layup was examined next. More specifically, the selected system consists of eight unidirectional T800/924 graphite-epoxy plies with a stacking sequence of $[\pm 45/0/90]_S$. Each layer has a thickness of 0.125 mm resulting in a total laminate thickness of 1 mm. The material properties for each single lamina in the principal directions of material symmetry are: $\rho = 1{,}500$ kg/m^3, $E_{11} = 161$ GPa, $E_{22} = 9.25$ GPa, $G_{12} = 6.0$ GPa, $\nu_{12} = 0.34$ and $\nu_{23} = 0.41$ [11]. The stiffness matrix for each lamina was rotated according to the angle between the fiber direction and the wave propagation direction [2]. In the following, wave propagation was assumed at 0° with respect to the fiber direction 1 (the extension to cases where this angle assumes different values is trivial). After all the matrices were rotated, the governing eigenvalue problem was solved as in the previous sections using the rotated stiffness matrices in the constitutive relations. Periodic Boundary Conditions (PBCs) were employed to gain computational efficiency [12]. The third-order elastic constants assumed for each lamina are: $A = 15$, $B = -33$ and $C = -14$ GPa [13]. The nonlinear post-processing was developed between 2.5 and 5.0 MHz. A complex primary mode

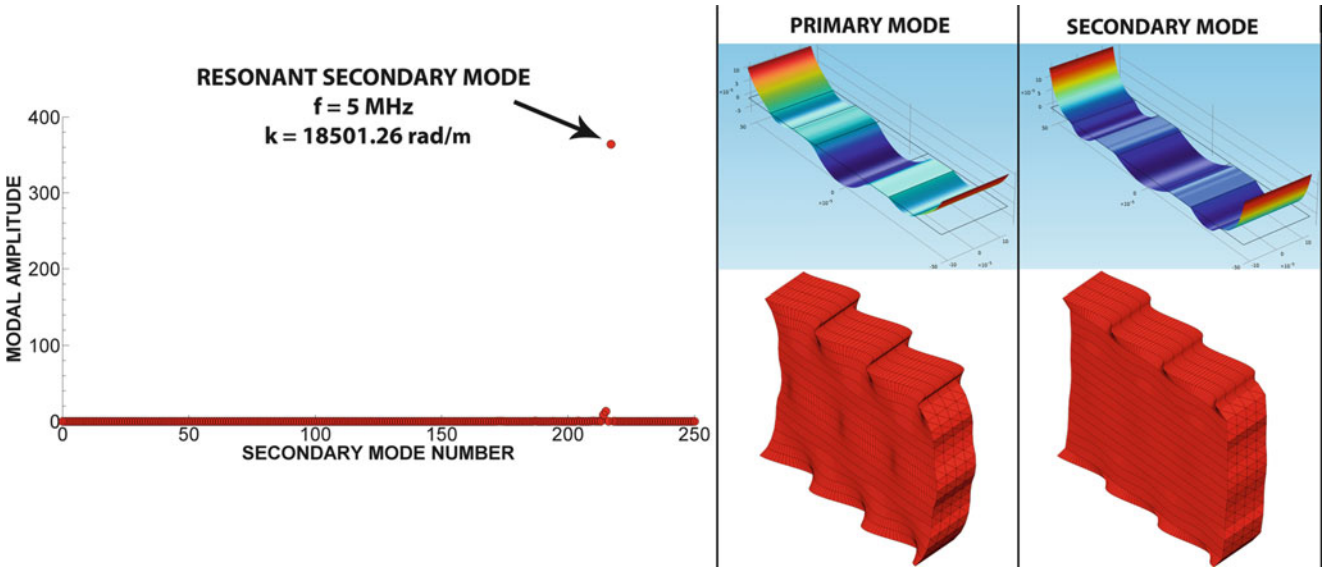

Fig. 16.3 Modal amplitude plot for secondary propagative modes, along with contour plots and 3D views of the selected primary and secondary modes for the elastic composite laminate

combining attributes typical of axial and flexural horizontal modes was selected as input. One of the propagative modes at the double harmonic (5 MHz) was found able to produce internal resonance. The results, in terms of modal amplitude plots, are shown in Fig. 16.3 along with the primary and secondary modeshapes. It can be noted from Fig. 16.3 how drastic is the predominance of the only resonant mode in terms of modal amplitude, when compared to all the other propagative secondary modes existing at 5 MHz. Both primary and secondary modes concentrate the wave energy near the center of the waveguide; consequently, this combination appears appealing for the inspection of the laminate because of the expected reduced wave leakage into surrounding areas.

16.4.3 Reinforced Concrete Slab

The complexity here arises from the coexistence of two domains with very different material properties. Previous studies have shown the influence of the reinforcement on the dispersion curves [12]. The present work analyzes the nonlinear features of the guided wave propagation for this particular heterogeneous system. Likewise the previous case PBCs are used to model the geometrical periodicity. The 2D periodic cell considered is 6 cm wide and 8 cm tall. The steel bars are assumed to be 1.6 cm in diameter (Fig. 16.4a). Material properties assumed for the concrete domain are: $\rho = 2{,}133$ kg/m^3, $C_{11} = 33.2$ GPa, $C_{66} = 11.8$ GPa [4]. For the steel bars, the following values were used: $\rho = 7{,}900$ kg/m^3, $C_{11} = 280$ GPa, $C_{66} = 80$ GPa [12]. The CO.NO.SAFE algorithm was used with 40 kHz as the primary frequency. The primary mode selected as input exhibits essentially a flexural horizontal displacement field.

The nonlinear results are presented in Fig. 16.4b. They reveal the presence of few asynchronous modes characterized by relatively large power transfer (modal amplitude values inside the circle) and only a single resonant secondary mode able to verify also the phase-matching condition. The nature of this identified advantageous combination of modes is represented in Fig. 16.4b.

16.5 Conclusions

The use of nonlinear guided waves is gaining increasing attention in the non-destructive evaluation and structural health monitoring communities. Proper application of nonlinear measurements requires a thorough understanding of the higher-harmonic generation phenomena that can be expected for the test waveguide. In the present work, the classical S.A.F.E. algorithm was extended to the nonlinear regime and implemented in a powerful multipurpose commercial FEM code

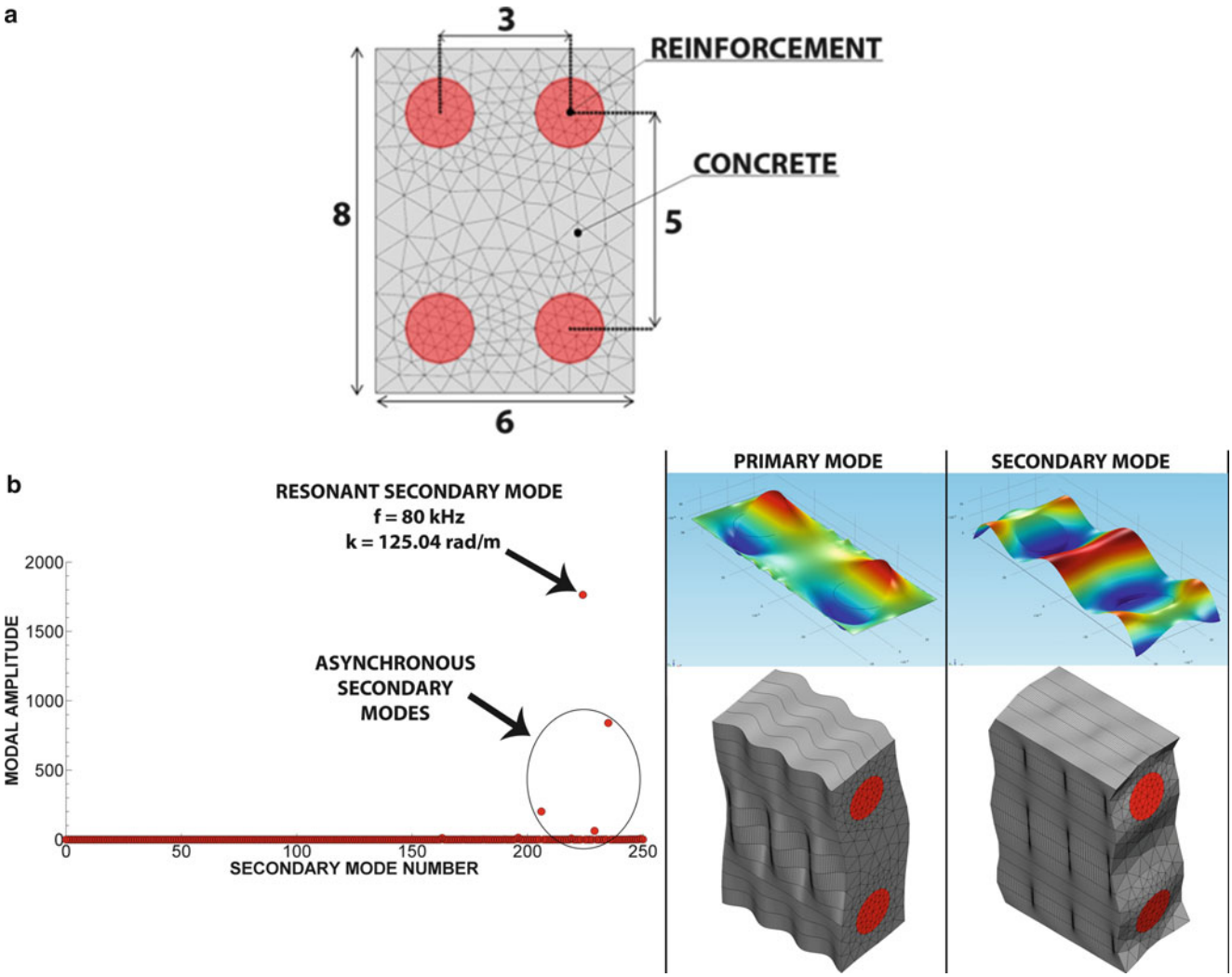

Fig. 16.4 (**a**) Geometrical details and finite element mesh for the periodic cell representative of a 8 cm thick reinforced concrete slab (dimensions in cm). (**b**) Modal amplitude plot for secondary propagative modes along with contour plots and 3D views of the selected primary and secondary modes for the reinforced concrete slab

(COMSOL). The result is a new tool that opens new possibilities for the analysis of dispersion characteristics and, most importantly here, nonlinear internal resonance conditions, for a variety of complex structural waveguides that do not lend themselves to alternative analyses such as purely analytical solutions.

The specific "complex" cases that were examined include: complex geometry (railroad track), multilayered composite panels (8-ply quasi-isotropic laminate), and heterogeneous periodic systems (reinforced concrete slab). In all these cases, the proposed algorithm successfully identified appropriate combinations of resonant primary and secondary modes that exhibit the desired conditions of synchronicity and large cross-energy transfer. These properties can be exploited in an actual system aimed at monitoring the structural condition of the waveguide by nonlinear waves (detect defects, measure quasi-static loads or instability conditions, etc.).

References

1. Auld BA (1990) Acoustic fields and waves in solids. Krieger, Malabar
2. Bartoli I, Marzani A, di Scalea FL, Viola E (2006) Modeling wave propagation in damped waveguides of arbitrary cross-section. J Sound Vib 295:685–707
3. Bermes C, Kim JY, Qu JM, Jacobs LJ (2007) Experimental characterization of material nonlinearity using lamb waves. Appl Phys Lett 90:0219011–0219013

4. Bouhadjera A (2004) Simulation of in-situ concrete conditions using a novel ultrasonic technique. In: Proceedings of 16th world conference on non-destructive resting, Montreal, Canada, 30 Aug–3 Sept 2004
5. Cawley P, Alleyne D (1996) The use of lamb waves for the long range inspection of large structures. Ultrasonics 34:287–290
6. Dace G, Thompson R, Rehbein D, Buck O (1991) Nonlinear acoustic, a technique to determine microstructural changes in material. Rev Prog Quant NDE 10B:1685–1692
7. de Lima WJN, Hamilton MF (2003) Finite-amplitude waves in isotropic elastic plates. J Sound Vib 265:819–839
8. Deng MX (2003) Analysis of second-harmonic generation of lamb modes using a modal analysis approach. J Appl Phys 94:4152–4159
9. Goldberg ZA (1960) Interaction of plane longitudinal and transverse elastic waves. Soviet Phys Acoust 6(3):306–310
10. Landau LD, Lifshitz EM (1959) Theory of elasticity. Wesley, London
11. Percival WJ, Birt EA (1997) A study of lamb wave propagation in carbon-fibre composites. Insight 39:728–735
12. Predoi MV, Castaings M, Hosten B, Bacon C (2007) Wave propagation along transversely periodic structures. J Acoust Soc Am 121:1935–1944
13. Prosser WH (1987) Ultrasonic characterization of the nonlinear elastic properties of unidirectional graphite/epoxy composites. NASA Contract Rep 4100:75–120
14. Rose JL (2002) Standing on the shoulders of giants: an example of guided wave inspection. Mater Eval 60:53–59
15. Sekoyan SS, Eremeev AE (1966) Measurement of the third-order elasticity constants for steel by the ultrasonic method. Meas Tech 0543–1972:888–893
16. Zarembo LK, Krasil'nikov VA (1971) Nonlinear phenomena in the propagation of elastic waves in solids. Soviet Phys USPEKHI 13:778–797

Chapter 17
Defect Detection in Composite Structures Using Lock-In Infrared Thermography

Arun Manohar and Francesco Lanza di Scalea

Abstract A Nondestructive Testing technique based on Lock-In thermography is proposed to detect delaminations present in a composite wind turbine blade. Image processing algorithms and statistical Multivariate Outlier Analysis were used in conjunction with the Lock-In thermography technique to counter 'blind frequency' effects and to improve the defect contrast. Receiver Operating Characteristic curves was used to quantify the gains obtained by using the proposed approach. Experiments were performed on a set of defects of various sizes that were incorporated during the construction of the wind turbine blade at different locations and depths.

Keywords Infrared thermography • Multivariate outlier analysis • Composites • Wind turbine blades • Defect detection

17.1 Introduction

The U.S. Department of Energy has recently set a target of adding 300 GW of wind power over the next 20 years [1]. During this period, a surge in production of wind turbine blades is expected. The Nondestructive Testing (NDT) community is still in the process of developing inspection techniques and standards for composite wind turbine blades [2]. Infrared thermography is an attractive NDT method for testing blades because of its full-field imaging capability. The problem of defect detection using infrared thermography has been studied extensively in the literature [3–7]. The most common implementation is based on Pulsed Thermography which is very well suited for detection of shallow defects. For deeper defects, Lock-In Thermography is generally preferred [8].

Lock-In Thermography [9–11] is based on the application of a periodic thermal energy input at very low frequency over a test object's surface. One of the main drawbacks of Lock-In Thermography is that 'blind frequencies' affect defect detection [9]. To address this shortcoming, the current paper proposes performing Lock-In tests at multiple frequencies, and subsequently applying Multivariate Outlier Analysis (MOA) to improve defect contrast and to counter the 'blind frequency' effects. Experiments were performed on 16 defects present in a 9 m test wind turbine blade at UCSD's Powell structural laboratories (Fig. 17.1a). The composite wind turbine blade was built using the CX-100 design developed by TPI Composites and Sandia National Laboratory [12]. The blade contains materials and construction techniques similar to those used for today's typical turbine blade with lengths in the 40 m range [13]. Several defects were added to the low-pressure side of the blade during the manufacturing stage. In this study, 16 delaminations defects were considered as shown in Fig. 17.1b. The implementation of these defects in the structure was accomplished by placing specially designed pillow inserts between the layers during the layup process. The inserts were developed at the Sandia National Laboratory and the thickness of the inserts used in the blade was measured at 0.25 mm. The diameters of the inserts used were 12.7, 25.4 and 50.8 mm.

A. Manohar (✉) • F. Lanza di Scalea
NDE & SHM Laboratory, Department of Structural Engineering, University of California, San Diego, 92093 La Jolla, CA, USA
e-mail: arunm@ucsd.edu

M. Rossi et al. (eds.), *Residual Stress, Thermomechanics & Infrared Imaging, Hybrid Techniques and Inverse Problems, Volume 8*, Conference Proceedings of the Society for Experimental Mechanics Series, DOI 10.1007/978-3-319-00876-9_17,

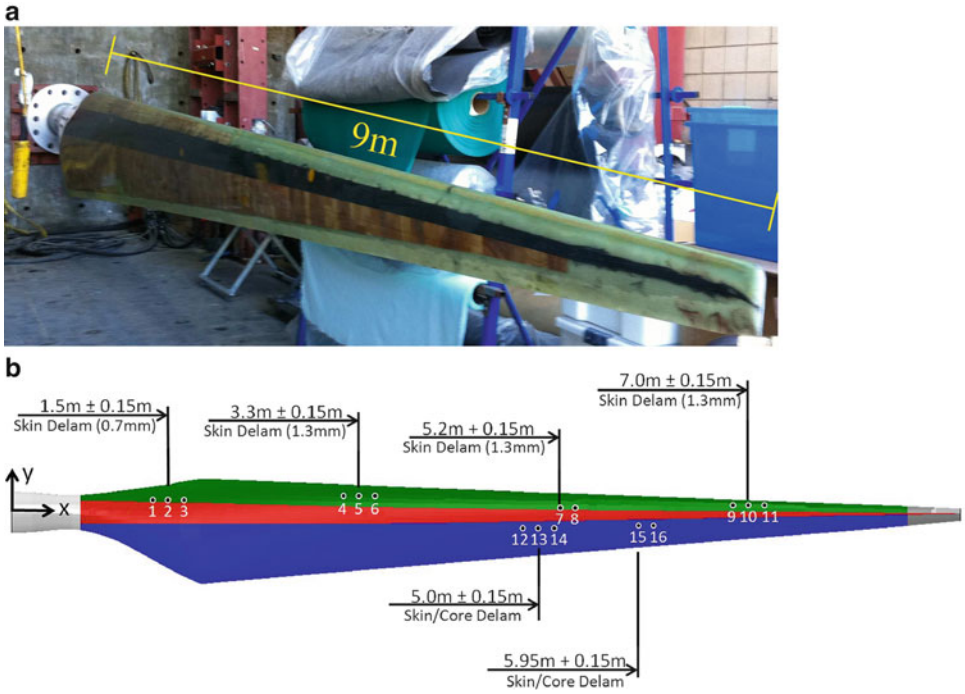

Fig. 17.1 (**a**) The CX-100 composite wind turbine blade cantilevered at the UCSD Powell labs (**b**) Schematic of the delamination defects present in the CX-100 wind turbine blade

17.2 Defect Detection Approach

Since the surface of the wind turbine blade was very reflective, the areas to be inspected were prepared by a thin coat of black, water-soluble paint. The paint layer improved the heat absorption at the surface and minimized the reflection of other heat sources present in the vicinity of the test area. For optimal detection of defects using the Lock-In technique, it is well established that the depth of the defect must be less than the thermal diffusion length [11]. The thermal diffusion length, z, is related to the thermal conductivity of the material, k, density, ρ, Lock-In frequency, f, and specific heat conductivity, c, by,

$$z = \sqrt{\frac{k}{\pi f \rho c}} \tag{17.1}$$

At some frequencies, commonly referred to as 'blind frequencies', the defects are undetected even though the thermal diffusion length is greater than the defect depth. Thus, the ability to detect defects within the object depends on the Lock-In frequency used. For a single-layer material, Eq. 17.1 can be used to compute the thermal diffusion length. However, the test specimen that was used in the presented study is a wind turbine blade which has layers of different materials whose properties and thickness are different. The calculation of the thermal diffusion length is not a straight-forward task. For the presented study, numerous experiments were performed at different Lock-In frequencies in order to determine the sensitive working range. Lock-In frequencies in the range of 30–70 mHz yielded the best results and were chosen for the experiments.

Lock-In Thermography is based on the application of a periodic thermal energy input to the surface of the object. When the resulting heat wave encounters a defect, some of it is reflected, causing a phase shift with respect to the input heat wave. The Lock-In Thermography setup that was used in the present study is shown in Fig. 17.2. The main components are the function generator, lighting dimmer pack, halogen lamps, IR camera and laptop. The function generator was used to generate the sinusoidal wave at a particular frequency and amplitude. The output of the function generator was fed into the lighting dimmer pack that amplified the power of the signal and delivered to the halogen lamps. The lamps heated the blade surface, which was imaged by the IR camera connected to the laptop for subsequent analysis. The IR camera used was a FLIR™ A320G camera with a maximum frame rate of 60 Hz. The detector is a focal plane array uncooled microbolometer with a spectral range of 7.5–13 μm, a resolution of 240 × 320 pixels, and Thermal Sensitivity of 50 mK.

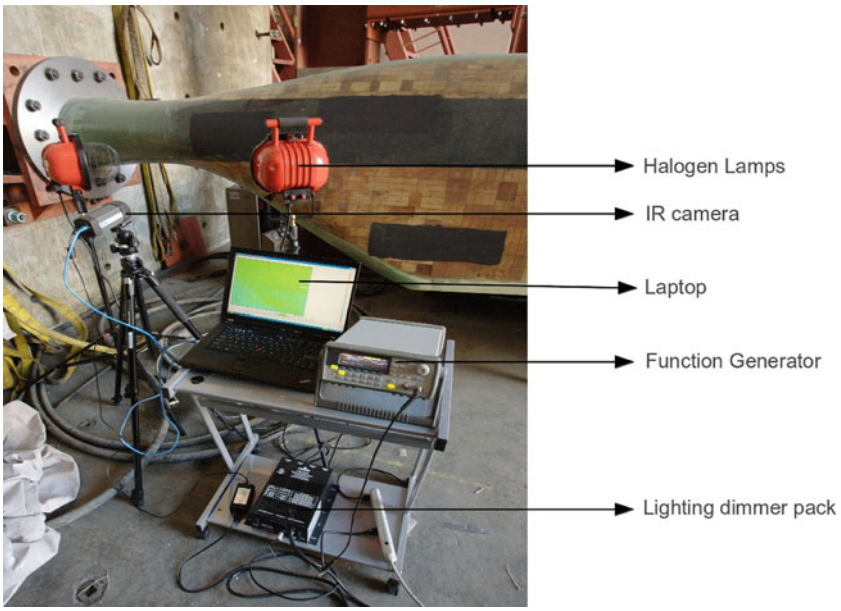

Fig. 17.2 Experimental setup used in Lock-In Thermography test

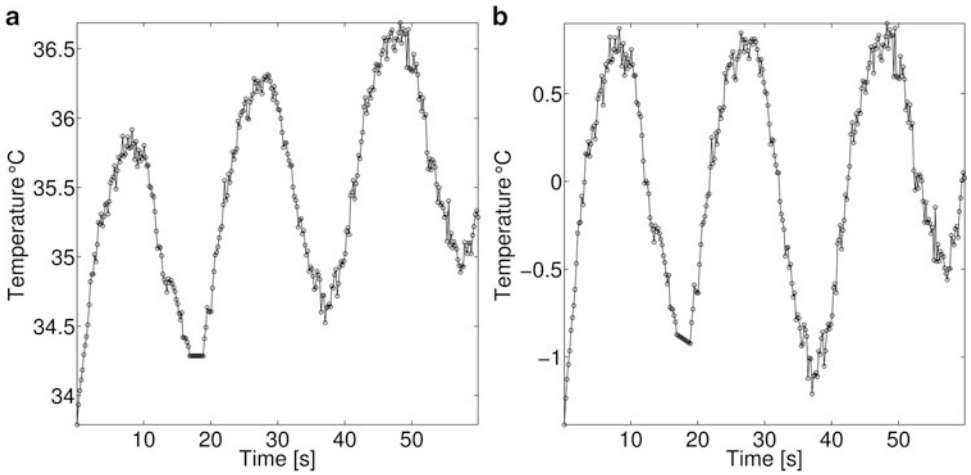

Fig. 17.3 Temperature-Time history measured at a point on the surface of the blade for three heating cycles at a 50 mHz Lock-In frequency (**a**) Before temperature slope removal (**b**) After temperature slope removal

For the Lock-In heating, a pair of halogen lamps that were rated at 1,400 W maximum total power was used to heat the test areas over three Lock-In time-periods. The temperature profile that was obtained at the surface can be compared to a sinusoid plus a constant temperature slope that is a consequence of the multiple heating cycles. A typical temperature profile at a sample location on the blade's surface is shown in Fig. 17.3a when three heating cycles were used at a Lock-In frequency of 50 mHz. At every location, linear fitting is performed to determine the temperature slope and the slope is removed from the raw data. The resulting temperature-time distribution that is obtained after the temperature slope removal is shown in Fig. 17.3b.

Fourier Transforms are then used to calculate the amplitude and phase at the Lock-In frequency at each spatial location. The phase and amplitude values are then combined at the different spatial locations to form the phase and amplitude images. The phase image is less susceptible to non-uniform heating and surface irregularities when compared to the amplitude image [11, 14], and it was used for subsequent processing. The phase and amplitude images that were obtained over an area

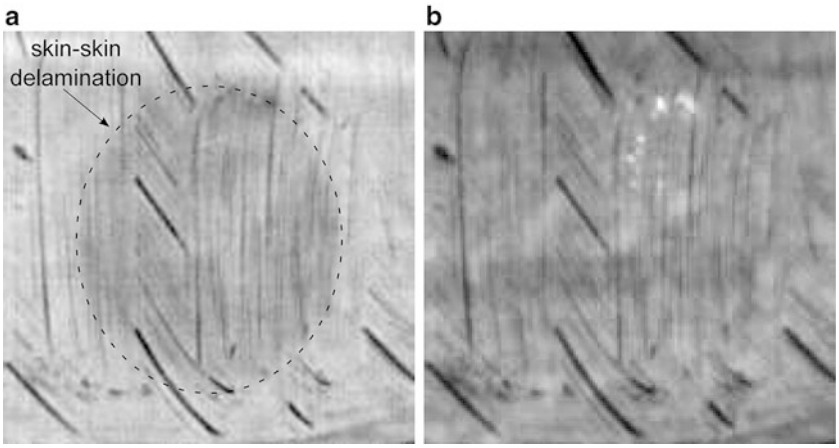

Fig. 17.4 (**a**) Phase image and (**b**) Amplitude image obtained from Lock-In heating at a 50 mHz frequency over an area containing a 50.8 mm diameter defect at a depth of 1.3 mm from the blade surface

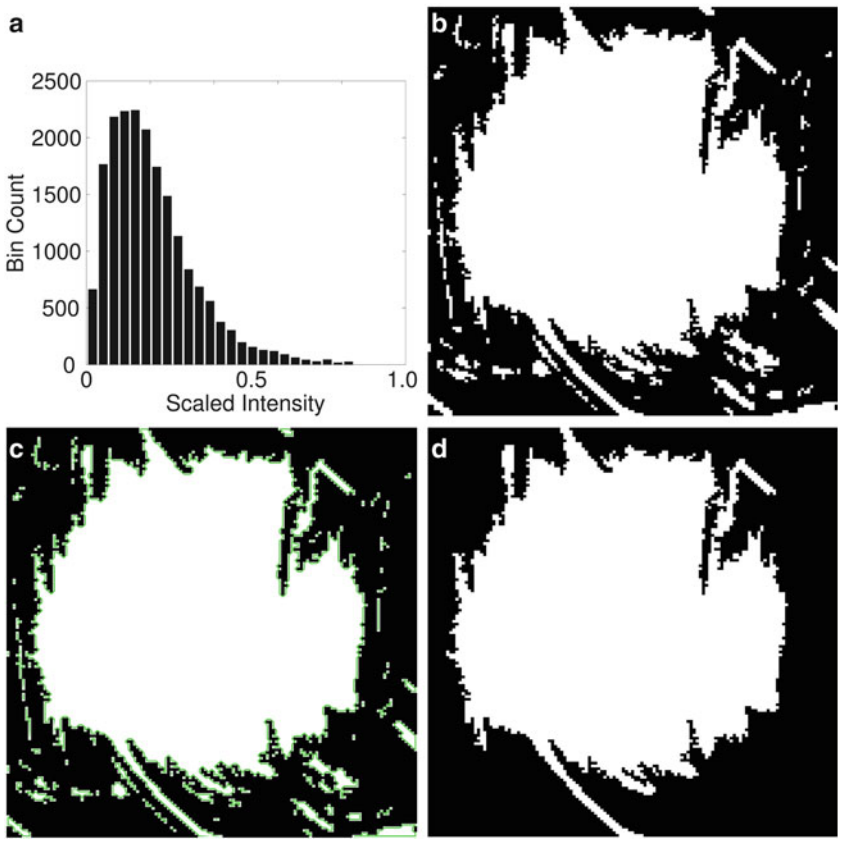

Fig. 17.5 Sequence of image processing steps performed on a phase image obtained over an area containing a 50.8 mm diameter defect at a depth of 1.3 mm from the blade surface (**a**) histogram of the intensity distribution in the phase image – intensity values are linearly scaled between 0 and 1 (**b**) binary image that is obtained by thresholding the scaled intensity value at 0.7, followed by application of morphological operations (**c**) boundaries of the different connected components (**d**) result of morphological image processing on the phase image shown in Fig. 17.4a

containing a 5.08 cm diameter skin-skin delamination at a depth of 1.3 mm from the blade surface are shown in Fig. 17.4a, b, respectively. Figure 17.4a shows the presence of the 50.8 mm diameter skin-skin delamination at a depth of 1.3 mm from the blade surface.

While the defect is visible, further contrast gains can be obtained through the use of image processing algorithms. Figure 17.5a shows the distribution of image intensity in the phase image in histogram form. The intensity values are linearly scaled between 0 and 1 using the maximum and minimum intensity values present in the image. Thresholding is performed at an intensity value to yield a binary image. Simple morphological operations are then performed on the thresholded binary image. The holes are filled in the binary image, followed by removal of isolated pixels (white pixel surrounded by eight black pixels). Figure 17.5b shows the binary image that is obtained when the phase image is thresholded at a value of 0.7 and

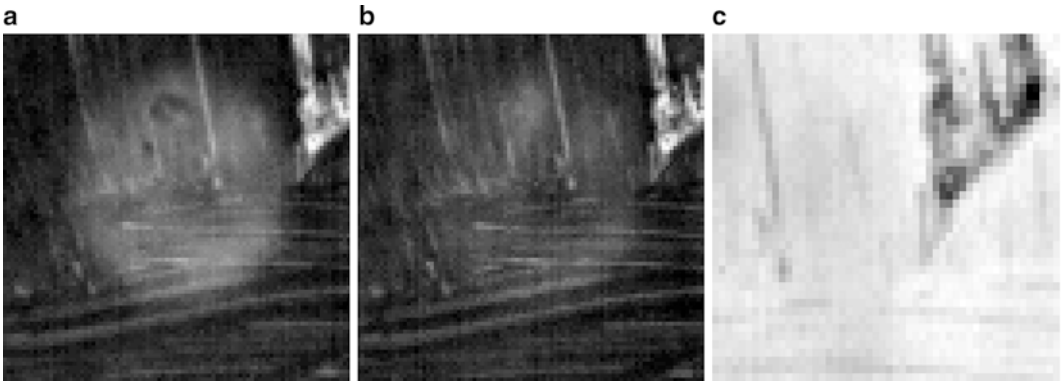

Fig. 17.6 Comparison of different Lock-In frequencies at a location containing a 2.54 cm diameter defect at a depth of 1.3 mm from the blade surface. The phase images were obtained at (**a**) 30 mHz, (**b**) 50 mHz and (**c**) 70 mHz frequency

after the application of the morphological operations. The different connected components are identified and labeled as shown in Fig. 17.5c. The area of the different connected components is then calculated, and the connected components whose area is less than 5 % of the image area are discarded. The final result is shown in Fig. 17.5d. This final result yields maximum contrast of the defect, and is also now suitable for the quantitative evaluation of the defect detection performance via computation of the Receiver Operating Characteristic curves.

Since 'blind frequencies' affect defect detection in Lock-In Thermography, five different Lock-In frequencies in the range 30–70 mHz were used at each defect location to ensure that at least one of the frequencies provides effective detection. MOA [14] is an efficient way of combining the spatially registered Lock-In data that are obtained at a defect location at different Lock-In frequencies. The discordancy test in the multivariate case is expressed by the Mahalanobis Squared Distance, D_ζ, which is a non-negative scalar defined as

$$D_\zeta = (x_\zeta - \bar{x})^T [K]^{-1} (x_\zeta - \bar{x}) \tag{17.2}$$

Where x_ζ is the potential outlier vector, $\bar{x}$ is the mean vector of the baseline, $[K]$ is the covariance matrix of the baseline, and T represents a transposed matrix. In this study, the data is five dimensional, corresponding to the five different Lock-In frequencies used. Figure 17.6 compares the phase images obtained using Lock-In heating at 30, 50 and 70 mHz, respectively. Notice that the phase images corresponding to Lock-In heating at 30 and 50 mHz clearly show the presence of defect. Lock-In heating at 70 mHz is much less effective. Apart from helping counter the 'blind frequency' effects, the use of MOA helps improving the Signal-to-Noise Ratio of the defective areas by statistically "adding" the contrast performance of multiple Lock-In frequencies.

ROC curves are a quantitative indicator of performance when comparing different detectors [15]. For each detector and the chosen detection threshold value, the True Positive Rate (TPR) and the False Positive Rate (FPR) can be calculated since the actual locations of the defects in the blade and their sizes are known. In this study, the performance across different thresholds is studied over the sixteen defects. The thresholds are varied between 0.1 and 0.9 in steps of 0.05. Figure 17.7 compares the performance of the different detectors against the MOA detector at a location containing a 5.08 cm diameter skin-skin delamination at a depth of 1.3 mm from the blade surface. The line connecting the coordinates (0, 0)–(1, 1) is the 'random guess' line. The best detector is the one that has an ROC curve furthest away from the 'random guess' line towards the top left corner of the ROC space.

To quantify the performance of the various detectors considered, the Area Under Curve (AUC) is computed for each of the different detectors for all the 16 defects. Based on the calculated AUC values, it can be concluded that in 51 of the 80 total cases, the use of MOA yields higher AUC over Lock-In heating at any of the individual frequencies. The mean gain in AUC that is obtained by using the MOA, compared to the 30, 40, 50, 60 and 70 mHz Lock-In frequencies is 0.96, 1.73, 1.79, 9.36, and 14.73 %, respectively. The overall gain in AUC obtained by MOA is 5.61 % over the individual detectors averaged over the 16 defects.

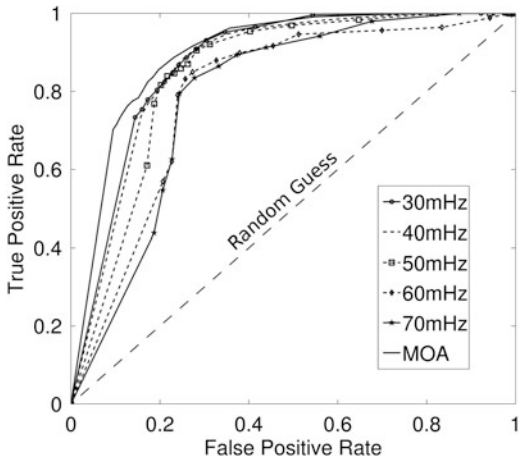

Fig. 17.7 Receiver Operating Characteristic curves comparing the performance of five different Lock-In frequencies and the MOA for different thresholds. The phase images were obtained over an area containing a 5.08 cm diameter defect at a depth of 1.3 mm from the blade surface

17.3 Conclusions

A novel approach based on Lock-In Thermography was proposed to address the problem of defect detection on composite wind turbine blades. Sixteen defects ranging in size between 12.7 and 50.8 mm, were considered for this study. The depths of the defects were in the range of 0.7–1.3 mm from the blade surface. Since 'blind frequencies' affect defect detection, Lock-In tests were performed at five different frequencies at each defect location, to ensure that any defect could be detected by at least one of the Lock-In frequencies. MOA was then performed on the spatially registered multi-frequency Lock-In data to combine in a statistically robust manner, the defect detection performance of the multiple Lock-In frequencies. Prior to the application of MOA, image processing algorithms including binarization and morphological operations were performed on the raw Lock-In thermal phase images. The defect detection performance of the single Lock-In frequencies, and the combined MOA, for various detection thresholds, was quantified via Receiver Operating Characteristic (ROC) curves. The ROC's plot the True Positive Rate (TPR) versus the False Positive Rate (FPR) computed for the known 16 test defects. The ROC results demonstrate that the approach of sweeping multiple Lock-In frequencies and combining the phase image results via MOA provides the nest overall defect detection performance compared to any single Lock-In frequency. This result is important in Infrared Thermographic detection of defects in composite structures, where Lock-In schemes are necessary to ensure enough penetration. The effectiveness of the MOA applied to Lock-In thermal phase images derives from (1) the statistical addition of defect contrast yielded by multiple Lock-In frequencies, and (2) the mitigation of the "blind frequency" problem affecting conventional Lock-In Thermography because several Lock-In frequencies are applied at each of the defective areas.

Acknowledgements The authors would like to thank the National Science Foundation (Grant #1028365, G. Maracas – Program Manager) and the von Liebig center at the University of California, San Diego. The authors would like to thank Dr. Michael Todd and Dr. Mohan Trivedi for their valuable inputs. Special thanks are extended to Jeffery Tippman, graduate student at UCSD NDE-SHM Lab, and Mark Rumsey and Dennis Roach of Sandia National Laboratories for advice on the design and defect lay-out of the CX-100 test blade.

References

1. U.S. Department of Energy (2008) 20% Wind energy by 2030
2. Roach D, Rackoq K, Duvall R (2010) Addressing the need for nondestructive inspection of wind turbine blades. Sandia National Laboratory
3. Shepard SM (2001) Advances in pulsed thermography. Thermosense XXIII 4360(1):511–515
4. Shepard SM, Lhota JR, Rubadeux BA, Wang D, Ahmed T (2003) Reconstruction and enhancement of active thermographic image sequences. Opt Eng 42(5):1337–1342
5. Sun JG (2006) Analysis of pulsed thermography methods for defect depth prediction. J Heat Trans 128(4):329–338
6. Ibarra-Castanedo C, Genest M, Servais P, Maldague XPV, Bendada A (2007) Qualitative and quantitative assessment of aerospace structures by pulsed thermography. Nondestruct Test Eval 22(2–3):199–215

7. Manohar A, Lanza di Scalea F (2011) Wavelet-aided MOA to enhance defect contrast in thermal images. Experimental Techniques
8. Pickering S, Almond D (2008) Matched excitation energy comparison of the pulse and lock-in thermography NDE techniques. NDT & E Int 41(7):501–509
9. Bai W, Wong BS (2001) Evaluation of defects in composite plates under convective environments using lock-in thermography. Meas Sci Technol 12(2):142
10. Meola C, Carlomagno GM, Squillace A, Vitiello A (2006) Non-destructive evaluation of aerospace materials with lock-in thermography. Eng Fail Anal 13(3):380–388. Papers presented at the first international conference on engineering failure analysis part III
11. Chatterjee K, Tuli S, Pickering SG, Almond DP (2011) A comparison of the pulsed, lock-in and frequency modulated thermography nondestructive evaluation techniques. NDT &E Int 44(7):655–667
12. Berry D (2007) CX-100 Manufacturing final project report. Sandia National Laboratory
13. Tippmann J, Manohar A, Lanza di Scalea F (2012) Wind turbine inspection tests at UCSD. Sensors and Smart Structures Technologies for Civil, Mechanical, and Aerospace Systems 2012. 8345(1):83451Q
14. Barnett V, Lewis T (1994) Outliers in statistical data, 3rd edn. Wiley, Chichester/New York
15. Kay S (1998) Fundamentals of statistical signal processing, volume II: detection theory. Prentice-Hall, Englewood Cliffs

Chapter 18
Digital Image Correlation for Identification of Vibration Modes

Olli Puustinen

Abstract We investigate the suitability of digital image correlation for the identification of vibration modes. The research focuses specifically on dynamic stereo-DIC measurements with two low speed cameras. First experiments are done in the laboratory conditions. Static deformations of a tensile test specimen and of a thin plate in bending are imaged, to establish a baseline for sensitivity to displacements and strains with our setup. Then the sensitivity is evaluated for dynamic laboratory experiments in which free vibrations of the thin plate are imaged. We will show that unknown vibration parameters, such as mode shapes of the plate, can be extracted from the measured data even for modes whose frequency is greater than several times the frame rate at which the images are captured. The method is finally applied to static and dynamic measurements of the flexibility and the vibrations of a structure during a field test in the context of a practical application.

Keywords DIC • Optical • Vibration • Mode shape • Natural frequency

18.1 Introduction

The object of this study is to investigate the suitability of digital image correlation [1] for the applications in mechanical engineering and especially for the vibration identification. In the experimental part static and dynamic strain and displacement measurements are performed with LaVision StrainMaster Digital Image Correlation system. In the static part the deformation of the tensile test specimen and the thin plate is imaged and measured and displacements and strains are calculated to establish a baseline for sensitivity to displacement and strains with our setup. The dynamic part includes the imaging of the vibration of the thin plate and the calculation of the natural frequencies and the mode shapes of the plate. The method is finally applied to static and dynamic measurements to investigate the flexibility of a structure during a field test.

18.2 Experimental Procedure

All experiments were performed with two LaVision StrainMaster ImagerProX 2 M pixel 14 bit CCD cameras with the resolution of 1,600 × 1,200 pixels and with the DaVis software. For image acquisition DaVis 7.2 and for strain and displacement analysis version 8.1 was used. For the calibration in the laboratory experiments LaVision's standard Type 7 3D calibration plate was used. The target plate is marked with uniformly spaced markers. The calibration was performed by obtaining three image pairs. The plate was tilted and rotated into different orientations during calibration. Three different orientations and positions were used.

All the test specimens were covered with a computer designed optimal surface pattern [2]. The surface pattern on the test specimen is presented in Fig. 18.1.

O. Puustinen (✉)
Department of Engineering Design and Production, Aalto University, 14200, FI-00076 Helsinki, Finland
e-mail: olli.p.puustinen@aalto.fi

M. Rossi et al. (eds.), *Residual Stress, Thermomechanics & Infrared Imaging, Hybrid Techniques and Inverse Problems, Volume 8*, Conference Proceedings of the Society for Experimental Mechanics Series, DOI 10.1007/978-3-319-00876-9_18,

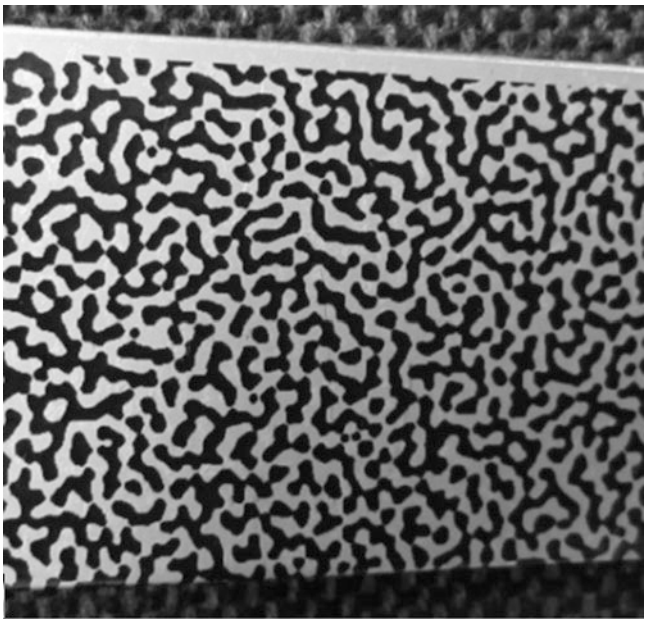

Fig. 18.1 Computer designed optimal surface pattern attached on a test specimen

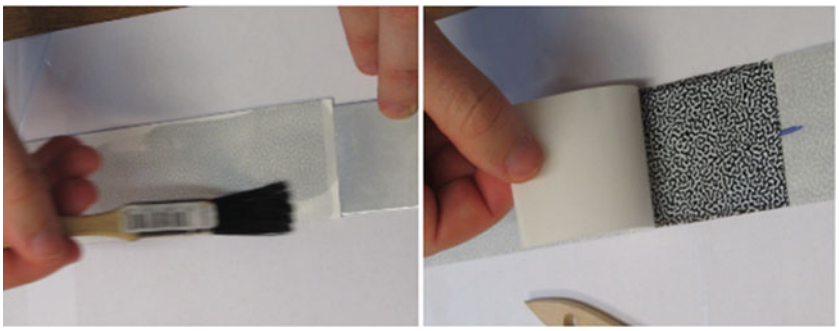

Fig. 18.2 Attaching the pattern on specimen using a laser tattoo paper

For these laboratory experiments the surface pattern was attached on the test specimen using a laser tattoo paper made by Crafty Computer Paper. This specific paper consists of two sets of paper, printing paper and adhesive paper. The pattern is printed on the printing paper and the adhesive paper is attached on that. The pattern will now stick on the adhesive film, which can be removed and placed on the specimen. By wetting the surface, the film can be removed so that the pattern will stick on the surface of the specimen. Using this method we can achieve a pattern, which sticks quite well on the surface of the specimen and is also flexible. Figure 18.2 illustrates the transfer process.

18.3 Imaging Free Vibrations of a Thin Plate

Before the dynamic experiment a statically bent 400 × 40 × 1 mm thin steel plate was investigated to establish a baseline for sensitivity to displacement and strains with our setup [3]. The plate was fixed from both ends and loaded in a tensile test machine until it buckled. This was imaged and the out-of-plane displacements were measured. After the measurement the strain values were calculated from the displacement data. Because of the static nature of the first measurement very high imaging frequency was not needed. To get enough pictures for further processing a frequency of 1 Hz was used. For the evaluation 220 images were taken. After the imaging the displacement and strain calculations were done with DaVis 8.1.

In this section some imaging results of vibration measurement are shown. The measurements were performed in stereo by using two cameras and therefore the out-of-plane displacements of the plate can be calculated. In Fig. 18.3 two images of the out-of-plane displacements over measured area at different time points are presented. Also a raw image from the beginning of the test is shown.

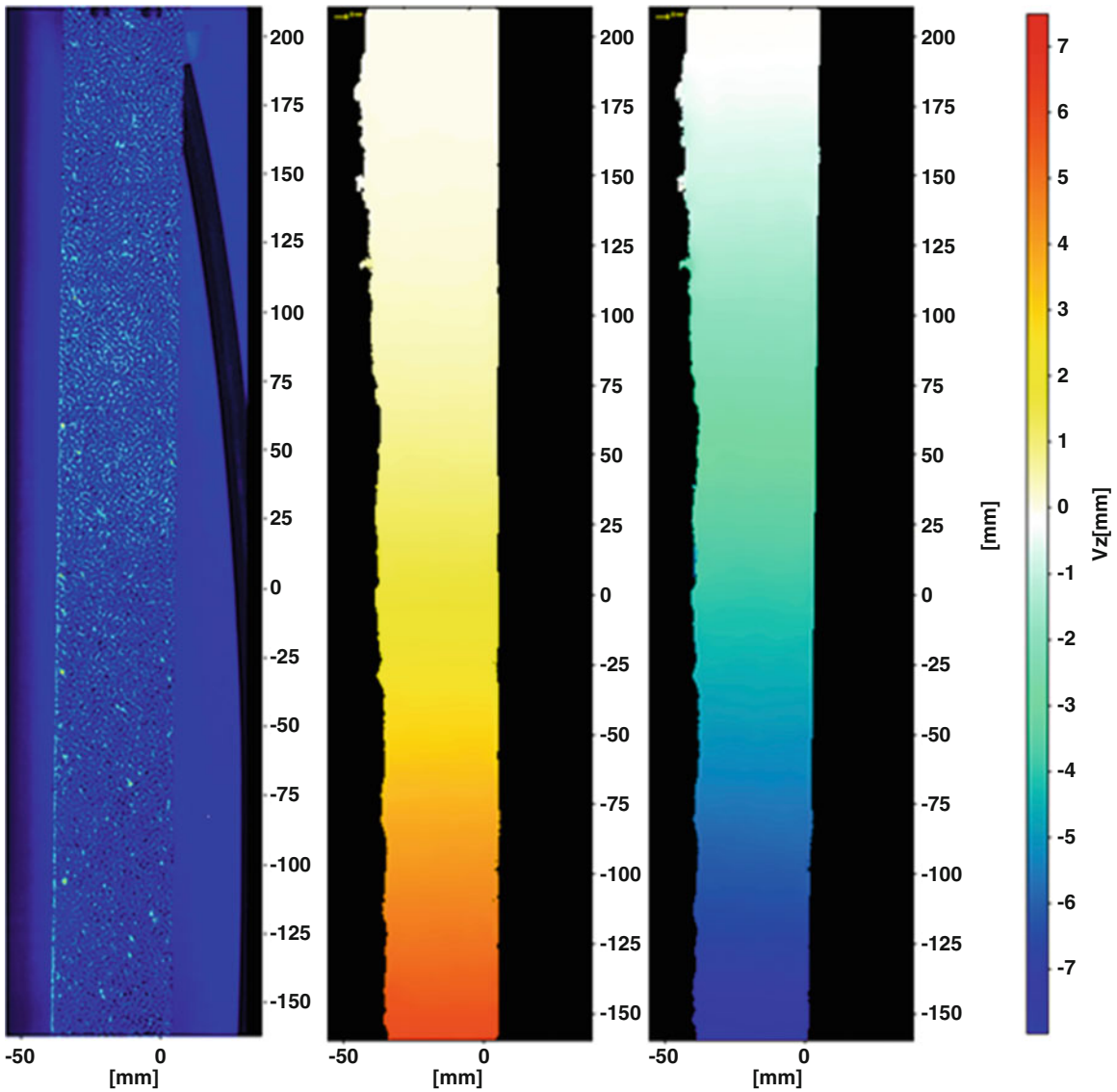

Fig. 18.3 A raw image at one time point and out-of-plane displacements at two different instants in time

In Fig. 18.4 the vibration data plot of third test, in which the displacements are plotted over time, is shown. The displacements in Fig. 18.4 are calculated average values over the whole area of the measured plate.

Figure 18.5 shows the z-displacement of the side profile of the plate. The fixed end of the plate is placed on the left side of the graph and the free end of the plate is placed right side. Each curves of different color present the shape of the side profile at different time points.

After the examination of the images and the graphs the data has been processed in Matlab software. The DaVis program does not allow much control over further processing of the measured data. Therefore all the further data processing is done with Matlab.

18.4 Solving Unknown Vibration Parameters

For the purpose of comparison, the first two mode shapes are calculated analytically. In the calculation the simple cantilever beam model [4] was used. According to this model mode shapes of the clamped – free beam and the equation for the natural frequencies are

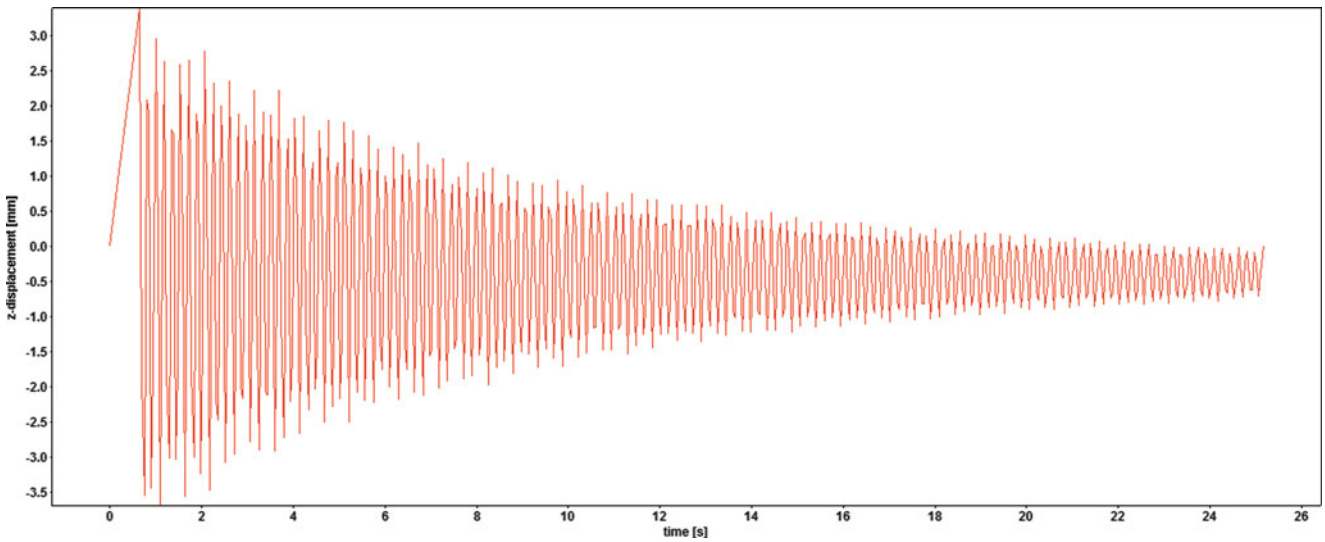

Fig. 18.4 Displacement – time plot (average displacement over the whole area)

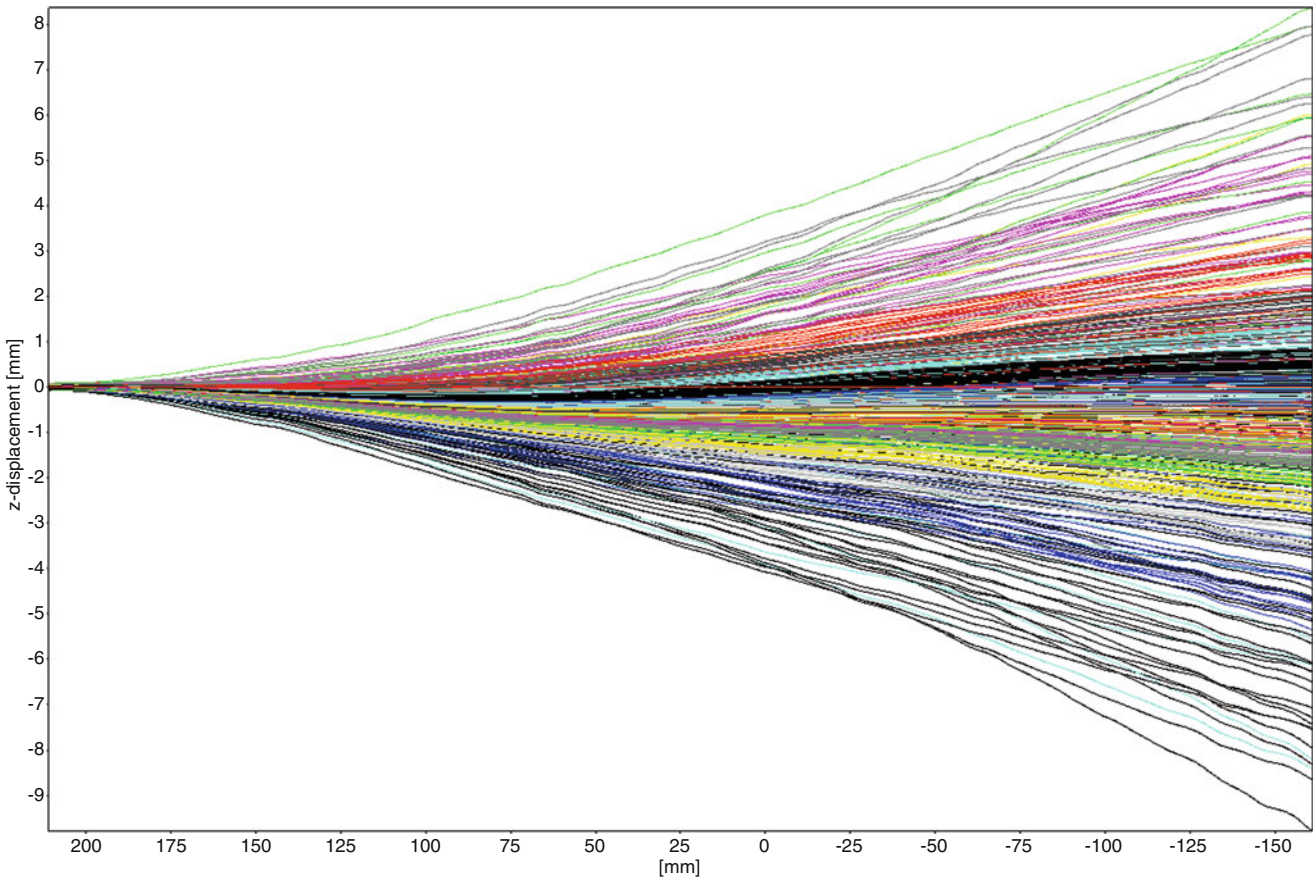

Fig. 18.5 z-displacement of the side profile of the plate. The y-axis shows the out-of-plane displacement and the x-axis shows the distance along the specimen

Table 18.1 Mode shape coefficients and natural frequencies

Mode	f_n	β_n	σ_n
1	5.4 ± 0.6 Hz	1.8751040	0.7341
2	33.7 ± 4.0 Hz	4.69409113	1.0185
3	94.5 ± 11.3 Hz	7.85475744	0.9992
4	185.2 ± 22.2 Hz	19.99554073	1.0000
5	306.1 ± 36.7 Hz	14.13716839	1.0000

$$\mathrm{f(x)} = \cosh \beta_{\mathrm{n}}\mathrm{x}\text{-}\cos \beta_{\mathrm{n}}\mathrm{x}\text{-}\sigma_n(\sinh \beta_{\mathrm{n}}\mathrm{x}\text{-}\sin \beta_{\mathrm{n}}\mathrm{x}), \tag{18.1}$$

$$f_n = \frac{1}{2\pi}{\beta_n}^2\sqrt{\frac{EI}{\rho a L^4}}, \tag{18.2}$$

where f_n is the natural frequency, E is the Young's modulus, $I = \frac{bh^3}{12}$, where b is the width and h is the thickness of the plate, is moment of inertia, ρ is density and a is the cross-sectional area and L is the length of the beam. The parameters β_n and σ_n are the mode shape coefficients and their values are presented in Table 18.1. The test specimen was made of stainless steel grade AISI 301 with density of 7,750 kg/m^3 and Young's modulus of 200 GPa. Thickness of the plate was varying a bit and is approximately h = 1.05 ± 0.05 mm. Also a small error ±10 mm in the length and a relative error of 1 % in the density and Young's modulus values is assumed. The total relative error of the natural frequencies can now be calculated from following equation. The values in Eq. 18.3 are assumed relative errors of different parameters.

$$\frac{\sigma f_n}{f_n} = \frac{1}{2}\frac{\sigma_E}{E} + \frac{1}{2}\frac{\sigma_\rho}{\rho} + \frac{\sigma_h}{h} + 2\frac{\sigma_L}{L} = 1\% + 1\% + 5\% + 5\% = 12\% \tag{18.3}$$

Table 18.1 shows also the first five analytically calculated natural frequencies of the plate. When the frame rate of the cameras is considered, the most interesting frequencies are the first two. For the plate, which was used in the test, the first two natural frequencies can be calculated as $f_1 = 5.4$ Hz and $f_2 = 33.7$ Hz.

Natural frequency values in Table 18.1 show that already a small variation in the thickness or length of a plate can make a relatively large change in the frequency. If the frequency can be measured more precisely than the parameters in Eq. 18.1, it could be also possible to use the frequency data to solve these parameters inversely. Analytically calculated mode shapes are shown in Fig. 18.6.

The 3D data of the experiment was transformed into Matlab and all the processing was done there. The rectangular area of interest was chosen over the plate and the average was taken along the horizontal direction. The vertical length of the area of interest was over the whole plate.

In Fig. 18.7 the time dependence diagram of the vibration is shown. This data was the base from which all the following graphs are calculated. The x-axis of the plot in Fig. 18.7 shows the time and the distance along the specimen is placed on the y-axis. The top of the plot (y = 0) presents the clamped end of the specimen. The color scale of the diagram represents the out-of-plane movement of the specimen, where blue reflects the movement towards the camera and red away from the camera.

Next the Fourier transform in time domain was taken. Figure 18.8 represent a surface plot of a Fourier transform of the data showed in Fig. 18.7. From Fig. 18.8 one may easily find the peak at the frequency of 5.6 Hz which represents the first mode of the vibration but it is also showing a peak at 6.2 Hz which corresponds to the second mode of the vibration. Due to the low sampling frequency the second mode, which can be found from the figure, is most likely an alias of the real second mode of the vibration. The shapes of the peaks in Fig. 18.8 represent the magnitude of the mode shapes of the vibration.

Next the mode shapes of the vibration of the plate, which we were able to solve, were calculated. The mode shapes with their natural frequencies are presented in Fig. 18.9. In the figure the green line represents the first mode and the red line represents the second mode. As said before, the second mode shown in the graph is the alias of the real second mode. The blue curve in the figure represents the DC component.

Next figures created with DaVis demonstrate the first two mode shapes of the plate. In Fig. 18.10 the first mode is shown left and middle and the second mode right.

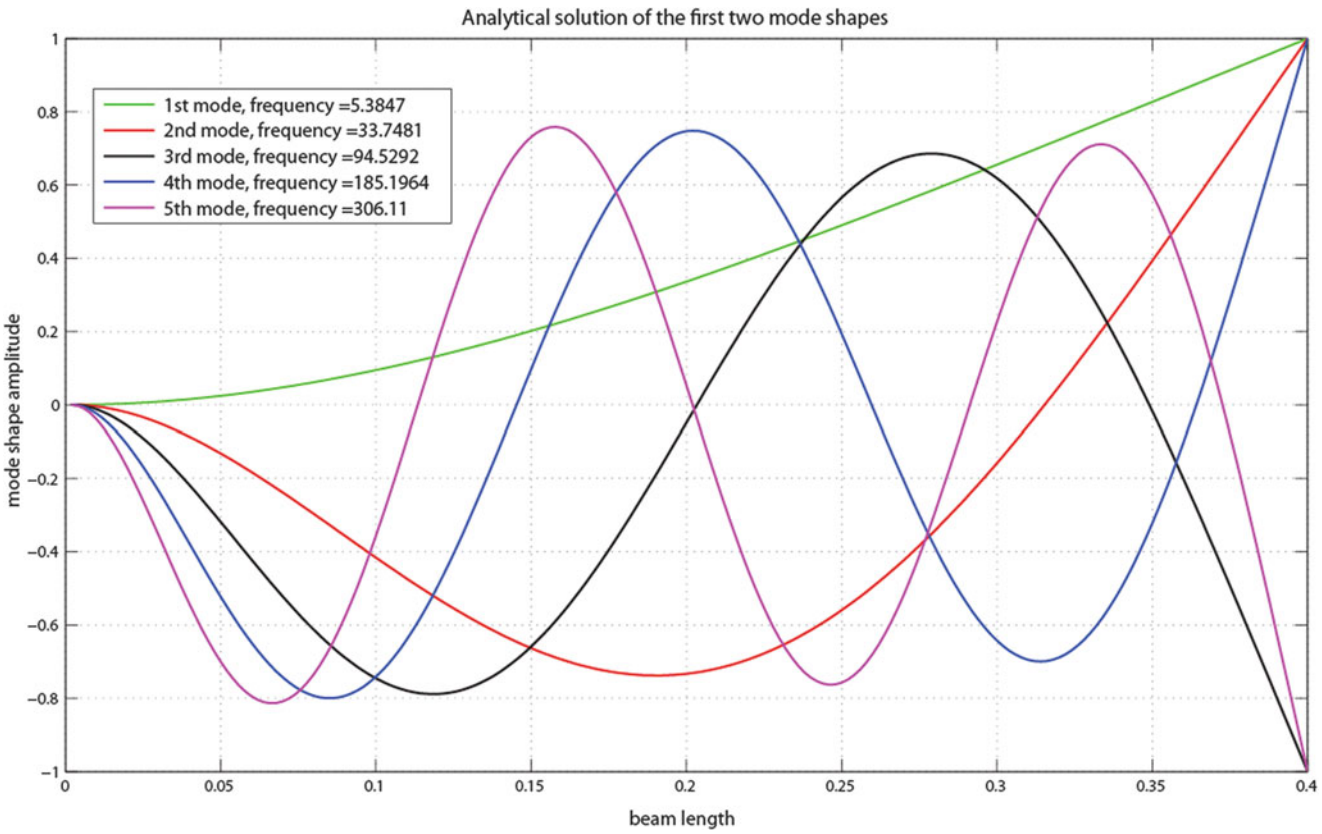

Fig. 18.6 Analytically calculated first five mode shapes

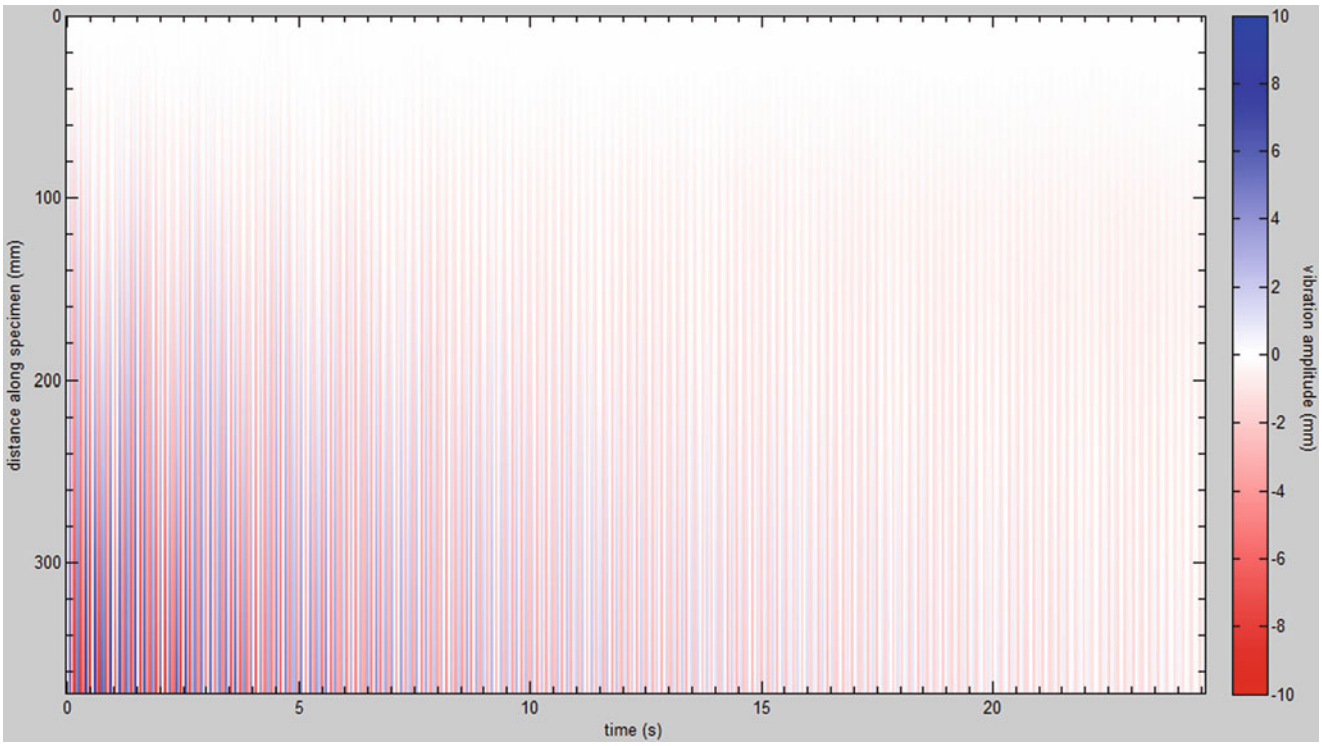

Fig. 18.7 Time dependence of the vibration

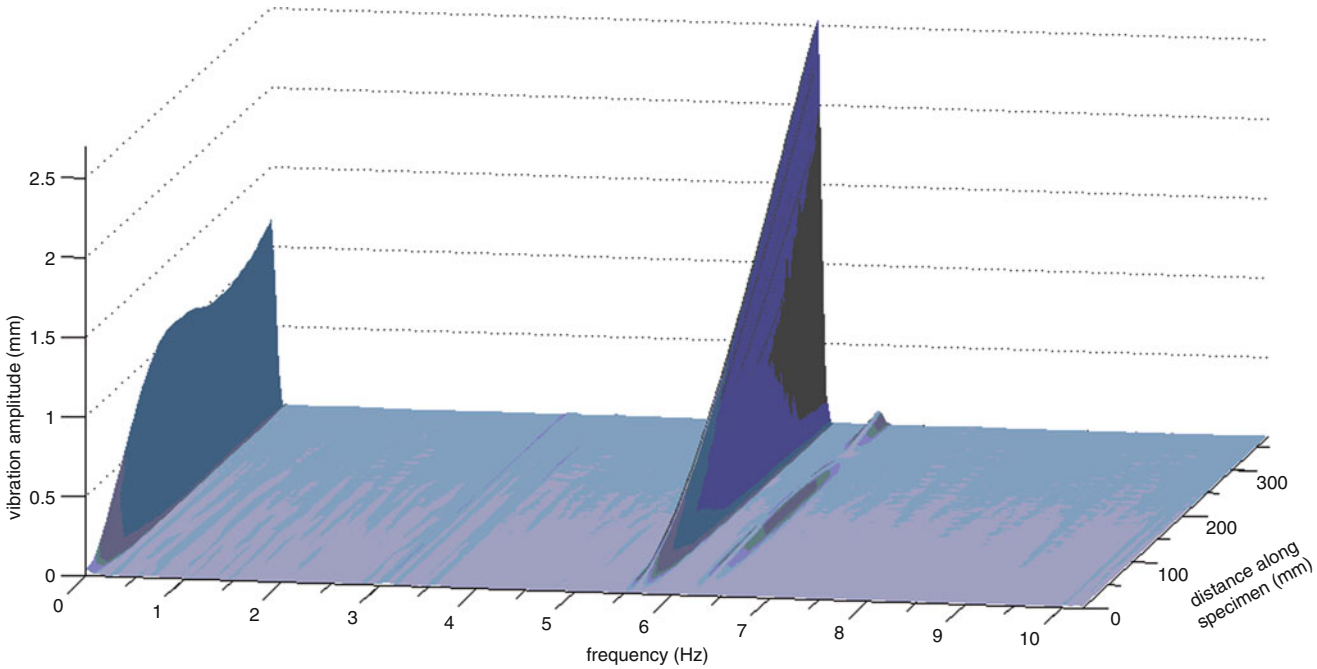

Fig. 18.8 FFT of the surface of the specimen

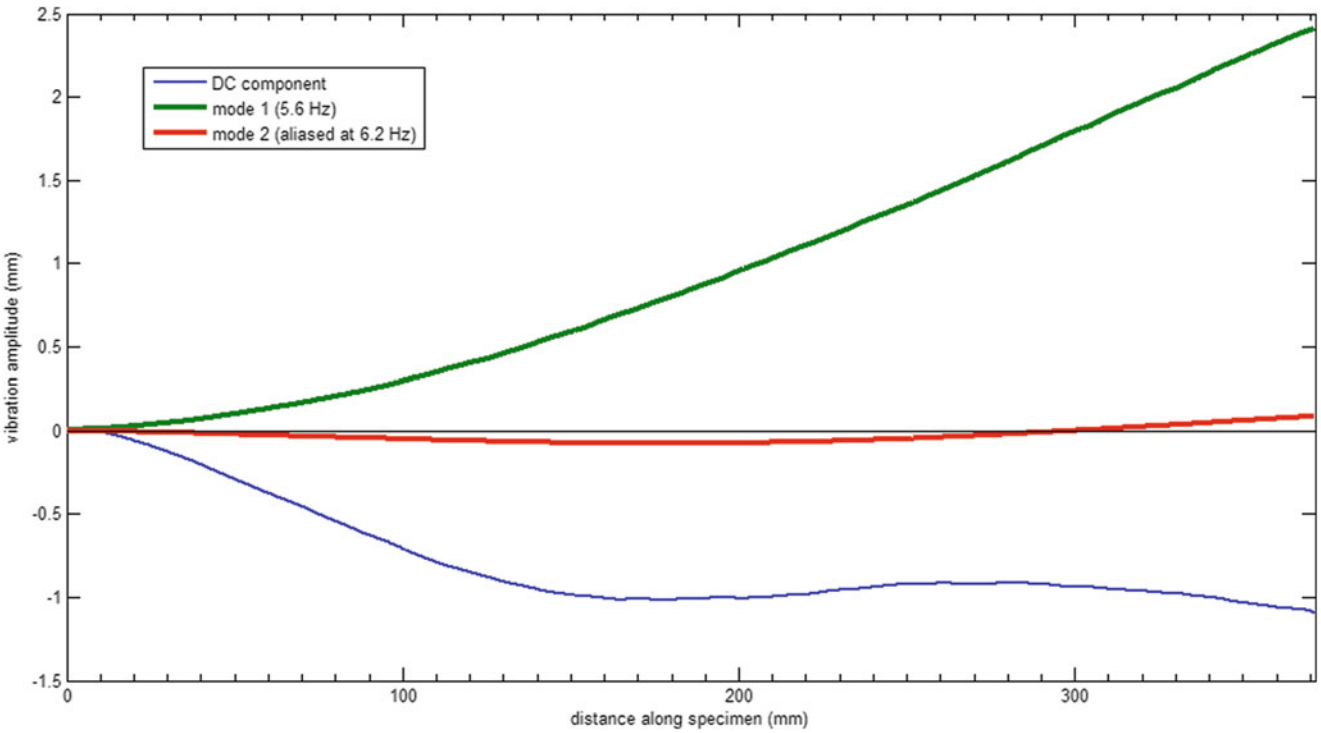

Fig. 18.9 Mode shapes of the vibration of the plate, in which the mode 2 is from alias frequency. The *blue line* represents the DC component of the vibration

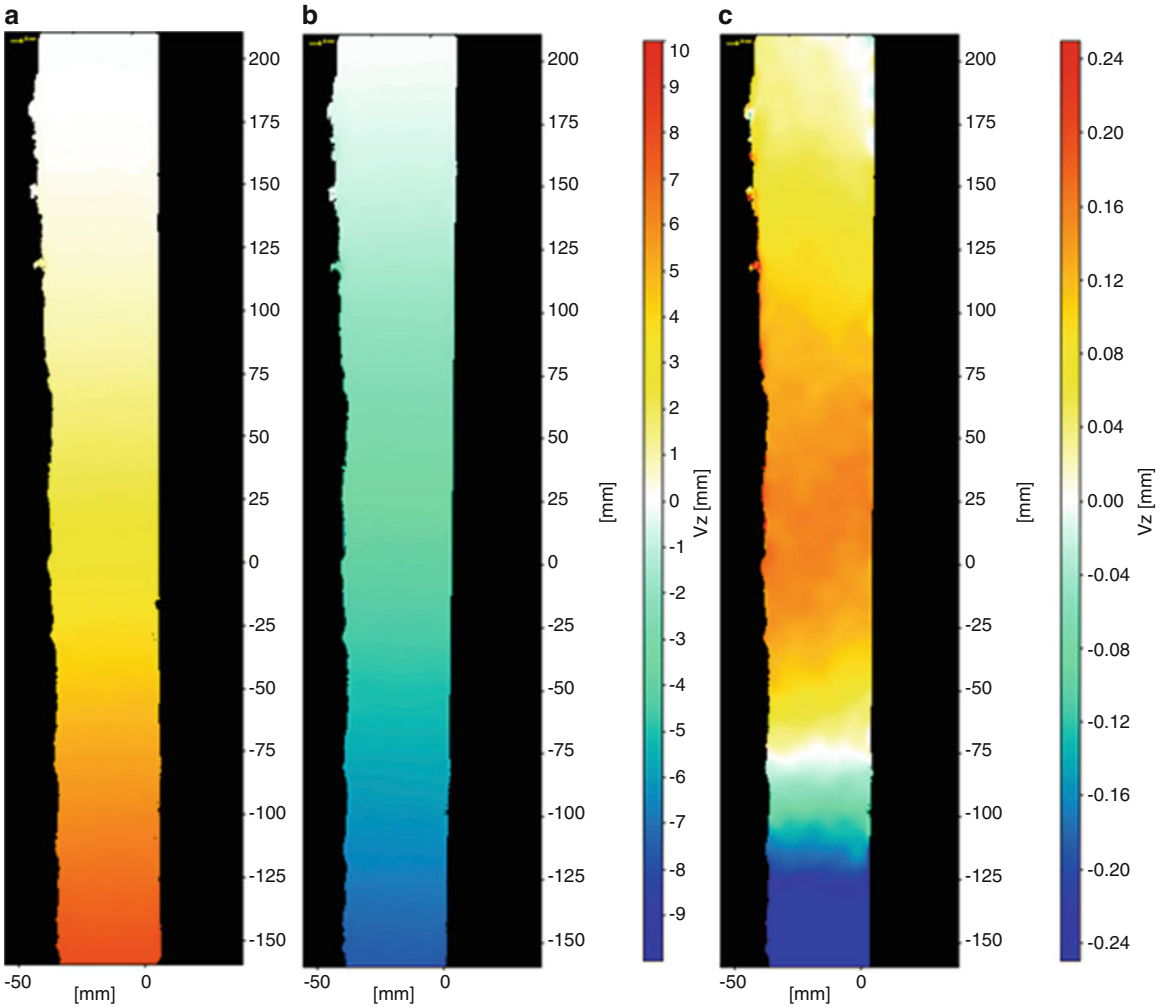

Fig. 18.10 (**a**) and (**b**) represent the first mode shape of the plate and (**c**) represents the second mode of the vibration

18.5 Conclusion and Further Work

The goal of this study was to identify vibrations of a rectangular plate by using the optical digital image correlation method and solve the first natural frequencies and vibration modes. Because of the limit of the sampling frequency of the cameras it was only possible to identify the first two modes of the vibration.

The analytically and experimentally calculated natural frequencies are presented in Table 18.2. As can be seen the measured first natural frequency is quite close to the analytical value. This small difference can come for example from the small variation of the plate thickness or length. Also the imaging process is very sensitive to noise so there can be small error in the experimental value. Nevertheless the values are close to each other.

In the values of the second natural frequency there is a difference caused by the too low sampling frequency. The calculated value of the second mode is in between of the DC component and the Nyquist frequency so it is most likely the alias of the real natural frequency of the second mode.

In spite of the difference in the natural frequencies it was still possible to find the real vibration modes of the first two natural frequencies. The calculated mode shapes are presented in Fig. 18.9. The measured mode shapes match quite well with the mode shapes which were calculated analytically.

LaVision's StrainMaster cameras, which were used during this thesis, had unquestionably too low frame rate for more accurate vibration measurement. However, already with the low speed camera it was possible to measure the lowest natural frequency of the vibrating object plate. If higher frequency vibration is needed to be measured, the high-speed DIC cameras would be necessary for valid measurement. Experiments which were done during this thesis show that it could be also

Table 18.2 Analytically and experimentally calculated values of the first two natural frequencies

	f_1	f_2
Analytical	5.4 Hz	33.7 Hz
Experimental	5.6 Hz	6.2 Hz (Alias)

possible to use DIC for field testing and in future for example to monitor machine vibrations. Also by combining the slower frame rate DIC measuring system with more accurate high-speed point measurements it could be possible to solve higher natural frequencies. DIC method works quite reliable in laboratory conditions especially in static cases, but the experiments, which are performed during this study, show that digital image correlation is also well suited for vibration measurements.

In future we are planning to use frame rate of 340 Hz cameras by Basler and try to solve higher frequency modes of a similar plate. After the laboratory experiments similar field tests were performed, where the flexibility and vibrations of a turret of a military vehicle were investigated. The field tests were successful but also for these tests the cameras which were used, were too slow. With the new higher frame rate camera system it is going to be possible to perform more accurate and complete measurements of this structure. We are also planning to combine a slower frame rate DIC measuring system with more accurate high-speed point measurements to make it possible to identify higher natural frequencies.

References

1. Sutton MA (2009) Image correlation for shape, motion, and deformation measurements basic concepts, theory and applications [s.1.]. Springer Science, New York. ISBN 978-0-387-78746-6
2. Bossyut S (2012) Optimized patterns for digital image correlation. Imaging methods for novel materials challenging applications, Springer, New York, NY, vol 3. ISSN 978-1-4614-4234-9
3. Puustinen OP (2013) Digital image correlation for identification of vibration modes, Master's thesis, Aalto University
4. Inman DJ (2007) Engineering vibration, 3rdth edn. Pearson Education, Upper Saddle River. ISBN 0-13-228173-2

Chapter 19
Application of VFM for the Simultaneous Identification of Visco-pseudo-hyper Elastic Constants of Rubbers

G. Chiappini, M. Sasso, M. Rossi, and D. Amodio

Abstract In this work, the Virtual Fields Method is employed in order to identify the parameters of constitutive models describing the visco-pseudo-hyper elastic behavior of rubber-like materials; a cruciform specimen is subjected to several biaxial loading/unloading cycles at different strain amplitudes, while load and full-field strain histories are recorded. The material is considered from its virgin state and no conditioning is performed, so not only the hyperelastic and viscoelastic characteristics have to be considered, but also the damage or Mullins effect has to be accounted for.

The numerical procedure here developed exploits the large amount of information provided by the experiment (over 18,000 pictures are processed) and put them into equations of virtual work where the models constants are unknown. It is worth to note that here all the material constants are determined simultaneously by solving a unique system of non linear equations, instead of determine them separately from different tests.

Keywords Virtual fields method • Viscoelasticity • Hyperelasticity • Mullins effect

19.1 Introduction

In this work a complete mechanical characterization of the material is presented, consisting in the execution of several experimental tests and on the calibration of the constitutive models describing the hyperelastic, viscoelastic and pseudo elastic behavior of the material. Rubbers are widely used in many engineering fields, including bellow seals, hydraulic hoses, tires, shock and vibration absorbers, and are often submitted to particular loading conditions, including large deformations and repeated cycles along different time periods.

From a mechanical point of view, elastomers usually show a strongly non linear relation between stress and strain, which is suitably studied in the framework of hyperelasticity; a number of numerical models are available in the literature. Indeed, large-strain response of hyperelastic materials in quasi-static conditions and without irreversible strain phenomena has been extensively researched since the works of Mooney [1]. Exhaustive documentation on this research topic can be also found in, Ogden [2]. Besides hyperelasticity, elastomers exhibit some inelastic phenomena, e.g., hysteresis, permanent set and stress softening. The latter, which is known as the Mullins effect [3, 4], consists in a change of the mechanical properties after that the material has been subjected to a deformation; it occurs from first few cycles and evolves toward a stabilization after a certain number of cycles (depending on the rubber, from less than 10 cycles to a 100). Both micro-mechanics and phenomenological explanations have been proposed on this effect; the Ogden-Roxburgh model [5] will be used in the present work, as it is implemented in commercial FEM codes [6]; since the material response in this model is governed by different forms of strain energy function on primary loading and unloading, it is referred to as a pseudo-elastic model. Dorfmann-Ogden also proposed a model for taking into account the permanent set in uniaxial conditions, which includes an additional term in the energy formulation for the residual strains that can be generalized for unloading occurring at any point of the primary loading path [7]. Furthermore, polymers have a unique response to mechanical loads and are properly treated as materials which in some instances behave as elastic solids, and in some instances as viscous fluids. As such, their

G. Chiappini (✉) • M. Sasso • M. Rossi • D. Amodio
Dipartimento di Ingegneria Industriale e Scienze Matematiche, Università Politecnica delle Marche,
via Brecce Bianche, 60131 Ancona, Italy
e-mail: g.chiappini@univpm.it

M. Rossi et al. (eds.), *Residual Stress, Thermomechanics & Infrared Imaging, Hybrid Techniques and Inverse Problems, Volume 8*,
Conference Proceedings of the Society for Experimental Mechanics Series, DOI 10.1007/978-3-319-00876-9_19,

mechanical properties are time dependent and cannot be treated mathematically by the laws of either solids or fluids [8]. The fundamental difference between polymers and other materials resides in the inherent rheological or viscoelastic properties: the constitutive relation between stress and strain is strongly influenced by time, even at room temperature. Different approaches to viscoelasticity are possible; among them, that based on fractional calculus has received considerable attention in recent years and has been used in characterizing the rheological behavior of viscoelastic materials by a number of authors [9, 10]; nevertheless, widely used are the classical models based on spring and dashpot, that lead in the time domain to material response functions described by a series of decaying exponential, known as Prony Series, which can be integrated to obtain the response to a generic load or strain history by the hereditary integral equation, further adapted for the large strain viscoelasticity [11]. Obviously, the correct modeling of all these aspects of the mechanical response is fundamental to obtain reliable results from analytical or FE computations involving elastomers, and a comprehensive material characterization is needed.

19.2 Constitutive Modeling of the Material

19.2.1 Hyperelasticity

The constitutive model here chosen for the description of the hyperelastic behavior of the rubber is the 3rd order Ogden model [2], as it is widely diffused and applied in several FEM codes and is able to describe the stress–strain relation of the material up to 400 % and more of elongation. Similarly to every model for hyperelasticity, it is based on the definition of a particular strain energy function W. For an isotropic and incompressible material W is usually expressed as a function of the principal stretches.

In plane stress condition, occurring for instance in the case of thin membranes subjected to in-plane loads, the principal Kirchhoff stresses are expressed by:

$$\sigma_1 = \lambda_1 \frac{\partial W}{\partial \lambda_1}, \ \sigma_2 = \lambda_2 \frac{\partial W}{\partial \lambda_2} \tag{19.1}$$

where W in the Ogden formulation is expressed by:

$$W = \sum_{p=1}^{3} \mu_p \left(\lambda_1^{\alpha_p} + \lambda_2^{\alpha_p} + \lambda_3^{\alpha_p} - 3\right)/\alpha_p \tag{19.2}$$

being λ_1, λ_2 and λ_3 the principal stretches. Exploiting the hypothesis of constant volume, Eq. 19.2 is reduced to:

$$\widetilde{W}(\lambda_1, \lambda_2) = \sum_{p=1}^{N} \mu_p \left(\lambda_1^{\alpha_p} + \lambda_2^{\alpha_p} + \lambda_1^{-\alpha_p}\lambda_2^{-\alpha_p} - 3\right)/\alpha_p \tag{19.3}$$

which can be analytically derived according to Eq. 19.1 to formulate the principal stresses as explicit functions of the parameters:

$$\sigma_1 = \lambda_1 \sum_{p=1}^{N} \mu_p \left(\alpha_p \lambda_1^{\alpha_p - 1} - \alpha_p \lambda_1^{-\alpha_p - 1}\lambda_2^{-\alpha_p}\right) \Big/ \alpha_p = \sum_{p=1}^{N} \mu_p \left(\lambda_1^{\alpha_p} - \lambda_1^{-\alpha_p}\lambda_2^{-\alpha_p}\right) \tag{19.4}$$

$$\sigma_2 = \lambda_2 \sum_{p=1}^{N} \mu_p \left(\alpha_p \lambda_2^{\alpha_p - 1} - \alpha_p \lambda_1^{-\alpha_p}\lambda_2^{-\alpha_p - 1}\right) \Big/ \alpha_p = \sum_{p=1}^{N} \mu_p \left(\lambda_2^{\alpha_p} - \lambda_1^{-\alpha_p}\lambda_2^{-\alpha_p}\right) \tag{19.5}$$

19.2.2 Visco-elasticity Behaviour

Regarding the viscoelasticity, the model here used is a six terms Prony series, with relaxation times chosen a priori in an evenly spaced from 10^{-1} s to 10^{4} s. Here a consolidated Prony series has been adopted in view of simulating the real behavior of an industrial component within a commercial FE software. The series of Prony used corresponds to a generalized Maxwell model with six branches, which summarizes the material stiffness function of time in the following way:

$$E(t) = E_0 \left[\alpha_\infty + \sum_{i=1}^{N} \alpha_i \exp\left(\frac{-t}{\tau_i}\right) \right] \tag{19.6}$$

where E_0 is the instantaneous stiffness (at an ideally infinite strain rate), while and α_i and τ_i are the relative moduli and relaxation times respectively. α_∞ represents the static stiffness (at an ideally zero strain rate) of the material, as a percentage of the instantaneous one. In the minimization procedure, implemented in Matlab®, the relaxation moduli are constrained to be positive and such that $\Sigma\alpha_i < 1$. These constraints have the physical meaning that the compression stress is monotonically decreasing with time but cannot change sign. It is important to note that the springs, and the corresponding stiffness in Eq. 19.6, are hyperelastic springs; for this reason the large strain viscoelasticity theory needs to be applied. Here, we adopted the typical updating formulas used in commercial FEM implementation [6], which in unixial stress condition reads:

$$\sigma_{i,n} = \sigma_{i,n-1} \exp\left(-\frac{\Delta t}{\tau_i}\right) + \alpha_i \exp\left(-\frac{\Delta t}{2\tau_i}\right)\left(\sigma_{h,n} - \sigma_{h,n-1}\right) \tag{19.7}$$

where the $\sigma_{i,n}$ denotes the Cauchy stress in the i-th Maxwell branch at the n-th calculation steps, while $\sigma_{h,n}$ denotes the purely hyperelastic stress. The overall time dependent stress becomes:

$$\sigma_n = \sigma_{\infty,n} + \sum\nolimits_i \sigma_{i,n} \tag{19.8}$$

where $\sigma_{\infty,n}$ is the quasi static hyperelastic stress, computed as the instantaneous stress reduced by a factor $1\text{-}\Sigma_i\alpha_i$.

19.2.3 Mullins Effect

Assume that the material response can be described in terms of an energy function of the form $W = W(F, \eta)$. In addition to the standard nonlinear elasticity theory, the scalar variable η has been added. Because of the influence of this new variable we refer now to W as a pseudo-energy function. For isotropic and incompressible material in equilibrium it is

$$\frac{\partial W(\mathrm{F}, \eta)}{\partial \eta} = \frac{\partial W(\lambda_1, \lambda_2, \eta)}{\partial \eta} = 0 \tag{19.9}$$

and stress is given by Eq. 19.3. During the deformation process η may be either active or inactive and switch between these two states, remaining continuous all the time. According to Ogden and Roxburgh [5], the strain energy function is:

$$W(\lambda_1, \lambda_2) = \eta \widetilde{W}(\lambda_1, \lambda_2) + \varphi(\eta) \tag{19.10}$$

where $\varphi(\eta)$ is called damage function and it is subjected to $\varphi(1) = 0$. It is clear that, when η_1 is inactive, that is $\eta_1 = 1$, this function reduces to the primary path. When η_1 is active, that is during the unloading or when reloading up to the maximum strain previously reached, the stresses are reduced of the factor η_1:

$$\sigma_1 = \eta\lambda_1 \frac{\partial W}{\partial \lambda_1}, \ \sigma_2 = \eta\lambda_2 \frac{\partial W}{\partial \lambda_2} \tag{19.11}$$

The formulation proposed for η by Ogden-Roxburgh is

$$\eta_1 = 1 - \frac{1}{r} erf\left[\frac{W_m - \widetilde{W}(\lambda_1, \lambda_2)}{m + \beta W_m}\right] \tag{19.12}$$

where r, m and β are the coefficients to be determined, W_m is the strain energy density reached at the load inversion point, and μ is the ground state shear modulus of the virgin material, equal to $0.5 \cdot \Sigma\alpha\mu$.

Nevertheless, since the tested material exhibits a non negligible permanent set, the Palmieri-Sasso model [7], which generalizes the permanent set model of Dorfmann-Ogden model for any inversion stretch, has been utilized. In this model, a second damage function η_2 and a residual strain potential N are introduced, so that the principal Cauchy stress becomes:

$$\sigma_{1,2} = \eta_1 \lambda_{1,2} \frac{\partial W}{\partial \lambda_{1,2}} + (1 - \eta_2)\lambda_{1,2} \frac{\partial N}{\partial \lambda_{1,2}} \tag{19.13}$$

The newly introduced functions η_2 and N are in the form:

$$\eta_2 = \tanh\left[\left(\widetilde{W}/W_m\right)^{\alpha}\right]/\tanh(1) \tag{19.14}$$

$$N(\lambda_1, \lambda_2) = \frac{1}{2}\left[\nu_1\left(\lambda_1^2 - 1\right) + \nu_2\left(\lambda_2^2 - 1\right) + \nu_3\left(\lambda_1^{-2}\lambda_2^{-2} - 1\right)\right] \tag{19.15}$$

On their turn, the coefficients ν_{i} in Eq. 19.15 and the exponent α in Eq. 19.14 are expressed by:

$$\alpha = J + K\left(\frac{W_m}{\mu}\right) \tag{19.16}$$

$$\nu_i = \mu\left[U - V \tanh\left(\frac{\lambda_{i,m} - 1}{Z}\right)\right] \tag{19.17}$$

where J, K, U, V, Z are the sought dimensionless parameters, $\lambda_{\mathrm{i,m}}$ is the i-th principal stretch at the inversion.

19.3 Application of VFM

In a generic inverse problem, where the geometry, the strain field and the applied load are given, the parameters governing the constitutive equations have to be identified. However, these unknown parameters that depend on the material and on the form of the adopted constitutive equations are not directly related to measured strain field; this means that a closed-form solution is not available. Besides constitutive laws, also other equations of continuum mechanics of solids must be verified at each point of the specimen; they are the equilibrium and congruence equations. The VFM [12–14] incorporates these considerations and exploits the large amount of experimental data provided by modern full-field acquisition methods like DIC; it is based on the principle of virtual work; for a given solid of volume V where the inertia and volume forces are negligible, this principle can be written as follows:

$$-\int_V \sigma_{ij}\varepsilon_{ij}^* dV + \int_{\partial V} T_i u_i^* dS + \int_V f_i u_i^* dV = \int_V \rho a_i u_i^* dV \tag{19.18}$$

where σ is the first Piola-Kirchhoff stress tensor, ε^* is the virtual displacement gradient tensor, T is the distribution vector of loadings acting on the boundary, ∂V is the part of solid boundary where the loading forces are applied, u^* is the virtual displacement vector, f is the distribution of volume forces acting on V, ρ is the density and a is the acceleration. An important feature is that the above equation is verified for any kinematically admissible virtual field (u^*, ε^*). In a general case the

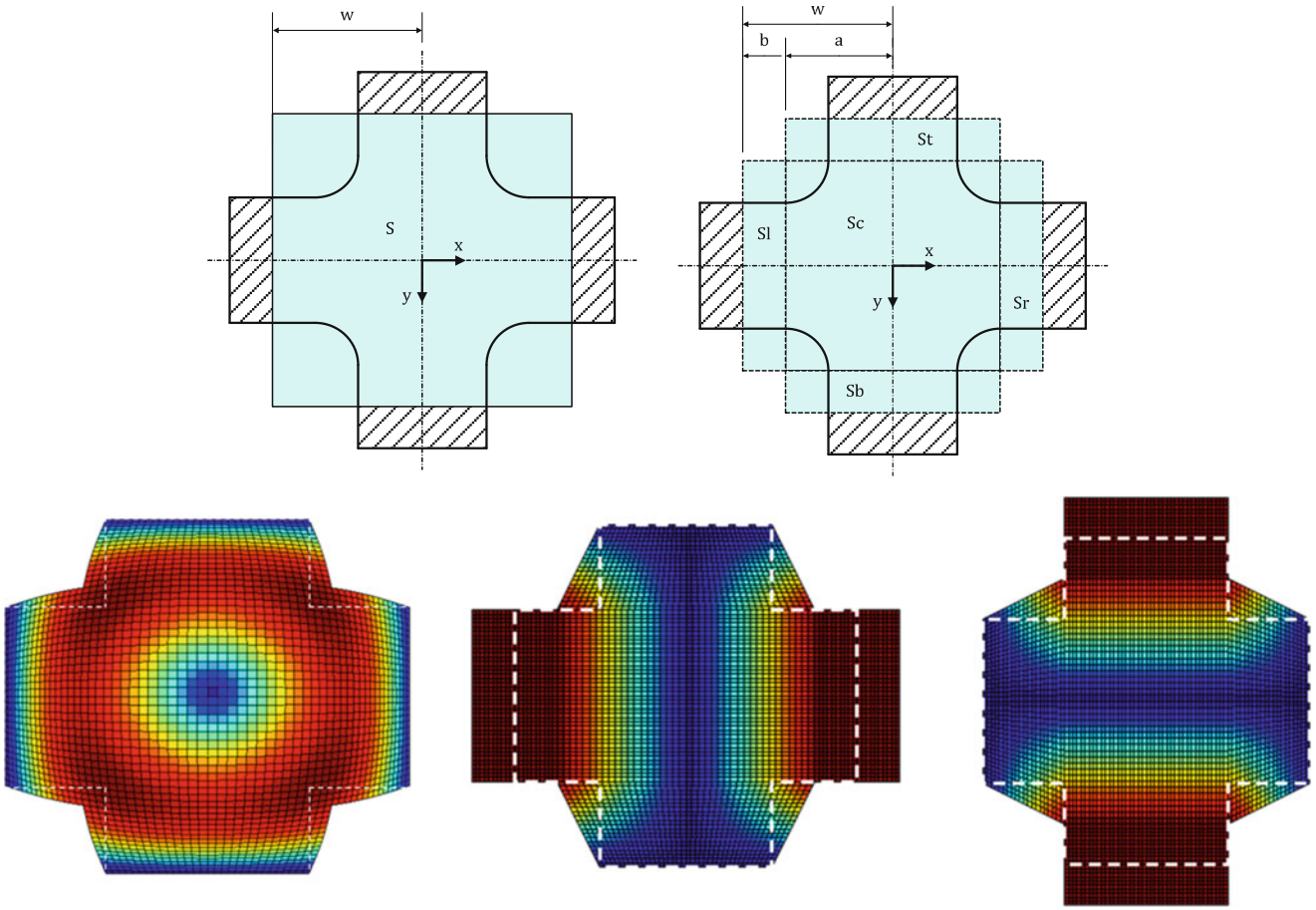

Fig. 19.1 Displacements associated with the three virtual fields

constitutive equation can be written as $\boldsymbol{\sigma} = g(\boldsymbol{\varepsilon})$, where g is a function of the actual strain components and is defined involving the material dependent parameters. Considering also a static case, whit no acceleration and no volume forces, Eq. 19.18 reduces to

$$-\int_V g_{ij}(\boldsymbol{\varepsilon})\varepsilon_{ij}^* dV + \int_{\partial V} T_i u_i^* dS = 0 \tag{19.19}$$

It is important to note that, if the actual strain field is heterogeneous, any new virtual field in Eq. 19.19 leads to a new equation involving the constitutive parameters. Hence, the VFM is based on Eq. 19.19 written with a given set of virtual fields, and the resulting system of equations is used to extract the unknown constitutive parameters. In Fig. 19.1 are represented the three displacement maps corresponding to the virtual fields used, the blue color indicates no displacement, while red indicates the maximum displacement. For reference, the virtual specimen is reported above the displacements fields. It can be noticed that the dimensions a, b and w are fictitious in general; here they correspond to the size of the regions of the undeformed configuration, in pixel, that are used for the implementation of the piecewise virtual displacement fields.

Considering a point on the surface of the specimen of x and y coordinates in a reference system with origin at the midpoint of the specimen, the first virtual field applied is expressed by the following equation:

$$\begin{cases} u^* = \dfrac{w}{\pi}\sin\left(x\dfrac{\pi}{w}\right)\cos\left(y\dfrac{\pi}{2w}\right) \\ v^* = \dfrac{w}{\pi}\sin\left(y\dfrac{\pi}{w}\right)\cos\left(x\dfrac{\pi}{2w}\right) \end{cases} \tag{19.20}$$

and consists of an expansion/contraction of the specimen with the edges stuck; this virtual field is equivalent to the imposition of the global balance of the work of internal actions, including shear, in the absence of external work; the Eq. 19.19 becomes:

$$\int_S \left(\sigma_{xx}\varepsilon^*_{xx}t\right)ds + \int_S \left(\sigma_{yy}\varepsilon^*_{yy}t\right)ds + \int_S \left(\sigma_{xy}\varepsilon^*_{xy}t\right)ds + \int_S \left(\sigma_{yx}\varepsilon^*_{xy}t\right)ds = 0 \tag{19.21}$$

For the second and third virtual field, represented in the central and right map of Fig. 19.1, the area occupied by the specimen was divided into five different areas, and has been assigned a different displacement law for each area, respecting the constraints of congruence between neighboring areas; in this case the displacements of the edges are not null but are such that it generates a virtual work by external horizontal forces. However it's important to note that, in second virtual field, the upper and lower edges of the virtual specimen have no displacements, and the left and right edges have only horizontal displacements; in this way, the VFM method is able to filter out any effects that are unknown or unmeasured in the clamps areas. So, the Eq. 19.19 for the these two virtual fields becomes:

$$\int_{Sl} \left(\sigma_{ij}\varepsilon^*_{ij}t\right)ds + \int_{St} \left(\sigma_{ij}\varepsilon^*_{ij}t\right)ds + \int_{Sr} \left(\sigma_{ij}\varepsilon^*_{ij}t\right)ds + \int_{Sb} \left(\sigma_{ij}\varepsilon^*_{ij}t\right)ds + \int_{Sc} \left(\sigma_{ij}\varepsilon^*_{ij}t\right)ds = 2aP_H \tag{19.22}$$

$$\int_{Sl} \left(\sigma_{ij}\varepsilon^*_{ij}t\right)ds + \int_{St} \left(\sigma_{ij}\varepsilon^*_{ij}t\right)ds + \int_{Sr} \left(\sigma_{ij}\varepsilon^*_{ij}t\right)ds + \int_{Sb} \left(\sigma_{ij}\varepsilon^*_{ij}t\right)ds + \int_{Sc} \left(\sigma_{ij}\varepsilon^*_{ij}t\right)ds = 2aP_V \tag{19.23}$$

where the unknowns are the constants of the material present in the analytical expression of terms σ_{ij}. These stress components are expressed as a function of the constitutive model chosen: visco-pseudo-hyper elastic models in plane stress condition.

19.4 Experimental Set-up

The experimental setup consists of a electromechanical tensile machine (Zwick®Z050 model), a CMOS camera with resolution 1280 × 1024 (Pixelink® B371F model) at 25 frame per second, and the biaxial testing fixture for cruciform shaped samples illustrated in Fig. 19.2a, which exploits the vertical movement of the crosshead to pull the specimen "arms" in both vertical and horizontal direction.

The cruciform sample is glued onto 'L'-shaped brackets, which are put in proper clamps in the biaxial testing machine; two load cells allow to read load values in the vertical and horizontal directions. Though this system is designed with

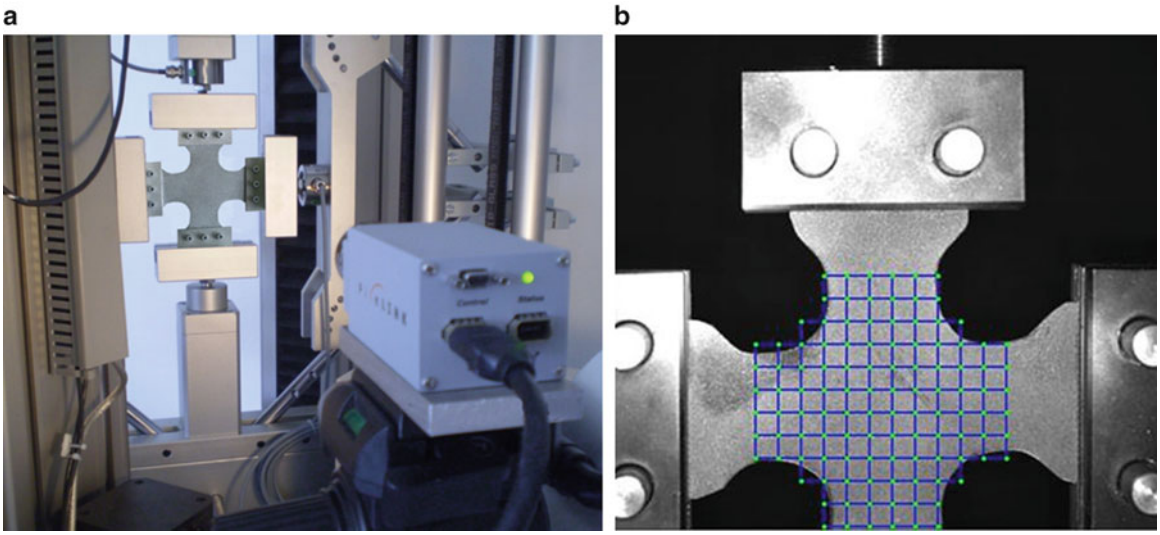

Fig. 19.2 **(a)** cruciform specimen framed by a CCD camera (**b**) virtual nodes grid on the image for the DIC analysis

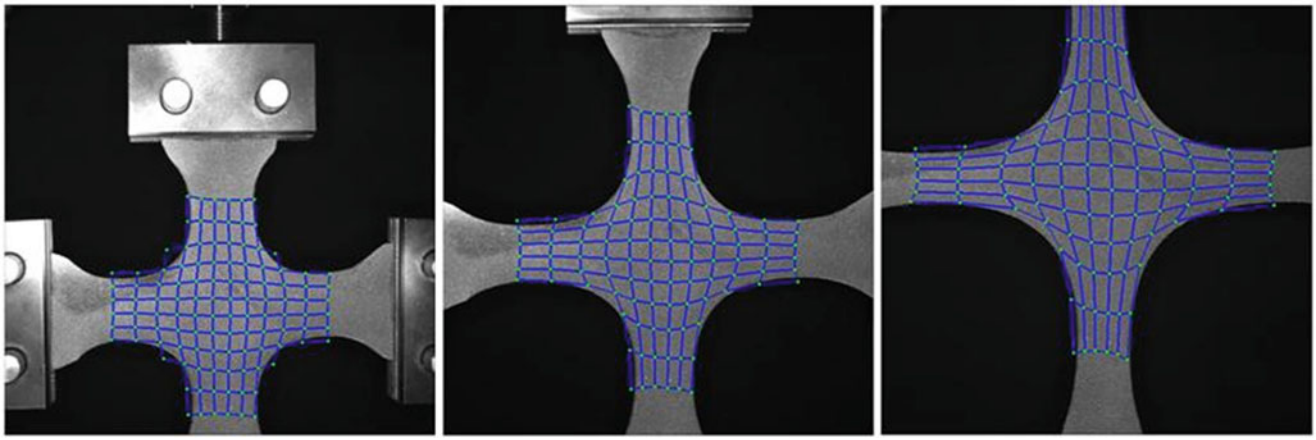

Fig. 19.3 Deformed grid nodes at 37.5 % (*left*), at 75 % (*middle*), at 150 % (*right*)

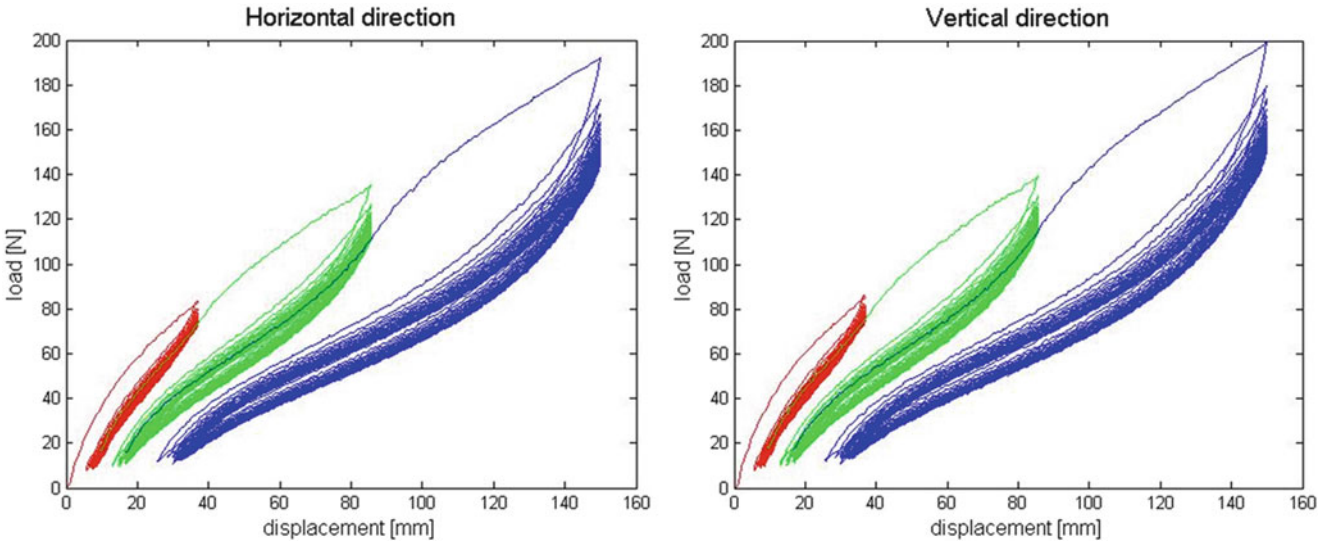

Fig. 19.4 Load–displacement curves on the two branches of the cruciform specimen

different possibilities of adjustment, in this work only a 45° diagonal configuration is used that generate a globally equal-biaxial stretching, because the shape of the sample allows to generate a strain field sufficiently heterogeneous. Figure 19.2b shows the first picture of the undeformed specimen grabbed by the camera, with a regular grid of nodes that are used in the DIC algorithm for the full-field computation of the strain distribution.

The sample has been subjected to loading/unloading cycles at three different levels of maximum strain (nominally 37.5 %, 75 % and 150 %, corresponding to 0.318, 0.600 and 0.916 in terms of logarithmic strain). In Fig. 19.3, it can be observed how the specimen (and the virtual nodes grid) is deformed at the three different crosshead positions. It is important to note that the machine has been operated in displacement control (with a crosshead speed of 150 mm/min), however, while the load → unload reversal occurred by imposing the strain level, the unload → reload inversion occurred when the global force fell below 10N.

Figure 19.4 shows the horizontal and vertical forces as functions of crosshead travel; in red is indicated the first cycle at 37.5 % of maximum elongation, in green is indicated second cycle performed up to 75 % and in blue is indicated the third cycle that have reached 150 %; the x axis indicates the vertical displacement (almost coincident with the horizontal one). For each amplitude, 30 cycles have been repeated.

While the specimen was undergoing stress cycles, the camera recorded digital images at a frequency of about 3.5 fps, for a total of 18,000 images, subsequently processed through DIC analysis software to obtain the distribution maps of strain components ε_x, ε_y, ε_{xy} and of the principal strains.

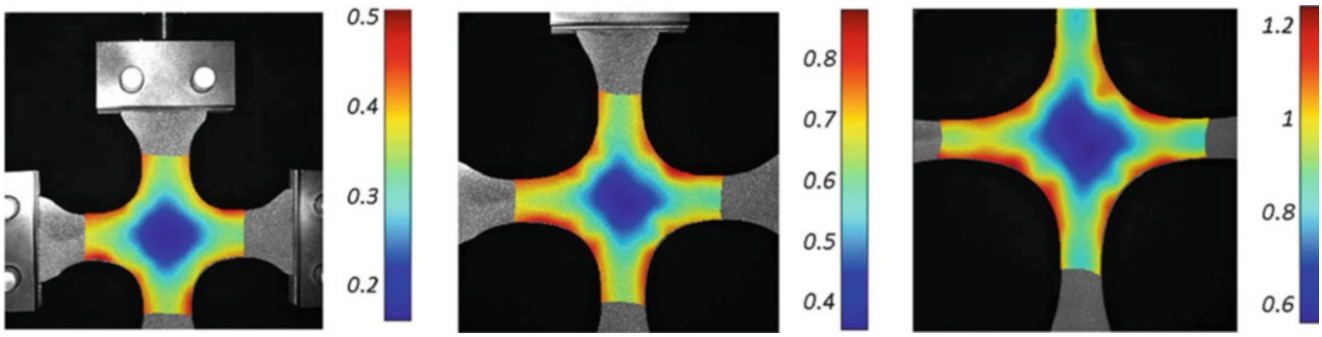

Fig. 19.5 Contour maps of first principal logarithmic strain: at 37.5 % (*left*), at 75 % (*middle*), at 150 % (*right*)

Table 19.1 Ogden model coefficients

μ_1 [MPa]	+0.8392
μ_2 [MPa]	+1.1718
μ_3 [MPa]	−1.1033
α_1	+0.0560
α_2	+2.2488
α_3	−0.0012

Table 19.2 Prony series coefficients

τ_i [s]	10^{-1}	10^{0}	10^{1}	10^{2}	10^{3}	10^{4}
α_i	0.6501	0.1701	0.0028	0.0154	0.0153	0.0316

Table 19.3 Coefficients of the Mullins model with permanent set

	r	m [MPa]	β [MPa]	
	3.3703	0.0836	0.5244	
J	K	U	V	Z
−0.0331	0.0073	8.5801	−15.4302	3.5718

In Fig. 19.5 are shown the contour maps relating to the first principal strain in correspondence of the three levels of inversion; one can note that the maximum principal strain in certain areas of the specimen is well above the average engineering value.

19.5 Fitting Results

A Matlab® numerical procedure has been implemented to minimize the discrepancy between experimental and numerical data, using VFM Eqs. 19.21, 19.22 and 19.23. In order to reduce the computational time, not all the experimental points have been used, but only five points in each loading or unloading stroke have been used; this led to a system of approximately 2,700 equations with 20 unknowns. The constrained minimization function *fmincon* has been adopted, which provided the best coefficients reported in Tables 19.1, 19.2 and 19.3.

The corresponding load–displacement curve (for horizontal direction) is shown in Fig. 19.6, compared with the experimental one; for the sake of clarity, only the first and last cycle for each amplitude are plotted.

A good agreement is observed in general, exception made for the decay of the stress peaks at the end of the loading paths, that is slightly emphasized by the numerical reconstruction.

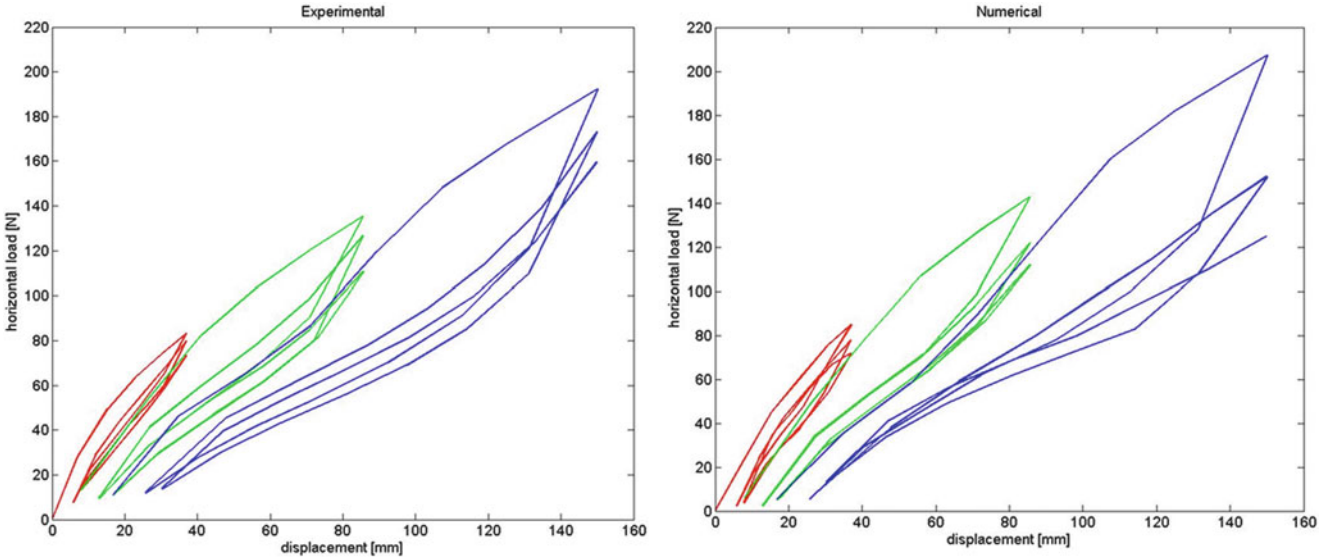

Fig. 19.6 *Horizontal load–displacement curves*, experimental (*left*) and numerical (*right*)

19.6 Conclusions

This work proposed a procedure for the comprehensive characterization of the mechanical behaviour of an elastomeric membrane. Using the experimental data from a unique cyclic test on a cruciform specimen, the coefficients of different constitutive models have been identified, by means of the Virtual Fields Method. The equations of the internal and external virtual work incorporated, simultaneously, the parameters of hyperelastic, viscoelastic and pseudo-elastic models available in literature. The matching between experimental and numerical was fairly good; so, even if further work is needed to improve and to validate the method, data suggests that is possible to characterize the complex behavior of rubber-like materials by a unique, more complex test, that involves all the phenomena to be investigated.

References

1. Mooney M (1940) A theory of large elastic deformation. J Appl Phys 11(9):582–592
2. Ogden RW (1984) Non-linear elastic seformation. Ellis-Horwood, Chichester
3. Mullins L (1947) Effect of stretching on the properties of rubber. J Rubber Res 16:275–289
4. Mullins L, Tobin NR (1957) Theoretical model for elastic behaviour of filler-reinforced vulcanized rubbers. Rubber Chem Technol J 30:551–571
5. Ogden RW, Roxburgh DG (1999) A pseudo-elastic model for the Mullins effect in filled rubber. Proc Roy Soc Lond A 455:2861–2877
6. ANSYS theory reference, release 13.0 – © 2010
7. Palmieri G, Sasso M, Chiappini G, Amodio D (September 2009) Mullins effect characterization of elastomers by multi-axial cyclic tests and optical experimental methods. Mech Mater 41(9):1059–1067
8. Brinson HF, Brinson LC (2008) Polymer engineering science and viscoelasticity: an introduction. Springer, Berlin
9. Sasso M, Palmieri G, Amodio D (2011) Application of fractional derivative models in linear viscoelastic problems. Mech Time-Depend Mater 15:367–387
10. Lewandowski R, Chorazyczewski B (2010) Identification of the parameters of the Kelvin-Voigt and the Maxwell fractional models, used to modeling of viscoelastic dampers. Comput Struct 88(1-2):1–17
11. Holzapfel GA (2000) Nonlinear solid mechanics: a continuum approach for engineering. Wiley, New York
12. Pierron F, Grediac M (2012) The virtual fields method, extracting constitutive mechanical parameters from full-field deformation measurements. Springer, New York
13. Palmieri G, Chiappini G, Sasso M, Papalini S (2009) Hyperelastic materials characterization by planar tension tests and full-field strain measurement. In: SEM annual conference and exposition on experimental and applied mechanics 2009. Albuquerque (NM), USA, vol 4, pp 2232–2238
14. Palmieri G, Sasso M, Chiappini G, Amodio D (2010) Virtual fields method on planar tension tests for hyperelastic materials characterization. Strain. doi:10.1111/j.1475-1305.2010.00759.x

Chapter 20
Anisotropy Evaluation of Paperboard With Virtual Fields Method

J.M. Considine, F. Pierron, K.T. Turner, and D.W. Vahey

Abstract Paperboard is most often used as a structural material in which stiffness is a critical mechanical property. As such, paperboard mills use stiffness as one of their quality control parameters. Some manufacturing variability of paperboard is caused by changing material anisotropy, a behavior that is difficult to characterize. This work introduces a novel load fixture, designed to produce full-field strains capable of anisotropic Q_{ij} evaluation without wrinkling the paperboard specimen. Anisotropic Q_{ij} evaluation was accomplished using the Virtual Fields Method (VFM), a generalized inverse method. A substantial effort was made to ensure material remained in its linear elastic regime. Q_{ij} determined by the VFM compared favorably with those determined by ultrasonic and tensile coupon tests. An appropriate virtual field mesh was established by a mesh density analysis.

Keywords VFM • DIC • Stiffness • Paperboard • Anisotropy

20.1 Introduction

Determination of mechanical properties of paper and paperboard is a critical part of quality control processes in paper mills because these properties largely regulate product value. Variability of mechanical properties is rarely acknowledged outside the industry [1]. One significant cause of variability is anisotropy. Anisotropy has many sources, some of which are fiber misalignment (i.e., predominant fiber direction is not aligned with direction of web travel), nonuniform drawing forces and uneven drying. As cellulose fiber materials are generally sold on a strength/weight or stiffness/weight basis, reduction of product variability and mechanical property improvement are persistent goals of paper manufacturers. Two tests, tensile coupon and ultrasonic, are the most common evaluations used for mechanical property determination; however, both have difficulty assessing anisotropy. Whereas tensile testing is destructive and requires multiple specimens at several angles of orthotropy, ultrasonic testing requires independent measurement of Q_{66} or Q_{12} [2] and depends on relatively few degrees of freedom.

Some degree of anisotropy in cellulose fiber composites, such as paper and paperboard, is expected, because cellulose fibers are themselves anisotropic [3]. Macroscopically, anisotropy is influenced by fiber orientation distribution and drying stresses [4, 5]. Online stiffness measurement is used in process control [6] to reduce anisotropy.

J.M. Considine (✉)
US Forest Service, Forest Products Laboratory, One Gifford Pinchot Drive, Madison, WI 53726, USA
e-mail: jconsidine@fs.fed.us

F. Pierron
University of Southampton, Southampton SO17 1BJ, UK
e-mail: F.Pierron@soton.ac.uk.

K.T. Turner
University of Pennsylvania, 245 Towne Building 220 S. 33rd St, Philadelphia, PA, USA 19104-6315
e-mail: kturner@engr.wisc.edu

D.W. Vahey
US Forest Service, Forest Products Laboratory, One Gifford Pinchot Drive, Madison, WI, USA 53726
e-mail: vahey@fs.fed

M. Rossi et al. (eds.), *Residual Stress, Thermomechanics & Infrared Imaging, Hybrid Techniques and Inverse Problems, Volume 8*, Conference Proceedings of the Society for Experimental Mechanics Series, DOI 10.1007/978-3-319-00876-9_20,

Full-field measurement techniques, such as DIC (digital image correlation), combined with analysis techniques developed to use this spatially dense data, offer another method to assess material anisotropy. In particular, VFM (Virtual Fields Method) [7] provides a unique combination of speed, programming simplicity, and multiple parameter assessment from a single test. VFM has been successfully employed to determine anisotropic plate bending stiffnesses [8] and through-thickness rigidities of thick composite tubes [9].

The objective of this paper is to demonstrate the use of VFM with full-field DIC-measured strain data to determine the anisotropic stiffnesses of a paperboard material by use of a novel load fixture. Appropriateness of this approach is demonstrated by comparison with stiffness determined by the two commonly used methods, namely ultrasonic and tensile coupon tests, which assume material homogeneity.

20.2 Material

Material was Whatman® (Kent, U.K.) Chromatography Paper 3MM CHR, often called filter paper. It had nominal physical properties of grammage 180 gm/m^2, thickness 0.28 mm and density 635 kg/m^3. Although no exact definition exists for the term paperboard, this filter paper had a thickness generally associated with paperboards and will be referred to as paperboard or filter paper. Filter papers are used in a variety of household, commercial, and scientific applications to capture particulate matter. The material was 100 % cellulose, composed entirely of cotton linters, a cellulose fiber that is typically 5–10 mm long. Paperboards are considered within the paper industry to be orthotropic. Paperboards contain variability from side-to-side of the web and along web length. Side-to-side variability is generally much greater than variability along web length. Paper machinery manufacturers have developed equipment to greatly reduce through-thickness variability.

20.3 Load Fixture

A specially designed load fixture is shown in Fig. 20.1. External forces are applied through four grips on the top half of the fixture and measured with Sensotec (Honeywell International, Inc., Columbus, Ohio) Model 31BR load cells (range ±444 N) attached to Sensotec Model GM signal conditioners. The four grips located on the bottom half of the specimen are stationary. Another fixture, not shown, was used to cut the specimen and properly locate and punch holes for each grip. Prior to placing the specimen within the fixture, an alignment jig was used to adjust the top four grips to a precise starting location such that the specimen would experience no forces upon initial placement in the fixture. The aluminum knobs shown in Fig. 20.1b are rotated to generate a particular radial tensile force at that location. Multiple load configurations were used to create a series of different full-field strains for Q_{ij} evaluation. For each load configuration, individual forces were kept constant or increased, with respect to the previous load configuration, so that relaxation stiffnesses were avoided.

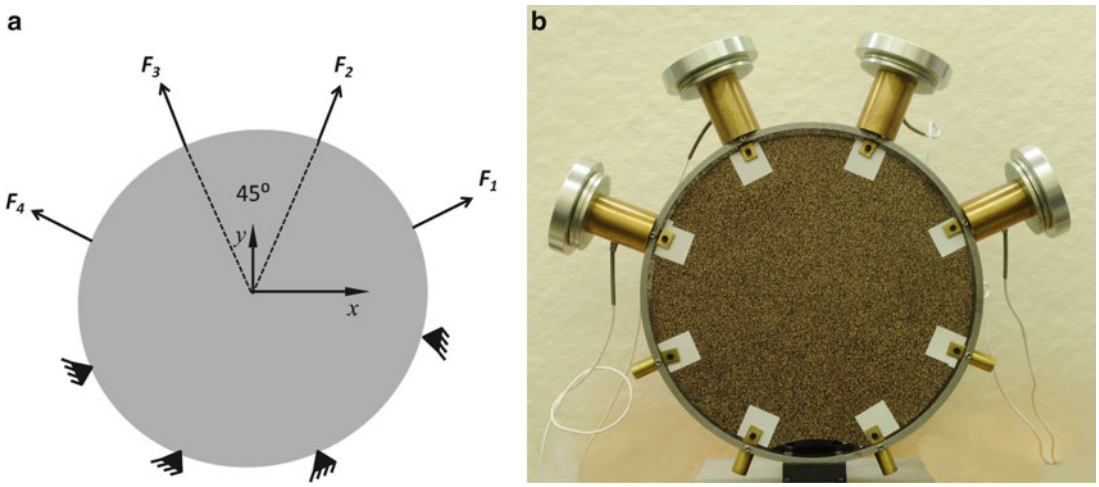

Fig. 20.1 Load fixture. (**a**) Schematic of load fixture. (**b**) Actual load fixture

Table 20.1 DIC system components and parameters

Technique used	Stereo image correlation
Camera	Allied vision technologies (Stadtroda, Germany) Stingray Model F504B
Lens	Computar (Commack, NY) M1614-MP2, 16 mm, f1.4
Lighting	Red LED, 4 × 3 array, wavelength 610–640 nm
Interface	IEEE 1394b – 800 Mb/s
Resolution	2, 452 × 2, 056
Sensor	Sony (Sony America, New York, NY) ICX655, CCD progressive
Sensor size	Type 2/3
Lens mount	C
Field of view	38. 7 cm × 32 cm
Facet size	21 pixels, approx 3. 3 mm × 3. 3 mm
Software	Istra (Dantec) 4-D v2.1.5
Smoothing	7 × 7 adaptive polynomial

The 24.5-cm-diameter specimen was gripped at eight locations 45° apart. Grips consisted of two small brass plates approximately 12 mm square. One plate had a threaded hole; the other a through-hole. Holes were punched at grip locations in the specimen, which was then clamped between plates with a small bolt. A torque wrench was used to ensure uniform clamping pressure for each grip. Special care was taken to prevent the top brass gripping plate from twisting and introducing undesirable stresses on the specimen.

20.4 Digital Image Correlation

We examined the paperboard surface with a Dantec®; (Dantec Dynamics, Inc., Holtsville, New York) DIC system whose details are listed in Table 20.1. Dot pattern was photocopied on specimens with a Sharp®; (Sharp Electronics Corp., Mahwah, New Jersey) MX-3100N copier. Static specimen images were captured by waiting 5 min after load application was adjusted. A single reference image was used for each test. For each specimen, the first load configuration had forces approximately 15 N greater, at each load grip, than forces for the reference image. Forces on the specimen for the reference image were used to ensure that the specimen was planar.

20.5 Virtual Fields Method

An abbreviated introduction to VFM is presented here; a recent book [7] provides a more thorough presentation. For a plane stress problem, the Principle of Virtual Work can be written as

$$\int_S \left(\sigma_1 \varepsilon_1^* + \sigma_2 \varepsilon_2^* + \sigma_6 \varepsilon_6^*\right) dS = \int_{L_f} \bar{T}_i u_i^* dl \tag{20.1}$$

where S is the area of 2-D domain, σ_i are stresses within S, ${u_i}^*$ are kinematically admissible virtual displacements, ${\varepsilon_i}^*$ are virtual strains associated with ${u_i}^*$, $\bar{T}_i$ are tractions applied on boundary of S, and L_f is the portion of S over which $\bar{T}_i$ are applied.

Assuming a linear elastic anisotropic material, the constitutive equation, using contracted index notation, is given by

$$\begin{Bmatrix} \sigma_1 \\ \sigma_2 \\ \sigma_6 \end{Bmatrix} = \begin{bmatrix} Q_{11} & Q_{12} & Q_{16} \\ Q_{12} & Q_{22} & Q_{26} \\ Q_{16} & Q_{26} & Q_{66} \end{bmatrix} \begin{Bmatrix} \varepsilon_1 \\ \varepsilon_2 \\ \varepsilon_6 \end{Bmatrix} \tag{20.2}$$

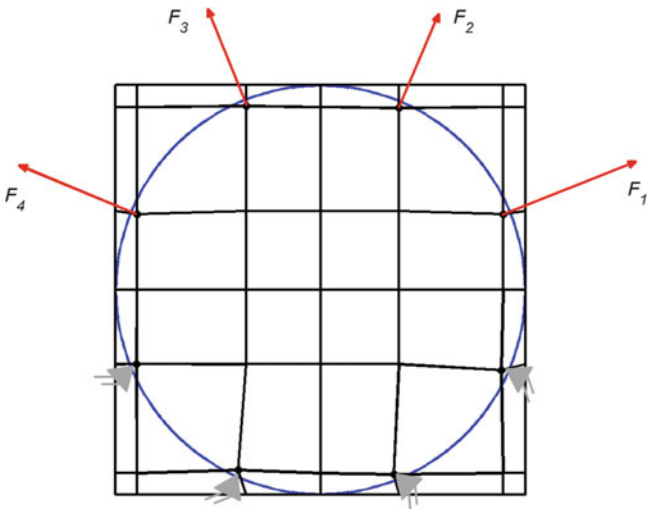

Fig. 20.2 Example of 36-element virtual mesh for Fig. 20.1a

Substituting Eqs. 20.2 into 20.1 gives

$$\int_S Q_{11}\varepsilon_1\varepsilon_1^* + \int_S Q_{22}\varepsilon_2\varepsilon_2^* dS + \int_S Q_{12}\left(\varepsilon_1\varepsilon_2^* + \varepsilon_2\varepsilon_1^*\right)dS + \cdots \tag{20.3}$$

$$\cdots + \int_S Q_{16}\left(\varepsilon_1\varepsilon_6^* + \varepsilon_6\varepsilon_1^*\right)dS + \int_S Q_{26}\left(\varepsilon_2\varepsilon_6^* + \varepsilon_2\varepsilon_6^*\right)dS + \int_S Q_{66}\varepsilon_6\varepsilon_6^* dS = \int_{L_f} \bar{T}_i u_i^* dl$$

If the material is homogeneous, then each Q_{ij} is a constant and can be placed outside the integrals in Eq. 20.3. In practice, six different $u_i{}^*$ are used in Eq. 20.3, one to identify each Q_{ij}. Special virtual fields simplify identification by choosing a $u_i{}^*$ so that only one integral term exists on the left side of Eq. 20.3. By approximating the integrals in Eq. 20.3 as discrete summations, a system of linear equations is developed whose solution requires minimal computation. DIC provides information on each ε_i throughout specimen surface and load cells provide values for each $\bar{T}_i$.

One of the most direct methods to create the virtual fields is to define a mesh of 4-node quadrilateral isoparametric elements, as shown in Fig. 20.2. In order to have a kinematically admissible virtual field, grip nodes are virtually fixed in both u and v displacement because they correspond to stationary grips in Fig. 20.1a. Additionally, load grips are restricted to radial displacement corresponding to forces F_4, F_3, F_2 and F_1. VFM elements in Fig. 20.2 are not precisely rectangular as some asymmetry of grip and force locations was created during fabrication. VFM meshes are not required to conform to specimen boundaries. Some VFM elements lie completely outside the specimen area, S, while other elements straddle the external boundary of S. Only terms in Eq. 20.3 with nonzero, experimentally-measured ε_i have a contribution to stiffness evaluation.

20.6 Supporting Tests

Ultrasonic tests were performed with a Nomura Shoji®; (Tokyo, Japan) SST-250 paper tester. Transmission probe oscillated at 25 kHz. A central circular region of 15-cm diameter was examined for each specimen. Ultrasonic velocity was measured from 0° to 175° in 5° increments. Q_{66} was determined by measuring shear wave velocity transmitted along the 2-principal material direction using a second, modified SST instrument. Remaining stiffnesses were determined by nonlinear regression of the stiffness transformation matrix [10].

Three tensile coupons were cut from each circular specimen after DIC and ultrasonic evaluations. Coupons were cut at 0°, 45°, 90° from 1-principal material direction. Coupons were 25 mm wide and each had a nominal gage length of 175 mm. Specimens were tested in an Instron®; (Instron Corp., Norwood, Massachusetts) Model 5865 load frame with a grip displacement rate of 0.5 mm/min. DIC images were captured at 1 Hz and used to determine longitudinal and transverse strains. Longitudinal strains were used to determine Q_{11} and Q_{22}; transverse strains were used to determine ν_{12}; Q_{66} was determined by stiffness transformation.

20.7 Results and Discussion

Table 20.2 gives VFM-evaluated Q_{ij} for the first and second tests of the same specimen, where tests are noted in column 1. Units are km^2/s^2, or specific stiffness units, and are equivalent to MN · m/kg. To minimize effects of relaxation on measurement, each subsequent load configuration had each of its forces held constant or increased from previous load configuration. After the first test, the specimen was removed from the load fixture, grips were reset to their initial locations, the specimen was re-installed in the fixture, and forces were introduced. Test 2 had small decreases in F_1 and F_4; however, it appears that corresponding large increases in F_2 and F_3 avoided relaxation of the material.

Results shown in Table 20.2 indicate the specimen was generally oriented with its primary principal material direction aligned vertically, because Q_{22} was greater than Q_{11}. Each test had reasonable agreement for Q_{11}, Q_{22}, Q_{12}, and Q_{66}, as demonstrated by acceptable COVs (coefficients of variation). COVs were generally below 10 % for the largest Q_{ij}. In both tests, increases in applied forces tended to give reduced Q_{ij}.

Amount of anisotropy, as indicated by non-zero Q_{16} and Q_{26}, was quite small. Habeger [2] suggested that anisotropy can be characterized by comparing non-orthogonality of directions for maximums of Q_{11} and Q_{22}. Using the mean values for Q_{ij} from Table 20.2 Test 1, 1- and 2-directions differ by 90.1°. Using mean values for the second test, 1- and 2-directions differ by 89.7°. Because the non-orthogonality was quite small, the specimen was considered orthotropic. One encouraging result was the generally consistent opposing signs for Q_{16} and Q_{26}, which is a necessary result from stiffness transformation of orthotropic materials.

Q_{11}, Q_{22}, Q_{12}, and Q_{66} decreased with increasing applied forces. This trend is shown graphically in Fig. 20.3, where "norm" refers to 2-norm for applied force and stiffness. The largest stiffness values, Q_{11}, Q_{22}, and Q_{66}, largely control the 2-norm. Because the evaluation procedure described here determined secant Q_{ij} and the selected material was known to be nonlinear, additional analyses were made to examine the possibility that the load configurations may have taken the material into nonlinear constitutive behavior.

Determination of material nonlinear behavior is not straightforward for this load fixture. Because the geometry was intentionally designed to produce sufficient strains, ε_i, for evaluation of all six Q_{ij}, it is not possible to directly determine onset of material nonlinear behavior. Furthermore, nonlinear behavior is unlikely to occur simultaneously for each Q_{ij}.

Table 20.2 Q_{ij} evaluation for each test of the specimen using mesh in Fig. 20.2. Stiffness units (km^2/s^2), Force units (N). LC – load configuration

Test	LC	Q_{11}	Q_{22}	Q_{12}	Q_{66}	Q_{16}	Q_{26}	F_1	F_2	F_3	F_4
1	1	2.87	6.81	0.61	1.29	− 0.12	0.06	16.9	17.3	19.0	17.8
	2	2.87	6.96	0.62	1.36	− 0.08	− 0.25	18.2	21.4	27.5	19.1
	3	2.61	6.12	0.75	1.37	− 0.06	− 0.42	19.1	22.7	27.6	20.9
	4	2.62	6.09	0.68	1.16	− 0.05	− 0.21	21.8	26.7	29.5	22.2
	5	2.59	5.86	0.72	1.26	0.00	− 0.33	24.0	30.7	32.7	25.4
	6	2.65	5.98	0.73	1.29	0.02	− 0.60	25.8	35.6	38.5	30.7
	7	2.52	5.90	0.71	1.21	0.05	− 0.58	28.5	37.4	39.1	32.0
	8	2.45	5.53	0.58	1.17	0.07	− 0.57	29.8	38.3	40.0	33.4
	9	2.35	5.55	0.63	1.16	0.06	− 0.61	33.4	42.3	45.3	37.4
	10	2.28	5.44	0.60	1.14	0.06	− 0.67	35.1	44.0	47.5	40.0
	Mean	2.58	6.02	0.66	1.24	− 0.01	− 0.42				
	COV (%)	7.49	8.50	9.60	6.89	− 1,264.91	− 55.48				
2	1	3.65	6.72	0.56	1.74	−0.08	0.13	17.8	16.0	17.9	15.6
	2	3.25	6.66	0.58	1.63	−0.10	0.35	17.3	20.0	21.3	14.7
	3	3.00	6.88	0.23	1.61	−0.31	0.37	18.2	22.7	24.3	17.3
	4	2.95	6.68	0.47	1.55	−0.07	0.07	20.5	26.7	27.8	20.0
	5	2.91	6.56	0.56	1.44	0.00	0.03	23.1	28.9	29.7	21.8
	6	2.83	6.05	0.31	1.29	0.03	0.17	25.4	30.7	31.4	21.8
	7	3.00	6.26	0.26	1.20	0.09	0.07	26.7	34.7	35.8	23.6
	8	2.93	6.02	0.27	1.22	0.09	0.12	29.4	36.5	37.9	25.4
	9	2.81	6.11	0.22	1.17	0.00	0.13	32.0	38.3	41.5	28.5
	10	2.72	6.08	0.34	1.17	−0.00	0.18	36.9	44.0	44.3	33.8
	Mean	3.01	6.40	0.38	1.40	−0.04	0.16				
	COV (%)	8.90	5.19	38.18	15.61	−331.35	69.44				

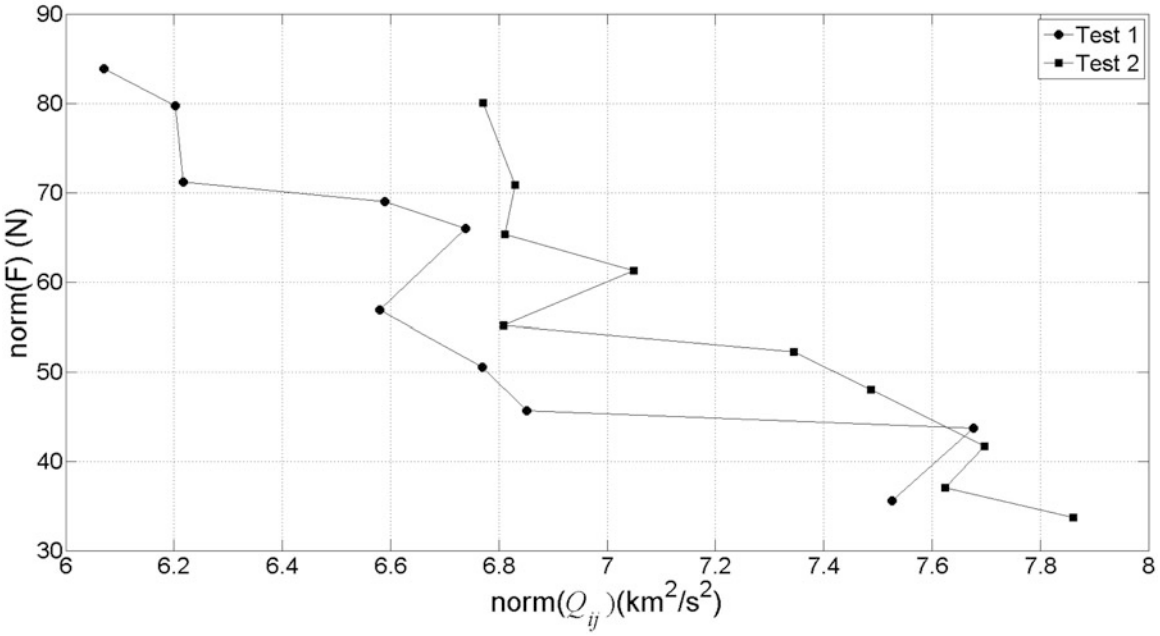

Fig. 20.3 Normalized stiffness, Q_{ij}, as affected by normalized applied force, F_i

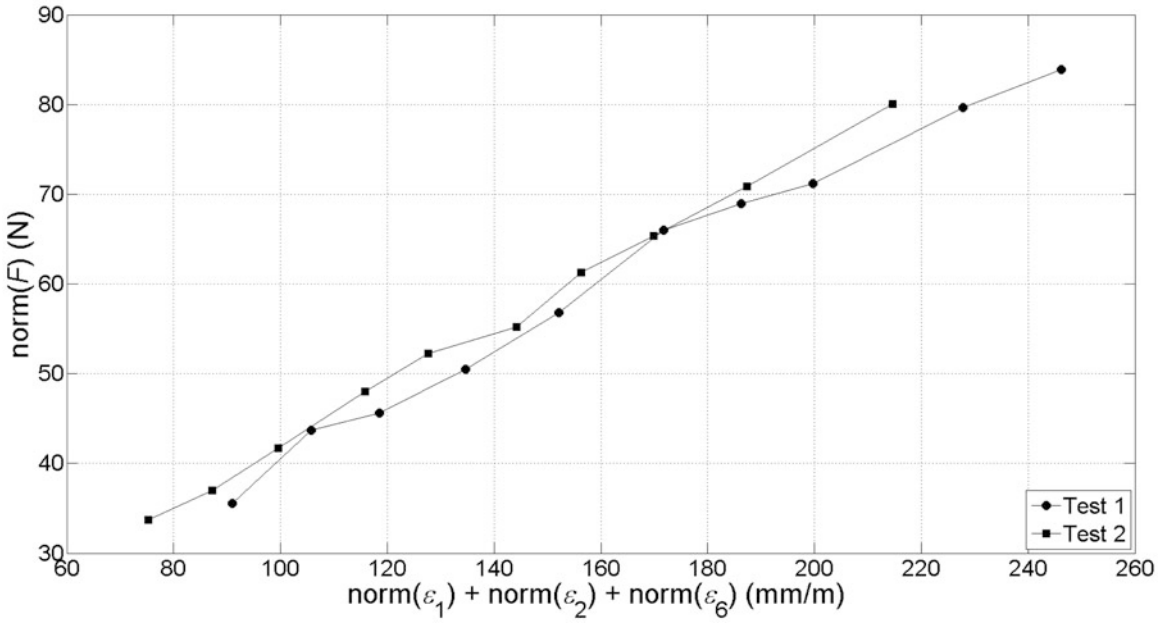

Fig. 20.4 Examination of applied forces and induced strain for Tests 1 and 2

Figure 20.4 examines the manner in which forces induced strain in these tests. This figure suggests that the specimen behaved linear elastically for each load configuration and for each test. Elastic behavior is illustrated by the relative coincidence of points for each test.

Table 20.3 compares Q_{ij} for VFM, ultrasonic, and tensile coupon tests. Both ultrasonic and tensile tests assume linear constitutive behavior. All three tests have reasonable agreement for Q_{11}, Q_{22}, and Q_{66}, which provides further evidence that the various load configurations in Tests 1 and 2 were within the linear material regime. VFM-evaluated Q_{12} were much

Table 20.3 Comparison of different methods for evaluating Q_{ij}, Units km^2/s^2

Test	Q_{11}	Q_{22}	Q_{12}	Q_{66}	Q_{16}	Q_{26}
VFM-Test1	2.58	6.02	0.66	1.24	− 0.01	− 0.42
VFM-Test2	3.01	6.40	0.38	1.40	− 0.04	0.16
Ultrasonic	3.33	7.12	1.94	1.68	0.12	− 0.14
Tensile	2.80	6.22	1.29	1.42	N/A	N/A

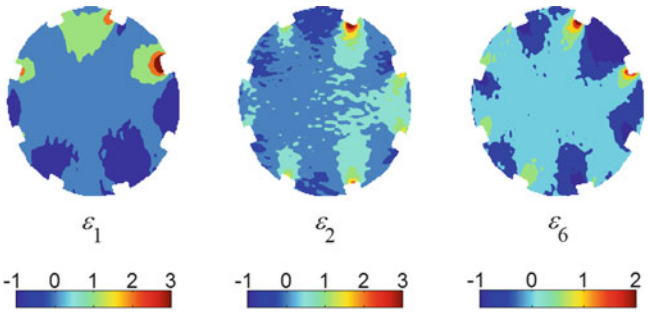

Fig. 20.5 Strains for Test 1, Load Configuration 10, Units (mm/m)

smaller than ultrasonic and tensile Q_{12}. Ultrasonic evaluation of Q_{12} is difficult and generally produces high values [11]. Additionally, Q_{66} and Q_{12} are effectively coupled in ultrasonic measurements because Q_{ij} are evaluated by stiffness matrix transformation. VFM-evaluated ν_{12} were 0.11 and 0.06 for Test 1 and Test 2 respectively, which falls below the range of ultrasonic ν_{12} values reported by Baum et al. [12]. Alternative explanations for Q_{12} disagreement between tests include number of Q_{ij} evaluations and specimen area examined for each test. VFM evaluation was based on the mean of 10 Q_{ij} identifications; ultrasonic values were based on a single test; three tensile coupons were evaluated, but Q_{12} was based on measurements made on two of those tensile coupons. If heterogeneity existed in the specimen, then relative area tested for each test would influence identification. Test areas were 471, 177, and 131 cm^2 for VFM, ultrasonic, and tensile tests, respectively.

To determine Q_{66}, significant effort was made to generate shear strains by creating a large force differential between adjacent loading grips. Figure 20.5 shows DIC-measured strains for Test 1, Load Configuration 10 where $F_1 - F_4$ were 36.9, 44.0, 44.3, and 33.8 N, respectively. For this configuration, ε_6 was near zero throughout the central region of the specimen. However, if the force differential became too large, the specimen developed wrinkles and the test was terminated. It is likely that some prior knowledge of approximate Q_{ij} may be used to create a specific load configuration optimized for stiffness evaluation. Accurate determination of Q_{66} for thin webs is a challenge and successful Q_{66} evaluation here demonstrates an alternative procedure, on a single specimen, without difficulties associated with ultrasonic and tensile tests.

VFM and ultrasonic tests had general agreement for both Q_{16} and Q_{26}. When Q_{16} and Q_{26} are very near zero, their evaluation tends to get masked by larger Q_{ij} for both VFM and ultrasonic tests. Ultrasonic test gave an angle of 90.1° between material 1- and 2-directions.

Figure 20.6 examines the influence of VFM element density on Q_{ij} evaluation. Unlike finite element convergence analyses, increased VFM element density does not improve accuracy of Q_{ij} identification, but tends to amplify noise present in experimentally measured strains. A very coarse mesh (i.e., 5^2 elements) smoothed strain gradients, which were real features that were intentionally introduced in the load fixture. Reduction of norm(Q_{ij}) above 15^2 elements was caused by increasingly ill-conditioned matrices used to evaluate virtual displacements, u_i^*, in Eq. 20.3.

20.8 Conclusion

This work introduced a novel load fixture designed to determine the anisotropic stiffnesses of paperboard with VFM. DIC was used to determine full-field strains under a variety of multi-axial load configurations. Because paperboard is considered to have nonlinear constitutive behavior, special analyses were introduced to examine material nonlinearity and elasticity. Analyses demonstrated that the material remained in the linear elastic regime because VFM-evaluated Q_{ij} were repeatable and compared favorably with those determined by ultrasonic and tensile coupon tests. Finally, the effect of VFM mesh density was examined to ensure that an appropriately sized mesh was used in the analysis.

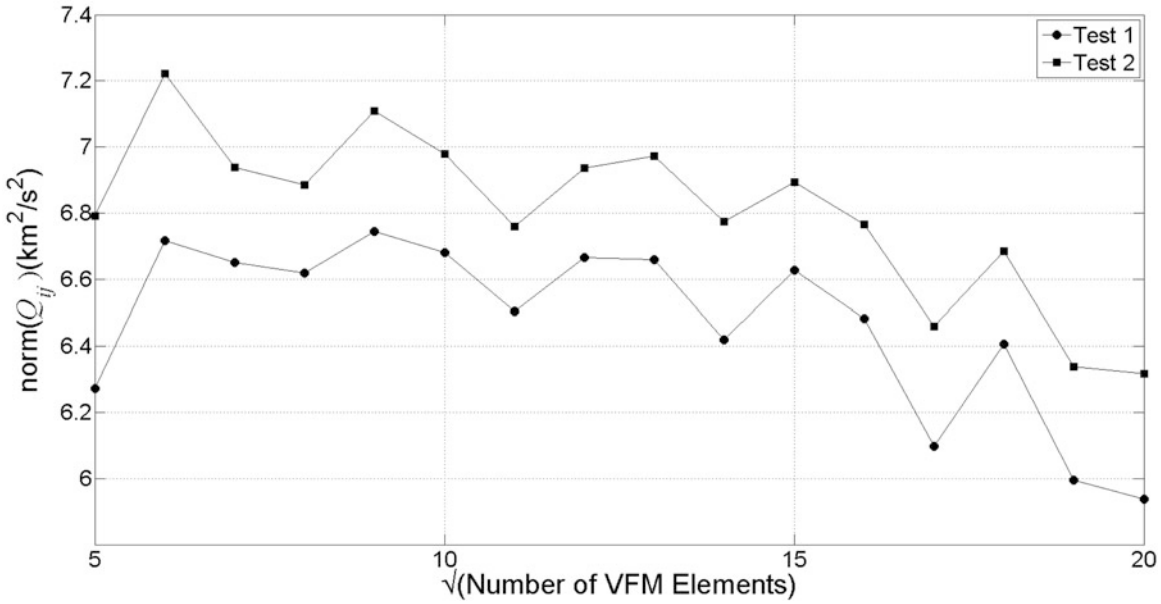

Fig. 20.6 Effect of mesh density on Q_{ij} evaluation

References

1. Allan R (2012) The cost of paper property variation is high. Appita 65(4):308–312
2. Habeger CC (1990) An ultrasonic technique for testing the orthotropic symmetry of polymeric sheets by measuring their elastic shear coupling-coefficients. J Eng Mater Technol-Trans ASME 112(3):366–371
3. Diddens I, Murphy B, Krisch M, Müller M (2008) Anisotropic elastic properties of cellulose measured using inelastic x-ray scattering. Macromolecules 41(24):9755–9759
4. Htun M, Andersson H, Rigdahl M (1984) The influence of drying strategies on the anisotropy of paper in terms of network mechanics. Fibre Sci Technol 20(3):165–175
5. Batten GL, Nissan AH (1986) Invariants in paper physics. Tappi J 69(10):130–131
6. Baum G (1987) Elastic properties, paper quality, and process control. Appita 40(4):289–294
7. Pierron F, Grédiac M (2012) The virtual fields method: extracting constitutive mechanical parameters from full-field deformation measurements. Springer, New York
8. Grédiac M, Vautrin A (1990) A new method for determination of bending rigidities of thin anisotropic plates. J Appl Mech-Trans ASME 57(4):964–968
9. Moulart R, Avril S, Pierron F (2006) Identification of the through-thickness rigidities of a thick laminated composite tube. Compos A-Appl Sci Manuf 37(2):326–336
10. Jones R (1975) Mechanics of composite materials. Taylor & Francis, London
11. Uesaka T, Mukarami K, Imamura R (1982) On the poisson's ratio of paper and its experimental determination. Tappi 65(8):115–116
12. Baum G, Brennan D, Habeger C (1981) Orthotropic elastic constants of paper. Tappi J 64(8):97–101

Chapter 21
Investigation of Fatigue Properties of Titanium Alloy Applying Variational Infrared Thermography

P.J. Hou, X.L. Guo, and J.L. Fan

Abstract This paper describes the application of the infrared thermographic method to estimate the fatigue life of titanium alloy. Using a variational thermographic method, fatigue tests were implemented in order to reckon the fatigue properties. Infrared thermogarphy provides thermal images which are closely related to the limiting fatigue stress. The deformation energy distribution can be determined on the hypothesis of the cycle index five million, relative to the limiting fatigue stress. This variational thermographic method, based on the infrared thermography, is applied to rapidly estimate the fatigue limit of titanium alloy. Through the comparison, the predicted fatigue behavior is confirmed in good agreement with the traditional fatigue results.

Keywords Infrared thermographic method • Fatigue behavior • Titanium alloy • Energy approach • S-N curve

21.1 Introduction

Fatigue design requires statistical processing of numerous tests. However, the traditional evaluation methods are often difficult to be performed for their time-consuming and expensive costing [1, 2].

So, a very important question is raised: How can we get a rapid estimate of the fatigue properties. The infrared thermographic method was first proposed by Risitano et al. [6] by using the surface temperature increments as the major fatigue indicator. Luong et al. [3–5] proposed to use the infrared thermographic method of the mean thermal energy dissipated under a given number of cycles to get this fatigue limit. The infrared thermographic method, based on the analysis of the heat during a loading fatigue test, was developed over the last 30 years. The fatigue limit can be evaluated in an extremely short time. Fatigue failure will take place once the accumulated energy, due to plastic deformation, reaches a constant threshold value. Based on this physical hypothesis, Fargione et al. [6] confirmed the connection between the fatigue limit and the quantity of heat dissipation by testing a given element to failure. Many attempts have been made to measure the fatigue limit fast, and so several studies were implemented. For instance, Pastor et al. and Fan et al. [7, 8] applied the infrared thermographic method to investigate metallic fatigue behavior, including fatigue limits, fatigue class, and Wöhler S-N endurance curves etc. In addition, Ummenhofer and Medgenberg [9] investigated the fatigue damage by a specialized data processing method and developed the infrared thermographic method. The results demonstrated accordance with the traditional test rather well. As a result of this, with the appearance of high resolution infrared camera, the infrared thermographic method has a great revolution to fatigue study.

In the present paper, in order to get a rapid estimate of the fatigue limit, we used the infrared thermographic method proposed by Luong et al. [4] to carry out the fatigue tests for titanium alloy. Pure titanium and titanium alloy are widely used as structural aerospace materials mainly because it is a light-weight and corrosion-resistant material, as a consequence it is important to understand the fatigue mechanisms. And the residual life prediction was proposed based on the hypothesis of the cycle index five million, relative to the limiting fatigue stress. The focus of the paper is to confirm the validity of the theoretical of the technique and to evaluate if the variational thermographic method is suitable in describing the residual life of titanium alloy.

P.J. Hou • X.L. Guo (✉) • J.L. Fan
State Key Laboratory of Structural Analysis for Industrial Equipment, Dalian University of Technology, Dalian 116023, China
e-mail: xlguo@dlut.edu.cn

M. Rossi et al. (eds.), *Residual Stress, Thermomechanics & Infrared Imaging, Hybrid Techniques and Inverse Problems, Volume 8*, Conference Proceedings of the Society for Experimental Mechanics Series, DOI 10.1007/978-3-319-00876-9_21,

21.2 Theoretical Models

21.2.1 The Infrared Thermographic Method

Fatigue damage is well known as energy dissipation accompanied by temperature changing. Most mechanical energy transform into heat energy during this process, then dissipates to the surroundings. The temperature linked with energy dissipation enables us to understand the energy transformation, toughness reduction and damping vibration of materials. Therefore, the fatigue process can be qualitatively evaluated using the relative temperature increment.

During fatigue tests, to avoid any possible errors induced by the environmental perturbation and the experimental system sensitivity, the relative temperature increment ΔT on the hot-spot zone of the specimen surface is used to describe fatigue damage status:

$$\Delta T = T_m - T_0 \tag{21.1}$$

where T_m is the average temperature on the zone; and T_0 is the initial temperature.

According to Luong [4], the fatigue limit is obtained as the stress level for which the temperature increment ΔT of two different increasing rate intersect into one point. As a consequence, it is rapid to determine the fatigue limit by employing the curves of the increase in temperature increment ΔT, and the temperature increment ΔT and the applied stress range Δσ have a well correlation, experimentally and theoretically:

$$\begin{aligned} \Delta T_s &= a \cdot \Delta\sigma + b \qquad for \quad \Delta\sigma < \Delta\sigma_0 \\ \Delta T_s &= A \cdot \Delta\sigma + B \qquad for \quad \Delta\sigma \geq \Delta\sigma_0 \end{aligned} \tag{21.2}$$

Where ΔT_s is the stable temperature increment; Δσ is the applied stress range; $\Delta\sigma_0$ is the fatigue limit; a, b, A, and B are material constant.

21.2.2 The Energy Approach

From the energy dissipation point, fatigue failure will take place as soon as possible when the quantity of the energy per unit volume reaches to a threshold value E_c. E_c, a constant value, is independent of loading sequence and level, and interaction of loading is not taken into account. Fargione et al. [6] defined an energetic parameter Φ, which enabled us to predict the whole S-N curve of materials. E_c is documented to be positive feedback to the energetic parameter Φ. This parameter can be intended by integrating the ΔT-N curve depicted by an infrared camera.

$$E_c \propto \Phi = \int_0^{N_f} \Delta T(N) \cdot dN \tag{21.3}$$

where N_f is the fatigue life.

A material from cyclic loading low than its yield limit but higher than its fatigue limit is defined by three phases. The temperature rapidly rises in the initial stage (phase 1), then goes to an asymptotic value (phase 2), finally it increases sharply before fatigue failure because of the plastic deformation (phase 3).

Due to the limited number of phase 1 and 3, the energetic parameter Φ can be simply expressed as:

$$\Phi = \Delta T_s \cdot N_f \tag{21.4}$$

Using the successive stepwise loading procedure, the energetic parameter is easily determined resorting to the infrared thermographic method. To rapidly determine the fatigue behavior of materials and components, it is possible to get the asymptotic temperature increment at each stress level, and then, based on Eq. 21.4, to calculate the relevant N_f. The entire S-N curve can be plotted using the couples of Δσ and N_f.

21.3 Experiment Investigations

21.3.1 Material and Specimen

The material used in the present research is TC4 titanium alloy, mainly composed of ≤0.30Fe, ≤0.10C, ≤0.05 N, ≤0.015 H, ≤0.20 O, 5.5–6.8 Al, and 3.5–4.5 V in wt %. It is widely used as structural aerospace materials mainly due to its very high yield strength of about 890 MPa and much low density of 4510 kg/m^3. And the dimension of the specimen is presented in Fig. 21.1.

21.3.2 Methods

Fatigue tests were carried out using a MTS810 servo-hydraulic machine with 100 kN capacity at room temperature without disturbance of the external heat resource. The testing system is also composed of infrared camera, lock-in module, computers and corresponding software [8] in Fig. 21.2.

Before tests, all the specimens were polished with fine grit papers, and then painted the specimens black to improve the heat radiation. The stress ratio is set as $R = -1$ with a frequency of 15 Hz. The stepwise loading procedure was applied to the same specimen. To avoid fatigue damage accumulation, the stress was applied from 50 MPa with steps of 10, 20, and 50 MPa every 1,000 cycles until fracture. In addition, the thermal images on the hot-spot zone were recorded by the infrared camera to perform the subsequent data analysis presented in Fig. 21.3.

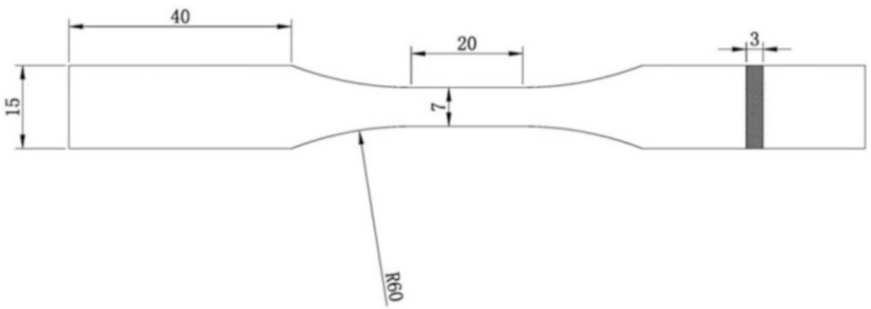

Fig. 21.1 Size of the specimen (unit: mm)

Fig. 21.2 Experimental system

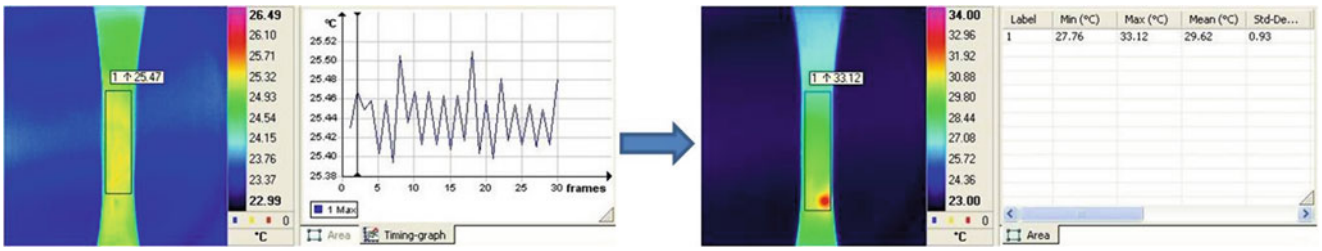

Fig. 21.3 Hot-spot zone evolution

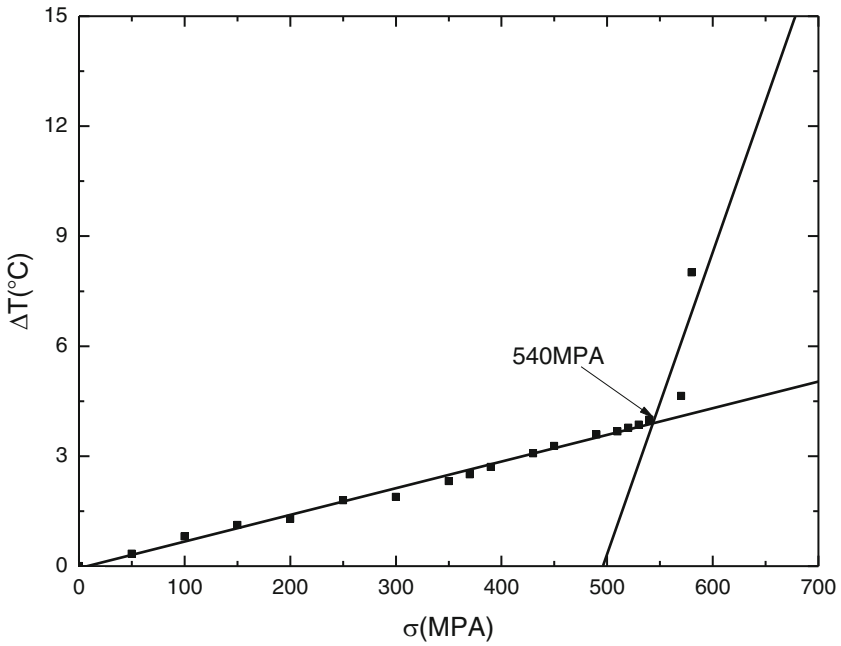

Fig. 21.4 ΔT-σ curve

21.4 Results and Discussion

21.4.1 Fatigue Limit

Temperature evolution is mainly attributed to the thermoelastic effect, plastic effect and heat conduction. The fluctuating temperature is due to the thermoelastic effect, and the temperature amplitudes increase with the increasing cyclic loading. Figure 21.4 is the curve of ΔT−σ used to get the fatigue limit by fitting the infrared data employing the Luong [4] method. During the test, the temperature of the specimen surface was detected by the infrared camera. From the Fig. 21.4, the fatigue limit of the TC4 titanium alloy is obtained as 540 MPa.

The elastic stress controls mechanical responses of tested specimens when the stress is less than 540 MPa. At this term, the specimen mainly takes place elastic deformation, and the temperature increment is mainly induced by non-plastic effects, i.e. viscosity effect etc. If the stress is higher than the fatigue limit, microcracks will initiate from the specimen boundaries, such as: the corner and the free surface. They initiate along the axial direction of 45°, and then coalesce to form a main crack. The main crack propagates perpendicular to the principal stress direction. The plastic strain energy accumulates during the fatigue evolution. Most of the mechanical energy is dissipated as heat energy heating up the specimen.

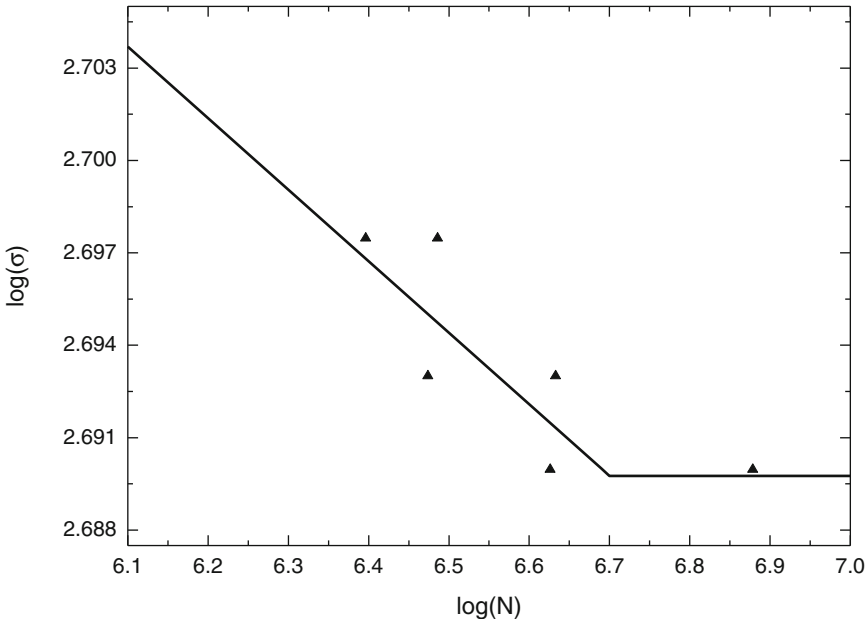

Fig. 21.5 The S-N curve by the traditional method

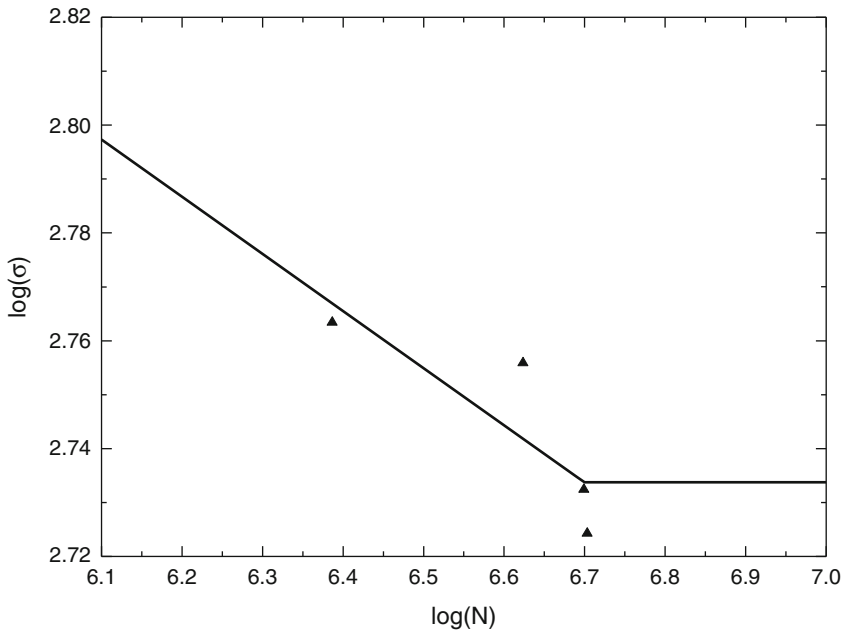

Fig. 21.6 The S-N curve by the energy approach

21.4.2 S-N Curve

It is well known that the S-N curve is the most common presentation of fatigue data. Here we assume that the cycle limit involved in the fatigue limit of TC4 titanium alloy aforementioned is five million. And the stable temperature increment ΔT_s corresponding to the fatigue limit was 3.90°C. Resorting to the stepwise loading procedure, all the stable temperature increment ΔTs relate to the applied stress level σ is able to be determined by the thermographic method mentioned above. The Eq. 21.4 allowed us to obtain the energetic parameter Φ, 1.95×10^7.

Using the least-square method, log(N) and log(σ) were fitted in the Fig. 21.5 by the limiting energy hypothesis. Figure 21.6 shows the S-N curve of titanium alloy using the traditional method. According to the Figs. 21.5 and 21.6, the two curves are very close through a direct comparison. Moreover, the fatigue limits between the traditional procedure σ_t and energy approach σ_e achieves good accordance. The S-N curves represent median line meaning 50 % survival probability with 95 % confidence level.

21.5 Conclusions

1. The variational themographic method enables us to rapidly evaluate the fatigue behavior of TC4 titanium alloy with a limited number of specimens.
2. The experimental tests demonstrate that the energetic parameter is a constant value which is a bulk property. It can be use to predict the fatigue behavior of materials and structures.

Acknowledgements The financial support of Natural Science Foundation of China (No.11072045) is gratefully acknowledged.

References

1. Fricke W (2003) Fatigue analysis of welded joints: state of development. Mar Struct 16:185–200
2. Crupi V, Guglielmino E, Maestro M et al (2009) Fatigue analysis of butt welded AH36 steel joints: thermographic method and design S–N curve. Mar Struct 22:373–386
3. Luong MP (1995) Infrared thermographic scanning of fatigue in metals. Nucl Eng Des 158:363–376
4. Luong MP (1998) Fatigue limit evaluation of metals using an infrared thermographic technique. Mech Mater 28:155–163
5. Luong MP (1990) Infrared thermovision of damage processes in concrete and rock. Eng Fract Mech 35:291–301
6. Fargione G, Geraci A, La Rosa G, Risitano A et al (2002) Rapid determination of the fatigue curve by the thermographic method. Int J Fatigue 24:11–19
7. Pastor ML (2008) Applying infrared thermography to study the heating of 2024-T3 aluminium specimens under fatigue loading. Infrared Phys Technol 51:505–515
8. Fan JL, Guo XL, Wu CW et al (2011) Research on fatigue behavior evaluation and fatigue fracture mechanisms of cruciform welded joints. Mater Sci Eng A 528(29–30):8417–8427
9. Ummenhofer T, Medgenberg J (2009) On the use of infrared thermography for the analysis of fatigue damage processes in welded joints. Int J Fatigue 31:130–137

Chapter 22
Monitoring Materials Under Impact with Infrared Thermography

Carosena Meola and Giovanni Maria Carlomagno

Abstract Infrared thermography is becoming ever more popular and is embracing a constantly wider range of applications going from medical diagnostics to building energy saving, comprehension of fluid-dynamic phenomena, etc. The present paper is concerned with the use of infrared thermography in the materials science field, relating to the behavior of a material under impact in a general sense. In particular, two different types of impact are considered: the impact of air jets over a surface for heat transfer purposes and the impact of a solid object against a composite material. Owing to the first topic, the attention is focused on the performance of the cooling devices, which generally are quench boxes equipped with arrays of nozzles. To this end, laboratory tests are performed in an attempt to show the influence of some parameters, such as nozzles flow rate and impinging distance, through measurements of convective heat transfer coefficients with the heated thin foil technique. Regarding the second item, an infrared imaging system is used to monitor the unsteady thermal response of some composite materials to low energy impact in order to gain more information about damage onset and propagation. For both types of tests, the usefulness of an infrared imaging device is highlighted.

Keywords Infrared thermography • Impact tests • Convective heat transfer • Heated-thin-foil technique • Composite materials

22.1 Introduction

Infrared Thermography (IRT) is a methodology which allows for: remote detection of thermal electromagnetic energy that is radiated from objects in the infrared band, conversion of such energy into a video signal and representation of the object surface temperature map. This represents a great potentiality to be exploited in a lot of application fields and for many different purposes. For example, IRT may be used for diagnosis (in medicine, architecture, maintenance), or for understanding of complex fluid-dynamic phenomena (flow instability, flow separation and reattachment), or for material characterization and procedure assessment, which can help improving design and fabrication of products. As technology evolves, infrared systems offer new opportunities for application; indeed, any process which is temperature-dependent may benefit from the use of an infrared device.

The attention of the present work is focused on the behavior of a material under impact in a general sense by considering either the impact of a gas, or of a solid object, onto a surface. In both cases an infrared imaging device is used to visualize the surface temperature variation due to the impact. The visualized temperature map may be exploited to gain two different types of information relating to the impacting fluid, or to the surface impacted by the object. In fact, in one case (gas impact) the surface temperature can be used to evaluate, through measurements of the convective heat transfer coefficient, the cooling/heating efficiency of the impacting fluid, which is to say the efficiency of the quench box producing the impinging mass flow rate. In the other case (object impact), the local heating up of the impacted surface is a symptom of occurred damage and then, the temperature map may be used to understand the failure modes of a material under impact.

C. Meola (✉) • G.M. Carlomagno
Department of Industrial Engineering – Aerospace Section, University of Naples Federico II, Via Claudio 21, 80125 Naples, Italy
e-mail: carmeola@unina.it

M. Rossi et al. (eds.), *Residual Stress, Thermomechanics & Infrared Imaging, Hybrid Techniques and Inverse Problems, Volume 8*, Conference Proceedings of the Society for Experimental Mechanics Series, DOI 10.1007/978-3-319-00876-9_22,

22.2 Impact by Air Jets

The temperature represents a critical parameter in many manufacturing processes like the glass tempering one, in which cooling efficiency plays a key role, especially for relatively thin glass sheets. In the last years, the design of innovative quenching (tempering) units, made by two nozzle arrays, with combined patent applications (able to increase production with higher level of mechanical properties, scrap reduction, less geometrical deformation, less cumbersome stretching, less time loss) has been the challenge of many researchers and specialists and is still an open question.

The heat transfer is influenced by many factors involving both geometrical (nozzle geometry, nozzle-to-nozzle spacing, impingement distance, etc.) and fluid flow conditions (jet velocity, turbulence, entrainment, spent air exhaust, etc.).

Therefore, experimental tests, needed for the validation of cooling devices, have provided a multitude of data. In the same time, the interest of many researchers was devoted to gain insights into the fluid-dynamics of impinging jets. As a consequence, literature is full of papers (theoretical, experimental and numerical) dealing with either a single, or an array of impinging jets, aimed at going through specific aspects such as the flow pattern after impingement [1], entrainment effects [2], unsteady effects [3], influence of nozzle shape [4], influence of shear layer dynamics [5] and data correlation [6, 7]. However, the majority of papers is concerned with relatively low effective (specific) mass flow rate values, while large values are often involved in real applications such as in glass tempering.

The tempering process produces inside the glass tensile stresses which increase its mechanical resistance, especially its flexural strength, and reduces the risk of breaking caused by thermal shocks. Tempered glass is also a safety product because it breaks shattering into small non-cutting fragments. The basic feature is to create a final condition of surface and edge compression with the core having compensating tensile stresses. This is achieved by heating the glass above approximately 600°C and rapidly cooling it by blowing air uniformly onto both of the glass plate surfaces, simultaneously. Indeed, the cooling phase is of paramount importance to obtain good tempered glass for two main reasons. It is important to transfer heat uniformly from both surfaces because uneven heat extraction may produce bows, or warps. Then, it is important to sustain the quench long enough till its stable condition, to avoid reheating of the glass surfaces from the still-hot core. Thus, of vital importance is the performance of the cooling devices, which generally are quench boxes equipped with arrays of nozzles. The governing parameters to be optimized are mainly: nozzles geometry, spacing between nozzles, flow rate and impinging distance.

Herein, it is shown as the problem can be solved in laboratory by using infrared thermography to evaluate the convective heat transfer coefficient h_c, between a plate and the jets issuing from an array of nozzles and impinging onto such a plate.

22.2.1 Experimental Setup and Test Procedure

The convective heat transfer coefficient h_c is evaluated with the steady state heated thin foil technique [8] which consists of heating a thin metallic foil, or a printed circuit board, by Joule effect and computing h_c with the formula:

$$h_c = \frac{q' - q'_l}{T_w - T_{aw}} \tag{22.1}$$

where q' is the Joule heating, q'_l includes losses due to tangential conduction and radiation, T_w is the wall temperature and T_{aw} the adiabatic wall temperature. In the present work both T_w and T_{aw} are measured with infrared thermography.

As shown in Fig. 22.1, the experimental apparatus [8], includes a target plate, which is a thin constantan foil (200 mm wide, 470 mm long and 0.050 mm thick) held flat by a stiffening fixture. The electric current to heat the target plate is provided by a direct current stabilized power supply. The cooling air jet, generated by a compressor, goes through a pressure regulating valve, a heat exchanger, a plenum chamber (quench box) where pressure and temperature are metered and flows through an array of 5 × 5 nozzles; the diameter of each nozzle is $d = 6.5$ mm and the spacing between nozzles in x and y directions is respectively $x_x = 40$ mm and $y_x = 20$ mm. The surface of the constantan target plate is covered, over the side viewed by the infrared camera, with a thin film of opaque paint of emissivity $\varepsilon = 0.95$ (measured with the infrared system itself).

The test procedure is the following: switch on the blower; reach the desired flow rate value; wait (about 2 h) to reach steady thermal conditions; then visualize the adiabatic wall temperature T_{aw} and acquire the cold image; put on the electric power supply; wait about 15 min to reach steady thermal conditions; visualize the wall temperature T_w and acquire the corresponding thermographic image (hot image). The temperature in the plenum chamber T_o is continuously checked to assure that both cold (T_{aw}) and hot (T_w) images are acquired at the same T_o value (generally, very small variations occur

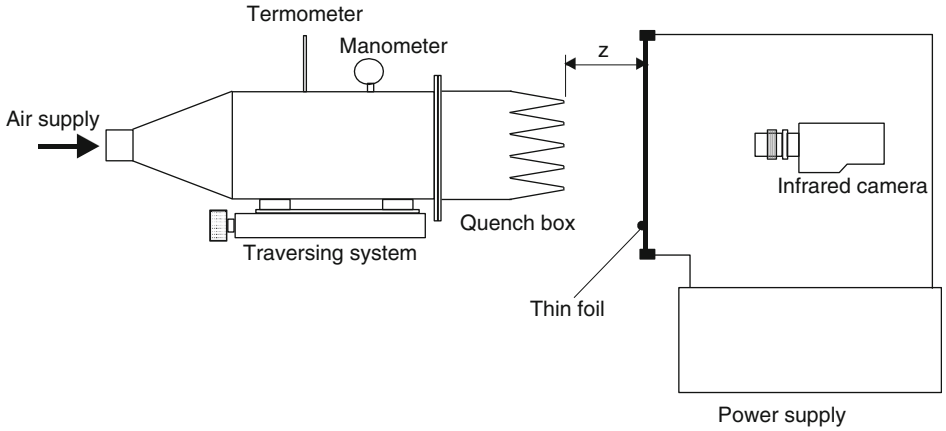

Fig. 22.1 Experimental setup

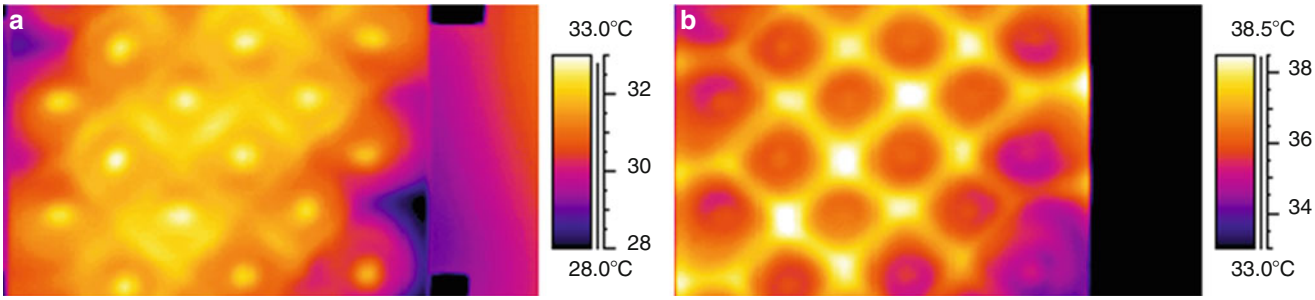

Fig. 22.2 T_{aw} and T_w maps for jets of $\Delta p = 130$ mbar, effective flow rate $m_{eff} = 6.6$ kgm^2/s impinging at $z/d = 4.6$ (**a**) T_{aw} map (**b**) T_w map

between the two acquisitions). Each data set is obtained by averaging 32 thermal images in time sequence to reduce measurement noise. Typical T_{aw} and T_w images for effective flow rate $m_{eff} = 6.6$ kgm^2/s, differential pressure $\Delta p = 130$ mbar and dimensionless impinging distance $z/d = 4.6$ are shown in Fig. 22.2.

The acquired images are analyzed and the h_c values (Eq. 22.1) are evaluated. Losses due to radiation $q_r^{'}$ are computed according to the radiosity relation that expresses heat transfer by radiation between two grey bodies, one having a much larger surface as compared to the other one:

$$q_r^{'} = \varepsilon\sigma\left(T_w^4 - T_a^4\right) \tag{22.2}$$

where ε is the total emissivity coefficient of the opaque paint, σ is the Stefan-Boltzmann constant and T_a is the ambient temperature. The tangential conduction $q^{'}$ is evaluated by means of the 2D laplacian of the wall temperature T_w:

$$q_c^{'} = sk_f\left(\frac{\partial^2 T_w}{\partial x^2} + \frac{\partial^2 T_w}{\partial y^2}\right) \tag{22.3}$$

where s and k_f are thickness and thermal conductivity coefficient of the foil and x and y the coordinates parallel to the foil surfaces. Losses due to natural convection are small as compared to other contributions and can be neglected. The convective heat transfer coefficient h_c can be reduced in dimensionless form in terms of the Nusselt number, Nu:

$$Nu = \frac{h_c d}{k_a} \tag{22.4}$$

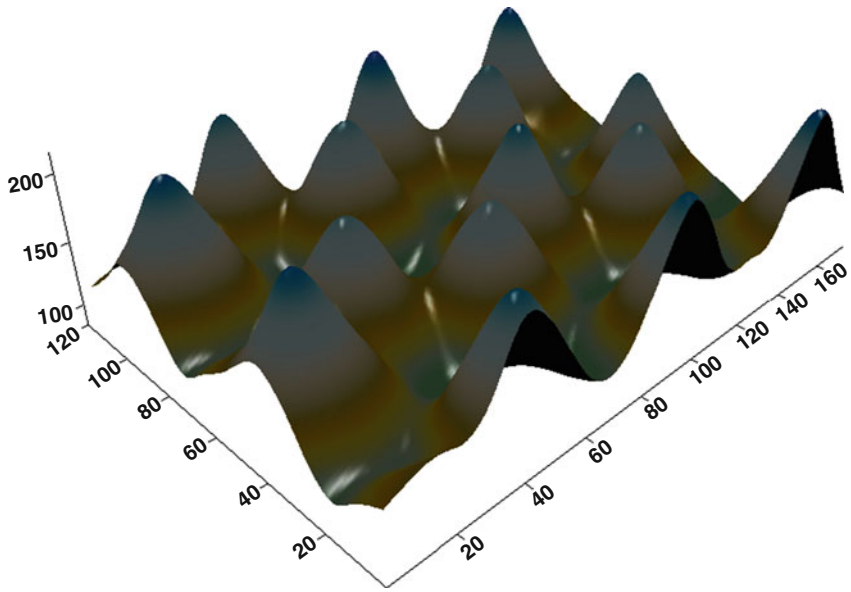

Fig. 22.3 3D Nusselt number map for the same conditions as in Fig. 22.2

with d nozzle diameter and k_a thermal conductivity coefficient of air evaluated at the film temperature T_f:

$$T_f = \frac{T_w + T_{aw}}{2} \tag{22.5}$$

Of course, k_a is determined point by point on the whole imaged surface. In particular, Nu is independent of the heat flux direction and so the plate can be either cooled, or heated, indifferently. A 3D map of the Nusselt number, for the same test conditions as in Fig. 22.2, is shown in Fig. 22.3. As expected, the Nusselt number attains maxima in correspondence of each jet axis and laterally decreases towards minima between adjacent jets.

22.2.2 Dimensionless Average Data Reduction

Data are also reduced in dimensionless form in terms of the average Nusselt number Nu_m defined as:

$$Nu_m = \frac{h_m D}{k_a} \tag{22.6}$$

with h_m the convective heat transfer coefficient averaged over the area of the hexagon indicated by the dashed area in Fig. 22.4. The effective flow rate is calculated as ratio between the measured flow rate $\dot{m}$ and the total blown area A_f:

$$m_{eff} = \frac{\dot{m}}{A_f} = \frac{\dot{m}}{n\, x_x y_y} \tag{22.7}$$

where n is the number of nozzles and x_x and x_y, as already specified, are the distances between nozzles in x and y directions. Values of Nu_m are plotted against the dimensionless impingement distance z/d for three different values of m_{eff} in Fig. 22.5. As can be seen, Nu_m increases with increasing m_{eff} and decreasing z/d.

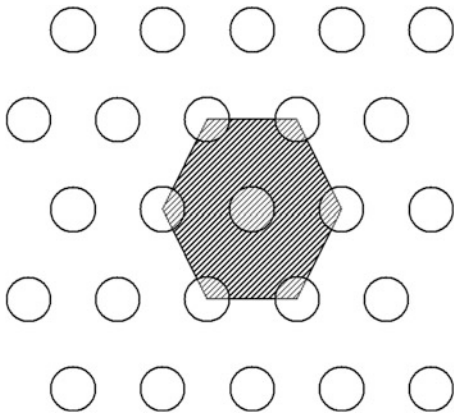

Fig. 22.4 Sketch of averaging area

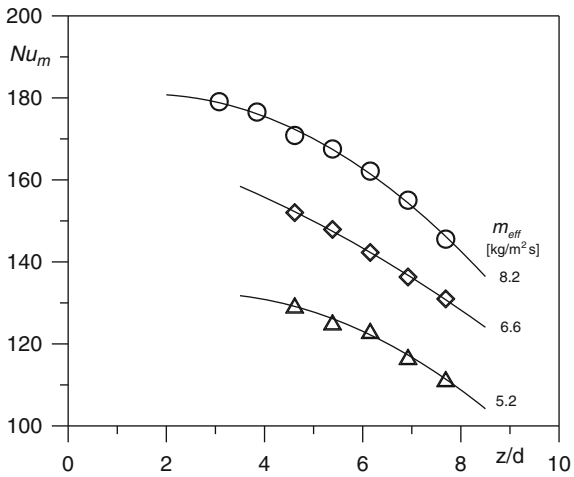

Fig. 22.5 Average Nusselt number against the impingement distance

22.3 Impact of a Blunt Object

The impact of a blunt object against a surface may cause a certain level of damage, which mostly mostly depends on the surface material and on the impact energy. Layered composites, due to their low interlaminar strength, are susceptible to delamination, often resulting in considerable loss in strength, and possibly leading also to catastrophic failures in service. Mostly dangerous is the impact at low energy, which, unlike in metals, does not produce visible damage on the composite surface, but buried delamination between the layers, which is often very slight and difficult to detect. Thus, it is very important, on one side, to understand the material behavior under impact for design purposes and, on the other side, to discover the occurred damage in its incipient stage for preventative measures. An infrared imaging device may be used to comply with both purposes. The use of infrared thermography was recently investigated by Meola et al. [9–11]; they proved that high frequency sampling rate (900 Hz) makes possible even to appraise the thermo-elastic effects which take place in a small time fraction [9]. Besides, Meola and Carlomagno [10] supplied information on the onset and propagation of impact damage in a glass fiber reinforced polymer and proposed a relationship between the damaged area and the impact energy owing to the effective striking surface.

Some images taken during an impact event are shown in the following. The attention is mainly focused on the onset of hot spots which also coincide with damage loci in an attempt to gain new understanding on the impact damage mechanisms from the thermal point of view. The analysis is performed by considering heat transfer by conduction. It is worth noting that, unlike the previous case (jet impact) which involved a steady state phenomenology because of the continuous air blowing, now the attention is focused on transient (unsteady) occurrences that accompany the impact of the object on the surface opposite to the observed one.

Fig. 22.6 Setup for impact tests with the Charpy pendulum (**a**) front side (**b**) rear side

22.3.1 Materials and Test Setup

Two different composite materials are considered:

- A glass fiber reinforced polymer (GFRP) obtained from unidirectional E-glass fibers embedded in translucent epoxy resin. Laminates 500 × 500 mm^2 of stacking sequence $[0_2/90_2]_S$ are fabricated by the hand lay-up technology and cured, under stamp, for 24 h at room temperature. After that, rectangular specimens 130 × 100 mm^2 are cut and post cured in oven at 60°C for 5 h. The overall thickness of each laminate is about 2.9 mm.
- A fiber metal laminate (FML) which includes three aluminum layers with two glass/epoxy layers in between them; specimens are 130 × 100 mm^2 and 1.5 mm thick. The external laminate surfaces are covered with a coating layer.

Impact tests are carried out with a modified Charpy pendulum including an impactor of hemispherical nose, 24 mm in diameter. Specimens are held from the shorter sides while are free to move along the two longer ones. Figure 22.6 shows the Charpy pendulum with the infrared camera positioned to view the specimen surface opposite to impact (Fig. 22.6a) and the lodging of specimens (Fig. 22.6b). The used infrared camera is the SC6000 (Flir systems), which is equipped with a QWIP detector, working in the 8–9 μm infrared band, of spatial resolution 640 × 512 pixels full frame and with a windowing option linked to frequency frame rate and temperature range. The impact energy is set by suitably adjusting the falling height of the Charpy arm.

22.3.2 Impact Tests and Data Analysis

Sequences of thermal images are acquired at 96 Hz during impact tests. More specifically, the acquisition starts few seconds before the impact and lasts for some time after to allow complete visualization of the thermal effects evolution with respect to the ambient temperature. To better account for the material thermal behavior, the first image ($t = 0$) of the sequence, i.e. the specimen surface (ambient) temperature before impact, is subtracted to each subsequent image so as to generate a map of temperature difference ΔT:

$$\Delta T = T(i,j,t) - T(i,j,0) \tag{22.8}$$

i and j representing lines and columns of the surface temperature map. Therefore, a sequence of ΔT images is created. Some ΔT images taken during impact are shown in Figs. 22.7 and 22.8. In particular, the images in Fig. 22.7 refer to a GFRP specimen impacted at energy $E = 7.5$ J, while those in Fig. 22.8 refer to a FML specimen impacted at $E = 4.5$ J. In both

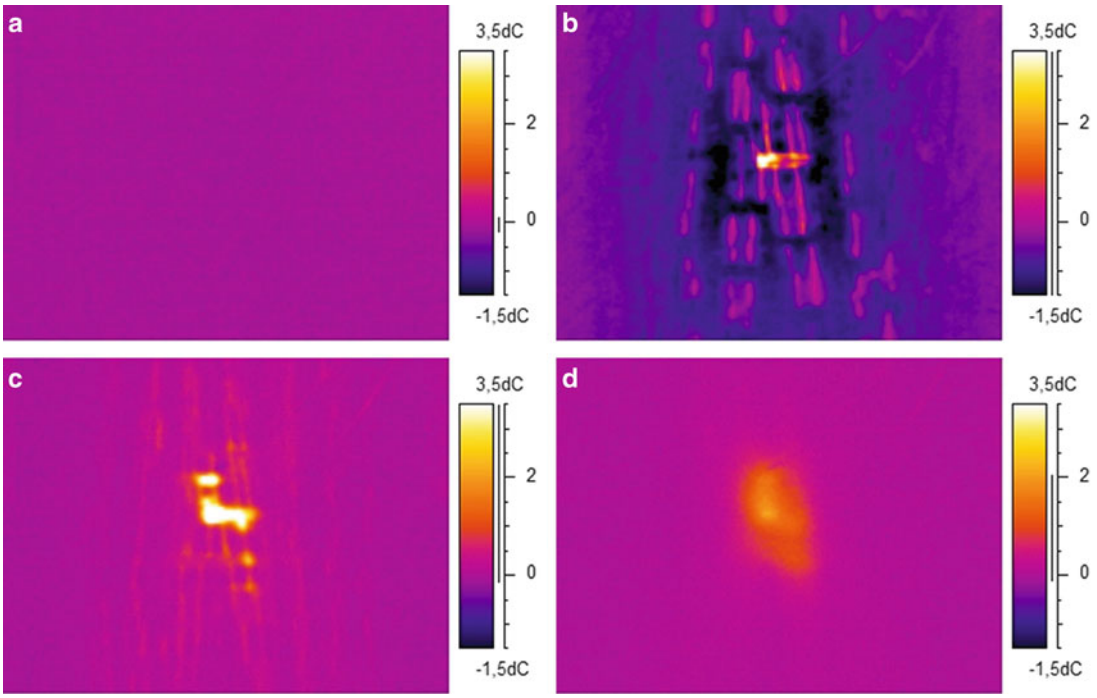

Fig. 22.7 Thermal images of a GFRP specimen taken under impact at $E = 7.5$ J (**a**) $t = 0$ s (**b**) $t = 0.0104$ s (**c**) $t = 0.104$ s (**d**) $t = 2.104$ s

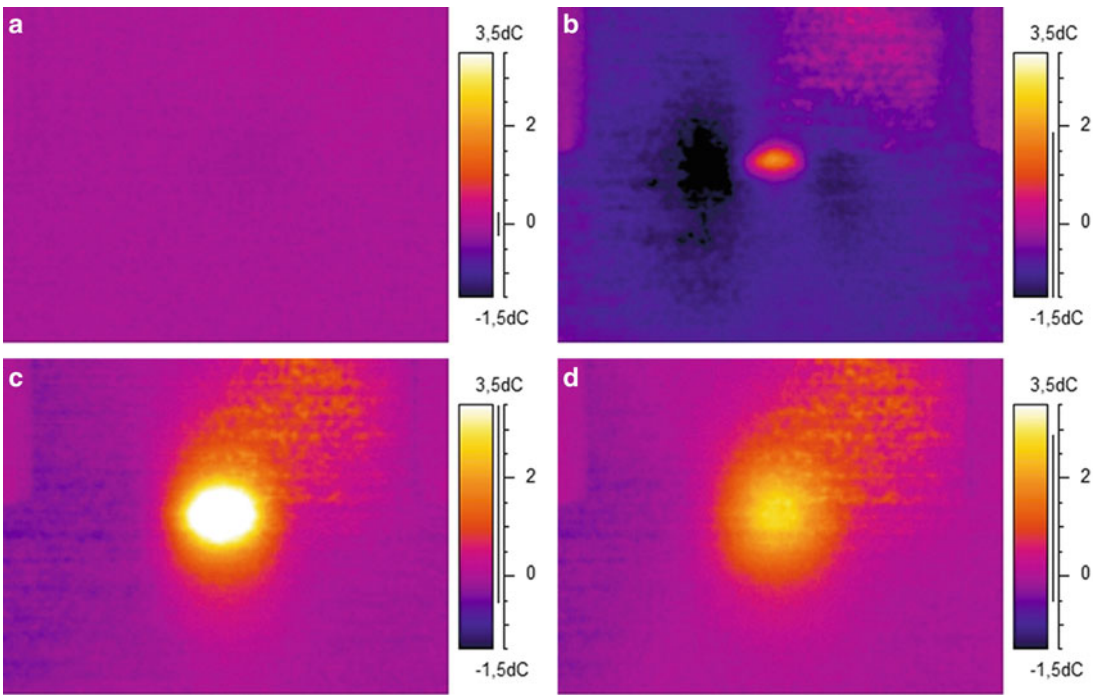

Fig. 22.8 Thermal images of a FML specimen taken under impact at $E = 4.5$ J (**a**) $t = 0$ s (**b**) $t = 0.0104$ s (**c**) $t = 0.031$ s (**d**) $t = 0.104$ s

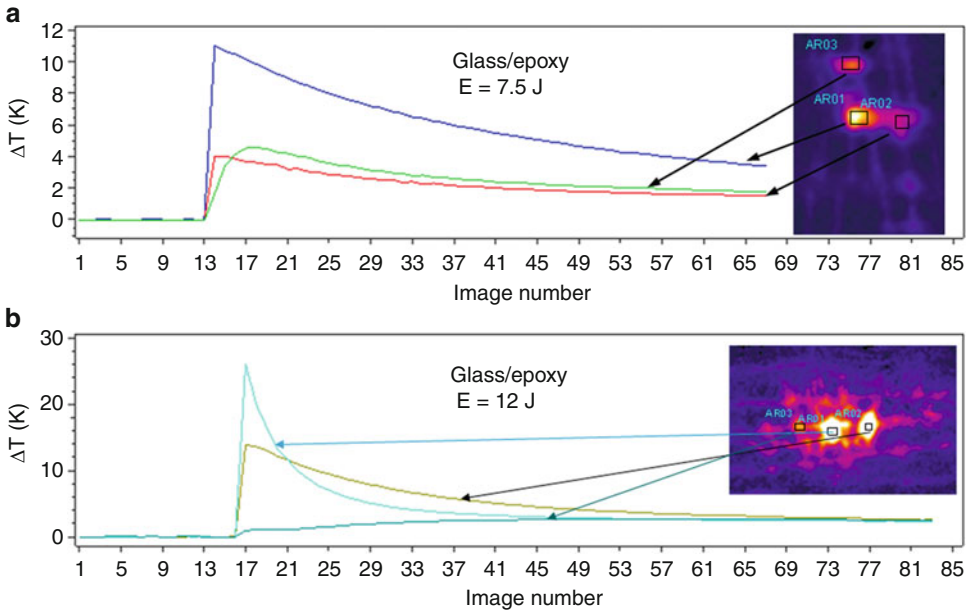

Fig. 22.9 ΔT against time in different hot spots for GFRP specimens (**a**) GFRP impacted at $E = 7.5$ J (**b**) GFRP impacted at $E = 12$ J

figures, the first image is showing an almost uniform $\Delta T = 0$ relating to the surface at ambient temperature before impact. The second image (Figs. 22.7b and 22.8b) is taken 1/96 s after the first one. As can be seen, on the GFRP surface (Fig. 22.7b) are clearly distinguishable the glass fibers with a hot spot in the central zone; such a hot spot enlarges fractions of a second later (Fig. 22.7c) while other smaller hot spots appear. More later, all the hot spots coalesce into a unique warm zone (Fig. 22.7d) due to lateral thermal conduction; of course, such a zone displays ΔT values lower than the hot spots in Fig. 22.7c because of heat diffusion and cooling down towards ambient temperature. It has to be considered that, during impact, kinetic energy passes from the impactor nose to the target; then, such energy is in part transformed into elastic energy and in part dissipated through failures, vibrations, or friction. Since most of the dissipated energy is converted into heat, the detection of the hot spots and their evolution supply information important for the comprehension of the impact damage mechanisms. By comparing Figs. 22.7 and 22.8, it is possible to see the different behavior of a FML material with respect to a glass/epoxy one. In fact, the image in Fig. 22.8b shows a central hot zone, which firstly enlarges quickly (Fig. 22.8c) and after tends to rapidly disappear (Fig. 22.8d); this behavior is completely different from that of the image in Fig. 22.7b, although both images are taken at the same time instant during the impact. This because the thermal effects are driven by the thermal behavior of the viewed external layer of the FML which is made of aluminum and therefore has a much higher thermal diffusivity.

For a quantitative analysis, ΔT values in three hot spots are plotted against the number of the image of the time sequence, for a GFRP impacted at $E = 7.5$ J in Fig. 22.9a and for a GFRP specimen impacted at $E = 12$ J in Fig. 22.9b. More specifically, in Fig. 22.9 are plotted average values in an area around each spot; such areas are named AR01, AR02 and AR03.

As can be seen, the plots of AR01 and AR02 (lines blue and red in Fig. 22.9a and lines light blue and brown in Fig. 22.9b) display an abrupt ΔT increase followed by a slower decrease. The average ΔT values in AR03 in Fig. 22.9a increases more slowly reaching the same maximum as in AR02. The average ΔT value in AR03 in Fig. 22.9b instead grows very slowly and intersects the decreasing branch of the light blue line (AR01 spot) at about 0.3 s later. Owing to such different time evolution and considering the stacking sequence and the thermal diffusivity, it is possible to infer that the spot AR03 in Fig. 22.9a is located still within the first layer of fibers; some delay being possibly due to a local resin thickening which affects the local thermal diffusion. Conversely, the spot AR03 in Fig. 22.9b refers to some damage occurred within an inner fibers layer.

As a final point, in Fig. 22.10 a comparison between the ΔT evolution in the FML specimen impacted at $E = 4.5$ J and in the glass/epoxy specimen (AR01) impacted at $E = 7.5$ J is shown. It is possible to see a certain difference in the slope of the rising tracts; this because the hot spot in glass/epoxy is due to the impact energy dissipated in the breakage of a superficial fiber, while the warm zone in FML is due to delamination underneath the aluminum layer at the interface with the glass/epoxy layer.

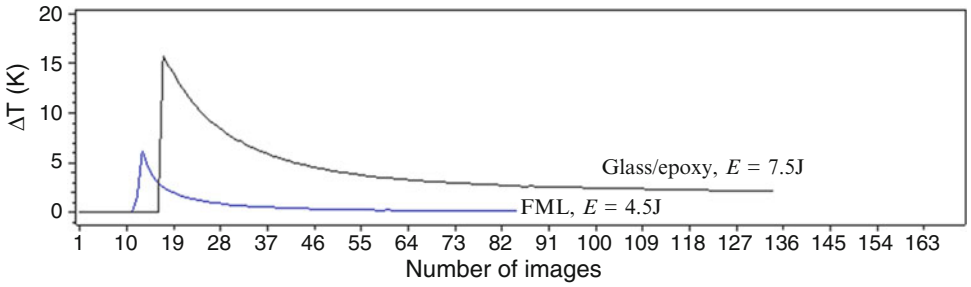

Fig. 22.10 A comparison of ΔT evolution with time in GFRP and FML specimens

22.4 Conclusions

It has been demonstrated as, by simply monitoring the temperature variation experienced by a plate under impact load, it is possible to gain information on either the impacting substance, or on the impacted one. Of course, this is possible by choosing the suitable model and applying the appropriate heat transfer mechanism. Then, from the evaluation of convective heat transfer coefficients, through the steady heated thin foil model it is possible to assess the performance of the flow rate impacting a surface, which also means assessing the performance of quench boxes. On the other side, considering the heat transfer mechanism by conduction through the thickness of a plate, it is possible to understand the reaction of such a plate against a body impacting on it. In the jet impact, a steady state phenomenology is monitored, because of the continuous air blowing, while, in the body impact, we are observing the transient (unsteady) occurrences that accompany the impact of the body on the surface opposite to the viewed one. The same infrared imaging device can be used to obtain both types of information by simply recording a sequence of images. The difference lies in the used test procedure and data analysis.

References

1. Glauert MB (1956) The wall jet. J Fluid Mech 1:625–643
2. Goldstein RJ, Sobolik KA, Seol WS (1990) Effect of entrainment on the heat transfer to a heated circular air jet impinging on a flat surface. J Heat Trans 112:608–611
3. Monkewitz BR, Bechert DW, Barsikow B, Lehmann B (1990) Self-excited oscillations and mixing in a heated round jet. J Fluid Mech 213:611–639
4. Meola C, de Luca L, Carlomagno GM (1995) Azimuthal instability in an impinging jet: adiabatic wall temperature distribution. Exp Fluid 18:303–310
5. Meola C, de Luca L, Carlomagno GM (1996) Influence of shear layer dynamics on impingement heat transfer. Exp Therm Fluid Sci 13:29–37
6. Meola C (2009) A new correlation of Nusselt number for impinging jets. Heat Trans Eng 30:221–228
7. Gregory JM, Browne EA, Peles Y, Jensen MK (2011) The effect of area ratio on microjet array heat transfer. Int J Heat Mass Trans 54:1782–1790
8. Meola C, Carlomagno GM (2006) Intensive cooling of large surfaces with arrays of jets. In: Proceedings of QIRT 2006, Padova, CD Room paper 064, 28–30 June 2006
9. Meola C, Carlomagno GM (2009) Infrared thermography to impact-driven thermal effects. Appl Phys A 96:759–762
10. Meola C, Carlomagno GM (2010) Impact damage in GFRP: new insights with infrared thermography. Compos Part A 41:1839–1847
11. Meola C, Carlomagno GM, Ricci F, Lopresto V, Caprino G (2011) Investigation of impact damage in composites with infrared thermography, 6th NDT in progress, Prague 10–12 Oct 2011.

Chapter 23
Damage Induced Evolution of the Thermal Diffusivity of SiC/SiC Composite

Jalal EL Yagoubi, Jacques Lamon, Jean-Christophe Batsale, and Marion Le Flem

Abstract This work is devoted to the experimental study of the effect of mechanical damage on the thermal diffusivity of SiC/SiC minicomposite test specimens. This sample geometry is very useful for understanding the damage mechanisms and their effect on mechanical and thermal properties. Relations between constituent properties (fiber/matrix/interface) and minicomposite mechanical behavior have been developed in the literature. Nevertheless, literature review showed that no experimental study has focused on the thermal properties of minicomposite under mechanical stresses. Lock-in thermography was used to measure the thermal diffusivity during tensile tests while acoustic emission technique allowed damage to be monitored. In this work, it is demonstrated that the evolution of thermal diffusivity is a reliable indicator of matrix damage. Drop in thermal properties appears to be highly sensitive to matrix crack density.

Keyword Damage • Diffusivity • Composite • Thermography • Acoustic emission

23.1 Introduction

Damage – thermal diffusivity relationship is a crucial issue for both structural health monitoring and thermal design of ceramic matrix composites. For more than a decade, SiC/SiC Ceramic Matrix Composites (CMC) have been investigated with a view to use in nuclear reactors of new generation as refractory fuel cladding. This structural element should combine mechanical strength, resistance to irradiation and oxidation, and high thermal conductivity [1–3]. The SiC/SiC shell must contain the fuel and transmit the large amount of heat produced by the nuclear reaction, under severe operating conditions (temperature, loading, irradiation). Although they consist of ceramic constituents, they exhibit a damageable elastic behavior and a much higher toughness than bulk ceramics. Damage results from cracks located in the matrix and at fibre/matrix interfaces which cause disruption of heat transfer and degradation of thermal conductibility with damage.

The local disturbances induced by cracks are revealed by infrared imaging. Thermal contrasts are potentially used in non-destructive testing of composites to detect delamination cracks in laminates [4] or in impact damage [5]. Pioneering work in [6] on unidirectional composites (RBSN/SiC_f) and in [7] on laminated composites has clearly demonstrated the effect of interfacial cracks on thermal diffusivity. The experimental results given in [8–10] for multidirectional reinforced composite, showed that measurements of thermal diffusivity during mechanical test monitor the progression of damage.

The mechanical behavior of CMCs and damage phenomena are well known in the literature [11–14]. However, the relationship between the degradation of thermal properties and damage has not been established experimentally.

J. EL Yagoubi (✉)
LCTS, UMR5801 Pessac, France

J. Lamon
LCTS, UMR5801 Pessac, France

LMT, Cachan, France

J.-C. Batsale
Arts et Metiers Paris Tech, UMR 5295, CNRS, Talence, France

M. Le Flem
CEA Saclay, Gif-sur-Yvette, Paris, France

M. Rossi et al. (eds.), *Residual Stress, Thermomechanics & Infrared Imaging, Hybrid Techniques and Inverse Problems, Volume 8*, Conference Proceedings of the Society for Experimental Mechanics Series, DOI 10.1007/978-3-319-00876-9_23,

Thus, the intent of the present paper is to tackle this problem by investigating the influence of damage modes on the thermal diffusivity of unidirectional composite (minicomposite) under uniaxial tension. The interest of minicomposites for the investigation of microstructure-property relations has been well demonstrated in numerous studies [14, 15]. First, from a practical point of view, the control of elaboration conditions (matrix infiltration) is not as complex as for multidirectional reinforced composites (2D, 2.5D and 3D). Then, the behavior of damaged woven composite is dictated by the longitudinal tows, which is reproduced in minicomposites [16]. Hence, minicomposite behavior has been studied extensively; This has enabled the understanding and modeling of matrix cracking and multiple fibre breaks in [13, 14] and static fatigue behavior in [17, 18]. However, no experimental study has focused previously on the thermal behavior of minicomposite under tensile load. A previous paper combined micromechanics-based equations of matrix multiple cracking and equations of heat transfer in the vicinity of cracks to end up with thermal conductivity-deformation relation [19]. This paper presents an original experimental approach based on a combination of various techniques for monitoring of damage and thermal behavior of minicomposites during tensile tests. Finally, thermal and mechanical behaviors of minicomposites are compared in order to deduce the relationship between damage and changes in thermal properties.

23.2 Minicomposite

Minicomposite test specimens were made of single yarns consisting of 500 commercial silicon carbide fibres, a Pyrocarbon (PyC) interphase of few tens of nanometres, and a silicon carbide matrix deposited via Chemical Vapor Infiltration (SiC CVI). Matrix thickness ranged from 2–3 μm at the core to 8–10 μm at the rim. Figure 23.1 shows porosity inherent to the CVI process of matrix deposition. Image analysis of polished sections was used for the determination of specimen cross section areas as well as the fractions of fibre (V_f) and matrix (V_m). Two batches of minicomposites were prepared:

M1 : reinforced by *Hi-Nicalon S* commercial fibres ($V_f = 0.38$);
M2 : reinforced by *Hi-Nicalon* commercial fibres (Hi-Ni) ($V_f = 0.3$);

The main properties of SiC fibres are given in Table 23.1.

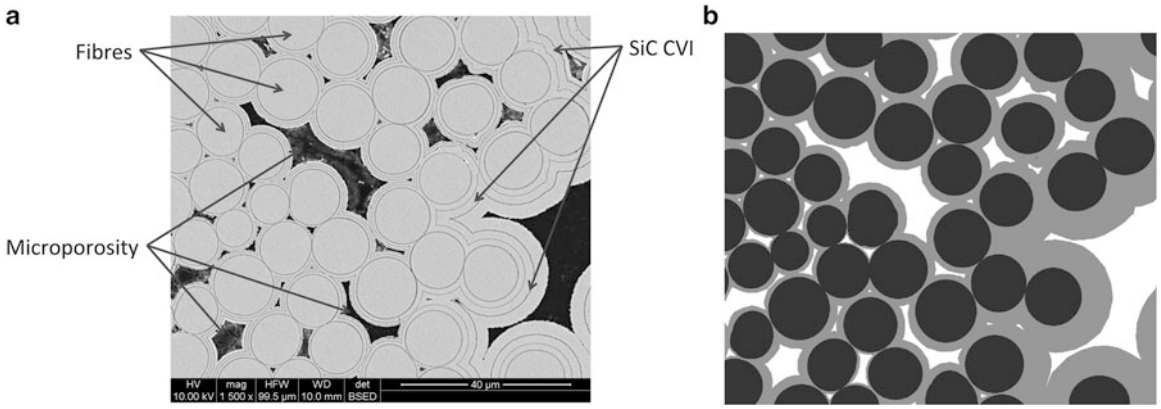

Fig. 23.1 (**a**) Scanning Electron Microscopy micrographs of the cross section of a SiC/PyC/SiC minicomposite showing the different phases (matrix, fibre and porosity) (**b**) Image analysis for the estimation of the fractions of fibres and matrix

Table 23.1 Selected properties of SiC fibres (at 25°C) [a][20] [b][21] [c][22]

Fibres	Hi-Ni-S	Hi-Ni
Young's modulus (GPa)	408[a]	270[a]
Strain to failure (%)	0.63[a]	1.04[a]
Density (g.cm^{-3})	3[a]	2.74[a]
Thermal conductivity (W.m^{-1}. K^{-1})	18[b]	8[b]
Specific heat capacity (J.kg^{-1}. K^{-1})	700[c]	690[c]

23.3 Experimental

The experimental setup (Fig. 23.2) has been developed in order to study simultaneously the thermal and mechanical behaviors of minicomposite. Minicomposites under load were heated using a laser beam while the thermal response was recorded using an Infrared camera. Acoustic emission technique was used for damage monitoring. It gives real-time information on initiation and evolution of damage. It was also useful to check that damage did not grow during the measurement of the thermal diffusivity when the load was kept constant. In the following, the experimental setup is described in detail.

23.3.1 Tensile Tests

Tensile tests were performed using an electromechanical testing machine (MTS). Metallic cylindrical tabs were glued at both ends of specimens. The spacing distance (gauge length) was 30 mm. Specimens strain was derived from the displacement of the upper crosshead using two inductive sensors (LVDT) for checking specimen straightness and grips alignment. A compliance calibration technique was used in order to estimate the deformation of grips that was subtracted from crosshead displacement (Cs = 0.3 μm.N^{-1}) [23]. Tensile tests were carried out under quasi-static conditions with a crosshead displacement rate of 0.05 mm/min. The crosshead displacement was kept constant during thermal measurements.

23.3.2 Damage Characterization

An acoustic emission sensor (*Pico* sensors from Euro Physical Acoustic) was placed on each machine grips. Acoustic emission events with an amplitude higher that the threshold (40 dB) were recorded during entire test, i.e. during loading-unloading at

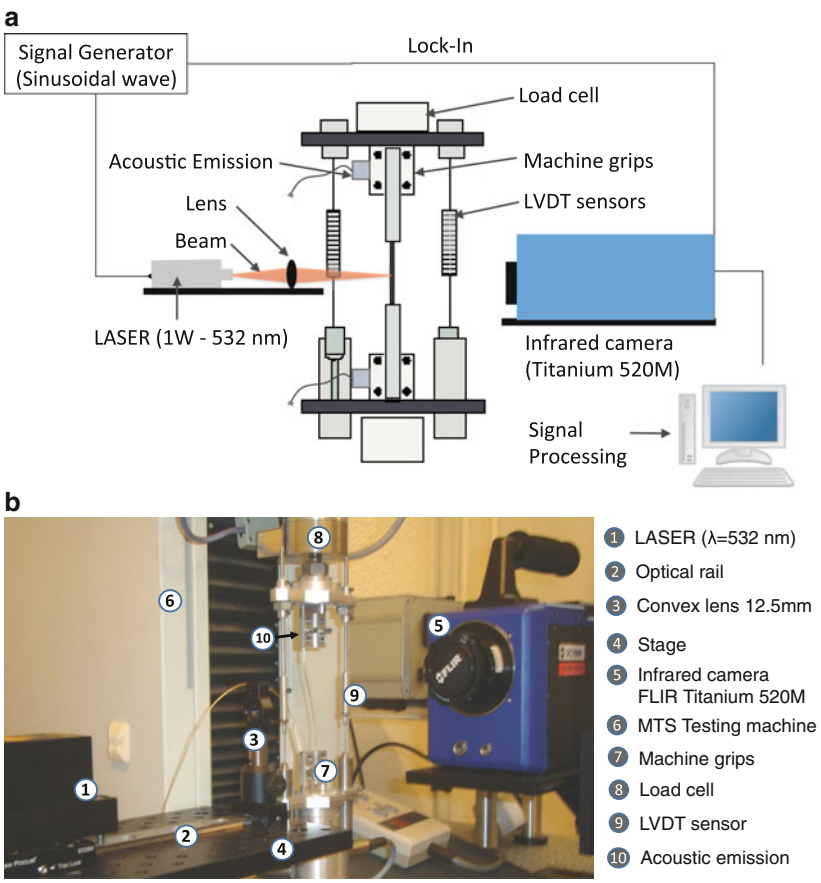

Fig. 23.2 Experimental setup for the measurement of thermal diffusivity under axial tensile test

constant rate as well as during the thermal diffusivity measurement under constant load. Then, the samples were observed after failure in a Scanning Electron Microscope, using backscattered electron imaging, in order to count the number of matrix cracks and measure crack spacing distance.

23.3.3 Thermal Diffusivity Measurement

The retained method was initially proposed by Angström [24] and adapted subsequently by several authors [25–27]. It consists in creating a local oscillating heat source in the material and to process the temperature profile along the axial direction. When periodical steady state is reached, a damped thermal wave out of phase propagates through the solid medium. The estimation procedure of longitudinal thermal diffusivity, detailed in the next section, is based on the evaluation of the damping and phase shift.

The local modulated heat source is provided by a laser beam of 532 nm wavelength emitted by a diode (1 W). The later is powered by a signal generator that produces sine waves at the selected frequency. Then, the laser beam passes through a lens to be focused on a diameter of about 100 µm at the surface of specimen. The thermal excitation system (diode and lens) is mounted on three axes precision positioning stage in order to accurately control the spatial position of the spot. Thus, a heat source is generated at the center of the minicomposite placed in the grips of the tensile machine.

An infrared camera (Titanium 520M from FLIR) captures the infrared signal (IR) emitted by the outer surface of specimen. It has 320 ×256 InSb sensors and is equipped with a 50 mm objective with an extension ring to reduce spatial resolution to a size of about 80 µm. Infrared images are recorded at 100 Hz. Then a dedicated software (Altair-LI also supplied by FLIR) is used to compute maps of damping and phase shift. It is worthnoting that the reference phase is assumed to be given by the signal generator that is connected to the appropriate Lockin input of the camera. Infrared signal processing to estimate thermal diffusivity, is detailed in the next section.

23.4 Infrared Signal Processing

In 1861, Angström [24] measured the thermal diffusivity of a long and homogeneous isotropic metallic bar. A periodic sinusoidal heat flux was generated, temperature was measured at the surface. Assuming one-dimensional heat transfer, this experiment can be described by the partial differential equation in Eq. 23.1 with the boundary and initial conditions given in Eq. 23.2:

$$\frac{\partial^2 T}{\partial x^2} - \frac{hp}{\lambda_x S} T = \frac{1}{a_x} \frac{\partial T}{\partial t} \tag{23.1}$$

Where h is the convective heat transfer coefficient, p is the perimeter, S is the cross-sectional area, λ_x and a_x are respectively longitudinal thermal conductivity and diffusivity.

$$\begin{aligned} t &= 0 && T(x,t) = 0 \\ x &= 0 && -\lambda_x \frac{\partial T}{\partial x} = \phi_o + \Delta\phi_o sin(\omega t + \varphi_o) \\ x &\to \infty && T(x,t) = 0 \end{aligned} \tag{23.2}$$

The local heat flux is described by the following quantities: ϕ_o is the offset, $\Delta\phi_o$ is the amplitude, ω is the pulsation and φ_o is the reference phase.

In the periodic steady state, the solution $T(x, t)$ of Eq. 23.1 is then expressed as the sum (Eq. 23.3) of a steady component, noted $\overline{T}(x)$ and a periodic component, noted $T^*(x, t)$ with a pulsation ω imposed by the heat flux at $x = 0$.

$$T(x,t) = \overline{T}(x) + T^* \tag{23.3}$$

For the purpose of thermal diffusivity identification, one focuses only on the periodic components given in Eq. 23.4:

$$T^* = A(x)cos(\omega t + \varphi(x)) \tag{23.4}$$

The amplitude and the phase difference of the wave are respectively given by Eqs. 23.5 and 23.6:

$$A(x) = A_o exp(-z_r x) \tag{23.5}$$

$$\varphi(x) = \varphi_o - z_i x \tag{23.6}$$

where z_i and z_r are as follows (Eqs. 23.7 and 23.8):

$$z_i = -\frac{\partial\varphi(x)}{\partial x} = \sqrt{\frac{1}{2a_x}\left[\sqrt{\left(\frac{hp}{\rho C_p S}\right)^2+\omega^2} - \frac{hp}{\rho C_p S}\right]} \tag{23.7}$$

$$z_r = -\frac{\partial \ln(A(x))}{\partial x} = \sqrt{\frac{1}{2a_x}\left[\sqrt{\left(\frac{hp}{\rho C_p S}\right)^2+\omega^2} + \frac{hp}{\rho C_p S}\right]} \tag{23.8}$$

The product of terms (z_i, z_r) is denoted z_π and given by the following equation (Eq. 23.9):

$$z_\pi = z_i.z_r = \frac{\omega}{2a_x} \tag{23.9}$$

Then, for several experiments conducted at different pulsations (k experiments), the previous scalar equation (Eq. 23.9) turns to a vectorial expression (Eq. 23.10):

$$\underline{Z_\pi} = \frac{1}{2a_x}\underline{\Omega} \tag{23.10}$$

where $\underline{\Omega}$ and $\underline{Z_\pi}$ are the vectors associated to ω and z_π.

Finally, longitudinal thermal diffusivity is calculated using the least squares method [27]:

$$a_x = \frac{1}{2(\underline{\Omega}^T \cdot \underline{\Omega})^{-1} \cdot \underline{\Omega}^T \cdot \underline{Z_\pi}} \tag{23.11}$$

23.5 Results and Discussion

23.5.1 Tensile Behavior

The tensile stress-strain curves (Fig. 23.3) exhibit the features of the well-known elastic damageable behavior of CMCs that has been investigated in previous papers [13, 14, 28]:

- an initial linear elastic domain of deformations for strains smaller than 0.1 %
- then, a non linear domain with upward curvature indicative of increasing compliance associated to transverse matrix cracking (for strains smaller than 0.3 %)
- a second linear domain indicative of constant compliance, that is attributed to deformation of fibres
- and for strains close to ultimate failure, a non linear domain with upward curvature, indicative of fibre failures.

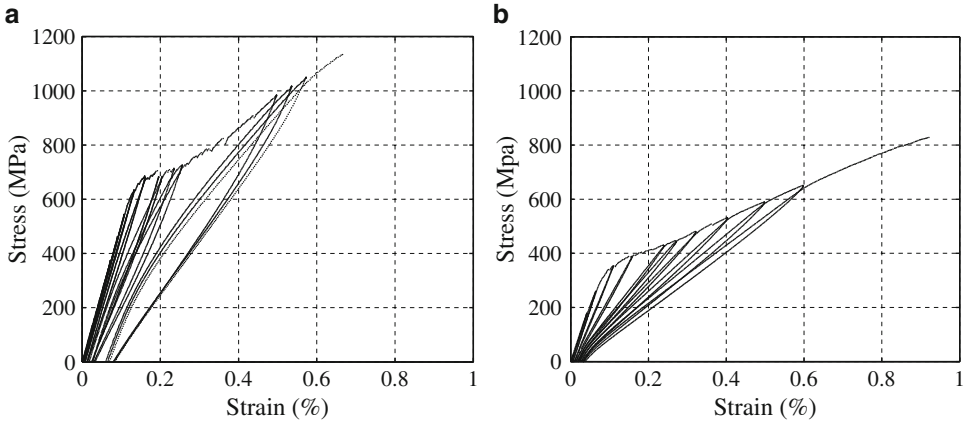

Fig. 23.3 Tensile stress-strain curves that exhibit the features of the well-known elastic damageable behavior of SiC/SiC composites. (**a**) M1 (Hi-Ni-S fibres). (**b**) M2 (Hi-Ni fibres)

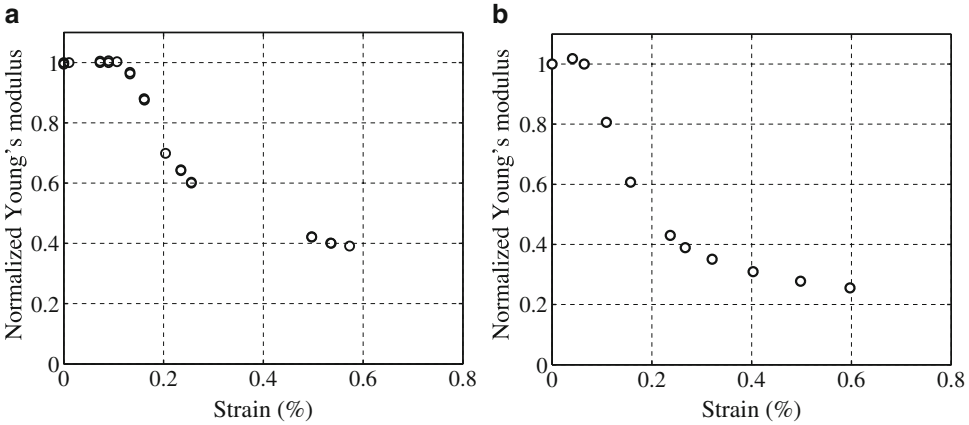

Fig. 23.4 Degradation of Young's modulus of SiC/SiC minicomposites extracted from loading-unloading cycles during axial tensile tests. (**a**) M1 (Hi-Ni-S fibres). (**b**) M2 (Hi-Ni fibres)

Table 23.2 Material's properties derived from tensile tests and microstructural observations

Minicomposite	M1	M2
Young's modulus (GPa)	395	360
Strain at the linear limit (%)	0.1	0.06
Strain at the matrix cracking saturation (%)	0.37	0.39
Strain to failure (%)	0.73	0.9
Mean crack spacing distance (at saturation) (μm)	376	128
Interfacial strength	Weak	Medium

Loading-unloading cycles demonstrate decrease in elastic modulus (Fig. 23.4). Furthermore, the presence of residual strains and hysteresis loop during loading-unloading, are both indicative of dissipative mechanisms such as cracking and friction at fibre/matrix interfaces. Finally, main material's features derived from the tensile tests are summarized in Table 23.2.

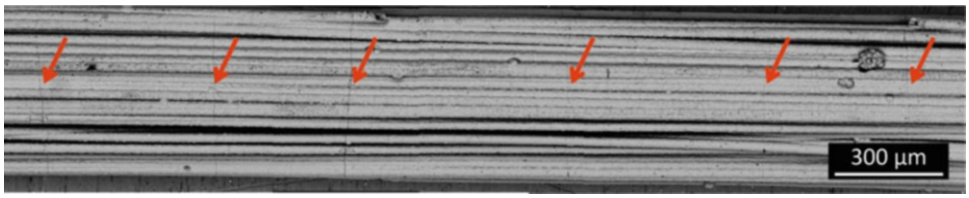

Fig. 23.5 Scanning Electron Microscopy micrographs showing randomly distributed matrix cracks after minicomposite failure

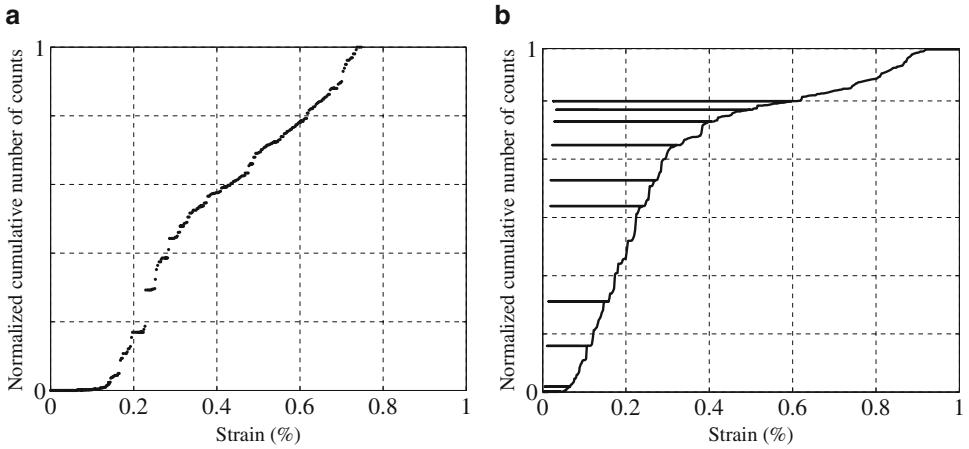

Fig. 23.6 Dimensionless cumulative number of acoustic emission counts during axial tensile tests. (**a**) M1 (Hi-Ni-S Fibres). (**b**) M2 (Hi-Ni Fibres)

23.5.2 Damage Characterization

23.5.2.1 Microscopy

Scanning Electron Microscopy images show matrix cracks perpendicular to fibre direction after minicomposite failure (Fig. 23.5). In the case of the minicomposite *M1*, the average crack spacing distance is 376 µm and the standard deviation is 167 µm. The material *M2* exhibits a higher crack density, the average crack spacing distance is 128 µm and the standard deviation is 43 µm. Then, one can derive the ultimate number of cracks (N_s) from the average crack spacing distance ($\langle \Delta L \rangle$) according to Eq. 23.12. Hence, when the matrix cracking is saturated, the total number of cracks is equal to 79 for *M1* and 234 for *M2*.

$$N_s = \frac{L - \langle \Delta L \rangle}{\langle \Delta L \rangle} \tag{23.12}$$

Where L is the minicomposite's length (L = 30 mm).

23.5.2.2 Analysis of Acoustic Emission

Figure 23.6 depicts the evolution of the cumulated number of counts during tensile tests. The cumulative number of counts has been shown to be equivalent to energy in previous work [29, 30]. It reveals the four domains that have been identified on the stress-strain curves:

- first, there was no acoustic emission at low strains below 0.08 % for minicomposite *M1* and 0.04 % for minicomposite *M2*, which indicates elastic deformations.

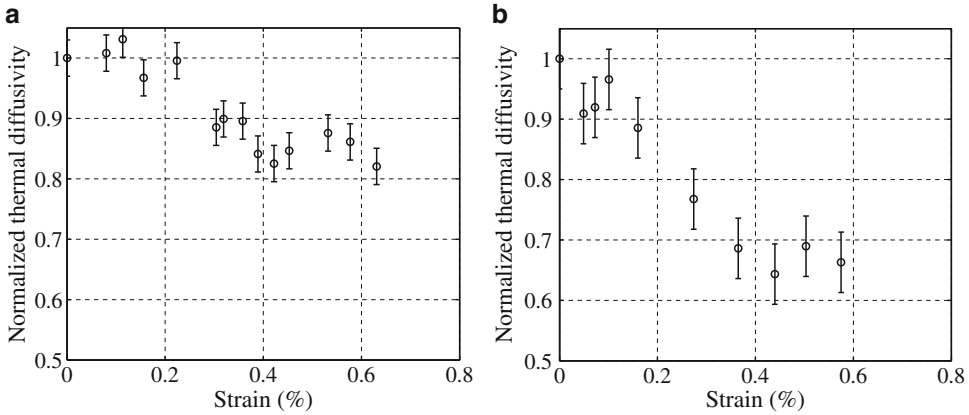

Fig. 23.7 Evolution of the longitudinal thermal diffusivity of minicomposites measured during axial tensile tests. (**a**) M1 (Hi-Ni-S fibres) ($a_o = 11\,\mathrm{mm^2.s^{-1}}$). (**b**) M2 (Hi-Ni fibres) ($a_o = 6.2\,\mathrm{mm^2.s^{-1}}$)

- the steady acoustic activity in the second part of the curve results from matrix cracking. It did not include fibre failures, as suggested by previous works [14, 16].
- in the third part, the acoustic activity is also steady and much less intense. It reflects a different and less severe phenomenon, such as fibre/matrix sliding.
- and, the final intense activity announces ultimate failure of fibres.

23.5.3 Thermal Diffusivity

Thermal diffusivity was estimated under constant load during the tensile tests. It is worth pointing out that acoustic activity was continuously recorded. The plots of cumulative number of counts clearly show that damage did not grow during the thermal characterization. The thermal diffusivity data reveals three of the domains that have been identified above (Fig. 23.7).

1. Under low strains corresponding to elastic deformations, thermal diffusivity was constant. This indicates that there was no disturbance, as expected with elastic behavior. Then, this shows that elastic deformations do not affect thermal diffusivity.
2. Under higher strains (<0.4 %) thermal diffusivity decreased by 10 % for minicomposite *M1* and by 30 % for *M2*. This agrees with the phenomenon of matrix cracking that occurs in this deformation range.
3. At strains >0.4 %, thermal diffusivity was constant. This suggests that new causes of disturbance did not appear. This is in agreement with the phenomena attributed to this domain of deformation (i.e. deformation of fibres and fibre sliding) that do not increase damage. Nevertheless, it is worth noting that the measurement of diffusivity was not possible at strains close to ultimate failure because of instability at the end of the test.

23.5.4 Relationship Between Damage and Thermal Diffusivity

In Fig. 23.8, the relative diffusivity (Eq. 23.13) is compared to acoustic emission (Eq. 23.15) and elastic modulus data (Eq. 23.14) for deformations up to 0.65 %. The agreement in data indicates that elastic modulus, thermal diffusivity and acoustic emission counts are equivalent indicators of matrix crack density.

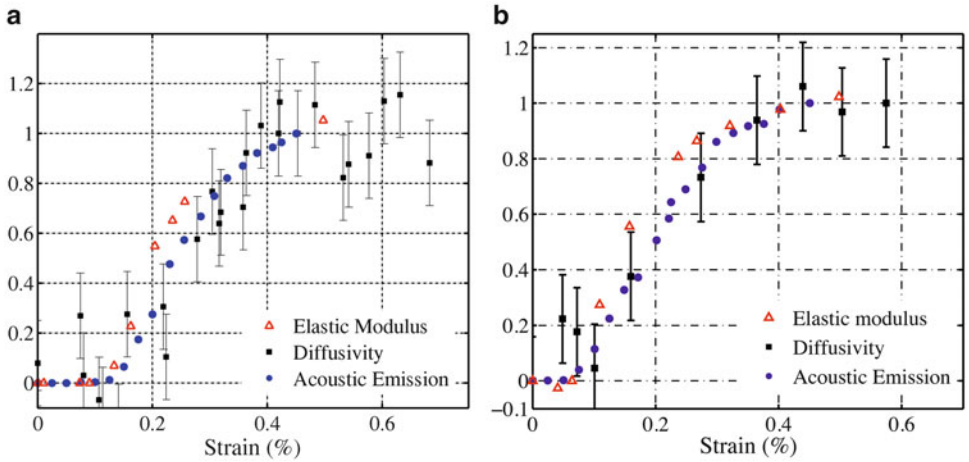

Fig. 23.8 Comparison of damage indicators derived from elastic modulus, thermal diffusivity and acoustic emission during axial tensile tests. (**a**) M1 (Hi-Ni-S fibres). (**b**) M2 (Hi-Ni fibres)

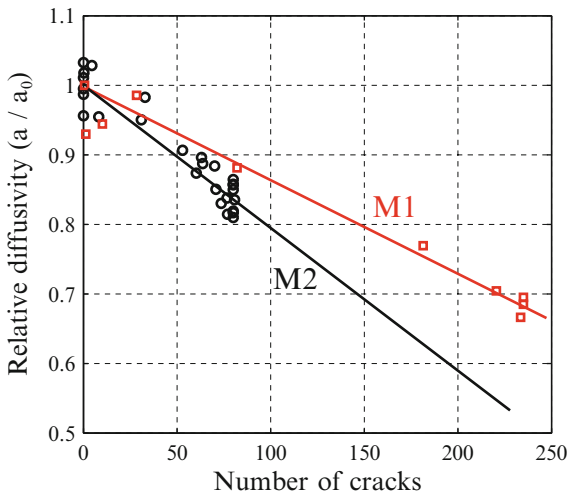

Fig. 23.9 Empirical relationship between number of cracks and diffusivity

$$d_a = \frac{a(\varepsilon)}{a_0} \tag{23.13}$$

$$d_E = \frac{E(\varepsilon)}{E_0} \tag{23.14}$$

$$d_{AE} = \frac{c(\varepsilon)}{c(\varepsilon_{sat})} \tag{23.15}$$

where a_0, E_0 are the initial thermal diffusivity and elastic modulus, c is the cumulated number of counts, and ε_{sat} is the strain at matrix cracking saturation. Then, Fig. 23.9 shows the empirical relationship between thermal diffusivity and number of matrix cracks derived from acoustic emission. Diffusivity is inversely proportional to the number of cracks according to Eq. 23.16. The slope β is 0.002 for *M1* and 0.0013 for *M2*.

$$\frac{a}{a_0} = 1 - \beta N \tag{23.16}$$

This relation was expected from the above comparison of acoustic emission and thermal diffusivity data since it has been shown in [30] that the number of acoustic emission counts during matrix cracking provides a satisfactory measurement of crack density. A close form for the coefficient β can be developed by combining models of fragmentation with thermal equations. This will be proposed in a next paper. Furthermore, because of the instability which is inherent to fibres failure, it was difficult to monitor the effect of fibre breakage on the thermal diffusivity. It seems that it can be concluded that thermal diffusivity measurement confirmed that fibre failures occurred at high strains above 0.7 %.

23.6 Conclusion

An experimental approach to damage-thermal diffusivity relationship was developed on SiC/SiC minicomposites. The longitudinal thermal diffusivity was measured during axial tensile tests using lock-in thermography. Evolution of damage was monitored by acoustic emission technique associated to SEM observations. Thermal diffusivity was found to be inversely proportional to the number of matrix cracks. Data on thermal diffusivity degradation confirmed previous results on damage in ceramic matrix composites. They indicated that matrix damage and fibre failures appear in sequence. They allowed understanding to be refined on damage mechanisms characterized by Young's modulus changes or acoustic emission count numbers. The longitudinal thermal diffusivity was found to be a reliable indicator of matrix damage in minicomposites under uniaxial tensile stresses. In the deformation range associated to matrix cracking, this is a damage parameter equivalent to Young's modulus and acoustic emission. Yet, elastic modulus decreased after saturation of matrix cracking, while diffusivity remained constant in the same deformation range which was attributed to sliding at fibre/matrix interface. This phenomenon is consistent with Young's modulus decrease, acoustic emission and residual strains increase. This mechanism did not affect thermal diffusivity.

The comparison of models of matrix fragmentation and thermal equations will be useful to assess the damage-thermal property relationships with a view to further extension to multiaxial conditions.

References

1. Jones R, Steiner D, Heinisch H, Newsome G, Kerch H (1997) Radiation resistant ceramic matrix composites. J Nucl Mater 245:87–107
2. Youngblood G, Senor D, Jones R, Graham S (2002) The transverse thermal conductivity of 2d-sic/sic composites. Compos Sci Technol 62:1127–1139
3. Zinkle S, Busby J (2009) Structural materials for fission and fusion energy. Mater Today 12:12–19
4. Balageas D, Déom A, Boscher D (1987) Characterization and nondestructive testing of carbon-epoxy composites by a pulsed photothermal method. Mater Eval 45:456–465
5. Bhatt R, Choi S, Cosgriff L, Fox D, Lee K (2008) Impact resistance of environmental barrier coated sic/sic composites. Mater Sci Eng A 476:8–19
6. Bhatt H, Donaldson K, Hasselman D, Bhatt R (1990) Role of the interfacial thermal barrier in the effective thermal diffusivity/conductivity of sic-fiber-reinforced reaction-bonded silicon nitride. J Am Ceram Soc 73:312–316
7. Hasselman D, Venkateswaran A, Tawil H (1991) Role of interfacial debonding and matrix cracking in the effective thermal diffusivity of sic-fibre-reinforced chemical vapour deposited sic matrix composites. J Mater Sci Lett 10:1037–1042
8. Krapez J, Spagnolo L, Frieb M, Maier H, Netter F (2004) Measurement of in-plane diffusivity in non homogeneous slabs by applying flash thermography. Int J Therm Sci 43:967–977
9. Bamford M, Batsale J, Fudym O (2009) Nodal and modal strategies for longitudinal thermal diffusivity profile estimation: application to the non destructive evaluation of sic/sic composites under uniaxial tensile tests. Infrared Phys Technol 52:1–13
10. Farooki J, Sheikh M (2006) Finite element modelling of thermal transport in ceramic matrix composites. Comput Mater Sci 37:361–373
11. Aveston J, Cooper G, Kelly A (1971) Single and multiple fracture. In: The properties of fiber fiber composites conference proceedings of the national physical laboratory. IPC Science and Technology Press, Surrey
12. Cao H, Bischoff E, Sbaizero O, Ruhle M, Evans A, Marshall D (1990) Effect of interfaces on the properties of fiber-reinforced ceramics. J Am Ceram Soc 73:1691–1699
13. Guillaumat L, Lamon J (1996a) Fracture statistics applied to modelling the non-linear stress-strain behavior in microcomposites: influence of interfacial parameters. Int J Fract 82:297–316
14. Lissart N, Lamon J (1997) Damage and failure in ceramic matrix minicomposites: experimental study and model. Acta Mater 45:1025–1044
15. Naslain R, Lamon J, Pailler R, Bourrat X, Guette A, Langlais F (1999) Micro/minicomposites: a useful approach to the design and development of non-oxyde cmcs. Composites A 30:537–547
16. Lamon J (2002) Micromechanics-based approach to the mechanical behavior of brittle matrix composites. Compos Sci Technol 61:2259–2272
17. Pailler F, Lamon J (2005) Micromechanics based model of fatigue/oxidation for ceramic matrix composites. Compos Sci Technol 65:369–374
18. Laforet A (2009) Rupture différée en fatigue statique, aux très hautes températures (800 °c-1300 °c) des fils hi-nicalon, des composites hi-nicalon pyc/sic et des composites hi-nicalon pyc/b4c. Phd thesis, University of Bordeaux

19. El Yagoubi J, Lamon J, Batsale J-C, Le Flem M (2010) Model of the influence of damage on the thermal properties of ceramic matrix composites. Ceram Eng Sci Proc 31:361–372
20. Dong S, Chollon G, Labrugère C, Lahaye M, Guette A, Bruneel J (2001) Characterization of nearly stoichiometric sic ceramic fibers. J Mater Sci 36:2371–2381
21. Yamada R, Igawa N, Taguchi T, Jitsukawa S (2002) Highly thermal conductive, sintered sic fiber-reinforced 3d-sic/sic composites: experiments and finite-element analysis of the thermal diffusivity/conductivity. J Nucl Mater 307:1215–1220
22. Sauder C (2004) Effect of irradiation on sic fibres. Internal report, LCTS
23. Gauthier W (2007) Delayed failure at intermediate temperatures (<800 °c) of sic-based tows and filaments. Phd thesis, Bordeaux University
24. Angström A (1861) Bestimmung der warme leitung durch periodische temperaturanderung. Ann Phys Chem 114:513–530
25. King R (1915) A method of measuring heat conductivities. Phys Rev 6:437–445
26. Starr C (1937) An improved method for the determination of thermal diffusivities. Rev Sci Instrum 8:61–64
27. Pradère C, Goyhénèche J, Batsale J-C, Dilhaire S, Pailler R (2006) Thermal diffusivity measurements on a single fiber with microscale diameter at very high temperature. Int J Therm Sci 45:443–451
28. Guillaumat L, Lamon J (1996) Probabilistic-statistical simulation of the non-linear mechanical behavior of a woven sic/sic composite. Compos Sci Technol 56:803–808
29. Forio P (2000) Thermomechanical behavior and lifetime of a sic/sic composite with a self healing matrix. Phd thesis, University of Bordeaux
30. Lamon J (2010) Stochastic models of fragmentation of brittle fibers or matrix in composites. Compos Sci Technol 70:743–751

Chapter 24
Identification of Welding Heat Sources from Infrared Temperature Measurements

B. Beaubier, K. Lavernhe-Taillard, R. Billardon, C. Boucq, P. Laloue, and B. Darciaux

Abstract Welding-brazing is one of the various processes involving a heat source and used by car manufacturers to assemble large thin steel sheets. The maximum temperature imposed to the assembled sheets by this welding-brazing process is lower than the maximum temperature imposed by many other welding processes. However, considering the dimensions of the assembled sheets – typically less than 1 mm in thickness and more than 1 m^2 in surface – and the fact that these sheets are subjected to various forming processes by plastic deformation before being assembled, the welding-brazing process may induce more or less localized undesirable deformations of the assembly. The work presented herein is part of a study the aim of which is to develop thermo-mechanical finite element simulations of the whole process in order to predict these deformations – which may help and reduce development time and cost. The validation of such numerical simulations is based on the comparison of numerical results and experimental evidences, which requires the development of well-controlled and highly instrumented tests. This paper is dedicated to the identification of the heat source model representing the welding-brazing operation. This identification is derived from the results of welding-brazing tests instrumented with thermocouples and infrared cameras. Micrographic observations in the vicinity of the welding-brazing joint are used to (partially) validate the numerical predictions of the Heat Affected Zone (HAZ).

Keywords Heat source • IR measurement • Heat transfer • Thermomechanical analysis

24.1 Introduction

More and more efforts are made to reduce vehicle development cost and time. The development of predictive numerical tools to simulate manufacturing and assembly processes plays a key role to reach this objective. Welding-brazing is one of the processes used by PSA Peugeot Citroën SA to assemble steel sheets with a joint made of a copper-silicon alloy. These sheets are thin – typically 0.67–1 mm thick – and large – typically larger than 1 m^2. Besides, before being assembled, these sheets are always subjected to various forming processes inducing plastic deformations and residual stresses. Hence, the thermo-mechanical loading imposed by the welding-brazing process may induce undesirable more or less localized deformations of the assembled vehicle body (Fig. 24.1). These deformations depend on the heat source, clamping tools and thermo-metallurgico-mechanical behaviour of the materials. Numerical simulations of the whole process should help and avoid expensive and long experimental test campaigns when developing a new vehicle. However, the validation of such simulations – involving many complex phenomena – requires to carry on well-controlled and highly instrumented experiments.

This study is dedicated to the identification of a representative heat source model to be used when simulating the welding-brazing process with general-purpose finite element code ABAQUS [1].

B. Beaubier (✉)
LMT Cachan (ENS Cachan//CNRS UMR 8535//UPMC), 61 Avenue du Président Wilson, 94235 Cachan Cedex, France

PSA Peugeot Citroën, Centre Technique de Vélizy B, Zone aéronautique Louis Bréguet, 78140 Velizy Villacoublay, France
e-mail: benoit.beaubier@lmt.ens-cachan.fr

K. Lavernhe-Taillard • R. Billardon
LMT Cachan (ENS Cachan//CNRS UMR 8535//UPMC), 61 Avenue du Président Wilson, 94235 Cachan Cedex, France

C. Boucq • P. Laloue • B. Darciaux
PSA Peugeot Citroën, Centre Technique de Vélizy B, Zone aéronautique Louis Bréguet, 78140 Velizy Villacoublay, France

M. Rossi et al. (eds.), *Residual Stress, Thermomechanics & Infrared Imaging, Hybrid Techniques and Inverse Problems, Volume 8*, Conference Proceedings of the Society for Experimental Mechanics Series, DOI 10.1007/978-3-319-00876-9_24,

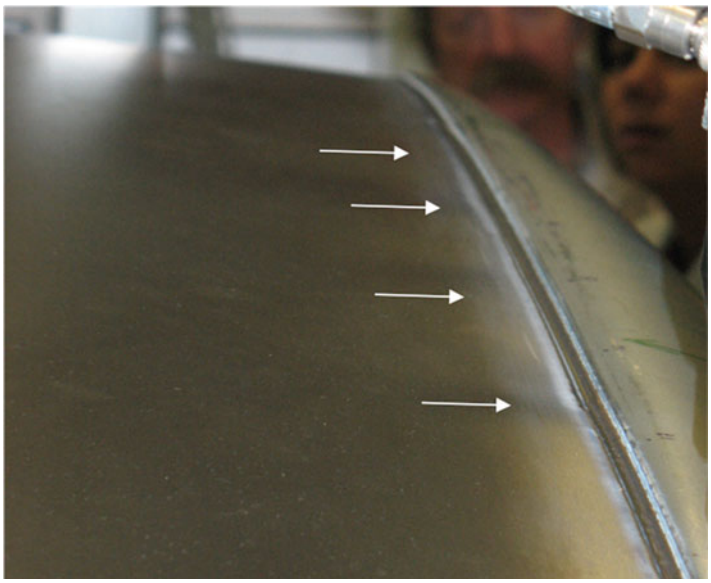

Fig. 24.1 Undesirable deformations induced by laser-brazing of the automotive roof

Table 24.1 Laser-brazing parameters used in the experimental test

Power (W)	Torch speed w_s (m/min)	Wire speed (m/min)	Clearance d (mm)	Angle α (°)	Angle β (°)	Intensity (A)
2,400	4	3.5	0	10	70	80

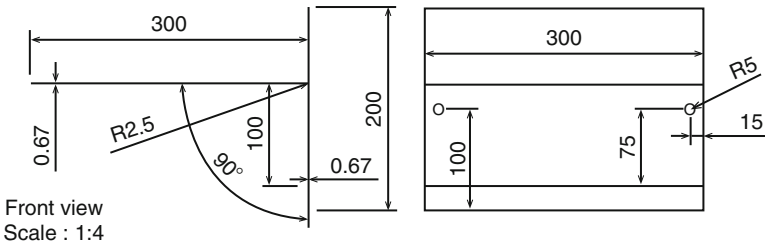

Fig. 24.2 Geometry of the welding-brazing assembly

24.2 Experimental Setup

Welding-brazing tests were performed to assemble 0.67 mm thick steel sheets with a copper-silicon alloy. The final geometry of the assembly is defined on Fig. 24.2. A plane sheet, referred as sheet (1), is laser-brazed with a V parting line on a bended sheet, referred as sheet (2), with a 90° angle.

The sheets are made of XES steel provided to PSA Peugeot Citroën by ARCELOR-MITTAL. The brazing material consists in a $CuSi_3$ filler wire provided by Air Liquide Welding.

The welding-brazing is performed with a YAG TRUMPF laser source. A power of 2.4 kW was used during this study – whereas nominal power of this source is 4 kW. Welding parameters are given in Table 24.1. Angles α and $\beta^* = 90° - \beta$ are defined in Fig. 24.3.

The temperature field on external surface of sheet (1) is measured using a FLIR SC3000 IR Camera [2]. The surface is painted in black using QUEEN black paint with very low emissivity (equal to 0.93 ± 0.03). The experimental setup is completed with 7 K-type thermocouples spot-welded on sheet (2). The locations of the thermocouples with respect to the brazing joint are defined in Fig. 24.4.

The hypotheses made to model the welding-brazing heat source are illustrated on Fig. 24.5. These hypotheses lead to a hybrid model – unlike volumetric models that are generally used to describe welding heat sources used to assemble thick parts [3]. This model consists in a 3D volumetric component that represents the heat input due to the welding-brazing joint deposit, and a 2D heat flux corresponding to the heat emitted by the laser beam. When being deposited, the joint is assumed to be at a constant temperature T_j. The surfacic heat source is modelled as a heat flux, Q_{beam}, which is, as a first

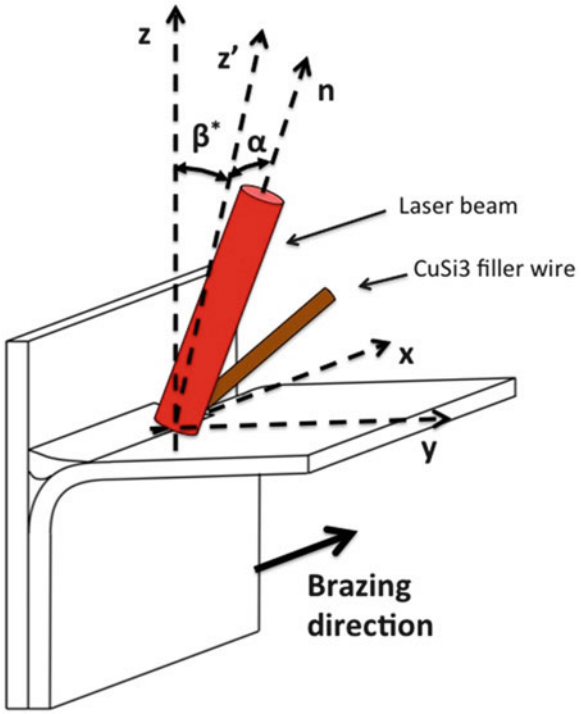

Fig. 24.3 Sketch of the laser welding-brazing operation with the filler wire

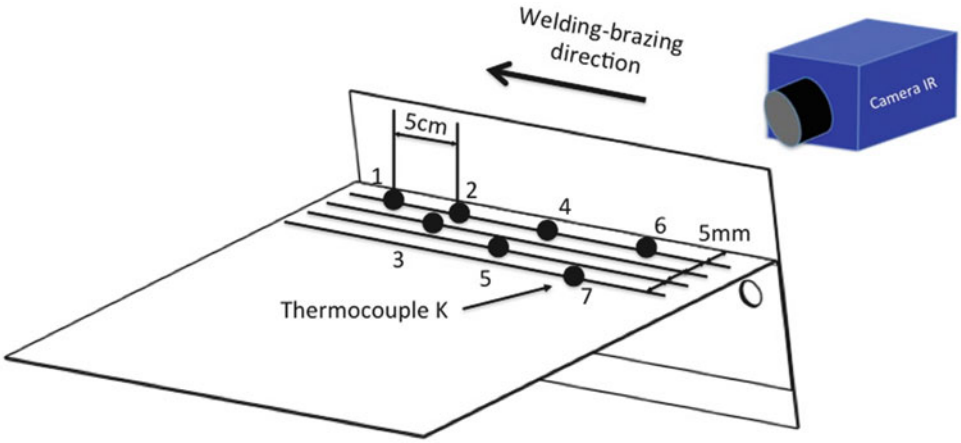

Fig. 24.4 Experimental setup used for heat source model identification

approximation, assumed to be constant and uniform over a cross-section of the laser beam. Furthermore, since temperature Tj is assumed to be close to the melting temperature of the copper-silicon alloy, i.e. roughly equal to 950 °C, the only unknown parameter representing the heat source is Q_{beam}.

The response of thermocouples 1, 2, 4 and 6 is depicted on Fig. 24.6. It appears that a steady state is reached after the heat source has moved along two-thirds of the total sample length. It is remarkable that the temperature reached by the thermocouples – that are located 5 mm away from the joint – does not exceed 260 °C.

The evolution of the temperature measured with the IR camera is depicted on Fig. 24.7 as a function of time along a line orthogonal to the laser-brazing joint – at a point where steady state has been reached. Figure 24.8 represents the temperature contour lines derived from Fig. 24.7.

Both sets of measurements, viz. with the thermocouples and the IR camera, are consistent. Moreover, it can be concluded that the heat source can be identified from the temperature measured with the IR camera at a given point during about 2 s.

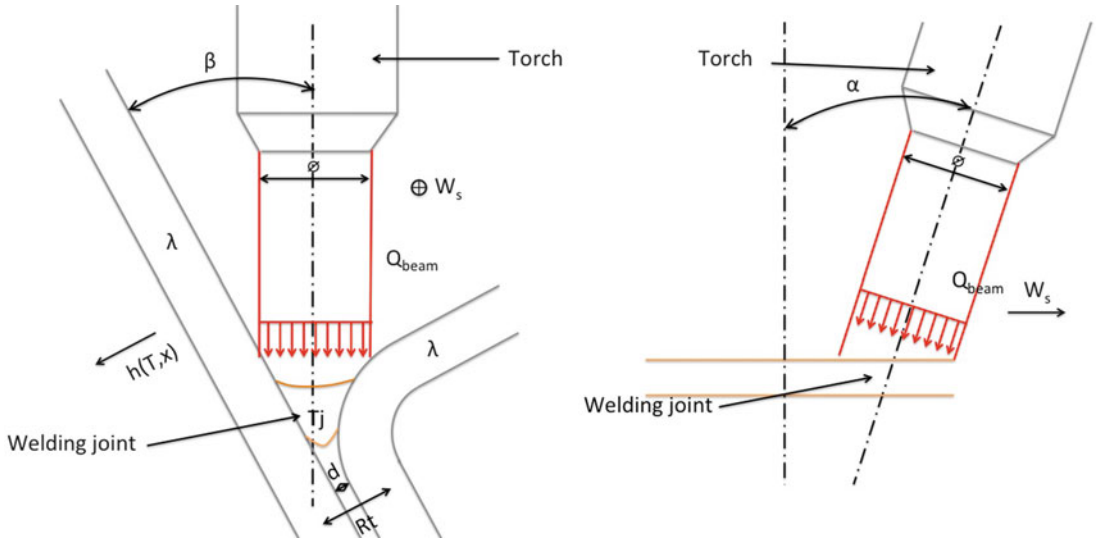

Fig. 24.5 Heat source modelling and laser brazing process parameters

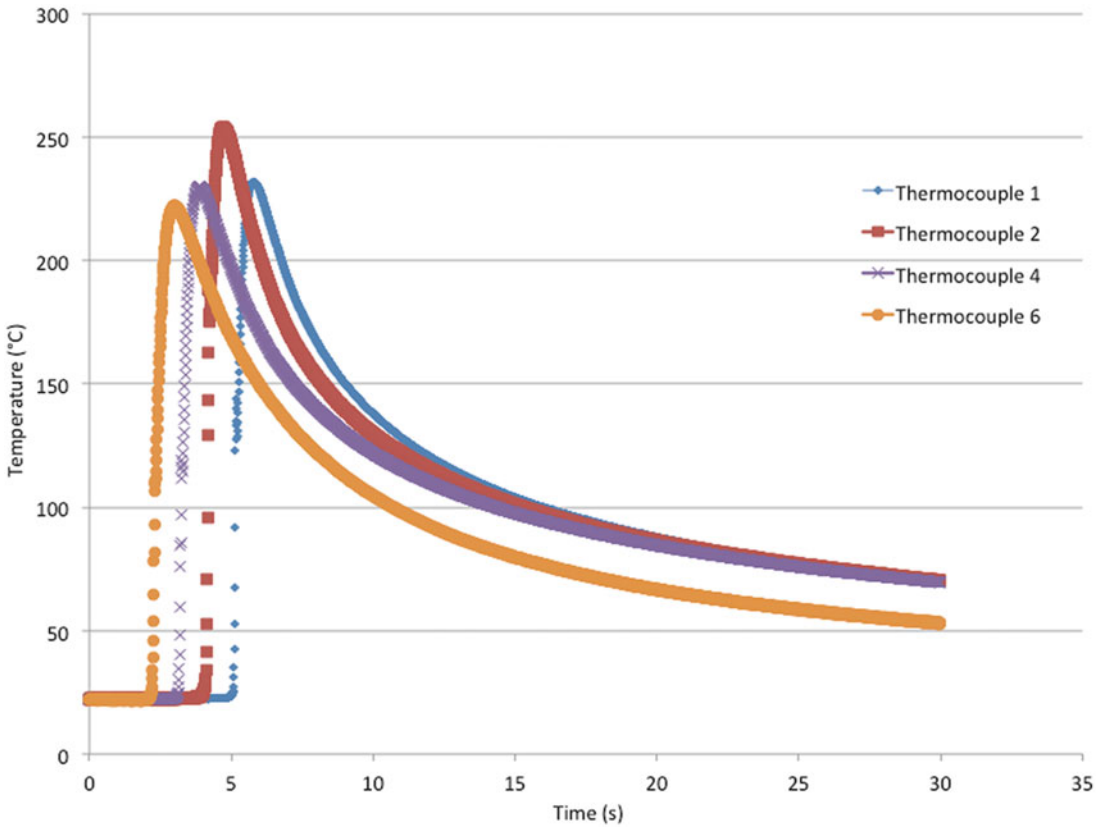

Fig. 24.6 Temperature evolution measured by thermocouples along the brazing joint

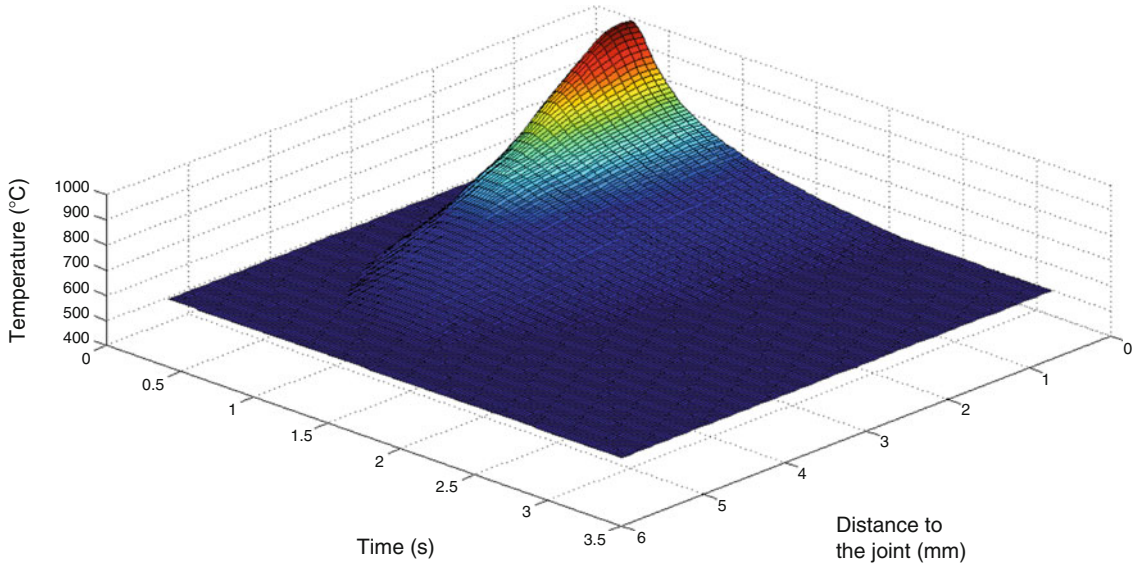

Fig. 24.7 Temperature time evolution along an orthogonal line to the brazing joint

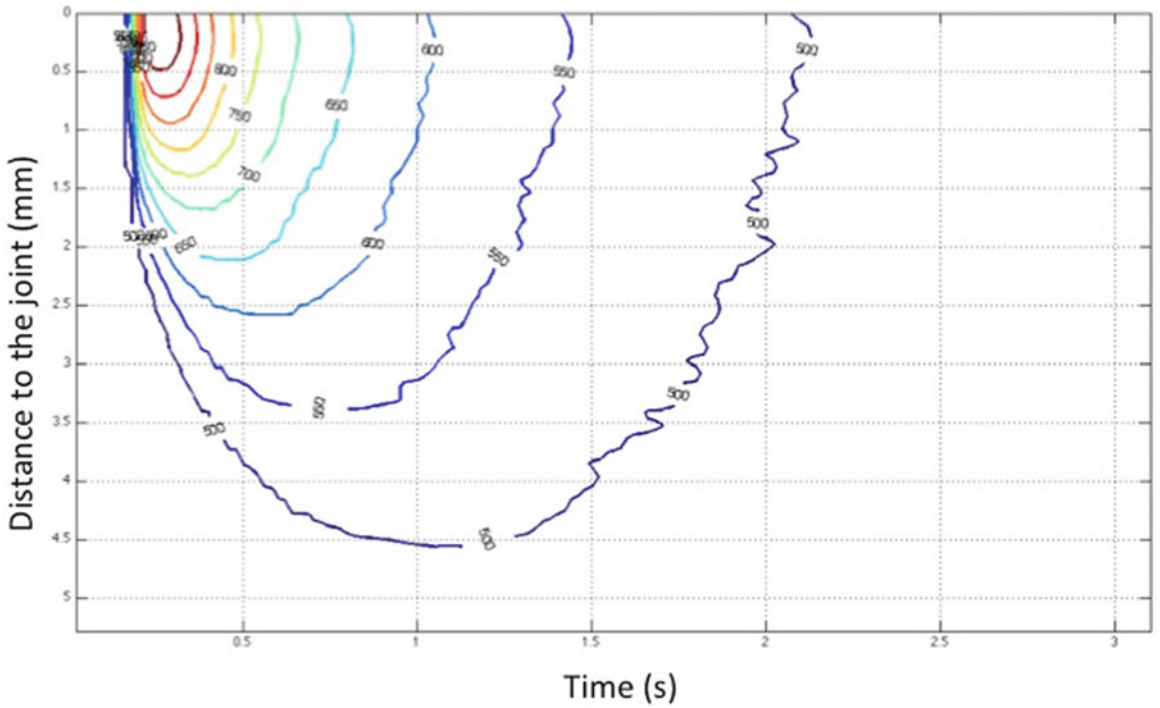

Fig. 24.8 Contour line of the temperature function of time and distance to the brazing joint

Metallurgical observations were also carried out in the vicinity of the joint as illustrated by Fig. 24.9. The microstructure of the sheet material appears as being affected by heat, not only beneath the face facing the brazing joint but also beneath the opposite face – and not in the core of the sheet. This change of microstructure corresponds to a recrystallization mechanism that is promoted by temperature and local hardening of the material. This observation is an indication that the initial hardening state of the material – as induced by the cold rolling process these steel sheets are submitted to – is not homogeneous through the thickness of the sheet.

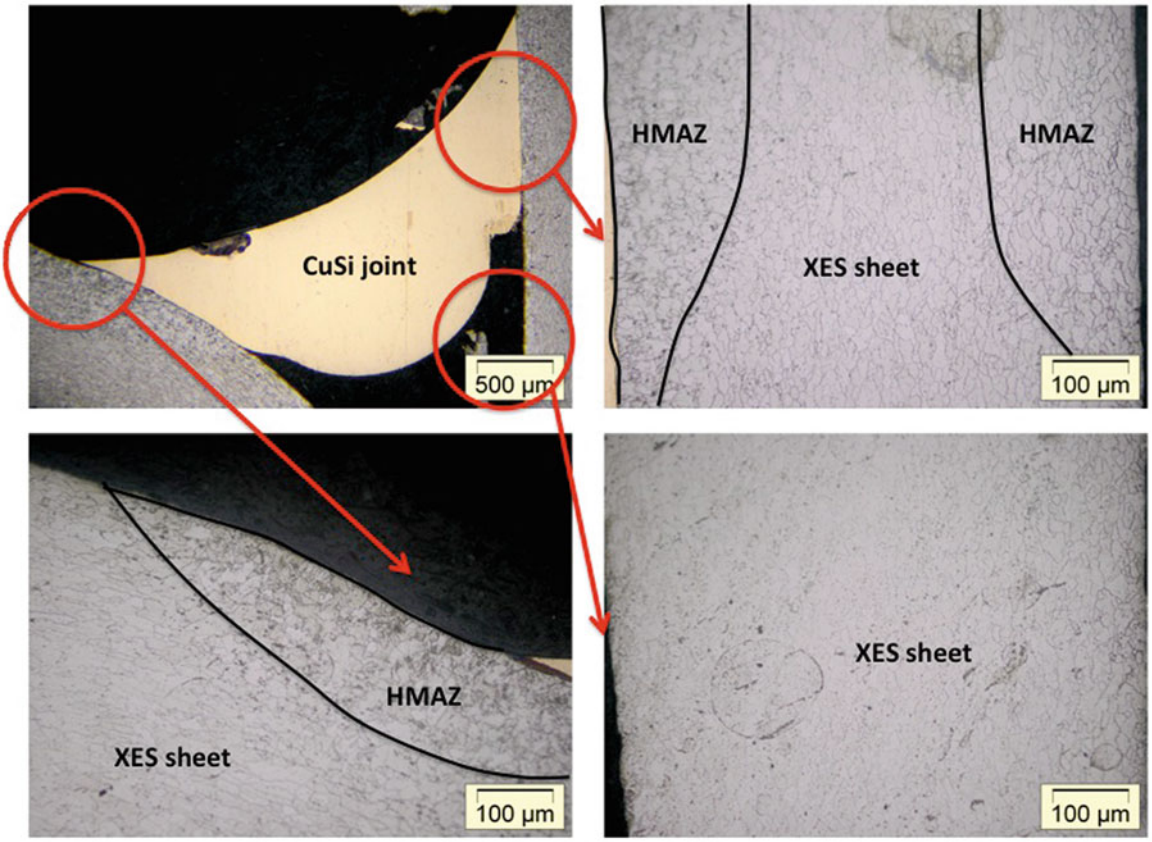

Fig. 24.9 Micrographies taken in the vicinity of the brazing joint

Besides, isothermal tension tests were performed on specimens cut from the XES steel sheet in order to characterize the thermo-mechanical behaviour of the material and identify ad hoc constitutive equations [4]. These experiments showed that the critical temperature above which material recrystallizes is as low as 450 °C. This observation together with the measurement of the extension of the Heat and Metallurgy Affected Zone in the vicinity of the brazing joint as defined on Fig. 24.9 can be used to validate heat transfer simulations of the welding-brazing process.

24.3 Identification of the Heat Source and Validation

Heat transfer numerical analyses of the welding-brazing tests were carried out using finite element code ABAQUS [1]. In the vicinity of the joint, the Heat Affected Zone – geometrically defined in accordance with previous experimental observations – is meshed with DC3D8 solid elements – that are compatible with thermo-mechanical numerical simulations. Conversely, in order to decrease computer cost, the remaining parts of the sheets are modelled with DS4 shell elements – that are also compatible with thermo-mechanical simulations. For this kind of mixed modelling, a proper connection between 3D and shell elements has to be ensured. For temperature a connection between the temperature of the master mesh (3D) and the slave mesh (shell) is performed. To cope with the temperature gradient through the thickness the proper degree of freedom (nsi) of the shell node must be connected to the proper node of the solid mesh (ni) (Fig. 24.10).

As a first approximation, the possible thermal exchange by solid contact between the sheets away from the brazing joint is not taken into account.

It is recalled that the only unknown parameter representing the heat source to be identified is Q_{beam}. The heat conductivity of the steel sheets is known. However, it must be noticed that the radiation and convection exchanges between the sheets and

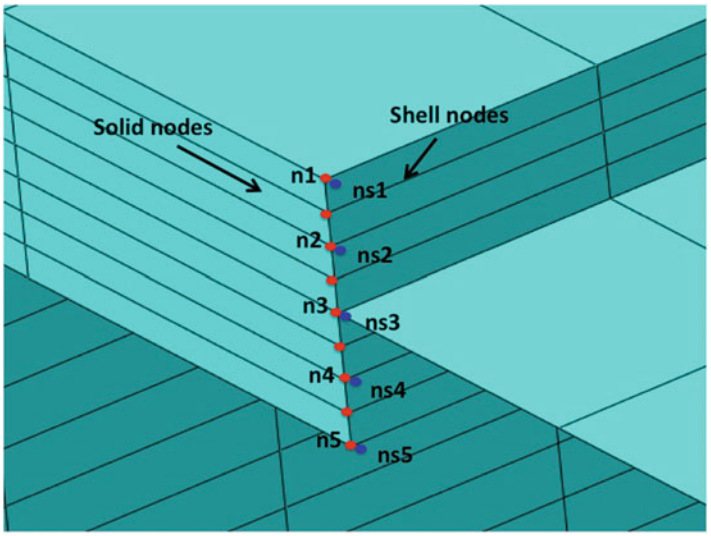

Fig. 24.10 Connection between 3D and shell meshes

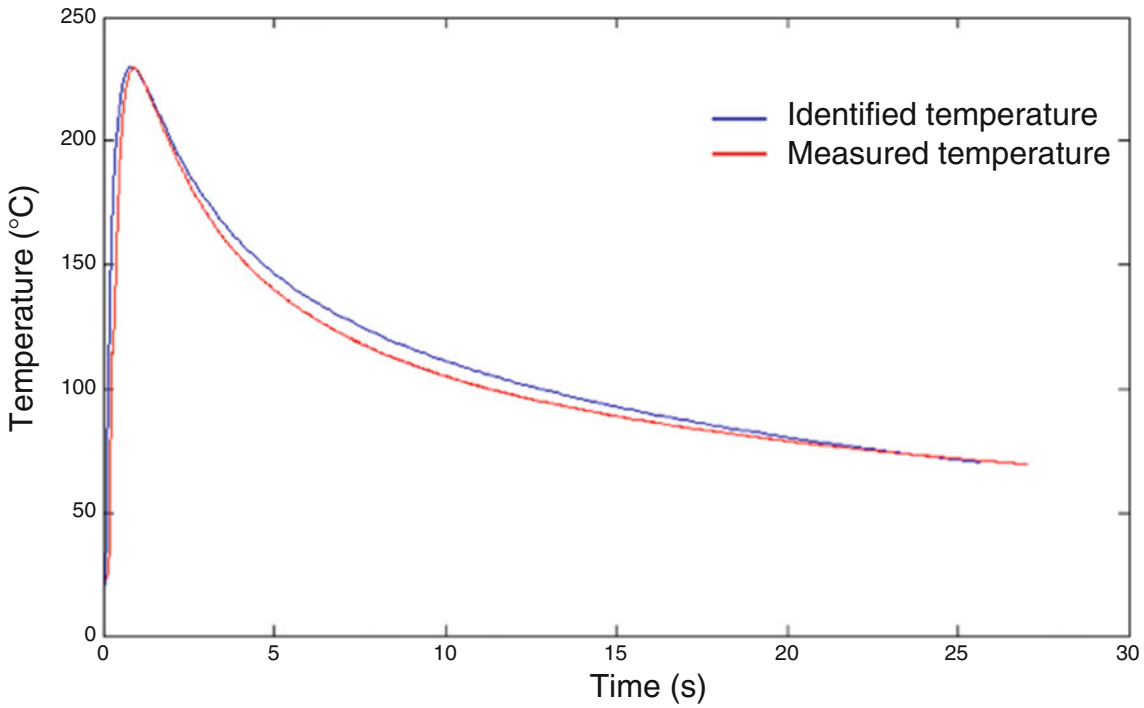

Fig. 24.11 Measured and simulated temperatures at the same position

the surrounding environment must also be considered as unknowns during the identification procedure. This heat exchange is modelled by a global exchange coefficient h(T).

Parameters Q_{beam} and h(T) were determined by an iterative identification procedure. It is recalled that at a given point in the vicinity of the brazing joint, the temperature increase during about 2 s is mainly dependent on the heat source parameter, Q_{beam}, whereas temperature evolution during cooling is mainly dependent on thermal exchange coefficient, h(T,x).

The result of the iterative identification procedure is illustrated by Fig. 24.11 where the temperature evolution as measured by a thermocouple at a particular point is compared with the numerical prediction.

24.4 Conclusions

A simple hybrid – surfacic and volumetric – model with few parameters is proposed to model a heat source representing a laser-brazing operation. A first identification of this model has been made using the results of a simple welding-brazing test campaign. Additional studies are in progress to identify the thermal resistance representing the contact between the steel sheets.

Furthermore, thermo-mechanical simulations will be developed to predict the deformations during the welding-brazing process. The validation of these simulations will be performed thanks to a new stereovision protocol developed for this study [5].

References

1. ABAQUS Version 6.11 Documentation, Dassault Systemes Simulia Corp., Providence, RI, USA, 2011
2. Gaussorgues G (1994) Infrared thermography, vol 5, Microwave technology series. Chapman & Hall, London, p 508
3. Goldak J, Chakravarti A, Bibby M (1984) A new finite element model for welding heat sources. Metall Trans 15B:299–305
4. Antoine R(2012) Caractérisation à chaud d'assemblages automobiles soudobrasés. Master Thesis, Arts et Métiers ParisTech
5. Beaubier B, Lavernhe-Taillard K, Besnard G, Lavernhe S, Hild F, Roux S (2012) CAD-based calibration of a 3D DIC system. In: SEM XII international congress and exposition on experimental and applied mechanics.

Chapter 25
Nondestructive Evaluation of Fiber Reinforced Polymers with Lockin Thermography

Carosena Meola, Veronica Grasso, Cinzia Toscano, and Giovanni Maria Carlomagno

Abstract The first use of infrared thermography (IRT), as non-destructive testing technique, dates back to the 1960; but, only recently it has been accepted amongst standardized techniques. At first, IRT suffered from perplexities and incomprehension but, starting from the 1980, it received renewed attention, with the exploitation and understanding of the underlying heat transfer mechanisms. The attention of the present paper is focused on the use of the lockin technique for non-destructive evaluation of fiber reinforced polymers. The intention is mainly to discover two different types of defects. One refers to the inclusion of the backing film, which may act as defect initiator site once the component becomes a load-bearing structure. The other one is the impact damage arising under low energy impact. Indeed, the damage produced by a low energy impact is the most risky one because it does not produce any external visible sign, while some internal damage occurs, which may grow in service with probable catastrophic consequences. Tests of the present investigation are performed with optical lockin thermography with results being presented as phase images. Regarding the impacted specimens, the aim is to highlight the damage distribution through their thickness.

Keywords Composites • Impact damage • Slag inclusion • Nondestructive evaluation • Lockin thermography

25.1 Introduction

Infrared Thermography (IRT) is generally referred to as a rather new technique of nondestructive testing (NDT) and evaluation of materials, since it has been only recently recognized amongst the standardized NDT techniques. However, the first commercial infrared system (named AGA Thermovision) entered the market in 1960. This system was initially used for the inspection of electric/electronic components and later implemented for NDT purposes, such as testing of Polaris rocket motors [1] and nuclear reactor fuel elements [2]. In the meantime, IRT became also attractive for the aerospace field. In 1992, it was considered an emergent technique by the American Society for Nondestructive Testing (ASNT) and it was fully recognized in the aerospace field in 2007 when the ASTM E2582, concerning application of flash thermography for inspection of aerospace composite panels, was released [3].

The first approaches were somewhat deceiving, because of difficulties in data interpretation, turning the interest towards other NDT techniques such as the ultrasonic method. It was over 20 years later that the heat transfer mechanisms [4] were identified for data analysis opening the door to the exploitation of infrared thermography. From that time up to now, there has been a proliferation of ideas regarding both hardware and software means for setting up effective techniques which are now amongst the well recognized NDT procedures in the aeronautical field. For more details the reader is addressed to international standards like the NAS410-08, or the European EN4179-09.

Basically, nondestructive testing with infrared thermography can be performed with two approaches, passive and active. In the first one, the material is at a temperature initially different (sometimes higher) from the ambient one because the part is inspected during, or suddenly after, a thermal operational cycle. For example in the aerospace field, passive thermography is suitable for assessing presence of water inside fuselage panels of landing aircraft. In the active approach, an external stimulation is necessary to induce adequate thermal contrasts. Along with the technical performance of IR imagers that is

C. Meola (✉) • V. Grasso • C. Toscano • G.M. Carlomagno
Department of Industrial Engineering, Aerospace Section, University of Naples Federico II, Via Claudio 21, Naples 80125, Italy
e-mail: carmeola@unina.it

M. Rossi et al. (eds.), *Residual Stress, Thermomechanics & Infrared Imaging, Hybrid Techniques and Inverse Problems, Volume 8*, Conference Proceedings of the Society for Experimental Mechanics Series, DOI 10.1007/978-3-319-00876-9_25,

permanently improving, the progress of IR-NDT is strictly connected to heating devices. Optical heating was, and still is, the preferred mode since it is simple to perform and effective for most of the applications. However, other systems, like air jets, could be used owing to the characteristics of the surface under test and to the related information to be acquired.

In the majority of cases, non destructive inspection of materials with an infrared imaging system is performed with the active mode, which consists in thermally stimulating the object (under exam) and monitoring its surface temperature variation during the transient heating, or cooling, phase. The presence of an inhomogeneity in the object material affects the heat propagation and causes a local surface temperature variation.

Basically, two thermographic techniques can be used for non destructive inspection: Pulse Thermography (PT) and Lockin Thermography (LT); other techniques may be tailored for a specific need, which are mainly variants of PT and LT because they include a different heating method, or a different processing algorithm.

The attention of the present work is devoted towards the use of lockin thermography for evaluation of some fiber reinforced polymers involving either slag inclusions, or impact damage.

25.2 Test Setup and Procedure

Tests are performed with optical lockin thermography (OLT), which basically includes: the infrared camera ThermaCam SC6000 coupled with the IrNDT lockin option, a halogen lamp for thermal stimulation and, of course, the specimen under inspection. A scheme of the test setup is given in Fig. 25.1.

In OLT, the thermographic system is coherently coupled to a thermal wave source which is operated in such a way that a sinusoidal temperature modulation results. This modulation is obtained from a non-linear electrical signal produced by the lock-in module which allows also for frequency variation. The thermal wave propagates inside the material and gets reflected when it reaches parts where the heat propagation parameters change (in-homogeneities). The reflected wave interferes with the surface wave producing an oscillating interference pattern, which can be measured in terms of amplitude, or phase angle, that, respectively, produces amplitude, or phase, images. The depth range for the amplitude image is given by the thermal diffusion length μ while the maximum depth p, which can be reached for the phase image, corresponds to 1.8 μ. A basic relationship relates the thermal diffusion length μ to the thermal diffusivity coefficient α and to the wave frequency f:

$$\mu = \sqrt{\frac{\alpha}{\pi f}} \tag{25.1}$$

Therefore, the material thickness, which can be inspected, depends on the wave period (the longer the period, the deeper the penetration) and on the thermal material properties (thermal diffusivity). Generally, tests start at a quite high wave frequency, at which only surface, or shallow, defects are visible. Later on, to inspect deeper layers, the frequency is reduced until the entire thickness has been traversed, or the minimum selectable frequency has been reached. Results are generally presented as phase images where a local variation of color indicates a local variation of phase angle and, in turn, a local variation of material thermal properties. The images may be stored for successive analysis to acquire information about size, depth and nature of defects.

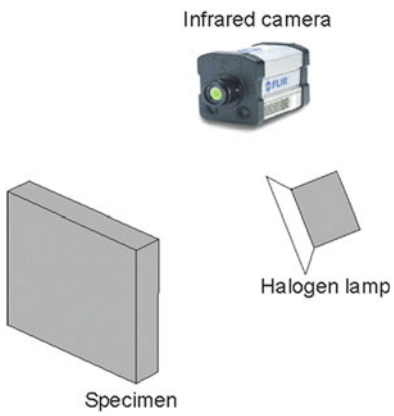

Fig. 25.1 Schematic setup for lockin thermography tests

25.3 Slag Inclusions

The manufacturing process of composites is quite complex, involving two, or more, different materials, time steps and setting up of many parameters; so, the final part is prone to slag inclusions. Often, fragments of the backing film remain entrapped which act as delamination initiator sites once the component becomes a load-bearing structure. Such fragments, if very thin, are difficult to be detected.

The geometrical limitations in the defects detection with infrared thermography were investigated by Meola et al. [5]. They analyzed both glass/epoxy and carbon/epoxy specimens with enclosed slag inclusions, of different materials and size, and located at different depth by using both pulse and lockin thermography performed with the Agema 900 infrared system. They found that, apart from the diameter (equivalent diameter), the defect thickness s plays a key role to mean that a thicker defect is better distinguishable than a thinner one of the same diameter. In particular, it was observed a strong decrease of the contrast for decreasing s/p below 0.1 (s and p being thickness and depth of defects); the latter was considered as limit for defects detection. As stated later by Meola [6], defects of low s/p values are better resolved with the rear heating phase thermography in which the transmitted part of the thermal wave is exploited rather than the reflected one. In fact, the transmitted signal is less affected by degradation due to lateral thermal diffusion within the material thickness.

In the following, a carbon/epoxy step wedged specimen similar to that analyzed by Meola et al. [5] is considered. It is 180 mm wide, 400 mm long and is divided into eight steps (50 mm each) along its length; the specimen thickness S varies in the range 2.6–6.6 mm. Three square Teflon inserts of thickness $s = 0.2$ mm and side $L = 6$, 12.7 and 16.9 mm respectively are positioned at half thickness in each step and regularly spaced along its width as sketched in Fig. 25.2. Then, the defect depth p varies in the range 1.3–3.3 mm, while s/p practically varies in the range 0.15–0.06. The camera is positioned at a distance necessary to view the entire specimen width and so the step wedged specimen is scrutinized into three views, which are named part 1 ($S = 2.6$–3.8 mm), part 2 ($S = 4.3$–5.5 mm) and part 3 ($S = 6.0$–6.6 mm).

Some phase images are reported in the following Figs. 25.3 and 25.4. In particular, Fig. 25.3 shows the phase images of part 1 (enclosing the three thinner steps 2.6, 3.2 and 3.8 mm thick) taken at heating frequencies $f = 0.2$ (Fig. 25.3a), 0.15 Hz (Fig. 25.3b) and 0.08 Hz (Fig. 25.3c). More specifically, for $f = 0.2$ Hz (Fig. 25.3a) defects appear visible only on the thinnest step (2.6 mm thick) but with a poor contrast. Such contrast enhances for a small decrease of the heating frequency to $f = 0.15$ Hz (Fig. 25.3b), when defects become distinguishable also in the successive 3.2 mm thick step. For $f = 0.08$ Hz (Fig. 25.3c), all defects in the three steps become visible.

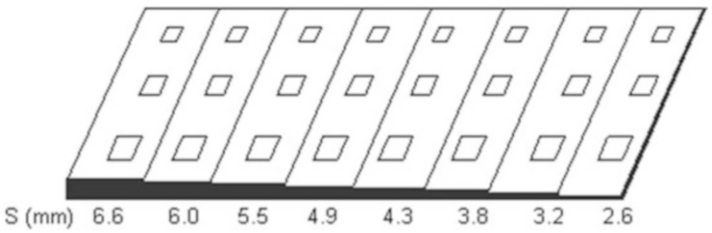

Fig. 25.2 Sketch of the step wedged specimen

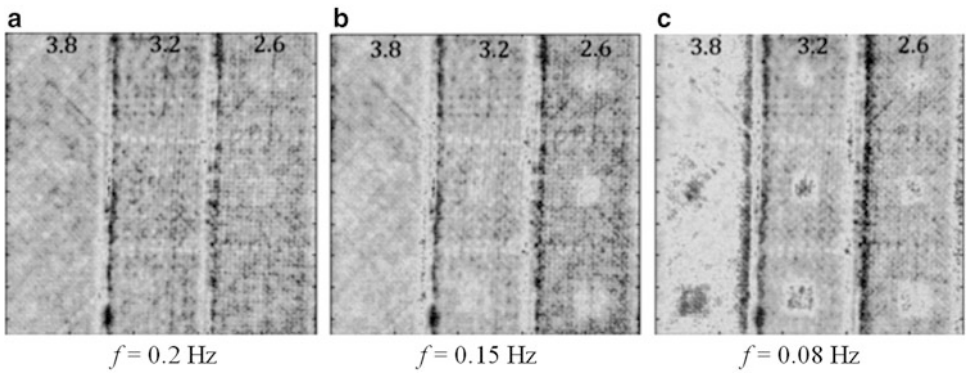

Fig. 25.3 Phase images of part 1 at different heating frequencies

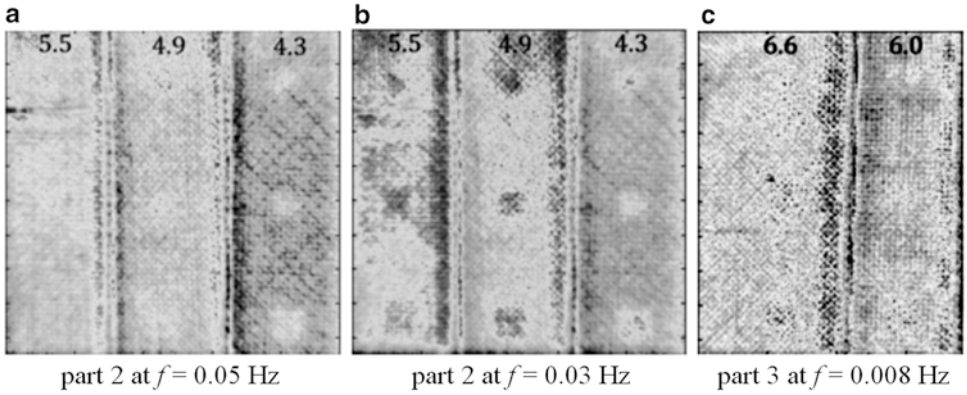

Fig. 25.4 Some phase images of parts 2 and 3

Figure 25.4 shows phase images of part 2 taken at two different heating frequencies $f = 0.05$ Hz (Fig. 25.4a) and $f = 0.03$ Hz (Fig. 25.4b) and of part 3 taken at $f = 0.008$ Hz (Fig. 25.4c). As can be seen, at the heating frequency of $f = 0.03$ Hz all defects in part 2 are resolved with a quite good contrast. Conversely, only signs of defects are perceptible on the thicker part 3 (even at the relatively low heating frequency of $f = 0.008$ Hz), while other details such as a non uniform distribution of resin becomes important preventing detection of inclusions. It has also to be observed that for part 3 the ratio s/p shrinks to 0.06 which is much smaller than the previously mentioned limiting value found by Meola et al. [6].

From a comparison between all the phase images herein shown, it can be observed that, by choosing the most adequate frequency, it is possible to detect defects and enhance their contrast; naturally, to the extent that the ratio s/p does not drop below a limiting value. Such value depends mainly on the relative thermal properties of host and buried defect materials and on the infrared imaging device sensitivity as well as its overall performance. In fact, the previous limiting value of 0.1 has been decreased to about 0.06 in the present case mainly thanks to the higher performance of the employed infrared camera and of the new lockin arrangement.

However, a factor to be always taken into account is the manufacturing process. Actually, by looking at the phase images (Figs. 25.3 and 25.4) it is possible to clearly see irregularities within the defects shape as well local variations of contrast. Such differences are to be ascribed mainly to the manufacturing hand lay-up process. More specifically, two main problems may arise during layering of a thin sheet of Teflon over a squashy surface (as maybe the resin impregnated fiber layer), which are: loss of planarity and contraction of the nominal area. In addition, local resin thickening may be associated with the loss of the original defect shape. Another factor, which may complicate the previous scenario, is the lateral thermal diffusion within the host material; this entails a blurring effect that increases with increasing the defects depth.

25.4 Impact Damage

One main weakness of composites is their vulnerability to impact; generally, they are able to absorb the impact energy within their polymeric matrix that distributes the energy in the material [7, 8]. In this way, a low energy impact does not produce perforation, but delamination between the layers with no visible surface manifestation. Often, layers delaminate under impact and tend to rejoin together very tightly once the impact force is removed. Therefore, this type of delamination is of difficult detection. Then, it is important to develop ad hoc NDT techniques, which may be able to discover delamination at its incipient stage and gain knowledge about the material behavior under impact for design purposes.

For the aims of this investigation, a glass fiber reinforced polymer (GFRP) obtained from unidirectional E-glass fibers embedded in translucent epoxy resin is considered. A laminate 500×500 mm^2 of stacking sequence $[0_2/90_2]_S$ is fabricated by the hand lay-up technology and cured, under stamp, for 24 h at room temperature. After that, rectangular specimens 130×100 mm^2 are cut and post cured in oven at 60 °C for 5 h; the overall thickness is about 2.9 mm. Such specimens are impacted with a Charpy pendulum [9] at energies in the range 7.5–12 J. They are evaluated by lockin thermography (Fig. 25.1) before and after impact.

Some phase images taken before and after impact are shown in the following Figs. 25.5 and 25.6 for the specimen GFRP-1 and in Figs. 25.7 and 25.8 for the specimen GFRP-2. In particular, Fig. 25.5 shows phase images of the specimen GFRP-1 before impact, taken at heating frequencies 0.1 Hz (Fig. 25.5a) and 0.05 Hz (Fig. 25.5b). It is possible to see some dark

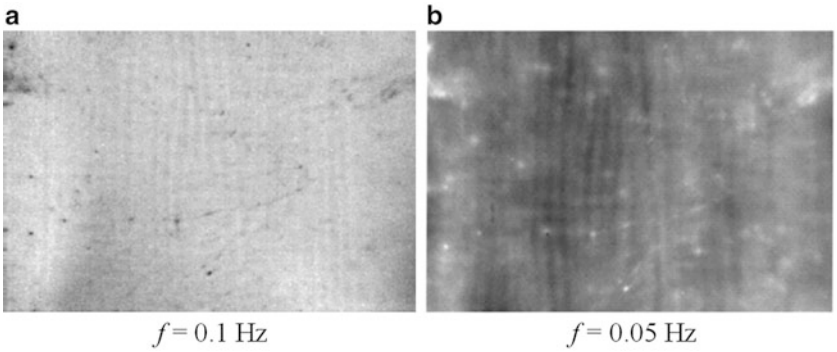

Fig. 25.5 Phase images of the specimen GFRP-1 before impact

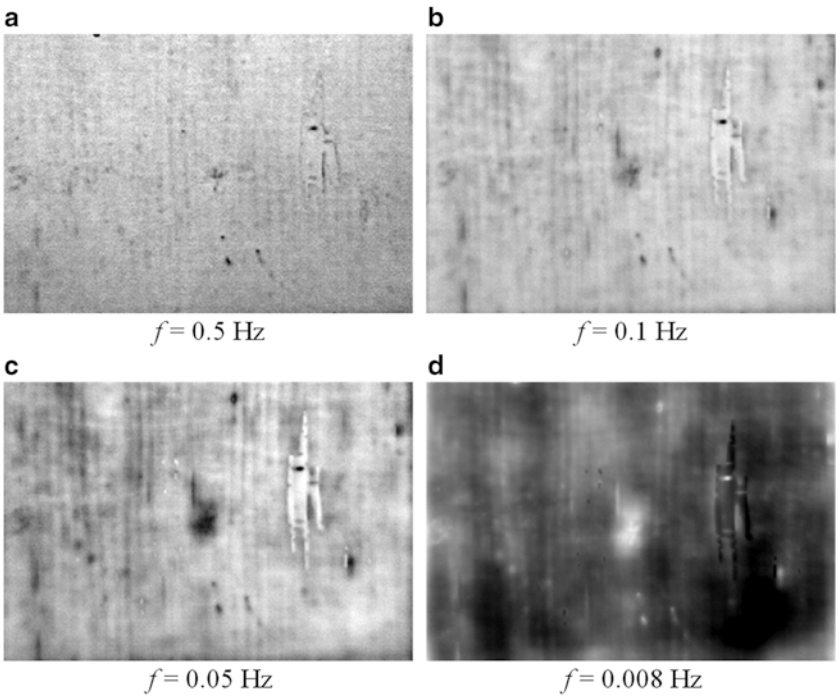

Fig. 25.6 Phase images of the specimen GFRP-1 after impact at $E = 7.5$ J

(Fig. 25.5a) and white (Fig. 25.5b) stains that account for local porosity distribution. It is worth noting that a change of grey level is experienced by features once they are surpassed by the thermal wave because of the blind frequency [10]. It is also possible to distinguish, especially in Fig. 25.5b, the fibers orientation involving also a certain misalignment. Instead in Fig. 25.6, phase images taken at different frequencies of the same specimen after impact at 7.5 J are reported; the viewed surface is that struck by the impactor. From the four images, taken at decreasing frequency, it is possible to reconstruct the quai-conical evolution of the damage through the specimen thickness. In fact, the phase image taken at $f = 0.5$ Hz (Fig. 25.6a) displays in its centre a slight mark, which enlarges as the frequency is decreased, that means (Eq. 25.1) going more in depth through the material. At last, for $f = 0.008$ Hz, which corresponds to a complete crossing of the entire specimen thickness, the classical peanut shape (on the rear surface) can be recognized.

Analogously in the following Figs. 25.7 and 25.8, the conditions of the specimen GFRP-2 before impact (Fig. 25.7) and the distribution of the impact damage through the thickness (Fig. 25.8) are illustrated. As a main difference the specimen GFRP-2 has fibers horizontally aligned on the viewed surface as clearly visible in the figures, this has led to a 90° rotation of the peanut structure. However, a larger extension of the damaged area is now observed because of the higher impact energy ($E = 12$ J); in particular, the peanut structure is clearly envisaged already for $f = 0.05$ Hz (Fig. 25.8c). Indeed, looking through Fig. 25.8c, it is possible to recognize a double peanut structure. One appears darker with lobes developing along the horizontal direction; this is likely located under the fourth ply at 90° at the interface with ply at 0° (note the stacking sequence $[0_2/90_2]_s$). The other peanut structure, which appears lighter and vertically oriented, is likely located within

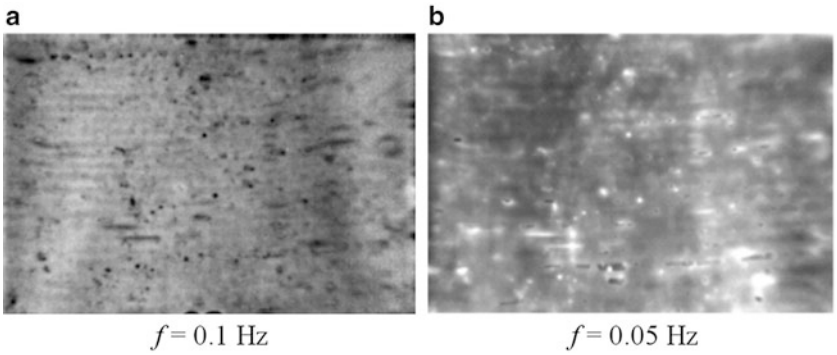

Fig. 25.7 Phase images of the specimen GFRP-2 before impact

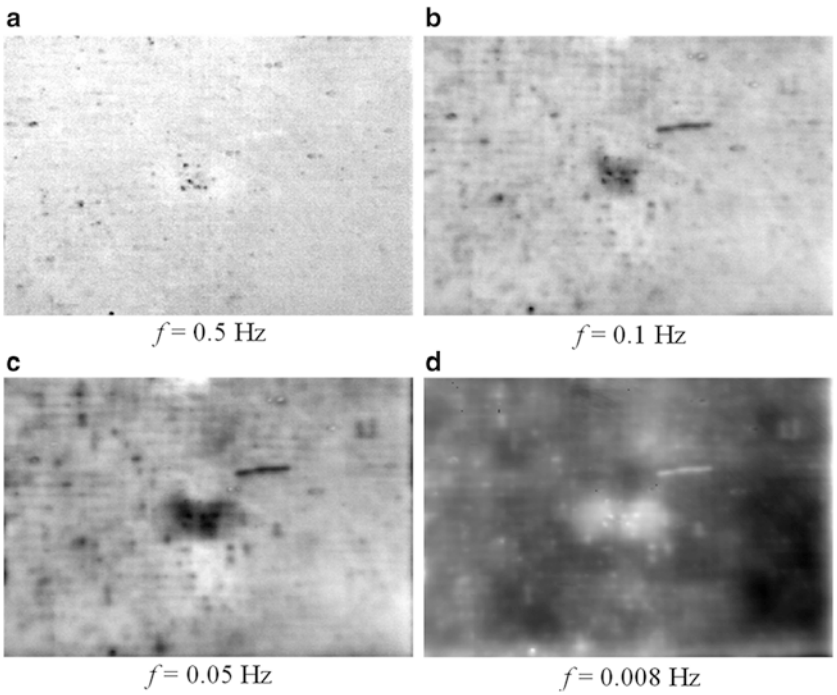

Fig. 25.8 Phase images of the specimen GFRP-2 after impact at $E = 12$ J

fibers at 90°. In addition, by comparing Fig. 25.7 to Fig. 25.5, it is possible to see that the specimen GFRP-2 is affected by a much greater level of porosity (Fig. 25.7b) with respect to the specimen GFRP-1 (Fig. 25.5b); however, porosity is almost away from the area of impact and so it cannot have a direct influence on the damage produced by the impact. Nevertheless, the presence of any defect may compromise the material strength and, in turn, its resistance as well its behavior to an impact event.

25.5 Conclusions

Lockin thermography has been used for nondestructive evaluation of fiber reinforced polymer composites by considering two types of reinforcing fiber: carbon and glass and by addressing two types of problems: slag inclusions and impact damage. The obtained results show that it is possible to discover inclusions, which are very thin, their thickness being less than 1/15 of their depth, and have thermal diffusivity very close to that of the material matrix. The technique effectiveness in depicting the impact damage evolution through the material thickness has also been demonstrated.

Of course, this may be enough in a rather qualitative (pass/fail) point of view, which is mostly the case in post-manufacturing inspection of parts. Conversely, a more accurate data processing may be required to extract quantitative information mainly for repairing purposes.

References

1. Beller WS (1965) Navy sees promise in infrared thermography for solid case checking. Missiles Rochets 16(22):1234–1241
2. Green DR (1968) Principles and applications of emittance-independent infrared non-destructive testing. Appl Optics 7:1779–1786
3. ASTM E2582-07 (2007) Standard practice for infrared flash thermography of composite panels and repair patches used in aerospace applications
4. Carslaw HS, Jaeger JC (1959) Conduction of heat in solids. Clarendon Press, Oxford
5. Meola C, Carlomagno GM, Giorleo L (2004) Geometrical limitations to detection of defects in composites by means of infrared thermography. J Nondestruct Eval 23:125–132
6. Meola C (2007) Nondestructive evaluation of materials with rear heating lock-in thermography. IEEE Sens J 7:1388–1389
7. Shyr TW, Pan YH (2003) Impact resistance and damage characteristics of composite laminates. Compos Struct 62:193–203
8. Baucom JN, Zikry MA (2005) Low-velocity impact damage progression in woven E-glass composite systems. Compos Part A 36:658–664
9. Meola C, Carlomagno GM, Ricci F, Lopresto V, Caprino G (2011) Investigation of impact damage in composites with infrared thermography. In: Mazal P (ed) Proceedings of 6th NDT in progress, Prague, 2011, pp 175–182
10. Meola C, Carlomagno GM (2004) Recent advances in the use of infrared thermography. Meas Sci Technol 15:R27–R58

Chapter 26
Realistic 3D FE Modelling of Peening Residual Stresses of Strain-Rate Sensitive Materials with Oblique Incident Angles

F. Yang, Z. Chen, S.A. Meguid, and M. Guagliano

Abstract Shot peening is a widely used treatment to improve the fatigue life of metallic components by introducing compressive residual stresses to the top layer of the components. Oblique incidence is often involved in the peening process due to geometric complexity of the real components. It is therefore the purpose of this study to conduct a realistic 3D finite element (FE) analysis of the peening process involving a large number of shots impinging simultaneously at a rate sensitive target made from Ti-6Al-4 V. A periodic cell model is developed to examine the effect of oblique incidence. The periodicity of the model is first validated by comparing the residual stress with that from a larger model. A parametric study is conducted to investigate the effect of shot impinging angles upon the residual stress generation. It is found that normal incidence leads to the largest residual stress magnitude and the compressive zone depth.

Keywords Shot peening • Residual stress • Finite element analysis • Oblique incidence • Rate sensitive

26.1 Introduction

Shot-peening is a cold-working treatment widely used to improve the fatigue life of metallic components in aerospace and automobile industries [1, 2]. It is accomplished by bombarding the surface of the component with small spherical shots at a relatively high impinging velocity. The impingement of shots causes an indentation surrounded by a plastic region. After peening, a field of compressive residual stress is left in the near surface layer due to inhomogeneous elasto-plastic deformation, which is beneficial for increasing the material hardness and retarding crack initiation under cyclic loading conditions [3]. The effectiveness of shot peening is related to a number of parameters including shot parameters such as the size, density, shape and mechanical properties of the shots, component parameters such as the geometry and mechanical properties of the target, and the process parameters such as mass flow rate, impact velocity, incident angle, distance from the nozzle and exposure time. In order to obtain a better control of the shot peening treatment, it is important to establish quantitative relationships between these parameters and the resulting residual stress pattern [4].

Finite element (FE) simulations have shown an increasing power in investigating shot-peening process due to its capability in separately investigating the effect of each parameter. Some researches simulated the single or a few shots impinging on a large area of the target. This includes the contributions made by Gariépy et al. [5], Klemenz et al. [6], Wu et al. [7], Meguid et al. [8]. However, in real shot peening practice, each incidence includes a large number of shots impinging on the target simultaneously. The adjacent shots would influence the residual stress distribution and make it different from that from a single or a few shots. For this purpose, Meguid et al. [9, 10], Majzoobi et al. [11] developed symmetry models of square base to describe the simultaneous impacts of multiple shots using mirror symmetry boundary conditions. Schiffner and Helling [12], on the other hand, used a symmetry cell of isosceles triangle base to investigate the effect of adjacent shots. All these results showed that the effect of adjacent shots cannot be neglected.

F. Yang • Z. Chen • S.A. Meguid (✉)
Mechanics and Aerospace Design Laboratory, Mechanical and Industrial Engineering, University of Toronto, Toronto, Canada
e-mail: meguid@mie.utoronto.ca

M. Guagliano
Mechanical Engineering Department, Politecnico di Milano, Via La Masa, 1, 20156 Milan, Italy

M. Rossi et al. (eds.), *Residual Stress, Thermomechanics & Infrared Imaging, Hybrid Techniques and Inverse Problems, Volume 8*, Conference Proceedings of the Society for Experimental Mechanics Series, DOI 10.1007/978-3-319-00876-9_26,

An important issue in shot peening is that the real target component often has a complex geometry. Therefore, oblique impingements are often involved in the shot peening process [2]. However, oblique impingements were not sufficiently and systematically investigated in the existing researches. Hong et al. [13] investigated a single shot impinging obliquely at a large plate. Miao et al. [14], Kim et al. [15], Schwarzer et al. [16] investigated the oblique impingements of multiple shots at a large region. Their work explored the effect of several parameters in the shot peening process. However, their models cannot be used to simulate the simultaneous impingements of a large number of shots. On the other hand, the symmetry cell models [9–11] are useful for simulating the simultaneous multiple shots of normal impingements, but they are not applicable for the case of oblique impingements. Investigations on the simultaneous oblique impingements of targets have not been found in literature. New models are needed for the simulation of multiple shots impinging simultaneously at oblique angles.

Another issue is related to the material properties of the target. The quick impingement of the shot causes rapid deformation of the target material. Some authors used rate insensitive models [8, 17, 18]. Others [9, 15, 19] considered strain rate sensitivity in their constitutive models. The results of [9] showed that the strain rate sensitivity of the target material cannot be neglected. In this paper, the strain rate sensitivity is included in our material model for the target.

In this paper, we provide an accurate FE simulation of a large number of shots impinging simultaneously and obliquely on a target made of rate sensitive material. The results of our work can provide an insight into the effect of obliquity in peening treatments.

26.2 Finite Element Modelling

The situation envisaged is that a large number of identical shots simultaneously impinge a metallic target at an identical incident angle θ as shown in Fig. 26.1a. The shots are assumed to be positioned in a periodic array with separation distance D between adjacent shots. Utilizing periodicity and symmetry, a representative computational cell including half a shot was generated and simulated as shown in Fig. 26.1b. A coordinate system was created so that z axis is along normal of the target and all shots move within the xz plane. The cell has a rectangular columnar geometry with dimensions of $D/\sin(\theta)$, $D/2$ and H along three coordinates, respectively. The cell length along x axis changes with the incident angle in order to feature the same flow density of the shot flux through area perpendicular to the flux direction. Considering the case with shots closely adjoining each other, D was taken as twice as the shot radius R. The height of the cell was taken as $4R$ since this value is large enough to screen the bottom boundary influence according to Ref. [9].

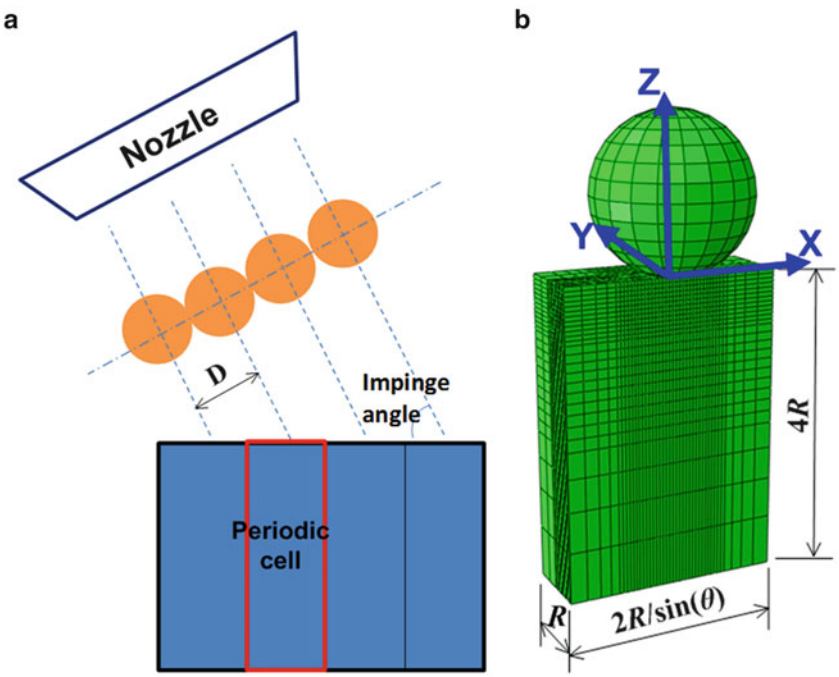

Fig. 26.1 FE model. (**a**) Schematic plot of the simulation situation; (**b**) mesh and the coordinate system

Instead of the symmetric boundary condition in Ref. [9, 10], periodic boundary condition was used for the two lateral facets at the ends of x coordinate to simulate the periodically distributed simultaneous oblique impingements. The periodic boundary was implemented by coupling each degree of freedom (DOF) of the corresponding nodes on the two opposite faces so that the two faces could deform synchronously. The two lateral facets at the ends of y coordinate were constrained using symmetric boundary condition. The nodes were constrained against all displacements and rotations on the bottom boundary.

The material models used by Meguid et al. [10] were also applied in this paper. The target was Ti-6Al-4V with Young's modulus $E = 114$ GPa, Poisson's ratio $v = 0.342$ and density $\rho = 4430$ kg/m^3. The initial yield stress is $\sigma_0 = 827$ MPa and the strain hardening parameters were extracted from the uniaxial stress–strain curve assuming isotropic hardening. The strain-rate sensitivity was accounted for using the data of Premack and Douglas [20]. These data were incorporated in the FE model by scaling the quasi-static stress–strain curve for different strain rates according to Fig. 7(b) in Ref. [10]. The shots were modeled as rigid balls with density $\rho_{shot} = 7850$ kg/m^3 and radius $r_{shot} = 0.18$ mm. The impinging velocity was chosen as $V = 75$ m/s according to Ref. [13]. The impinging angle is 60° unless otherwise specified. The shot was modeled as a rigid ball with an analytical spherical surface and the corresponding point mass and point rotational inertia positioned at its centre. The target was discretized using eight-node solid elements with reduced integration. The mesh was refined near the contact region with element size of $0.05R$. The impact contact between the shot and the target was implemented using a penalty algorithm with a friction coefficient of 0.3 according to Ref. [9]. The FE model was developed using the commercial code ABAQUS/EXPLICIT version 6.1.

26.3 Verification of the Periodicity for the Proposed FE Model

Periodicity requires that the simulated cell can represent any larger region that is an integral multiple of the cell. To check the implementation of periodicity for the newly proposed periodic model, a larger model as 18 times as the original cell model was created. The larger model included nine shots in a 3×3 array. The length was 3 times as that of the original model. The width was 6 times as that of the original model since the original model only included half of a shot. Periodic boundary conditions were applied on the four lateral boundaries to couple the corresponding DOFs. Other parameters were kept the same as the original cell model. Figure 26.2a, b compare the contour plots of the residual stress σ_{xx} in xz plane for the larger model and the original model, respectively. Figure 26.3a, b compare the contour plots of the residual stress σ_{xx} on target surface for the larger model and the original model, respectively. These results show that the original model including half a shot and the larger model including nine shots generated consistent residual stress distribution results. Figure 26.4 compares the trajectories of the shot centers in the original model and the larger model. The locations of the four representative shots from the larger model were indicated in Fig. 26.3a. All the trajectory curves match very well with each other. These consistencies confirm that the requirement of periodicity can be satisfied using our proposed model.

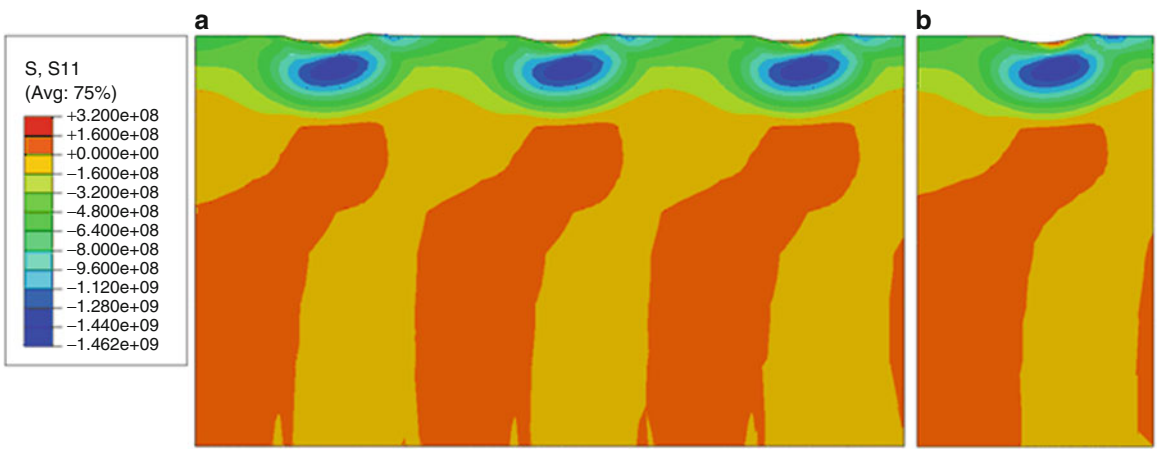

Fig. 26.2 Comparison of the contour plots of the residual stress σ_{xx} in xz plane for (**a**) the larger model and (**b**) the original model

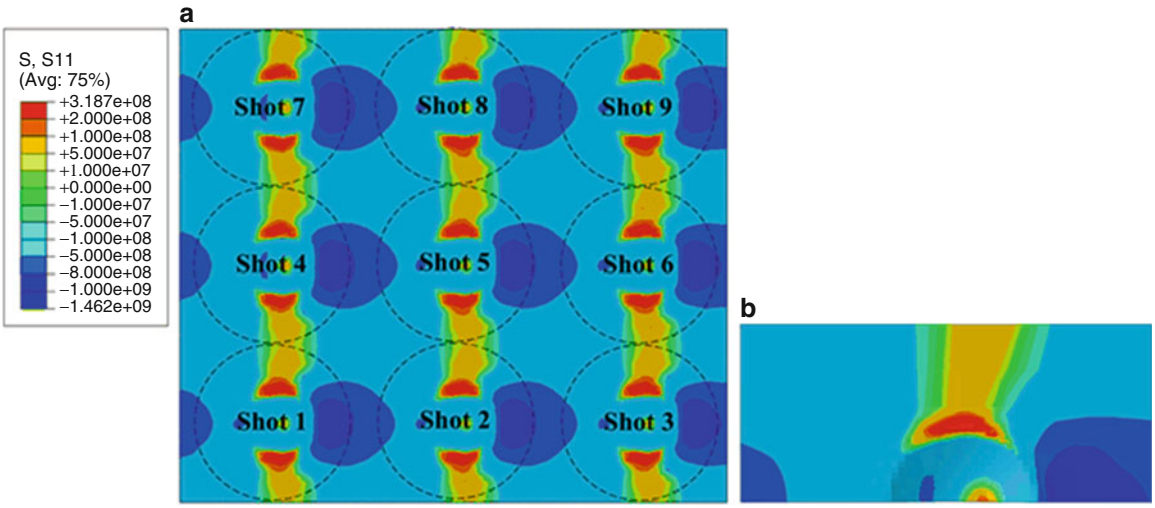

Fig. 26.3 Comparison of the contour plots of the residual stress σ_{xx} on target surface for (**a**) the larger model and (**b**) the original model

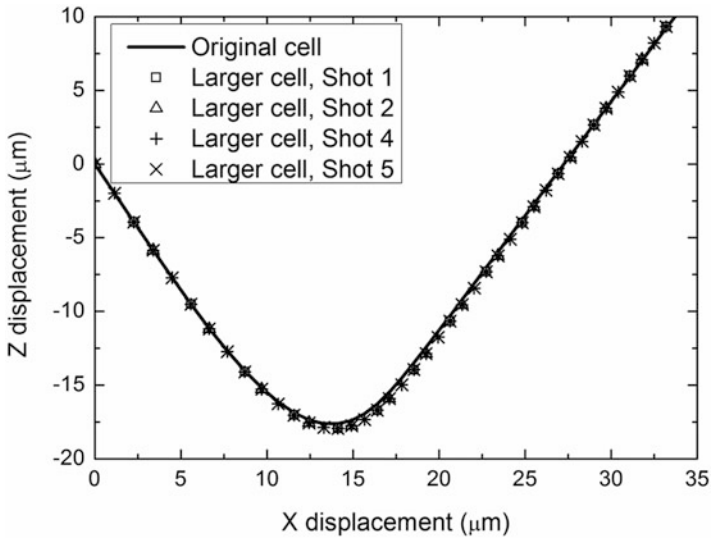

Fig. 26.4 Comparison of the trajectories of the shot centers

26.4 Effect of the Incident Angle on the Residual Stress Distribution

A parametric study was conducted to investigate the effect of the incident angle on the obtained residual stress distribution. For this purpose, a series of simulations were carried out with different impinging angles of shots. Other conditions remain the same. Five angles were investigated as 30°, 45°, 60°, 75° and 90°. For all the simulation cases the shot initially impinged at the origin which is positioned at the center of the top edge. Figure 26.5 compares the contour plots of the obtained residual stress σ_{xx} within the xz plane in the same legend. It is found that increase of the impinging angle leaded to an increase of the compressive zone area. This tendency can be more clearly seen in Table 26.1 from the depth of the compressive residual stress zone $d_{compressive}$, which is determined from the zero stress position on the line along depth direction through the maximum stress location. Table 26.1 also lists the magnitude and the x, z locations of the maximum residual stress σ_{xx}. It indicates that the maximum residual stress also increases with the impinging angle. The depth of the maximum stress location is deeper for a larger incident angle. While the x distance from the impinging location for the maximum stress location is larger for the smaller incident angle. Figure 26.6 compares the contour plots of the residual stress on the top surface of target. It indicate that the magnitudes of the residual stresses increase as the incident angle increases. These results indicate that the normal incidence is the most effective scenario regarding to the residual stress development.

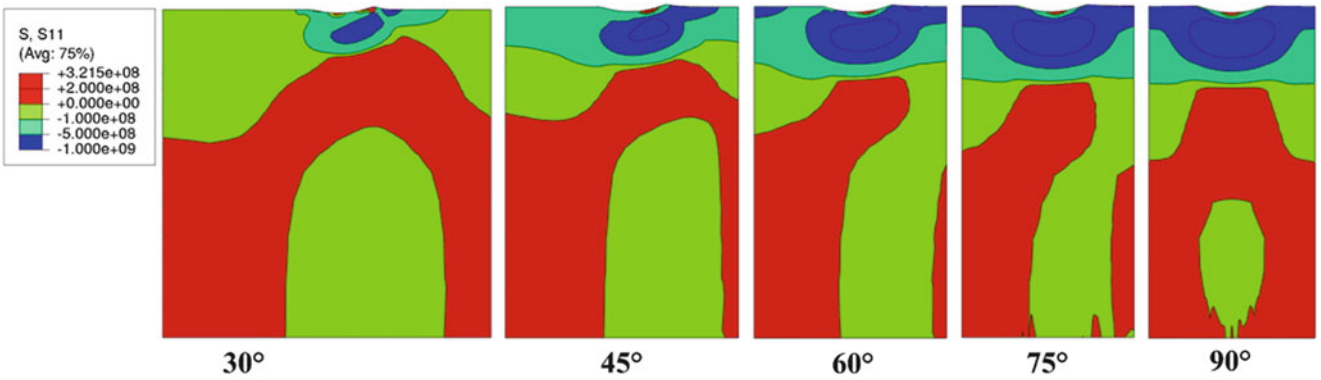

Fig. 26.5 Comparison of contour plots of the residual stress σ_{xx} in xz plane for different impinging angles

Table 26.1 Effect of impinging angle on the distribution characteristics of residual stress σ_{xx}

θ (°)	$d_{compressive}$ (mm)	$\sigma_{xx,\ max}$ (MPa)	x_{max} (mm)	z_{max} (mm)
30	0.0925	1,020	0.0842	−0.0247
45	0.123	1,314	0.0630	−0.0371
60	0.153	1,492	0.0377	−0.0468
75	0.160	1,616	0.0102	−0.0565
90	0.164	1,641	0.0	−0.0546

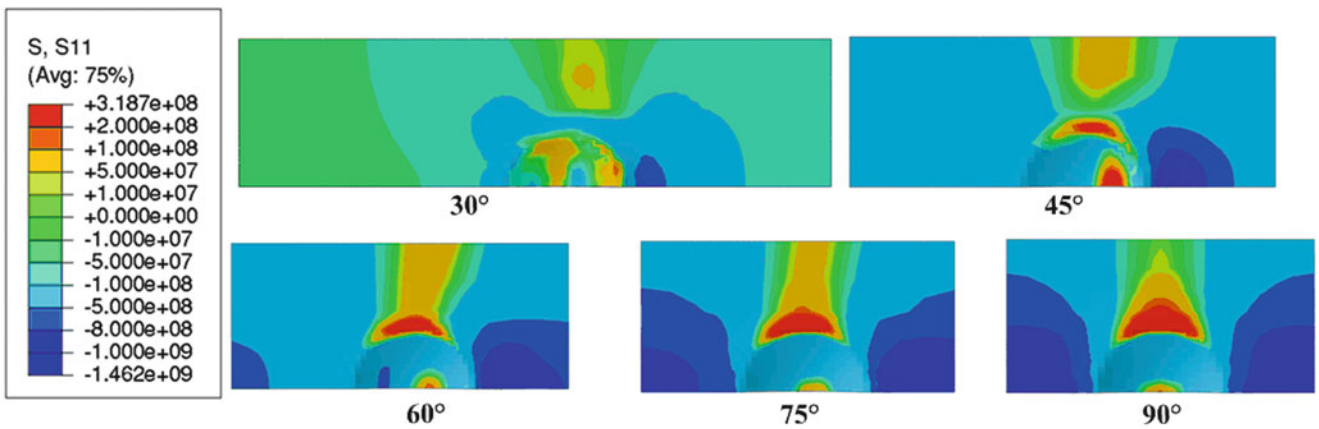

Fig. 26.6 Comparison of contour plots of the residual stress σ_{xx} on target surface for different impinging angles

26.5 Conclusions

A 3D FE analysis of a large number of shots simultaneously impinging a rate sensitive component obliquely has been presented. It is intended to provide insight into the effect of oblique impingement, often encountered in the peening process as a result of the geometric complexity of treated components. A periodic cell model is developed by coupling the DOFs of the corresponding nodes on two opposite periodic boundaries. The periodicity of the model is validated by comparing the residual stress results with those obtained from a larger model. A parametric study is then conducted to investigate the effect of incident angle upon the resulting residual stress profile. It is found that normal incidence leads to the largest residual stress magnitude and the largest compressive zone area, therefore is the most beneficial incidence scenario regarding to residual stress generation.

References

1. Meguid SA (1986) Impact surface treatment. Elsevier Applied Science, Amsterdam
2. Schulze V (2006) Modern mechanical surface treatment. Wiley-VCH, Weinheim
3. Kobayashi M, Matsui T, Murakami Y (1998) Mechanism of creation of compressive residual stress by shot peening. Int J Fatigue 20:351–357
4. Guagliano M (2001) Relating Almen intensity to residual stresses induced by shot peening: a numerical approach. J Mater Process Technol 110:277–286
5. Gariépy A, Larose S, Perron C, Lévesque M (2011) Shot peening and peen forming finite element modelling – towards a quantitative method. Int J Solids Struct 48:2859–2877
6. Klemenz M, Schulze V, Rohr I, Lohe D (2009) Application of the FEM for the prediction of the surface layer characteristics after shot peening. J Mater Process Tech 209:4093–4102
7. Wu XQ, Wang X, Wei YP, Song HW, Huang CG (2012) Parametric study on single shot peening by dimensional analysis method incorporated with finite element method. Acta Mech Sin 28(3):825–837
8. Meguid SA, Shagal G, Stranart JC, Daly J (1999) Three-dimensional dynamic finite element analysis of shot-peening induced residual stresses. Finite Elem Anal Des 31:179–191
9. Meguid SA, Shagal G, Stranart JC (2002) 3D FE analysis of peening of strain-rate sensitive materials using multiple impingement model. Int J Impact Eng 27:119–134
10. Meguid SA, Shagal G, Stranart JC (2007) Development and validation of novel FE models for 3D analysis of peening of strain-rate sensitive materials. J Eng Mater Tech 129:271–283
11. Majzoobi GH, Azizi R, Alavi NA (2005) A three-dimensional simulation of shot peening process using multiple shot impacts. J Mater Process Technol 164–165:1226–1234
12. Schiffner K, gen Helling CD (1999) Simulation of residual stresses by shot peening. Comput Struct 72:329–340
13. Hong T, Ooi JY, Shaw BA (2008) A numerical study of the residual stress pattern from single shot impacting on a metallic component. Adv Eng Soft 39:743–756
14. Miao HY, Larose S, Perron C, Lévesque M (2009) On the potential applications of a 3D random finite element model for the simulation of shot peening. Adv Eng Soft 40:1023–1038
15. Kim T, Lee H, Hyun H, Jung S (2013) Effects of Rayleigh damping, friction and rate-dependency on 3D residual stress simulation of angled shot peening. Mater Des 46:26–37
16. Schwarzer J, Schulze V, Vöhringer O (2006) Finite element simulation of shot peening – a method to evaluate the influence of peening parameters on surface characteristics. In: Wagner L (ed) Shot peening. Wiley-VCH, ICSP-8, Garmisch-Partenkirchen, pp 507–515
17. Edberg J, Lindgren L, Mori K (1995) Shot peening simulated by two different finite element formulations. In: Shen S, Dawson P (eds) Simulation of materials processing: theory, methods and applications. Balkema Publishers, Rotterdam, pp 425–430
18. Frija M, Hassine T, Fathallah R, Bouraoui C, Dogui A (2006) Finite element modelling of shot peening process: prediction of the compressive residual stresses, the plastic deformations and the surface integrity. Mat Sci Eng A 426:173–180
19. Mylonas GI, Labeas G (2011) Numerical modelling of shot peening process and corresponding products: residual stress, surface roughness and cold work prediction. Surf Coat Tech 205:4480–4494
20. Premack T, Douglas AS (1995) Three-dimensional analysis of the impact fracture of 4340 steel. Int J Solid Struct 32:2793–2812

Chapter 27
Water Cavitation Peening by Ultrasonic Vibration for Improvement of Fatigue Strength of Stainless Steel Sheet

Tomohiro Sasaki, Shun Hasegawa, Masayuki Nakagawa, and Sanichiro Yoshida

Abstract Water cavitation peening has been applied to thin sheets of austenitic stainless steel of 0.1 mm in thickness. The influence of cavitation peening on various factors related to the fatigue property of the material has been investigated. It has been found that the fatigue limit is increased by about approximately 10 %, while no significant changes in the surface roughness and the microstructure are observed. The residual stress evaluated by Full Width at Half Maximum (FWHM) of X-ray diffraction, and the mean value of micro-hardness on the surface are slightly decreased in the peened specimen. To investigate the origin of increase in fatigue strength, deformation behavior in the tensile test has been measured using electronic speckle pattern interferometry. The optical fringe patterns by ESPI (Electronic Speckle-Pattern Interferometry) during the transitional process from the elastic deformation to the yielding have shown that local plastic deformation due to the strain concentration was suppressed by the cavitation peening.

Keywords Cavitation • Peening • Ultrasound • Surface treatment • Fatigue • Speckle interferometry

27.1 Introduction

Peening process is widely used as a surface treatment to improve the fatigue strength of mechanical components. Here compressive residual stress introduced by peening is believed to counteract on the crack initiation. Recently, cavitation peening technique [1–5] has been developed as a means of shot-less peening. In this technique, impact induced by cavitation bubbles upon collapsing on the surface of the work is utilized to cause compressive residual stress. The cavitation bubbles are formed by high-speed water jet [1–4] or ultrasonic oscillator submerged in water [5]. The cavitation peening process can be applied to thin metal sheets or soft metals because the effect of surface damage due to excessive plastic deformation is relatively small.

In the present work, the cavitation peening generated by an ultrasonic vibrator has been applied to thin sheets of austenitic stainless steel, and the effect of residual stress, microstructure, and micro-hardness on the fatigue behavior has been investigated. Consequently, the fatigue limit has been found to increase, while no significant changes in the factors related to the fatigue resistance have been found. This suggests that the improvement of fatigue property of the thin sheet metal by the cavitation peening arises from other factors. In order to some insight into the origin, deformation behavior in tensile test has been investigated using electronic speckle pattern interferometry.

T. Sasaki (✉) • S. Hasegawa
Department of Engineering, Niigata University (Japan), Niigata University, Ikarashininocho 8050, Nishi-ku, Niigata-shi, Niigata 9502181, Japan
e-mail: tomodx@eng.niigata-u.ac.jp

M. Nakagawa
Industrial Research Institute of Niigata Prefecture (Japan), 1-11-1 Abuminishi, Chuou-ku, Niigata-shi, Niigata 9502181, Japan

S. Yoshida
Department of Chemistry and Physics, Southeastern Louisiana University, SLU 10878, Hammond, LA 70402, USA
e-mail: syoshida@selu.edu

M. Rossi et al. (eds.), *Residual Stress, Thermomechanics & Infrared Imaging, Hybrid Techniques and Inverse Problems, Volume 8*, Conference Proceedings of the Society for Experimental Mechanics Series, DOI 10.1007/978-3-319-00876-9_27,

27.2 Experimental Details

The material used in this study was cold-rolled stainless-steel sheet (18Cr-8Ni steel, AISI304) of 0.1 mm in thickness. The mean crystal grain size of the base metal was approximately 30 μm. The specimens used for the fatigue test and the tensile test were prepared by cutting the steel sheet in the roll direction with an electrical discharge machine. The specimen geometry is shown in Fig. 27.1. The yield stress obtained from the tensile tests was 1,248 MPa.

The schematic of water cavitation peening equipment is illustrated in Fig. 27.2. An ultrasonic transducer with the power of 2.5 kW and the vibration frequency of 19 kHz was used for the water cavitation peening. The cavitation bubbles are generated by vibration via an ultrasonic horn with the tip diameter of 25 mm in water. The vibration amplitude of the horn tip under no load condition in air was about 25 μm in peak-to-peak. The distance between the specimen and the ultrasonic horn tip was 1 mm. The specimen was placed on a X-stage reciprocating with a constant speed of 5.0 mm/s and a stroke of 50 mm. The cavitation peening was applied for 360 s to both sides around the necking part of specimen.

Load controlled fatigue test was performed on the peened specimen and the un-peened specimen. A sinusoidal waveform at 40 Hz was employed for the loading configuration. The minimum load was a constant of 30 N, and the maximum loads were 549–749 N (55–75 % of the yield strength of specimen).

X-ray diffraction analysis was conducted to the peened surface. The X-ray tube of Cu-Kα was operated at 40 kV and 30 mA. The specimen in this study was processed by cold rolling, thus the microstructure had the dual phase of austenite and

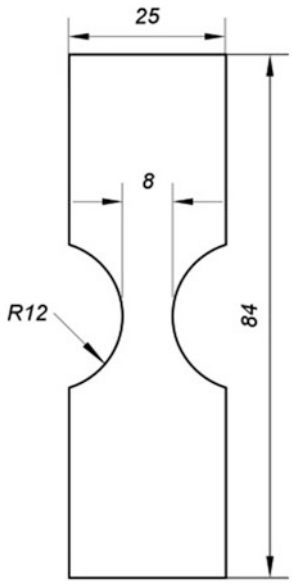

Fig. 27.1 Specimen used for fatigue test

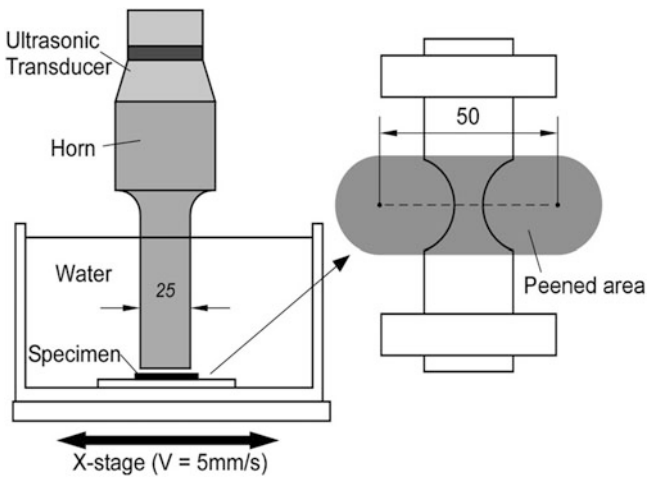

Fig. 27.2 Ultrasonic cavitation peening equipment

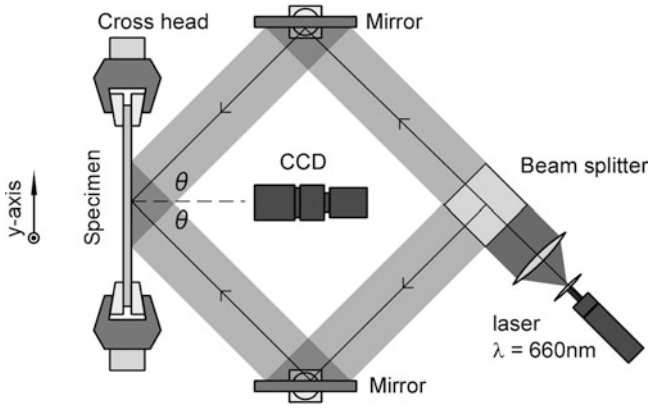

Fig. 27.3 Experimental arrangement

strain induced martensite. In addition, it was difficult to measure the residual stress by $\sin^2 \psi$ method because of anisotropy caused by the rolling texture. Therefore, the residual stress was qualitatively evaluated by a FWHM of a (220) plane peak of austenite.

Deformation process in the uniaxial tensile test was observed by ESPI. Figure 27.1a shows the optical configuration which has sensitivity of the longitudinal displacement along tensile direction (Y-axis). A dual beam ESPI [6] setup was arranged horizontally parallel to the tensile direction. The light source was a continuous wave, semiconductor laser oscillating at 660 nm. The laser beam was split into two paths by a beam splitter, and the two beams illuminated the tensile specimen at an incidence of 38°. When the specimen was stretched by the tensile machine and the longitudinal displacement occurred on the surface of specimen, the brightness of the superposed speckle field by the two beams changed. The image of the specimen during the tensile test was captured by the CCD camera at a constant rate of 15 fps (frames per second). The images of speckles due to these optical configurations were recorded into computer. The change in the brightness of speckles due to each optical configuration was calculated numerically by subtracting 256 bit brightness data. Consequently, the displacement contour representing the longitudinal displacement was obtained as the fringe pattern. The crosshead speed in the tensile test was at a constant of 1.7×10^{-3} mm/s (Fig. 27.3).

Each contour in the fringe pattern represents equal value of the in-plane displacement components. Relationship between the relative number of contour, n and the displacement component along the v, is given as a following equation [1].

$$n = \frac{2}{\lambda} u \sin\theta \tag{27.1}$$

where λ is the wavelength of the light source and θ is the angle of beam incidence. The coordinate in the pixel value of black fringes appeared were measured in the subtracted image, and the fringe number was indexed from the stationary end of specimen. The displacement values at measurement points on the fringe were obtained by Eq. 27.1. The values at the other coordinates in the image were computed by bilinear interpolation. Longitudinal strain, ε_{yy}, is given by $\partial v/\partial y$.

27.3 Result and Discussion

27.3.1 Fatigue Resistance

Figure 27.4 shows the S-N plot of the base metal (un-peened) and the peened specimen. The number of cycle to failure tends to be greater in the peened specimen shown by "○" compared to the un-peened specimen ("●"). The fatigue limit in the peened specimen was found to increase by 10 %. It can be stated that the fatigue resistance was improved by the cavitation peening process. X-ray diffraction peak of the specimens and the FWHMs are shown in Fig. 27.5. The results are compared with a measurement result of an annealed specimen in order to compare with the low strain condition.

The diffraction peak is broadened by the cold working, thus the FWHM shows a large value in the un-peened and the peened specimens. However, the FWHM in the peened specimen decreases compared to the un-peened. The peak location slightly shifts to a larger angle by the peening. These values are indicative of that microscopic strain on the surface was relaxed by the peening. Compressive residual stress on the surface is considered to be saturated by the rolling. On the other

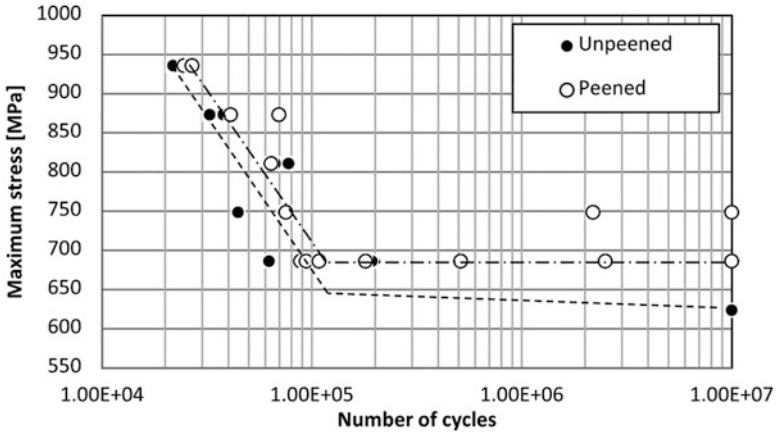

Fig. 27.4 S-N plot

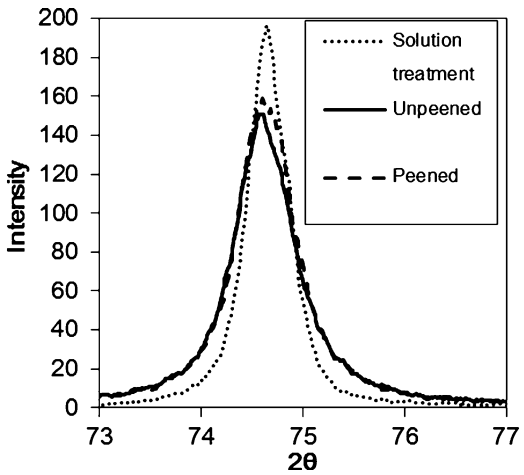

Fig. 27.5 X-ray diffraction pattern for (220) peak of austenite

hand, optical micrographs of specimens are shown in Fig. 27.6. The observation was carried out for the same location before and after the peening. The surface roughnesses measured by a stylus type surface roughness tester were respectively 0.5901 and 0.5907 μm in maximum height of the depth. It can be stated that there was almost no morphological change in the surface by the peening. Furthermore, the micro-hardness on the surfaces was shown in Fig. 27.7. The values of hardness have variances with the range from 450 HV to 800 HV associated with the dual phases of the austenite and the strain induced martensite. The mean hardness was found to show slight decrease by the peening. These results imply the decrease in the micro-strain on the surface by the peening, and this fact leads to the relaxation of residual stress. It may be concluded that the compressive residual stress does not affect the improvement fatigue resistance in this study.

27.3.2 Deformation Behavior in the Yielding

The fatigue test in this study was performed under the yield stress of specimen. Fatigue may progress by local plastic deformation or crack occurrence associated with microscopic inhomogeneity in the material. Upper graph in Fig. 27.8 shows the load–displacement curves of the un-peened specimen. The base material used in this study was a thin sheet with cold-working, thus the mechanical property is different from that of general austenitic stainless steels. The clear yield points and the yield drop were observed in the load–displacement curve. The difference in the deformation behavior between the peened specimen and the un-peened specimen appeared in transitional process from elastic deformation to the yielding. The lower images shown in Fig. 27.8 indicate the displacement contours (fringe pattern) of the un-peened specimen obtained at several load levels. The patterns represent displacement along the tensile axis resulting from a constant time interval of 3.3 s (50 frames in CCD capture). The applied load corresponding to the fringe patterns were shown in the

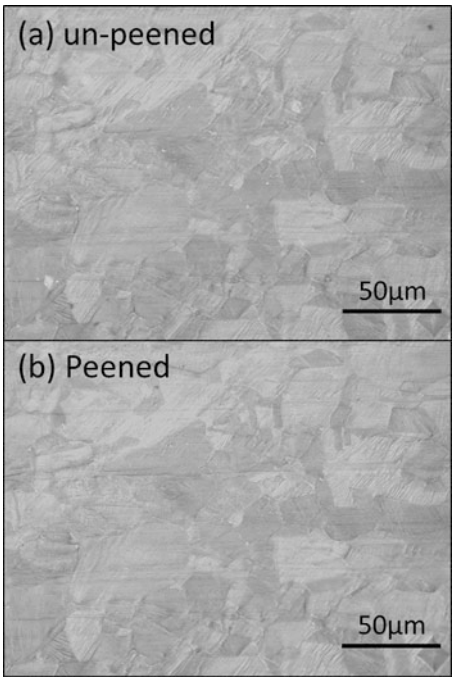

Fig. 27.6 Optical micrographs of the un-peened and the peened surfaces

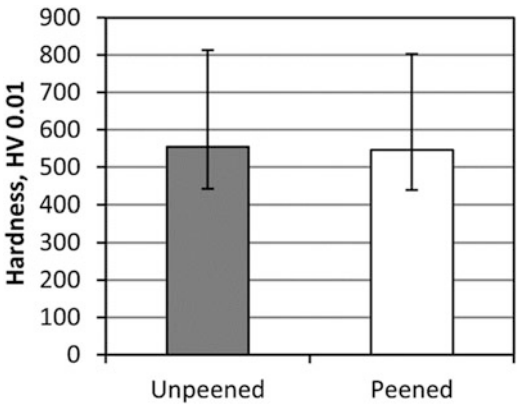

Fig. 27.7 Micro-hardness on the surface

load–displacement curve. The fringes in the elastic range (Fig. 27.8a) were distributed in all the area of specimens. The deformation can be considered to be entirely elastic. Before the yielding, the fringes begin to concentrate to one side of the neck of specimen as shown in Fig. 27.9b, while the curve is almost linear in this load range. The concentrated fringes develop to a discontinuous region as shown in Fig. 27.8c. Figure 27.9 shows the optical micrograph of the area of fringe concentration. The shear bands inclined at about 54° to the tensile axis are observed and form a mesh pattern. A shear band is formed by propagation of the grain slips. This indicates that local plastic deformation occurred at the neck. The shear band subsequently grows toward the other side of neck until the maximum load. In the fringe pattern of Fig. 27.8d, the band consisting of the large number of fringes is observed as a white band. When the white band grew across the width of specimen as shown in Fig. 27.8e, macroscopic plastic deformation began with drifting of the shear band. In contrast, the fringe patterns in the peened specimen showed a uniform change as shown in Fig. 27.10. The fringe concentration at the beginning of local plastic deformation more gradually progresses as compared with the behavior in the un-peened specimen (Fig. 27.10a–c). The interval of fringes decreases with increase in the applied load and consequently forms a white band similar to the un-peened specimen at the yield strength.

Figure 27.11 shows results of strain analysis for the deformation behavior shown in Figs. 27.8 and 27.10. The strain obtained from the fringe pattern indicates the values in the time interval corresponding to the subtracted frames. The analysis

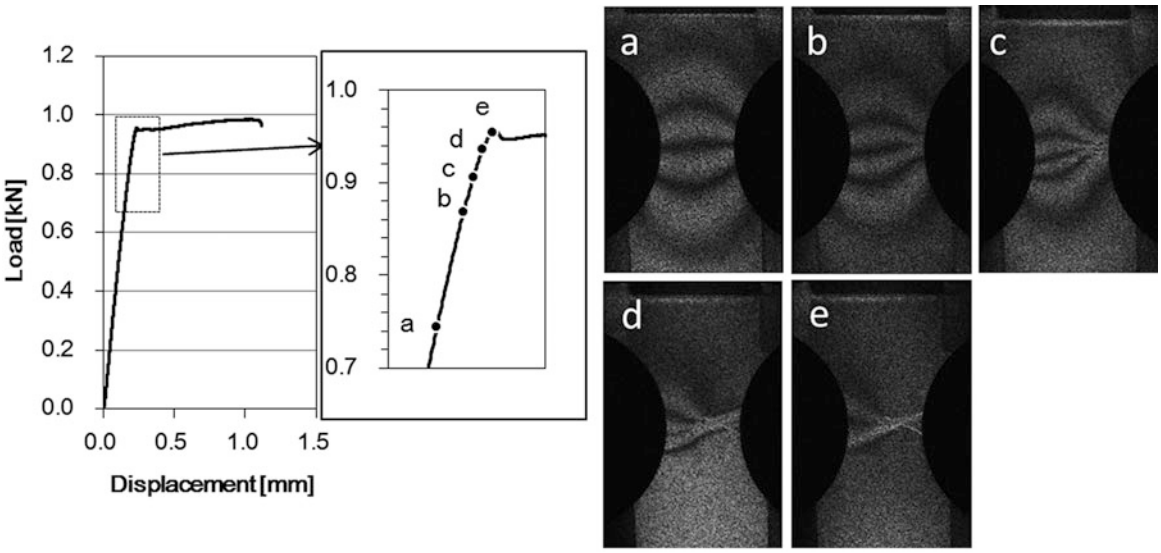

Fig. 27.8 Load–displacement curve and fringe patterns before the yielding in the un-peened specimen

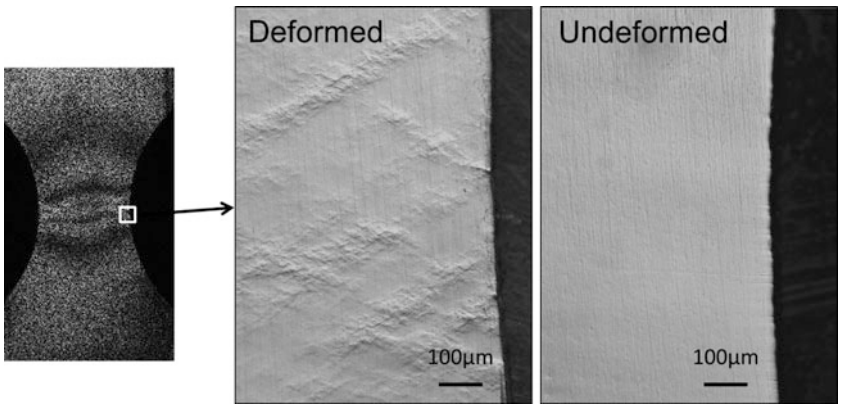

Fig. 27.9 Optical micrographs of the fringe concentration area

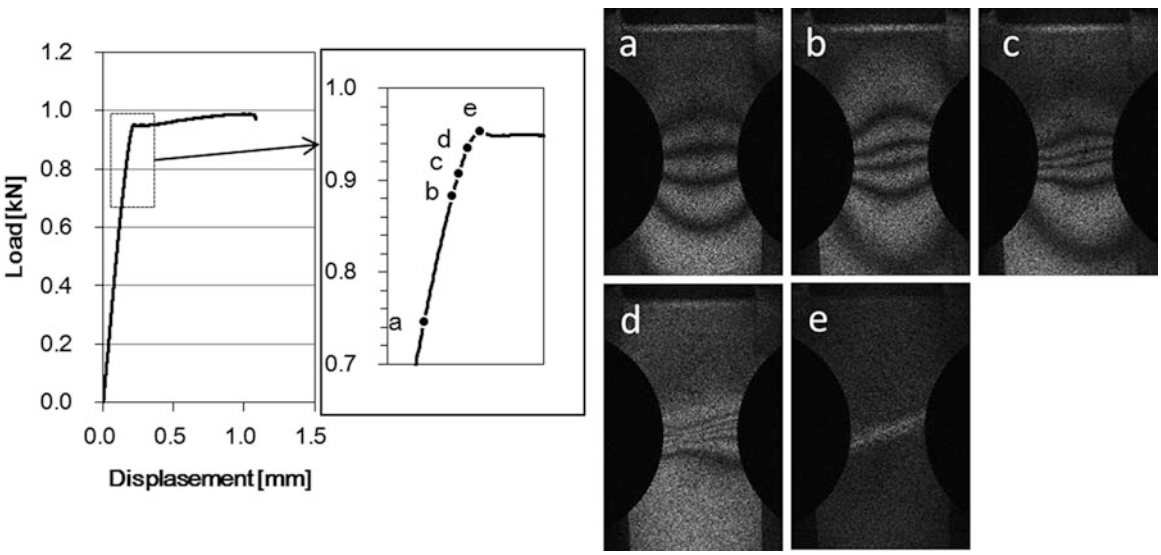

Fig. 27.10 Load–displacement curve and fringe patterns before the yielding in the peened specimen

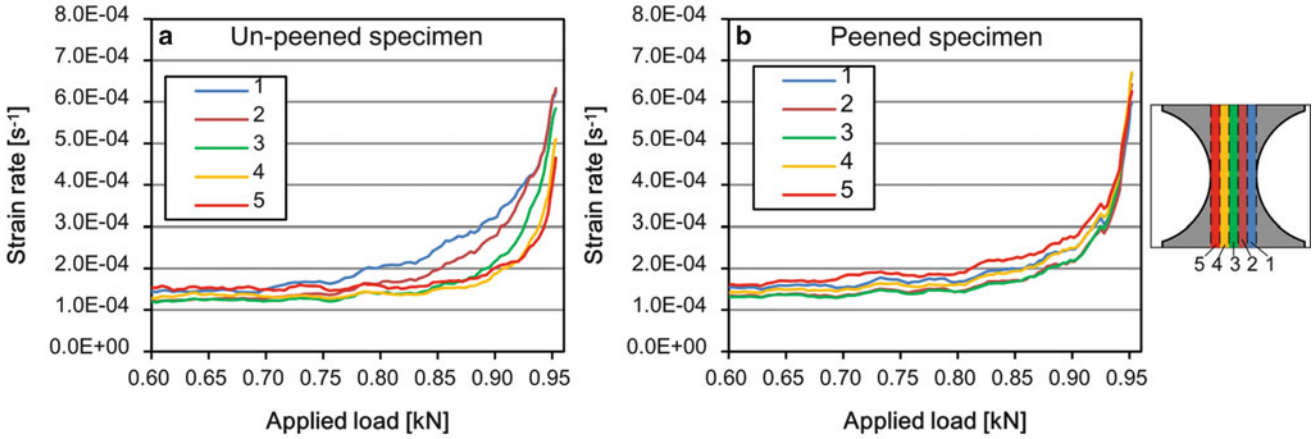

Fig. 27.11 Variation of strain rate around the neck of specimen

was performed for five regions with 1.6 × 30 mm as shown in Fig. 27.11, and the maximum values in the region were plotted against the applied load. In the un-peened specimen, the strain rate starts to increase from the one side of specimen (in order of No.1–5), while in the peened specimen, the increase in strain rate rapidly occurs at the all regions. The relaxation of micro-strain by the peening as observed in the results of X-ray diffraction and micro-hardness leads to homogenization on the surface, and this effect might suppress the crack initiation by stress concentration in the fatigue test.

27.4 Summary

Cavitation peening was applied to thin austenitic stainless steel sheets, and the effect of peening on the fatigue resistances, the residual stress on the surface, the surface morphology, and the micro-hardness distribution were investigated. The cavitation peening improved the fatigue strength of the specimen by about 10 %. The residual stress evaluated by FWHM of X-ray diffraction, and the micro-hardness on the surface showed slight decreases in the peened specimen. It has been concluded that the microscopic strain preliminary induced by cold working was relaxed by the cavitation peening. The effect of the peening process appeared in the deformation behavior in the transition of elastic deformation to the yielding. The optical fringe pattern measured by ESPI showed that the local plastic deformation due to strain concentration was suppressed in the peened specimen. The results has revealed the effect of the cavitation peening on the homogenization of the surface. The improvement of fatigue resistance by the cavitation peening is probably due to the effect of the homogenization on the surface.

References

1. Soyama H, Park JD, Saka M (2002) Use of cavitating jet for introducing compressive residual stress. J Manuf Sci Eng Trans ASME 122:83
2. Soyama H, Saito K, Saka M (2002) Improvement of fatigue strength of aluminum alloy by cavitation shotless peening. J Eng Mater Tech Trans ASME 124:135
3. Odhiamabo D, Soyama H (2003) Cavitation shotless peening for improvement of fatigue strength of carbonized steel. Int J Fatigue 25:1217
4. Ramulu M, Kunaporn S, Jenkins M, Hashish M, Hopkins J (2002) Fatigue performance of high-pressure water jet peened aluminum alloy. J Press Vess Technol Trans ASME 124:118
5. Nakagawa M, Watanabe T (2004) Introducing compressive residual stress on metal surface by irradiating ultrasonic wave with horn in water. J Jpn Weld Soc 22:587, in Japanese
6. Rastogi PK (1993) In: Sirohi RS (ed) Speckle metrology Marcel Dekker, New York, p 41

Chapter 28
Effect of Residual Stress on Spallation of NiCrBSi Coating

Chen-Wu WU

Abstract The impact induced spallation characteristics of two specimens with NiCrBSi coating developed by different treatments are investigated. Two typical spallation patterns corresponding to the two kinds of specimens are observed. Theoretical analysis indicates that the difference in spallation characteristics is due to the residual stress. The initial stress states for the two kinds of specimens are investigated. The outcomes verify that the compressive residual stress within the coating will lead to large buckling region of the coating upon impact.

Keywords Coating • Impact • Residual stress • Spallation • Buckling

28.1 Introduction

Hard alloy coatings are widely used on the surface of the parts to improve its resistance to wear, impact and thermal degradation. The adhesion of the coating to the substrate is crucial for the integrity of the component. Wu et al [1, 2] developed an impact testing method to evaluate the interface adhesion of coating to substrate. In such method, a front-end-coated light bullet is accelerated by powder gun or gas gun and impinged at the substrate side of the coated specimen. The input compressive stress pulse would be reflected into tensile stress pulse at the test interface and ultimately makes the coating to separate from the substrate. Moreover, their recent work also showed that the residual stress would influence the impact responses of the coatings [3]. After the interface debonding, the off-plane displacement of the test coating will introduce large in-plane tensile stress within the coating. Such in-plane stress will be influenced by the residual stress of the test coating. Furthermore, the residual stress in the coating may also influence the propagation of the interface cracking. Generally speaking, the interface debonding and coating stress should be mutually dependent. This may be the principle mechanism why residual stress would affect the impact response of the coatings.

In the present work, the method of Bullet Impact is applied to study the dynamic fracture behavior of the NiCrBSi coating on superalloy substrate. It has been shown that the residual stress within the NiCrBSi coatings can be different with different processing conditions [4, 5]. In particular, the large residual stress can be reduced or even reversed by remelting after spraying. As mentioned, the residual stress would greatly influence the fracture behaviors of the coating upon impact. Therefore, this research focuses on relating the spallation pattern of the coating with its residual stress state.

First, experiments were conducted to investigate the spallation behaviors of the coating. The results reveal that two distinct spallation patterns could be obtained for the coatings with different processing conditions, by which different interface adhesion and different residual stress state were developed. Then, the residual stresses of the two kinds of specimen were measured by XRD and related to the spallation patterns. Finally, the cause of the different spallation patterns is discussed by considering the effect of residual stress. It is demonstrated that the residual stress can significantly influence the cracking pattern of the coating when subjected to impact by a front-end coated bullet.

C.-W. WU (✉)
Institute of Mechanics, Chinese Academy of Sciences, No. 15 Beisihuanxi Road, Beijing 100190, China

Department of Engineering Technology and Industrial Distribution, Texas A&M University, College Station, Texas 77843, USA
e-mail: chenwuwu@imech.ac.cn; cwwu@tamu.edu

M. Rossi et al. (eds.), *Residual Stress, Thermomechanics & Infrared Imaging, Hybrid Techniques and Inverse Problems, Volume 8*, Conference Proceedings of the Society for Experimental Mechanics Series, DOI 10.1007/978-3-319-00876-9_28,

28.2 Experimental Description and Results

28.2.1 Description of the Test

According to the bullet impact method, experiments are carried out as depicted in Fig. 28.1a, b. Two types of NiCrBSi coatings are tested, of which one is as-sprayed coating and the other coating is subjected to re-melting after spraying. The thickness of the superalloy substrate and coating is 5 and 0.3 mm, respectively. The planar dimension of the specimen is about 150 × 100 mm. The cylindrical nylon bullet is used with its front end coated with nickel foil. The bullet diameter is 12.7 mm and the bullet coating, nickel foil thickness is about 20 μm. And the length of the bullet body is approximately 50 mm, which is enough to avoid the disturbance from the secondary pulse reflected from the bullet rear of the bullet [1]. After the impact test, the specimen is observed and optical images are taken to investigate its spallation morphology.

28.2.2 Test Results

The coated bullet accelerates to about v = 100 m/s and impinges at the specimen substrate. The typical spallation morphology is shown in Fig. 28.2a, b, of which the bullets after test have also been provided. Obviously, the nylon bullets front-end exaggeratedly cracked and expanded into mushroom geometry due to the severe impact.

The magnified central impacted region is shown in Fig. 28.3a, b. One can see that the clear separation is developed in the impact region for the remelted specimen (Fig. 28.3a), comparing to interface debonding and radial cracking of the as-sprayed specimen (Fig. 28.3b). Comparing to the re-melted coating, a larger spallation area on the as-sprayed specimen was observed.

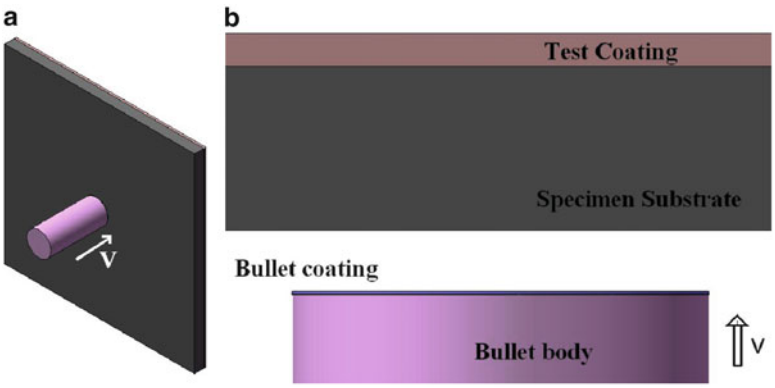

Fig. 28.1 (**a**) Sketch of the impact test and (**b**) magnified part of the specimen and bullet

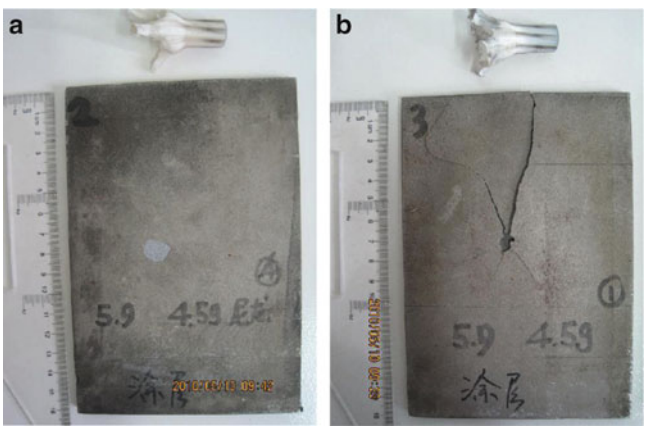

Fig. 28.2 Photo after test for (**a**) re-melted coating and (**b**) as-sprayed coating

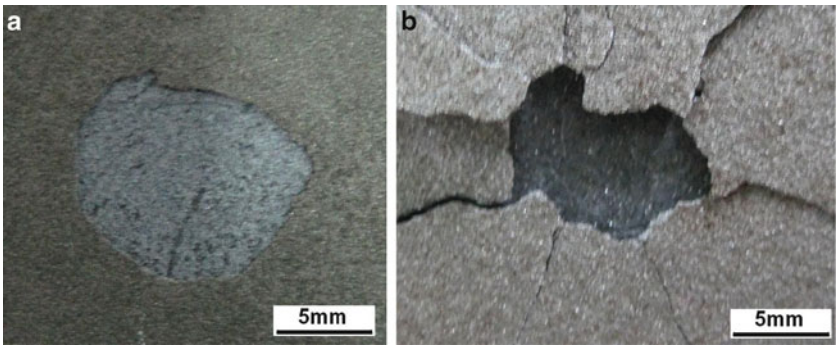

Fig. 28.3 Surface morphology for (**a**) re-melted coating and (**b**) as-sprayed coating

As for the difference in the material states of the two kind of specimen, the remelting process would change the properties of the coating, the interface bonding condition as well as the residual stress state. Strictly speaking, such factors may all contribute to the dynamic fracture behaviors of the coatings. Considering the fact that there is not enough evidence at present for the change of coating properties and interface bonding condition, only the effect of the residual stress state on the impact failure of the coatings is taken into account.

28.3 Residual Stresses and Its Effect

The XRD method [6] was used to measure the surface residual stress in the coating as shown in Fig. 28.4a and a typical test result is shown in Fig. 28.4b. The residual stresses were tested at the locations at different distances from the adjacent free edge of the specimens. Two orthogonal surface stress components are measured for each test point considering the rectangle geometry characteristic of the specimen. The tested orthogonal stress components are parallel to the orthogonal free edges of the specimen.

The measured results reveal that the tested points are almost of equiaxial residual stress states. The algebraic average residual stresses are obtained from the two stress components. The residual stresses versus the distance from the adjacent free edge are graphed in Fig. 28.5a, b. Figure 28.5a, b represent the residual stresses of remelted coating and as-sprayed coating, respectively. Considering the uncertainty of the measurement, about 20 % of the measured value should be regarded as test error. It is indicated that the absolute value of the residual stresses for both coating decrease from the center to the free edge of the specimen, for which it is conceivable that the residual stress should be gradually released by the free edge.

Basically, even considering the test uncertainty, the measurement results still indicate that large compressive residual stress exists in the as-sprayed NiCrBSi coatings. However, this residual stress will be reduced greatly or even changed into small tensile stress by the remelting treatment.

Such difference in residual stress may lead to the difference in the spallation patterns as shown in Figs. 28.2 and 28.3, with which the theoretical descriptions on the spallation process are sketched as in Fig. 28.6a, b. In Fig. 28.6a, b, the last picture of each case is shown in half plane view while the others are shown in cross section view. The off-plane displacement of the coating under bullet impact will result in large tensile stress in the coating, especially around the edge of the impact region. Such tensile stress will lead to fracture of the coating as shown in Fig. 28.6a. As for the clear interface separation between coating and substrate, there is not much deflection in the coating relative to the substrate. Thus the impact induced interface normal stress would not be significantly influenced by the in-plane residual stress [3]. Therefore the interface debonding will arise once the reflected stress pulse arrive or exceed the interface strength σ_{inter} [2],

$$2v(\rho c)_1(\rho c)_2(\rho c)_3/\left(\left((\rho c)_1+(\rho c)_2\right)\left((\rho c)_2+(\rho c)_3\right)\right) \geq \sigma_{inter} \tag{28.1}$$

where, v is the initial impinged velocity of the bullet, ρ and c represents density and elastic wave velocity of the medium, respectively. The subscripts 1, 2 and 3 are representing bullet coating, specimen substrate, and specimen coating.

In summary, as shown in Fig. 28.6a, the remelted coating subjected to impact test would mainly experience three conditions in stages: interface debonding, coating fracture and coating fragment flying away.

If large compressive residual stress exists within the coating, the compressive residual stress may offset the tensile stress resulted from impact. On the other hand, the large compressive residual stress will lead to buckling of the coating after the interface debonding. The buckling will lead to propagation of interface crack, as shown in Fig. 28.6b. Once the interface

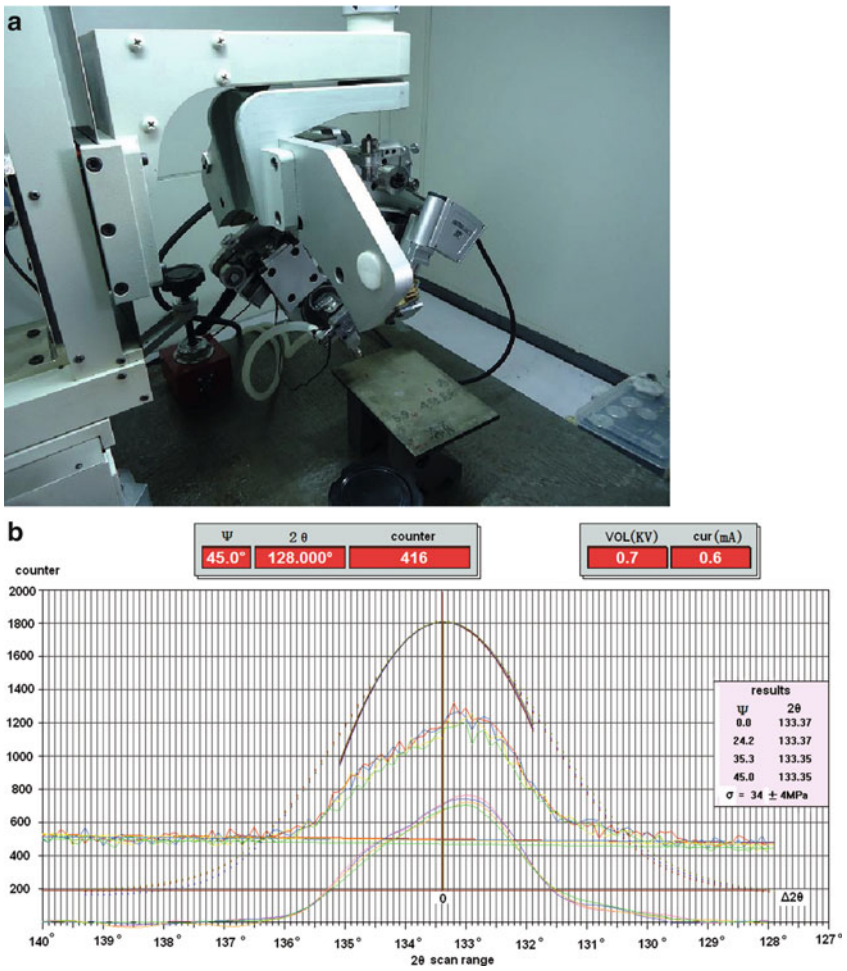

Fig. 28.4 (**a**) Photo of residual stress measurement and (**b**) typical test result

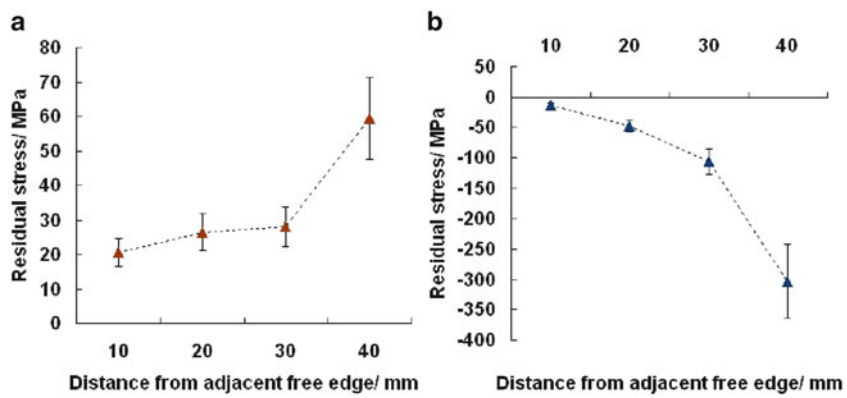

Fig. 28.5 Residual stresses of (**a**) re-melted coating and (**b**) as-sprayed coating

debonding is fully developed by the tensile stress pulse within the impact region, the circular plate buckling theory can be approximately applied. Furthermore, the circular coating separated from the substrate is of boundary constraint more flexible than being clamped while more rigid than pinned. Therefore, we can estimate the critical buckling radial stress σ_{cr} as [7, 8],

$$\sigma_{cr} \approx 0.7875 \times \left(E/\left(1-\nu^2\right)\right) \times (h/r)^2. \tag{28.2}$$

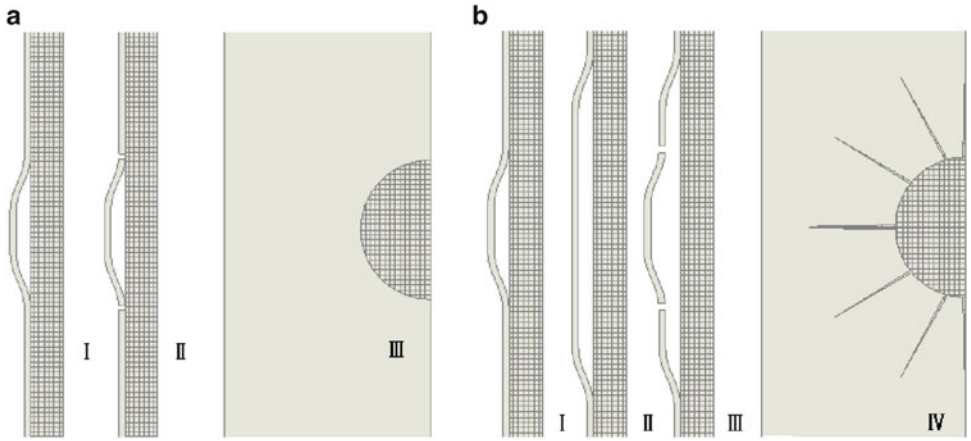

Fig. 28.6 Half size diagram for spallation of (**a**) re-melted coating and (**b**) as-sprayed coating

where E, ν is the elastic modulus and Poisson's ratio of the coating, respectively; h and r represent the thickness and the radius of the debonding region, respectively. If the elastic parameters [9] of the NiCrBSi coating of $E \approx 200$GPa, $\nu \approx 0.15$ and geometrical parameters $h \approx 0.3$ mm, $r \approx 6$ mm are substituted into Eq. 28.2, the critical buckling stress should be about 400 MPa. As shown in Fig. 28.5b, the largest stress component is about 300 MPa. After being transmitted to the polar coordinate component, the radial residual stress should be about 420 MPa. Considering the fact that a dynamic lateral loading with impact, the actual critical buckling stress should be lower than that estimated by Eq. 28.2. Thus, it is believable that the buckling would appear after interface debonding is developed within the impact region. Upon buckling of the coating, the in-plane residual stresses will influence the interface stress due to the coating inclination relative to the substrate. From the energy point of view, the off-plane deformation of coating will partially release the residual stress. Such reduction in elastic energy can increase the energy release rate of the interface crack. Generally speaking, the interface crack will propagate if the elastic energy release rate exceeds the interface fracture toughness. Therefore, the interface crack propagation will be enhanced by the residual stress. Of course, the center region of the coating will also crack along the circumferential direction as the tensile stress would increase with the further off-plane displacement of the coating segment covered by impact region.

In summary, the as-sprayed coating subjected to impact test would experience conditions in four stages: interface debonding, coating buckling with interface crack propagation, coating fracture and coating fragment flying away. The major difference in the spallation process of the two kinds of coating is the large buckling of the as-sprayed coating. This should be attributed to the contribution of the large compressive residual stress within these coating. As for the fact that the remelting treatment can reduce the residual stress, the remelted coating would not experience the large buckling stage. However, it is noteworthy that the remelting process may also increase the interface fracture toughness, which can hold back the interface crack propagation and therefore prevent the buckling of the coating.

28.4 Conclusion

Two kinds of NiCrBSi coating are subjected to bullet impact test and two corresponding distinct spallation patterns are observed. Residual stress measurements based on XRD indicate that large compressive residual stresses were developed within the as-sprayed coating while the remelting treatment reduced such residual stress to a negligible level. Due to the high compressive residual stress within the as-sprayed coating, large regime buckling of the coating will appear under impact. It is demonstrated theoretically that the distinction in the spallation of the coating could have been resulted from the difference in their residual stress states. Considering the fact that the remelting treatment can also change the interface strength, further investigation is needed to separate the contribution of the improvement in interface properties.

Acknowledgements This work was supported by the National Natural Science Foundation of China (Grant No. 11002145). The author is very grateful to Prof./Dr. Jyhwen WANG from TA&MU for the helpful discussion and revision in writing. Thanks are also due to Z.-L. WU from NUST, Z.-T. WANG from NUST, X.-X. CHENG from CAS and Y.-C. YUAN from CAS for their assistance in carrying out the experiments.

References

1. Wu CW, Wu ZL, Zhang K, Chen GN (2009) Evaluation of film-substrate adhesion via impact using coated bullets. J Mech Mater Struct 10 (4):1703–1709
2. Wu ZL, Wu CW, Chen GN, Zhang K (2010) On a novel method of impact by a front-end-coated bullet to evaluate the interface adhesion between film and substrate. Prog Org Coat 68(1–2):19–22
3. Wu CW (2011) Effect of residual stresses on spallation of the film under impact by coated bullet. Exp Appl Mech 6:239–252
4. Simunovic K, Franz M, Maric G (2008) Investigation and estimation of residual stress in flame sprayed and fused NiCrBSi coatings. Metalurgija 47:93–97
5. Bergant Z, Grum J (2009) Quality improvement of flame sprayed, heat treated, and remelted NiCrBSi coatings. J Thermal Spray Technol 18(3):380–391
6. Prevey PS (1986) X-ray diffraction residual stress techniques. In: American Society for Metals (ed) Metals handbook, vol 10. American Society for Metals, Metals Park, pp 380–392
7. Szilard R (1974) Theory and analysis of plates. Prentice-Hall, Englewood Cliffs, New Jersey
8. Kerr AD (1962) On the instability of circular plates. J Aeronaut Sci 29(4):486–487
9. Lu SP, Kwon OY, Guo Y (1986) Wear behavior of brazed WC/NiCrBSi (Co) composite coatings. Wear 254:421–428

Chapter 29
Multiaxial Fatigue Resistance of Shot Peened High-Strength Aluminium Alloys

M. Benedetti, V. Fontanari, D. Bergamini, M. Bandini, and D. Taylor

Abstract This paper is aimed at investigating multiaxial fatigue of shot peened Al-7075-T651 alloy. Plain axi-symmetric specimens were subjected to combined in-phase tension and torsion loading, under nominal load ratio $R = 0.05$ and biaxiality ratio $\lambda = \tau_a/\sigma_a = 2$. The results from multi-axial tests are discussed together with those obtained under pure tension and pure torsion loading. Fatigue crack initiation sites have been investigated through scanning electron microscopy fractography and the role of surface roughness on fatigue resistance has been analyzed. The initial and the stabilized residual stress profiles were used to discuss the improvement in the fatigue response in the hypothesis of crack initiation and early crack propagation as fatigue controlling parameters. For this purpose, several multiaxial fatigue criteria were used to account for the residual stress field.

Keywords Multiaxial fatigue • Al-7075-T6 • Shot peening • Residual stresses • Fatigue criteria

29.1 Introduction

Aluminium alloys are an attractive class of materials for aircraft and automotive industry because of their high specific static strength. In aerospace, aluminium alloys face ever stiffer competition from composites. In the automotive context, more and more engine parts are being made from them. Usually, high static mechanical properties are induced in aluminium alloys by dispersion hardening through solution and ageing heat treatments. However, aluminium alloys exhibit poor plain fatigue resistance [1] and high notch fatigue sensitivity [2]. Accordingly, stress raisers, like holes, fillets and grooves, always present in machine parts, are particularly detrimental to the fatigue response of these alloys, thus limiting their use in highly stressed mechanical components characterized by complex shapes. For this reason, aluminium alloys are frequently subjected to shot peening, particularly effective in incrementing the plain and notch fatigue strength of steels and light alloys. The shot peening mainly results in three fatigue related modifications of the surface layers: roughness, residual stresses and work hardening. Clearly, the surface roughening after shot peening is detrimental to the fatigue resistance due to the stress concentration exerted by the surface dimples. In the literature, it is commonly accepted that the improvement of fatigue strength is mainly induced by the introduction of compressive residual stresses in the surface region, responsible for both retarded fatigue crack initiation and lower small crack growth rates [3, 4]. The role of work hardening on the fatigue response is essentially indirect, since it strongly affects the stability of residual stresses by preventing them from relaxing due to accumulation of plastic deformation [5].

M. Benedetti (✉) • V. Fontanari • D. Bergamini
Department of Industrial Engineering, University of Trento, via Mesiano 77, 38100 Trento, Italy
e-mail: matteo.benedetti@ing.unitn.it

M. Bandini
Peen Service s.r.l, via Pollastri 7, 40138 Bologna, Italy
e-mail: m.bandini@peenservice.it

D. Taylor
Department of Mechanical Engineering, Trinity College Dublin, Dublin 2, Ireland
e-mail: dtaylor@tcd.ie

M. Rossi et al. (eds.), *Residual Stress, Thermomechanics & Infrared Imaging, Hybrid Techniques and Inverse Problems, Volume 8*, Conference Proceedings of the Society for Experimental Mechanics Series, DOI 10.1007/978-3-319-00876-9_29,

Up to now, the majority of investigations have been focused on uniaxial loading, whereas the effect of shot peening under multiaxial fatigue loading is poorly understood. This topic is however of great interest, mainly for two reasons: (i) shot peening introduces a fairly equibiaxial residual stress field, so it is desirable to know the response of high-strength Al alloys under multiaxial loading in order to conveniently calibrate multiaxial fatigue criteria that can account for this biaxial stress field. (ii) Structural parts made of high-strength Al alloys for aerospace applications (e.g., aircraft fittings, gears and shafts) are frequently subjected in service to multiaxial loading (axial, torsion, bending); therefore, it is interesting to quantify the beneficial effect of shot peening in the presence of such external multiaxial stress field.

This paper is aimed at investigating multiaxial fatigue of shot peened Al-7075-T651 alloy. Plain axi-symmetric specimens were subjected to combined in-phase tension and torsion loading, under nominal load ratio $R = 0.05$ and biaxiality ratio $\lambda = \tau_a/\sigma_a = 2$. The results from multi-axial tests are discussed together with those obtained under pure tension and pure torsion loading. Fatigue crack initiation sites have been investigated through scanning electron microscopy fractography and the role of surface roughness on fatigue resistance has been analyzed. The initial and the stabilized residual stress profiles were used to discuss the improvement in the fatigue response in the hypothesis of crack initiation and early crack propagation as fatigue controlling parameters. For this purpose, several multiaxial fatigue criteria were used to account for the residual stress field.

29.2 Materials Experimental Procedures

The experimentation has been performed on the aluminium alloy Al-7075-T6, widely used for aeronautical applications, supplied in the form of extruded bars with 15 mm diameter. The bulk material properties have been determined on five standard monotonic tensile tests (initial strain rate of $1{\cdot}10^{-3}$ s^{-1}) performed in the longitudinal orientation. The results, summarized in Table 29.1, show yield strength higher than 500 MPa, combined with good material ductility (total elongation of 15 %).

The fatigue characterisation has been carried out on plain axi-symmetric hourglass specimens whose geometry is illustrated in Fig. 29.1. The microstructure has been tested with the stress axis parallel to the L-direction. The first type of samples (Fig. 29.1a), with threaded end connections, has been used for pure tension tests. The second type of samples (Fig. 29.1b), with straight-sided collet-grip, has been used for pure torsion and combined tension-torsion tests.

Part of the specimens has been subjected to controlled shot peening: the parameters of the peening treatment considered are summarized in Table 29.2. The treatment employs small ceramic beads leading to a gentle and superficial effect, which allow for higher fatigue performance as compared with larger beads [6].

Pure tension fatigue tests have been carried at a nominal frequency of 150 Hz using a resonant testing machine (Fig. 29.2a), whereas pure torsion and combined tension-torsion fatigue tests have been carried out at a nominal frequency

Table 29.1 Monotonic tensile properties of the Al-7075-T651 alloy

E (GPa)	$\sigma_{Y0.2}$ (MPa)	UTS (MPa)	σ_F (MPa)	T.E. (%)	R.A. (%)
72 (±1)	515 (±5)	575 (±5)	760 (±10)	15 (±2)	20 (±2)

E elastic modulus, $\sigma_{Y0.2}$ 0.2 % yield stress, *UTS* ultimate tensile strength, σ_F true fracture stress, *T.E.* total elongation, *R.A.* reduction in area

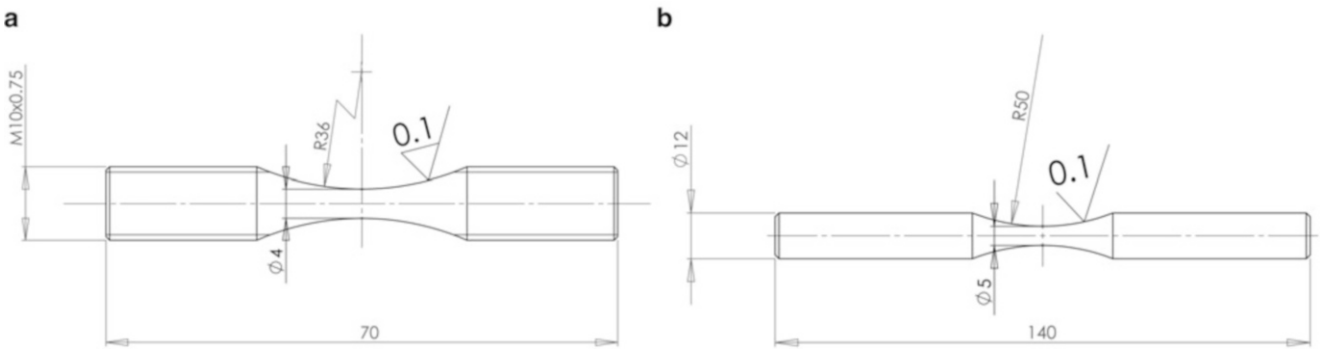

Fig. 29.1 Geometry of the specimens used in this study. (**a**) Pure tension and (**b**) pure torsion and combined tension-torsion specimens. All dimensions are given in mm

Table 29.2 Shot peening parameters

Treatment	Material	Bead size (μm)	Bead hardness (HV_1)	Bead composition	Almen intensity	Angle of impingement	Coverage (%)
B120	Ceramic	60–120	700	ZrO_2 67 % SiO_2 31 %	4.5 N	90°	100

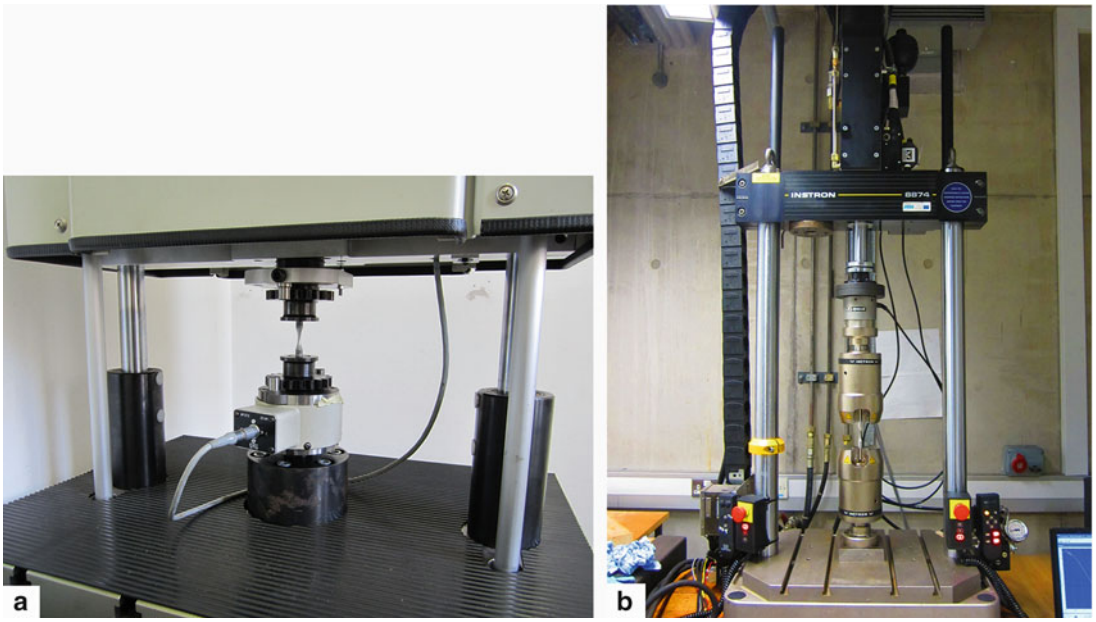

Fig. 29.2 Testing machines used in the present study. (**a**) resonant testing machine for pure tension tests, (**b**) servo-hydraulic biaxial machine for pure torsion and combined tension-torsion tests

of 2 Hz using an Instron 8874 servo-hydraulic biaxial machine with a 10 kN axial load cell and a torsion load cell of 100 Nm. All tests have been performed under load control, loading ratio R = 0.05, in laboratory environment. Combined tension-torsion fatigue tests were carried out with a biaxiality ratio (i.e. the nominal torsion stress to the nominal (maximum) tensile stress) equal to 2 and phase angle equal to 1 (in-phase loading).

Different stress levels corresponding to fatigue lives in the range between nearly 10^4 and 10^6 cycles have been considered. Pure tension tests were terminated at 3×10^6 cycles when no fracture occurred, while pure torsion and combined tension-torsion tests were interrupted at 1×10^6 cycles. The fatigue curves corresponding to 50 % of failure probability, represented by the S-N curve:

$$\sigma_{P50} = \sigma_{0P50} \times N_f^{-\frac{1}{k}} \tag{29.1}$$

were determined by fitting the $\log(N_f)$ versus $\log(\sigma)$ results. The uncertainty range was assumed to be constant and approximated by its centroid value. As a representative value of the scatter, the following expression was used:

$$T\sigma = 1 : \sigma_{P90}/\sigma_{P10} \tag{29.2}$$

P_{90}, P_{10} denote the 90 % and 10 % levels of failure probability, respectively.

The analysis of the residual stress field induced by the peening treatments was carried out by measuring the stress profile by XRD technique. For this purpose, an AST X-Stress 3,000 X-Ray diffractometer (radiation Cr Kα, irradiated area 1 mm^2, $\sin^2\psi$ method, 11 diffraction angles (2θ) scanned between −45° and 45°) was used. The in-depth measurements were performed step-by-step removing a very thin layer of material using an electro-polishing device.

Both initial and stabilized residual stress fields were measured. For this purpose, measurements were performed on tested specimens after failure in a region far enough from the fracture surface (about 2 mm) so that the material rupture was supposed not to have altered the residual stress field [6].

29.3 Results and Discussion

29.3.1 Fatigue behaviour

The results of the pulsating bending fatigue tests as well as the P50 fatigue lines are compared in Fig. 29.3a–c for pure tension, pure torsion and multi-axial loading, respectively, in the different material variants considered. The parameters representing the fatigue curves corresponding to 50 % of failure probability, according to Eq. 29.1 and the results scatter, expressed by Eq. 29.2 are listed in Table 29.1.

The peening treatment considered was effective in prolonging the fatigue life of the material, even in the presence of multi-axial loading, as well as in reducing the large scatter in fatigue results displayed by the virgin material. This improvement depends on the loading type, being more remarkable for torsion and combined tension-torsion with respect to pure tension. This can be explained by the fact that under pure tension the entire cross section of the specimen is subjected to the same external stress, while under torsional loading the outer material layer undergoes higher stress levels with respect to the core. The beneficial effect exerted by the superficial compressive residual stress field induced by shot peening is then expected to be different in the two loading conditions (Table 29.3).

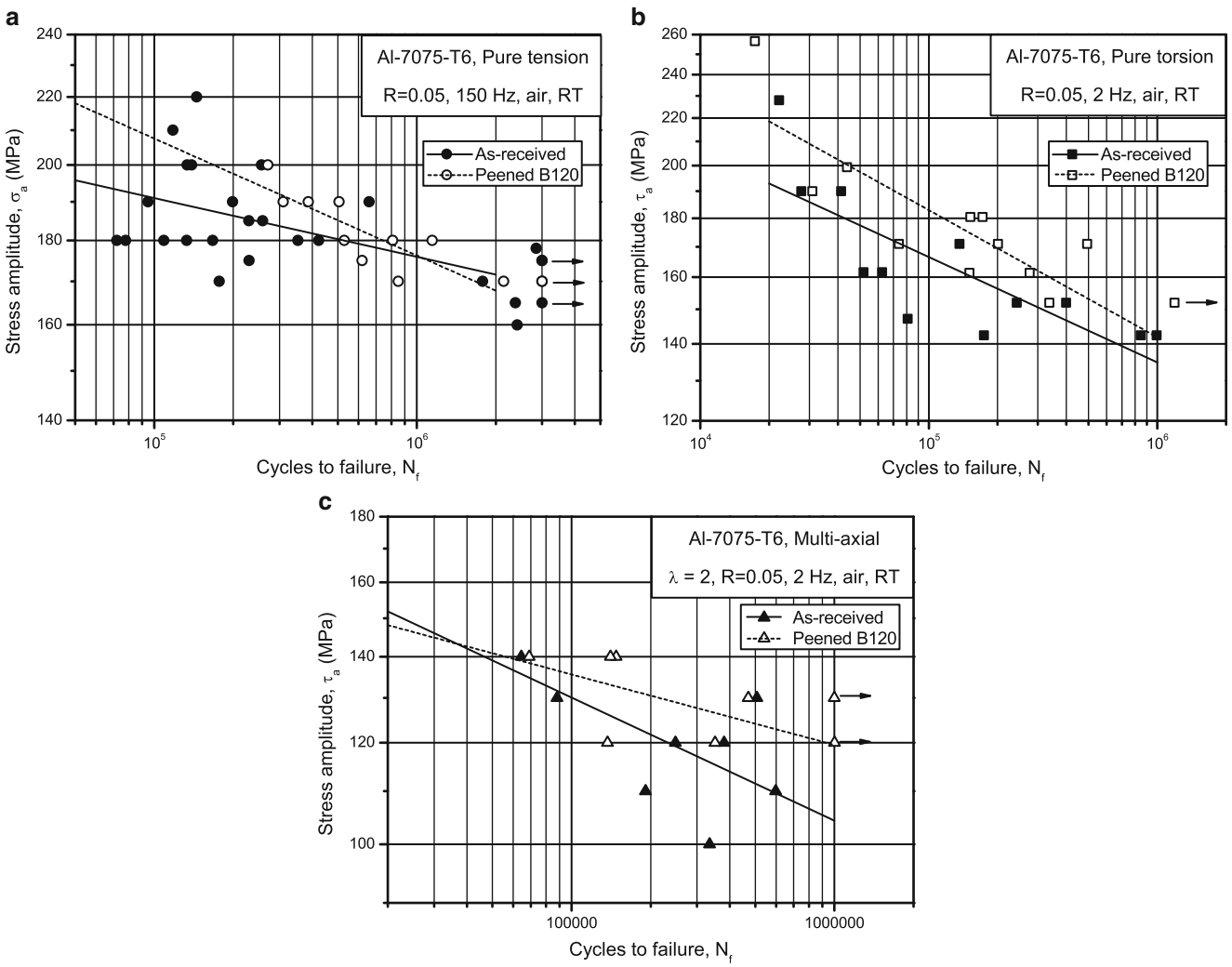

Fig. 29.3 Fatigue curves of the as-received and peened conditions: (**a**) pure tension, (**b**) pure torsion, and (**c**) combined tension-torsion loading. Run-out tests are marked by *arrows*

Table 29.3 Principal results of fatigue tests

		Wöhler curve		
Loading	Condition	k	σ_{P50} (MPa)	$T\sigma$
Pure tension	As-received	11	480	1:1.25
	Peened B120	9	650	1:1.23
Pure torsion	As-received	28	290	1:1.18
	Peened B120	14	470	1:1.08
Multi-axial	As-received	10	390	1:1.25
	Peened B120	18	255	1:1.18

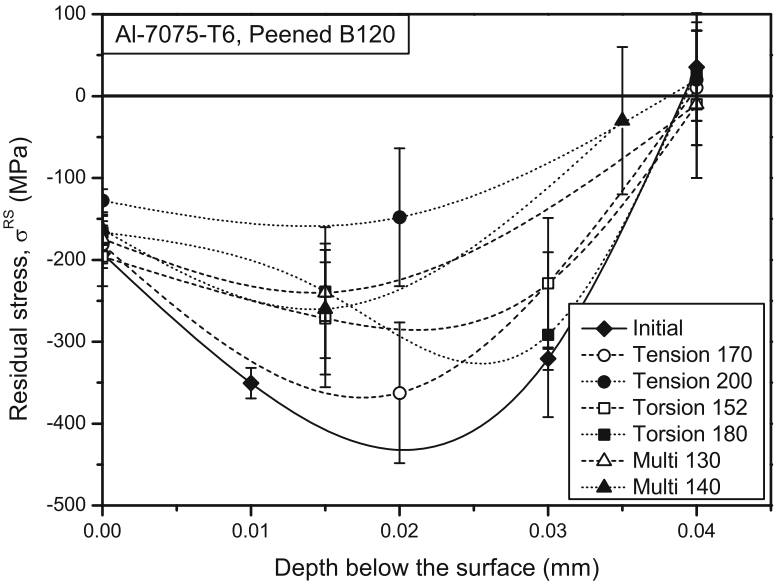

Fig. 29.4 Evolution of the residual stress profile during fatigue life. The plot legend indicates, beside the fatigue loading type, the stress amplitude expressed in MPa

29.3.2 Residual Stress Field

XRD measurements were carried out on the fatigue samples in order to characterize the residual stress field prior to and after fatigue testing. The obtained stress profiles are illustrated in Fig. 29.4. The initial residual stress profile displays a sub-superficial compressive residual stress peak located nearly 20 μm below the surface and a depth of the surface layer interested by compressive residual stresses equal to about 40 μm. The surface compressive residual stress amounts nearly 200 MPa. The error of the residual stress measurements is low (less than 50 MPa) within a depth of about 20 μm, where the fatigue response is mostly dictated [6], whereas it increases noticeably at higher depths, presumably due to the very elongated grain structure of the internal material layers that have not undergone recrystallization and hence grain refinement during shot peening.

Figure 29.4 also illustrates the evolution of the residual stress field during fatigue life at two stress levels for each fatigue loading type. It can be noted that the surface residual stress value remains approximately constant, being higher than 150 MPa, except for the pure tension test conducted at the highest stress level. The subsuperficial material layers undergo significant residual stress relaxation, which is more pronounced for the pure tension test conducted at the highest stress level.

29.3.3 Fractographic Analysis

SEM observations carried out on the fracture surfaces of unpeened specimens revealed surface crack initiation under both pure tension (Fig. 29.5a) and multiaxial loading (Fig. 29.5b). The plane of crack initiation is approximately orthogonal to the specimen's axis under pure tension, while it is inclined by an angle of about 30° under multiaxial loading (Fig. 29.5c). Crack nucleation was found to occur in the superficial layers, about 50 μm below the surface, in the peened specimens subjected to

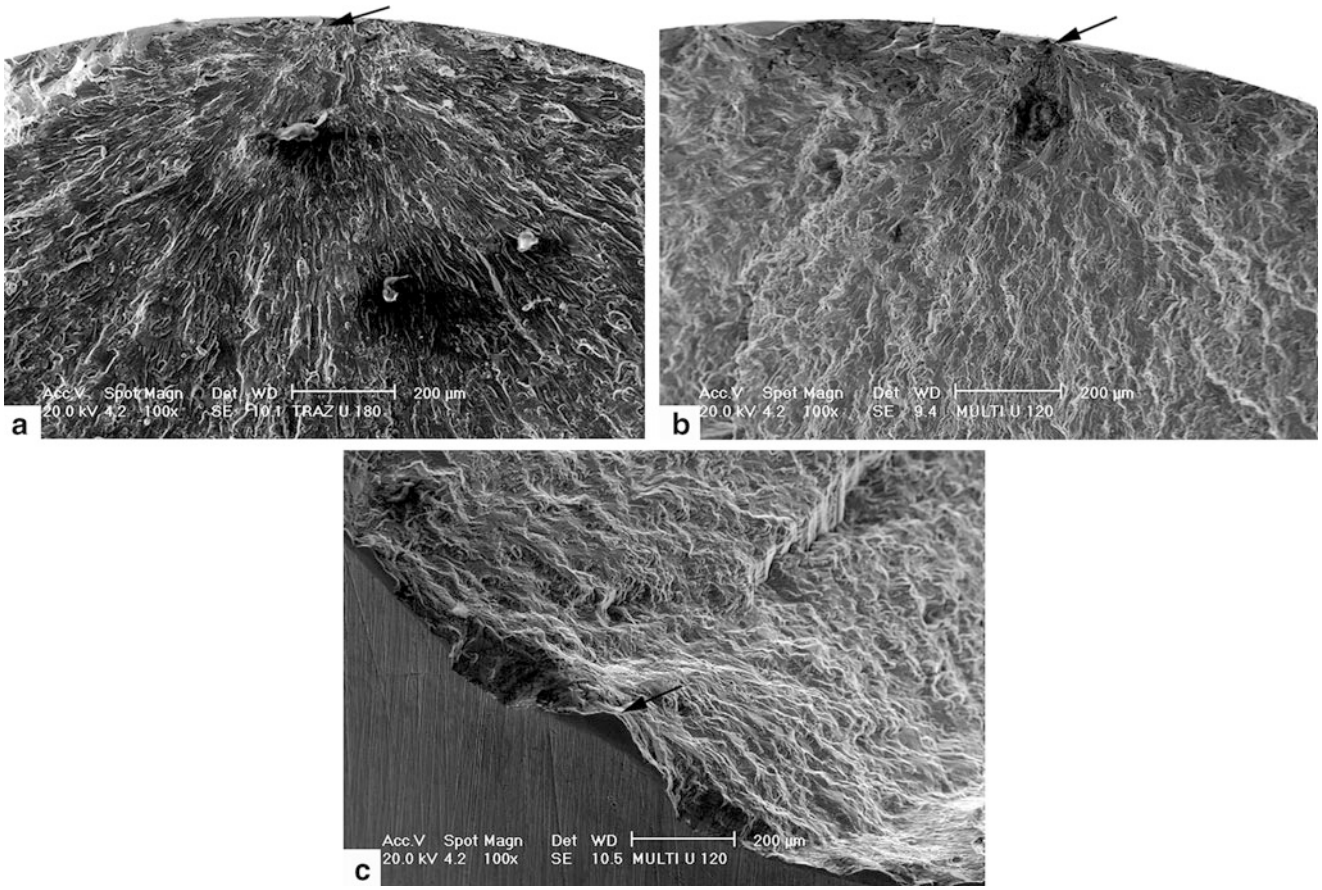

Fig. 29.5 SEM micrographs of the fracture surfaces around the fatigue crack initiation sites in unpeened specimens. (**a**) pure tension ($\sigma_a = 180$ MPa, $N_f = 1 \times 10^5$), (**b**) and (**c**) combined tension-torsion ($\tau_a = 120$ MPa, $N_f = 2 \times 10^5$)

pure tension (Fig. 29.6a) and multiaxial loading (Fig. 29.6b). Similarly to the as-received condition, the plane of crack initiation is approximately orthogonal to the specimen's axis under pure tension, while it is inclined by an angle of about 30° under multiaxial loading (Fig. 29.6c). No information about crack nucleation site under pure torsion was found because the relative sliding between the crack faces destroyed the morphology of the fracture surfaces.

29.3.4 Fatigue Life Prediction

One of the aim of the present work was to identify the most suitable multiaxial fatigue criterion for predicting the fatigue behaviour of high-strength Al alloys, even in the presence of a residual stress field. For this purpose, the uniaxial fatigue data collected under pure tension and pure tension have been used to calibrate the material constants of three well-established multiaxial fatigue criteria: Sines [7], Crossland [8] and Fatemi Socie [9].

The Sines criterion includes the octahedral shear stress amplitude, or equivalently the Von Mises equivalent stress amplitude $\sigma_{VM,a}$, and the mean hydrostatic pressure p_m in a linear equation of the form:

$$\sigma_{VM,a} + \alpha_S \cdot p_m = \beta_S \tag{29.3}$$

Similarly, the Crossland criterion includes the Von Mises equivalent stress amplitude $\sigma_{VM,a}$, and the maximum hydrostatic pressure $p_{\max}$ in a linear equation of the form:

$$\sigma_{VM,a} + \alpha_S \cdot p_{\max} = \beta_S \tag{29.4}$$

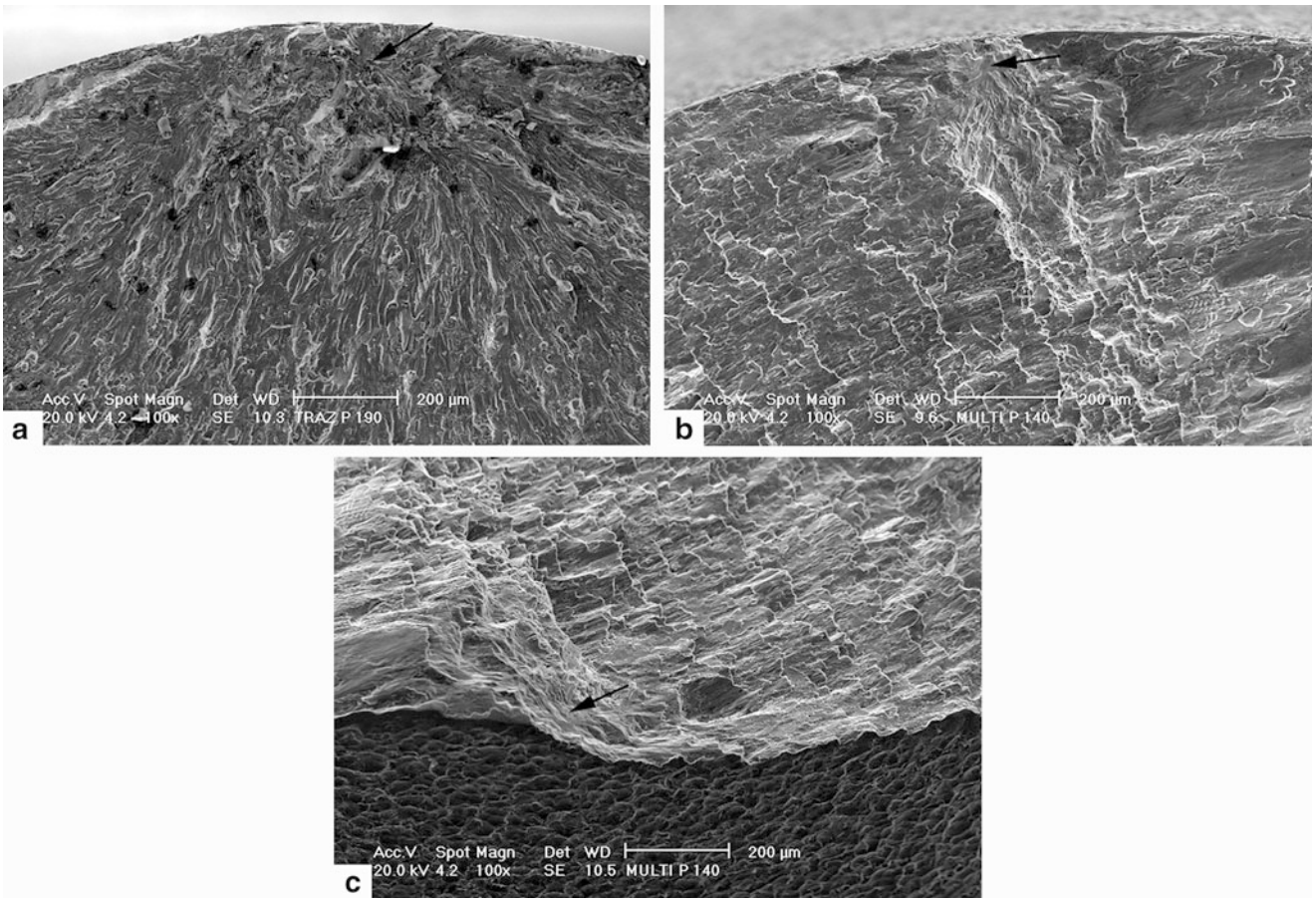

Fig. 29.6 SEM micrographs of the fracture surfaces around the fatigue crack initiation sites in peened specimens. (**a**) pure tension ($\sigma_a = 190$ MPa, $N_f = 5 \times 10^5$), (**b**) and (**c**) combined tension-torsion ($\tau_a = 140$ MPa, $N_f = 1 \times 10^5$)

Both Crossland and Sines criterion have been developed for proportional loading, since they assume a fixed orientation of principal axes associated with the alternating components of strain.

The Fatemi Socie criterion is suitable also for non-proportional loading and is based on the identification of the critical plane experiencing the maximum range of shear strain γ_a. In addition, it incorporates the mean stress by using the maximum value of normal stress $\sigma_{n,\max}$, acting the plane of maximum shear strain range.

$$\gamma_a \left(1 + \alpha_{FS} \frac{\sigma_{n,\max}}{\sigma_Y}\right) = \beta_{FS} \tag{29.5}$$

Figure 29.7a compares the predictions made by the three fatigue criteria with the experimental results from the multiaxial fatigue tests carried out on the unpeened samples. It can be noted that all the criteria are in satisfactory agreement with the experimental data, especially Crossland and Fatemi Socie.

The fatigue strength of the peened material is mainly dictated by the surface roughness and the residual stresses [6, 10]. The effect of the surface roughness was taken into account by incorporating into the fatigue criteria the stress concentration factor determined in [6] for a similar peening treatment. Residual stresses were treated as mean stresses superimposed to the oscillating stresses caused by the external cyclic load. Specifically, the surface residual stress value and an equibiaxial stress field were considered according to Ref. [6]. Figure 29.7b–d compare the predictions made by the three fatigue criteria with the experimental results of the peened specimens subjected to pure tension, pure torsion and multiaxial loading, respectively. It can be noted that the Crossland criterion gives the best fatigue life estimations with respect to Sines and Fatemi Socie criteria. Moreover, material response under pure torsion is satisfactorily predicted over the entire life interval, whereas the response under pure tension and multiaxial loading is overestimated in the low cycle regime, presumably due to relaxation of the surface residual stress observed in these loading conditions at high stress amplitudes.

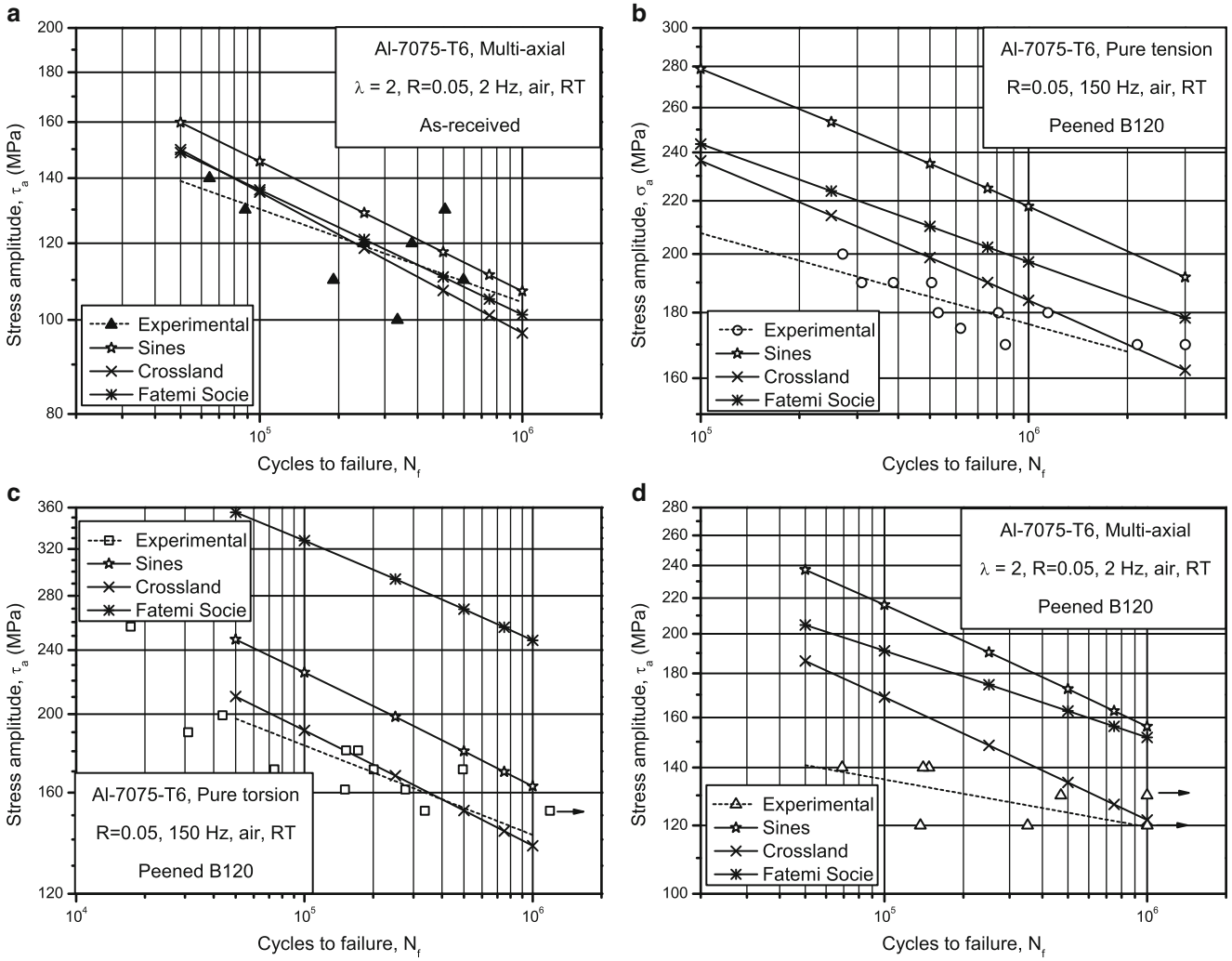

Fig. 29.7 Comparison between experimental and calculated fatigue curves. (**a**) unpeened material under multiaxial loading. Peened material under (**b**) pure tension, (**c**) pure torsion and (**d**) multiaxial loading

29.4 Conclusions

The multiaxial fatigue behaviour of unpeened and peened Al-7075-T6 alloy has been experimentally investigated exploring fatigue lives comprised between 10^4 and 10^6 cycles. The following conclusions can be drawn:

1. Shot peening is an effective method to improve the fatigue endurance of Al-alloys. Dispersion in fatigue resistance is greatly reduced by shot peening.
2. Surface residual stresses are nearly stable during the fatigue life, especially at low stress levels. Subsuperficial layers have a larger tendency to residual stress relaxation if they are subjected to tension.
3. The Crossland multiaxial fatigue criterion can satisfactorily predict the multiaxial fatigue response of unpeened and peened high-strength Al alloys under proportional loading.

References

1. ASM handbook (1991) Properties and selection: nonferrous alloys and special-purpose materials, vol 2, 10th edn. American society for metals, Materials Park
2. Bian JC, Tokaji K, Ogawa T (1994) Notch sensitivity of aluminium-lithium alloys in fatigue. J Soc Mat Sci Jpn 43:840–846
3. Guagliano M, Vergani L (2004) An approach for prediction of fatigue strength of shot peened components. Eng Fract Mech 71:501–512
4. Wagner L (1999) Mechanical surface treatments on titanium, aluminum and magnesium alloy. Mater Sci Eng A263:210–216
5. McClung RC (2007) A literature survey on the stability and significance of residual stresses during fatigue. Fatig Fract Eng Mater Struct 30:173–205
6. Benedetti M, Fontanari V, Scardi P, Ricardo CLA, Bandini M (2009) Reverse bending fatigue of shot peened 7075-T651 aluminium alloy: the role of residual stress relaxation. Int J Fatig 31:1225–1236
7. Sines G (1959) Behavior of metals under complex static and alternating stresses. In: Sines G, Waisman JL (eds) Met fatigue. McGraw-Hill, New York, pp 69–145
8. Crossland B (1956) Effect of large hydrostatic pressures on the torsional fatigue strength of an alloy steel. In: Proceeding of the international conference on fatigue of metals, Institution of Mechanical Engineers, London
9. Fatemi A, Socie D (1988) A critical plane approach to multiaxial damage including out-of-phase loading. Fatig Fract Eng Mater Struct 11(3):149–165
10. Benedetti M, Fontanari V, Bandini M (in press) A simplified and fast method to predict plain and notch fatigue of shot peened high-strength aluminium alloys under reverse bending. Surf Coat Technol. doi:10.1016/j.surfcoat.2011.12.008

Chapter 30
Quantifying Residual Strains in Specimens Prepared by Additive Layer Manufacturing

A.N. Okioga, R.J. Greene, and R.A. Tomlinson

Abstract Residual stresses and strains are prevalent in many components, especially those that are made using additive layer manufacturing. The residual strains are superposed onto any applied load, which in experimental analysis may lead to inaccurate results. The manufacture of a component with known residual strains in all build orientations will enable it to be tested in its green state with results similar to an annealed counterpart. This study has been conducted to explore the relationship between the orientation build of the component, and its thickness in relation to the amount of residual strain it contains. The samples tested are made using Objet FullCure720 RGD720, and have an incremental thickness in order to determine the relationship between specimen thickness and residual strain. The test method used is photoelasticity, in which three analytical methods are implemented – Tardy compensation, Null-balance compensation and six-step phase-stepping. It was established that one of the build orientations possesses no residual strains, and the phase-stepping technique produces the most accurate results. This comparative analysis will aid the development of a simplistic method for manufacturing and testing components with minimal residual strains via additive layer manufacturing. Eliminating the need for post-processing will therefore enable time and cost savings.

Keywords Additive layer manufacturing • Build specifications • Photoelasticity • Residual strains

Nomenclature

α	Relative retardation
θ	Isoclinic angle
σ	Principal stress (MPa)
f_σ	Stress optic coefficient
i_n	Light intensity
N	Fringe order
t	Through thickness of specimen (mm)
X, Y, Z	Global axes of coordinates

30.1 Introduction

Additive layer manufacturing is a technique that consists of building a component in layers. It is very useful in industry as it allows for the manufacture of intricate components in a rapid manner and reduces the waste material. Because of its high levels of precision, it is also used to make lattices and meshes for low density components. In addition to this, the same

A.N. Okioga (✉) • R.A. Tomlinson
Department of Mechanical Engineering, University of Sheffield, S1 3JD, Sheffield, UK
e-mail: anne.okioga@gmail.com

R.J. Greene
Strain Solutions Ltd, S41 8NG Chesterfield, UK

M. Rossi et al. (eds.), *Residual Stress, Thermomechanics & Infrared Imaging, Hybrid Techniques and Inverse Problems, Volume 8*, Conference Proceedings of the Society for Experimental Mechanics Series, DOI 10.1007/978-3-319-00876-9_30,

component can be replicated with little effort, as, for some additive manufacturing processes the production machine is only required to read a Computer Aided Design (CAD) file, so larger batches of the same component can be easily manufactured to a high level of accuracy and similarity.

There are many different types of additive manufacturing techniques, depending on the materials used and the form in which the raw materials are. Some of the processes that require a powdered raw material for manufacturing components are: laser sintering – for thermoplastics and elastomers; laser melting – for alloys; and electron beam melting – specifically for non-ferrous alloys [1]. For material deposition processes, wire extrusion and blown powder processes are utilised. However, the most common process is 3D printing, which is widely accessible and relatively simple to use, as the designed component provides the build information via a CAD file. 3-D printing is a quick and effective method of creating complex components with precision, hence its use in this study. The 3-D printing process is suitable for creating prototypes for testing using photoelastic techniques, as some plastics used in the printing process possess birefringent characteristics. It alleviates the strenuous task of producing intricate moulds and casting, hence allowing for greater accuracy and efficiency in the production and testing of the samples.

Conventionally, when additive manufacturing is used to create components, there is residual strain created in the direction of build due to shrinkage during curing of the material, as shown in a study conducted by Quintana et al. [2]. This is not a major deterrent, as relatively simple heat treatment methods allow for the alleviation of these stresses. However, the heat treatment process requires specific apparatus that may be inaccessible to the user. Additionally, most thermoplastics have a degree of sensitivity to moisture absorption from the environment, therefore the characteristics of the sample may change slightly and degradation in material properties could result from excessive exposure to the environment [3]. It is therefore more time efficient and financially lucrative to allow for a procedure that will enable the testing of the component in its green state i.e. directly after build without further post processing, and therefore the aim of this study is to perform a quantitative procedure to determine the specific residual strains within a component that is manufactured via additive manufacturing, and an analysis on build orientation is carried out to inspect the most suitable orientation of build for minimal residual stresses.

30.2 Materials and Experimental Methods

The material selected for this study was Objet FullCure720, manufactured by Stratasys Inc. This material is transparent and exhibits birefringence, therefore it is ideal for photoelastic studies. To initialise the manufacturing process, a CAD file is created and loaded into the printer system as a .stl file, which will determine the geometry of the final product. The build layer, which is the thickness of each layer that is used to create the component, is then selected, which dictates the intricacy of the product, hence manufacture duration. The manufacturing process involves layering heated material onto a platform with thicknesses in the order of microns. The head of the printer deposits material as it moves along the platform and once it has completed the layer, it repeats the process layer by layer to eventually create the 3-D model designed in the CAD file.

A specimen was designed to fulfil the following objectives:

1. To investigate the variation of strain with an increase in specimen thickness;
2. To examine the effect that build orientation has on residual strain, with particular interest in obtaining a ‘strain-free’ orientation for simplicity in analysis;
3. To determine the effect of residual strains experienced in the component with respect to the build-up layer;
4. To measure the specimen thickness at which triaxial effects are present, which create distortions and inhibit clarity of results.

The test components viewed as useful for the fulfilment of all these objectives were sets of staircase blocks (Fig. 30.1), which have incremental thicknesses and could incorporate all the information, whilst providing the same build environment, therefore minimising changes and anomalies that can be brought about due to differences in build conditions. The CAD file created contained three different specimens in the three build orientations, where the point of interest regarding the orientation was the through-thickness of the ‘step’. Due to the rigidity of a set build-up layer in the printer prior to manufacture, two batches of the blocks were made consecutively – one with a build-up layer of 16 μm and the other with 32 μm.

To gain a measure of the residual strains, photoelastic methods were implemented, as they provide a quick and effective visualisation of the strains experienced within the component. A circular polariscope was used, and this yields isochromatic fringes. The stress optic law (Eq. 30.1) is then implemented to obtain the principal stress difference ($\sigma_1 - \sigma_2$):

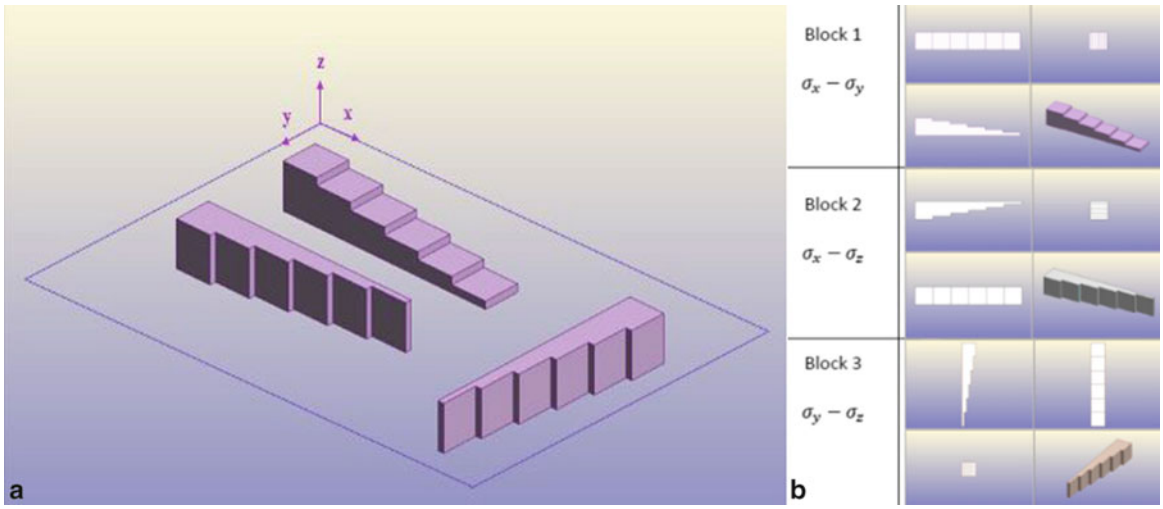

Fig. 30.1 CAD drawings of the mutually perpendicular staircase blocks with (**a**) the build orientations specified by the global coordinates x, y and z and (**b**) the orthogonal drawings to show build variation with respect to the orientations

$$\sigma_1 - \sigma_2 = \frac{Nf_\sigma}{t} \tag{30.1}$$

where N is the isochromatic fringe order, f_σ the stress optic coefficient and t the through-thickness of the birefringent specimen [4]. Since this is an elastic situation, the strains can be inferred from the stresses. The three main analytical techniques used are Tardy method, Null Balance Compensation and Phase-stepping. These are implemented for comparative studies, in order to validate results and determine the most effective photoelastic method of the three for this particular application.

The Tardy method is the simplest approach, as it only requires the use of the grey-field spectrum of the polariscope. The analyser is rotated by a known angle and a specific point of interest monitored to view the changes in fringe order – this enables fractional fringes to be determined, as the fringe moves by a known distance in the sample, and the rotation gives the angle by which the change has occurred [4]. As this study involved samples with minimal residual stresses, it was found to be more effective to study each 'stair' partition and rotate the analyser to a point at which the fringe appears. For greater simplicity, monochromatic sodium light ($\lambda = 589.3$ nm) was used, in order for the specific full fringes to be determined.

Null balance compensation is a quantitative method of obtaining point to point fringe readings within the polariscope [4] using a Null Balance Compensator manufactured by the Vishay Measurements Group. This is an instrument used to establish accurate fringe readings by introducing a variable birefringence with known calibration that is adjusted to cancel out the refractive index of the specimen under observation. This is because the magnitude of birefringence of the null balance compensator and specimen are equal in magnitude, but opposite in direction, resulting in a net birefringence of zero, indicated by a black fringe. The adjustment is carried out using a dial, whose turning gives a specific counter reading and, using the calibration chart that accompanies the compensator, fringe order is easily obtained, with respect to the counter reading. Because there is a linear relationship between the counter reading and fringe order, it is also a simple way of obtaining the fringe order, hence the strains within the component. However, the greatest limitation of this method is the tedious analysis due to a point to point data acquisition, and at very low fringes, there is no clear distinction in the determination of fringe order. It is therefore ideal for initial calibration, but a more robust analytical technique is required to define the holistic strain state of the system.

Phase-stepping is the most appropriate method for studying the specimen, as it gives a full field automated analysis by using images presented by the rotation of both the output quarter wave plate and analyser, which varies the light intensities from the specimen. In this method, there can be up to eight light intensities used for analysis, making it an over deterministic process, hence reducing the threshold of error. In this particular study, the implementation of the six step phase-stepping process developed by Patterson, Ji and Wang [5] is implemented, with the orientations in Table (30.1) yielding simultaneous Eqs. 30.2 and 30.3 that provided the formulae used to determine the isoclinic angle (θ) and relative retardation (α) from the different light intensities (i_n). Relative retardation is related to fringe order using Eq. 30.4.

Table 30.1 Orientations for the output elements in the implementation of the six-step phase-stepping technique developed by Patterson, Ji and Wang: with the equations. yielding the isoclinic angle Eq. 30.2, retardation Eq. 30.3 and fringe order Eq. 30.4 [5]

Intensity	Output $\lambda/4$ plate orientation	Analyser orientation
i_1	0	$\pi/4$
i_2	0	$-\pi/4$
i_3	0	0
i_4	$\pi/4$	$\pi/4$
i_5	$\pi/2$	$\pi/2$
i_6	$3\pi/4$	$3\pi/4$

$$\theta = \frac{1}{2} tan^{-1}\left(\frac{i_5 - i_3}{i_4 - i_6}\right) \tag{30.2}$$

$$\alpha = \frac{1}{2} tan^{-1}\left(\frac{i_4 - i_6}{(i_1 - i_2)cos2\theta}\right) \tag{30.3}$$

$$\alpha = 2\pi \mathrm{N} \tag{30.4}$$

Three build orientations are being investigated (Fig. 30.1), therefore the staircase blocks are observed in the plan and side views (Figs. 30.2, 30.3, and 30.5). This allows the stress differences, as shown in Table 30.2, to be calculated.

Six blocks were manufactured – three blocks of each build layer, each built in a specific orientation as shown in Figs. 30.1 and 30.2, with dimensions shown in Fig. 30.2b.

30.3 Results

An initial visual inspection was carried out in the circular polariscope in dark field configuration, as shown in Fig. 30.3. In order to present a clear contrast in the resulting fringe orders and allow for the same conditions throughout the analytical process, the staircase blocks were separated into their build-up layer categories, and stacked on top of each other, with the thinnest through-thickness at the farthest left in both set-ups.

From visual inspection, it is seen that there is an increase in fringe order as the through-thickness of the specimen increases. This is mostly evident in blocks 2 and 3, which display significant fringe orders. Therefore an increase in transmission length gives a higher fringe order, because the light has a further travelling distance and therefore retardation – hence the difference in refraction is greater, when we consider that the difference in principle stresses remains constant (Eq. 30.1).

It is also evident that the build orientation is highly significant if residual strains are to be alleviated. As shown in Fig. 30.3, the blocks built in the z-direction have negligible residual strain when the through-thickness is viewed – they display dark fringes throughout all the thicknesses. This allows for the testing of a component in its green state – depending on the thickness. However, as the thickness increases, the black fringes appear to be slightly lighter, which signifies that there is some residual strain in the component at a thickness above the optimal thickness. As thickness increases, there tends to be a slight change in residual strain, although not as significant as in the other build directions. Using this method, it is more evident to discern the changes in fringe order, hence select a suitable range of thicknesses, in this case below 15 mm.

It is also seen in Fig. 30.3 that there is a similarity between the X and Y build orientations, with the variation increasing with a change in through-thickness. This could be useful when constructing components whose loading information is required in two directions. As identified in Fig. 30.4, the residual stress from a side profile changes significantly, showing blocks 2 and 3, built in orientations x and y (Fig. 30.1) now possess virtually no residual strains. The stacking arrangement is still the same as in Figs. 30.2 and 30.3, with the exception of block 2 (central block) being inverted for balancing purposes. However, the results still harmonize with block 3.

It has also been established that the finer the build-up layer, the greater the residual strains experienced in the component. Referring to Figs. 30.3 and 30.4, the blocks with a build-up layer of 16 μm (left) had the greater possession of residual strains in comparison to those with the build-up layer of 32 μm. To confirm this, null balance compensation was implemented to

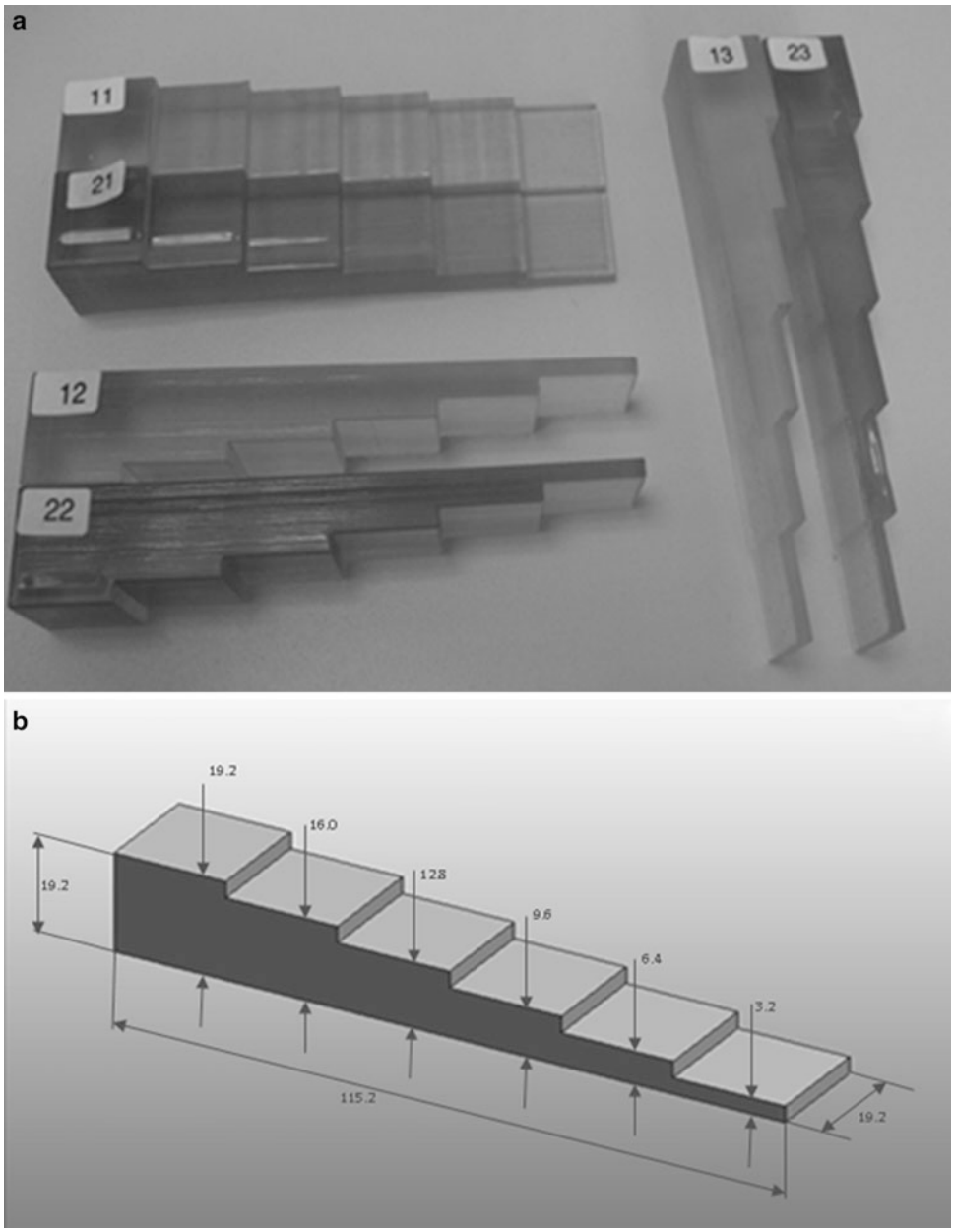

Fig. 30.2 The staircase blocks in their orientation of manufacture, in relation to Fig. 30.1 (**a**) Staircase blocks in their build orientation, and (**b**) dimensions of the staircase blocks (mm)

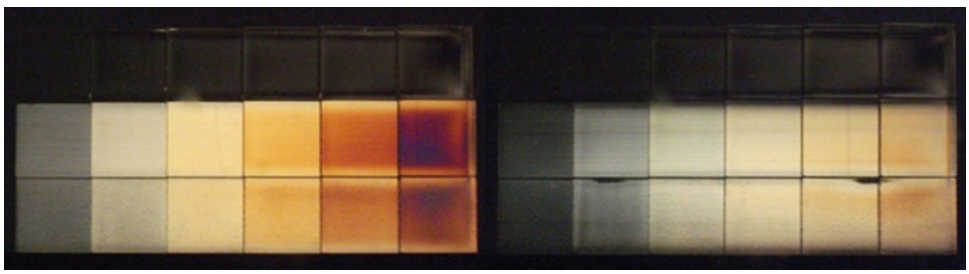

Fig. 30.3 Dark-field fringe information of the staircase blocks for the build-up layers, 16 μm (*left*) and 32 μm (*right*) The blocks are stacked on top of each other in the order block 1(*top*), block 2 (*centre*) and block 3 (*bottom*) and viewed in the Z direction – from the definitions in Fig. 30.1

Table 30.2 Nomenclature of blocks for analysis, related to orientation and build layup, as shown in Fig. 30.2

Block number	Definition
11	16 μm build-up layer for block 1 ($\sigma_x - \sigma_y$)
12	16 μm build-up layer for block 2 ($\sigma_x - \sigma_z$)
13	16 μm build-up layer for block 3 ($\sigma_y - \sigma_z$)
21	32 μm build-up layer for block 1 ($\sigma_x - \sigma_y$)
22	32 μm build-up layer for block 2 ($\sigma_x - \sigma_z$)
23	32 μm build-up layer for block 3 ($\sigma_y - \sigma_z$)

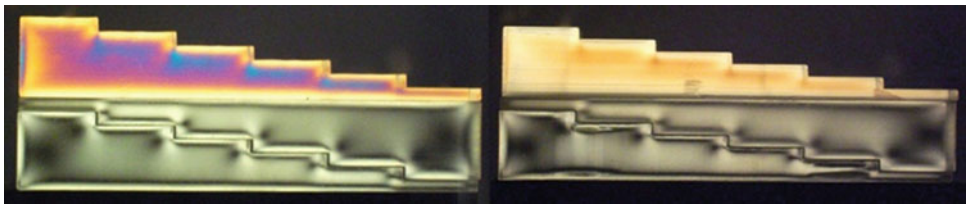

Fig. 30.4 Dark-field fringe information of the side profile of the staircase blocks for the build-up layers, 16 μm (*left*) and 32 μm (*right*) In this case, the blocks are being viewed in the X-Y plane which yields residual strain in block 1, as the staircase build layers are stacked in this plane, causing the shrinkage of the block to be most prominent

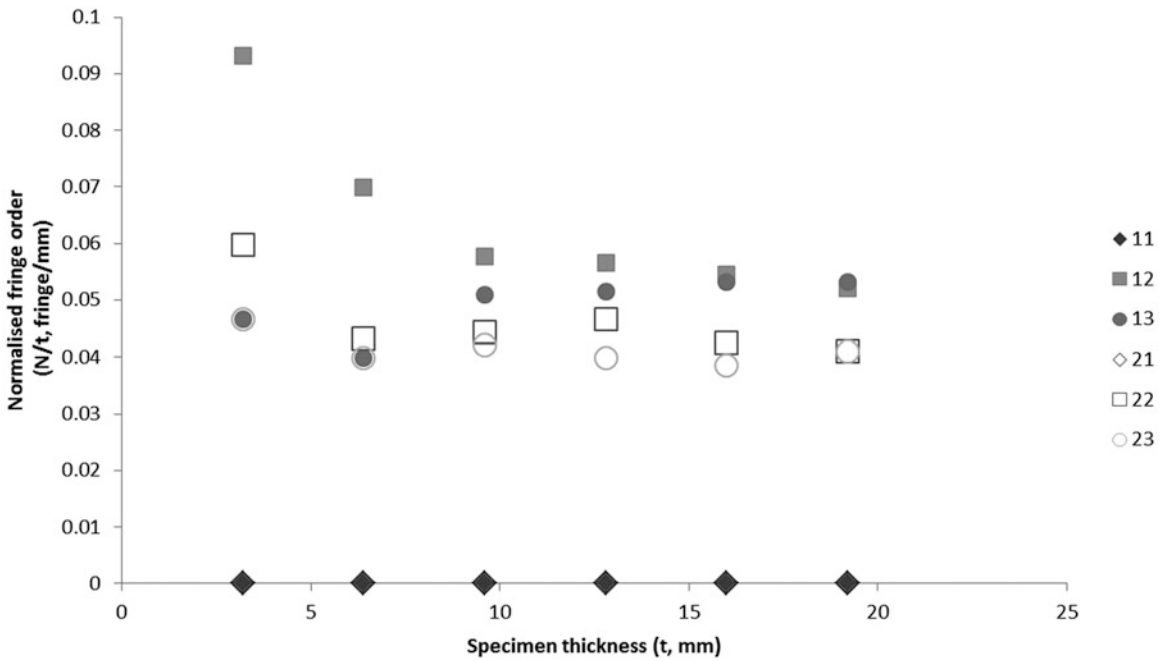

Fig. 30.5 Numerical results of the Null Balance Compensation for the test specimen as labelled in Table (30.2), showing evidently that build orientation 1 is ideal as it contains minimal residual stresses when viewed in the Z direction

determine the specific variation (shown in Fig. 30.5). When a smaller build-up layer is implemented (closed symbols), there are more partitions in the component that undergo curing and therefore there is greater shrinkage in the component, leading to greater residual strains.

Because it has been established that the blocks with the 16 μm build-up layer possessed greater residual strains, those with the 32 μm build-up layer were analysed to complete a comparative analysis between the three named photoelastic methods that tests for their performance at low strains. The results yielded when all methods are compared numerically indicate that at

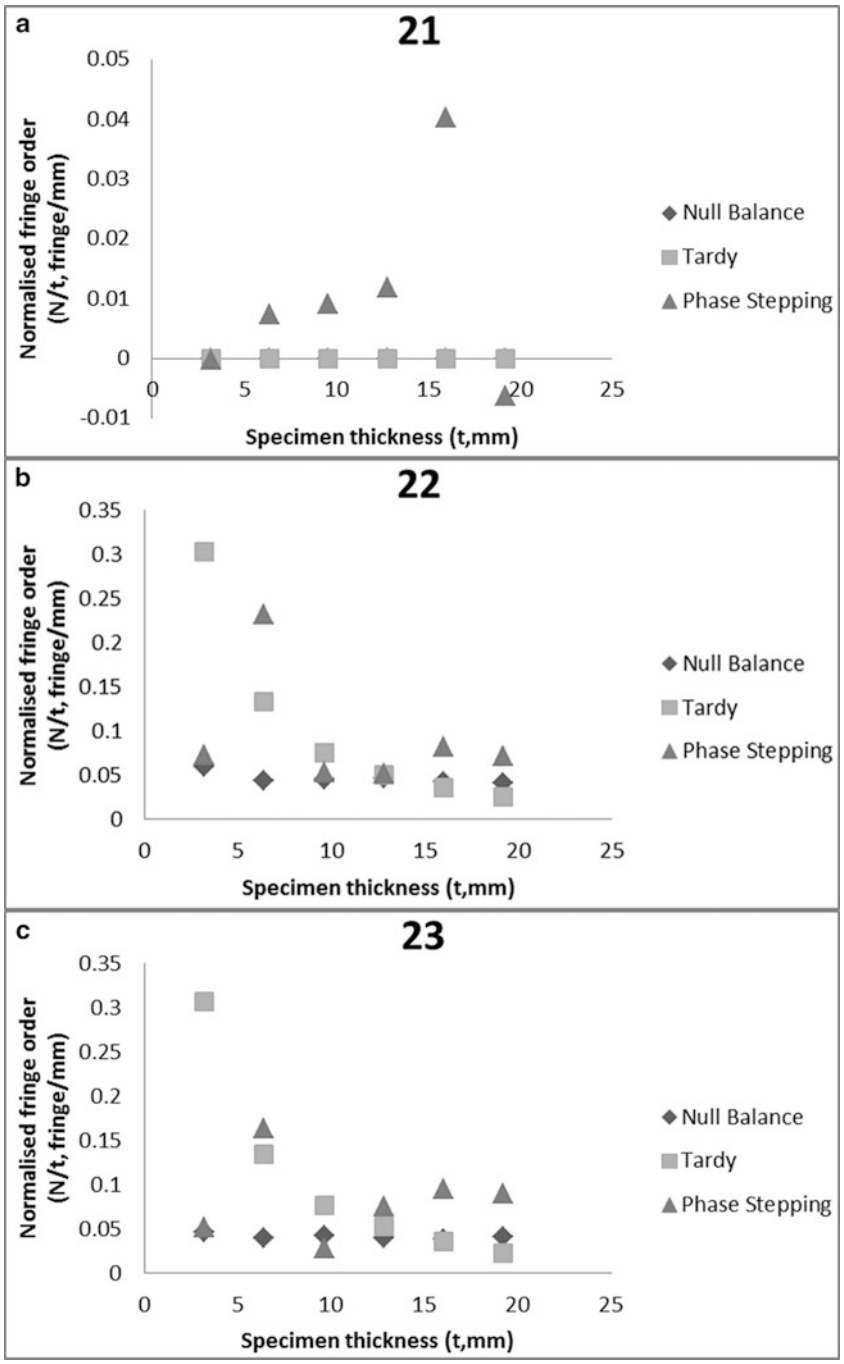

Fig. 30.6 Numerical results comparing the three analytical methods for the 32 μm staircase blocks (**a**) 21, which allows the identification of low values of N, (**b**) 22 and (**c**) 23, which display similar results indicating that there are relatively uniform residual strains through the thickness, especially at through-thicknesses above 10 mm when all methods are utilised

very small specimen through-thicknesses, there exists a wide margin error between all three photoelastic techniques, as represented graphically in Fig. 30.6. This resulting margin is especially true for the Tardy method, which, as indicated, has the greatest variation from all the other methods. Also, the phase-stepped values of the second 'stair', in both samples 22 and 23 have an anomalous result, which will be investigated further. If these two points are discounted, the resulting plots relating through thickness to normalised fringe order is consistent with the null balance results. The reason for this is that once the thickness has been normalised, there should be consistency in the fringe order throughout the specimen. However, at thicknesses above 10 mm, the residual strain has greater consistency through all the methods, and, therefore, from this analysis, it is suggested, if utilising the Tardy method with any of the others for comparative analysis, the specimen thickness should be no less than 10 mm if residual strains are to be quantified, rather than annealed whilst viewing specimen in all three dimensions.

Nevertheless, as shown in Fig. 30.6a, the phase-stepping result indicates that if an orientation, such as that which was used to manufacture block 21, is being used to create a component and one direction of view is the sole interest, it is more advantageous to work with through-thicknesses below 15 mm. From visual inspection via Tardy Method and Null Balance Compensation, the orientation yields zero residual strain. However, when phase-stepping is implemented, it is seen that residual strains are present – although the normalised fringe order is approximately 0.01 fringe/mm for a range of through-thicknesses, but it changes greatly at a thickness above 15 mm. This is a possible indication that there are triaxial effects causing distortion if the component produced has a through-thickness above 15 mm.

30.4 Conclusion

In this application, it has been established that it is possible to test a material in its green state after 3D printing, as, if the component is built in a specific orientation (in this case, Z direction), when analysed for residual stresses, they are negligible. This implies that loads can be applied in that direction to the material, and the residual stresses will not superpose any information onto the results. However, it was also recognised that this is true for a narrow thickness range, between 10 mm and 15 mm, and for a thorough analysis, it is best to apply a digital photoelasticity technique, such as phase stepping, as it allows for greater accuracy, as there is no element of human judgement in the determination of the residual strains experienced in components built via 3D printing.

References

1. Gibson I, Rosen DW, Stucker B (2010) Additive manufacturing technologies: Rapid prototyping to direct digital manufacturing, Springer
2. Quintana R et al (2010) Effects of build orientation on tensile strength for stereolithography-manufactured ASTM D-638 type I specimens. Int J Adv Manuf Technol 46:201–215
3. Cooke W, Tomlinson RA, Burguete RL, Johns D, Vanard G (2011) Anisotropy, homogeneity and ageing in an SLS polymer. Rapid Prototyp J 17(4):269–279
4. Doyle JF, Phillips JW (1989) Manual on experimental stress analysis, Fifth Edition, *Society for Experimental Mechanics, Chapter 6*
5. Patterson EA, Ji W, Wang ZF (1997) On image analysis for birefringence measurements in photoelasticity. Opt Laser Eng 28:17–36

Chapter 31
Parameter Determination of Anisotropic Yield Criterion

Jin-Hwan Kim, Frédéric Barlat, and Fabrice Pierron

Abstract The present study aims at identifying all the anisotropic elasto-plastic material properties from simple uniaxial tension tests performed in two directions on steel sheet specimens having a complex geometry. A digital image correlation technique is used for the full-field heterogeneous strain measurement. An appropriate elasto-plastic constitutive model is adopted. The virtual fields method (VFM) is used as an inverse procedure to determine the constitutive parameters, which are calculated using tensile test results obtained in rolling and transverse directions.

Keywords Optical method • Inverse method • Plasticity • Anisotropy • Advanced high strength steel

31.1 Introduction

Finite element analysis of metal forming is widely used in industrial practice to reduce time and costs in production. The accurate determination of the elasto-plastic material properties of sheet metal is essential in providing reliable input in metal forming analysis. Prior thermo-mechanical processing of sheet metal induces directional properties on the material. To characterize the anisotropic plastic properties, several tests need to be performed. For instance, for the well-known stress-based Hill 1948 model (plane stress state) [1] and Yld2000-2d model [2], four tests (three uniaxial tensile tests at 0°, 45° and 90° from the rolling direction and one biaxial tensile test) are required to derive the coefficients. This makes the identification procedure time consuming and costly.

In this study, a new methodology is applied to identify the anisotropic yield function coefficients with reduced number of uniaxial tensile tests. Especially, the expensive biaxial tensile test is not needed for the identification, which is a big advantage in a practical point of view. In order to derive the anisotropic coefficients, simple tensile tests of thin sheet metal specimens having a complex geometry are performed to acquire sufficient heterogeneous stress information. Full-field logarithmic strain fields are measured through a digital image correlation technique. Then, an appropriate constitutive model, which describes the anisotropic behavior adequately, is chosen. To determine the constitutive parameters, here the necessity of an analytical tool arises. In this study, the virtual fields method (VFM) is used for an inverse identification of the plastic material parameters from the heterogeneous stress state. In this paper, the methodology is introduced and validated on a virtual test, using finite element simulations. Next, the proposed methodology is applied to identify the anisotropic parameters of Hill 1948 yield criterion using experimental measurements.

J.-H. Kim (✉) • F. Barlat
Graduate Institute of Ferrous Technology, Pohang University of Science and Technology, San 31 Hyoja-dong, 790-784 Nam-gu, Pohang, Gyeongbuk, Republic of Korea
e-mail: jinkim@postech.ac.kr; f.barlat@postech.ac.kr

F. Pierron
School of Engineering Sciences, University of Southampton, Highfield, SO17 1BJ Southampton, UK
e-mail: F.Pierron@soton.ac.uk

M. Rossi et al. (eds.), *Residual Stress, Thermomechanics & Infrared Imaging, Hybrid Techniques and Inverse Problems, Volume 8*, Conference Proceedings of the Society for Experimental Mechanics Series, DOI 10.1007/978-3-319-00876-9_31,

31.2 Methodology

31.2.1 Materials

An advanced high strength steel (AHSS) sheet, Dual Phase (DP) 780, is selected in this study. DP steels exhibit high strength, high strain hardening and good ductility, making those versatile for many automotive applications.

31.2.2 Stereo Digital Image Correlation

The full-field measurement technique applied here is the stereo digital image correlation (SDIC), which is a 3D version of the digital image correlation (DIC) [3]. In DIC, the area of interest (AOI) is composed of many small correlation windows (subset, facet). The grayscale intensity distributions of all the subsets in undeformed and deformed stages are correlated, allowing the measurement of 2D coordinates of each subset during deformation. SDIC utilizes two cameras with different incidence angles for the calculation of 3D coordinates of each subset. The SDIC set-up is shown in Fig. 31.1.

Two 2448 $\times$ 2048 pixels 14 bit CCD cameras are used for SDIC. In order to use DIC, a speckle pattern is required on the AOI of the surface where the full-field displacements are measured. A random pattern is made by spraying matt white paint as a base and black dots are applied as seen in Fig. 31.1. Before loading a steel sheet specimen, a reference (undeformed) image is recorded and sets of pictures at a constant acquisition rate are taken simultaneously by the two cameras. Synchronized load data is obtained from the analog output of the tensile tester when images are taken. In this study, the Vic-3D software (www.correlatedsolutions.com) is used for the calculation of undeformed and deformed coordinates of AOI from the speckle pattern images.

31.2.3 Logarithmic (True) Strain

Next, the deformation gradient is obtained from the undeformed and deformed coordinates of each measurement data point following the analytical procedure (interpolation method) used in [4] and the theory of finite deformation. The whole AOI is meshed with triangular elements. Then, the deformation gradient F in each triangle can be calculated assuming a plane stress state and incompressibility ($\det(F) = 1$). Then the Logarithmic strain tensor E_{ln} is derived from the deformation gradient F through the left stretch tensor V ($V^2 = F^T F$) as in Eq. 31.1 [5].

Fig. 31.1 Views of stereo image correlation set-up

$$E_{\ln} = \sum_{\alpha=1}^{3} \ln(\lambda_\alpha) r_\alpha \otimes r_\alpha \tag{31.1}$$

where λ_α and r_α are the eigenvalues and eigenvectors of the left stretch tensor V.

31.2.4 Constitutive Model

It is essential to choose an appropriate constitutive model which can describe the plastic behavior in order to derive accurate stress fields from the measured strain fields. In this study, Hill 1948 yield criterion for anisotropic material under plane stress is assumed as an initial study. The associated plasticity flow rule and Swift hardening law are used.

Hill 1948 yield criterion (plane stress):

$$\Phi(\sigma_{ij}, \varepsilon_p) = \sqrt{(H+G)\sigma_{xx}^2 + (H+F)\sigma_{yy}^2 - 2H\sigma_{xx}\sigma_{yy} + 2N\sigma_{xy}^2} - \sigma_s(\varepsilon_p) = 0 \tag{31.2}$$

Swift law:

$$\sigma_s = K(\varepsilon_0 + \varepsilon_p)^n \tag{31.3}$$

where σ_s is the current yield stress and ε_p the equivalent plastic strain. In this case, the number of parameters to be identified is six (H, F, N, K, ε_0 and n) because $H + G = 1$ (from the condition that the initial yield stress in the rolling direction is equal to the initial yield stress in a simple tensile test).

31.2.5 The Virtual Fields Method

In this study, the virtual fields method (VFM) [6] is adopted to process the deformation fields obtained experimentally for the identification of the constitutive parameters. The VFM is based on a relevant use of the equilibrium equations through the principle of virtual work. The equilibrium equation in the case of elasto-plasticity for static loading, and in absence of volume forces, can be written as follows:

$$-\int_V \left[\int_0^t \dot{\sigma} dt\right] : \varepsilon^* dV + \int_{S_f} T.u^* dS = 0 \tag{31.4}$$

where $\dot{\sigma}$ is the stress rate which is a function of $\dot{\varepsilon}$ (actual strain rate), σ (actual stress) and unknown constitutive parameters, V the measurement volume, T the surface tractions acting on S_f, ε^* the virtual strain field derived from u^* (the virtual displacement field).

Proper choice of virtual fields enables the identification of material parameters if actual strain and load information are provided by the experiment. In the case of elasto-plasticity, the identification is performed through an iteration procedure [7]. Since the constitutive parameters in the stress formula are unknown, initial values are estimated for the identification. The quadratic gap between the internal virtual work and the external virtual work is minimized, leading to identification of unknown parameters. In this study, virtual fields are defined empirically for the identification, which means that the virtual fields are chosen by trial and error using simulated data. The virtual fields providing the most robust identification are determined. These virtual fields are then kept for the identification with the actual experimental data. The virtual fields selected in this study are shown in Eq. 31.5.

$$u_x^* = \sin(y), \quad u_y^* = y \tag{31.5}$$

31.3 Results and Discussion

31.3.1 Numerical Validation

To validate the proposed approach, simulated measurements were produced using the Abaqus software. The initial step was to find the geometry, which can provide the most heterogeneous stress state. Various geometries were investigated using von Mises yield criterion with linear hardening. Plane stress state was assumed. The specimen configuration chosen in this study is shown in Fig. 31.2a and the heterogeneous stress components at each measurement point obtained with this geometry are plotted in the principal stress space as shown in Fig. 31.2b. The next step was to identify the anisotropic material parameters using the VFM. Hill 1948 yield criterion with Swift hardening law under plane stress was assumed. The same identification process used in the experiments was applied to the identification using the simulated data. To obtain similar number of measurement points as in the experiments, very fine mesh size was applied first. Three nodes triangular shell elements were used. After obtaining the undeformed and deformed coordinates of simulated measurement points, the whole AOI was meshed with triangular elements. Then, the logarithmic strain fields of the AOI were calculated and the VFM was applied to find the material parameters.

It was found that there is only one global optimum in the case of von Mises yield criterion with linear hardening (the number of parameters: two). However, there exist many local optima with Hill 1948 yield criterion with Swift hardening law (the number of parameters: six). Only when the initial guesses were close to the reference values, which were input in the FE simulations, all the parameters were identified correctly. Therefore, it was decided to combine two tensile tests in two different directions, one in the rolling direction and the other in the transverse direction. Interestingly, the VFM retrieved all the constitutive coefficients within tolerable small errors regardless of the initial guesses in this case.

31.3.2 Experimental Results

Tensile tests in two different directions were carried out as recommended from the FE simulation. Fig. 31.3 shows the three logarithmic strain fields of the DP780 specimen obtained from the tensile test in the rolling direction. The direction y is the rolling direction and the direction x the transverse direction. The nicely distributed strain maps indicate that the alignment of the specimen and the full-field measurement quality with DIC are very satisfactory.

In Table 31.1, the identified parameters by the VFM with two tests are compared to the reference values obtained with the conventional methods (three uniaxial tensile tests at 0°, 45° and 90° from the rolling direction and one biaxial tensile test). It can be seen that the identified values by the VFM and the previous data are in reasonably good agreement. Slight

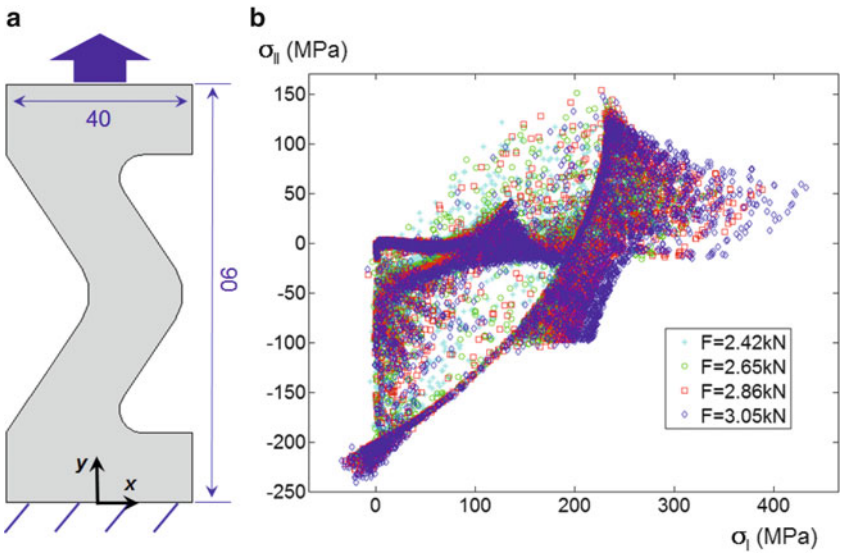

Fig. 31.2 (**a**) Specimen geometry (units: mm) (**b**) heterogeneous stress state

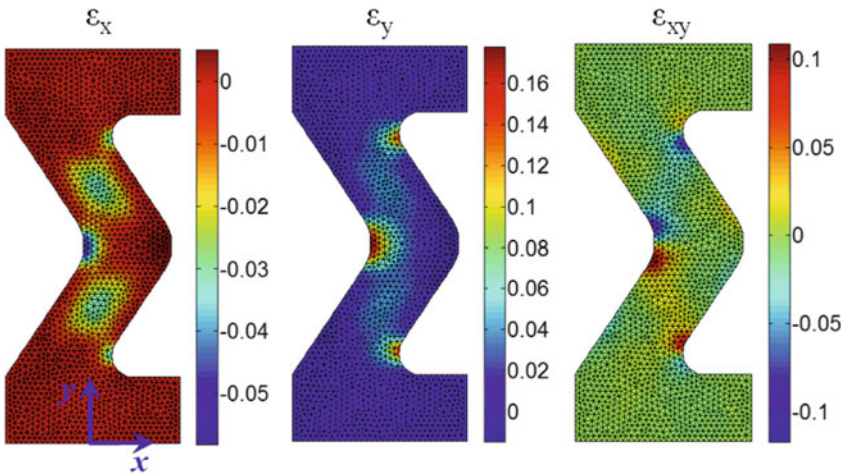

Fig. 31.3 Heterogeneous logarithmic strain fields of the DP780 specimen

Table 31.1 The identified parameters by the VFM

	K	ε_0	n	H	F	N
Reference	1,267.91	0.000094	0.1391	0.4951	0.4967	1.5242
Identified	1,182.58	0.0024	0.1478	0.6516	0.4207	1.5110

deviations of H and F parameters are mainly because the biaxial information is a bit insufficient. It is considered that this can be improved if one more tensile test result in 45° direction is provided to the VFM. It can be concluded that the identification of all anisotropic plastic parameters is feasible only when the tests can provide sufficient heterogeneous information for the yield locus.

31.4 Conclusions

The present study took full advantage of the combination of the VFM and the full-field measurement technique with the simple tensile tests in order to determine the anisotropic plastic properties of Hill 1948 yield criterion of an advanced high strength steel specimen. Identification was successfully carried out with the VFM and the full-field measurements. The current approach will be applied to more sophisticated yield criterion such as Yld2000-2d model in the future. In this case, due to the increased number of parameters to be identified, more attention should be paid on selection of the virtual fields and on the optimization algorithm.

References

1. Hill R (1948) A theory of the yielding and plastic flow of anisotropic metals. Proc Roy Soc Lond A 193:281–297
2. Barlat F, Brem JC, Yoon JW, Chung K, Dick RE, Lege DJ, Pourboghrat F, Choi S-H, Chu E (2003) Plane stress yield function for aluminum alloy sheets-part 1: theory. Int J Plast 19(9):1297–1319
3. Sutton MA, Orteu JJ, Schreier H (2009) Image correlation for shape, motion and deformation measurements. Springer Publishing Company, Incorporated
4. Avril S, Badel P, Duprey A (2010) Anisotropic and hyperelastic identification of in vitro human arteries from full-field measurements. J Biomech 43(15):2978–2985
5. Dassault Systemes (2010) Abaqus version 6.10, User's manual.
6. Pierron F, Grédiac M (2012) The virtual fields method. Springer, New York
7. Avril S, Pierron F, Pannier Y, Rotinat R (2008) Stress reconstruction and constitutive parameter identification in plane-stress elasto-plastic problems using surface measurements of deformation fields. Exp Mech 48(5):403–420

Chapter 32
Performance Assessment of Inverse Methods in Large Strain Plasticity

Marco Rossi, Marco Sasso, Gianluca Chiappini, Dario Amodio, and Fabrice Pierron

Abstract The Virtual Fields Method (VFM) is an inverse method which allows to identify the constitutive parameters of materials from full-field measurements. The method relies on the principle of virtual work and, traditionally, is mainly used to characterize the material properties. Nonetheless the VFM can also be used as an inspection tool to compare constitutive models or experimental configurations. For instance, it can be adopted to compare different constitutive models in order to find out which one is more suitable to describe the mechanical behaviour observed during an experiment. In this paper this idea is applied in the case of large strain plasticity. A sensitivity study was conducted to evaluate how the specimen geometry and the texture orientation influence the identification of the constitutive parameters. Then the method was used to compare the performances of three constitutive models in reproducing the plastic behaviour of a given material. The studied models are isotropic von Mises, Hill48 for normal and planar anisotropy. The work was conducted on simulated data.

Keywords Plasticity • Inverse method • Virtual fields method • Benchmark • Anisotropy

32.1 Introduction

A large number of plasticity models are nowadays available to describe the plastic behaviour of metals. These models try to reproduce the complex phenomena which occurs in plasticity, e.g. anisotropy, kinematic hardening, void growth etc. Starting from the classical von Mises plasticity theory, many other models have been developed, for instance Hill48 for anisotropic plasticity [1], the Yld2000-2d model proposed by Barlat et al. [2] which has been extended in [3], Vegter and van den Boogaard [4] used a piecewise description of the yield locus using Bézier splines, Bai and Wiezbicki [5] included the dependence on the third stress invariant.

In practical engineering applications, the choice of a suitable theoretical model plays an important role. Indeed an advanced model usually requires a more complex identification procedure and also the implementation in FE codes will be more complicated. It is useful, in this case, to have a benchmark procedure that allows to have simple indications on which is the best solution.

The virtual fields method (VFM) is an identification procedure used to identify the constitutive parameters in materials [6]. This method has been used in many applications [7] in particular in the plasticity fields several papers have been already published. One of the advantages of the VFM compared to other methods, as the FE model updating [8], is the computation time which is commonly very low since no FE computations are involved in the identification algorithm.

M. Rossi (✉) • M. Sasso • G. Chiappini • D. Amodio
Università Politecnica delle Marche, via brecce bianche, 60131 Ancona, Italy
e-mail: m.rossi@univpm.it; m.sasso@univpm.it; g.chiappini@univpm.it; d.amodio@univpm.it

F. Pierron
University of Southampton, Engineering Sciences, Highfield, SO17 1BJ Southampton, UK
e-mail: F.Pierron@soton.ac.uk

M. Rossi et al. (eds.), *Residual Stress, Thermomechanics & Infrared Imaging, Hybrid Techniques and Inverse Problems, Volume 8*, Conference Proceedings of the Society for Experimental Mechanics Series, DOI 10.1007/978-3-319-00876-9_32,

For this reason the VFM represents a suitable benchmarking tool, indeed, in a reasonably short amount of time many different constitutive models can be compared. Here, the experimental test is aimed to select the appropriate constitutive model rather than to identify the parameters of an a priori chosen constitutive model. The idea will be explained in this paper using simulated experiments.

Once the constitutive model is chosen using this technique further tests can be conducted to have a correct identification.

32.2 Theoretical Background

The VFM can be applied to many applications, the complete theory is detailed in [6]. Here, in particular, the VFM is applied to plasticity at large deformations. The procedure consists in the minimization of a cost function which represents the equilibrium equation written using the principle of virtual works. Dealing with large strains, the finite deformation theory has to be employed to compute stress and strain. Let us denote $\boldsymbol{\Psi}$ the cost function and $\boldsymbol{\xi} = \{p_1, p_2, \ldots, p_N\}$ a vector of the N constitutive parameters which have to be identified. It follows:

$$\boldsymbol{\Psi}(\boldsymbol{\xi}) = \sum_{i=1}^{N_{vf}} \sum_{j=1}^{N_{step}} \left| \int_V \mathbf{T}_j^{1PK} : \delta \mathbf{F}_i^{\bullet} \, dv - \int_{\partial V} \left(\mathbf{T}_j^{1PK} \mathbf{n} \right) \cdot \delta \mathbf{v}_i \, dS \right| \tag{32.1}$$

$\mathbf{T}^{1\mathrm{PK}}$ is the first Piola-Kirchhoff stress tensor, $\delta\mathbf{v}$ is a virtual displacement field defined by the user, $\delta\mathbf{F}^{\bullet}$ is the corresponding virtual displacement gradient tensor, V is the volume of the specimen in the zone of interest, ∂V is the boundary surface and $\mathbf{n}$ is the surface normal in the undeformed configuration. The cost function is computed for each measurement step of the test and for each defined virtual field. N_{step} and N_{vf} are the number of measurement steps and adopted virtual fields, respectively. The first integral of Eq. 32.1 can be viewed as the virtual work of the internal forces and the second one as the virtual work of the external forces. The stress is computed using the first Piola-Kirchhoff stress tensor, i.e.:

$$\mathbf{T}^{1PK} = \det(\mathbf{F}) \, \boldsymbol{\sigma} \, \mathbf{F} \tag{32.2}$$

where $\boldsymbol{\sigma}$ is the Cauchy stress tensor and $\mathbf{F}$ the deformation gradient. The Cauchy stress tensor is obtained from the strain field measured in the specimen surface using a full-field measurement technique. The constitutive model is used to pass from strain to stress, therefore the Cauchy stress is a function of the constitutive parameters $\boldsymbol{\xi}$. According to the VFM, the parameter vector $\boldsymbol{\xi}$ is iteratively varied by a minimization algorithm in order to find out the best set of parameters which minimize the cost function of Eq. 32.1. The procedure is discussed in depth in Rossi et al. [9] where the theoretical approach is presented for a general three-dimensional state of stress.

Such a method can be adapted to different plasticity models. In this paper three of them have been used, the standard von Mises plasticity, the Hill48 model for normal anisotropy and the Hill48 model for planar anisotropy [10]. The equivalent stress for von Mises is:

$$\sigma_{eq} = \sqrt{\sigma_x{}^2 - \sigma_x \sigma_y + \sigma_y{}^2 + 3\tau_{xy}{}^2} \tag{32.3}$$

for Hill48, in case of normal anisotropy:

$$\sigma_{eq} = \sqrt{\sigma_x{}^2 - \frac{2R}{1+R}\sigma_x \sigma_y + \sigma_y{}^2 + \frac{2(1+2R)}{1+R}\tau_{xy}{}^2} \tag{32.4}$$

where R is the Lankford parameter [11]. In case of planar anisotropy, the equivalent stress becomes:

$$\sigma_{eq} = \sqrt{(g+h)\sigma_x{}^2 - 2h\sigma_x \sigma_y + (f+h)\sigma_y{}^2 + 2n\tau_{xy}{}^2} \tag{32.5}$$

where f, g, h and n are parameters which can be computed from the Lankford parameter at different orientations. If we assume that the equivalent plastic strain σ_{eq} is equivalent to the yield stress in the rolling direction, i.e. 0°, it can be shown that [12]:

Table 32.1 Parameters to be identified

Plasticity model	Parameters	#
Von Mises	K,ε_0,N	*3*
Hill48 for normal anisotropy	K,ε_0,N,R	*4*
Hill48 for planar anisotropy	K,ε_0,N,R_0,R_{90},R_{45}	*6*

$$g = \frac{1}{1+R_0};\ f = \frac{1}{1+R_{90}};\ h = \frac{R_0}{1+R_0};\ n = \left(\frac{1}{2}+R_{45}\right)\left(1+\frac{R_0}{R_{90}}\right)g \tag{32.6}$$

Where R_0, R_{90} and R_{45} are the values of the Lankford parameters measured at orientation 0°, 90° and 45° respectively. The same hardening law was used for the three models, i.e. the Swift law [10]:

$$\sigma_{eq} = K(p+\varepsilon_0)^N \tag{32.7}$$

where σ_{eq} is the equivalent stress of Eqs. 32.3, 32.4, and 32.5, p is the equivalent accumulated plastic strain and K, ε_0 and N are the parameters to be identified. Summarizing, the number of parameters for the different models are listed in Table 32.1, the three models have an increasing complexity with 3, 4 and 6 parameters. From a practical point of view, the choice of the Hill48 model for planar anisotropy requires at least three tests in three different directions to evaluate the six parameters.

In the following sections it is shown how the VFM can be effectively used to choose the most suitable model for a given application.

32.3 Validation on Simulated Data

The procedure was tested using strain fields coming from a FE model. The FEM results and the used geometry are illustrated in Fig. 32.1. The geometry is a simple notched specimen. Such geometry is rather easy to manufacture from sheet metal specimens and it is often used to identify the material properties, also in plasticity [12]. The material orientation is such that the 0° is oriented with the tensile direction that is the vertical direction (y) in this case.

The strain fields illustrated in Fig. 32.1 look quite heterogeneous, however, unfortunately, the stress components activated during the test does not vary significantly. Indeed, in order to maximize the effectiveness of the VFM procedure, the experiment should generate an heterogeneous stress/strain field which cover a large set of stress/strain states. In Fig. 32.2, the stress components obtained during the simulated test, normalized with respect to the equivalent stress, are illustrated.

From Fig. 32.2 it turns out that only a small part of the stress space is covered with the used experiments. More effective geometries can be evaluated in future studies. The benchmark is performed using three imaginary materials, one isotropic, one with normal anisotropy and one with planar anisotropy. The used parameters reproduce the behaviour of steel sheet metals Table 32.2.

For each material, the VFM was applied using the three plasticity models. At the end of the minimization procedure the value assumed by the cost function is used as benchmark value to identify the best model. It is worth nothing that, in this case, the focus is not on the accuracy of the identified parameters, but on the possibility of using a simple test to choose the best constitutive model.

Two virtual fields were used in the evaluation of the cost function of Eq. 32.1, that is:

$$\delta\mathbf{v}_1 = \begin{cases} \delta v_x = 0 \\ \delta v_y = y/L \end{cases}$$
$$\delta\mathbf{v}_2 = \begin{cases} \delta v_x = \dfrac{x}{W}\dfrac{(|y|-L)}{L} \\ \delta v_y = 0 \end{cases} \tag{32.8}$$

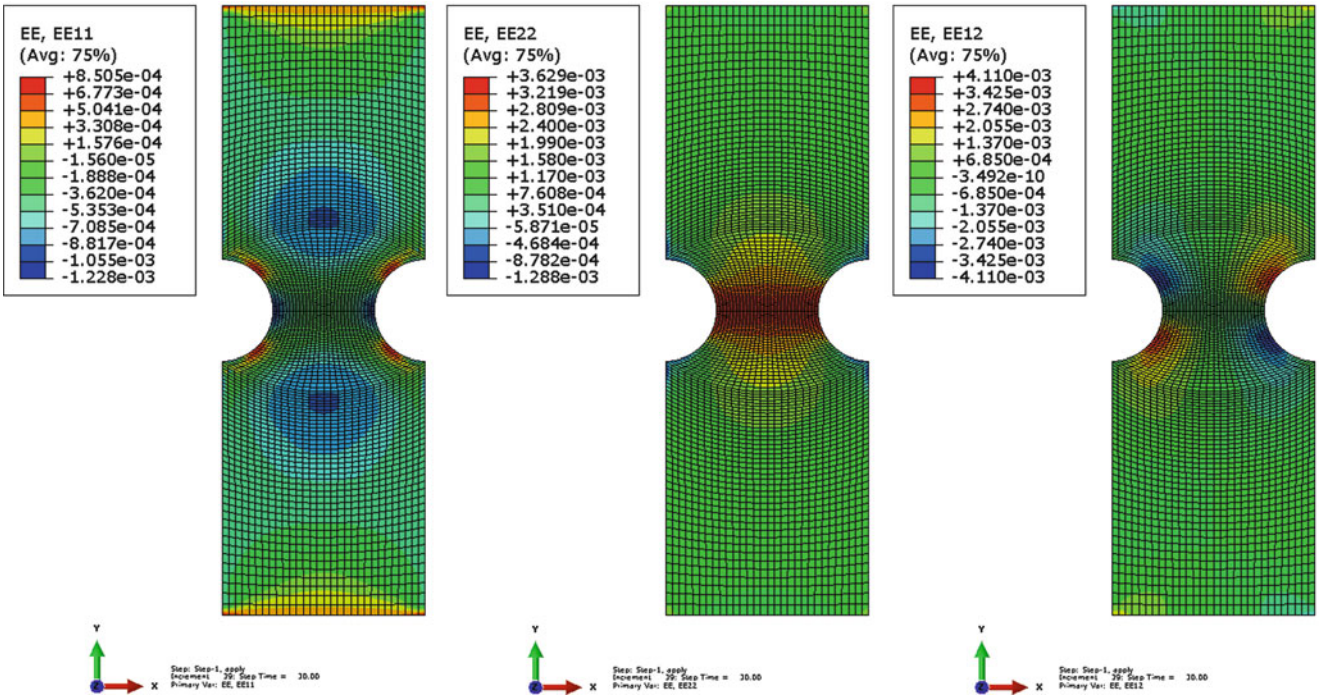

Fig. 32.1 Specimen geometry and computed strain fields, ε_{xx}, ε_{yy} and ε_{xy}, respectively

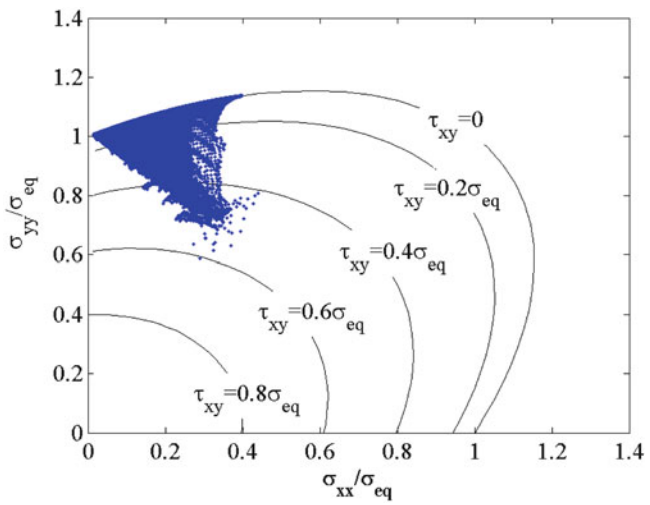

Fig. 32.2 Stress components obtained with the used notched specimen. The stress components are normalized with respect to the equivalent stress σ_{eq}

Table 32.2 Materials used in the FE model

	Input parameters					
Material	K [MPa]	ε_0	N	R/R_0	R_{45}	R_{90}
Isotropic	1,000	0.02	0.5	–	–	–
Normal anisotropy	1,000	0.02	0.5	1.8	–	–
Planar anisotropy	1,000	0.02	0.5	1.8	1.1	2.5

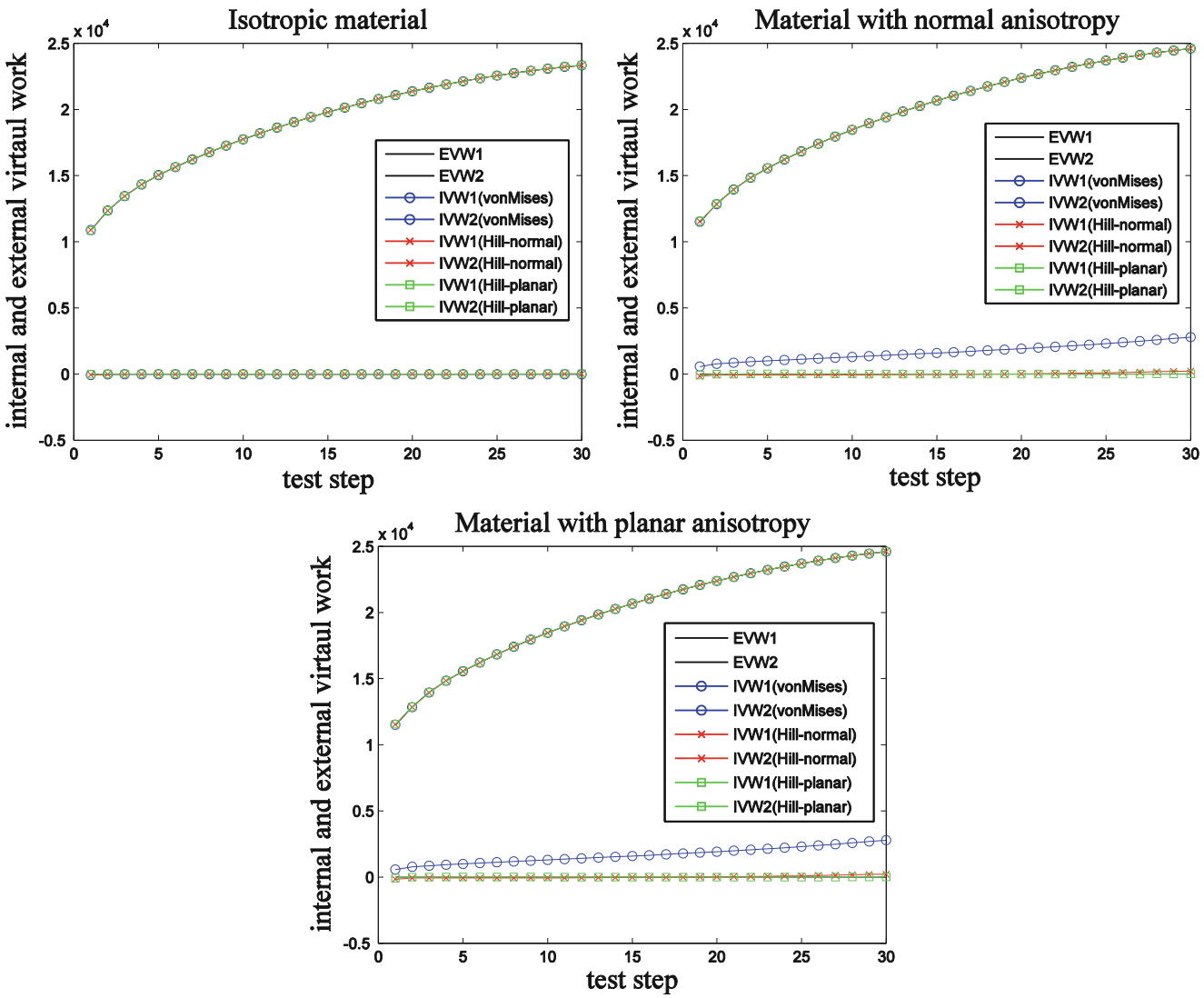

Fig. 32.3 Comparison between internal (*IVW*) and externale (*EVW*) virtual work in the three investigated material at the end of the identification procedure

L is the semi-length of the inspected area and W is the semi-width of the middle section. The coordinate system is chosen such as the origin is placed at the centre of the specimen. The virtual work of the external forces for the two virtual fields is:

$$\int_{\partial V} \left(\mathbf{T}_j^{1PK}\mathbf{n}\right) \cdot \delta\mathbf{v}_1 \, dS = 2f_j \tag{32.9}$$

$$\int_{\partial V} \left(\mathbf{T}_j^{1PK}\mathbf{n}\right) \cdot \delta\mathbf{v}_2 \, dS = 0 \tag{32.10}$$

where f_j is the total tensile force at increment j. The results are illustrated in Fig. 32.3 in terms of comparison between the internal and external virtual work for the three considered materials. In Table 32.3 the results in terms of final value of the cost function is shown. In Table 32.4 the identified parameters in the different benchmark tests is listed.

When an isotropic material is used, the cost function is almost the same using the three models. In this case it is obviously more convenient using the simple von Mises model with three parameters. In case of normal anisotropy the cost function value obtained with the von Mises model is much higher than the other two which are very similar. This is clear also from the graphs of Fig. 32.3. When a material with planar anisotropy is used, a large difference is observed between von Mises and the Hill models however, in this case the cost function using the Hill-normal model is eight times larger than the one used the Hill-planar model.

Table 32.3 Cost function values

	Cost function value		
Input material	von Mises	Hill-Normal	Hill-Planar
Isotropic	23.2	9.3	11.6
Normal anisotropy	2,301	20.5	18.6
Planar anisotropy	1,670	80.3	11.8

Table 32.4 Identified parameters

	Identified parameters					
Models	K [MPa]	ε_0	N	R/R_0	R_{45}	R_{90}
Isotropic material						
von Mises	999.2	0.020	0.5018	–	–	–
Hill-normal	1,000.3	0.020	0.5018	0.995	–	–
Hill-Planar	836.5	0.020	0.4898	0.9698	1.109	0.6212
Material with planar anisotropy						
von Mises	1,152.7	0.0194	0.5008	–	–	–
Hill-normal	1,001.8	0.0197	0.5023	1.7859	–	–
Hill-Planar	734.0	0.0204	0.4752	1.8077	1.8184	0.7122
Material with normal anisotropy						
von Mises	1,144.6	0.0168	0.4844	–	–	–
Hill-normal	1,038.2	0.0171	0.4869	1.5611	–	–
Hill-Planar	1,004.6	0.0185	0.4919	1.8953	1.0413	1.6483

The distinction between normal and planar anisotropy is more difficult to individuate, this is probably due to the specimen geometry which generates a stress/strain field not very heterogeneous, see Fig. 32.2.

The interesting outcome of this study is that, looking at the identified parameters of Table 32.4 the benchmark is effective even if the VFM procedure is not able to correctly identify the parameters.

32.4 Conclusions

In this paper a benchmark procedure to choose the best plasticity model for a given application is presented. The procedure relies on the cost function obtained using the VFM. The low computational cost of the VFM allows to compare many different models in a reasonable amount of time. The procedure has been tested on simulated experiments. The chosen experiment is tensile test on notched specimens which produce a moderate heterogeneous stress/strain field. Using the described procedure it is possible individuate the best model even though the VFM procedure is not able to correctly identify the constitutive parameters. This shows the potentiality of the proposed procedure for testing applications, however the test geometry should be optimized and the procedure should be validated on real experimental cases.

References

1. Hill R (1948) A theory of yielding and plastic flow of anisotropic metals. Proc Roy Soc Lond Ser A Math Phys Sci 193:281–297
2. Barlat F, Brem JC, Yoon JW, Chung K, Dick RE, Lege DJ, Pourboghrat F, Choi SH, Chu E (2003) Plane stress yield function for aluminium alloy sheets-part I. Int J Plast 19:1297–1319
3. Barlat F, Aretz H, Yoon JW, Karabin ME, Brem JC, Dick RE (2005) Linear transformation based anisotropic yield functions. Int J Plast 21:1009–1039
4. Vegter H, van den Boogaard AH (2006) A plane stress yield function for anisotropic sheet material by interpolation of biaxial stress states. Int J Plast 22:557–580
5. Bai Y, Wierzbicki T (2008) A new model of metal plasticity and fracture with pressure and Lode dependence. Int J Plast 24(6):1071–1096
6. Pierron F, Grédiac M (2012) The virtual fields method. Springer, New York
7. Grédiac M, Pierron F, Avril S, Toussaint E (2006) The virtual fields method for extracting constitutive parameters from full-field measurement: a review. Strain 42:233–253

8. Avril S, Bonnet M, Bretelle A-S, Grédiac M, Hild F, Ienny P, Latourte F, Lemosse D, Pagano S, Pagnacco E, Pierron F (2008) Overview of identification methods of mechanical parameters based on full-field measurements. Exp Mech 48:381–402
9. Rossi M, Pierron F (2012) Identification of plastic constitutive parameters at large deformations from three dimensional displacement fields. Comput Mech 49:53–71
10. Chackrabarty J (2000) Applied plasticity. Springer, New York
11. Lankford WT, Snyder SC, Bausher JA (1950) New criteria for predicting the press performance of deep drawing sheets. Trans Am Soc Metals 42:1197–1232
12. Rossi M, Broggiato GB, Papalini S (2008) Application of digital image correlation to the study of planar anisotropy of sheet metals at large strains. Meccanica 43:185–199

Chapter 33
Optical: Numerical Determination of the Flow Curves of Anisotropic Steels and Failure Prediction

G. Mirone

Abstract A combined experimental – numerical method is presented here for the stress–strain characterization of ductile anisotropic metals.

The experimental side of the method is based on the simultaneous video acquisition of tensile round bars from two different angles, for determining the true stress-true strain curves of highly anisotropic ductile metals.

Then the material-independent *MLR* correction, derived in previous works from numerical simulations of tensile tests with many different metals, is applied to the experimental true stress- true strain curve, so obtaining an accurate post-necking flow curve of the material.

The proposed procedure is applied to tensile specimens of an X100 steel for piping, machined with different notches along different orientations within a rolled plate cut from a large size pipe.

The flow curves and the Hill parameters identifying the behavior of the X100 steel are derived by applying the proposed procedure to the tests of smooth specimens alone; the experiments with notched specimens are then simulated by finite elements, using as input the material data from smooth bars. The experimental – numerical comparison evidences the accuracy of the whole material data used and, in turn, the suitability of the proposed procedure.

Finally, the Bao-Wierzbicki damage model is implemented in a subroutine ran together with a new series of FE analyses, obtaining failure predictions very close to experiments.

Keywords Damage • Fracture • Anisotrpopy • Necking • Triaxiality

33.1 Introduction

The stress–strain characterization of anisotropically plastic metals is based on the experimental derivation of two series of stress–strain data: the hardening curve, defining the evolving size and position of the yield surface as the plastic strain flows, and the parameters defining the shape of the yield surface. Both these series of data are defined according to the yield criteria adopted.

While for soil-like and pressure-dependent granular materials the yield surface is a tapered cylinder (variable cross sections), [1–3], for metals it is not yet completely clarified whether or not the hydrostatic stress affects the elastoplastic stress–strain response and, then whether or not the cross section of the yield surface is constant or not.

The effect of the second stress invariant is just taken into account by the isotropic and kinematic hardening functions, while the effect of the third stress invariant, causing non-circularity of the cross-section of the yield surface, is modeled by various models for plastic "induced" anisotropy [4–6]. In this paper we deal with a highly anisotropic X-100 steel for piping whose anisotropy is mainly due to rolling and cold-forming of the pipe sheet, so the Hill model for plane stress-induced anisotropy is adopted.

Whatever anisotropy model is used, the hardening curve must be derived from experiments in which the evolving cross section and load are acquired. The true curve obtained in this way must be then postprocessed in the post-necking strain range, for eliminating the effect of neck-induced triaxiality on the load/area ratio, and finally obtaining the real hardening curve [7–11].

G. Mirone (✉)
Università di Catania, Viale A. Doria 6, Catania, Italy
e-mail: gmirone@diim.unict.it

M. Rossi et al. (eds.), *Residual Stress, Thermomechanics & Infrared Imaging, Hybrid Techniques and Inverse Problems, Volume 8*, Conference Proceedings of the Society for Experimental Mechanics Series, DOI 10.1007/978-3-319-00876-9_33,

Due to the remarkable anisotropy the cross section of the round bar specimens loses its circularity very soon after the first yielding, and becomes a very flat ellipse at the test end, so, the usual optical techniques for acquiring the true curve in the post necking range cannot be used anymore; here a method is presented for overcoming this obstacle.

Once the true curve is obtained with the new procedure proposed, the post-necking correction method developed in [12] for isotropic-plasticity materials, is implemented here also for the highly anisotropic X100 steel.

The anisotropy material constants are derived partially from experiments with smooth specimens machined along different orientations, partially from reverse-engineering methods helped by finite elements simulations.

The quality of the material characteristic data so obtained is evaluated by simulating other experiments, different from those used for the characterization. As closely are simulated the non-characterization tests, as better the material data is.

Then also the ductile damage is modeled according to various damage models, for predicting failure initiation; again, the comparison of the failure predictions with experiments indicates how accurate are the models implemented.

The effect of triaxiality in determining/accelerating failure is modeled as in the Wierzbicki approach [13–16], while the effect of the Lode angle (or the third stress invariant) on failure is modelled in a different way based on various other viewpoints [17–23].

33.2 Stress–Strain Characterization of Anisotropic Materials by Tension Tests

The true stress – true strain curve, simply named "true curve", takes into account for the large strains and the cross section decrease occurring in the tensile specimen:

$$\begin{aligned} \sigma_{True} &= \frac{F}{A} \\ \varepsilon_{True} &= Ln\left(\frac{A_0}{A}\right) \end{aligned} \tag{33.1}$$

As the specimen deforms uniformly and maintains its constant cross section, the data in Eq. 33.1 is equal to the equivalent stress necessary for characterizing the elastoplastic stress–strain response of isotropic metals:

$$\begin{aligned} \sigma_{True} &= \frac{F}{A} \\ \varepsilon_{True} &= Ln\left(\frac{A_0}{A}\right) \end{aligned} \tag{33.2}$$

Where F is the current load, A_0 is the initial cross section and A is the current cross section.

If the tensile round specimen is made of isotropic materials, then the cross section can be determined by simply measuring the radius ($A_0 = \pi\, a_0{}^2$, and $A = \pi\, a^2$), but if the material is not plastically isotropic, then the specimen cross section after yielding can be considered elliptical, with semiaxes a and b.

$$\begin{aligned} \sigma_{True} &= \frac{F}{\pi \cdot a \cdot b} \\ \varepsilon_{True} &= Ln\left(\frac{a_0{}^2}{a \cdot b}\right) \end{aligned} \tag{33.3}$$

Then, both a and b must be determined from experiments, and in Fig. 33.1 is depicted the scheme for explaining how such a task can be accomplished.

Two cameras acquire video sequences of the evolving specimen shape from two different sight lines, in principle at random angles.

Assuming that the distances between each camera and the specimen is much greater than the cross section size, follows that the sight lines *r2* are parallel each other and to the axis of camera 1, as well as the *r2* lines are parallel each other and to the axis of camera 2.

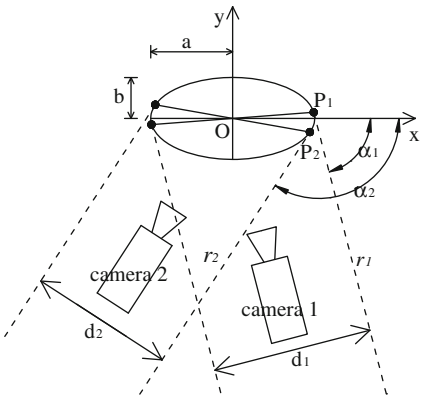

Fig. 33.1 Elliptical cross section and cameras setup

Each couple of dashed parallel lines defining an apparent diameter can be described by Eq. 33.4 below:

$$y_i = \pm q_i + m_i \cdot x \tag{33.4}$$

where

$$\begin{cases} m_i = Tan(\alpha_i) \\ q_i = \dfrac{d_i}{2 \cdot Cos(\alpha_i)} \end{cases} \tag{33.5}$$

with the subscript $i = 1, 2$ referring to data from the first or the second camera, respectively.

The elliptical cross section can be represented by the following equation:

$$\frac{x^2}{a^2} + \frac{y^2}{b^2} = 1 \tag{33.6}$$

so the points $P1$ and $P2$ can be obtained as intersections between axes (33.4) and the ellipse (33.6).

Generally, the intersection between an axis and an ellipse lying on the same plane consists of two points; by coupling the equations of an ellipse with that of a line, the following equations are derived, returning the x coordinates of the two intersection points:

$$x_i = \frac{a^2 d_i Sec(\alpha_i) Tan(\alpha_i) \pm \sqrt{4a^{2\cdot} b^4 - a^{2\cdot} b^2 d_i{}^2 Sec(\alpha_i) + 4a^4 b^2 Tan(\alpha_i)^2}}{2 \cdot \left(b^2 + a^2 Tan(\alpha_i)^2\right)} \tag{33.7}$$

if the intersecting axes are r_1 and r_2 in Fig. 33.1, the two intersection points for each axis degenerate in a single tangent point like P_1 and P_2 and the terms under square root in Eq. 33.7 must vanish: this condition gives a new equation for each video camera:

$$\begin{cases} 4a^{2\cdot} b^4 - a^{2\cdot} b^2 d_1{}^2 Sec(\alpha_1) + 4a^4 b^2 Tan(\alpha_1)^2 = 0 \\ 4a^{2\cdot} b^4 - a^{2\cdot} b^2 d_2{}^2 Sec(\alpha_2) + 4a^4 b^2 Tan(\alpha_2)^2 = 0 \end{cases} \tag{33.8}$$

By solving the coupled Eq. 33.8, the final expression for the semiaxes is obtained:

$$\begin{cases} a = \sqrt{\dfrac{(d_1 \cdot Sec(\alpha_1))^2 - (d_2 \cdot Sec(\alpha_2))^2}{4\left(Tan(\alpha_1)^2 - Tan(\alpha_2)^2\right)}} \\ b = \sqrt{(d_1 \cdot Sec(\alpha_1))^2 - Tan(\alpha_1)^2 \cdot a^2} \end{cases} \tag{33.9}$$

So three experimental measurements (the two apparent diameters d_1, d_2 together with the angle α between camera mountings and main anisotropy axis), are sufficient for deriving the cross section of tensile specimens made of anisotropically yielding metals. And the knowledge of the current cross section together with that of the current load allow to easily calculate the true curve through Eq. 33.3.

Given that the anisotropy directions do not change nor rotate during a tension test, α can be measured only once at the test end, before the specimen halves are removed from their fixtures.

The proposed procedure can be applied to round tension specimens machined along any orientation, with smooth or arbitrarily notched shapes.

For the induced anisotropy is adopted the Hill 48 yield criteria,

$$\begin{aligned} f(\tilde{\sigma}) = {} & a_1 \cdot (\sigma_y - \sigma_z)^2 + a_2 \cdot (\sigma_x - \sigma_z)^2 + a_3 \cdot (\sigma_x - \sigma_y)^2 \\ & + 3 \cdot a_4 \cdot {\tau_{yz}}^2 + 3 \cdot a_5 \cdot {\tau_{xz}}^2 + 3 \cdot a_6 \cdot {\tau_{xy}}^2 \leq {\sigma_{Eq-ISO}}^2 \end{aligned} \tag{33.10}$$

and, given that the strain history generating the material anisotropy is mainly of the plane-stress type (rolling and cold working of pipes metal sheet), the Hill 48 criteria takes the following simplified form:

$$\begin{aligned} a_1 &= \frac{{\sigma_{Av}}^2}{2}\left(\frac{1}{{\sigma_{90}}^2} + \frac{1}{{\sigma_N}^2} - \frac{1}{{\sigma_0}^2}\right); & a_4 &= \frac{{\sigma_{Av}}^2}{2{\sigma_N}^2} \cdot \sqrt{\frac{2 \cdot r_{45} + 1}{3}} \\ a_2 &= \frac{{\sigma_{Av}}^2}{2}\left(\frac{1}{{\sigma_0}^2} + \frac{1}{{\sigma_N}^2} - \frac{1}{{\sigma_{90}}^2}\right); & a_5 &= \frac{1}{2} \\ a_3 &= \frac{{\sigma_{Av}}^2}{2}\left(\frac{1}{{\sigma_0}^2} + \frac{1}{{\sigma_{90}}^2} - \frac{1}{{\sigma_N}^2}\right); & a_6 &= \frac{1}{2} \end{aligned} \tag{33.11}$$

with

$$\begin{aligned} \sigma_N &= \sigma_0 \sqrt{\frac{r_{90} \cdot (1 + r_0)}{r_0 + r_{90}}} = \sigma_{90} \sqrt{\frac{r_0 \cdot (1 + r_{90})}{r_0 + r_{90}}} \\ \sigma_{Av} &= \frac{\sigma_0 + 2 \cdot \sigma_{45} + \sigma_{90}}{4} \end{aligned} \tag{33.12}$$

Six constants are then necessary for completely identifying the anisotropy response of the material: σ_0, σ_{45}, σ_{90}, which are the first-yield stresses of smooth tensile specimens machined at 0°, 45° and 90° to the rolling direction, and r_0, r_{45}, r_{90}, expressing the strain ratios $\varepsilon_{Width}/\varepsilon_{Thick}$ between the strain along the width and that along the thickness of the same 0°, 45° and 90° specimens.

The strongest underlying assumption of the Hill criteria is that the yield stresses ratios and the strains ratios along the various directions are constant all over the strain histories, so, for determining the hardening curve $\sigma_{Av}(\varepsilon_{Eq}')$, just the hardening curve along a single direction can be derived by experiments and then opportunely scaled by the constant ratios.

In this work, smooth and notched tensile round specimens are machined along the longitudinal (0°) direction of a pipeline made of steel of the X100 grade. The size of the available steel block was not sufficient for machining specimens of appropriate size also at 45° and 90° to the rolling direction.

Then, the hardening curve and the parameters $\sigma_0 = 648$ MPa; $r_0 = 0.525$ are obtained from the experiments with smooth specimens; the yield stress $\sigma_{90} = 750$ MPa is provided by the steel supplier, while σ_{45}, r_{45} and r_{90} must be derived by reverse engineering, due to the unavailability of specimens at 45° and 90°.

The experimental procedure proposed here for deriving the true stress–true strain curves is applied to the available 0° specimens, but the method is not restricted to any material orientation.

Three identical smooth round tension specimens are machined (slightly elongated ISO 6892 specimens), Fig. 33.2 and Table 33.1 showing their shape and dimensions.

The cameras are supported by a fixture holding them at a 90° angle each other, and a goniometer is placed below the specimen fixture for reading the angle between anisotropy semiaxes and camera sight axes, at the end of each test (see Fig. 33.3).

From each video sequence, single frames are extracted at selected time intervals, at which also the load is read from the testing machine sample file.

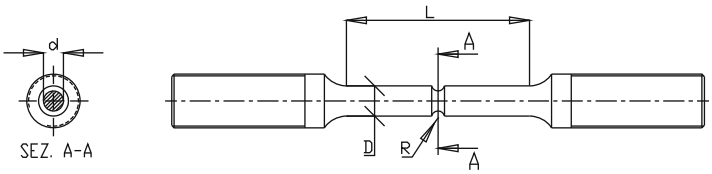

Fig. 33.2 Specimens geometry

Table 33.1 Specimens dimensions

Specimen	d [mm]	D [mm]	R [mm]	L [mm]
Smooth	9	9	∞	55

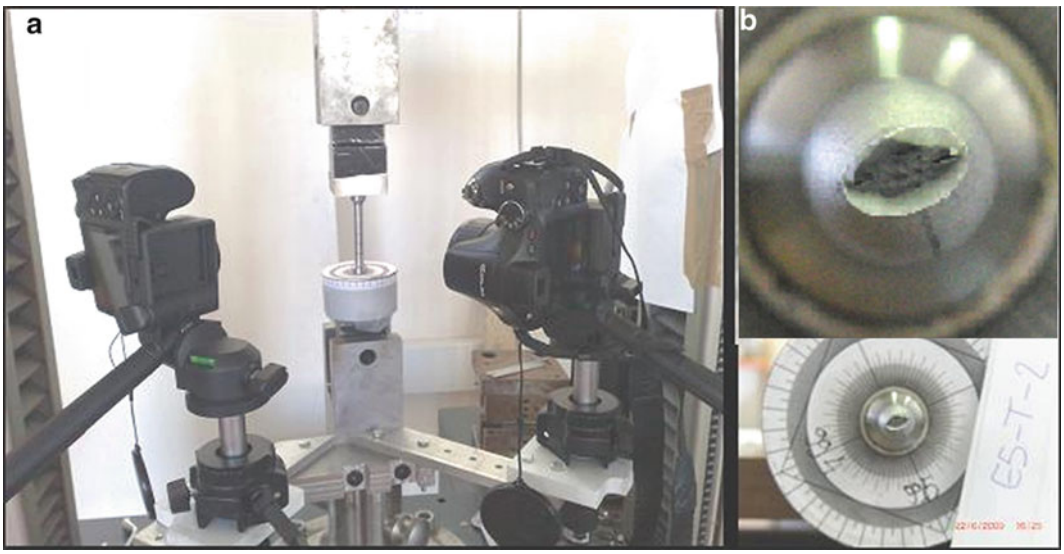

Fig. 33.3 Experimental setup and fractured specimens sections

Simple image analysis measurements give the apparent diameters *d1* and *d2* of Eq. 33.9, so the semiaxes and the current cross section can be calculated. Then, Eq. 33.3 give the experimental true curve for the 0° smooth specimens.

The true curve is finally corrected by the MLR function in the post-necking range for obtaining the flow curve $\sigma_0(\varepsilon_{Eq'})$:

$$MLR(\varepsilon - \varepsilon_N) = 1 - 0.6058 \cdot (\varepsilon - \varepsilon_N)^2 + 0.6317 \cdot (\varepsilon - \varepsilon_N)^3. - 0.2107 \cdot (\varepsilon - \varepsilon_N)^4$$
$$\sigma_0(\varepsilon_{Eq}) = \sigma_{0True}(\varepsilon_{True}) \cdot MLR(\varepsilon - \varepsilon_N). \tag{33.13}$$

In Fig. 33.4 is reported the experimental estimation of the true stress σ_{0True} (scattered points), the best fit curve of experimental points (higher solid curve) and the neck-corrected flow stress (lower solid curve).

Among the remaining unknown anisotropy parameters, those from 45°-oriented specimens are found to play a negligible role on the available experimental data, while r_{90} strongly affects the ellipticity ratio of 0° smooth specimens. So r_{90} is varied in FE analyses until the semiaxes ratio from FE evolves as it does in the experiments (see Fig. 33.5) and the value of 660 Mpa, 0.60 and 0.85, identifying the constants set named "Hill 22", are adopted for σ_{45}, r_{45} and r_{90}, respectively.

33.3 Experiments and FE Simulations for Validating Material Data

Other specimens are machined from the X100 steel block, according to Fig. 33.6 and Table 33.2.

The true curves of the notched tensile specimens are obtained according to the procedure presented here, as also in these cases the considerable anisotropy leads to highly elliptical cross sections (see Fig. 33.7), requiring double camera video samplings.

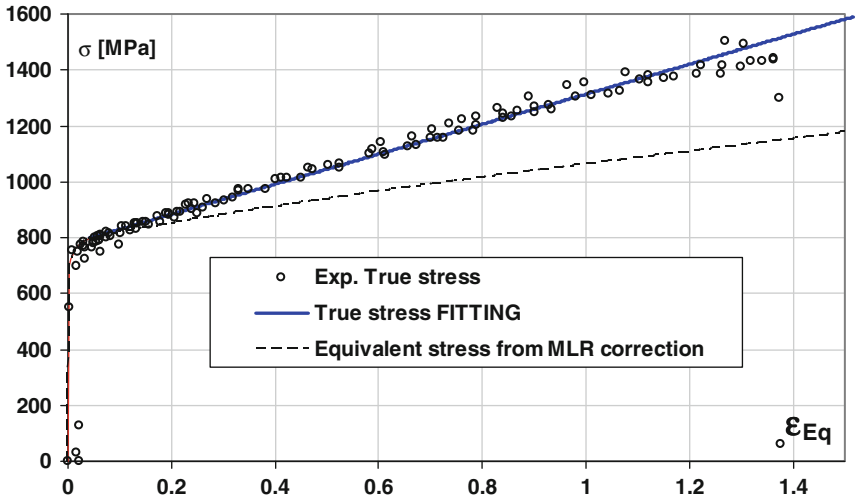

Fig. 33.4 Experimental true curve, best fit and MLR-corrected flow stress $\sigma_0(\varepsilon_{Eq}')$

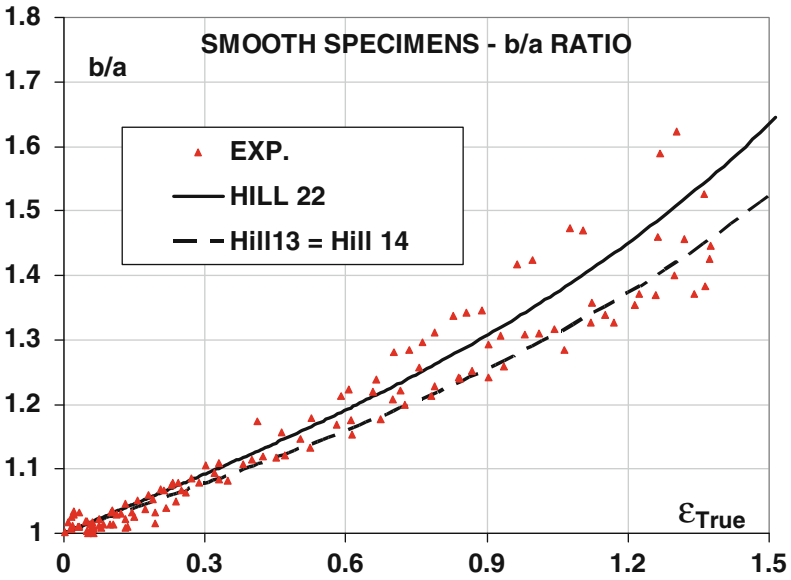

Fig. 33.5 Experimental true curve, best fit and MLR-corrected flow stress $\sigma_0(\varepsilon_{Eq}')$

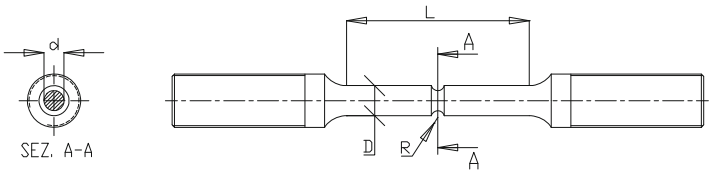

Fig. 33.6 Round notched tension specimens

Below are reported the experimental data from the tests of the above specimens, together with the numerical predictions obtained by using the material data of the previous section for the simulations of the current tests.

For the tensile tests are reported the true stress-true strain curves, the load-elongation curves and the ellipticity ratio of semiaxes, while for the fracture specimens, only the load – notch opening curves are considered Fig. 33.8.

All the numerical predictions for the tensile tests are very close to the experimental findings up to failure, confirming that the material data obtained are capable of correctly describing the stress–strain behavior of the material.

This means that the experimental procedure for determining the true curve (dual camera and elliptical cross section model) and the post-necking correction of such a curve (MLR function derived from isotropic materials) are also suitable for characterizing materials exhibiting very pronounced induced anisotropy.

Table 33.2 Dimensions of round notched tensile specimens

Specimen	d [mm]	D [mm]	R [mm]	L [mm]
R2	6	9	2	55
R10	6	9	10	55

Fig. 33.7 Fractured notched tension specimens

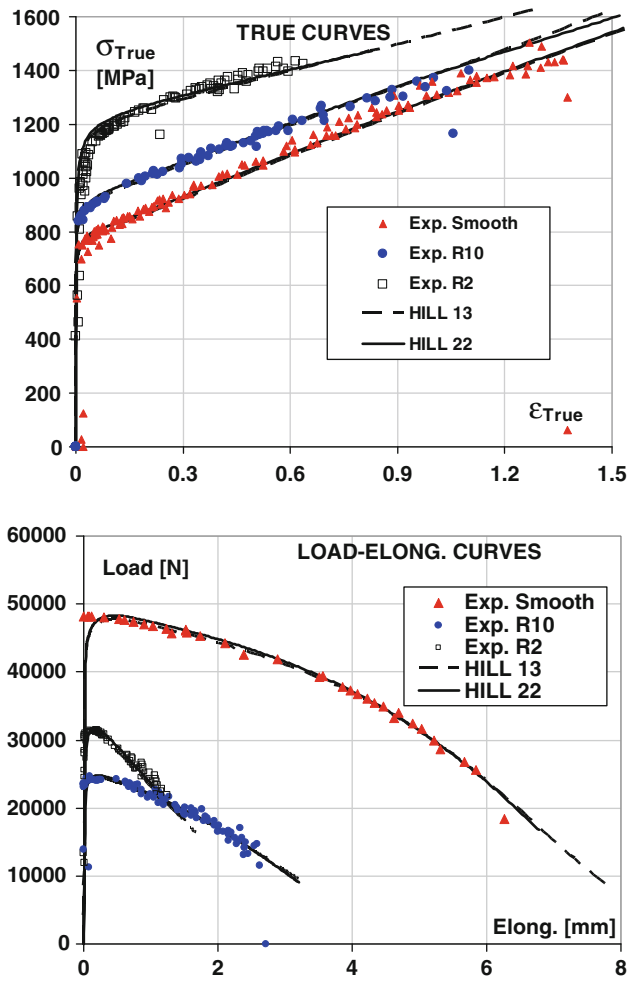

Fig. 33.8 True curves and load-elongation curves from tensile tests

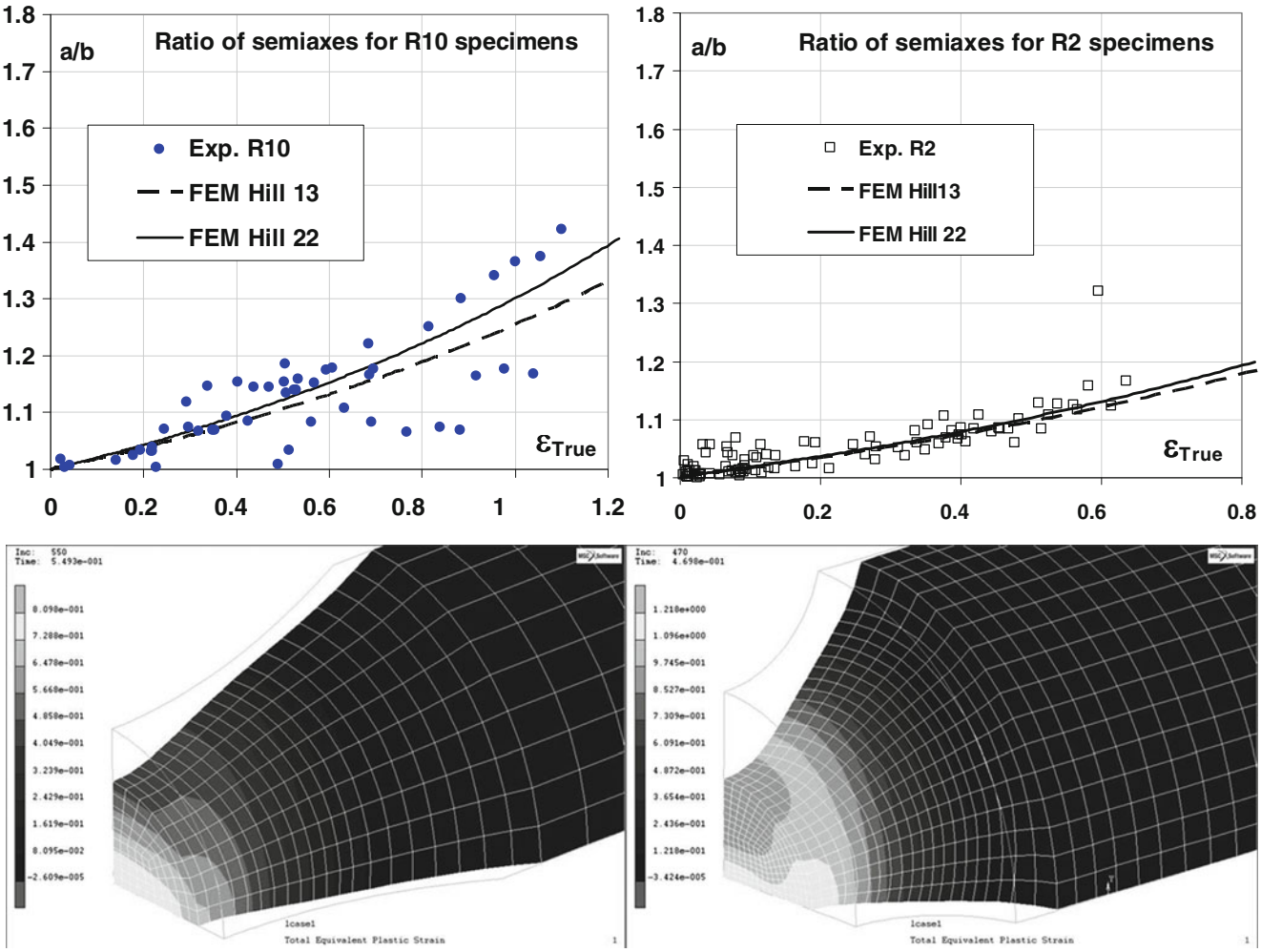

Fig. 33.9 Ellipticity ratio curves from tensile tests and deformed FE meshes of notched specimens

After failure initiates and rapidly propagates in the necked cross sections, experimental curves abruptly disappear, while the numerical curves, "unaware" of any failure, continue without any visible discontinuity up to the last step of the elongation imposed to the FE model Fig. 33.9.

33.4 Triaxiality, Lode Angle and Damage Modeling

According to most current theories about ductile fracture, failure initiation is a local phenomenon promoted by the stress triaxiality (expressing the 1*st* stress invariant), the plastic strain (promoted by the 2nd stress invariant) and the Lode angle (expressing the 3rd stress invariant).

Triaxiality factor and normalized Lode angle are defined as in Eq. 33.14:

$$TF = \frac{\sigma_H}{\sigma_{Eq}}$$
$$X = \frac{27 \cdot \sigma'_1 \cdot \sigma'_2 \cdot \sigma'_3}{2 \cdot \sigma^3{}_{Eq}} \tag{33.14}$$

Local failure is assumed to be the consequence of a damage function $D(\varepsilon_{Eq}{}', TF, X)$ reaching a critical value. Here the path dependence of damage and failure is ensured by imposing that D contains an integral function, the effects of variables TF and X are assumed to be uncoupled, and the critical value is assumed to be a material constant:

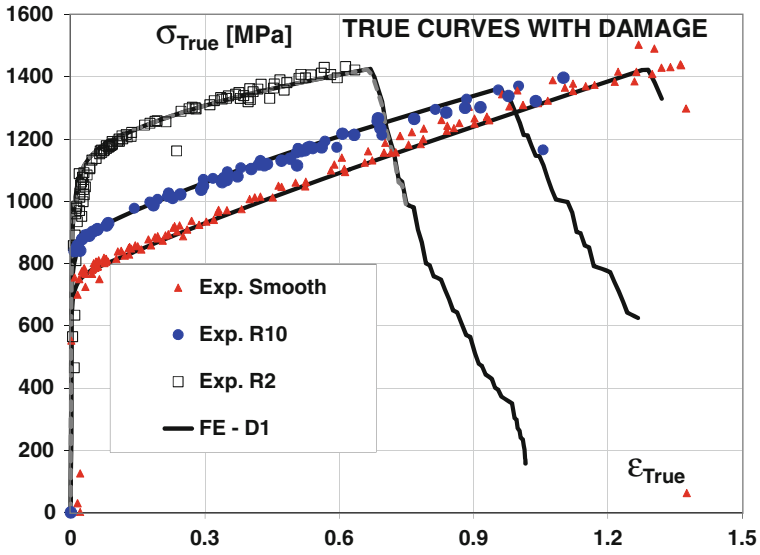

Fig. 33.10 True curves from FE with damage

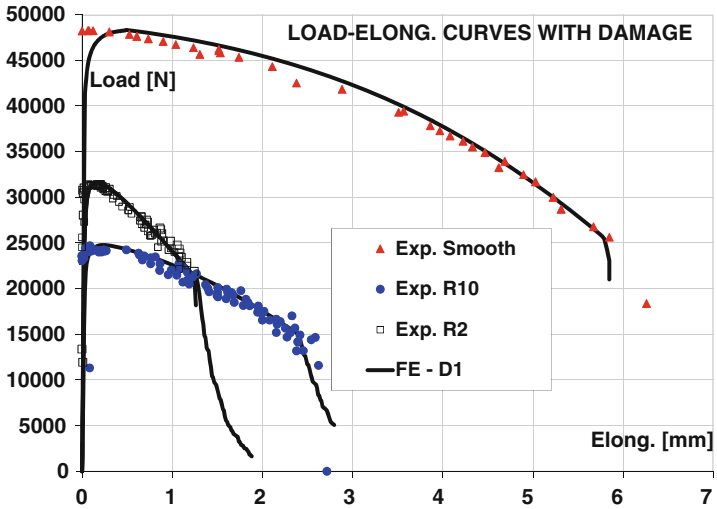

Fig. 33.11 Load-elongation curves from FE with damage

$$D(\varepsilon_{Eq}, TF, X) = \frac{\int_0^{\varepsilon_{Eq}} f(\varepsilon_{Eq}, TF) d\varepsilon_{Eq}}{\int_0^{\varepsilon_{Eq}} g(\varepsilon_{Eq}, TF) d\varepsilon_{Eq}}$$
$$D(\varepsilon_{Cr}, TF, X) = D_{cr} \tag{33.15}$$

where ε_{Cr} is the critical strain at which local failure initiates.

So, after the critical damage is evaluated along a given stress/strain/triaxiality/Lode angle history for which experimental data is available, the critical strain can be predicted for every other arbitrary stress/strain/triaxiality/Lode angle history, and a general failure criteria is inferred in this way.

The dependence of damage on *TF* is assumed to be that proposed by Bao and Wierzbicki, so the damage function becomes:

$$D(\varepsilon_{Eq}, TF, X) = \frac{\int_0^{\varepsilon_{Eq}} TF \cdot d\varepsilon_{Eq}}{g(\varepsilon_{Eq}, X)} \tag{33.16}$$

The curves FE-D1 in Figs. 33.10 and 33.11 show the numerical response where the effect of *X* on damage is switched off (only *TF* and ε_{Eq} affect failure).

As visibile in Eqs. 33.14, 33.15 and 33.16, the effect of the Lode angle on failure of axisymmetric specimens can be almost neglected because X is close to unity all over the test and also because the specimens undergo a very fast fracture propagation; on the contrary, the above effect is extremely important when modeling the C(T) fracture specimens because these exhibit much lower values of X at the crack front and because the slow crack propagation largely affects the overall response of the fracture specimen.

33.5 Conclusions

A method is proposed in this paper for deriving the true curve of round specimens made of highly anisotropic steels, all over the strain history including the post-necking range, up to failure.

Also, a material-independent necking-correction function, developed in previous works for many different isotropic metals, is used here proving its suitability for anisotropic steels as well.

The accuracy of the complete experimental-analytical procedure for calculating the true curve and for correcting it in the post-necking phase, is verified by using the obtained material curve as the input for FE simulations of various tests (notched round tension bars and C(T) fracture specimens) substantially differing from those used for the derivation of the whole material curve (smooth round tensile bars).

In case of axisymmetric tension tests, the material behaviour can be simulated by the stress–strain data alone, with a remarkable degree of accuracy, because the fracture phenomenon only occurs at the very final stages of the test and does not influence the overall specimen response.

References

1. Drucker DC, Prager W (1952) Soil mechanics and plastic analysis for limit design. Q Appl Math 10(2):157–165
2. Bigoni D, Piccolroaz A (2004) Yield criteria for quasi brittle and frictional materials. Int J Solids Struct 41:2855–2878
3. Bai Y, Wierzbicki T (2007) A new model of metal plasticity and fracture with pressure and Lode dependence. Int J Plast 24:1071–1096
4. Barlat F, Lege DJ, Brem JC (1991) A six-component yield function for anisotropic materials. Int J Plast 7:693–712
5. Hill R (1993) User-friendly theory of orthotropic plasticity in sheet metals. Int J Mech Sci 35(1):19–25
6. Bron F, Besson J (2004) A yield function for anisotropic materials: application to aluminum alloys. Int J Plast 20:937–963
7. Bridgman PW (1956) Studies in large flow and fracture. Mcgraw Hill, New York, NY
8. Alves M, Jones N (1999) Influence of hydrostatic stress on failure of axisymmetric notched specimens. J Mech Phys Solids 47:643–667
9. La Rosa G, Mirone G, Risitano A (2003) Post-necking elastoplastic characterization, degree of approximation in the Bridgman method and properties of the flow-stress/true-stress ratio. Met Mater Trans A 34A(3):615–624
10. Ling Y (1996) Uniaxial true stress–strain after necking. AMP J Technol 5:37–48
11. Zhang ZL, Hauge M, Odegard J, Thaulow C (1999) Determining material true stress–strain curve from tensile specimens with rectangular cross section. Int J Solids Struct 36:2386–2405
12. Mirone G (2004) A new model for the elastoplastic characterization and the stress–strain determination on the necking section of a tensile specimen. Int J Solids Struct 5(41):3545–3564
13. Bao Y, Wierzbicki T (2004) On fracture locus in the equivalent strain and stress triaxiality space. Int J Mech Sci 46:81–98
14. Wierzbicki T, Bao Y, Lee Y-W, Bai Y (2005) Calibration and evaluation of seven fracture models. Int J Mech Sci 47:719–743
15. Xue L (2009) Stress based fracture envelope for damage plastic solids. Eng Fract Mech 76:419–438
16. Brunig M, Chyra O, Albrecht D, Driemeier L, Alves M (2008) A ductile damage criterion at various stress triaxialities. Int J Plast 24:1731–1755
17. Mirone G (2007) Role of stress triaxiality in elastoplastic characterization and ductile failure prediction. Eng Fract Mech 74:1203–1221
18. Mirone G (2008) Elastoplastic characterization and damage predictions under evolving local triaxiality: axysimmetric and thick plate specimens. Mech Mater 40:685–694
19. Xue L, Wierzbicki T (2008) Ductile fracture initiation and propagation modelling using damage plasticity theory. Eng Fract Mech 75:3276–3293
20. Coppola T, Cortese L, Folgarait P (2009) The effect of stress invariants on ductile fracture limit in steels. Eng Fract Mech 76:1288–1302
21. Mirone G, Corallo D (2010) A local viewpoint for evaluating the influence of stress triaxiality and Lode angle on ductile failure and hardening. Int J Plast 26:348–371
22. Gao X, Zhang T, Hayden M, Roe C (2009) Effects of the stress state on plasticity and ductile failure of an aluminum 5083 alloy. Int J Plast 25:2366–2382
23. Gao X, Zhang T, Zhou J, Graham SM, Hayden M, Roe C (2011) On stress-state dependent plasticity modeling: significance of the hydrostatic stress, the third invariant of stress deviator and the non-associated flow rule. Int J Plast 27:217–231

Chapter 34
Advanced Biaxial Cruciform Testing at the NIST Center for Automotive Lightweighting

Mark A. Iadicola, Adam A. Creuziger, and Tim Foecke

Abstract Modeling of sheet metal forming operations requires mechanical properties data at very large tensile strains and various biaxial strain paths. Typically these data are developed along strain ratio paths that are linear and monotonic, but actual forming strain paths are nonlinear and not necessarily monotonically increasing. A unique planar-biaxial testing facility at the National Institute of Standards and Technology (NIST) has been designed to address non-linear strain paths and other long standing measurement needs. The system uses a combination of four independently controlled hydraulic actuators, with either displacement, force, or strain feedback control, to deform the material, while measurements of the material response is accomplished through a unique combination of digital image correlation and X-ray diffraction. Results of commissioning tests are presented for displacement and force control along different axes. The system was able to deform the sample in the elastic and plastic regimes. The results show the difference between the displacement and strain paths followed, as well as some unexpected behavior (e.g. buckling). Other expanded system capabilities for future use are briefly described.

Keywords Biaxial deformation • Cruciform • Digital image correlation • X-ray diffraction • Infrared imaging

34.1 Introduction

The drive for improved fuel efficiency is pushing the auto industry to remove weight from their entire vehicle fleet. A major target for this lightweighting is the sheet metal components (e.g. unibody frame, doors, hoods, deck lids, and fenders). One method to achieve these goals is moving to advanced high-strength or lower density sheet metals, but designers need more robust material models for these materials to make full use of their potential. The more robust models must be calibrated through the entire forming strain range (plastic strains often >0.20 m/m) and complex strain paths (e.g. plane-strain followed by uniaxial transverse deformation). Classic models calibrated using simple uniaxial tests are not sufficient to capture the evolving material properties during complex and/or multistage forming processes. More complex models require more complex data for calibration. These data often are developed through bilinear strain paths, where samples are strained in a first stage, unloaded, machined, and then deformed through a second linear strain path. The possible effects of unloading and machining include changes in the material response. Biaxial deformation is occasionally used, but typically is performed over a single linear strain path, especially for tests to very high strains (e.g. bulge testing). Cross-shaped (cruciform) biaxial testing could be used to perform some nonlinear strain paths without unloading, but currently is typically used for linear strain paths and still suffers from biaxial failure at strains (typically <0.05 m/m) well below the forming limits (strains ≈ 0.30 m/m) for the same material [12]. These tests also require modeling (that assumes a constitutive law) to relate the applied loads to the stress and strains in the gauge section.

To address these and other long standing issues the National Institute of Standards and Technology Center for Automotive Lightweighting (http://www.nist.gov/lightweighting/) in Gaithersburg, MD has developed an advanced biaxial testing facility over the last few years which uses a unique combination measurement systems integrated into a high capacity biaxial testing machine. The facility is designed to test cross-shaped high strength sheet metal samples, although other shapes and

M.A. Iadicola (✉) • A.A. Creuziger • T. Foecke
Materials Sciences and Engineering Division, National Institute of Standards and Technology, Gaithersburg, MD, USA
e-mail: mark.iadicola@nist.gov

M. Rossi et al. (eds.), *Residual Stress, Thermomechanics & Infrared Imaging, Hybrid Techniques and Inverse Problems, Volume 8*, Conference Proceedings of the Society for Experimental Mechanics Series, DOI 10.1007/978-3-319-00876-9_34,

materials can be tested. The overall system is designed to permit large biaxial strain through controlled non-linear and non-monotonic strain paths without unloading the sample. The mechanical testing machine can run a static test in force, displacement, or strain control, or any logical combination of these methods, on each axis. The strain control and measurement is achieved through a combination of non-contacting two-dimensional (2D) real-time and three-dimensional (3D) post-processed digital image correlation (DIC) systems. An X-ray diffraction (XRD) method similar to [5, 9] is used to determine the surface biaxial stress state through measurement and analysis of the crystal lattice strains at a spot in the specimen gauge section. Optional non-contacting measurement of surface temperature can be performed using a 2D infrared (IR) imaging camera system. This paper describes the facility's basic mechanical testing capabilities (using force and displacement control) for one candidate specimen shape, and presents the results from some of the commissioning testing. The additional strain control and other measurement systems will be described in a general way with the details left for future work.

34.2 Facility Description

The biaxial cruciform mechanical testing machine is oriented horizontally (Fig. 34.1a) with the surface of the specimen level and about 1.5 m (5 ft) above the laboratory floor. The XRD and 3D-DIC systems are attached to the machine frame above the specimen, and the IR camera and 2D-DIC systems are attached to the machine frame below the specimen (Fig. 34.1). The 3D-DIC and IR systems could be repositioned without loss of functionality, but when the 2D-DIC system is used for strain control the system must have clear line-of-sight of the specimen gauge section. The XRD system is hung from a moveable gantry frame, and when XRD measurements are required the gantry is positioned directly above the specimen (Fig. 34.1a). In this paper, we will only discus the basic mechanical testing system and 3D-DIC measurement systems. Details of the other systems (i.e. 2D-DIC, infrared imaging, and X-ray diffraction) will be discussed in a future paper.

34.2.1 Mechanical System

The mechanical testing system in based on four independently controlled hydraulic actuators (X1, X2, Y1, and Y2 shown in Fig. 34.1) aligned in orthogonal pairs (X-axis and Y-axis). Each actuator has a $\pm$500 kN force capacity, and has a $\pm$50 mm displacement range from a reference distance of 640 mm between grip faces on each axis. Control feedback signals include: displacement position from four linear variable differential transformers (LVDTs) and force from four load cells, one for each actuator. The actuators can be programmed individually or in pairs using various combinations of these control signals. For cruciform testing, the actuators are typically controlled in axis pairs (matrix mode). In matrix mode, each axis displacement is the sum of the actuator displacement for each pair (positive tension and negative compression, resulting in a total range of $\pm$100 mm), and the difference between the displacements for each axis is an offset displacement (e.g. negative toward X1 and positive toward X2). The force in matrix mode is reported as the average between each actuator in the pair (positive tension and negative compression), and the difference between the force on each pair of actuators along an axis is reported as an offset force for that axis. For cruciform shaped samples, the offset force is typically controlled to zero to prevent shearing of the specimen arms on the orthogonal axis. The system allows the specific signal used for control during a test to be changed without unloading the specimen (e.g. force control to a given displacement followed immediately by displacement control to an additional amount of force), but does not allow a switch from matrix mode to independent actuator control while under load. The control modes are also axis independent allowing one axis to be controlled by one signal while the other is controlled by a different signal (e.g. simultaneous force control on X-axis and displacement control on the Y-axis). Care must be taken in programming a logical loading sequence that does not result in an unstable and uncontrollable situation. A classic example is the use of displacement control during compression testing where buckling may occur, as opposed to using force control that can become unstable if buckling occurs. The designed maximum loading rates for matrix mode control are 50 kN/s in force control and 20 mm/s at maximum force in displacement control.

34.2.2 Digital Image Correlation

Digital image correlation analysis measures the motion of a high contrast pattern on the surface of a specimen [16]. This can be accomplished with a single camera to measure the 2D displacement of a flat surface, or using a multi-camera system to measure the 3D shape and motion of a flat or curved surface. The cruciform facility has three DIC systems: one real-time 2D-DIC for control feedback (not used in the examples shown here) and two full-field 3D-DIC systems to measure strains in the gauge section and loading tabs that require post-processing analyses.

Each of the 3D-DIC systems uses a pair of Point Grey GRAS-50S5M-C five mega pixel CCD cameras viewing the specimen surface from a slightly oblique angle (Fig. 34.1). One system views only the middle 50 mm by 50 mm of the gauge area (using a pair of Sigma 105 mm f/2.8 EX DG telephoto macro lenses), while the other has a field of view approximately 200 mm by 200 mm (using a pair of Schneider-Kreuzach XenoPlan 1.9/35-0901 compact lenses) to monitor the end tabs extending from the gauge area. In this way, the strain response of both the global (overall view) and local (center of the gauge section) areas of the specimen are measured on the top of the specimen independent of the 2D-DIC strain control monitored on the bottom surface (Fig. 34.1). The 3D-DIC cameras have a maximum frame rate of 5 Hz at full resolution. An estimate of the noise and systematic errors can be made using an analysis of the undeformed pattern as imaged by this camera system configuration. Based on this analysis the total uncertainty (assuming $\pm$ one standard deviation) is $\pm 140 \times 10^{-6}$ strain and $\pm 280 \times 10^{-6}$ strain for the global and local systems, respectively. Engineering strain (e) is used throughout this paper, but other strain measures could be used as well.

34.2.3 Data Acquisition and Synchronization

Since each system is running almost completely independent of the other systems, synchronization of the data can be a challenge. The mechanical testing system can acquire the control and feedback signals during procedures for later analysis. There is also the ability to acquire more external signals (digital or analog). The 3D-DIC system can acquire up to eight analog signals simultaneously with the image acquisition, which are selected here to record force and displacement signals from the mechanical testing system.

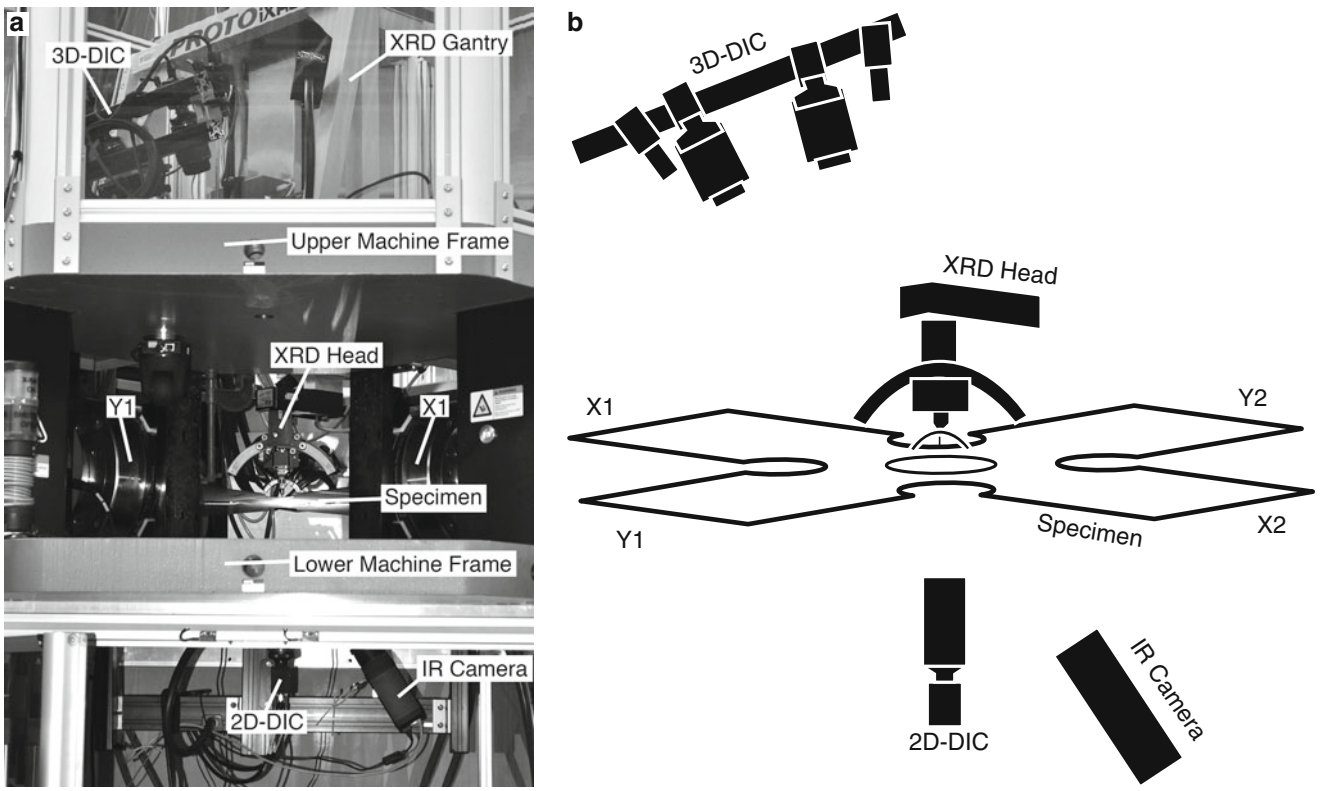

Fig. 34.1 (**a**) Annotated photograph and (**b**) schematic representation of the cruciform specimen, various measurement systems, and actuator positions (*X1*, *X2*, *Y1*, and *Y2*)

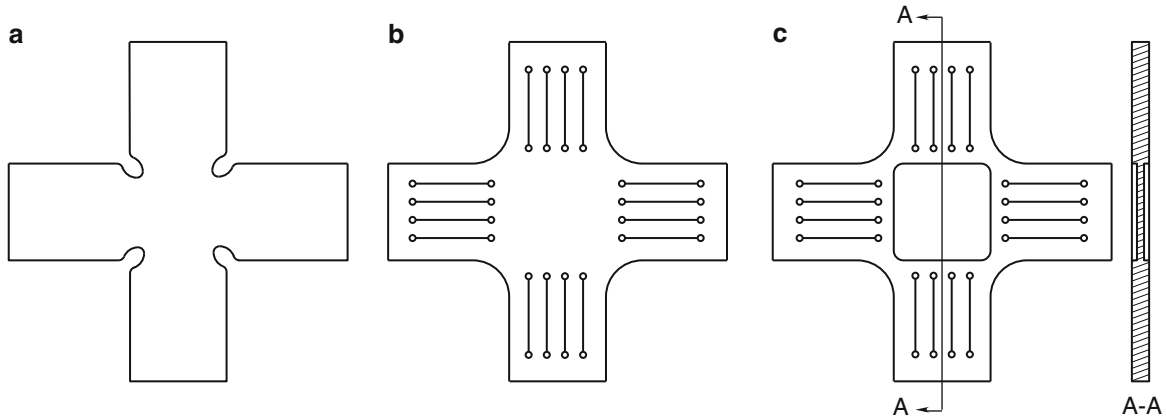

Fig. 34.2 Cruciform specimen design themes commonly seen in the literature: (**a**) reentrant corners, (**b**) relief slits in the arms, and (**c**) reduced thickness in the gauge area

34.2.4 Other Measurement Systems

In order to follow a realistic non-linear strain path, accurate strain control will be required. A two-axis contact extensometer measurement was attempted, but resulted in premature failure due to specimen damage caused by the extensometer's point contacts. Various non-contact strain measurement methods were considered, and a 2D-DIC system was determined to balance the needs for accurate real-time high-strain measurement and ease of use. This system has recently been added below the specimen (Fig. 34.1). An X-ray diffraction system is mounted above the specimen (Fig. 34.1), and is designed to serve multiple purposes. The first is to be used to measure the interatomic lattice strain to estimate the stress at a point using the "$\sin^2\psi$" method [14], similar to [5, 9], but for cruciform specimens rather than forming limit specimens. The system shown in Fig. 34.1 has two detector pairs that permit measurement of two different reflections. These could be used to measure two phases in the same sample simultaneously, and may be used to determine the load partitioning between multiple phases. Another potential use for the XRD system is to monitor the amount of phase transformation seen in particular alloys during plastic deformation (e.g. transformation induced plasticity, TRIP, steels). An infrared camera has been added below the specimen for use monitoring adiabatic heating during plastic deformation or phase transformations. This system could also be used for during elevated temperature testing. Detailed descriptions and testing of these systems will be included in a future paper.

34.3 Biaxial Specimen Design

The use of cruciform shaped specimens to determine the biaxial mechanical properties of sheet metal material is quite common [2, 4, 6, 8, 10, 12, 15], but the exact design of the specimen varies widely [1, 3, 7, 11, 13, 17]. Most designs try to develop a uniform strain region in the gauge section for simple linear strain paths. This is done through either adding reentrant radii at the meeting point of the arms (Fig. 34.2a), or constraint relief slits in the arms (Fig. 34.2b), or a combination of both. Finite element analyses are typically used to optimize on a basic design with some success, and these same analyses are needed to estimate the stress in the gauge section based upon the load imposed on the arms and an assumed constitutive law. These specimen geometries invariably fail outside the center gauge section at strains well below the biaxial forming limit strains, due to inevitable stress and deformation concentrations in the corners or near the slits in the arms. In some designs, the center of the gauge section is machined to a thinner cross-section (Fig. 34.2c) to achieve higher strains or even failure in the middle of the gauge area. Although this is less desirable than using the as-received sheet, it is a reasonable starting point for specimen design. In this paper, the specimens use a geometry similar to [1], but enlarged in the plane of the specimen (Fig. 34.3). Abu-Farha et al [1] reported achieving failure in the center of the gauge section for heated specimens. The results of our testing show that this simple scaling in the plane of testing was not sufficient to force failure in the middle of the gauge area (see Sect. 34.4), but did permit the basic commissioning testing of our biaxial cruciform system. The specimen as designed in Fig. 34.3 was able to achieve plastic strains in the gauge area, but was also susceptible to buckling along some loading paths.

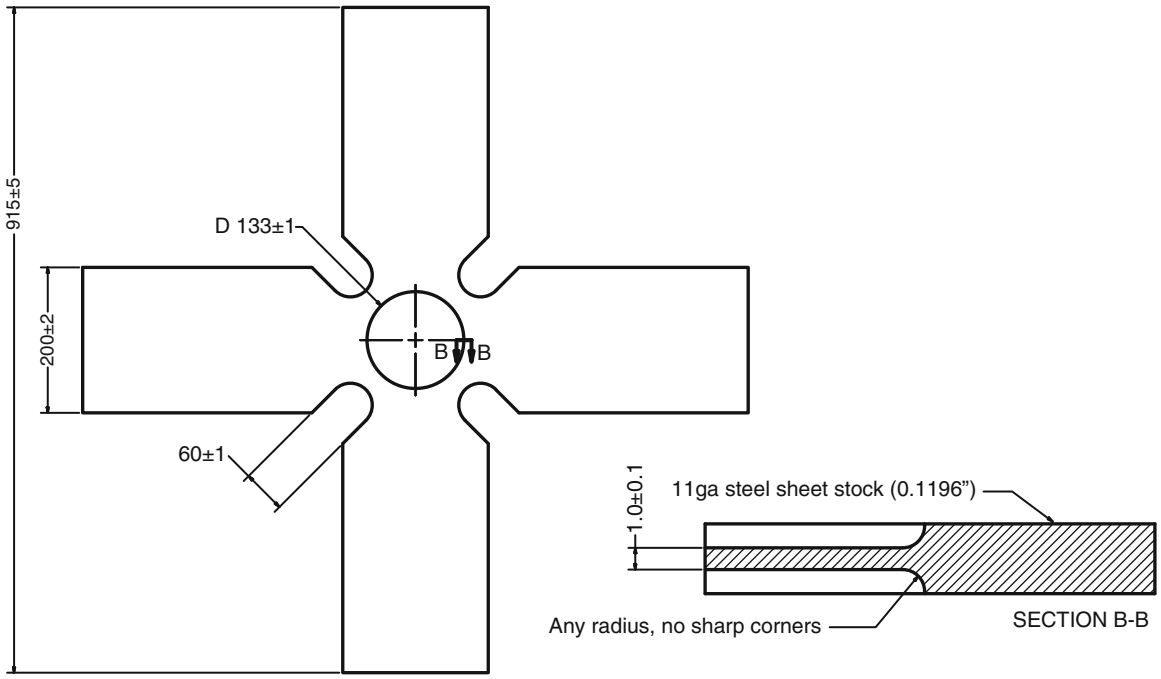

Fig. 34.3 Cruciform geometry used in examples shown here (dimensions in mm)

34.4 Results

A series of tests were performed to verify the capacity, control, and measurement systems of the new facility. The results presented here are a small portion of those tests, and demonstrate just some of the systems capabilities. Examples 1 and 2 are cruciform tests performed exclusively in force or displacement control along simple paths. The 2D-DIC system for strain control was not yet installed at the time of these tests. For both examples shown here, the system control was in matrix-mode with the offset force on each axis set to 0 kN. In Example 1, the strains were intended to be limited to the elastic regime, but some small plastic straining (residual strain when unloaded) did occur near the end of the test. In Example 2, strains well into the plastic regime were intended, but resulted in nonlinear buckling behavior. No buckling was seen in Example 1.

34.4.1 Example 1: Force and Displacement Control in the Low Strain Regime

In this example, a mild steel sample machined to the specimen geometry shown in Fig. 34.3 was used. The intention of this test was to verify the displacement and force control in the elastic regime, but some plastic deformation did occur. Figure 34.4a, b, and c show the resulting paths followed in displacement, force, and strain space, respectively. This is the data acquired by the 3D-DIC system, and the strain measured by analyzing the images including the specimen loading tabs. Each path has key points labeled A through I where control paths were changed. The arrows show the direction of time increasing along each segment of the path, and the matrix control mode is noted as "dc" for displacement control and "fc" for force control (strain control is not used in this example). For this example, the same control mode was applied to both axes, which is denoted by the "XY" label for each control mode (Fig. 34.4). Force offset control is used on both axes and set to 0 kN. Equi-biaxial force control is demonstrated on segment A-B, where as equi-biaxial displacement control is demonstrated on segment D-E. Segments B-C and C-D demonstrate displacement control resulting in behavior between the uniaxial and equi-biaxial strain conditions. At the end of segment C-D, there is a 4 min pause when the system was placed in manual control and unloaded slightly to balance the forces between the axes before the equi-biaxial unloading segment D-E. Uniaxial force control (not to be confused with uniaxial deformation) is demonstrated in segments E-F-G in the X-direction and G-H-I in the Y-direction, where the transverse force is held near zero in each case. During these segments plastic deformation occurred. The results of the plastic deformation can be seen at point G (at zero force) where there is a residual strain, and similarly for point I (at zero force) where there is a residual strain. It is interesting to note that

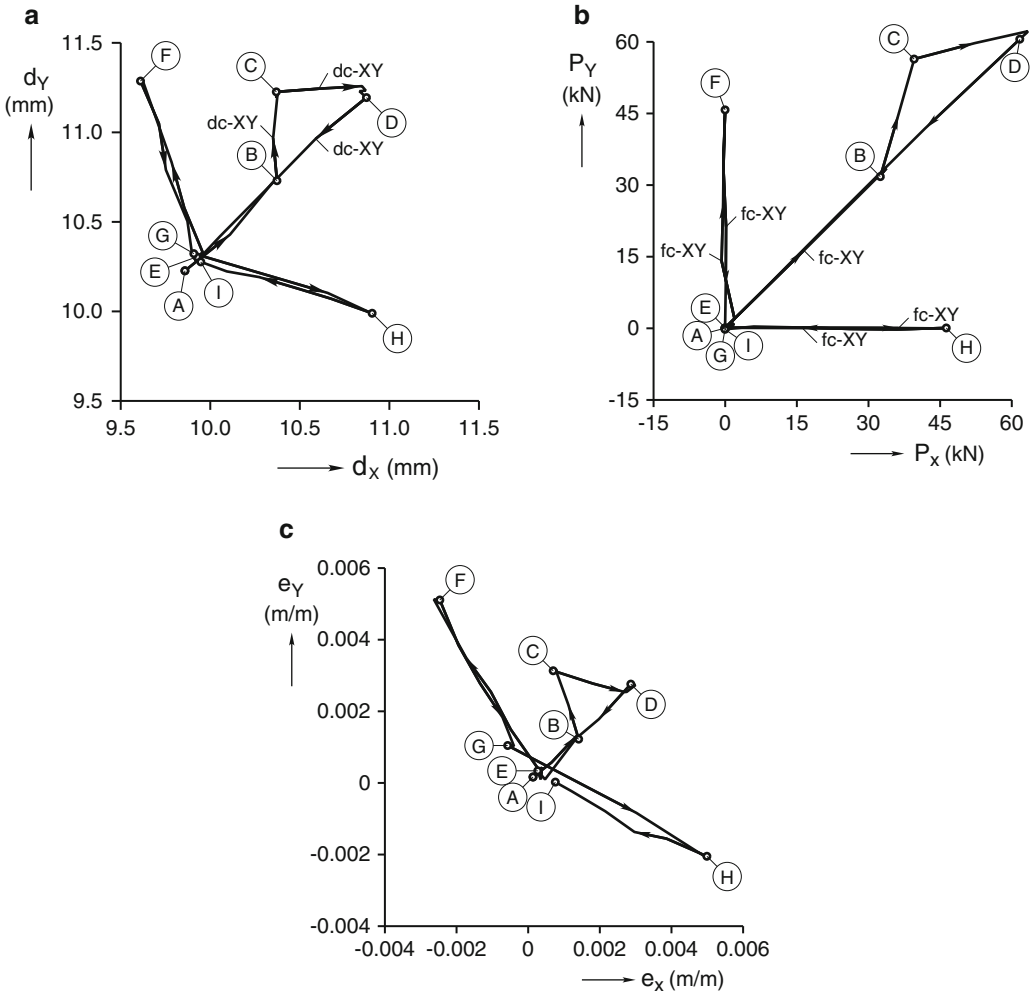

Fig. 34.4 Results for Example 1 (**a**) displacement, d, (**b**) force, P, and (**c**) strain, e, along the specimen X and Y axes. Key points in the loading paths are labeled by letters A through I, and the progression is denoted by the arrow on each segment. "dc" denotes displacement control and "fc" denotes force control, with suffix "X" is applied to the X-axis and "Y" if applied to the Y-axis. Uncertainties in displacement and force are on the order of the line thicknesses shown in (**a**) and (**b**), and in strain are ±0.00014 m/m

segments E-F-G and G-H-I that exhibit plastic deformation do not exceed the load levels for segments A through E where no residual strain was seen (Fig. 34.4c). This example also demonstrates an important point in understanding cruciform testing, which is that even in the elastic range (A through E) the shape of the paths are not identical in displacement (Fig. 34.4a) and strain space (Fig. 34.4c), thus the grip/arm displacement ratio does not indicate the applied strain ratio in the gauge section even for elastic deformation.

34.4.2 Example 2: Combined Force and Displacement Control in the Plastic Regime

Example 2 uses the same specimen as Example 1, but deforms the sample well into the plastic regime. This example also combines the control modes in each segment such that one axis might be in displacement control while the other is in force control. Figure 34.5a, b, and c plot the resulting paths in displacement, force, and strain space, respectively, similar to Fig. 34.4 for Example 1. Again, key points are labeled with letters A through J where the control paths were changed, and arrows show the direction along these paths. The matrix control modes are still shown as "dc" and "fc" for displacement and force, respectively, but "X" and/or "Y" are added to show to which axis this is applied. For example, segment B-C labeled "fc-XY" is performed in force control along both axes, where as segment A-B labeled "dc-Y" and "fc-X" is performed in

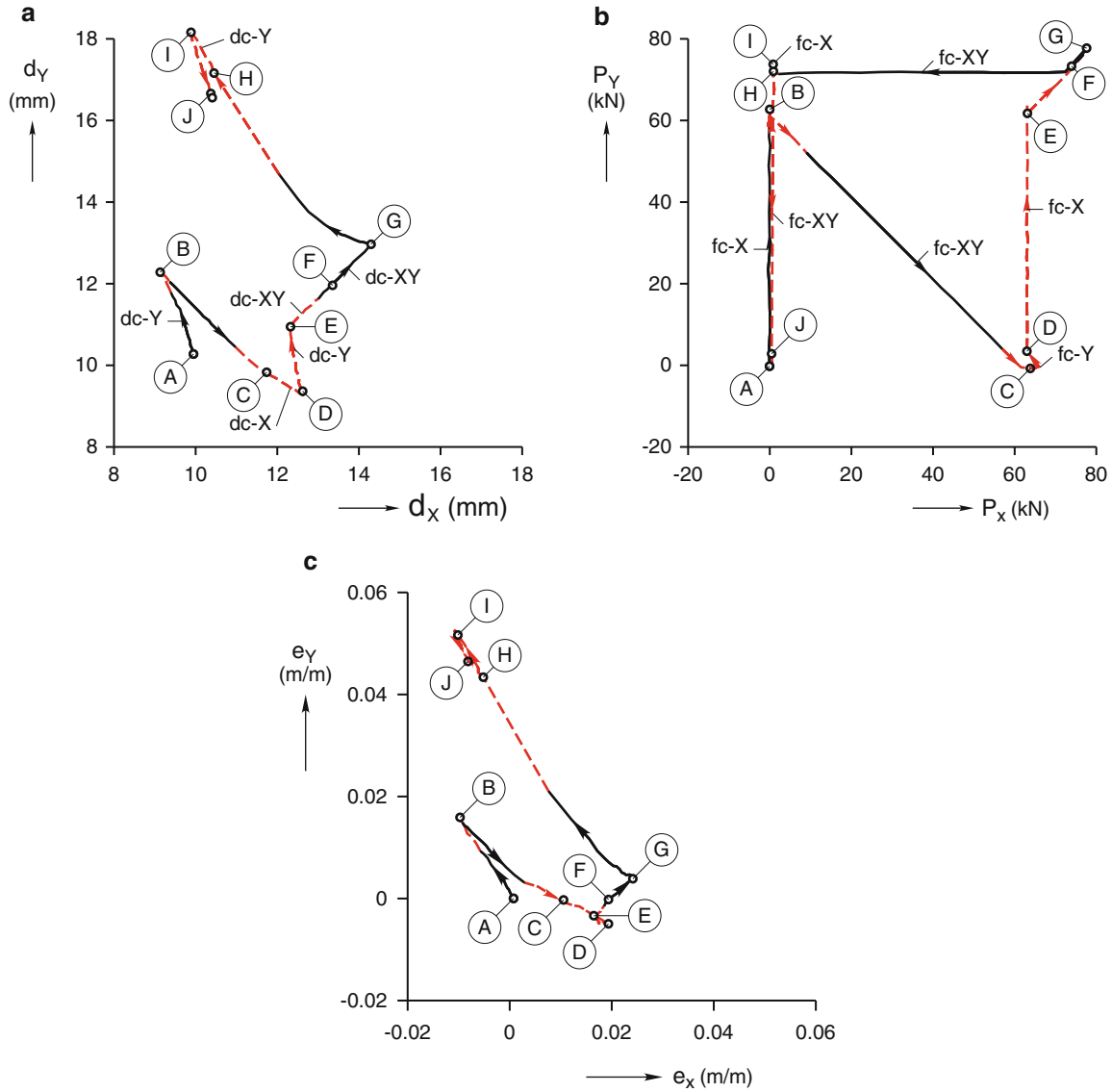

Fig. 34.5 Results for Example 2 (**a**) displacement, d, (**b**) force, P, and (**c**) strain, e, along the specimen X and Y axes. Key points in the loading paths are labeled by letters A through J, and the progression is denoted by the arrow on each segment with dashed lines when buckling is present. "dc" denotes displacement control and "fc" denotes force control, with suffix "X" is applied to the X-axis and "Y" if applied to the Y-axis. Uncertainties in displacement and force are on the order of the line thicknesses shown in (**a**) and (**b**), and in strain are ±0.00014 m/m

displacement control along the Y-axis with simultaneous force control along the X-axis. Again, the offset force is set to 0 kN along both axes. Since this is the same specimen as Example 1, point A is located at the same displacement, force, and strain as the end point (I) in Example 1. Note that the residual strain after Example 1 (I in Fig. 34.4c) is not as visible at the initial point in Fig. 34.5c because the axis range is much larger in Fig. 34.5c than in Fig. 34.4c.

Similar to Example 1, the shape of the displacement and strain paths do not agree, this is especially true in the segments where buckling is present. Buckling occurred at three locations in the loading paths. For clarity dashed lines (Fig. 34.5) are used for segments where the specimen was buckled. The first occurred near the end of segment A-B, and was a small (±0.35 mm out-of-plane) "S" shaped buckle along the X-axis of the gauge section (Fig. 34.6a). During segment B-C this buckle is removed, but another larger buckle forms (±1.75 mm out-of-plane) with the same shape along the Y-axis in the gauge section (Fig. 34.6b). This larger buckle remained through segments C-D and D-E, and was finally flattened by the end of segment E-F. The third and final buckle occurs at the end of segment G-H, and is another large "S" shaped buckle (±2.25 mm out-of-plane) aligned again with the X-axis (Fig. 34.6c). Since the system was in force control and this buckle occurred near $P_X = 1$ kN, the buckling resulted in a sudden jump in displacement (Fig. 34.5a) and strain (Fig. 34.5c) during

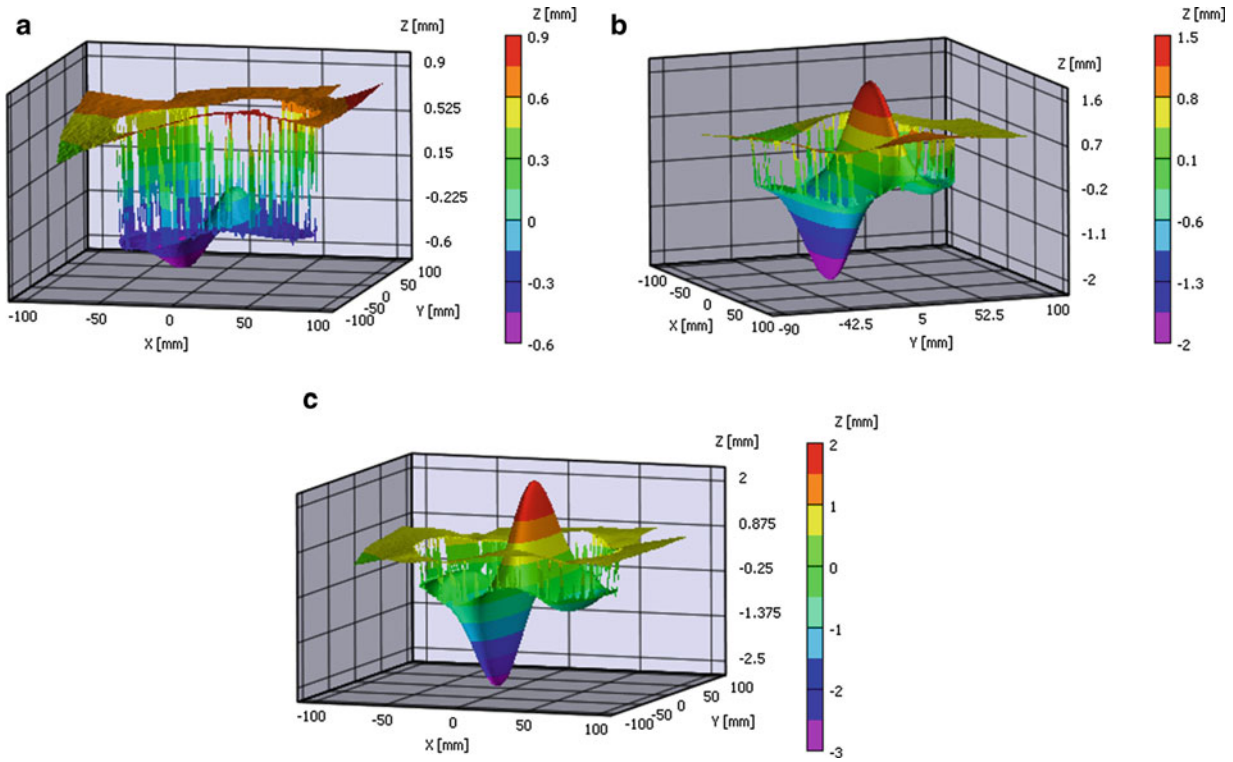

Fig. 34.6 3D-DIC height, Z, contour data in perspective plot showing buckling in Example 2 during segments (**a**) A-B, (**b**) C-D, and (**c**) G-H in Fig. 34.5

segment G-H that is barely visible in the force (Fig. 34.5b) near point H. This final buckling remained to the end of the test. The onset of each buckling event occurred when the force along one axis approached zero. One might expect the specimen design in Fig. 34.3 with a reinforced (thicker) area around the thinner gauge section could result in the some elastic compressive force being transferred from the thicker reinforced ring to the thinner gauge section along the axis being unloaded resulting in buckling. This is consistent with each buckle shape (Fig. 34.6) being along the axis that is approaching zero force (Fig. 34.5b). Modeling is planned to verify this hypothesis. This may result in a specimen design that has an envelope of applicability that is limited in part by a no buckling restriction.

Without 3D shape data, assessment of when the buckling occurred would be difficult, and quantifying the shape almost impossible. In addition to providing this 3D shape, the 3D-DIC system also has the advantage that its measurement of strain is not effected by the out-of-plane motion that may result in fictitious strains when using typical 2D strain mapping systems. The maximum strains achieved were $(e_X)_{max} = 0.036$ and $(e_Y)_{max} = 0.054$, in the X and Y directions respectively. Although these are less than the expected forming limit strains for this material, the strain level is close to or above the strain limits seen for a specimen without a reduced thickness gauge section for a similar material [12].

34.5 Summary

Based on the testing performed and the results shown here the new biaxial testing facility at the National Institute of Standards and Technology Center for Automotive Lightweighting meets or exceeds its basic design specifications. Mechanical control has been demonstrated using various combinations of force and displacement control in both the elastic and plastic regimes. Full-field displacement and strain mapping was sufficient to track the specimen response, and is capable of tracking strain localizations and buckling phenomena. The specimen geometry used was not sufficient to obtain failure in the center of the gauge section, and will require further development. The geometry did show that it is very sensitive to potential buckling. Based on the results shown here, the system is capable of testing complex loading paths without unloading and re-machining the samples, assuming a specimen geometry can be found that does not buckle or result in premature failure at the edges of the gauge area.

34.6 Disclaimer

Certain commercial equipment, instruments, or materials are identified in this paper in order to specify the experimental procedure adequately. Such identification is not intended to imply recommendation or endorsement by the National Institute of Standards and Technology, nor is it intended to imply that the materials or equipment identified are necessarily the best available for the purpose.

References

1. Abu-Farha F, Hector LG Jr, Khraisheh M (2009) Cruciform-shaped specimens for elevated temperature biaxial testing of lightweight materials. JOM 61(8):48–56
2. Banabic D (2004) Anisotropy and formability of AA5182-0 aluminium alloy sheets. CIRP Ann Manuf Technol 53:219–222
3. Boehler JP, Demmerle S, Koss S (1994) A new direct biaxial testing machine for anisotropic materials. Exp Mech 34:1–9
4. Ferron G, Makinde A (1988) Design and development of a biaxial strength testing device. J Test Eval 16:253–256
5. Foecke T, Iadicola MA, Lin A, Banovic SW (2007) A method for direct measurement of multiaxial stress–strain curves in sheet metal. Metall Mater Trans A Phys Metall Mater Sci 38A:306–313
6. Geiger M, Hussnätter W, Merklein M (2005) Specimen for a novel concept of the biaxial tension test. J Mater Process Technol 167:177–183
7. Green DE, Neale KW, MacEwen SR, Makinde A, Perrin R (2004) Experimental investigation of the biaxial behaviour of an aluminum sheet. Int J Plast 20:1677–1706
8. Hoferlin E, Van Bael A, Van Houtte P, Steyaert G, De Mare C (2000) The design of a biaxial tensile test and its use for the validation of crystallographic yield loci. Model Simul Mater Sci Eng 8:423–433
9. Iadicola MA, Foecke T, Banovic SW (2008) Experimental observations of evolving yield loci in biaxially strained AA 5754-O. Int J Plast 24(11):2084–2101
10. Ikeda S, Kuwabara T (2004) Work hardening behavior of IF and low carbon steel sheets under biaxial tension. Tetsu-to-Hagane J Iron Steel Inst Jpn 90:34–40
11. Kuwabara T, Ikeda S, Kuroda K (1998) Measurement and analysis of differential work hardening in cold-rolled steel sheet under biaxial tension. J Mater Process Technol 80–81:517–523
12. Kuwabara T, van Bael A, Iizuka E (2002) Measurement and analysis of yield locus and work hardening characteristics of steel sheets with different r-values. Acta Mater 50:3717–3729
13. Müller W, Pöhlandt K (1996) New experiments for determining yield loci of sheet metal. J Mater Process Technol 60:643–648
14. Noyan IC, Cohen JB (1987) Residual stress: measurement by diffraction and interpretation. Springer-Verlag, New York
15. Shiratori E, Ikegami K (1968) Experimental study of the subsequent yield surface by using cross-shaped specimens. J Mech Phys Solids 16:373–394
16. Sutton MA, Orteu J-J, Schreier H (2009) Image correlation for shape, motion and deformation measurements: basic concepts, theory and applications. Springer, New York
17. Yu Y, Wan M, Wu XD, Zhou X-B (2002) Design of a cruciform biaxial tensile specimen for limit strain analysis by FEM. J Mater Process Technol 123:67–70

Chapter 35
An Enhanced Plasticity Model for Material Characterization at Large Strain

L. Cortese, G.B. Broggiato, T. Coppola, and F. Campanelli

Abstract An experimental campaign on some isotropic steels for pipeline applications has been put forth. It was based on tests with different stress states: tension on smooth and notched geometries, torsion, three point bending, plane strain, and combined tension-torsion. The aim was the characterization of the material elasto-plastic behavior up to large strain and the calibration of a ductile damage model for failure estimation.

Results from tension and torsion were to be used for plasticity behavior description: from both of them, it is possible to retrieve the material true-stress true-strain curve until final failure. Unexpected differences were found. A critical interpretation led to the hypothesis that the ordinary isotropic *J2*-plasticity modelization could not predict all experimental evidences, starting from medium deformations, with increasing errors when plastic strain builds up. To approach this issue, an enhanced plasticity model has been developed and implemented into FEM code. It is a modification of a formulation widely used for geomaterials, which can take into account the influence of triaxiality and deviatoric effects on plastic accumulation. In addition, it allows a progressive transition from the Von Mises criterion, which demonstrated to be accurate for small strains, to a more complex formulation. A preliminary calibration of the model has been provided. This has been accomplished using a multiple-target inverse approach, exploiting experimental global data and FEA, by means of a dedicated optimization procedure. Appreciable improvements have been observed in terms of experimental-numerical match.

Keywords Ductile materials • Mechanical testing • Large strains • *J2-J3* plasticity model • Inverse calibration

35.1 Introduction

The *J2*-plasticity is the most used theory for ductile isotropic materials; as its name suggests, it assumes that yielding and flow stress are governed by the second deviatoric stress invariant only.

Limits of *J2*-plasticity are well-known since the works of Lode [1], Ros and Eichinger [2], Taylor and Quinney [3], who demonstrated that the model was not able to accurately reproduce all experimental evidences.

Nevertheless, the correlation with experimental outcomes was found to be sufficiently good, in particular for the low-medium plastic range, so that the *J2*-plasticity, also thanks to its ease of calibration and implementation, has been widely employed for research purposes and industrial practice. The use of more comprehensive theories has been for a long time considered to add just more difficulties than benefits [4].

Nowadays, due to the improved ductility shown by materials, the correct identification of the plastic behavior up to very large strains has become a compelling instance, particularly for engineering applications where the modeling of stress and strain distribution at critical points, originated from complex loading conditions, is needed. Moreover, also ductile damage accumulation strongly depends on the state of stress, so that plasticity issues cannot be neglected for a good assessment of ultimate resistance of materials. It is then no coincidence that, in recent years, attempts to overcome *J2*-plasticity drawbacks have come from the ductile damage community.

L. Cortese, Ph.D. (✉) • G.B. Broggiato, Ph.D. • F. Campanelli, M.Sc.
Mechanical and Aerospace Engineering Department, Sapienza Università di Roma, via Eudossiana, 18, 00184 Rome, Italy
e-mail: luca.cortese@uniroma1.it

T. Coppola, M.Sc.
Centro Sviluppo Materiali S.p.A. (CSM), via di Castel Romano, 100, 00128 Rome, Italy

M. Rossi et al. (eds.), *Residual Stress, Thermomechanics & Infrared Imaging, Hybrid Techniques and Inverse Problems, Volume 8*, Conference Proceedings of the Society for Experimental Mechanics Series, DOI 10.1007/978-3-319-00876-9_35,

Several alternative plasticity models have been proposed. Starting from extensive experimental studies [5–7], Brunig [8] and Kuroda [9] have found out that a plasticity model involving the first stress invariant also allows a more accurate prediction of deformation, localization and fracture behaviors in pressure-sensitive materials.

The contribution to yielding and flow stress of the third deviatoric stress invariant (*J3*) has also been investigated, and the opportunity of including it in the yield function has been discussed by the way of theoretical considerations, experimental tests and micromechanical analyses [10–12]. For many materials, the introduction of a *J3* term in the yield function [13, 14] seems to accommodate a systematic discrepancy between the Von Mises (i.e. *J2*) criterion and the experimental results. Plasticity models involving three stress invariants are put forth and experimentally validated in [15–17]. Here, the third deviatoric stress invariant is incorporated into the so-called Lode parameter, for the first time introduced in [1], to provide a method of differentiating between the Tresca and the Von Mises yield criteria.

It has to be mentioned that soil and rock mechanics has long recognized [18–20] a need for including the Lode stress parameter into constitutive laws. Indeed, the yield function proposed here comes from a customization of the one devised by Bigoni and Piccolroaz for geomaterials [20].

Starting from outcomes of an experimental campaign, this paper aims to formulate and make effective, through a proper calibration procedure, an enhanced plasticity model that would be able to overcome some drawbacks of the classical *J2* plasticity theory.

In the next section, experimental evidences from tension and torsion tests, proving deficiencies of J2-plasticity, at least at large strains, are reported for three ductile isotropic steels.

Afterwards, an enhanced *J2-J3* based model plasticity is proposed and outlined, and it is tuned through a multiple-target inverse calibration procedure.

35.2 Experimental Results

Three steels, supplied in form of seamless pipes commonly used in automotive applications (*33MnB5* and *25MnCr6*) and in oil pipeline construction (*API 5L grade 65*), have been tested. Their overall mechanical properties, together with the delivery state and pipe dimensions are outlined in Table 35.1.

These materials, widely used in actual applications, exhibit a highly ductile behavior, much higher than many others tested in the literature.

All materials can be regarded as fully isotropic. Proof of isotropic behavior may be deduced from their tensile properties in longitudinal and tangential direction, as also demonstrated for steels coming from the same family [21]. Moreover, all of them are supplied after the final high temperature heat treatment, which reset any deformation induced anisotropy due to the manufacturing process.

Specimens were extracted in the pipe longitudinal direction, at mid thickness position. Their dimensions have been defined according to the available thickness, choosing smaller geometries (type 2 in Fig. 35.1b) for lower thickness pipes.

An extensive experimental campaign has been carried out on these steels, with the initial goal of calibrating a ductile damage prediction model.

Tension tests on smooth and notched cylindrical bars have been executed on a 250 kN servo-hydraulic MTS machine; torsion tests have been performed on a custom-made tension-torsion biaxial machine designed and built by some of the authors [22]. Both the equipments are available for testing at the Mechanical and Aerospace Engineering Department of Sapienza Università di Roma. Bending tests and plane strain tensile tests have been performed at the laboratories of Centro Sviluppo Materiali Spa (Castel Romano, Roma).

In a preliminary step, true stress-true strain curves derived from tension tests have been employed to describe material hardening. Such curves were obtained directly from experimental data until the onset of necking, while the large strain range was characterized by means of an inverse calibration procedure [23], under the assumptions of *J2*-plasticity.

Table 35.1 Mechanical properties of investigated materials

		Pipe dimension [mm]				
	Delivery state	Diameter	Thickness	Yield stress [MPa]	Ultimate stress [MPa]	Elongation at break [%]
Grade 65	*Quenched and relieved*	406	20	440	530	18
33MnB5	*Annealed*	65	8	455	615	15
25MnCr6	*Normalised*	80	10	380	560	28

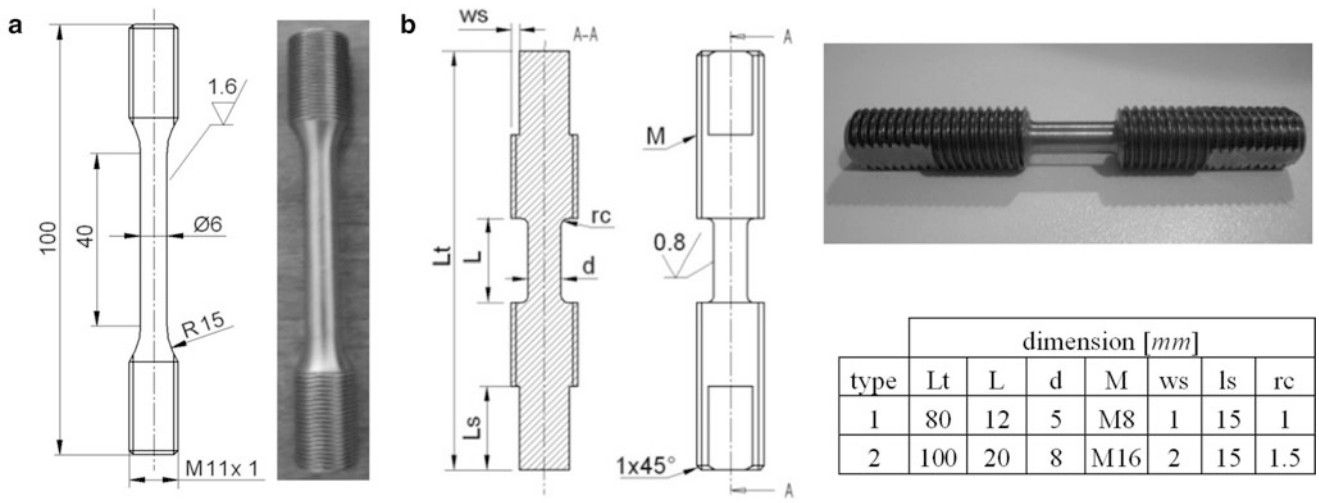

	dimension [*mm*]						
type	Lt	L	d	M	ws	ls	rc
1	80	12	5	M8	1	15	1
2	100	20	8	M16	2	15	1.5

Fig. 35.1 Specimen geometries: (**a**) tension test; (**b**) torsion test

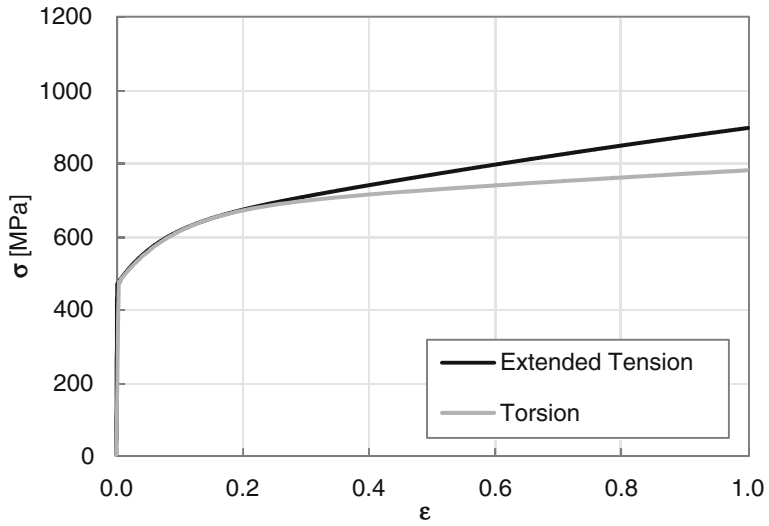

Fig. 35.2 *Grade 65*: true stress-true strain curves from tension and torsion tests

At a later stage, also data from torsion tests have been used to determine true stress-true strain curves: in this case, a direct calibration procedure is available [24]; again, *J2*-plasticity was assumed.

Figure 35.1 shows specimen geometries for tension and torsion tests.

Provided that *J2*-plasticity is accurate, the stress–strain curves coming from both approaches should have to be identical. Conversely, a remarkable discrepancy has been found.

Figures 35.2 and 35.3 report curves derived through the two calibration approaches: it can be noticed that, starting from low-medium deformation, they begin to differ. This is systematically observed for all tested materials. The difference becomes larger as further deformation builds up. Regularly, torsion curves are lower than tension ones.

Such differences cannot be due to any error in the inverse calibration procedure used to determine the true stress-true strain curve after necking from tensile test. In fact, for all materials, necking occurs at $0.09 \div 0.11$ of plastic strain, while curves start diverging appreciably from at least 0.20 on. Furthermore, if extended curves were wrong because of an incorrect inverse calibration, numerical simulation of tensile test using curves from torsion would match experimental results. This does not happen. For the sake of brevity outcomes of such verification are not reported here.

In order to account for this discrepancy, the hypothesis is that, at least at large strains, subsequent yielding is governed not only by the second deviatoric invariant stress but also by Lode parameter and, possibly, by hydrostatic pressure.

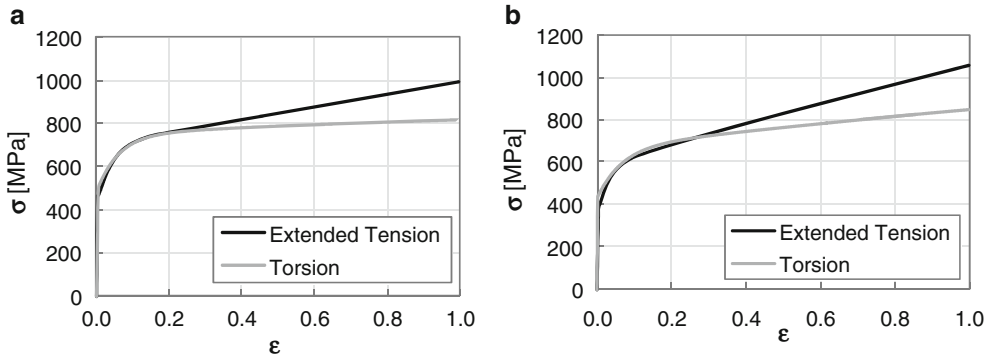

Fig. 35.3 True stress-true strain curves from tension and torsion tests: (**a**) *33MnB5* (**b**) *25MnCr6*

35.3 Formulation of the Enhanced Plasticity Model

The plasticity theory described in this section is valid under the assumptions of material homogeneity and isotropy, plastic incompressibility [25], isotropic hardening behavior, pressure insensitivity (i.e., no yielding occurs under hydrostatic tension or compression).

It is worth mentioning that the latter assumption is reasonable for investigated materials, but can be easily removed if necessary: the proposed model has a general formulation that, by means of a proper calibration (different from the one discussed here), could be used to describe a pressure-sensitive behavior also.

The adopted yield function comes from a customization of the unified yield function by Bigoni and Piccolroaz [20], which, in its formulation for pressure-insensitive materials, reduces to:

$$F = \frac{q}{g(X)} - k \tag{35.1}$$

where $q = \sqrt{3J_2}$ is the equivalent Von Mises stress; $g(X)$ is a function of the Lode parameter $X = \frac{27}{2}\frac{J_3}{q^3}$:

$$g(X) = \left[\cos\left(\beta\frac{\pi}{6} - \frac{1}{3}\arccos(\gamma X)\right)\right]^{-1} \tag{35.2}$$

The function $g(X)$ is able to model the shape of the yield surface deviatoric section.

The three material parameters are:

- k, which characterizes the isotropic hardening effect and depends on the accumulated plastic strain;
- $\beta \in [0; 2]$ which governs the so-called strength-differential phenomenon;
- $\gamma \in [0; 1)$ which gives a sort of polygonal shape to the yield surface, with more or less pronounced sharp corners.

Function (35.1) reduces to classical yielding function for suitable values of β and γ: Von Mises criterion is obtained for $\beta = 1$ and $\gamma = 0$; Tresca criterion is obtained for $\beta = 1$ and $\gamma \to 1$.

Readers should refer to Bigoni and Piccolroaz work [20] for a more exhaustive investigation on Eq. 35.1.

From here on, inspired by Eq. 35.1, an enhanced plasticity model (EPM) is devised.

First of all, to determine material constant k, the expression (35.1) can be specialised for a uniaxial state of stress. In this case $X = 1$, $q = \sigma_Y$ so that:

$$k = \frac{\sigma_Y}{g(X = 1)} \tag{35.3}$$

Furthermore, according to Figs. 35.2 and 35.3, it seems reasonable to postulate that investigated materials yield according to a Von Mises criterion for low plastic deformations; as the equivalent plastic strain ε^p reaches a threshold value (ε_{th}), subsequent yield surface distorts in the deviatoric plane. Such a distortion is governed by the accumulation of plastic strain, so that the new yield surface can be described by:

$$q\frac{g(X = 1)}{g(X)} - \sigma_Y = 0 \tag{35.4}$$

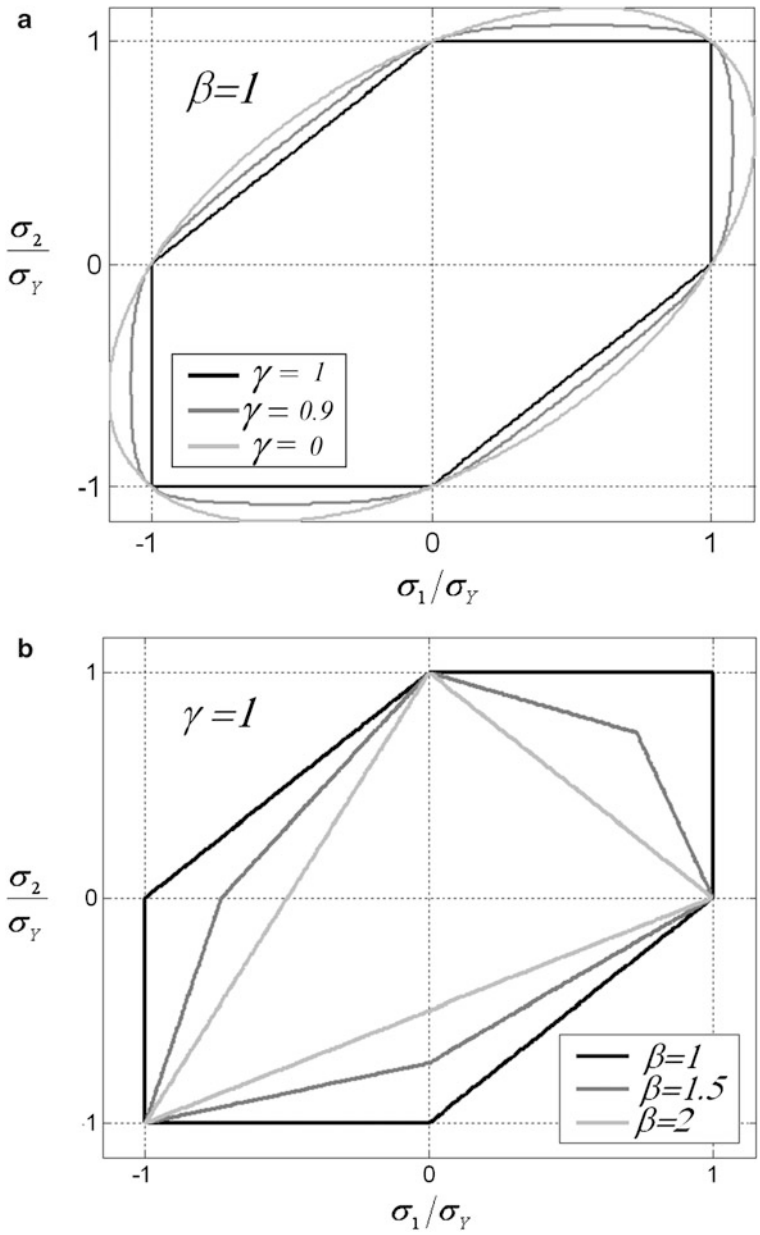

Fig. 35.4 Yield surface, section with $\sigma_3 = 0$: (**a**) variation of γ at fixed β; (**b**) variation of β at fixed γ

with:

$$\beta = \begin{cases} 1 & \varepsilon^p \leq \varepsilon_{th} \\ \beta(\varepsilon^p) & \varepsilon^p > \varepsilon_{th} \end{cases} \quad \text{and} \quad \gamma = \begin{cases} 0 & \varepsilon^p \leq \varepsilon_{th} \\ \gamma(\varepsilon^p) & \varepsilon^p > \varepsilon_{th} \end{cases}$$

Note that for $X = 1$ (as in tensile stress state), (35.4) reduces to the Von Mises criterion independently from the level of plastic deformation: this is consistent with the assumption that led to Eq. 35.3.

Since γ is initially zero and must go towards 1, yield surface evolves to a polygonal shape with corners (Fig. 35.4a).

It can be proven that the curves in Figs. 35.2 and 35.3 diverge too much for the effect being caught by a variation of the yield function produced by the γ parameter alone. Concerning β, it follows that it must increase towards 2 to capture the experimental evidences; as a consequence of this parameter variation, the yield surface tends to lose its symmetry as shown (Fig. 35.4b).

Based on the above mentioned remarks, the following laws are selected to describe variation of β and γ with equivalent plastic strain:

$$\beta = \begin{cases} 1 & \varepsilon^p \leq \varepsilon_{th} \\ 2 - \exp[-b(\varepsilon^p - \varepsilon_{th})] & \varepsilon^p > \varepsilon_{th} \end{cases} \text{ and } \gamma = \begin{cases} 0 & \varepsilon^p \leq \varepsilon_{th} \\ 1 - \exp[-a(\varepsilon^p - \varepsilon_{th})] & \varepsilon^p > \varepsilon_{th} \end{cases} \tag{35.5}$$

Hence, parameters to be identified are ε_{th}, a, b.

Besides the yield function, a proper flow rule has to be postulated. Here, an associated flow rule is assumed:

$$d\varepsilon_{ij}^p = d\varepsilon^p \frac{dF(J_2, J_3)}{d\sigma_{ij}}$$

$d\varepsilon^p$ is the equivalent plastic strain increment, $\frac{dF}{d\sigma_{ij}}$ are derivatives of Eq. 35.1 with respect to tensor stress components.

As stated in [14], as far as pressure-sensitive materials concern, the flow rule is associative in the deviatoric plane only, in order to fulfill plastic incompressibility.

35.4 Calibration Procedure

The plasticity model has been coded into MSC Marc FEM software as user subroutine.

Parameters ε_{th}, a, b have been calibrated by exploiting experimental data of the *Grade 65*: the first parameter has been trivially identified from stress–strain curves (see Fig. 35.2), ε_{th} being the equivalent deformation value where tension and torsion start to differ significantly from each other. For all the others, an inverse calibration has been performed. At the end, the procedure allowed to select the parameter set that provided the best match between experimental tests and their numerical simulation. The comparison has been carried out in terms of force-displacement and torque-rotation global quantities of tension, torsion and combined tests. The geometry used for the biaxial test is shown in Fig. 35.5.

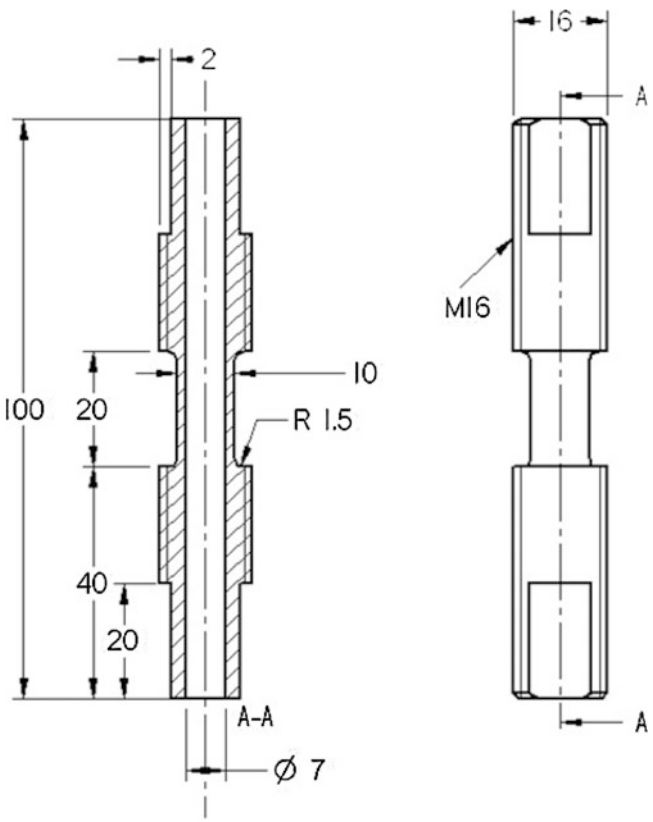

Fig. 35.5 Specimen geometry for tension-torsion combined testing

Table 35.2 Best fit parameters of the plasticity model for steel grade 65

ε_{th}	a	b
0.2	4.2	0.15

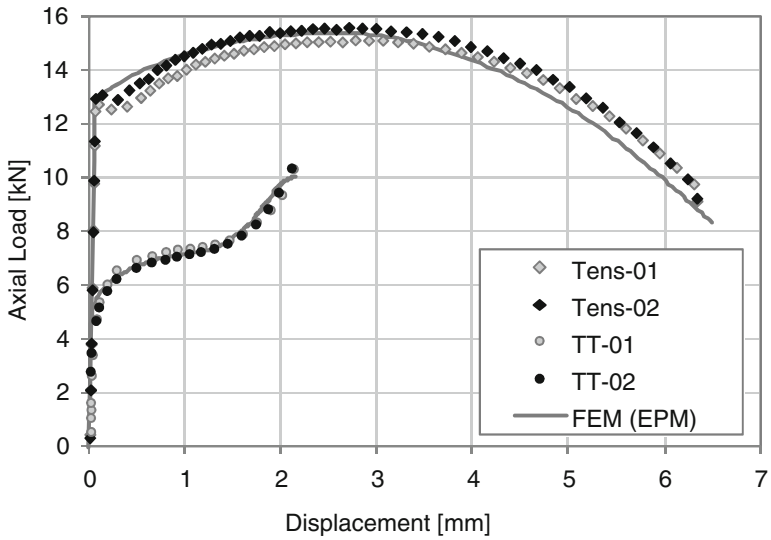

Fig. 35.6 Load–displacement curves: comparison between experimental and best fit EPM results from FEM analysis

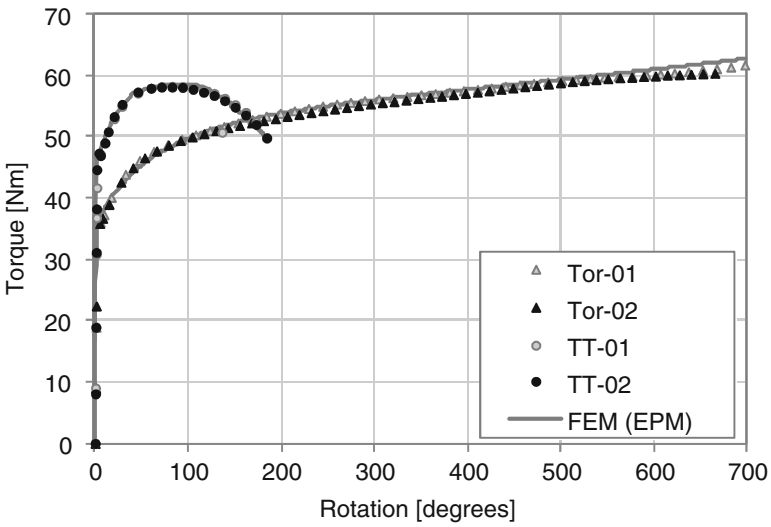

Fig. 35.7 Torque-rotation curves: comparison between experimental and best fit EPM results from FEM analysis

The displacement to rotation ratio of this test has been kept constant and equal to *0.67 mm/rad* (so far just one combination has been run and used, but others are on the way).

A *c++* code has been developed to handle this optimization process and the interaction with FEM analysis. Both zero and first order methods (simplex and Levengberg-Marquard respectively) have been used for the minimization procedure. The *L2* norms of the difference vectors (between experimental and corresponding numerical data of the tests) have been considered as error functions.

Table 35.2 reports the best fit parameters obtained with this methodology:

Figures 35.6 and 35.7 show the experimental-numerical match in terms of global quantities, for the different kinds of tests. Numerical data are collected from FEM simulations, and are relative to the final calibrated EPM model runs. In Fig. 35.6, load–displacement curves are presented, for the tension test (Tens-01/Tens-02) and for the axial load component of the biaxial test (TT-01/TT-02). Figure 35.7 illustrates torque-rotation results of the torsion test (Tor-01/Tor-02) and of the twist part of the biaxial test (TT-01/TT-02).

The level of agreement is excellent, with maximum error below 5 % for all tests.

35.5 Conclusion and Further Development

Starting from some experimental evidences showing some limits of the *J2* plasticity theory in the range of large strains, an enhanced plasticity model has been developed and implemented into a commercial FEM code. This model assumes that plastic evolution is governed by the *J2* and *J3* invariants of the deviatoric stress tensor. Tension, torsion and biaxial tests have been performed on a grade 65 steel, and the results have been used to setup the model. The calibration has been accomplished by means of an inverse procedure: the best parameter set has been found minimizing the error between global quantities, collected from the three kinds of tests, and the corresponding outcomes of the FEM simulations of the tests themselves. The resulting experimental-numerical match was indeed very good. This proves how the proposed model can be properly tuned, and also how it is able to predict experiments under different multiaxial states of stress. As future developments, other biaxial tests, with different combination of loads, will be executed, to make the calibration even more sound, and to provide additional data for validation purposes. Also all alloys will be shortly investigated.

References

1. Lode W (1926) Versuche über den Einfluß der mittleren Hauptspannung auf das Fließen der Metalle Eisen Kupfer und Nickel. Zeitschrift für Physik 36(11–12):913–939
2. Ros M, Eichinger A (1929) Versuche zur Klaerung der Frage der Bruchgefahr III, Metalle. EMPA-Bericht Nr 34:1–72
3. Taylor GI, Quinney H (1932) The plastic distortion of metals. Philos Trans Royal Soc Lond A 230(681–693):323–352
4. Mendelson A, Plasticity: theory and application, MacMillian series in applied mechanics Landis F (ed), The MacMillian Company, New York, p 92, p 109, 1968.
5. Spitzig WA, Sober RJ, Richmond O (1975) Pressure dependence of yielding and associated volume expansion in tempered martensite. Acta Metall 23(7):885–893
6. Richmond O, Spitzig WA (1980) Pressure dependence and dilatancy of plastic flow. In: Theoretical and applied mechanics: proceedings of the 15th international congress of theoretical and applied mechanics, Toronto, Canada. North-Holland Publishing Company, Amsterdam, pp 377–386
7. Wilson CD (2002) A critical reexamination of classical metal plasticity. J Appl Mech, Trans ASME 69(1):63–68
8. Brunig M (1999) Numerical simulation of the large elastic–plastic deformation behavior of hydrostatic stress-sensitive solids. Int J Plast 15(11):1237–1264
9. Kuroda M (2004) A phenomenological plasticity model accounting for hydrostatic stress-sensitivity and vertex-type of effect. Mech Mater 36(3):285–297
10. Prager W (1945) Strain hardening under combined stresses. J Appl Phys 16(12):837–840
11. Ohashi Y, Tokuda M (1973) Precise measurement of plastic behaviour of mild steel tubular specimens subjected to combined torsion and axial force. J Mech Phys Solids 21(4):241–261
12. Miller MP, McDowell DL (1992) Modeling large strain multiaxial effects in FCC polycrystals. Int J Plast 12(7):875–902
13. Brunig M, Berger S, Obrecht H (2000) Numerical simulation of the localization behavior of hydrostatic-stress-sensitive metals. Int J Mech Sci 42(11):2147–2166
14. Yang F, Sun Q, Hu W (2009) Yield criterions of metal plasticity in different stress states. Acta Metall Sin (Engl Lett) 22(2):123–130
15. Bai Y, Wierzbicki T (2008) A new model of metal plasticity and fracture with pressure and Lode dependence. Int J Plast 24(6):1071–1096
16. Gao X, Zhang T, Zhou J, Graham SM, Hayden M, Roe C (2011) On stress-state dependent plasticity modeling: significance of the hydrostatic stress, the third invariant of stress deviator and the non-associated flow rule. Int J plast 27(2):217–231
17. Hu W, Wang ZR (2005) Multiple-factor dependence of the yielding behavior to isotropic ductile materials. Comput Mater Sci 32(1):31–46
18. Bardet JP (1990) Lode dependences for isotropic pressure-sensitive elastoplastic materials. J Appl Mech 57(3):498–506
19. Menétrey P, Willam KJ (1995) Triaxial failure criterion for concrete and its generalization. ACI Struct J 92:311–318
20. Bigoni D, Piccolroaz A (2004) Yield criteria for quasibrittle and frictional materials. Int J Solids Struct 41:2855–2878
21. Bufalini A, Morana R, Nice PI, Nasvik H, Kjørholt H, Bailey BM, Adam MK, Jiral DG, Ross RC, Smith B, Ueda M, Ohe T (2010) Evaluation of mechanical performance and stress-corrosion-cracking resistance of post expanded carbon steel and CRA casing grades. Paper SPE 133382, presented at the SPE ATCE, Florence
22. Broggiato GB, Cortese L (2008) Sviluppo di un sistema di prova biassiale per la caratterizzazione del legame elasto-plastico e del danneggiamento duttile. In: Proceedings of XXXVII AIAS, 37th conference of italian association for stress analysis, Sapienza Università di Roma, Rome, 2008
23. Ling Y (1996) Uniaxial true stress–strain after necking. AMP J Technol 5:37–48
24. McClintock FA, Argon AS (1966) Mechanical behavior of materials. Addison-Wesley, Boston
25. Spitzig WA, Richmond O (1984) The effect of pressure on the flow stress of metals. Acta Metall 32(3):457–463

Chapter 36
Residual Stress and Phase Transformation Map for Impact Fatigued Zirconia

M. Allahkarami and J.C. Hanan

Abstract Chipping failure is a principle concern of bi-layer porcelain-zirconia restoration ceramics. Residual stress and phase transformation play a key role in the strength. In order to study the monoclinic to tetragonal phase transformation and residual stress in the fatigued zirconia layer, several 2D X-ray diffraction frames on a flat disk sample were collected. Phase transformations were mapped using 2D micro X-ray diffraction of 441 frames at 50 × 50 μm spacing automatically positioned on an impact region. Yttria–zirconia tetragonal phase transformations to monoclinic zirconia and monoclinic yttria were observed, mostly at the impacted area. Residual stresses were measured using the micro X-ray diffraction $\sin^2\psi$ method. Important observations include the range in measured residual stress from a compressive stress, −300 MPa, up to a tensile stress of +650 MPa; and up to 100 % phase transformation from tetragonal to monoclinic.

Keywords Residual stress • Phase transformation • Diffraction mapping • Zirconia • 2D X-ray frame

36.1 Introduction

Zirconia core veneered with porcelain crowns have been used widely for clinical restoration due to their superior aesthetics, excellent biocompatibility, inertness, low plaque accumulation and remarkable strength. Residual stresses created as a result of thermal expansion coefficient mismatch between the core and veneer layer is desired to be compressive at the porcelain surface. Compressive residual stress at the surface of a crown inhibits crack initiation and improves damage tolerance. This works similar to the introduction of a surface layer of compressive residual stress in high cycle fatigue (HCF) turbine engine components [1]. Compressive residual stress at the crown surface makes the crown a more durable, longer lasting restoration by preventing moisture, saliva, and other corrosive materials from entering surface defects. When tensile load is applied to compressive residual stress surfaces, the compressive residual stress first compensates the tensile load [2].

Although yttria stabilized tetragonal zirconia (Y-TPZ) exhibits a flexural strength of 900–1,200 MPa, a structural phase transformation from tetragonal to monoclinic phase may take place under local stresses long before the far field stresses reach this limit [3]. Such stress induced phase transformations involve volume expansion that changes the compressive residual stress induced into the porcelain surface [14]. The structure expansion due local phase transformation from tetragonal to monoclinic is believed to act as a crack closure mechanism and adds more strength [4, 5]. Maximum service loads of a restoration may experience in a patient's mouth is 4–6 times bellow than ultimate strength of zircinia ceramic core material. However even with such a low bite load, a considerable number of failures have been reported at early years of service [6]. Such early failure could be attributed to fatigue cased by cyclic load and the presence of residual stresses induced by grain anisotropy and thermal expansion mismatch. In spite of the low magnitude loads, it is expected that tetragonal to monoclinic phase transformations take place.

A 2D X-ray diffraction technique has been implemented to map phase transformations for a sectioned crown that was loaded to fracture, but only elastic strain for the (101) tetragonal peak was used for stress correlation with the phase transformation [7]. Biaxial residual stress measurements with the $\sin^2\psi$ method using a laboratory micro X-ray diffraction system, is well established. Zhang et al., validated the result of stress measurements in zirconia with X-ray diffraction by

M. Allahkarami • J.C. Hanan (✉)
Mechanical and Aerospace Engineering, Oklahoma State University, Tulsa, OK, USA
e-mail: jay.hanan@okstate.edu

M. Rossi et al. (eds.), *Residual Stress, Thermomechanics & Infrared Imaging, Hybrid Techniques and Inverse Problems, Volume 8*, Conference Proceedings of the Society for Experimental Mechanics Series, DOI 10.1007/978-3-319-00876-9_36,

comparing it with nano indentation [8]. A method of combined phase transformation and residual stress measurement by X-ray diffraction has also been reported, but only for line scans [2]. A two dimensional phase mapping combined with residual stress measurement requires a long time to on conventional laboratory scale diffraction systems. Using a 2D detector, the exposure time is remarkably reduced [9, 10]. Diffraction phase mapping using 2D detectors could be performed even on non flat samples [11]. In this present work, using an accurate motorized five axis stage, point size beams down to a few μm in diameter, 2D area detectors, and a laser video auto z-alignment system, 2D maps of phase transformation and residual stress were collected on a fatigued zirconia disk sample.

36.2 Materials

The material under study is a 1 mm thick disk made of sintered polycrystalline zirconia stabilized by the addition of 3 mol% yttrium oxide (3Y-TZP). The zirconia disk was fabricated with typical dental laboratory thermal treatment procedures for fabrication of all ceramic zirconia-porcelain systems. In order to simulate the dentin layer, the disk sample was mounted on a polymer base [12]. The load applied to dental restorations in their service life is limited to 150 N maximum [12]. To create a stress induced phase region, a cyclic load of 150 N at the peak and at a frequency of two cycles per second was applied to a 0.5 mm zirconia layer using a 1.9 mm tungsten carbide ball indenter with a custom load frame [13, 14]. To ensure that the sample remains accurately aligned on the translation stage after a particular cyclic loading step, a precision kinematic base was used.

36.3 Method

The residual stress measurements were conducted using a Bruker D8 Discover Laboratory X-ray diffractometer equipped with a Hi-star 2D area 1024 × 1024 pixel detector. The detector was kept at the maximum sample distance of 299.5 mm, as frames collected at a long detector distance have more strain resolution and diffraction rings are more distinguishable. A focusing optic was used to achieve a beam diameter of 50 μm with Cu-K_α radiation at tube parameters of 40 kV/40 mA. Bruker's General Area Diffraction Detection System (GADDS) in SLAM command mode was used for data collection. In SLAM command mode, GADDS automatically invokes commands from a script file. GADDS initializes given measurement configurations such as 2θ, sample height (z), measurement coordinates on sample (x,y), rotation (φ) and tilt (χ) using a precise motorized five axis sample stage. Calibration of the system was checked by collecting a diffraction pattern from a NIST standard polycrystalline corundum sample prior to conducting the experiment.

36.4 Results and Discussion

The contact region under the indenter is of particular interest since it represents a locally impacted region similar to the clinical situation. A gradient of material properties between the center of impact and a far field region is expected. Due to impact fatigue, phase transformation from tetragonal to monoclinic zirconia occurs in relation with the superimposed residual stresses, which also adjusts after the phase transformation. Measuring a gradient change in the phase transformation coupled with residual stresses in the contact region with a non-destructive test is one goal of this work.

Selecting a proper mesh size is an important step for designing XRD mapping experiments. Optical microscope observation, as illustrated in Fig. 36.1a, shows cracks only in a small region under indenter tip. Both the sample and indenter are made from high toughness materials and are hard to deform, resulting in a small impact region when they are in contact. Figure 36.1b shows a top view from optical microscopy of the sample superimposed with a target grid (red).

A simulation of a single indent using ABAQUS 6.9, illustrated in Fig. 36.2, also indicates that the impact region is small and very intense at the contact region. The stress field also extends a similar distance into the depth of the zirconia compared to the diameter of the indenter. X-rays of 8 keV, as used here, only penetrate 25 μm into the surface.

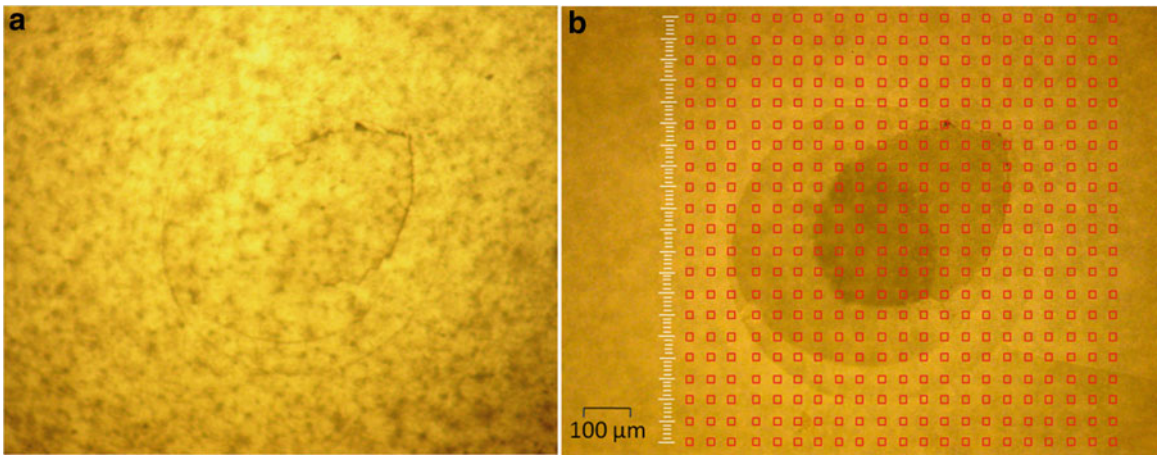

Fig. 36.1 (**a**) Area under the indenter and in the vicinity of the indenter (**b**) impact region superimposed with a target grid

After 40 k cyclic fatigue steps, at the area under the indenter and in the vicinity of the indenter, phase transformations were mapped using 2D micro X-ray diffraction of 441 frames at 50 µm × 50 µm spacing automatically positioned on the impact region. More details on experimental parameter selection for phase mapping is published by authors in previous reports [2, 3]. Comparing frames shown in Fig. 36.3a, b and c; X-ray diffraction at a far distance from the indenter shows the zirconia was completely tetragonal and with no observable monoclinic peaks, while measurement in the middle of the contact region indicated significantly intense monoclinic reflection peaks. Frames collected at halfway between the center of the impact and far distance showed monoclinic peaks in addition to tetragonal peaks, as shown in Fig. 36.3b. Figure 36.3d illustrates χ integration of the 2D diffraction data as intensity versus 2θ. This suggests that the phase transition discussed above was created by impact damage.

The micro X-ray diffraction patterns collected have a combination of monoclinic Zirconium Oxide peaks (011,110,−111,111, and −102) and tetragonal zirconia peaks (101 and 110) at 2θ diffraction angles between 18° and 38°. All peak intensities were extracted for the data set using GADDS mapping software and results were saved as a matrix. Contour plots of the transformed structure, as shown in Fig. 36.4a, indicates that the zirconia poly-crystalline tetragonal structure greatly exhibits phase transformation to monoclinic at the impacted region up to 100 %. This phase transformation is generally associated with stress concentration under the indenter tip, as shown in Fig. 36.4b.

For residual stress measurements in high 2θ angles, a total of 1,746 frames were collected. This means at each of 441 measurement locations, four frames with different sample tilt values were collected to cover 60° of ψ angle. All frames cover 2θ from 63° to 83°. The (004) tetragonal zirconia peak and (−231) monoclinic zirconia peaks were selected for stress calculation using the $\sin^2\psi$ method [2].

In spite of the fact that there are localized variations, a correlation between the phase transformation and residual stress exists. The residual stress varies in the range of ±100 MPa far away from indent. But is more volatile between a compressive stress of −300 MPa up to a tensile stress of +650 MPa at the contact zone. Figure 36.5 shows a scatter plot for the correlation between residual stress and phase transformation content. It reveals that when the phase transformation is less than 50 %, the residual stress value is mostly tensile and less than 200 MPa. When 30–50 % of the tetragonal phase has not transformed to monoclinic, the residual stress is mostly compressive, while after this percentage of phase transformation, the residual stress was tensile and linearly increased up to 650 MPa.

This result is in contrast to earlier work published from single load to failure where the transformation to monoclinic phase in zirconia was associated with a resulting relief of residual stress. Here the residual stress is greatest when the transformation to monoclinic is more severe. This suggests the transformation can be different in low load fatigue. Possibly, this is due to a more gradual transformation. Some have observed microcracking associated with the phase transformation [15]. Such microcracking could relieve residual stresses.

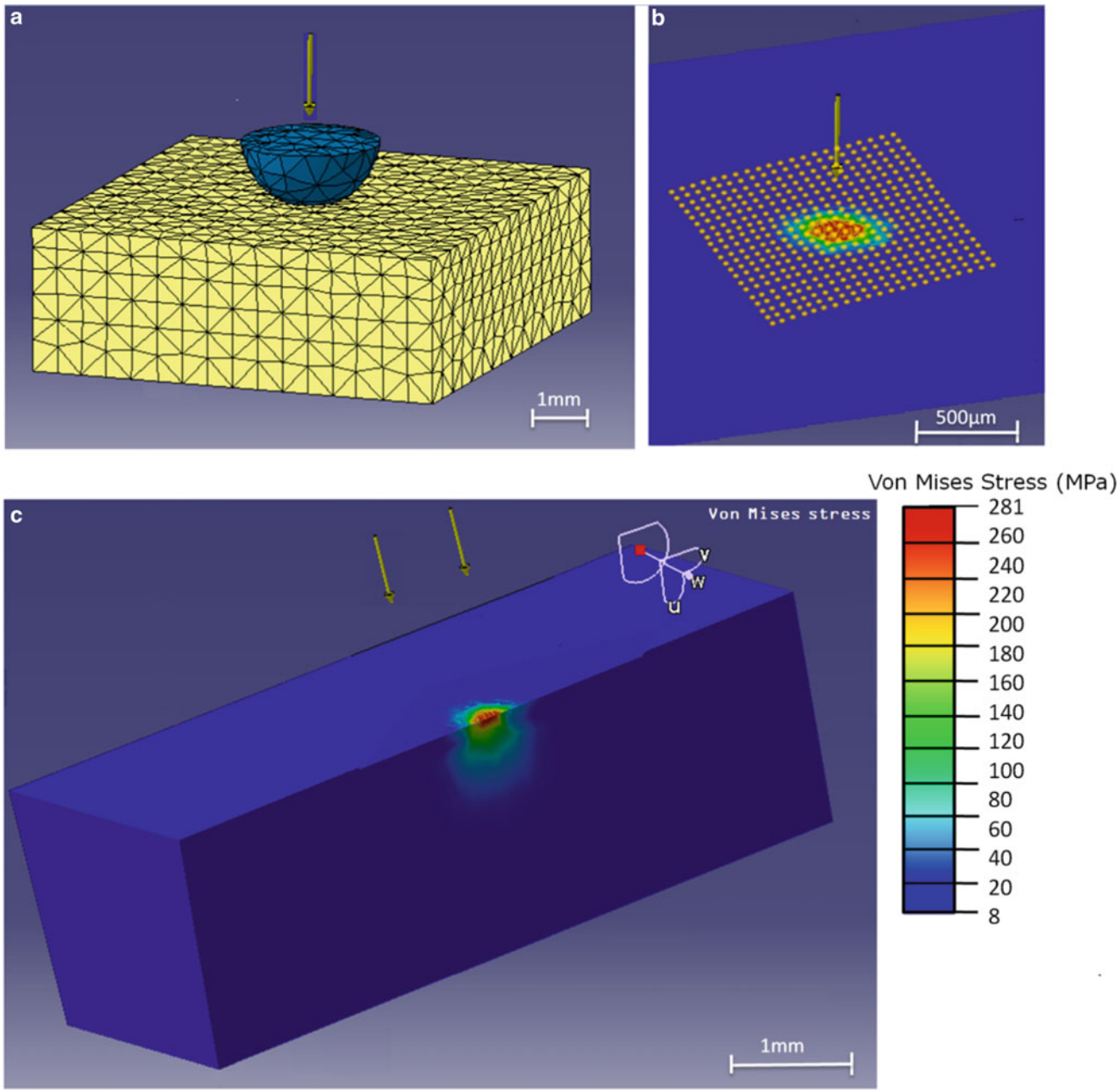

Fig. 36.2 (**a**) Simulation model illustrated with a course mesh for visulzation (the actual model was cunsructed with much finer mesh). (**b**) X-ray diffraction measurment grid super imposed on a stress distribution map in the surface of the flat zirconia sample under compression by a rigid Tungestan carbide indenter. (**c**) Stress distribution cross sectional view

While the local stresses can be high from the indentation, local stresses from grain-grain interactions can be even more significant [16]. These local stresses superimposed on the applied stress are the likely initiation of first early fatigue cycle phase transformations. Seeing that the residual stresses increase with transformation suggests that the transformation zone would continue to grow more severe with additional loading events. Clearly, this mechanism can be a contribution to the limited lifetime of ceramic dental restorations and needs further study.

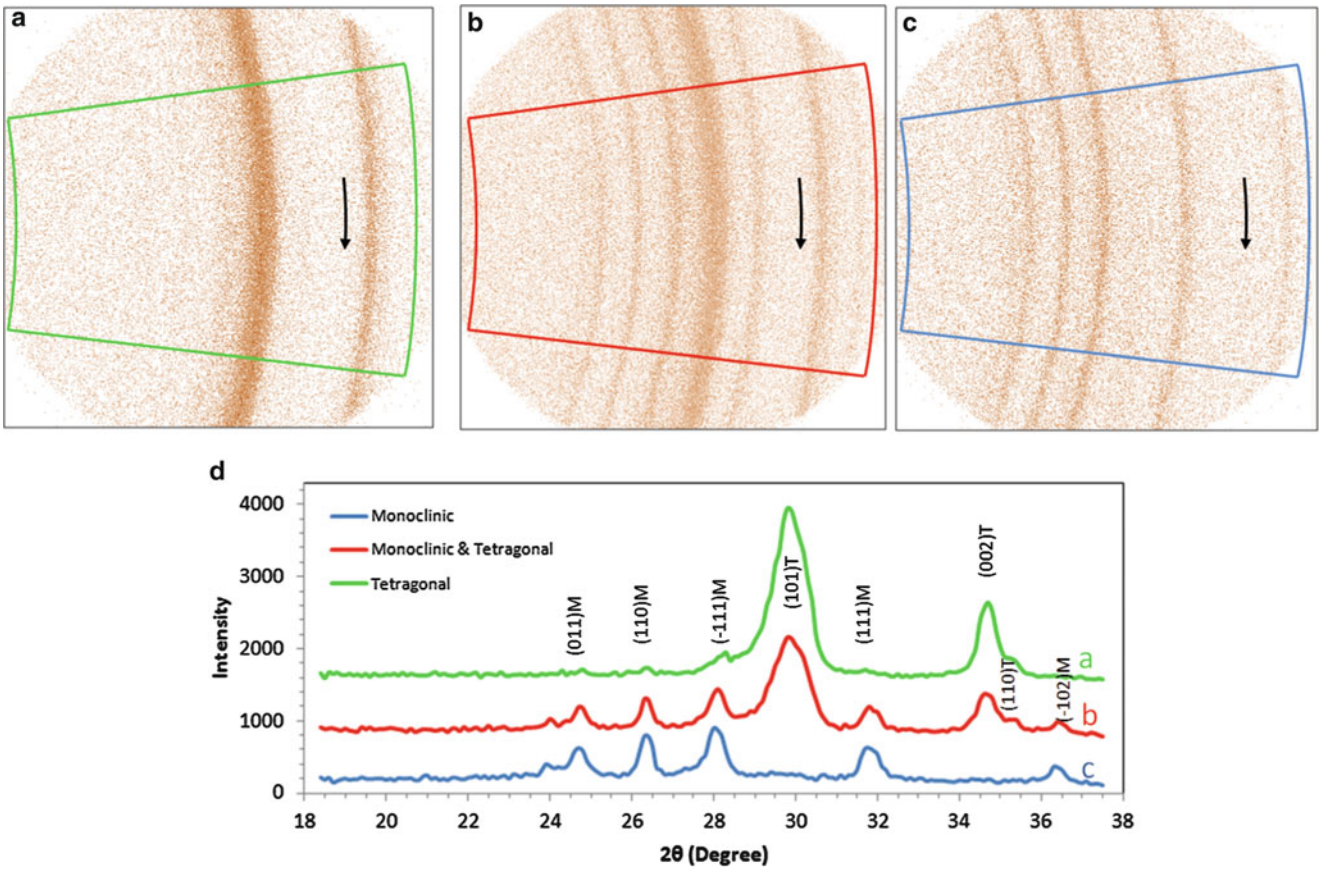

Fig. 36.3 X-ray diffraction frames: (**a**) far from the contact region, (**b**) middle of the contact region, (**c**) center of the contact region, (**d**) Indexed micro-XRD spectra showing phase identification for the above corresponding frames

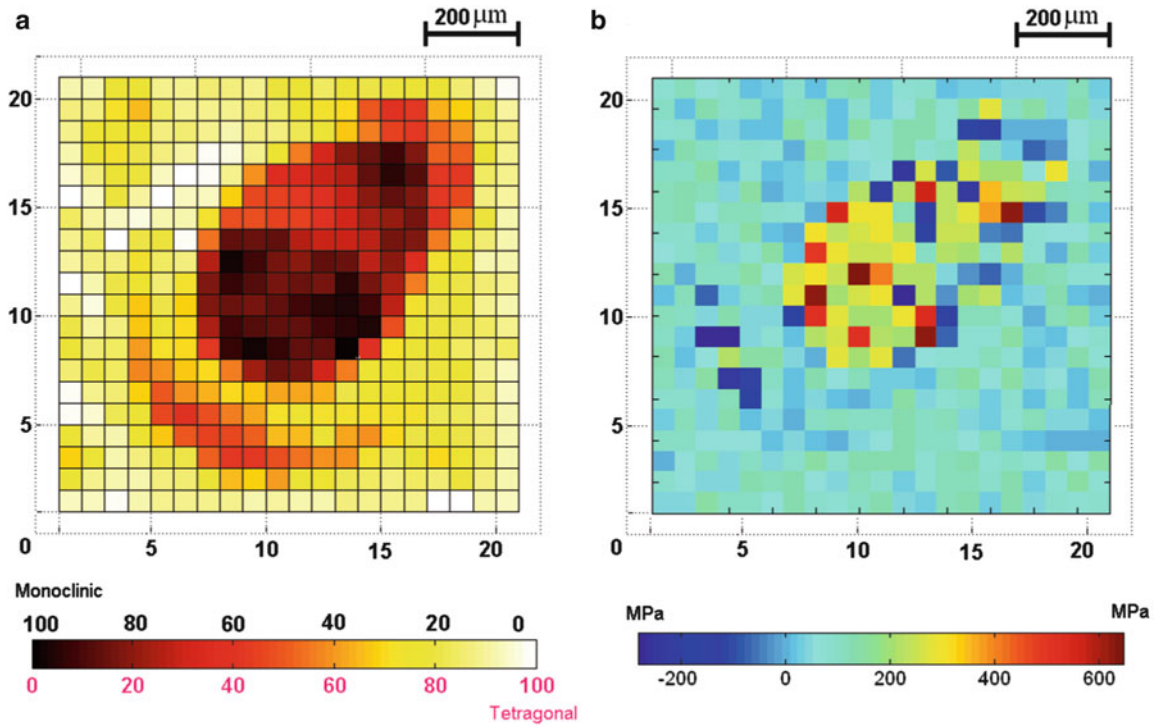

Fig. 36.4 (**a**) Color plot that represents the total area under three monoclinic peaks, (**b**) biaxial residual stress map

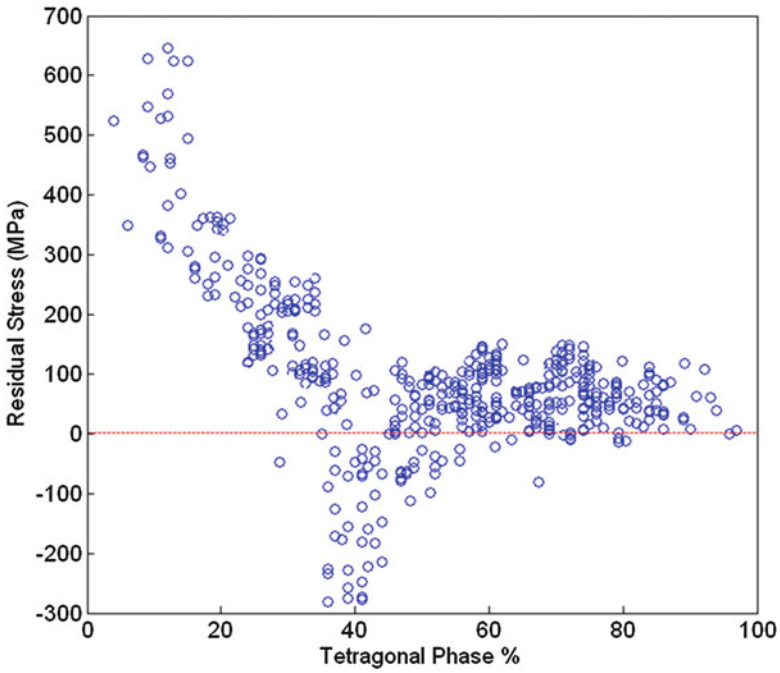

Fig. 36.5 Scatter plot for the correlation between phase transformation and residual stress measurements

36.5 Conclusion

The experimental procedure used here fatigued zirconia disks in order to determine the effect on the residual stress state and phase transformation. The results indicate that cyclic fatigue at a relatively small load does change the state of the residual stress in the sample with associated phase transformation. It was observed that the zirconia polycrystalline tetragonal structure exhibits up to 100 % phase transformation at the impacted region from clinically relevant fatigue loads with a resulting compressive residual stress of −300 MPa up to a tensile residual stress of +650 MPa in the fully transformed region.

Acknowledgment The ceramic sample was provided by Dr. E. D. Rekow's team at NYU School of Dentistry. Partial research support provided by the Oklahoma Health Research award (project number HR07-134), from the Oklahoma Center for the Advancement of Science and Technology (OCAST).

References

1. Prevéy P, Jayaraman N, Ravindranath R (2005) Design credit for compressive residual stresses in turbine engine components. In: Proceedings of the 10th National Turbine Engine HCF conference, New Orleans, 8–11 March 2005
2. Allahkarami M, Hanan JC (2012) Residual stress delaying phase transformation in Y-TZP bio-restorations. Phase Transit 85(1–2):169–178
3. Allahkarami M, Hanan JC (2012) Residual stress and phase transformation in Zirconia restoration ceramics. Adv Bioceram Porous Ceram V Ceram Eng Sci Proc 574:37–47
4. Bale HA (2010) Measurement and analysis of residual stresses in zirconia dental composites using micro X-ray diffraction. Ph.D. dissertation, Oklahoma State University
5. Scott HG (1975) Phase relationship in zirconia-yttria systems. J Mat Sci 10:1527–1535
6. Butler EP (1985) Transformation-toughened zirconia ceramics: critical assessment. Mat Sci Technol 1:417–432
7. Sailer I, Feher A, Filser F, Gauckler LJ, Luthy H, Hammerle CH (2007) Five-year clinical results of zirconia frameworks for posterior fixed partial dentures. Int J Prosthodont 20:383–388
8. Allahkarami M, Hanan JC (2011) Mapping the tetragonal to monoclinic phase transformation in zirconia core dental crowns. Dent Mater 27:1279
9. Zhang Y, Allahkarami M, Hanan JC (2012) Measuring residual stress in ceramic zirconia–porcelain dental crowns by nanoindentation. J Mech Behav Biomed Mater 6:120–127
10. He BB (2009) Two-dimensional X-ray diffraction. Wiley, Hoboken

11. He BB, Preckwinkel U, Smith KL (2003) Comparison between conventional and two-dimensional XRD, advances in X-ray analysis. 46:37–42
12. Allahkarami M, Hanan JC (2011) X-ray diffraction mapping on a curved surface. J Appl Crystallogr 44:1211–1216
13. Lawn BR, Deng Y, Thompson VP (2001) Use of contact testing in the characterization and design of all-ceramic crownlike layer structures, a review. J Prosthet Dent 86:495–510
14. Bale H, Tamura N, Coelho P, Hanan JC (2009) Impact fatigue deformation and residual stress evolution in dental ceramics. Fatigue and fracture in non-metallic materials, society of experimental mechanics annual conference & exposition on experimental and applied mechanics
15. Garvie RC, Swain MV (1985) Thermodynamics of the tetragonal to monoclinic phase transformation in constrained zirconia microcrystals. J Mater Sci 20:1193–1200
16. Bale HA, Tamura N, Coelho P, Hanan JC (2008) Interface residual stresses in dental zirconia using Laue micro-diffraction. Adv X-ray Anal 52:368–375

Chapter 37
Characterization of Silicon Photovoltaic Wafers Using Infrared Photoelasticity

T.-W. Lin, G.P. Horn, and H.T. Johnson

Abstract Reliability of silicon photovoltaic (PV) wafers is strongly influenced by defects and residual stresses from the crystallization and wire-sawing processes. Information about defects and stress in each wafer is important for improving the solar cell efficiency. An approach is developed for characterization of defects and residual stresses on silicon PV wafers. Utilizing a lock-in photoelastic imaging technique, the infrared grey-field polariscope (IR-GFP), retardation images are generated for individual silicon PV wafers taken from industry-grown single crystal stock. Full-wafer scale retardation images are compared with band-to-band photoluminescence (PL) images from the same wafers. The lock-in photoelastic imaging allows for better identification of defects than standard band-to-band PL imaging. Analytical models of elasticity are used to generate retardation patterns for dislocations and the residual thermal stresses. The theoretical retardation profiles are compared with the photoelastic image for defect identification and residual stress analysis. The approach is capable of relatively rapid wafer imaging, automated defect detection and stress analysis, and thus may be suitable for integration as an in-line reliability control process.

Keywords Silicon • Dislocation • Residual thermal stress • Photoelasticity • Defect detection

37.1 Introduction

Residual thermal stresses and defects such as dislocations can affect performance of silicon photovoltaic (PV) wafers. Manufacturing processes of the PV wafers involve crystallization of silicon material and subsequent cutting and wire-sawing, which generate residual stresses, dislocations, and cracks. Solar cells with high densities of defects and high residual stresses are found to have reduced efficiencies due to the shorter carrier lifetime. Defects act as recombination sites for electrons and holes, shortening their diffusion lengths in the silicon PV wafers [1, 2].

During the crystallization process, silicon undergoes solidification and cooling from its melting temperature to room temperature. The temperature gradient within the ingot causes thermal stress in the material. Large residual stresses in the bulk silicon crystal often result in undesired wafer deformation. Dislocations become active in the crystal when the thermal stresses on a particular slip system produce a resolved shear stress larger than its critical value at elevated temperatures [3, 4]. PV wafers with high residual stresses are vulnerable to fracture during the solar cell fabrication processes, if there exist defects acting as stress concentrators [5]. Understanding the defects and residual stress distribution in each wafer is important for improving the reliability and performance of the PV solar cells.

There are several non-destructive techniques for characterization of the as-cut silicon PV wafers. Infrared transmission (IRT) imaging is used to locate defects that are not observable in visible light. The spatial resolution of IRT is limited by the wavelength of the light source, making it difficult to detect smaller defects with this method. X-ray topography is capable of imaging slip bands and dislocation loops. High temperature applications are possible since the x-ray image provides good contrast even at 1,000 °C [6]. However, a synchrotron radiation facility is required for this method. Photoluminescence (PL) is widely used for measuring minority carrier lifetime in PV wafers [7]. Defects such as dislocations show up on PL images

T.-W. Lin (✉) • G.P. Horn • H.T. Johnson
Department of Mechanical Science and Engineering, University of Illinois at Urbana-Champaign,
1206 W. Green St, 61801 Urbana, IL, USA
e-mail: lin142@illinois.edu

M. Rossi et al. (eds.), *Residual Stress, Thermomechanics & Infrared Imaging, Hybrid Techniques and Inverse Problems, Volume 8*,
Conference Proceedings of the Society for Experimental Mechanics Series, DOI 10.1007/978-3-319-00876-9_37,

as darker regions, since the PL signal emitted from these sites is lower. Although the intensity of the PL signal reveals the location of defects and dislocations in the wafer, their associated stress fields are not available. Photoelasticity is used for experimentally analyzing different types of defects in the PV wafer, including cracks, inclusions, grain boundaries, and dislocations [2, 5, 8]. The birefringence image given by photoelastic measurement shows changes in the refractive indices due to strain in the wafer. Both the stresses associated with defects and the thermally induced stresses are measureable. Among various photoelastic methods, the infrared grey-field polariscope (IR-GFP) has demonstrated the ability to perform rapid silicon wafer inspection at rates that may be applicable to industrial applications [9].

In this study, infrared photoelastic measurement of silicon PV wafers is performed using IR-GFP. Analytical model is used for calculating the dislocation stress and the residual thermal stress that occurs during crystallization of the silicon ingot. The birefringence image generated using IR-GFP is explained based on thermal elasticity and dislocation stress theories. It is possible to interpret the GFP image and understand the generation mechanism of the thermally induced and the dislocation associated stress fields.

37.2 Characterization Methods

The silicon PV wafers are mono-crystalline, grown using an 8 in. Czochralski (CZ) process. A particular crystal orientation is selected by using a seed crystal. The seed crystal is brought in contact with the silicon melt and pulled out of the melt with a relative rotation to the crucible [10]. Therefore, the solidified silicon grows into a cylindrical ingot. After the silicon ingot is grown, subsequent cutting and wire-sawing processes are performed. The dimensions of the as-cut square PV wafer are 150 mm on each side and 300 μm in thickness.

Photoelastic measurement of industrial as-cut silicon PV wafers is carried out using an IR-GFP system built by Stress Photonics. A charge-coupled device camera with resolution of 1380 × 1030 pixels is utilized in the system, with an adjustable focusing camera lens to achieve a 20 × 24 cm^2 field of view.

A GFP image of a representative silicon PV wafer is shown in Fig. 37.1a. The intensity on the image indicates magnitude of the optical retardation caused by the stress-induced birefringence in the wafer. The relation between the birefringence $(n_1 - n_2)$ and the optical retardation is

$$\delta = d(n_1 - n_2) \tag{37.1}$$

where d is the thickness of the wafer and n_1 and n_2 are refractive indices along the fast- and slow-optical axes that are perpendicular to each other. The change of the refractive indices depends on the impermeability tensor B_{ij}, which contains dielectric properties of the silicon. Therefore, Eq. 37.1 can be written as

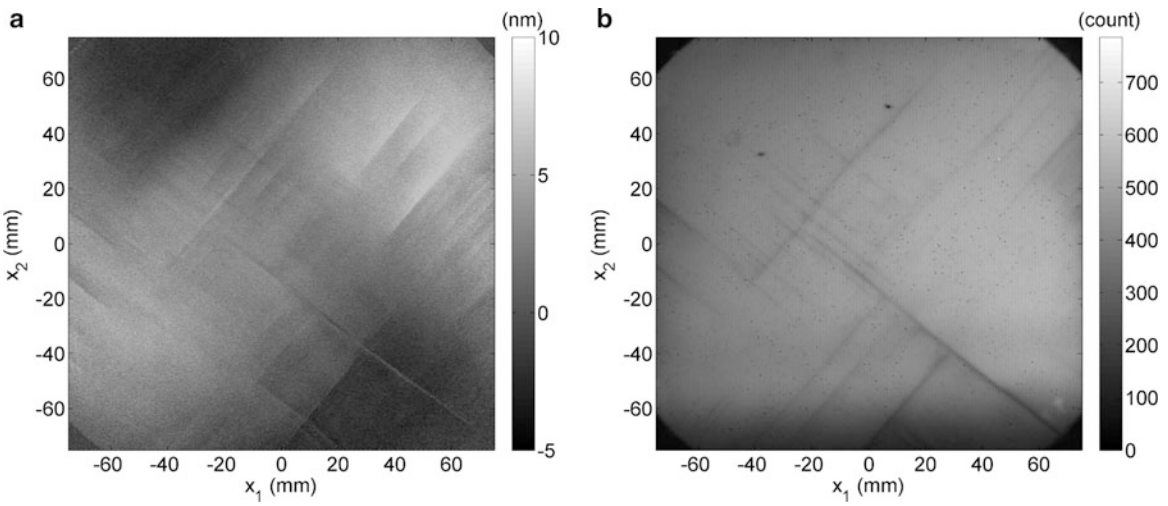

Fig. 37.1 Measurement of PV wafer A using (**a**) IR-GFP, maximum and minimum retardations are 13.8 and −5.2 nm, respectively; (**b**) PL image, showing intensity of the illuminated signal; the dislocation slip bands present on both images, while the thermal residual stress profile presents only on the GFP image

$$\delta = \frac{n_0^3 d}{2}(B_1 - B_2) \tag{37.2}$$

where B_1 and B_2 are the principal values of B_{ij}, and n_0 is the original refractive index of silicon when there is no stress in the crystal [11]. For incident light that propagates normal to the wafer surface, the birefringence is related to the difference of the two principal values of the tensor B_{ij} that are associated with the two in-plane principal axes. The impermeability tensor depends on the stress states in the silicon through Pockels' law, or

$$B_{ij} = \pi_{ijkl}\sigma_{kl} \tag{37.3}$$

where π_{ijkl} are the elasto-optical coefficients of the silicon. The theoretical retardation is calculated for each point in the silicon wafer according to the stress state of the point. For comparison between the experimental and the theoretical results, a 2D retardation profile image can be found by integrating the retardation through the thickness of the wafer, since the measured GFP image is obtained in the same way.

Photoluminescence (PL) measurements are performed to obtain band-to-band image of the PV wafers. A laser with 800 nm wavelength is used as the excitation source of the PL signal. Electrons in the silicon are excited into the conduction band and drop back to the valence band by illuminating light with wavelength of 1.1 μm. Defects in the wafer can introduce other paths for electrons and holes to recombine without the illumination.

37.3 Results and Discussion

Qualitative inspection of a typical IR-GFP image of a silicon PV wafer shows a superposition of two distinct stress fields. A macro-scale stress pattern is shown across the wafer in Fig. 37.1a, where dark regions are located on the upper-left and lower-right corners, and bright regions are located on the upper-right and lower-left corners. Grey represents zero retardation on the GFP image, while dark and bright regions indicate high retardation with opposite sign. The center of the wafer shows relatively low retardation. The four-lobe shape that consists of the dark and bright regions is due to the residual thermal stresses.

There are also thin lines of highly concentrated retardation distributed across the wafer and oriented at 45° to the wafer edge. The intensity of the retardation signal of each line is localized along the line direction and is distinct from the background intensity. It shows a bright region on one side of the feature and a dark region on the other side. The orientation of the lines and highly concentrated residual stress fields suggest that dislocation slip bands in the PV wafer result in these lines in the GFP image.

Figure 37.1b shows a PL image of the same PV wafer. Similar to the GFP image, the dislocation slip bands are also observed in the PL image. The lower PL intensity indicates a shorter minority carrier lifetime at the slip bands, which is due to a higher recombination rate of electrons and holes [1]. Therefore, the PL imaging has become the standard method for the qualitative detection of defects in the solar industry. One of the significant differences between the PL image and the GFP image is that the four-lobe pattern does not present in the PL image, thus the defect signal is uniquely identified through PL. However, the PL image does not provide any information regarding the residual stress state of the wafers from the defects or the thermal processes. The GFP image provides all of those qualitative results from the PL image, with additional information about the stress states in the wafer.

Characterization of the silicon PV wafers using IR-GFP has an advantage in its ability to image the stress fields associated with the slip bands. In some cases, this allows location of defects that are not visible with PL imaging. Figure 37.2 shows the GFP image of another silicon PV wafer (Fig. 37.2a) and the PL image of the same wafer (Fig. 37.2b). From the PL image, one might conclude that this is a relatively defect-free wafer. However, the GFP image shows several dislocation slip bands near the center and upper parts of the wafer. It also shows the four-lobe pattern due to the residual thermal stress. Defects such as dislocations in the wafer are often associated with localized stress fields. Since the stress-influenced area is larger than the size of the defect, it is possible for IR-GFP to resolve very small defects that are not visible in the PL image. Precipitates, vacancies, and newly initiated cracks are not easily visible, especially when their sizes are close to the optical limitation of the instrument. For silicon PL imaging, it often requires an exposure time from a few seconds up to a minute. The PL image becomes smeared due the scattering of the PL light and or the insufficient incident light, which can lower the contrast and reduce the resolution of the PL image [7].

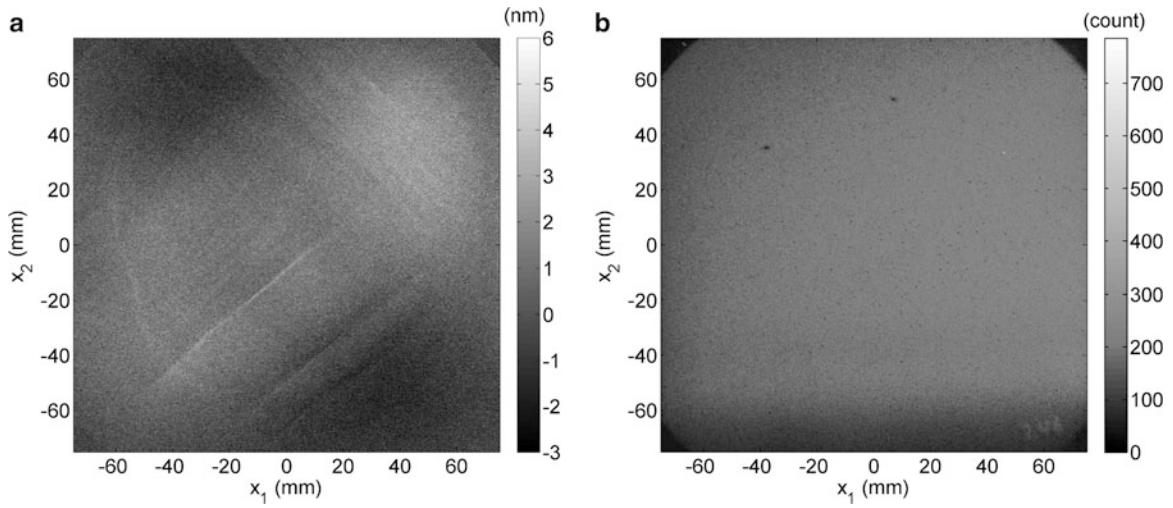

Fig. 37.2 Measurement of PV wafer B using (**a**) IR-GFP, maximum and minimum retardations are 8.6 and −8.3 nm, respectively; (**b**) PL image, which does not show the dislocation slip bands and the thermal residual stress profile

To explain the characteristic features of the GFP image, it is essential to study the generation mechanisms of the stresses that develop during the silicon crystallization process. During the crystal growth of the silicon, the temperature in the silicon ingot is close to the melting temperature, while the temperature on the surface of the ingot is lower. Residual thermal stresses occur due to this temperature difference.

An analytical thermo-elastic model is applied to describe the thermal stress field in the silicon ingot grown with the CZ process. For simplicity, the geometry of the ingot is assumed to be a cylinder with infinite length. Thus, the problem can be solved assuming plain-strain conditions in the ingot. Furthermore, axisymmetric stress fields are expected since there is symmetry about the axis of the cylinder. In polar coordinates, the prescribed temperature at the center of the ingot is denoted as T_0 at $r = 0$ and the temperature on the surface of the ingot remains at T_R, where $r = R$. By solving the axisymmetric plane-strain problem, following [12], the nonzero thermal stress components associated with the prescribed temperatures are the hoop stress and the radial stress expressed by

$$\sigma_{rr} = \frac{2\alpha E(T_0 - T_R)}{(1-\nu)} \sum_{s=1}^{\infty} \frac{e^{-mt}}{\beta_s^2 J_1(\beta_s)} \left\{ J_1(\beta_s) - \frac{R}{r} J_1\left(\frac{r}{R}\beta_s\right) \right\} \tag{37.4}$$

$$\sigma_{\theta\theta} = \frac{2\alpha E(T_0 - T_R)}{(1-\nu)} \sum_{s=1}^{\infty} \frac{e^{-mt}}{\beta_s^2 J_1(\beta_s)} \left\{ J_1(\beta_s) + \frac{R}{r} J_1\left(\frac{r}{R}\beta_s\right) - \frac{r}{R}\beta_s J_0\left(\frac{r}{R}\beta_s\right) \right\} \tag{37.5}$$

where $m = K\beta_s^2/\rho c R^2$, α is the thermal expansion coefficient, K is the thermal conductivity, c is the specific heat, ρ is the density, E is the Young's modulus, ν is the Poisson's ratio, J_0 and J_1 are Bessel's function of the first kind, and β_s (s = 1,2, . . .) are the roots of $J_0(\beta_s) = 0$. A time constant t is assumed as the duration for the surface temperature to change from T_0 to T_R. The stress fields are transformed in Cartesian coordinates. The retardation from thermal residual stress is calculated using Eqs. 37.1, 37.2, and 37.3. A plot of the theoretical retardation profile due to thermal stress is given in Fig. 37.3a.

A time constant $t = 0.01$ and a temperature difference of 1,000 °C is chosen to fit the theoretical plot to the experimental result. Figure 37.3a shows the four-lobe retardation field due to the thermal stresses. Once the retardation profile of the residual thermal stress is found, comparison between the GFP image and the theoretical retardation profile can be used to identify defects in the wafer. Deviation between the experimental and theoretical retardation profiles gives the location of the defects.

In order to interpret the linear features caused by the dislocation slip bands, it is necessary to understand the crystallographic structure of the PV wafer. The CZ-grown single crystal silicon wafer has [001] wafer surface normal direction. Silicon has diamond crystal structure and cubic symmetry. There are 12 slip systems in the crystal, with the close-packed planes {111} and the slip directions $<1\,\bar{1}\,0>$. For simplicity, only edge dislocations are considered here. The location of the edge dislocation is assumed in the PV wafer, based on its orientation on each slip plane. As an example, the slip system with

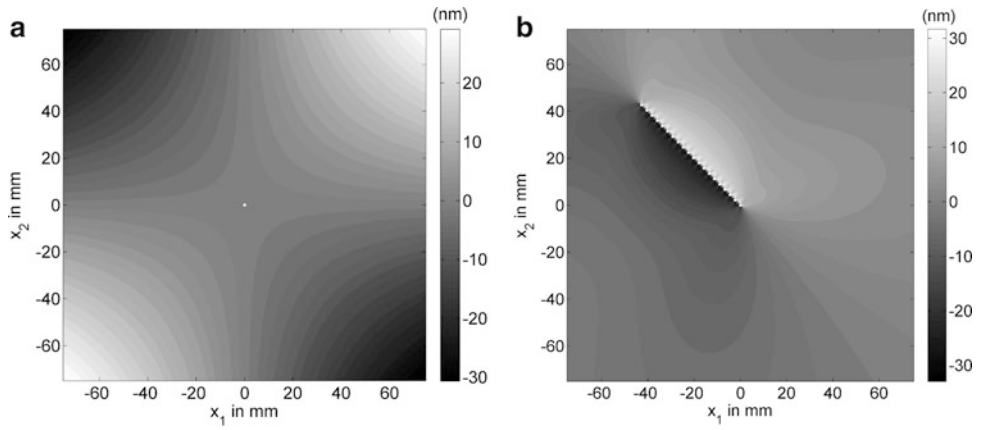

Fig. 37.3 Theoretical retardation profile due to (**a**) an estimated residual thermal fields and (**b**) an array of 20 edge dislocations in (111) plane and $[1\bar{1}0]$ slip direction

(111) slip plane and $[1\,\bar{1}\,0]$ slip direction is considered. The stress fields of each edge dislocation are expressed by the theory of isotropic linear elasticity [13], which gives

$$\sigma_{11} = -D\mathrm{x}_2 \frac{\left(3\mathrm{x}_1^2 + \mathrm{x}_2^2\right)}{\left(\mathrm{x}_1^2 + \mathrm{x}_2^2\right)^2}, \tag{37.6}$$

$$\sigma_{22} = D\mathrm{x}_2 \frac{\left(\mathrm{x}_1^2 - \mathrm{x}_2^2\right)}{\left(\mathrm{x}_1^2 + \mathrm{x}_2^2\right)^2} \tag{37.7}$$

$$\sigma_{12} = D\mathrm{x}_1 \frac{\left(\mathrm{x}_1^2 - \mathrm{x}_2^2\right)}{\left(\mathrm{x}_1^2 + \mathrm{x}_2^2\right)^2}, \tag{37.8}$$

$$\sigma_{33} = \nu(\sigma_{11} + \sigma_{22}) \tag{37.9}$$

where $D = Gb/2\pi(1-\nu)$, G is the shear modulus, b is Burgers vector of the edge dislocation in silicon. These stress fields are transformed in crystal coordinates of the wafer.

The retardation due to the dislocation stresses is calculated using Eqs. 37.1, 37.2, and 37.3 and plotted in Fig. 37.3b. An array of 20 edge dislocations is selected as an example for the plot. The theoretical retardation plot of the dislocation slip bands has positive value on one side and negative on the other side, which corresponds to the line patterns shown in Figs. 37.1a and 37.2a. The width of the slip band is approximately the thickness of the PV wafer. This is expected since the dislocation lines are oriented on the (111) slip plane and intersect both the front and back surfaces of the wafer [6].

37.4 Conclusions and Future Work

This study provides a method for characterization of the stress fields and the defects in single crystal silicon PV wafers. Using IR-GFP for the infrared photoelastic measurement, the dislocation slip bands and the thermally induced residual stress fields in the wafer are visualized. Comparison between the GFP images and PL images shows that the IR-GFP measurement is able to reveal defects that are not detected by the PL technique. Both the global stress field due to CZ crystallization and the localized dislocation stress field are analyzed using simple linear elastic models. The stress fields shown in the GFP images are interpreted by comparing to plots generated from the theoretical models.

The IR-GFP system used for this study utilizes a visible light charge-coupled camera as its sensing component. The dynamic sensing range of the camera is primarily in the range of the visible light, with a smaller sensitivity for the near-infrared range. It is desirable to use an infrared camera with better sensitivity in the near-infrared and mid-infrared range.

Acknowledgements The wafer specimens studied here were provided by SolarWorld Industries, America. This assistance is gratefully acknowledged.

References

1. Ostapenko S, Tarasov I, Kalejs JP, Haessler C, Reisner E-U (2000) Defect monitoring using scanning photoluminescence spectroscopy in multicrystalline silicon wafers. Semicond Sci Technol 15(8):840–848
2. He S, Danyluk S, Tarasov I, Ostapenko S (2006) Residual stresses in polycrystalline silicon sheet and their relation to electron–hole lifetime. Appl Phys Lett 89(11):111909
3. Leroy B, Plougonven C (1980) Warpage of silicon wafers. J Electrochem Soc 127(4):961–970
4. Shimizu H, Aoshima T (1988) Thermal warpage of large diameter Czochralski-grown silicon wafers. Jpn J Appl Phys 27(12):2315–2323
5. Ganapati V, Schoenfelder S, Castellanos S, Oener S, Koepge R, Sampson A, Marcus M a, Lai B, Morhenn H, Hahn G, Bagdahn J, Buonassisi T (2010) Infrared birefringence imaging of residual stress and bulk defects in multicrystalline silicon. J Appl Phys 108(6):063528
6. Danilewsky AN, Wittge J, Croell A, Allen D, McNally P, Vagovič P, Dos Santos Rolo T, Li Z, Baumbach T, Gorostegui-Colinas E, Garagorri J, Elizalde MR, Fossati MC, Bowen DK, Tanner BK (2011) Dislocation dynamics and slip band formation in silicon: in-situ study by X-ray diffraction imaging. J Cryst Growth 318(1):1157–1163
7. Trupke T, Bardos RA, Schubert MC, Warta W (2006) Photoluminescence imaging of silicon wafers. Appl Phys Lett 89(4):044107
8. Fukuzawa M, Yamada M (2006) Photoelastic characterization on multicrystalline silicon substrates for solar cell. Mater Sci Semicond Proc 9 (1–3):266–269
9. Horn G, Lesniak J, Mackin T, Boyce B (2005) Infrared grey-field polariscope: a tool for rapid stress analysis in microelectronic materials and devices. Rev Sci Instrum 76(4):045108
10. Sinno T, Dornberger E, Von Ammon W, Brown R, Dupret F (2000) Defect engineering of Czochralski single-crystal silicon. Mater Sci Eng R Rep 28(5–6):149–198
11. He S, Zheng T, Danyluk S (2004) Analysis and determination of the stress-optic coefficients of thin single crystal silicon samples. J Appl Phys 96(6):3103
12. Jaeger J (1945) LI. On thermal stresses in circular cylinders. Philos Mag Ser 7 36(257):418–428
13. Hull D, Bacon DJ (2011) Introduction to dislocations, 5th edn. Butterworth-Heinemann, New York/Oxford, pp 63–83

Chapter 38
Acoustic Emission Analysis of Aluminum Specimen Subjected to Laser Annealing

C. Barile, C. Casavola, G. Pappalettera, and C. Pappalettere

Abstract This paper deals with the study of acoustic emissions (AE) from aluminum Al5068 specimen during local annealing process by a laser diode source. The heating cycle, obtained by irradiating the surface of the specimen, causes a change in the local stress state which can be studied by X-Ray diffractometry; at the same time acoustic emissions can be recorded as a consequence of residual stress relieving.

This hybrid approach provides evidence of the presence of a correlation between stress relieving and the number of signals of acoustic emissions recorded during the heating and the cooling stages. Annealing cycle was repeated several times and acoustic emissions were detected during each cycle; the amount of residual stresses along the longitudinal direction was measured at the end of each cycle as well. The number of acoustic signals exhibits the typical behavior due to the Kaiser effect while residual stresses show a quite regular decrease from cycle to cycle. Mechanical tensile tests have also been performed on the same specimen tested at four different loads. In this case too, experimental results show evidence of Kaiser effect, however a steeper reduction of the number of signals is observed with respect to the thermal tests.

Keywords Aluminum • Acoustic emission • Laser annealing • Residual stress relaxation • Mechanical test

38.1 Introduction

Acoustic emissions are generated in solid materials subjected to both thermal and mechanical stresses or deformations. They can be related to several sources i.e. motion of dislocations, crack nucleation, crack propagation etc. The acoustic emissions technique detects stress waves produced during the transient release of energy in stressed materials [1, 2], it is a non-invasive technique that can act both in active and in passive way.

AE are detected in the ultrasonic range of frequencies by using high sensitivity piezoelectric sensors having the resonance frequency equal to the frequency of the ultrasound signal to be monitored. The AE technique is characterized by the possibility to detect the energy release of stressed component even when it depends on a strictly localized phenomena. In this work, in fact, a high power laser diode was focused on an aluminum specimen in a localized spot, in order to relax the residual stress. Despite of the huge amount of work which has been done in characterizing the different sources of acoustic emissions, much work has to be done in studying the stress relaxation process as a generator of acoustic events.

This paper aims to connect the stress relaxation obtained by the annealing process with the level of detected acoustic signals. The specimens analyzed were subjected to thermal cycles in order to induce local stress relaxation. X-ray diffractometer was used to quantify the amount of relaxed stress. AE sensors were used to detect the acoustic emission events generated during the annealing process. Mechanical tests were also performed and in this case too AE signals were detected. Kaiser effect was observed both in thermal and mechanical tests but showing a different damping behavior.

C. Barile • C. Casavola (✉) • G. Pappalettera • C. Pappalettere
Dipartimento di Meccanica, Matematica e Management, Politecnico di Bari, Viale Japigia 182, 70126 Bari, Italy
e-mail: casavola@poliba.it

M. Rossi et al. (eds.), *Residual Stress, Thermomechanics & Infrared Imaging, Hybrid Techniques and Inverse Problems, Volume 8*, Conference Proceedings of the Society for Experimental Mechanics Series, DOI 10.1007/978-3-319-00876-9_38,

38.2 Materials and Methods

38.2.1 Thermal Tests

Acoustic emission events are identified by a set of shots (*hits*) [3]. If a voltage threshold value is fixed, the hits represent the number of times the voltage generated from the PZT sensor overcomes that threshold. Every shot is characterized by an intensity value proportional to the energy of the detected event [4]. Preliminary experiments were carried out to find an optimal value for the threshold. A too low value of the threshold, in fact, would introduce too much noise in the measurement; on the other hand if the value is too high no signal can be detected. A value of 30 dB was used during the entire experimental plan, this value is in agreement with the findings of [5] for annealed Al 2219.

During the experimental tests, acoustic emissions were monitored both during laser annealing cycle and during cooling; subsequently the efficiency of the cycle, in terms of obtained stress relaxation, was evaluated by means of an X-ray diffractometer (XRD). In other words residual stresses were evaluated on the *as received* sample and at the end of each heating cycle. In order to perform this measurement an XRD with a Cr source was used. Beam was collimated through a 3 mm diameter collimator.

The experimental tests were carried out on prismatic aluminum specimen (Al 5068), with $10 \times 10 \times 160$ mm dimensions. Two sensors (Table 38.1 [6]) were placed on the surface of the specimen 30 mm far apart one from each other (Fig. 38.1), and at the same distance from the area heated by the laser beam.

First of all the initial state of residual stresses was measured on the specimen. Successively the laser was focused at the center of the analyzed area.

Due to the elliptical shape of the laser spot, two different and orthogonal directions of measurement were chosen in order to estimate the effects of the different power density in both directions. Longitudinal and transverse ones were replicated three times for each point.

The cycle was realized through a high power laser diode (GaAlAs), with a nominal power of 100 W and a wavelength of 830 nm (Fig. 38.2).

Table 38.1 Main characteristics of the Mistras Pico sensor used in this work

Characteristichs of the Pico sensor	
Peak sensitivity	54 dB
Operating frequency range	200–750 kHz
Resonant frequency	250 KHz
Temperature range	−65–177 °C
Dimension	5 × 4 mm

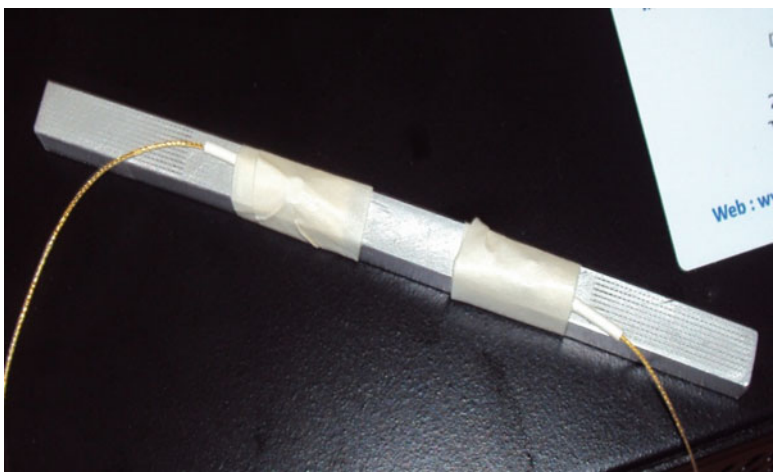

Fig. 38.1 Sensors positioning

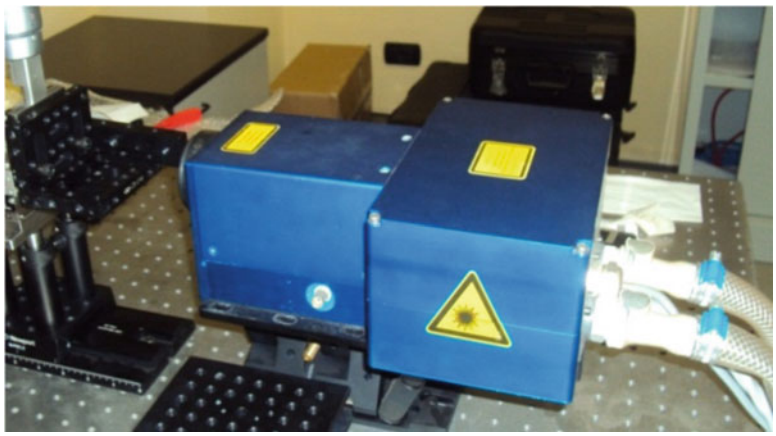

Fig. 38.2 Diode pump solid-state laser used for the laser annealing cycle

A proper cycle was defined to reach an effective relaxation of residual stress. Laser and cycle parameters were chosen on the basis of already existing studies [7]. The following parameters defines the adopted thermal cycle:

- Current 5 A;
- Laser power 16.3 W;
- Heating cycle 20 s;
- Cooling 240 s.

Acoustic emissions were monitored and recorded continuously during the heating cycle. At the end of the cycle a new diffractometric measure was carried out on the same point previously measured and annealed, in order to quantify the effective relaxation. Annealing cycles were repeated three times for each point.

38.2.2 Mechanical Tests

In this part of the experimental, acoustic emissions from the sample were recorded during a tensile mechanical tests. Iterative loops of loading and unloading [8] were applied on the specimen. The load value was reached under displacement control. This operation was repeated five times for each set maximum loading value. Then a new set of cycles was executed up to an increased load value. An uniaxial electro-mechanical MTS static machine was used, having a load capacity of 30 kN (Fig. 38.3).

Four loading and unloading cycles for each of the following loading levels: 8, 11, 14 and 17 kN. Each cycle was replicated five times.

At the beginning of a new set of cycles the specimen was removed and repositioned to ensure the start of the test on a zero load.

During all tests, acoustic emissions were recorded and monitored continuously.

38.3 Results and Discussion

38.3.1 Thermal Tests

Results of the diffractometric measurements and the number of recorded Hits per each cycle are reported in Table 38.2.

As reported in Table 38.2 it results that the number of the recorded hits decreases during consecutive cycles. This phenomenon is more evident if a fitting of the number of hits as a function of the number cycle is done. In this way it can be observed that the number of counts for each cycle of thermal load tends to decrease as a negative exponential function. The exponent depends on the sequential number of the thermal cycle. Figure 38.4 compares the different exponential curves corresponding to three different annealed point.

Fig. 38.3 Uniaxial static testing machine MTS Alliance RT/30

Table 38.2 Diffractometric measurements and number of hits per cycle

# Cycle	# Hits	σ [MPa]
1	8	−116.6
2	2	−106.4
3	1	−94.1
4	1	−84.8

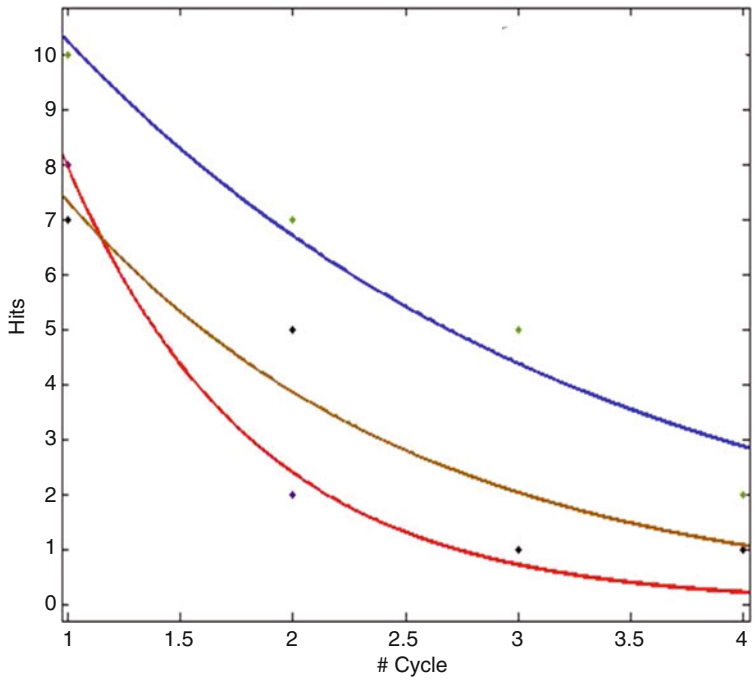

Fig. 38.4 Fitting of the number of hits versus the # of cycle. The three *curves* refer to the result obtained on three different points

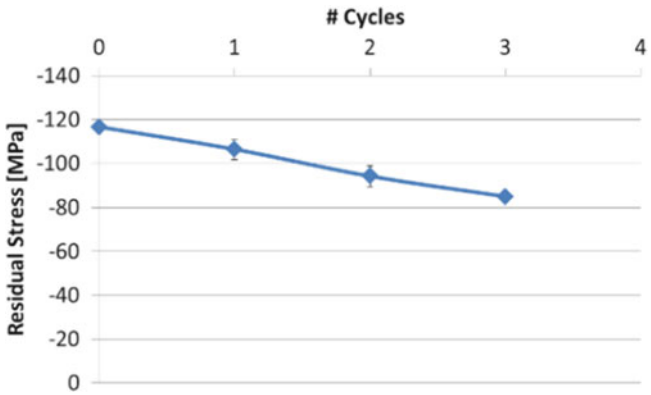

Fig. 38.5 Residual stress [MPa] versus number of cycles

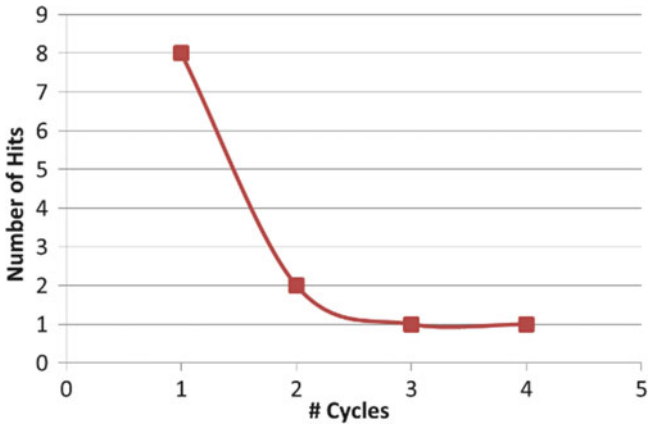

Fig. 38.6 Number of recorded hits versus number of cycles

Since all the thermal cycles are equal (i.e. with the same times and the same temperatures both during heating and cooling), reducing the number of counts in the various cycles can be considered representative of the presence of thermal Kaiser effect. This effect causes the tendency to decrease the number of hits in thermal cycles after the first one, according to a negative exponential law:

$$\#\ \text{Hits} = a^* e^{(b*N)} \tag{38.1}$$

Where N corresponds to the number of the thermal cycle.

The average value found for the exponential coefficient was b $= -1.202$.

This correlation between the thermal behavior and the counts of acoustic emissions may be better understood considering that the application of thermal loads, cause the formation and/or the propagation of micro cracks and defects [9]. They represent a source of acoustic emissions. Jointly to this phenomenon and due to the same thermal cycle, a variation of residual stress is obtained. This interpretation of data justifies the acquisition of a greater number of hits for the first cycle than in the other ones.

Kaiser effect affected thermal cycles after the first one, resulting in a reduction of the number of hits per cycle. This trend can be justified by considering that if the same thermal load is applied for all the cycles, after the first one [10] there is no longer formation and/or propagation of micro-cracks. The thermal stress, in fact, is not sufficient to allow crack propagation. For this reason there is no further activity of acoustic emissions except than that connected to residual stress relaxation.

Growing the number of thermal cycle repetition this phenomenon becomes more evident, because fewer defects cause emissions; it remains a residual term of acoustic emissions caused by the variation of the residual stress.

In Figs. 38.5 and 38.6 it is shown that the effect of the applied thermal cycle is a quite constant reduction of residual stress while, contemporarily the number of recorded hits drop down drastically.

Table 38.3 Number of hits in five load step

Test	8 KN	11 KN	14 KN	17 KN
1	3,263	5,088	6,048	6,604
2	1,891	2,590	2,998	3,898
3	1,610	2,605	3,190	3,680
4	1,603	2,670	3,209	3,650
5	1,585	2,359	3,008	3,634

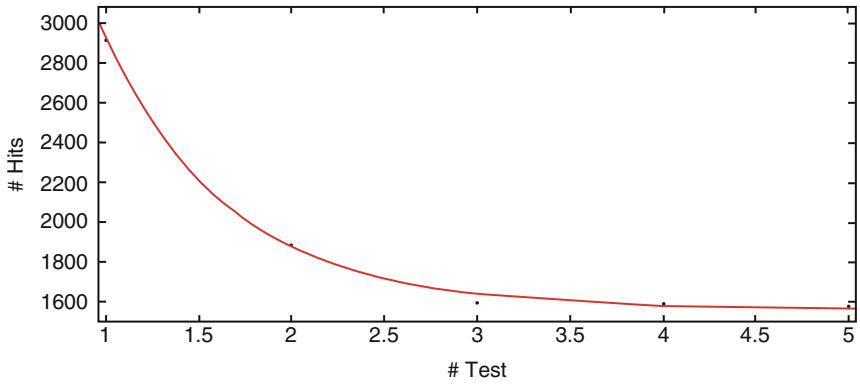

Fig. 38.7 Plot of the number of hits versus the number of test in mechanical tensile test

38.3.2 Mechanical Tests

The behavior observed during the annealing was found also during tensile mechanical tests even if appearing different from a quantitative point of view.

In Table 38.3 acoustic emission data, in terms of recorded hits, are shown for each loading cycle.

Mechanical cycles of loading and unloading, after the first one, determined a decrease in terms of recorded Hits. In Fig. 38.7a is reported, as an example, the curve referred to the test performed at 8 KN. The curve trend is very similar to the thermal one, but the damping is much greater than in the previous case.

Mechanical applied loads caused the nucleation and/or propagation of micro-craks and internal/superficial defects. These events produced acoustic emissions signals. During the first load application there is a considerable amount of acoustic emissions, even more than two orders greater than that observed in thermal tests. The difference between mechanical and thermal test can be attributed to the difference in the of stressed volume in the two tests. Thermal load was focused on a small spot on the surface of the specimen, mechanical one involved the whole specimen.

After the first load application, the number of cracks and defects didn't increase substantially. So the emission linked to this phenomenon is almost absent, causing a considerable reduction of the number of the recorded acoustic emissions. The number of counts for each following load cycle had a tendency to decrease, according to a negative exponential function. It results interesting to underline that the number of emissions detected didn't tend to zero but reached a minimum value, depending on the load applied. This value is related with the background noise connected to acoustic signals produced by the tensile machine itself.

A constant term has to be added to the exponential equation in order to properly describe the behavior of the number of hits as a function of subsequent loading cycles.

$$\#\ \text{Hits} = a^{*} e^{(b*N)} + c \tag{38.2}$$

Where N corresponds to the number of the mechanical cycle.

The constant c represents is introduced to quantify the background noise of testing machine, i.e. a minimum number of emissions (proportional to the applied load) recorded in any test carried out.

Experimental tests show a proportionality between the applied load and the number of emissions recorded. So applying a greater load corresponds to record a greater number of hits.

This type of test confirms the presence of the Kaiser effect in mechanical tests as in thermal one. The exponent characteristic of this function is smaller than in thermal case (larger in absolute value). The calculated mean value for b in the case of mechanical loading was $b = -7.68$ to be compared with the value $b = -1.202$ obtained during thermal tests. This can be explained in view of the fact that the effect of the residual stress variation was not present in mechanical tests, and so the acoustic emission was totally related to the nucleation and/or propagation of micro cracks and internal defects.

38.4 Conclusions

In this work the correlation between the acoustic emission and a localized annealing treatment of stress relaxation was analyzed. Results obtained allowed to identify a negative exponential law to describe the number of hits recorded in each thermal cycle. Results showed a relation between the application of thermal gradient and acoustic emissions, confirming the release of elastic energy during the residual stress relaxation. The presence of a thermal Kaiser effect justifies the falling detections in following cycles. Mechanical tests were also carried out. These tests confirm the presence of the Kaiser effect however, without the influence of residual stress relaxation, the exponential falling appear to be steeper.

References

1. Miller RK, McIntire P (1987) Acoustic emission testing, vol 5, 2nd edn, Nondestructive testing handbook. American Society for Nondestructive Testing, Columbus, Ohio, pp 275–310
2. Drouillard TF, Glenn TG (1985) Production acoustic emission testing of braze joint. J Acoust Emiss 1(2):8l–85l
3. Pao YH (1978) Theory of acoustic emission, elastic waves and non-destructive testing of materials, AMD 20. American Society of Mechanical Engineers, New York, USA, pp 107–128
4. Enoki M, Kishi T, Kohara S (1983) Determination of microcracking moment tensor of quasi-cleavage facet by AE source characterization, progress in acoustic emission III. In: Proceedings of the eighth international acoustic emission symposium, The Japanese Society for Non-Destructive Inspection, pp 763–770
5. Venkitakrishnan PV, Sinha PP, Krishnamurthy R (2005) Study and analysis of residual stresses due to various secondary processes in AA 2219 annealed sheet using acoustic emissions and hole drilling methods. NDT&E Int, 38:615–622
6. www.mistrasgroup.com
7. Viotti MR, Sutério R, Albertazzi A, Kaufmann GH (2004) Residual stress measurement using a radial in-plane speckle interferometer and laser annealing: preliminary results. Opt Lasers Eng 42:71–84
8. Kaiser J (1953) Erkenntnisse und Folgerungen aus der Messung von Geräuschen bei Zugbeanspruchung von Metallischen Werkstoffen. Arch Eisenhüttenwes 24(1–2):43–45
9. Miller RK, McIntire P (1987) Acoustic emission testing, vol 5, 2nd edn, Nondestructive testing handbook. American Society for Nondestructive Testing, Columbus, Ohio, pp 58–61, 84–88
10. Dunegan HL, Tetelman AS (1971) Acoustic emission. Res Dev 22(5):20–24

Chapter 39
Optical Analysis of Weld-Induced Residual Stress by Electronic Speckle-Pattern Interferometry

Sean Craft, Saugat Ghimire, Bishwas Ghimire, T. Sasaki, and Sanichiro Yoshida

Abstract Electronic Speckle-Pattern Interferometry (ESPI) is applied to analysis of residual stress induced by laser welding. A thin plate of stainless-steel is butt-welded to a carbon-steel plate of the same dimension to form a dissimilar-weld specimen. Similarly, a pair of stainless-steel plates and that of carbon-steel plates are respectively butt-welded to each other to form similar-weld specimens. The dimensions of the dissimilar and simlar-weld specimens are all the same. A tensile load is applied to the specimen perpendicular to the weld line and at a constant pulling rate until the stress on the sample is approximately a quarter of the yield stress. The resultant deformation is monitored with an ESPI setup sensitive to the in-plane displacement component parallel to the tensile axis. Interferometric images are formed at a fixed time interval, and fringe patterns representing contours of the in-plane displacement are created by subtracting the image taken at each time step from several time steps after. Resultant fringe patterns show behaviors that can be interpreted as revealing residual stress.

Keywords Residual stress • Electronic speckle-pattern interferometry • Laser welding • Nondestructive analysis • In-plane deformation

39.1 Introduction

Residual stresses are locked in materials. They arise from a wide range of manufacturing processes and can cause serious problems such as unwanted distortion, weakness, and even failure. Unlike stress due to external loading, they are hidden inside the material and cannot be directly measured from outside. Analysis of residual stress therefore requires a certain step to change the stress state and read out the resultant change in displacement or strain. Prevailing techniques such as the layer removal [1], hole-drilling [2] and incremental slitting methods [3] relax the residual stress through removal of the surrounding material and determine the residual stress from the resultant strain redistribution. These are well-established and reliable technique, but destructive by nature and limited to localized area analysis. As a non-destructive method, analysis with local laser heating [4] is available. Most residual stress is caused by some sort of heating action during the manufacturing process coupled with thermal gradient during the cooling process. For this type of residual stress, the laser heating technique is effective as it essentially relaxes the residual stress by reversing the process. However, estimation of thermal load by laser radiation is not straightforward.

Considering the above situation, we are interested in developing a non-destructive technique of residual stress analysis, and have recently started an experimental project. Our idea is rather straightforward; we apply a tensile load to a specimen of minimum strength and within the elastic regime, read out the response of the specimen as a full-field displacement pattern using optical interferometry and make diagnoses based on the observed displacement pattern. In this study, we made analyses on residual stress caused by welding of thin-plates – welding is one of the most common causes of residual stress in the metalwork and is a classic problem of mechanical engineering [5]. The aim of this paper is to report on preliminary results of

S. Craft • S. Ghimire • B. Ghimire • S. Yoshida (✉)
Department of Chemistry and Physics, Southeastern Louisiana University, SLU 10878, 70402 Hammond, LA, USA
e-mail: syoshida@selu.edu

T. Sasaki
Department of Engineering, Niigata University (Japan), Niigata University, Ikarashin Ninocho 8050, 950-2181
Nishi-ku, Niigata-shi, Niigata, Japan

M. Rossi et al. (eds.), *Residual Stress, Thermomechanics & Infrared Imaging, Hybrid Techniques and Inverse Problems, Volume 8*,
Conference Proceedings of the Society for Experimental Mechanics Series, DOI 10.1007/978-3-319-00876-9_39,

the project. The experimental procedures are described along with the analysis of the displacement patterns. These results can be interpreted as representing qualitative features of the residual stress caused by the welding, and thereby indicates the feasibility of the present method for quantitative analysis.

39.2 Experimental

39.2.1 Specimens

Table 39.1 lists the materials and welding conditions of the specimens. Typically, two plates of 100 mm (wide) × 50 mm (long) × 0.3 mm (thick) stainless steel (SUS 304) are butt-welded together, along the 50 mm sides, and cut, normal to the weld line, into 5 specimens that are 20 mm wide × 100 mm long (the SUS-SUS welded). Similarly, two plates of low-carbon steel (SPCC) of the same width and length as the SUS plate and 0.4 mm thick are butt-welded and cut into specimens of 20 mm × 100 mm (the SPCC-SPCC welded).[1] For the SUS-SPCC weld, a plate of SUS and one of SPCC, of the same dimensions as used above, are butt-welded together and then cut into specimens of 20 mm × 100 mm in the same manner as described above. The heat source of the welding was a pulsed Nd:YAG laser. On welding, the plates were held on the table and the laser beam was applied from the top along the butted sides of the plates.

In butt-welding, residual stress is caused by heat arising during the welding process coupled with a thermal gradient during the cooling process. Figure 39.1 schematically illustrates typical residual stresses in a similar-weld specimen and dissimilar-weld specimen. In the similar weld-specimen case, the residual stress is mainly caused by the temperature gradient along the weld line. When the welding is initiated from one end of the butted side, say from the bottom side as in Fig. 39.1a, the material at the joint shrinks as it is cooled after the laser beam passes away. On the other hand, the part of the material currently being joined tends to expand as it is heated by the laser beam. Consequently, if the plates are not held to the table, they tend to rotate as indicated by the dashed line in Fig. 39.1a. To avoid this opening, the holding mechanism keeps applying counteracting force. Consequently, when the welding is completed, the top end of the welded region is compressed (restrained from expansion), and the bottom end is stretched (restrained from shrinking). In the case of a dissimilar-weld specimen, in addition to the same tendency as the similar weld-specimen case, the side of the weld line where the material has higher thermal expansion tends to be stretched (because when cooled it tends to shrink more) and the other side tends to be compressed.

39.2.2 Loading Pattern and Strain Measurement

To investigate residual stress, it is essential that the applied load does not cause permanent deformation. To avoid permanent deformation, we applied a tensile load to the specimen up to approximately a quarter of the yield stress, and relaxed the load by reversing the direction of the test machine's dynamic head, and moving it at a constant speed until the load was zero; care

Table 39.1 Specimen's materials and welding conditions

	SUS	SPCC		Welding condition	
Young's modulus (E)	193	211.4	GPa	Heat source	Nd:YAG laser
Density	8,000	7,850	kg/m^3	Mode	Pulse
sqrt(E/r)	4.911	5.189	km/s	Average power	1.5–2.1 kW
Thermal expansion coefficient	17.3	11.7	ppm/K	Frequency	2 Hz

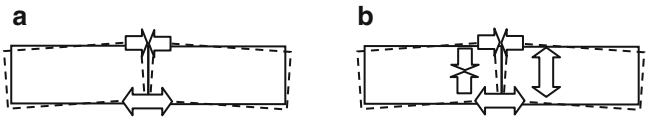

Fig. 39.1 Residual stress in (**a**) similar welded and (**b**) dissimilar welded specimens

[1] The thickmess of the SUS and SPCC plates were different simply because of the availability of the materials.

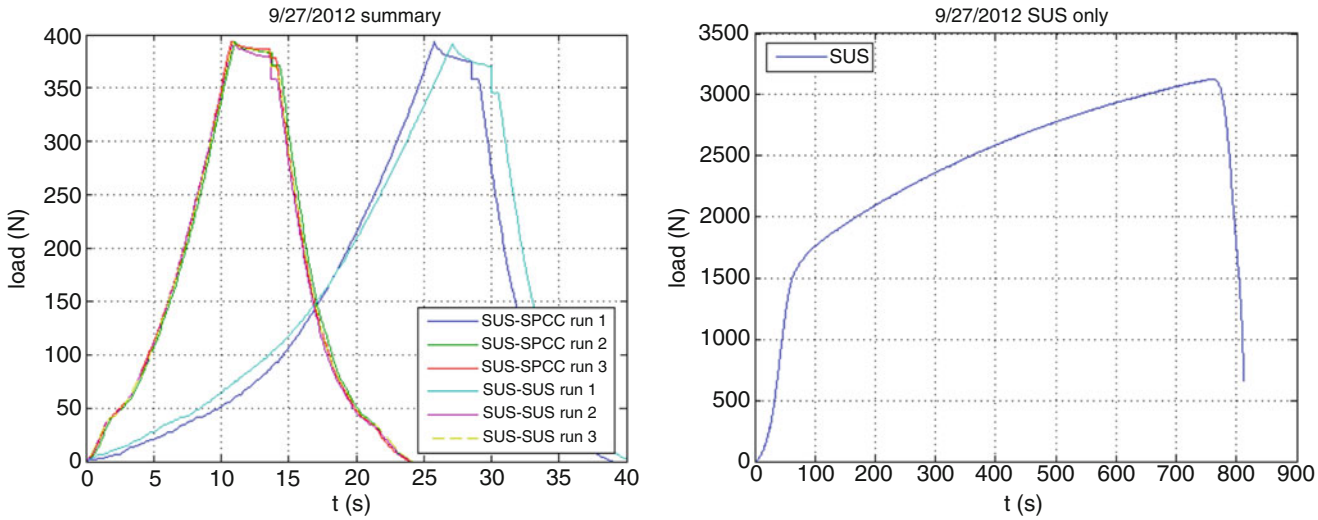

Fig. 39.2 Loading characteristics of welded specimens (*left*) and SUS specimen (*right*)

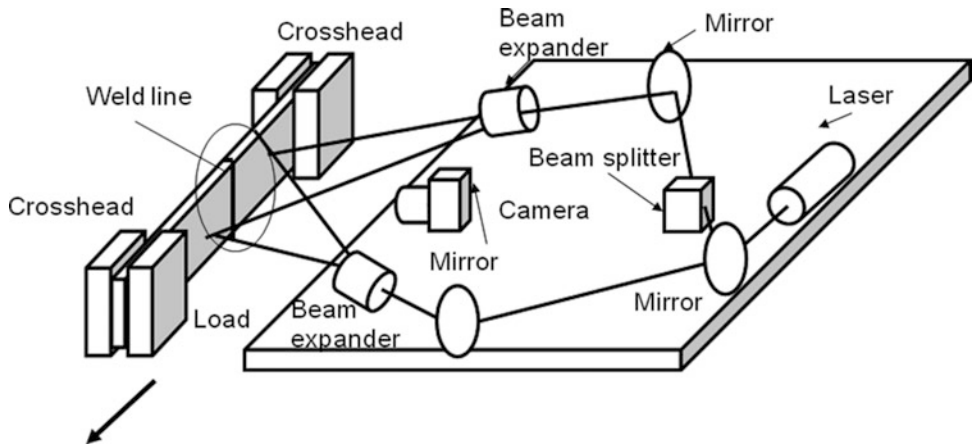

Fig. 39.3 ESPI setup

was taken to avoid negative loading. Subsequently, without dismounting the specimen from the test machine, we repeated the same tensile-compress cycles across several runs. The repetitions were important to confirm that the specimen did not experience permanent deformation, and also to ensure that slip effects were minimized as the head's grip on the sample becomes firmer after the first run. The test machine's head speed was set at a constant rate of 30 μm/s for both the tensile and compress phases. Figure 39.2a shows the loading characteristics of the specimen for the first three cycles of a similar and dissimilar-weld specimen (SUS-SUS welded and SUS-SPCC welded) comparing them with the loading characteristics of a pure SUS specimen of the same material and dimension shown in Fig. 39.2b. As seen in (a), the loading characteristics of the second and third runs overlap with each other, indicating that the deformation is elastic. The different behaviors for the first runs are believed to be due to slippage of the specimen inside the grip. This is evidenced by the fact that when a specimen was reloaded with the same tensile-compress pattern after being dismounted from the test machine at the end of the third run, the loading characteristics of the fourth run was similar to that of the first run, while the loading characteristics of the fifth and sixth runs overlapped with those of the second and third runs. Note that the maximum load of 400 N in (a) is approximately a quarter of the yield load seen in (b).

Figure 39.3 illustrates the arrangement of strain measurement with an Electronic Speckle-pattern Interferometer (ESPI) setup. The specimen was loaded horizontally, and the ESPI was sensitive to in-plane displacement of the specimen whose

weld line was vertical. The CCD camera took the image of the specimen at a constant frame rate of 30 frames per second. The image data was sent to computer memory and subtracted from the image taken 10–15 frames earlier. In this fashion, so called-fringe patterns representing contours of equi-displacement lines were formed.

39.3 Results and Discussion

39.3.1 Comparison of SUS-SUS, SPCC-SPCC and SUS-SPCC Welded Specimens

We tested the three types of specimens, the similar weld specimens of SUS-SUS and SPCC-SPCC welded, and the dissimilar weld specimen of SUS-SPCC welded. Careful examination of fringe patterns in all the specimens in the entire loading range tested revealed specific differences between the similar-weld and dissimilar-weld specimens. Figure 39.4 shows the differences. Here, the left column shows pairs of fringe patterns observed in the SUS-SUS welded (the top two, a1 and a2), SPCC-SPCC welded (the middle two, b1 and b2) and the SUS-SPCC welded (the bottom two, c1 and c2). The plot placed to the right of each pair is the corresponding loading characteristics. In the similar weld specimens, common to the SUS-SUS and SPCC-SPCC welded, the fringe patterns are characterized by the initial pattern consisting of vertical fringes on one side of the weld line (at the horizontal center of the image) followed by patterns consisting of horizontal lines on both sides of the weld line. In the left column (images) of Fig. 39.4, (a1) and (b1) represent the former pattern whereas (a2) and (b2) represent the latter. These patterns were observed only in an initial stage of tensile cycle and a final stage of compress cycle where the load is low. In the right column of Fig. 39.4, the points where each fringe pattern was observed are indicated on the loading characteristics. Notice that the loading characteristics show a small plateau when these patterns were observed. In the other loading range, the similar and dissimilar weld specimen did not show a notable difference in the observed fringe patterns. The dissimilar-weld specimen showed horizontal fringes on both sides of the weld all the time. From these observations, we suspect that the small plateau in the loading characteristics is related to the residual stress associated with the welding. More will be discussed on this in the next section.

39.3.2 Comparison of Unheated and Heated Welded Specimens

To determine whether or not the small plateau observed in Fig. 39.4 is related to residual stress due to welding, we repeated the same procedure as discussed in the preceding section using a pair of welded specimens. One of the pair was heated after the welding (heat-treated) whereas the other was not heat-treated. The post-weld heating treatment is known to relax any residual stress. Figure 39.5 compares the loading characteristics of the SUS-SUS weld specimen with the heating treatment (dashed line) and the SUS-SUS weld specimen without treatment. It is seen that the untreated specimen shows a small plateau similar to the one in Fig. 39.4 (a3) but the treated specimen does not show a clear plateau.

Figure 39.6 shows fringes observed in the unheated (left) and heated (right) SUS-SUS weld specimen. The straight line running vertically along the horizontal center of the image is the weld line. (a) – (c) in Fig. 39.5 indicate the load levels when these fringes were taken. Fringes are faint in both the untreated and treated specimen for (a) and (b). The dashed lines are traces of the faint fringes inserted for better visualization. In (a) and (b), apparently the unheated and heated cases show different fringe patterns from each other; in the case of the unheated, the right half of the specimen show curved, horizontal fringes both in (a) and (b) similar to Fig. 39.3 (a1). On the other hand, there is little to no difference between the unheated and heated cases for (c).

The observations in Figs. 39.5 and 39.6 can be interpreted as follows. From the fringe patterns, it is speculated that when the specimen has residual stress, one half of the specimen rotates as a rigid body with negligibly small deformation and the other half stretches.[2] As indicated in Fig. 39.1a, a similar-weld specimen typically is stretched near the end where the welding is initiated and compressed at the other end where the welding is completed. When such a specimen is pulled perpendicularly to the weld line, the compressed end stretches more easily than the already stretched end. This explains the rotating half of the specimen. The other half (non-rotating half) of the specimen can be explained by assuming that this

[2] In fringe patterns formed by an ESPI setup sensitive to horizontal in-plane displacement, horizontally parallel contours represent pure rotation or shear, and vertically/ parallel contours stretch or compression.

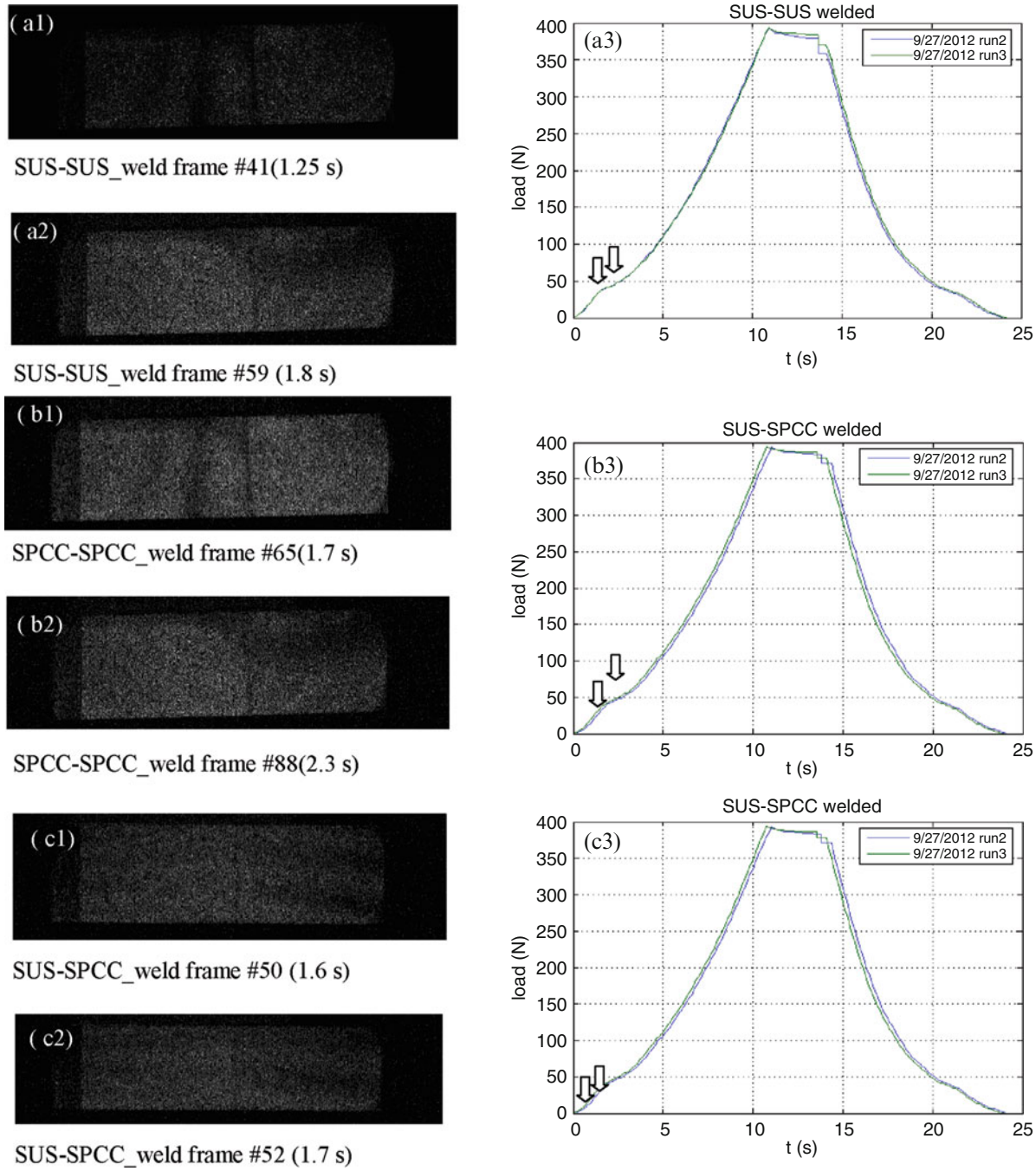

Fig. 39.4 Fringe patterns observed in the SUS-SUS, SPCC-SPCC and SUS-SPCC specimens and corresponding loading characteristics. The fringe images were observed in the second run of the tensile-compress cycle

stretch-compression phenomenon due to residual stress occurs predominantly on one side of the weld line. When the compressed end is relaxed and the stretched end further stretched by the external force (exerted by the test machine), the boundary near the weld line of the non-rotating half displaces in the tensile direction resulting in rather uniform stretch over the enter region of this half. When the specimen is heated after the welding, on the other hand, the residual stress due to the weld is relaxed. Therefore, both side of the specimen across the weld line behave more or less in the same fashion. The fringe patterns in the right column of Fig. 39.6 indicate this. When the stress level reaches (c) in Fig. 39.5, the fringe patterns observed in the untreated and treated specimens show basically the same feature; both sides of the specimen rotate. This can be interpreted as that by this time the compression due to the residual stress has been relaxed and therefore the behavior of

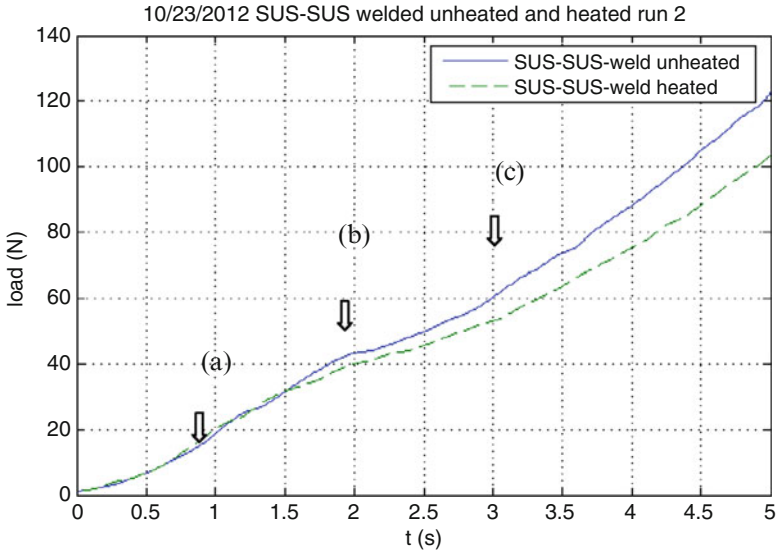

Fig. 39.5 Loading characteristics of post-welding heat-treated and untreated SUS-SUS weld specimens

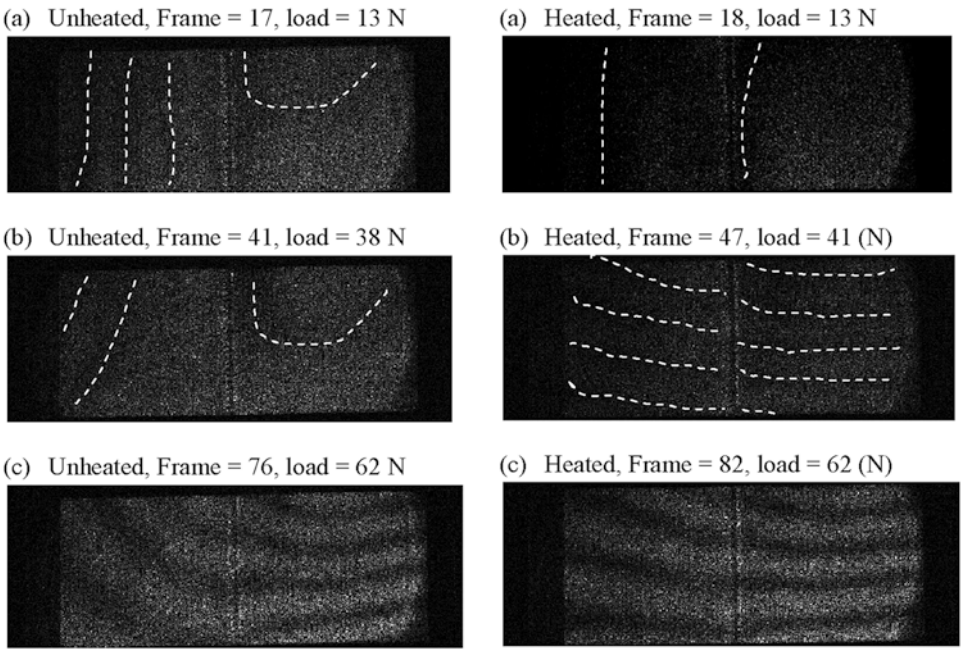

Fig. 39.6 Fringes observed in untreated (*left*) and heat-treated SUS-SUS welded specimen

the untreated specimen is similar to that of the treated specimen. It is not clear why both halves of the specimen show rotation-like motion. It is interesting to note that the different behaviors in the fringe pattern between the treated and untreated specimens occur near the small plateau in the loading characteristics. It is considered that while the compressed end (which is due to the residual stress) relaxes, the test machine's head exerts less force as it moves (the pulling rate is still constant, but the force experienced by the sample/head is lessened because more strain is occurring than tensile stress). This can naively explain the presence of the small plateau. More investigation is definitely necessary for more conclusive argument.

39.4 Conclusions

The present study indicates the feasibility of the described method to analyze residual stress arising from welding. The observed ESPI fringes differentiate the similar-welded and dissimilar-welded specimens. The observed difference can be interpreted as explaining the qualitative feature of residual stress of the respective case, i.e., residual stress in similar-weld specimens is mainly due to temperature gradient along the weld line whereas that in dissimilar-weld specimen is also caused by the difference in thermal expansion. Comparison of fringe patterns between similar-weld specimens with and without post-heating treatment supports these arguments.

Acknowledgement This study has been supported in part by the National Science Foundation International Research Experience for Student Grant (IRES-0927033) awarded to Southeastern Louisiana University, the Tokyo Denki University internal research grant, Southeastern Louisiana University Orr grant, and the National Research Foundation of Korea (grant No. 2011–001790).

References

1. Eijpe MPIM, Powell PC (1998) Determination of residual shear stress in composites by a modified layer-removal method. J Mater Sci 33:2019–2026
2. Schajer GS, Yang L (1994) Residual-stress measurement in orthotropic materials using the hole-drilling method. Exp Mech 12:324–333
3. Roberts SJ, McCartney LN, Broughton WR (2011) A novel method of determining stress distribution in plates using the incremental slitting technique. J Strain Anal Eng Des 46:280–297
4. Vikram CS, Pchersky MJ, Feng C, Engelhaupt D (1996) Residual-stress analysis by local laser heating and specle-correlation interferometry. Exp Tech 20:27–30
5. Bate SK, Green D, Buttle D (1997) A review of residual stress distribution s in welded joints for the defect assessment of offshore structures, Health safety exclusive – offshore technology report, Her Majesty's Stationery Office, Norwich NR3 1BQ, ISBN 0-7176-2411-0

Chapter 40
Shape Is Not Enough to Test Hypotheses for Morphogenesis

Victor D. Varner, Gang Xu, and Larry A. Taber

Abstract During embryogenesis, tissues and organs often undergo dramatic changes in shape. Identifying the forces that drive these shape changes is crucial to understanding morphogenetic mechanisms. Here, we show how experiments in conjunction with finite-element modeling can be used to study the source, distribution, and evolution of passive and actively generated tissue stresses during development. This paper focuses on two illustrative examples: head fold formation and folding of the cerebral cortex. Because different combinations of forces may produce similar shapes, morphogenetic mechanisms cannot be determined by matching global changes in geometry alone. Other types of data are needed, including stress and strain distributions. Here, tissue stress is estimated using dissection experiments, while strains are measured by tracking the motions of tissue labels. The results provide new insight into the physical mechanisms that drive the formation of the head fold in the early embryo and cortical folding in the brain at later stages of development.

Keywords Residual stress • Biomechanics • Finite-element models • Embryo • Development

40.1 Introduction

The presence of residual stress in the cardiovascular system has been known at least since 1960, when Bergel [1] found that artery rings spring open following a transmural cut. More than two decades later, investigators studied the functional significance of residual stress [2–4]. In the aorta, for example, Chuong and Fung [5, 6] showed that residual stresses help homogenize wall stress at normal physiological pressures. This leads to greater efficiency, as smooth muscle in small arteries would then perform nearly equal work across the wall when the muscle contracts to regulate blood flow [7]. Moreover, Fung and others have shown that residual stress in arteries evolves following a perturbation in blood pressure, suggesting that these stresses may play an important role during functional adaptation [8, 9].

In the embryo, Beloussov and colleagues have been studying residual stress since the 1970s [10]. Like Bergel, Fung, and others, these investigators characterized residual stress by cutting the tissue and observing the resulting deformation. Their results led them to propose a fundamental principle called the Hyper-restoration (HR) Hypothesis [11]. The basic idea of HR is that embryonic tissues respond actively to changes in stress in a way that tends to restore the original stress state, but generally overshoots the original stress to the opposite side. For example, a decrease in tension elicits active contraction which increases the tension to a value greater than it was originally. Beloussov suggests that the overshoot then triggers a new response, and so on, potentially driving a morphogenetic event to completion [11, 12].

Although the validity of the HR Hypothesis is uncertain [13, 14], the importance of stress in morphogenesis is clear. Most embryonic tissues and organs do not simply grow into their final shapes. Rather, they undergo rather complex

V.D. Varner
Department of Chemical and Biological Engineering, Princeton University, Princeton, NJ 08544, USA

G. Xu
Department of Engineering and Physics, University of Central Oklahoma, Edmond, OK 73034, USA

L.A. Taber (✉)
Department of Biomedical Engineering, Washington University, St. Louis, MO 63130, USA
e-mail: lat@wustl.edu

M. Rossi et al. (eds.), *Residual Stress, Thermomechanics & Infrared Imaging, Hybrid Techniques and Inverse Problems, Volume 8*, Conference Proceedings of the Society for Experimental Mechanics Series, DOI 10.1007/978-3-319-00876-9_40,

deformations from relatively simple initial morphology [15]. These deformations are driven by mechanical stresses exerted by neighboring tissues, as well as stresses generated intrinsically by active processes including differential growth, actomyosin contraction, actin polymerization, cell intercalation, and cell migration [16].

It is important to realize that the term "residual stress" may not be appropriate for biological tissues, as stress can be generated by mechanisms acting in various constituents at several different length scales. For example, a single radial cut does not relieve all residual stress in an arterial ring; hence, multiple cuts are necessary to characterize the stress distribution across the wall [17]. But how many cuts are needed? Sometimes just a few cuts can provide a reasonable estimate of stress at the tissue level [8]. But what about at the cell and subcellular levels, where most of the stress-generating activity occurs? In theory, one can keep dissecting a tissue almost indefinitely. So it may be better to just use the term "stress" and clearly state the conditions, length scale, and tissue constituents where the stress occurs.

From an engineering perspective, one important reason to determine evolving stress distributions in the embryo is to test computational models. Typically researchers determine morphogenetic mechanisms by perturbing development and observing the resulting effects. Using intuition, they then propose a hypothesis to explain what they observe and conduct further experiments to test their hypothesis. There can be several problems with this approach: (1) The inherent complexity of morphogenesis can make intuition misleading; (2) similar shapes sometimes can be generated by multiple mechanisms; and (3) perturbing one mechanism may trigger a backup response, which may have evolved to help minimize developmental defects. Models can help limit the number of possibilities by showing which mechanisms are physically plausible. Moreover, stress and strain distributions can help distinguish between different mechanisms, which may produce essentially the same morphology but different stress and strain fields.

To illustrate how computational modeling can be integrated with measurements of stress and strain to deduce physical mechanisms, we herein consider two problems: (1) head fold (HF) formation and (2) folding of the cerebral cortex in the brain.

40.2 Methods

To study HF formation, fertile white Leghorn chicken eggs were incubated at 38.5 °C to obtain embryos at stages 5–7 (23–29 h) as defined by Hamburger and Hamilton [18], who divided the 21-day incubation period of the chick into 46 stages. Whole embryos were cultured using a filter paper method [19]. Optical coherence tomography (OCT) was used to acquire 3-D images.

Tissue strains during morphogenesis were measured by tracking the motions of fluorescent tissue markers [20]. Tissue stress was characterized by using micropipettes to excise circular plugs of tissue and analyzing wound geometry [21]. To minimize a possible wound healing response, only 30–45 s elapsed between wounding and image capture.

Cortical folding was studied in brains extracted from ferrets on postnatal days P6, P18, and adult (9- and 12-month old) immediately after sacrifice. A vibratome was used to cut 600-μm-thick coronal slices. To probe tissue stress, a razor blade was used to make radial and circumferential cuts in brains fully submerged in aCSF.

Finite-element models were created using COMSOL Multiphysics. A theory for finite volumetric growth [22] was used to simulate morphogenesis [20, 23].

40.3 Results and Discussion

During its earliest stages of development, the chick embryo is a relatively flat membrane consisting of three primary germ layers called ectoderm, mesoderm, and endoderm [15]. The mesoderm, which is composed mainly of loose (mesenchymal) cells, lies between the other two layers, which are cell sheets (epithelia). The HF and brain are primarily of ectodermal origin.

Head Fold Formation. The HF, the first major 3-D structure to form in the embryo, essentially initiates brain, heart, and foregut development. The HF is a crescent-shaped ridge that lies anterior to the relatively thick neural plate (NP) (Fig. 40.1a), which later develops into the brain and spinal cord. As the HF forms, it contacts the vitelline membrane (Fig. 40.1b). Although biologists have studied this problem since the late 1800s, the mechanisms of HF formation have remained poorly understood [20].

Recently, we proposed a new hypothesis for HF formation that includes three sets of driving forces [20]: (1) convergent extension, which causes the NP to elongate longitudinally and shorten transversely; (2) active cell-shape changes that cause

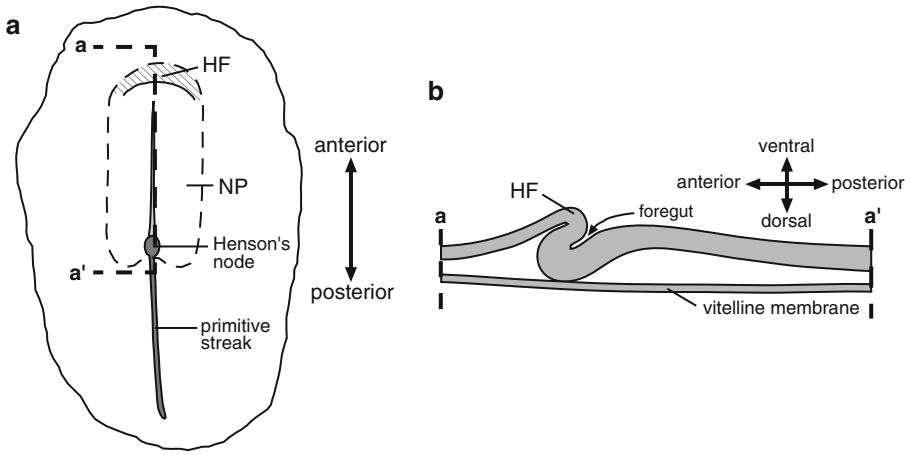

Fig. 40.1 (**a**) Schematic of HH stage 7 chick embryo (*HF* head fold, *NP* neural plate) (**b**) Midline section a–a′ (From [20])

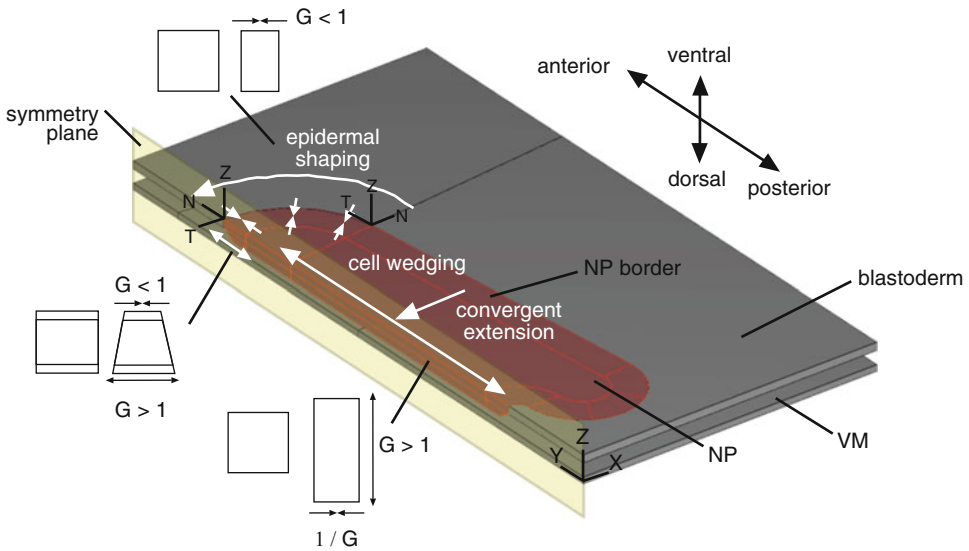

Fig. 40.2 Finite-element model for head fold formation. *Top layer*: ectoderm; *bottom layer*: vitelline membrane (*NP* neural plate, *G* growth) (From [20])

cells to become wedge shaped (cell wedging) within the HF region; and (3) active transverse shortening (epidermal shaping) in a region anterior to the HF. All of these processes are based on experimental observations [20].

To test our hypothesis, we created a 3-D finite-element model consisting of two neo-Hookean plates representing the ectoderm and vitelline membrane (Fig. 40.2). The NP is a thickened region of the ectoderm, and frictionless contact between the initially separated plates is assumed. All driving forces are simulated via growth [20]. For example, convergent extension is modeled as positive longitudinal growth and negative transverse growth within the NP, while cell wedging is simulated by a linear growth gradient across the plate thickness. In addition, the ectoderm is subjected to equibiaxial tension.

Our initial model included only convergent extension and cell wedging, and material properties were assumed to be homogeneous. This model yielded good agreement with experimental HF shape [24], which has been considered by some modelers as adequate validation. A simple example shows that accurate reproduction of normal morphology may not be sufficient, however. Consider bending of a cantilever beam by differential growth. In case 1, the bottom half of the beam grows uniformly, while the top layer remains passive. In case 2, a linear distribution of axial growth is specified across the beam thickness (simulates cell wedging). Although the beam bends into a circular shape for both cases, the stress distributions are fundamentally different (Fig. 40.3). In fact, cell wedging bends the beam without creating stress. Hence, matching morphology alone is not enough to validate a model for morphogenesis.

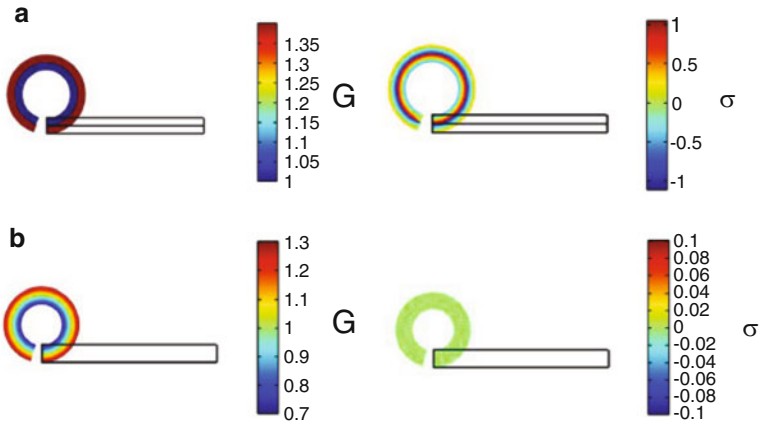

Fig. 40.3 Bending of cantilever beam (**a**) Growth of *bottom layer* (**b**) Cell wedging (G axial growth, σ bending stress)

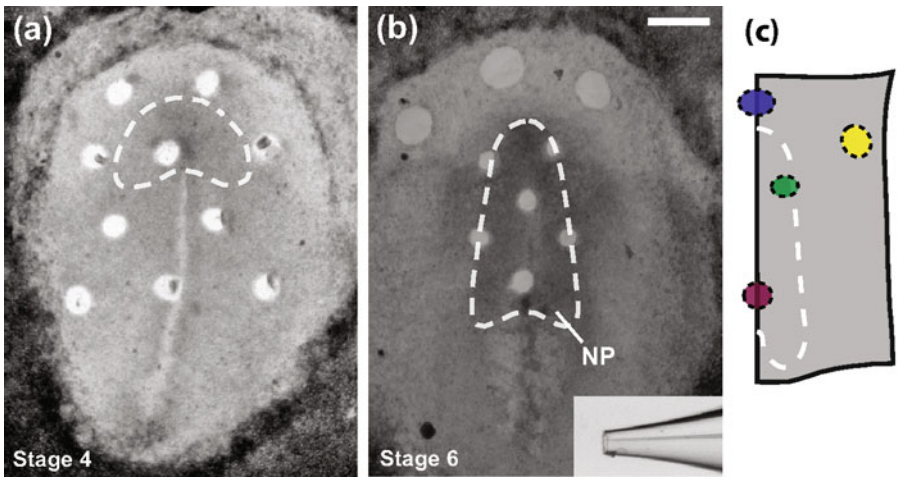

Fig. 40.4 Holes punched into embryo to characterize stress (**a**) Before head fold begins to form, holes open uniformly to indicate equibiaxial tension (**b**) After head fold formation, greater tension occurs outside the neural plate (NP, *dashed curve*), while compression is present inside the NP (**c**) Results from model are in reasonable agreement with data (From [20])

To further test the model, we measured morphogenetic strains during HF formation. Numerical and experimental patterns of normal strain were in reasonable agreement, but, contrary to the data, the model predicted discontinuous shear strains across the NP border [24]. The discontinuity in the model was caused by the relatively thicker and therefore stiffer NP. Speculating that the elastic modulus of the NP is actually smaller than that of surrounding tissue, we measured material properties using microindentation tests. The results showed that the modulus of the NP is about half that of the surrounding tissue [24]. With the adjusted properties, the model then gave a continuous shear strain distribution, but the softer NP made HF geometry less accurate. Including the third driving force (transverse shortening) fixed this problem (see Fig. 40.5a), but there still was a need for further testing.

Next, we estimated tissue stress by punching circular holes at various locations in the ectoderm [20, 21]. Before HF formation, all holes were relatively circular and opened to about the same size, larger than the tip diameter (Fig. 40.4a). This indicates that the embryo is initially in a state of relatively uniform equibiaxial tension. During HF formation, the hole size (immediately after punching in other embryos) indicates still greater tension outside the NP but compression inside the NP (Fig. 40.4b). Simulating these experiments with the model yielded similar results (Fig. 40.4c).

Finally, we examined the predicative capability of the model by perturbing morphogenesis. In one experiment, we cut holes to disrupt the stresses on either side of the HF. In another experiment, we removed the vitelline membrane before culture. For both perturbations, the model predicts that the HF acquires an abnormal v-shape, consistent with the experimental results (Fig. 40.5b). Taken together, these results support our hypothesis, although further testing is needed.

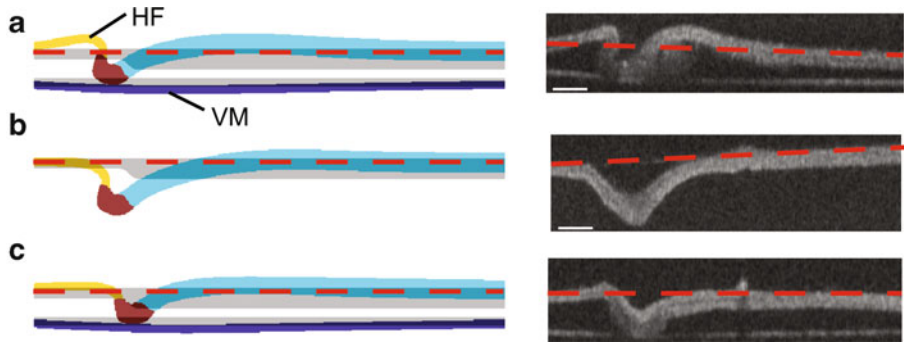

Fig. 40.5 Effects of mechanical perturbations on head fold (HF) morphology (*left column*: model; *right column*: experiment). Longitudinal midline sections are shown (**a**) Control embryo (**b**) Vitelline membrane (VM) removed (**c**) Cuts made to relieve stress on left and right sides of HF (From [20])

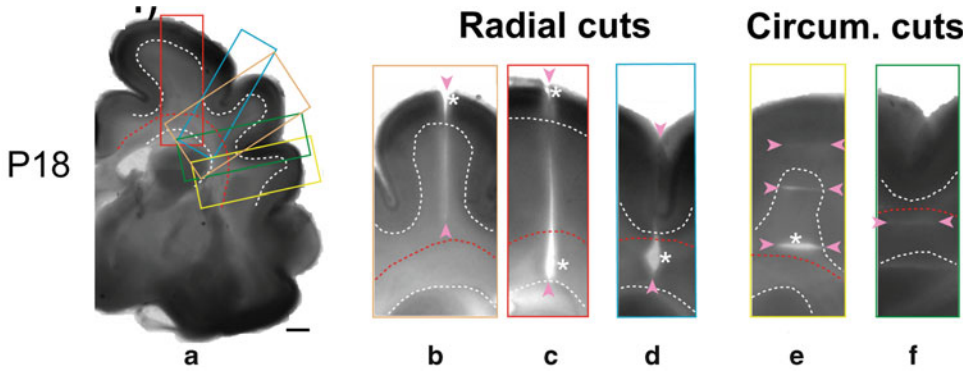

Fig. 40.6 Cuts reveal stress in ferret brain slice 18 days after birth. Importantly, radial cuts through a gyrus (**b**) do not open in interior of gyrus, contradicting the axon tension hypothesis. *Arrowheads* indicate cuts; *asterisks* indicate cut openings (From [23])

Cortical Folding. The cerebral cortex is an outer layer of gray matter in the brain that folds into characteristic patterns in most large mammals. Abnormal folding is associated with various neurological disorders [25]. The mechanisms that cause this folding are intrinsic to the brain [26], but otherwise cortical folding remains a poorly understood process.

During the past few decades, two hypotheses have dominated thinking on this topic. The first is based on differential growth [27], whereby differences in growth rate between cortical layers cause the surface to buckle or fold. The second postulates that folding is driven by tension generated in axons [28], which pull strongly interconnected cortical regions together, causing folds to develop. Until recently, however, both hypotheses have been based primarily on speculation.

Since these two mechanisms would be expected to produce different stress fields, we used dissection experiments to examine stress in the brain during the folding process [23]. Ferret brains were used for this purpose, since cortical folding in these animals occurs during the first few weeks after birth [29, 30]. Cuts were made at various locations and orientations in fresh brain slices. A cut that opened indicated tension perpendicular to the cut; a cut that did not open indicated little stress or compression.

Radial cuts through gyri (outward folds) opened near the brain surface and in the interior white matter tract, which consists primarily of axons. These results indicate that axons are indeed under considerable tension (Fig. 40.6c). However, little or no tension was found across the interior of gyri (Fig. 40.6b), contradicting the axon tension hypothesis.

To test the differential growth hypothesis, we created a model for a brain slice. First, isotropic growth of the gray matter puts the white matter tract (red region) into tension (Fig. 40.7a). Next, growth is specified in one region of the cortex to give a single gyrus, and then another region grows to give a second gyrus. We also assumed that the gray matter (subplate) between the cortex and the white matter tract grows in response to stress through feedback laws. The resulting folds are similar to experiments (compare Figs. 40.6a and 40.7c). To test this phased differential growth model further, we simulated radial cuts. As in the experiments, the cuts opened in the white matter tract (Fig. 40.7e, g). They also opened at the outside of gyri (Fig. 40.7e) but remained closed at the outside of sulci (inward folds, Fig. 40.7g). All of these results agree with our experimental data (Fig. 40.6). Hence, our model supports the differential growth hypothesis.

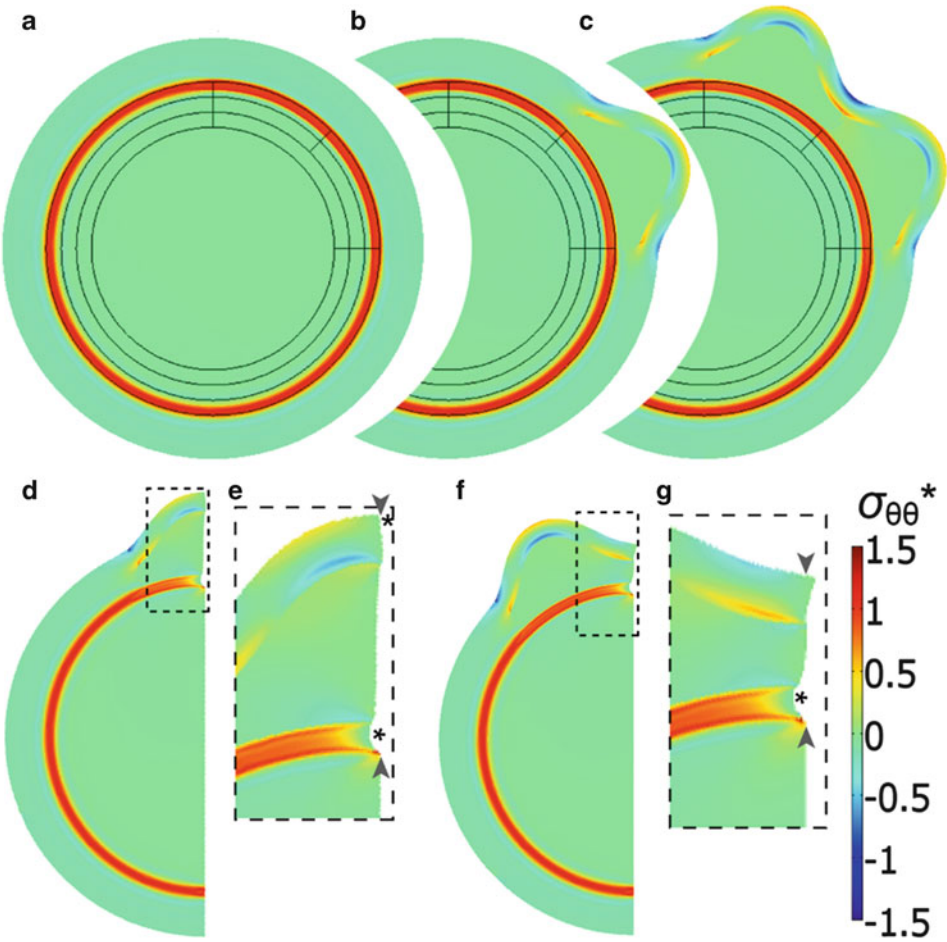

Fig. 40.7 Phased differential growth model for cortical folding (**a**–**c**) Cortex grows regionally to produce two gyri. Radial cuts through gyrus (**d**, **e**) and sulcus (**f**, **g**) indicate stresses in agreement with experiments (see Fig. 40.6) (From [23])

40.4 Conclusions

For several reasons, determining the physical mechanisms of morphogenesis is a particularly challenging problem in mechanics. The problems often involve complex geometry, are highly nonlinear with multiple solutions, and are driven by both passive and active stresses generated at multiple scales. Combining experiments and computational modeling is a useful approach to solving these problems. In general, models must be able to predict realistic stress and strain distributions in addition to morphology.

Acknowledgments This work was supported by NIH grants R01 HL083393 and R01 NS070918, as well as NSF grant DMS-054070.

References

1. Bergel DH (1960) The viscoelastic properties of the arterial wall. University of London, London
2. Vaishnav RN, Vossoughi J (1983) Estimation of residual strains in aortic segments. In: Hall CW (ed) Recent developments in biomedical engineering. Pergamon Press, New York, pp 330–333
3. Fung YC (1991) What are the residual stresses doing in our blood vessels? Ann Biomed Eng 19:237–249
4. Fung YC (1990) Biomechanics: motion, flow, stress, and growth. Springer, New York
5. Chuong CJ, Fung YC (1986) On residual stresses in arteries. J Biomech Eng 108:189–192

6. Chuong CJ, Fung YC, Schmid-Schonbein GW, Woo SLY, Zweifach BW (1986) Residual stress in arteries, Frontiers in biomechanics. Springer, New York, pp 117–129
7. Fung YC (1997) Biomechanics: circulation. Springer, New York
8. Fung YC, Liu SQ (1989) Change of residual strains in arteries due to hypertrophy caused by aortic constriction. Circ Res 65:1340–1349
9. Fung YC, Liu SQ (1991) Changes of zero-stress state of rat pulmonary arteries in hypoxic hypertension. J Appl Physiol 70:2455–2470
10. Beloussov LV, Dorfman JG, Cherdantzev VG (1975) Mechanical stresses and morphological patterns in amphibian embryos. J Embryol Exp Morph 34:559–574
11. Beloussov LV (1998) The dynamic architecture of a developing organism: an interdisciplinary approach to the development of organisms. Kluwer, Dordrecht
12. Beloussov LV, Luchinskaya NN, Ermakov AS, Glagoleva NS (2006) Gastrulation in amphibian embryos, regarded as a succession of biomechanical feedback events. Int J Dev Biol 50:113–122
13. Taber LA (2009) Towards a unified theory for morphomechanics. Phil Trans Roy Soc A Math Phys Eng Sci 367:3555–3583
14. Taber LA (2008) Theoretical study of Beloussov's hyper-restoration hypothesis for mechanical regulation of morphogenesis. Biomech Model Mechanobiol 7:427–441
15. Gilbert SF (2010) Developmental biology, 9th edn. Sinauer Associates, Sunderland
16. Davies JA (2005) Mechanisms of morphogenesis: the creation of biological form. Elsevier, San Diego
17. Vossoughi J, Hedjazi Z, Borris FS, Langrana NA, Friedman MH, Grood ES (1993) Intimal residual stress and strain in large arteries. In: Proceedings~summer bioengineering conference, ASME, New York, ppp 434–437
18. Hamburger V, Hamilton HL (1951) A series of normal stages in the development of the chick embryo. J Morphol 88:49–92
19. Voronov DA, Taber LA (2002) Cardiac looping in experimental conditions: the effects of extraembryonic forces. Dev Dyn 224:413–421
20. Varner VD, Voronov DA, Taber LA (2010) Mechanics of head fold formation: investigating tissue-level forces during early development. Development 137:3801–3811
21. Varner VD, Taber LA (2010) On measuring stress distributions in epithelia. In: Garikipati K, Arruda EM (eds) IUTAM symposium on cellular, molecular and tissue mechanics. Springer, New York, pp 45–54
22. Rodriguez EK, Hoger A, McCulloch AD (1994) Stress-dependent finite growth in soft elastic tissues. J Biomech 27:455–467
23. Xu G, Knutsen AK, Dikranian K, Kroenke CD, Bayly PV, Taber LA (2010) Axons pull on the brain, but tension does not drive cortical folding. J Biomech Eng 132:071013
24. Varner VD, Taber LA (2012) On integrating experimental and theoretical models to determine physical mechanisms of morphogenesis. Biosystems 109:412–419
25. Pang T, Atefy R, Sheen V (2008) Malformations of cortical development. Neurologist 14:181–191
26. Welker W, Jones EG, Peters A (1990) Why does the cerebral cortex fissure and fold? A review of the determinants of gyri and sulci, Cerebral cortex. Plenum, New York, pp 3–136
27. Richman DP, Stewart RM, Hutchinson JW, Caviness VS Jr (1975) Mechanical model of brain convolutional development. Science 189:18–21
28. Van Essen DC (1997) A tension-based theory of morphogenesis and compact wiring in the central nervous system. Nature 385:313–318
29. Smart IH, McSherry GM (1986) Gyrus formation in the cerebral cortex of the ferret. II. Description of the internal histological changes. J Anat 147:27–43
30. Smart IH, McSherry GM (1986) Gyrus formation in the cerebral cortex in the ferret. I. Description of the external changes. J Anat 146:141–152

Chapter 41
FBG Based In Situ Characterization of Residual Strains in FDM Process

Antreas Kantaros and Dimitris Karalekas

Abstract Additive Layered Manufacturing has emerged as a popular manufacturing direction to accelerate product creation. Layered manufacturing can build parts that have traditionally been impossible to build because of their complex shapes or variety of materials. Layered manufacturing processes accumulate residual stresses and strains during material build up. Theses stresses may cause layer delamination and part distortion. This paper presents the work done on investigating residual strain accumulation in one of the most used additive processes, namely the Fused Deposition Modeling (FDM) and as a function of two typically selected process parameters. The developed residual strains at the end of the fabrication process were recorded using an optical sensor with a short fiber Bragg grating (FBG), embedded at the midplane of FDM built prismatic specimens. To assess the strain development without constraining effects from any adhesion to the building platform surface, measurements were taken at free-standing state at the end of the fabrication process. It is demonstrated that the magnitude of the solidification induced residual strains is significant and depends significantly on the selected material deposition direction (bead orientation) as a result of the formation of poor interbead interfaces and void (air gap) regions.

Keywords Fused deposition modeling • Layer manufacturing • Processing parameters • Residual strains • Fiber Bragg grating

41.1 Introduction

Layered manufacturing (LM) methods or solid freedom fabrication (SFF) technologies have been widely used for rapid prototyping (RP) purposes such as fabrication of complex shapes and models for visualization, verification and assembly purposes during product creation. In recent years, layered manufacturing has evolved from rapid prototyping techniques to rapid manufacturing methods where functional parts with tailored properties are produced for potential end use in a product. This process, where the objects are produced by sequential deposition of material layers, is characterized by the accumulation of residual stresses and strains during material build up. These stresses arise from the contraction that takes place as a result of the deposition of a layer, which causes distortions and in same cases layer delamination or cracking. Many authors have investigated such fabrication stresses in these technologies [1, 2].

Fused deposition modeling (FDM) is a layered manufacturing technology that produces parts of complex geometry by the layering of extruded materials, such as Acrylonitrile-butadiene-styrene (ABS) plastic. The ABS material is initially in the raw form of a flexible filament which is then partially melted and extruded through a heated nozzle in a prescribed parallel road pattern onto a platform layer by layer at chamber temperature. The deposited material (individual roads) cools, solidifies, and bonds with the neighboring material. In FDM, as in other LM processes, the heating and rapid cooling cycles of the work materials will aggravate non-uniform thermal gradients and cause stress build-up that consequently results in part distortions and dimensional inaccuracy. Once the build process is completed, the FDM build part can be viewed as a laminate composite structure with anisotropic material properties. The mechanical

A. Kantaros • D. Karalekas (✉)
Laboratory of Advanced Manufacturing Technologies and Testing, University of Piraeus,
Karaoli and Dimitriou 80, GR-185 34 Piraeus, Greece
e-mail: dkara@unipi.gr

M. Rossi et al. (eds.), *Residual Stress, Thermomechanics & Infrared Imaging, Hybrid Techniques and Inverse Problems, Volume 8*,
Conference Proceedings of the Society for Experimental Mechanics Series, DOI 10.1007/978-3-319-00876-9_41,

properties of FDM parts are not only controlled by the build material, but also influenced by the selected fabrication parameters. Analysis of past research suggests that part quality of FDM parts relates to part strength, surface quality and dimensional accuracy and it depends significantly on few primary control factors such as layer thickness, deposition direction of filament roads, road (or raster) width, gap sizes between filaments and stacking sequence of the vertically stacked layers of bonded fibers (roads).

In recent years, several researchers have investigated the anisotropic nature of FDM parts and the effect of various process parameters such as layer thickness and part orientation, on the properties of the built parts [3]. It is also concluded, that since semi-molten filament is extruded from nozzle tip and solidified in a chamber, maintained at certain temperature, change of phase is likely to occur [4]. As a result volumetric shrinkage takes place causing weak interlayer bonding and high porosity resulting in reduced load bearing area. What is more, the material used for part fabrication must have lower glass transition temperature and linear shrinkage rate because the extruded material is cooled from glass transition temperature to chamber temperature resulting in the development of inner stresses responsible for the appearance of inter- and intra-layer deformation in the form of cracking, de-lamination or even part fabrication failure [5]. It is experimentally demonstrated that bond quality between adjacent filaments depends on envelope temperature and variations in the convective conditions within the building part [6]. The extrusion phenomenon in FDM is also studied and the conclusion reached was that process parameters are critical to the part accuracy [7]. A parametric study of part distortions in FDM using 3D FEA showed that the scan speed is the most significant factor to part distortions followed by the layer thickness. Furthermore, they reported that residual stresses increase with layer thickness and road width, to a less extent though [8].

Several works have been conducted aiming at studying the influence of process parameters on the strength of FDM fabricated parts. Characteristically, it is observed that raster orientation causes alignment of polymer molecules along the direction of deposition during fabrication and tensile, flexural and impact strength depends on orientation [4]. Additionally, it is empirically shown that mechanical properties like tensile strength and flexural strength uniformly decreases with increase in orientation angle [9]. The major reasons for decrease in mechanical properties may be caused due to void formation and thermally induced stresses in FDM built parts. Such detrimental effects may be reduced by proper adjustment of part orientation along with other process parameters. Moreover, it is reported that layer thickness, raster (road) angle and air gap influence the elastic performance of ABS prototypes manufactured by FDM [10]. Further to this, it is pointed out that orientation is an important process parameter for part strength, dimensional accuracy, surface finish, part build time and cost in layered manufacturing [11].

This paper describes an undertaken work concentrated on investigating in-situ the magnitude of the solidification induced residual strains in FDM built parts fabricated using different processing parameters. In the presented experimental study, two important processing parameters of fused deposition modeling were considered: (a) layer thickness and (b) stacking sequence (road or raster orientation).

41.2 Experimental

41.2.1 Specimen Preparation

Prismatic specimens of 10 × 10 × 40 mm (width × height × length) were fabricated out of ABS at room temperature using a RapMan 3.0 open-source FDM 3D printer. Six types of specimens were manufactured using two different processing parameters. The first processing parameter was layer thickness, where half of the specimens were built having a layer thickness of 0.25 mm and the rest of 0.5 mm. The second processing parameter was road (raster) orientation, where three orientations were investigated: (a) unidirectional or 0°, the roads are aligned with the long dimension of the specimen, (b) transverse or 90°, roads perpendicular to the long dimension of the specimen, and (c) default or +45°/−45° crisscross, representing the machine's default road orientation.

Each specimen contained an embedded optical fiber of 0.125 mm in diameter centrally located at the midplane of the specimen and along its long (axial) direction. The optical fiber was equipped with a FBG of 10 mm length, operating at a Bragg wavelength of 1,550 nm. Full spectrum measurements of FBG were taken using a Micron Optics sm125 optical sensing interrogator. The FDM printing begins with the fabrication of the support layers and continues with the layer by layer fabrication up to the midplane layer of the specimen. When half of the specimen is fabricated, the FDM printer pauses for 3 s and the nozzle returns to its zero position away from the specimen. During this time interval, the FBG sensor is placed on the midplane layer and a reference Bragg wavelength (λ_{B0}) measurement is taken. Then, the printer nozzle returns and continues with the layer by layer fabrication until the whole specimen is constructed. In order to keep the FBG sensor

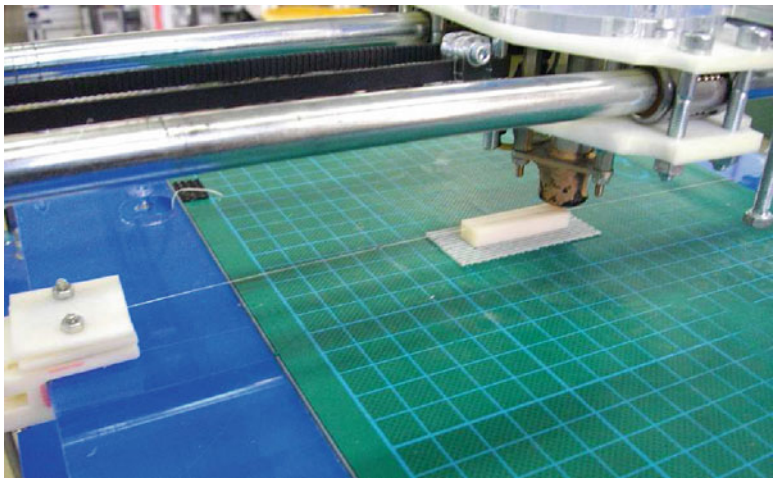

Fig. 41.1 Picture of prismatic specimen containing an embedded FBG sensor, fabricated using a RapMan 3.0 open-source FDM 3D printer

perfectly aligned during embedment two holding fixtures were designed and manufactured using the same RapMan FDM-printer. These holding devises were mounded on the build platform edges and at opposite sides of the specimen's long direction (Fig. 41.1). At the end of the printing process the specimen remains on the build platform for 2 h to allow cooling to ambient temperature and FBG recordings were at that point.

41.2.2 FBG Working Principles

In general, optical fibers present several advantages over common measuring techniques such as low susceptibility to electromagnetic interference, low cost, low weight and small size. Such sensors can be used to monitor several parameters such as fabrication strains and temperature during cure as well as to evaluate the component's structural integrity in service after cure. Many works involving FBG sensors for in-situ cure monitoring in polymeric and composite materials have been reported [12–15].

The principle of the FBG sensor is based on the measurement of the changes in reflective signal, which is the center wavelength (λ_{B0}) of back-reflected light from the Bragg grating, and depends on the effective refractive index (n_{eff}) of the core and the periodicity (Λ) of the grating, [16], as expressed by the Bragg condition $\lambda_{B0} = 2n_{eff}\,\Lambda$. When the FBG is embedded into a homogeneous axial strain ε_x, assuming that the two later strains on the fiber (ε_y, ε_z) are related to the axial one by $\varepsilon_y = \varepsilon_z \approx -\nu_f\,\varepsilon_x$ (where ν_f is the fiber's Poisson ratio), and/or a uniform temperature change ΔT, the difference in wavelength $\Delta\lambda_B = \lambda_B - \lambda_{B0}$, obtained from the peak shift of the spectra, before and after loading, is:

$$\frac{\Delta\lambda_B}{\lambda_{B0}} = (1 - p_e)\varepsilon_x + \left(\alpha_f + \xi\right)\Delta T \tag{41.1}$$

where, λ_{B0} is the Bragg wavelength at a reference state, p_e is the strain-optic coefficient which can be determined experimentally, [17], (where, $p_e = 0.215$), α_f is the thermal expansion coefficient of the fiber (where, $\alpha_f = 8 \times 10^{-7}\,^{\circ}\mathrm{C}^{-1}$) [18] and ξ is the thermo-optic coefficient of the fiber (where, $\xi = 8.916 \times 10^{-6}\,^{\circ}\mathrm{C}^{-1}$), respectively [19].

When the FBG sensor is embedded into a host material which is cured and then both experience uniform temperature changes, the Bragg equation is modified to account for the thermally induced axial strains in the fiber as a result of the mismatch in the coefficients of thermal expansion (CTE) between the optical fiber (α_f) and the host material (α_m). Therefore, a more generalized equation can be written as:

$$\frac{\lambda_B - \lambda_{B0}}{\lambda_{B0}} = \frac{\Delta\lambda_B}{\lambda_{B0}} = (1 - p_e)\,\varepsilon_{res} + (1 - p_e)(\alpha_m - \alpha_f)\Delta T + (\alpha_f + \xi)\Delta T \tag{41.2}$$

In the previous equation ε_{res} accounts for the solidification induced residual strains and $(\alpha_m - \alpha_f)\Delta T$ for the strains ε_T due to thermal expansion mismatch. If the strain is constant through out the sensor, the resulting spectrum appears as a simple shift to a lower or higher wavelength depending on whether the strain is compressive or tensile in nature.

41.3 Results and Discussion

41.3.1 Residual Strains Measurement

As mentioned before, the FBG sensor was placed in the central part of the built prismatic specimens since hoop and radial strains are negligible compared to axial ones, [20], have demonstrated that the fiber and the surrounding material have the same strains. At the end of the fabrication process, λ_B, was measured for every specimen and compared to the reference wavelength, λ_{B0}, before embedment. Since each of these measurements was conducted at ambient temperature, Eq. 41.2 reduces to:

$$\frac{\lambda_B - \lambda_{B0}}{\lambda_{B0}} = \frac{\Delta\lambda_B}{\lambda_{B0}} = (1 - p_e)\,\varepsilon_{res} \tag{41.3}$$

where, ε_{res} is the fabrication induced residual strains along the optical fiber direction.

For the selected layer thicknesses and build orientations the residual strains along the long axis of the test specimens, as calculated from the FBG recordings and the use of Eq. 41.3, are presented in Tables 41.1 and 41.2. It is observed that the residual strains for the specimens having a layer thickness of 0.25 mm are significantly lower than the ones of larger layer thickness. Examination of the 0.25 mm thickness specimens revealed that they exhibited a lower filament width and a higher raster to raster air gap distance when compared to the 0.5 mm ones. Furthermore, insufficient adhesion between adjacent layers was evident for the 0° direction specimens. Examining the results presented for 0.5 mm thickness specimens, can be seen that the fabrication induced residual strains for the longitudinal and crisscross directions are comparable and almost double to the corresponding ones for the transverse direction.

Although the 3D printer's software did not have the option for the user to choose a specific filament width and raster to raster air gap distance, changes made in its open source g-code permitted the fabrication of a new set of specimens of 0.25 mm thickness, designated as 0.25B hereafter, having a wider filament (raster) width leading to a lower raster to raster air gap distance. The FBG-based calculated residual strains for this case are presented in Table 41.3. As expected, the third batch of specimens exhibited higher residual strains due to the modification of the filament width and air gap parameters. Increase of residual stresses with raster width, to a less extent though, has been also reported [8]. It is observed that in this case the strains for the transverse and crisscross specimens are comparable and of significant magnitude. On the other hand, the longitudinal specimen exhibited somewhat higher residual strains than the corresponding ones obtained from the previous batch of the same thickness, yet though much lower than the transverse and crisscross ones measured for the same batch of specimens.

Table 41.1 Measured maximum wavelength and corresponding calculated residual strains for specimens of 0.25 mm layer thickness

Layer thickness (mm)	Build (road) orientation	Calculated residual strains ε_{res}, (με)
0.25	Longitudinal, 0°	528.7
0.25	Transverse, 90°	966.3
0.25	Crisscross, ±45°	2,925.2

Table 41.2 Measured maximum wavelength and corresponding calculated residual strains for specimens of 0.5 mm layer thickness

Layer thickness (mm)	Build (road) orientation	Calculated residual strains ε_{res}, (με)
0.5	Longitudinal, 0°	5,549.9
0.5	Transverse, 90°	2,751.0
0.5	Crisscross, ±45°	5,539.9

Table 41.3 Measured maximum wavelength and corresponding calculated residual strains for specimens of 0.25 mm layer thickness and smaller road to road air gap distance

Layer thickness (mm)	Build (road) orientation	Calculated residual strains ε_{res}, (με)
0.25B	Longitudinal, 0°	932.6
0.25B	Transverse, 90°	6,729.7
0.25B	Crisscross,±45°	6,364.0

Lower longitudinal residual stresses when compared to the transverse ones have also been reported [8]. By performing three-dimensional finite element analysis simulations of the FDM process with layer thickness of 0.254 mm they have found that the short-raster tool path resulted to higher residual stresses than the long raster and alternate-raster patterns. Additionally, the interlayer bonding in the 0° orientation specimens can be significantly weaker than the other two directions. It is reported [4] that mechanically tested FDM test samples of 0°-orientation were fractured by individual layers as a result of weak interlayer bonding.

41.4 Conclusions

In this study, the use of an optical fiber to record in-situ the solidification induced strains in FDM built specimens is presented. A series of samples with an embedded fiber Bragg grating (FBG) sensor in their midplane were fabricated using two important processing parameters, layer thickness and build orientation namely. The experimental results show that their magnitude is significant and sensitive to the investigated process parameters. It was found that the residual strains obtained for the 0° direction, where the roads are aligned to the long dimension of the specimen, were constantly lower than the corresponding ones in the transverse, 90°, and crisscross, ±45°, directions when a layer thickness of 0.25 mm was selected. When the thickness of each deposited layer was increased to 0.5 mm the measured strains in the 0°and 90° directions were comparable.

Acknowledgements This work has been funded by the THALIS Program of the Hellenic Ministry of Education and within the context of MIS 380278 research project.

References

1. Karalekas D, Rapti D (2002) Investigation of the processing dependence of SL solidification residual stresses. Rapid Prototyp J 8:243–247
2. Karalekas D, Aggelopoulos A (2003) Study of shrinkage strains in a stereolithography cured acrylic photopolymer resin. J Mater Process Technol 136:146–150
3. Vasudevarao B, Natarajan DP, Razdan A, Mark H (2000) Sensitivity of RP surface finish to process parameter variation. Partnership for Research in Stereo Modeling, Department of Industrial Engineering, Arizona State University
4. Es-Said OS, Foyos J, Noorani R, Mandelson M, Marloth R, Pregger BA (2000) Effect of layer orientation on mechanical properties of rapid prototyped samples. Mater Manuf Process 15:107–122
5. Wang TM, Xi JT, Jin Y (2007) A model research for prototype warp deformation in the FDM process. Int J Adv Manuf Technol 33:1087–1096
6. Sun Q, Rizvi GM, Bellehumeur CT, Gu P (2008) Effect of processing conditions on the bonding quality of FDM polymer filaments. Rapid Prototyp J 14:72–80
7. Jiang KY, Gu YH (2004) Controlling parameters for polymer melting and extrusion in FDM. Key Eng Mater 258–259:667–671
8. Zhang Y, Chou K (2008) A parametric study of part distortions in fused deposition modeling using three dimensional element analysis. J Eng Manuf 222:959–967
9. Sood AK, Chaturvedi V, Datta S, Mahapatra S (2011) Optimization of process parameters in fused deposition modeling using weighted principal component analysis. J Adv Manuf Syst 10:241–259
10. Lee B, Kim S, Kim H, Ahn S (2007) Measurement of anisotropic compressive strength of rapid prototyping parts. J Mater Process Technol 187–188:627–630
11. Pandey PM, Venkata Reddy N, Dhande SG (2007) Part deposition orientation studies in layered manufacturing. J Mater Process Technol 185:125–131
12. Leng J, Asundi A (2002) Real time cure monitoring of smart composite materials using extrinsic Fabry-Perot interferometer and fiber Bragg grating sensors. Smart Mater Struct 11:249–255
13. Antonucci V, Giordano M, Cusano A, Nasser J, Nicolais L (2006) Real time monitoring of cure and gelification of a thermoset matrix. Compos Sci Technol 66:3273–3280
14. Karalekas D, Cugnoni J, Botsis J (2008) Monitoring of process induced strains in a single fibre composite using FBG sensor: a methodological study. Compos Part A Appl Sci Manuf 39:1118–1127
15. Parlevliet PP, Bersee HEN, Beukers A (2010) Measurement of (post-)curing strain development with fibre Bragg gratings. Polym Test 29:291–301
16. Measures RM (2001) Structural monitoring with fiber optic technology. Academic Press, San Diego. ISBN 0124874304
17. Giaccari P, Dunkel GR, Humbert L, Botsis J, Limberger HG, Salathé RP (2005) On a direct determination of non-uniform internal strain fields using fibre Bragg gratings. Smart Mater Struct 14:127–136
18. Jin XD, Sirkis JS, Chung JK (1997) Optical fiber sensor for simultaneous measurement of strain and temperature. Proc SPIE 3042:120–127
19. Neumann EG (1988) Single mode fibers I: fundamentals. Springer-Verlag, Berlin
20. Colpo F, Humbert L, Botsis J (2007) Characterization of residual stresses in a single fibre composite with FBG sensor. Compos Sci Technol 67:1830–1841

Chapter 42
Polynomial Fitting Techniques for IRT Inspection

Shanglei Li, Anish Poudel, and Tsuchin Philip Chu

Abstract This paper discusses the use of polynomial surface fitting techniques for the infrared thermography (IRT) evaluation of the graphite epoxy composite laminate. The composite laminate had 12 inserted Teflon films in different layers so as to simulate delamination defects. Based on the initial IRT inspection, it was determined that the raw IR images were not able to detect all 12 defects. In order to improve the detection capability and remove the heating pattern, a fitted heating pattern was generated by using the polynomial surface fitting method. Then, this pattern was deleted by applying the subtract function. It was demonstrated that this applied method not only removed the non-uniform heating effect, but also preserved all defect information and enhanced the thermal contrast of the raw IR images.

Keywords Polynomial surface fitting • Subtract function • Graphite epoxy laminates • IRT • NDE

42.1 Introduction

Composites are increasingly being used as the main building materials in modern civil, mechanical, and aerospace structures. The main reason behind this is that composites offer outstanding thermal and physical properties compared to traditional metals and their alloys. These attractive properties of composites include higher strength-to-weight ratio, superior fatigue life, higher stiffness, and lower coefficient of thermal expansion. However, composites are prone to damage mechanisms which can occur during the processing stages or during in-service operations. Some of the flaws that are often encountered include delaminations, cracks, disbonds, impact damage, porosity, inclusions, fiber wrinkling or waviness, and fiber and ply misalignment [1]. It is very important to identify and characterize these defects in composites because they can greatly reduce the stiffness, compressive strength, and tensile performance of the structure. For this, various nondestructive evaluation (NDE) methods are often considered. Infrared thermography (IRT) is one of the proven NDE methods which is predominantly applied during the inspection of composites [2–11]. But, infrared (IR) image quality in a multi layered composite is subjected to blurring and the degradation of the acquired signal due to the diffusive nature of the process. Various literatures have reported the use of several image enhancement pixel based techniques to improve the quality of IR images for better defect detection in composites [9, 12–16]. In this paper, step-heating IRT approach was employed to test graphite epoxy composite laminates with artificially simulated delamination defects. The polynomial surface fitting technique was then used to estimate the heating pattern in an IR image which was then subtracted from the original IR image to obtain a clear and enhanced IR image. This technique was able to detect defects in composite laminates with greater confidence by removing the heating pattern compared to the raw IR image.

S. Li (✉)
Department of Electrical and Computer Engineering, Southern Illinois University Carbondale,
1230 Lincoln Drive, Carbondale, IL 62901, USA
e-mail: shanglei@siu.edu

A. Poudel • T.P. Chu
Department of Mechanical Engineering and Energy Process, Southern Illinois University Carbondale,
1230 Lincoln Drive, Carbondale, IL 62901, USA

M. Rossi et al. (eds.), *Residual Stress, Thermomechanics & Infrared Imaging, Hybrid Techniques and Inverse Problems, Volume 8*,
Conference Proceedings of the Society for Experimental Mechanics Series, DOI 10.1007/978-3-319-00876-9_42,

42.2 Polynomial Fitting

Thermal contrast is commonly used in IRT to evaluate defect visibility, enhance image quality, and ultimately for quantitative purposes [16]. There are several types of contrasts such as absolute contrast, running contrast, normalized contrast, and standard contrast [10]. However, the thermal contrast is affected by heating patterns such as the synchronization of heat sources, reflected light from the surrounding environment, surface roughness, color, and emissivity of the surface of the specimen. These effects will lead to the reduction in defect contrast, blurring and degradation of the acquired signal which can cause difficulties during IR inspection. In order to improve the detection capability and remove the heating pattern, a fitted heating pattern was first estimated by using the polynomial surface fitting algorithm on the obtained raw IR image. Then, this pattern was deleted by applying the subtract function. The implementation of heating estimation and image correction is based on two assumptions: (1) The heating effect is a slow variance function compared to thermal contrast changing of defects; (2) Obtained IR images can be considered as a combination of ideal image, heating effect (pattern), and independent noise. The heating pattern can be considered as an additive factor and it can be removed by subtracting the estimated heating pattern.

In this study, for an obtained IR image $I(x, y)$ with a resolution of $m \times n$, the heating pattern is defined as an additive factor to the ideal IR image intensities and the obtained IR image can be modeled as:

$$I(x, y) = f(x, y) + h(x, y) + n(x, y) \tag{42.1}$$

Where:

$f(x, y)$ is the ideal IR image.
$h(x, y)$ is the heating pattern.
$n(x, y)$ is the independent thermal noise.

By estimating the heating pattern $h(x, y)$ with polynomial surface fitting and eliminating the noise $n(x, y)$ with Wiener filter, the ideal IR image can be obtained:

$$f(x, y) = I(x, y) - h(x, y) \tag{42.2}$$

To estimate the heating pattern of $h(x, y)$, let $(x_i,\ y_j)$ be the coordinates of a pixel in the pattern image, and $z_{i,j}$ indicate the temperature of pixel (x_i, y_j). A two dimensional fifth order polynomial of x and y is utilized to implement surface fitting which is constrained with lease square method. A desired surface fitting equation of non-uniform heating pattern $h(x_i,\ y_j)$ is given by:

$$h(x_i, y_j) = \left(a{x_i}^5 + b{x_i}^4 + c{x_i}^3 + d{x_i}^2 + ex_i + f\right) \cdot \left(g{y_j}^5 + h{y_j}^4 + i{y_j}^3 + j{y_j}^2 + ky_j + l\right) \tag{42.3}$$

Equation 42.3 is expanded and rewritten as follows, where the subscript of coefficient A indicates the power of x_i and y_j respectively.

$$h(x_i, y_j) = A_{55}{x_i}^5{y_j}^5 + A_{54}{x_i}^5{y_j}^4 + A_{53}{x_i}^5{y_j}^3 + \ldots + A_{11}x_iy_j + A_{10}x_i + A_{01}y_j + A_{00} \tag{42.4}$$

The unknown coefficients must yield zero first derivatives to obtain the minimum least square error. For the fifth order polynomial surface fitting, there are 36 unknown coefficients in Eq. 42.4. The coefficients A in Eq. 42.4 can be solved by plotting known values x_i, y_j and $z_{i,j}$.

In order to subtract the estimated heating pattern from the raw IR image, the image subtraction technique is applied. The image subtraction is an image processing technique that can help to identify small temperature changes, suppress the influence of thermal reflections, and visualize time derivatives if applied consecutively [10]. IR image subtraction subtracts a reference image from each image of a recorded sequence or subtracts each image from its precursor and is expressed as:

$$\Delta U_{subtraction} = U_{source} - U_{reference} \tag{42.5}$$

The subtracted image of $f(x,y)$ can be expressed as:

$$\Delta f(x,y)_{subtraction} = f(x,y)_{source} - f(x,y)_{reference} \tag{42.6}$$

Combining Eq. 42.6 with Eq. 42.2, we get:

$$\Delta f(x,y)_{subtraction} = \left[I(x,y)_{source} - I(x,y)_{reference}\right] - \left[h(x,y)_{source} - h(x,y)_{reference}\right] \tag{42.7}$$

The first part of Eq. 42.7: $[I(x,y)_{source} - I(x,y)_{reference}]$ is the result of obtained IR image subtraction. The second part: $\left[h(x,y)_{source} - h(x,y)_{reference}\right]$ is the result of heating pattern subtraction which contains no defect information. Thus, $\Delta f(x,y)$ is the desired enhanced IR image.

42.3 Experimental Setup and Procedure

The material used in this study was a graphite epoxy composite laminate with artificially simulated delamination defects as shown in Fig. 42.1. This panel had dimensions of 300 × 300 × 1.68 mm. The sample had 12 rectangular Teflon inserts of thickness 0.1 mm with changeable distance. The experimental setup used for conducting infrared thermography tests is shown in Fig. 42.2. This infrared thermography system is similar to that described in an outside work [17]. A continuous heat flux was applied for approximately 5 s by using four 500 W, 120 V halogen linear tubes. An infrared camera was used to record the thermal response every 0.03 s for a total of 300 frames.

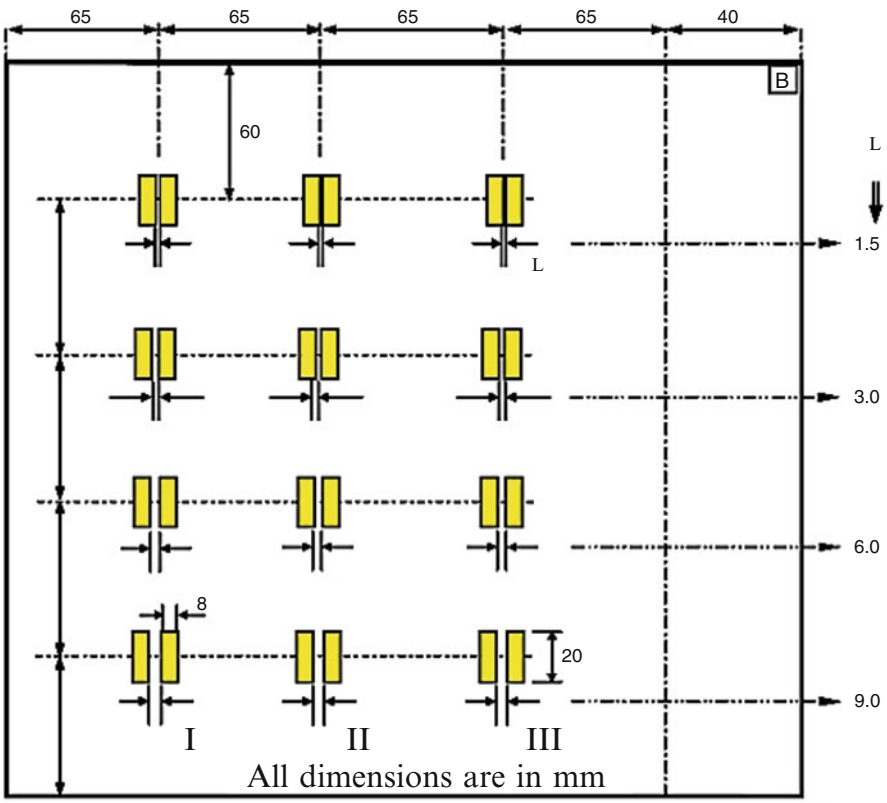

Fig. 42.1 Delamination defect map in graphite epoxy composite laminate. Position of the Teflon throughout the thickness (*I*) between layer 1 and 2; (*II*) between layer 4 and 5; (*III*) between layer 7 and 8

42.4 Results and Discussion

Figure 42.2 shows the thermal images of composite laminate at frame 90 and 170 (0.03 s per frame) during the heating stage. The obtained IR image sequence resolution is 240 × 330 pixels.

The dotted yellow regions in Fig. 42.3 indicate areas of non-uniform heating in composite laminate. These were very difficult to analyze due to the lower thermal contrast and overlapped defect information within non-uniform heating zones. In order to improve the thermal contrast of defects and make defect detection an easy process, an estimated heating pattern was generated and subtracted from the raw IR image to obtain the enhanced image. Figure 42.4 shows the fitted surface with fifth order polynomial for frames 90 and 170 respectively. In the Fig. 42.4a, b red indicates the hot spot in the specimen, while blue indicates the cold area of the specimen. Similarly, the gray level as shown in Fig. 42.4c, d indicates the temperature variance in 2D images. From these, the heating effect (pattern) is clearly observed in the estimated images.

Figure 42.5a shows the raw IR image subtraction result for the same graphite epoxy panel. This is based on the first part of the Eq. 42.7 as mentioned earlier. Based on the results as shown in Fig. 42.5a, it was observed that after the image subtraction, not only the defects, but also the non-uniform heating area was enhanced. This phenomenon caused IR image degradation and made defect detection difficult. Figure 42.5b shows the non-uniform heating patterns estimated by polynomial surface fitting and image subtraction, which is based on the second part of the Eq. 42.7.

In order to eliminate the non-uniform heating effect as shown in the Fig. 42.5b, a background image containing no defect information, only the heating pattern, needed to be subtracted from the desired image. This can be obtained by applying the second part of the Eq. 42.7. Figure 42.6a shows the corrected subtraction images obtained after subtracting the heating pattern from corrupted IR images.

Defects that were difficult to be detected in Fig. 42.3 are now clearly observed in Fig. 42.6a. From the results as shown in Fig. 42.6, the hot spot in the middle of the specimen was removed and the thermal contrast was enhanced, thus increasing the detectability of defects. A similar procedure was applied in the cooling stage using frame 180 and 270 and the results obtained are shown in Fig. 42.6b.

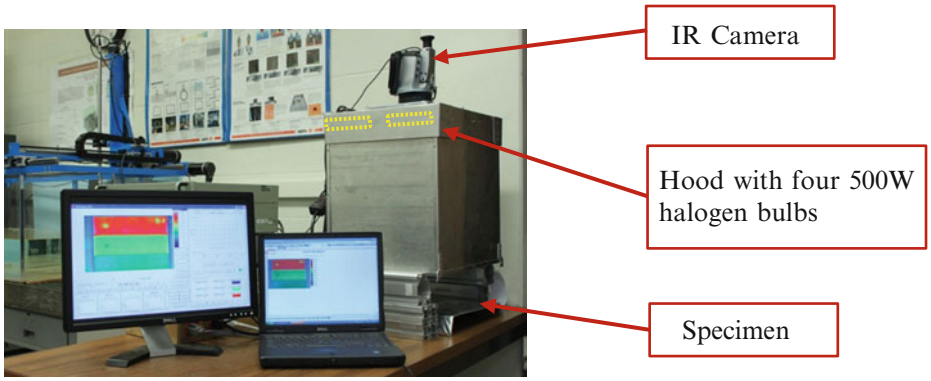

Fig. 42.2 Infrared thermography test setup for graphite epoxy composite laminates

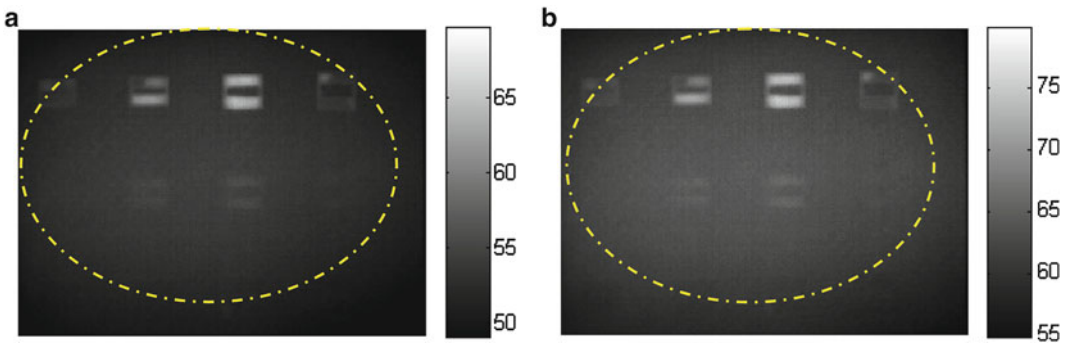

Fig. 42.3 Infrared thermal images of graphite epoxy laminates at (**a**) frame 90; (**b**) frame 170

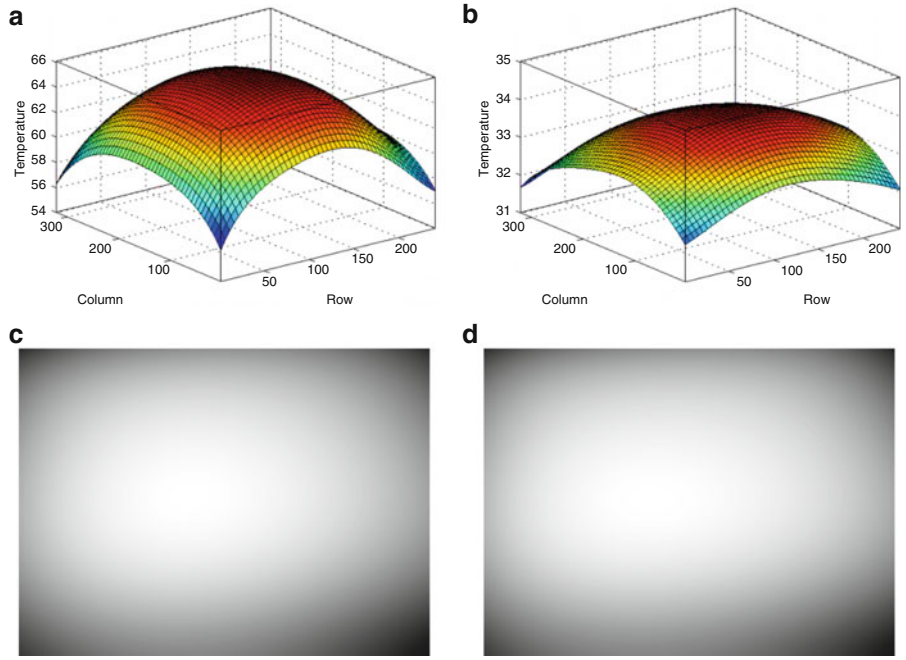

Fig. 42.4 Pictorial representation of fifth order polynomial surface fit for the infrared images (**a**) 3D fitted surface of frame 90; (**b**) 3D fitted surface of frame 170; (**c**) heating pattern for frame 90; (**d**) heating pattern of frame 170

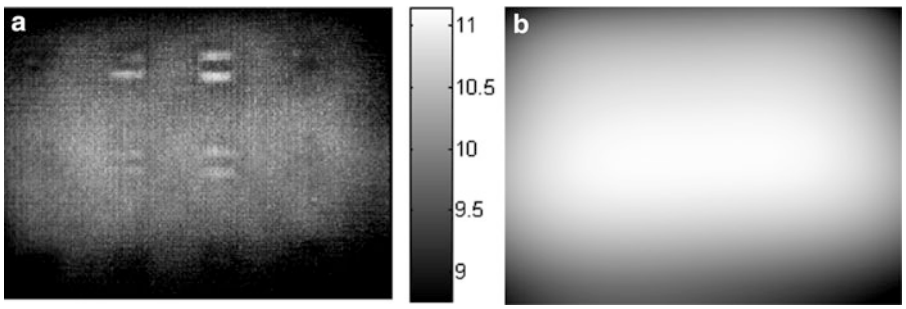

Fig. 42.5 (**a**) Image subtraction result of raw IR image; (**b**) simulated heating pattern of subtracted image

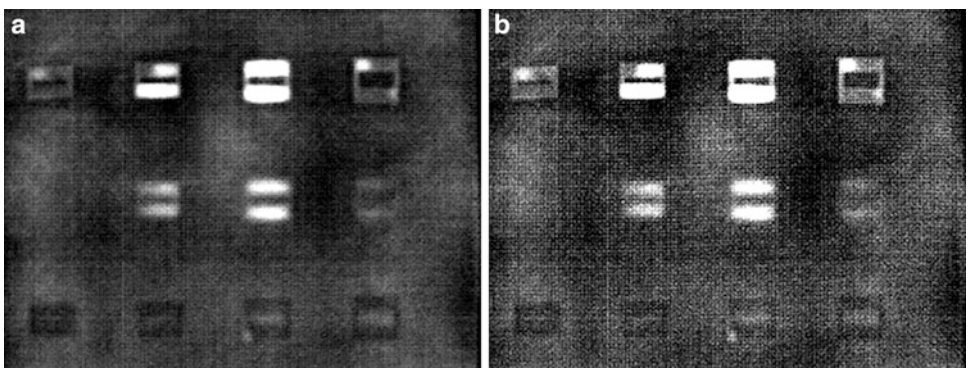

Fig. 42.6 Corrected subtraction IR images by using the heating pattern for (**a**) heating stage of frame 90 and 170; (**b**) cooling stage of frame 180 and 270

Table 42.1 Experimental comparison of CNR & PSNR

		CNR (dB)	PSNR (dB)
Heating stage	*Raw IR image frame 90*	1.7927	13.4128
	Raw IR image frame 170	1.6828	15.2668
	Raw IR image frame 170−90	2.0242	14.4792
	Result image	2.3071	–
Cooling stage	*Raw IR image frame 270−180*	2.1625	13.1755
	Result image	3.2086	–

For objective evaluation, the result and raw IR images at different frames were compared. Peak signal-to-noise ratio (PSNR) and contrast signal-to-noise ratio (CNR) were employed for quantitative assessment. The PSNR is given as:

$$PSNR = 10 \cdot \log_{10}\left(\frac{{MAX_I}^2}{MSE}\right) \tag{42.8}$$

Where:

MAX_I is the maximum possible pixel value of the image. In this study, all pixels are represented using 8 bits Gray level, here MAX_I is 255.
MSE is the mean squared error.

Similarly, the CNR is given as:

$$CNR = \frac{S_i - S_o}{\sqrt{\sigma_i^2 + \sigma_o^2}} \tag{42.9}$$

Where:

S_i and S_o are the mean values inside and outside the ROI respectively
σ_i and σ_o are the standard deviations respectively

From Table 42.1, it can be verified that the CNR of the result image is higher than anyone of the raw IR images. Further, note that the PSNR value of result image is 14.33 dB greater than the raw IR image and 13.82 dB greater than the subtracted images on average. Since the proposed method provides good performance in both of CNR and PSNR, we can see that the proposed polynomial fitting method is effective in the IR image enhancement.

42.5 Conclusion

The polynomial surface fitting method was applied to eliminate the heating pattern in the IR images of the composite laminates. Based on the results, it was demonstrated that this method not only eliminates the non-uniform heating effect efficiently, but also preserves defect information and enhances the thermal contrast.

References

1. Lubin G, Peters ST (1998) Handbook of composites. Chapman & Hall, London
2. Brady RP, Kulkarni MR, Chu TP, Russell S (1999) Thermal image analysis for the in-situ NDE of composites. J Compos Technol Res 21 (3):141−146
3. Chu, TP, Poudel, A, Filip, P (2012) C/C composite brake disk non-destructive evaluation by IR thermography. In: Proceedings conference on thermosense − thermal infrared applications XXXIV, SPIE, Baltimore, Maryland, USA. http://proceedings.spiedigitallibrary.org/proceeding.aspx?articleid=1385503
4. Chu TP, Don J, Pan Y, Poudel A (2012) Defect characterization in commercial carbon-carbon composites. World J Eng 9(6):481−486
5. Pan YP, Miller RA, Chu TP, Filip P (2009) Thermal diffusivity mapping of carbon/carbon composites. Mater Eval 67(5):540−546
6. Hung MYY, Chen YS, Ng SP, Shepard SM, Hou Y, Lhota JR (2007) Review and comparison of shearography and pulsed thermography for adhesive bond evaluation. Opt Eng 46(5):051007

7. Shepard SM (2001) Advances in pulsed thermography In: Proceedings Thermosense XXIII Conference, SPIE, Orlando, FL, pp. 511−515. http://proceedings.spiedigitallibrary.org/proceeding.aspx?articleid=912247
8. Shepard SM, Lhota JR, Ahmed T, Rubadeux BA and Wang D (2001) Quantification and automation of pulsed thermographic NDE. In: Proceedings of nondestructive evaluation of materials and composites V conference, SPIE, Newport Beach, CA, pp 73−78. http://proceedings.spiedigitallibrary.org/proceeding.aspx?articleid=908620
9. Shepard SM, Hou J, Lhota JR, Golden JM (2007) Automated processing of thermographic derivatives for quality assurance. Opt Eng 46(5):051008
10. Maldague X (2001) Theory and practice of infrared technology for nondestructive testing. Wiley, New York
11. Vollmer M, Mollmann K-P (2010) Infrared thermal imaging: fundamentals: research and applications. Wiley-VCH, Weinheim
12. Cramer KE, Winfree WP (2011) Fixed eigenvector analysis of thermographic NDE data. In: Safai M, Brown JR (eds) Thermosense: thermal infrared applications Xxxiii. SPIE, Bellingham
13. Luo B, Liebenberg B, Raymont J, Santospirito SP (2011) Automatic thermographic image defect detection of composites. In: Safai M, Brown JR (eds) Thermosense: thermal infrared applications Xxxiii. SPIE, Bellingham
14. Manohar A, di Scalea FL (2011) Wavelet aided multivariate outlier analysis to enhance defect contrast in thermal images. In: Proceedings of conference on sensors and smart structures technologies for civil, mechanical, and aerospace systems, WILEY, SEM Conference, Uncasville, Connecticut. http://onlinelibrary.wiley.com/doi/10.1111/j.1747-1567.2011.00771.x/abstract
15. D'Orazio T, Leo M, Guaragnella C, Distante A (2007) Analysis of image sequences for defect detection in composite materials. In: Advanced concepts for intelligent vision systems, Proceedings, Springer, Delft, The Netherlands 4678, pp 855−864. http://link.springer.com/chapter/10.1007/978-3-540-74607-2_78
16. Benitez H, Ibarra-Castanedo C, Bendada A, Maldague X, Loaiza H, Caicedo E (2007) Modified differential absolute contrast using thermal quadrupoles for the nondestructive testing of finite thickness specimens by infrared thermography. In: 2006 Canadian conference on electrical and computer engineering, Memphis, TN, pp 4
17. Li S, Chu TP (2013) The application of polynomial fitting techniques to IRT inspections. In: Proceedings of ASNT 22nd research symposium, ASNT, 2013

Chapter 43
In-Flight Infrared Thermography for Studies of Aircraft Cabin Ventilation

T. Dehne, J. Bosbach, and A. Heider

Abstract To improve the convenience of aircraft cabins, Cabin Displacement Ventilation (CDV) was investigated during flight tests in an Airbus A320 with an automatically rotatable infrared camera. For this purpose a programmable, step motor driven infrared camera setup was developed, allowing for time resolved acquisition of the temperatures on the interior cabin surfaces during the whole flights. From the temporal development of the surface temperatures the cooling and heating performance of pure CDV as well as a hybrid system (HV), where 30 % of the fresh air was supplied through the original lateral outlets, was analyzed and characterized. Static measurements reveal a characteristic, yet homogeneous temperature distribution in the cabin for both scenarios, pinpointing to a homogeneous cooling of the heat loads in the whole cabin. In order to study the performance of CDV and HV, dedicated "pull-up" and "pull-down" scenarios, those are abrupt changes of the inflow temperature with the objective to study the heating and cooling dynamics, were conducted during the flight tests. Analysis of time resolved measurements discloses that the cooling performance of the cabin is limited by thermal diffusion of heat inside of the interior cabin materials.

Keywords Indoor air flow • Displacement ventilation • Environmental control • Flight test • Aircraft cabin

43.1 Introduction

In passenger aircraft, cabin air pressure, cabin air quality and comfortable cabin air temperatures have to be maintained by an environmental control system (ECS). Herewith, the cabin ventilation system, which is part of the ECS, is essential to provide oxygen as well as to discharge carbon dioxide, excess air humidity, heat loads and unpleasant exhalation [1, 2]. Due to the general trend of rising heat loads in modern passenger aircraft cabins [3], a growing interest in new, more efficient, yet passenger friendly ventilation systems for aircraft cabins can be observed in the literature. Besides the heat removal efficiency, the thermal passenger comfort, which is governed by the fluid temperatures, air velocities and surface temperatures as well as the air quality, plays a key role. The purpose of this study was to examine a new ventilation system for aircraft cabins under flight conditions and to prove its potential benefits under real conditions.

43.2 Aircraft Cabin Ventilation Systems

Passenger comfort and herewith thermal passenger comfort, which is determined by the ventilation system, plays an important role in commercialization of modern aircrafts. At present, the ventilation systems in passenger aircraft are based upon the principle of mixing ventilation (MV see Fig. 43.1a), where fresh and used air are mixed in the shear layers of fresh air jets with rather high momentum (typical inflow velocities are of the order of 1 m/s) [4]. The advantages of MV are moderate temperature stratifications and high surface cooling rates. However, MV is prone to draft, especially at high heat loads and often lacks from a comparably high amount of short circuit flows, which limit the heat removal efficiency.

T. Dehne, M.Eng. (✉) • J. Bosbach • A. Heider, Dipl. Phys.
German Aerospace Center (DLR), Institute of Aerodynamics and Flow Technology, Bunsenstrasse 10, D-37073 Göttingen, Germany
e-mail: tobias.dehne@dlr.de

M. Rossi et al. (eds.), *Residual Stress, Thermomechanics & Infrared Imaging, Hybrid Techniques and Inverse Problems, Volume 8*, Conference Proceedings of the Society for Experimental Mechanics Series, DOI 10.1007/978-3-319-00876-9_43,

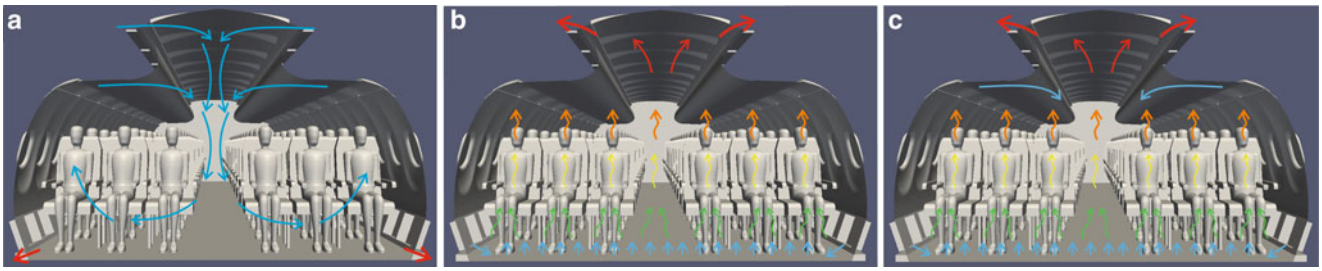

Fig. 43.1 Ventilation concepts for aircraft cabins (**a**) Mixing Ventilation (MV), (**b**) Cabin Displacement Ventilation (CDV) and (**c**) Hybrid Ventilation (HV) which is a combination of MV and CDV

Therefore as an alternative ventilation concept, cabin displacement ventilation (CDV, Fig. 43.1b) has been investigated by means of Computational Fluid Dynamics (CFD) [5–9] and experiments in aircraft cabin mock-ups [6, 7] since a few years. CDV provides low incoming flow velocities (u ~ 0.1 m s) near the floor level whereby a lower velocity and turbulence level can be attained. The fresh air rises near the passengers and heat loads by buoyancy before it leaves in the upper cabin part and thus removes heat, carbon dioxide and contaminants.

To examine the advantages of MV and CDV, many studies were conducted in the last years, see e.g. [4–16]. Yin et al. [5] studied and compared MV and CDV in a Boeing 767 aircraft cabin section. They advise CDV for a possible use in airplanes because of diminished CO_2 concentration and increased relative humidity in the passenger zone.

Müller et al. [6] as well as Schmidt et al. [8] investigated MV, CDV and a hybrid system (see Fig. 43.1c) in an A320 cabin mock-up sectin. They found a trend to "hot heads" for CDV in contrast to a higher draft risk for MV. As long as the vertical temperature stratification can be kept small enough, CDV prospects an improved passenger thermal comfort over MV. MV, CDV and a personalized air distribution system were compared in a Boing 767 aircraft cabin section by Zhang et al. [7] by means of CFD. The results show the most uniform air temperature, but the highest air velocities and CO_2 concentrations for MV. The personalized air distribution system, which supplied the passenger breathing zone with outside air, creates the best cabin environment. Recently, Bosbach et al. [16] investigated a ceiling based cabin displacement ventilation (CCDV) system experimentally in a Dornier 728 aircraft cabin. They compared velocity and temperature distributions and the heat removal efficiency of six different ventilation systems (MV, CDV, CCDV and hybrid CCDV/CDV cases). It was found, that CCDV allows well to balance out the potential benefits and drawbacks of MV and CDV.

In the current study, CDV and a hybrid ventilation (HV) system, where CDV is supported by the lateral MV air outlets, which carry 30 % of the fresh air, are investigated and compared under real flight conditions. While the resulting flow velocities and fluid temperatures were already presented and discussed elsewhere [11, 17], this study demonstrates further benefits of the dynamic performance of CDV and HV regarding control of the surface temperatures.

43.3 Experimental Set-up

43.3.1 General Description

The measurements presented in the following were conducted in the Advanced Technology Research Aircraft (ATRA), which is an Airbus A320 and the largest test bed of the German Aerospace Center, at a flight level of about 37,000 ft and a Mach number of Ma = 0.78. For the study, the largest part of the AFT temperature zone has been refurbished to CDV, where the experiments were conducted. A detailed description of the flight test installation is given in [11]. Before take-off, ground tests were performed to ensure a homogenously heating up of the passenger dummies and the cabin materials and to see the changes between ground and flight conditions.

After reaching the flight level, a waiting time of 85 min was held to achieve static thermal conditions. Two ventilation scenarios were investigated. First pure CDV, for which low-draft air outlets have been installed at the position of the DADO panels. Secondly, a hybrid case (HV), where 70 % of the fresh air was supplied through these new outlets and 30 % was supplied through the original lateral outlets, was studied. During both scenarios, the air was leaving the cabin through the pre-existing ceiling air outlets, see Fig. 43.1b, c.

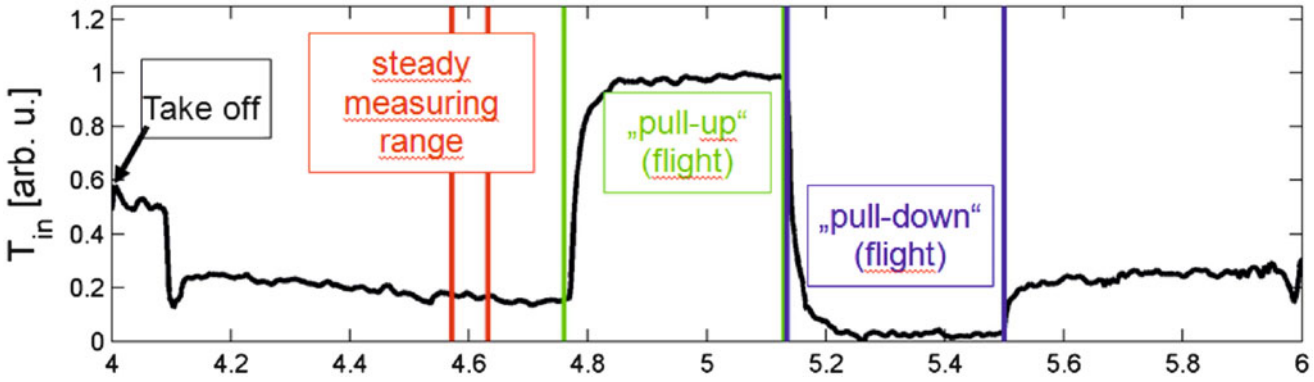

Fig. 43.2 Climate phases during the flight tests for CDV

Fig. 43.3 (**a**) Rotation stage for the infrared camera, and (**b**) flight test instrumentation with thermal passenger dummies and rotating infrared camera in the modified cabin section

To study the heating ("pull-up") and cooling ("pull-down") performance of the two ventilation systems, abrupt changes of the inflow temperature were conducted after the steady measurements. An overview of the different phases in terms of the inflow temperature is given in Fig. 43.2.

To detect the surface and flow temperatures as well as the flow velocities, a computer controlled two axis rotating infrared (IR) camera set-up and in addition more than 200 temperature, air flow velocity, pressure and humidity sensors were installed in the measurement section. The results of the steady measuring range as well as the heating and cooling dynamics of the infrared camera were discussed in this paper.

43.3.2 Infrared Camera

To investigate the surface temperatures of the cabin materials, a programmable, step motor driven, automatically rotatable infrared camera set-up was developed and installed in the front part of the measurement section, see Fig. 43.3a, b. To get an overview of the whole cabin, the set-up is able to rotate the camera into eight positions every minute. Like this, we were able to compile a panorama picture from the taken images every minute. The camera has a resolution of 640 × 480 pixels and a sensitivity of 0.08 K.

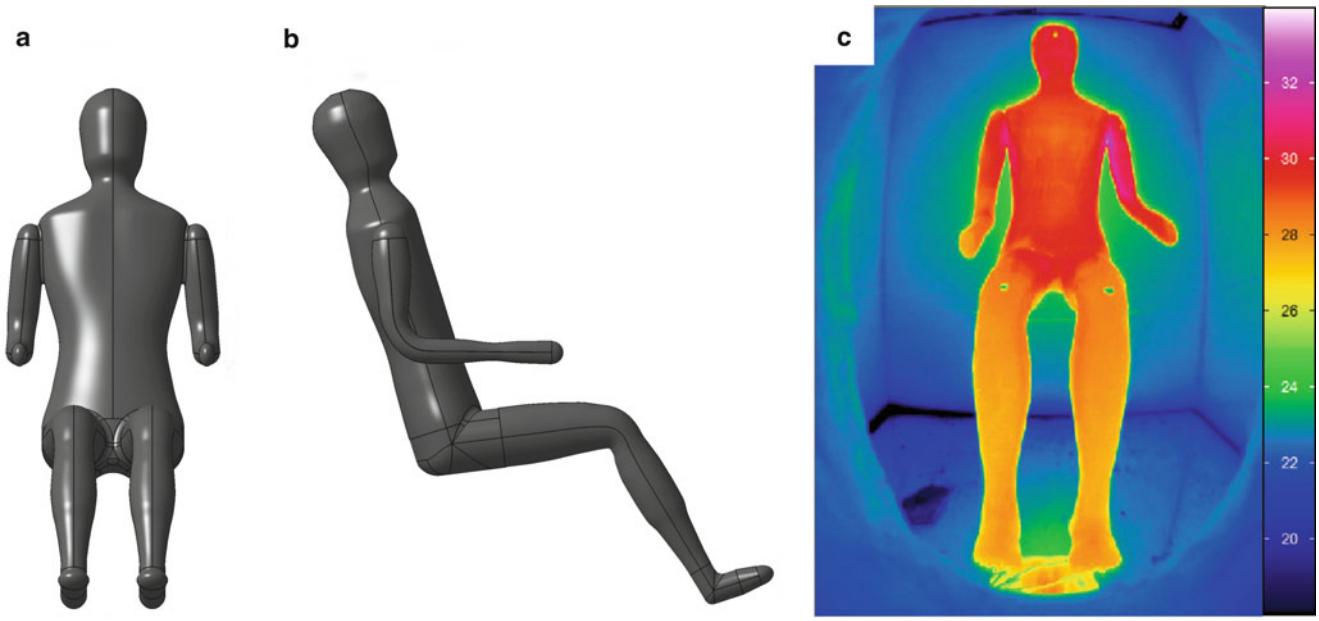

Fig. 43.4 Thermal passenger dummies (**a**) front view, (**b**) side view and (**c**) inside a test environment for approval of the technical specifications

43.3.3 Thermal Passenger Dummies

To realistically simulate the thermal boundary conditions during the tests, 63 thermal passenger dummies (Fig. 43.4a, b) were developed and placed on 11 seats rows in the measurement section (Fig. 43.3b). The role of the dummies is to provide realistic heat loads and obstructions, as the passengers do under operational conditions. Each dummy provides a heat load of 75 W. To guarantee the comparability of the dummies, each passenger model has been investigated in a thermal box prior to the flight and ground tests, see Fig. 43.4c. Clearly, the heated passenger dummy can be detected, which reveals a characteristic and realistic temperature fingerprint. The latter results from the fact, that the dummies are constructed to provide a constant heat flux density over the whole surface. Only at the head, the heat flux density is slightly increased in order to simulate the thermal impact of a real passenger in the experiments.

In the cabin environment, the passenger dummies have mainly three possibilities to release their heat load. First, the heat can be transported away from the dummy surface by free convection. The second possibility is forced convection which will be evocated by external movement. Finally discharge of the heat by thermal radiation exchange with the surrounding surfaces plays an essential role. The exact composition of these processes can vary between different seat positions and ventilation scenarios and will have an impact on the resulting surface temperatures. If e.g. the surrounding flow velocities are low, the dummies have to release their energy mainly by thermal convection and//or radiation, which would result in higher surface temperatures.

43.4 Results

Consequently, the static and also the dynamic surface temperatures in the cabin are important to characterize CDV and HV. With panorama pictures of the internal surface temperature distribution, which were created from the single recorded IR views, the temperature distribution among the different seat positions could be detected. Furthermore panorama pictures show the temperature distribution of the surrounding surfaces. Figure 43.5 depicts the static temperature fields of the flight tests (a) CDV, (b) HV from which, for the sake of comparability, the mean inflow temperature has been subtracted. The central part of the images corresponds to a look in the back of the cabin and shows the side panels, ceiling panels, hat racks and floor, where the temperature distribution is very similar in CDV and HV. A first look at the panorama pictures reveals a very homogenous temperature distribution between different seat positions for the whole cabin. However, characteristic

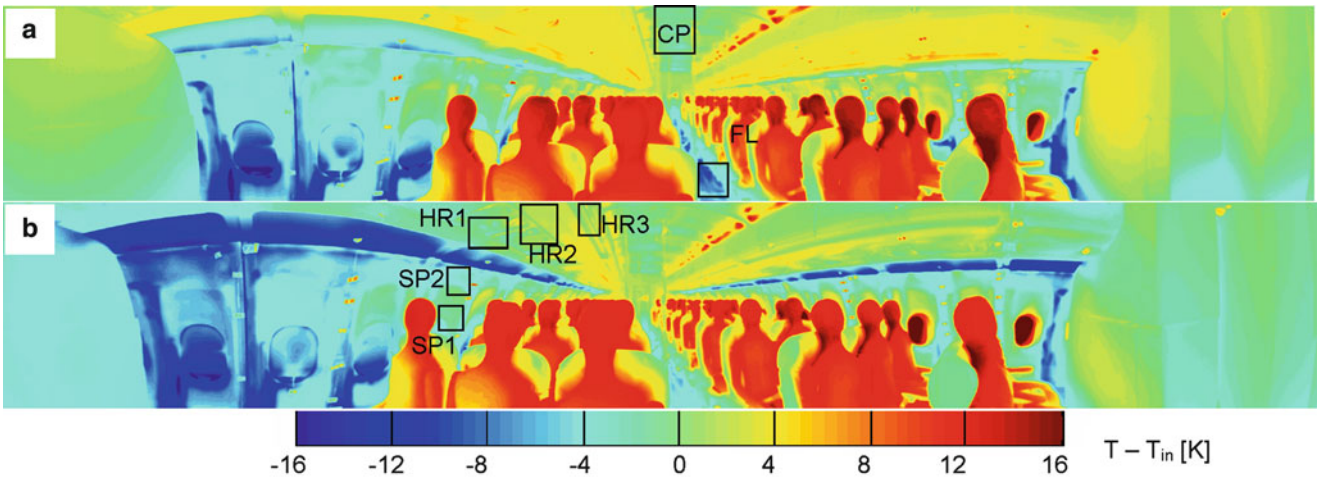

Fig. 43.5 Cabin surface temperature distribution of (**a**) CDV and (**b**) HV by panorama IR- thermography. The *rectangles* in (**c**) and (**d**) depict the evaluation areas for Fig. 43.8 (*FL*, floor, *SP* side-panel, *HR* hat-rack, *CP* ceiling-panel)

differences between HV and CDV can be found. First, there is a temperature difference between the window seats on the right hand (flight direction) and the left hand cabin side, which is caused by solar radiation on the left cabin side, even though the window shutters were closed during the test flights. The floor reveals lower temperatures for CDV than HV due to the higher volume flow at CDV. Further differences between CDV and HV are cooler lateral outlets, hat racks and side walls at HV. While the head temperatures are slightly higher at CDV due to the lower velocity and turbulence level caused by the lateral air jets, the chest temperatures are higher at HV due to the lower air flow rate in the lower part. An exception is the wall seats, where the chest temperatures are lower at HV due to the lower wall temperatures. Because of the radiation and thermal convection of the dummies there are higher internal temperatures at CDV as compared with HV.

To investigate the heating and cooling performance, "pull-up" and "pull-down" scenarios were conducted after the static measurements (Fig. 43.2). To study the dynamics, the inflow temperature was increased and decreased abruptly by about $\Delta T_p \cong 10$ K. In the following, the results for the pull-up scenario are shown. While the air temperatures, which have been investigated in parallel, follow the changed inflow temperature quite fast [11], a slow dynamics has been observed at the interior cabin surfaces.

Panorama pictures of the surface temperature distribution at different points in time after begin of the pull-up of HV are compiled in Fig. 43.6. In order to allow for identification of temperature changes, the initial temperature distribution (T_0) prior to the pull-up has been subtracted and the result has been normalized to ΔT_p.

The first panorama picture after 250 s shows large temperature changes at the lateral inlets and near to it. The other parts of the cabin show small surface temperature modifications during this period, because mainly the exchange of the cabin air with the cool air takes place during this period, which is a prerequisite for surface temperature changes. Fig. 43.6b) and the following figures clearly reveal how subsequently the surface temperature changes take place, starting at the lateral inlets. For the pull-down scenarios the surface temperature changes start first in the lower part of the cabin and later affect also the upper part, which are discussed in [10].

To compare the characteristics of the ventilation systems and the temperature jumps, the differences between the pull-up and pull-down scenario of CDV and HV after 1,500s are compared in Fig. 43.7. Higher temperature changes for HV near the lateral outlets, caused by the higher velocity and turbulence level, were observed. Figure 43.7 shows smaller floor temperature and higher ceiling temperature changes for pull-up in comparison with pull-down. At CDV, the temperature changes start in the lower part of the cabin, while at HV first the regions in the surrounding of the lateral outlets are affected. As a consequence, the racks, side panels and dummies are cooled faster at HV as compared to CDV.

In order to characterize the dynamic response of the cabin interior, the time that a certain mean temperature needs to reach 30 % of the applied temperature jump, $t_{0.3}$, was calculated from the thermography images and plotted in Fig. 43.8 for the pull-up and pull-down scenario at CDV and HV. Depicted are the arithmetic averages of different cabin parts (see Fig. 43.5). On the floor, a major delay time can be observed for both ventilation systems, which is generally higher for pull-down, because the warm air rises up at pull-up due to buoyancy. The two measurement ranges SP1 and SP2 reveal a great difference between CDV and HV at the side walls, which we ascribe to the pressure gradient induced by the lateral air jets. The latter increase the air exchange in this region by entrainment and removal of air in the shear layers. Until position HR2,

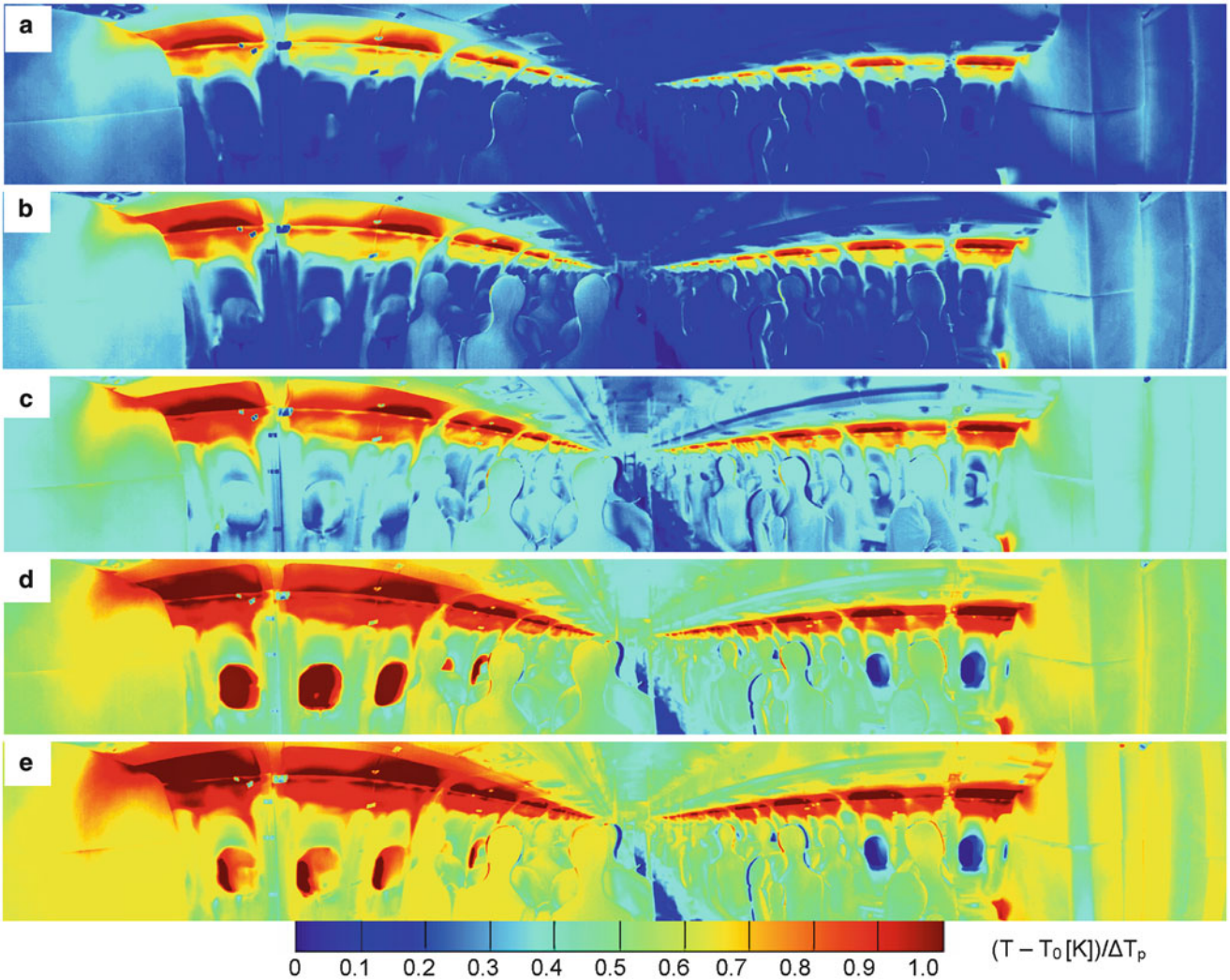

Fig. 43.6 Normalized differences of surface temperatures ($(|T - T_0|)/\Delta T_p$) upon pull up for HV after (**a**) 250 s (**b**) 500 s (**c**) 1,000 s (**d**) 1,500 s (**e**) 2,000 s as measured by panorama IR- thermography. T_0 denotes the surface temperature distribution before the pull up and ΔT_p the temperature jump

the higher turbulence level at HV causes faster changes of the surface temperatures as compared to CDV. In the upper part of the cabin (HR3 and CP), $t_{0.3}$ becomes very similar for both systems.

Very similar values were found from evaluation of local temperature sensors in [17], where besides floor, hat rack and ceiling temperatures also fluid temperatures in the passenger zone have been evaluated. It was found, that $t_{0.3}$ of the air temperatures is generally smaller for CDV for $z < 1$ m and smaller for HV for $z > 1$ m as well as at the cabin surfaces. The observed faster fluid temperature changes in the passenger zone were ascribed to the attraction of fresh air by the heat loads due to the buoyancy dominated flow at CDV.

43.5 Summary

For the first time cabin displacement ventilation (CDV) and a hybrid ventilation (HV), where 30 % of the fresh air was supplied through the original lateral outlets, have been investigated under flight conditions. The tests were performed in the refurbished AFT zone of an Airbus 320 aircraft, i.e. the "Advanced Technology Research Aircraft" (ATRA) of the German Aerospace Center. Here the focus was kept to measurements performed with a rotatable infrared camera set-up, allowing for time resolved acquisition of the surface temperatures during the flight tests. Measurements under static flight conditions

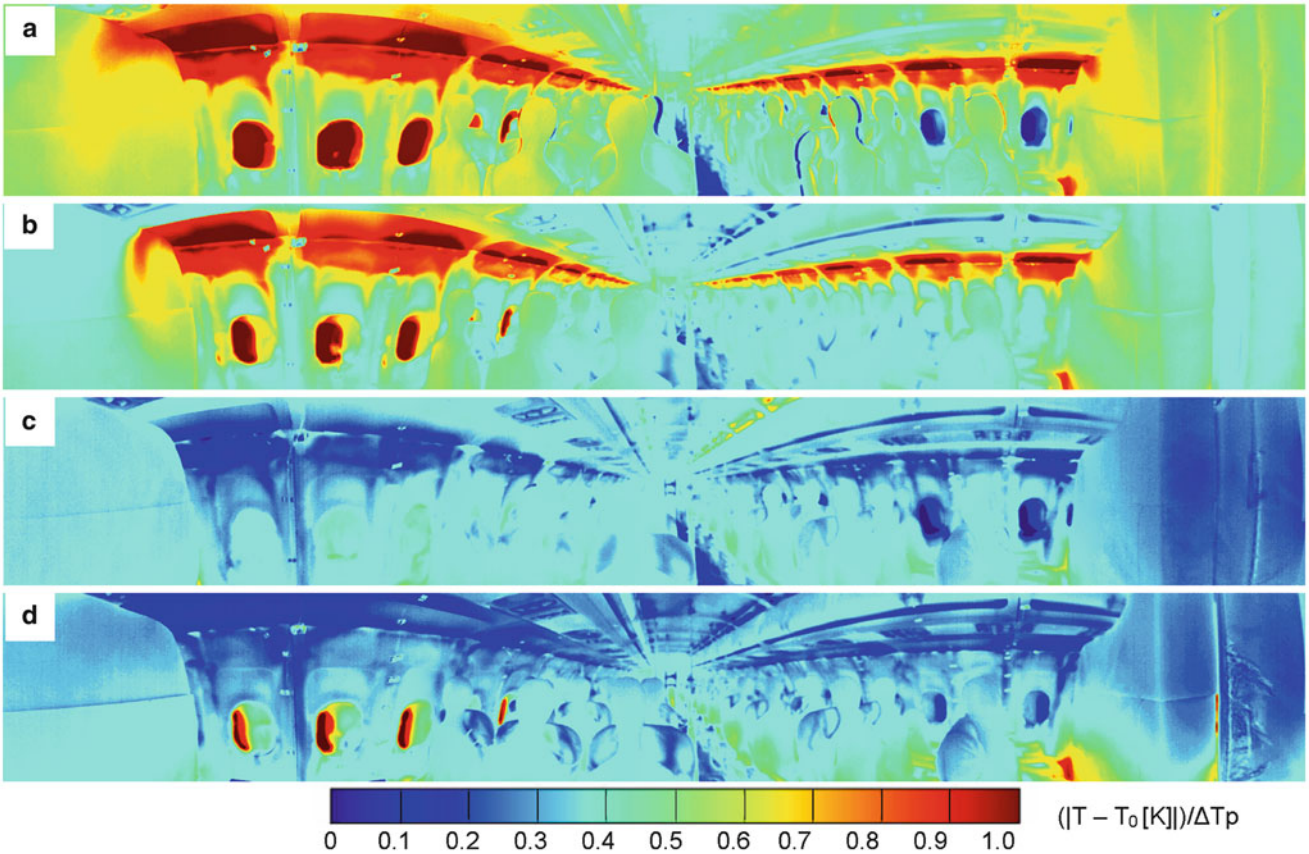

Fig. 43.7 Normalized differences of surface temperatures $|T - T_0|$ after 1,500 s for (**a**) pull up HV, (**b**) pull down HV (**c**) pull up CDV and (**d**) pull down CDV. ΔT_p denotes the temperature jump and T_0 the surface temperature distribution before ΔT_p

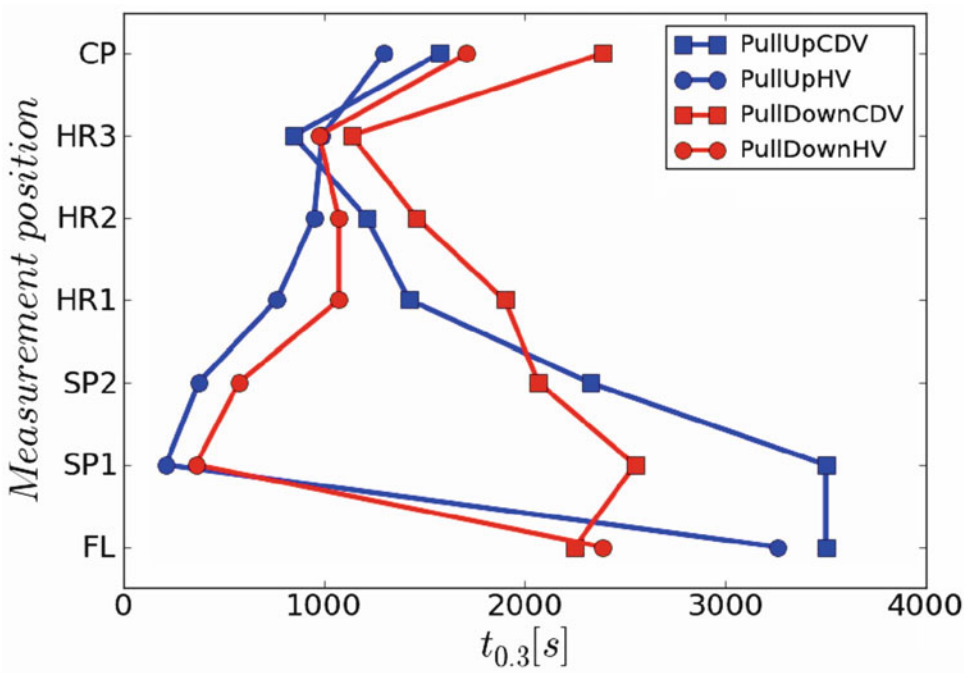

Fig. 43.8 Time that the spatially averaged temperature in the respective evaluation area needs to reach 30 % of the applied temperature jump ΔTp ($t_{0.3}$) for different positions for CDV (*squares*) and HV (*circles*) during pull up (*blue*) and pull down (*red*). The *lines* are just a guide to the eye

unveil a homogeneous temperature distribution between the seat positions for both ventilation systems. Supply of air through the lateral outlets at HV results in reduced wall temperatures and an improved surface cooling performance at the walls. While in the upper cabin part, the performance of CDV and HV regarding control of the surface temperatures is very similar, HV is up to 30 % faster regarding temperature control in the lower cabin part.

Acknowledgements

This project was supported by the German Federal Ministry of Economics and Technology under grant number 20K0806D on the basis of a decision of the German Bundestag. The responsibility of the content is the authors.

We thank all colleagues at Airbus Operations and the German Aerospace Center, who contributed to the successful preparation and performance of the ground and flight tests.

References

1. Hunt E, Reid D, Space D, Tilton F (2013) Commercial airliner environmental control system, engeneering aspects of cabin air quality. http://www.google.de/url?sa=t&rct=j&q=&esrc=s&source=web&cd=2&cad=rja&ved=0CD0QFjAB&url=http%3A%2F%2Fwww.smartcockpit.com%2Fdownload.php%3Fpath%3Ddocs%2F%26file%3DEngineering_Aspects_of_Cabin_Air_Quality.pdf&ei=r0ESUafINsjssgaQkoCwBA&usg=AFQjCNEcSaJ1n2XTQNHwfpMCzmaUpUhR9Q&bvm=bv.41934586,d.Yms. Website open at 6th Feb 2013
2. Hunt H, Space D (2013) The airplane cabin environment issues pertaining to flight attendant comfort http://www.donaldson.com/en/aircraft/cabinairquality/supportDocs/18%20Issues%20Pertaining%20to%20Flight%20Attendant%20Comfort.pdf. Website open at February 6th, 2013
3. Knepple RA (2012) Die energie-autarke Kabine - das Ende der klassischen Bordnetze, Deutscher Luft- und Raumfahrtkongress, Berlin10–12 Sept 2012
4. Kühn M, Bosbach J, Wagner C (2009) Experimental parametric study of forced and mixed convection in a passenger aircraft cabin mock-up. Build Environ 44(5):961–970
5. Yin S, Zhang T (2009) A new under- aisle displacement air distribution system for wide- body aircraft cabins. In: Eleventh international IBPSA conference, Glasgow, 27–30 July 2009
6. Müller D, Schmidt M, Müller B (2011) Application of a displacement ventilation system for air distribution in aircraft cabins. In: AST 2011, Hamburg, Mar 31–Apr 1 2011
7. Zhang T, Chen Q (2007) Novel air distribution systems for commercial aircraft cabins. Build Environ 42:1675–1684
8. Schmidt M, Müller D, Gores I, Markwart M (2008) Numerical study of different air distribution systems for aircraft cabins. In: 11th international conference on indoor air quality and climate, Copenhagen, 17–22 Aug 2008
9. Zhang T, Chen Q (2005) Comparison of different ventilation systems for commercial aircraft cabins. In: Proceedings of indoor air 2005, Vol IV. Beijing, pp 3205–3210
10. Dehne T, Bosbach L, Heider A (2012) Dynamics of aircraft cabin ventilation by in-flight infrared thermography. In: Eleventh quantitative infrared thermography QIRT conference, 2012, Neapel
11. Bosbach J, Heider A, Dehne T, Markwart M, Gores I, Benfeldt P (2012) Evaluation of cabin displacement ventilation under flight conditions. In: 28th international congress of the aeronautical sciences ICAS2012, Brisbane, 23–28 Sept 2012, ISBN 978-0-9565333-1-9
12. Zhang Z, Chen X, Mazumdar S, Zhang T, Chen Q (2009) Experimental and numerical investigation of airflow and containment transport in an airliner cabin mockup. Build Environ 44:85–94
13. Mazumdar S, Chen Q (2007) Impact of moving bodies on airflow and containment transport insider aircraft cabins. In: Roomvent 2007, Helsinki
14. Gao NP, Niu JL (2008) Personalized ventilation for commercial aircraft cabins. J Aircr 45(2):208–512
15. Mangili A, Gendreau MA (2005) Transmission of infectious diseases during commercial air travel. Lancet 365:989–996
16. Bosbach J, Lange S, Dehne T, Lauenroth G, Hesselbach F, Allzeit M (2012) Alternative ventilation concepts for aircraft cabins. In: Deutscher Luft- und Raumfahrtkongress, Berlin, 10–12 Sept 2012
17. Bosbach J, Heider A, Dehne T, Markwart M, Gores I, Bendfeldt P (2012) Flight testing of alternative ventilation systems for aircraft cabins. In: 18 DGLR-Fach-symposium der STAB, Stuttgart, 6–7 Nov 2012

Chapter 44
Study of Elastomeric Membranes for Vibration Dampers in Non-stationary Conditions

M. Sasso, G. Chiappini, M. Rossi, and E. Mancini

Abstract The present work describes the study carried out to characterize the constitutive and operating behavior of a rubber membrane; the application under examination consists of a air-oil separator for dampers of helicopter rotor blades. The main requirements are that the membrane must be mounted inside the main tube through a manual reversal movement, must withstand a differential pressure of 3 bar in exercise and 7.5 bar in the acceptance test, without tearing and respecting the dimensions allowable within the damper, and it must ensure a tight seal. Moreover, the membrane will be subjected to cycles of elongation and shortening due to the operation of a piston which, by means of a suitable contrast spring, allows the consumption and charging of the oil in the damper. The study was conducted using FEM simulations that take into account large displacements and the hyperelastic, viscoelastic and pseudo-elastic characteristics of the rubber material, in order to simulate the global behavior of the membrane starting from the very first loading cycles and for a given time duration.

Keywords Elastomers • Viscoelasticity • Hyperelasticity • Mullins effect • FEM

44.1 Introduction

The present work concerns the study of a membrane, made of elastomeric material, used for the task of air-oil separation in dampers of helicopter rotors. In these dampers, the damping action takes place for the viscous effect due to the passage of oil through calibrated holes; the fact that the oil within the damper must have a certain overpressure with respect to the outside, coupled with the fact that small oil leakage are unavoidable, leads to the need of a feeding system of the oil, able to guarantee the sealing and to reduce the pressure loss. In dampers commonly used, this is accomplished by means of movable metal elements; however, this solution presents some drawbacks, especially for the reliability and wear of the contact seals.

In this paper instead, a feasibility study is conducted on the replacement of the "traditional" metal plate with a rubber membrane which carries out the dual task of: allowing the preservation of a differential pressure without rupture, and ensuring the sealing of the oil itself, in particular in correspondence of the outer tube. Figure 44.1 shows in detail the area of the damper which contains the membrane.

The study here presented consists in the simulation by a commercial finite element code; the main results of the various stages of assembly and operative life of the membrane will be shown. With regard to the material, the main phenomena related to rubber-like materials have been taken into account, such as hyperelasticity, viscoelasticity, and pseudo-elasticity (or mullins effect); the calibration of the relevant constitutive models has been carried out through an extensive experimental campaign, according to the methods described in [1–4].

M. Sasso (✉) • G. Chiappini • M. Rossi • E. Mancini
Dipartimento di Ingegneria Industriale e Scienze Matematiche, Università Politecnica delle Marche,
via Brecce Bianche, 60131 Ancona, Italy
e-mail: m.sasso@univpm.it

M. Rossi et al. (eds.), *Residual Stress, Thermomechanics & Infrared Imaging, Hybrid Techniques and Inverse Problems, Volume 8*,
Conference Proceedings of the Society for Experimental Mechanics Series, DOI 10.1007/978-3-319-00876-9_44,

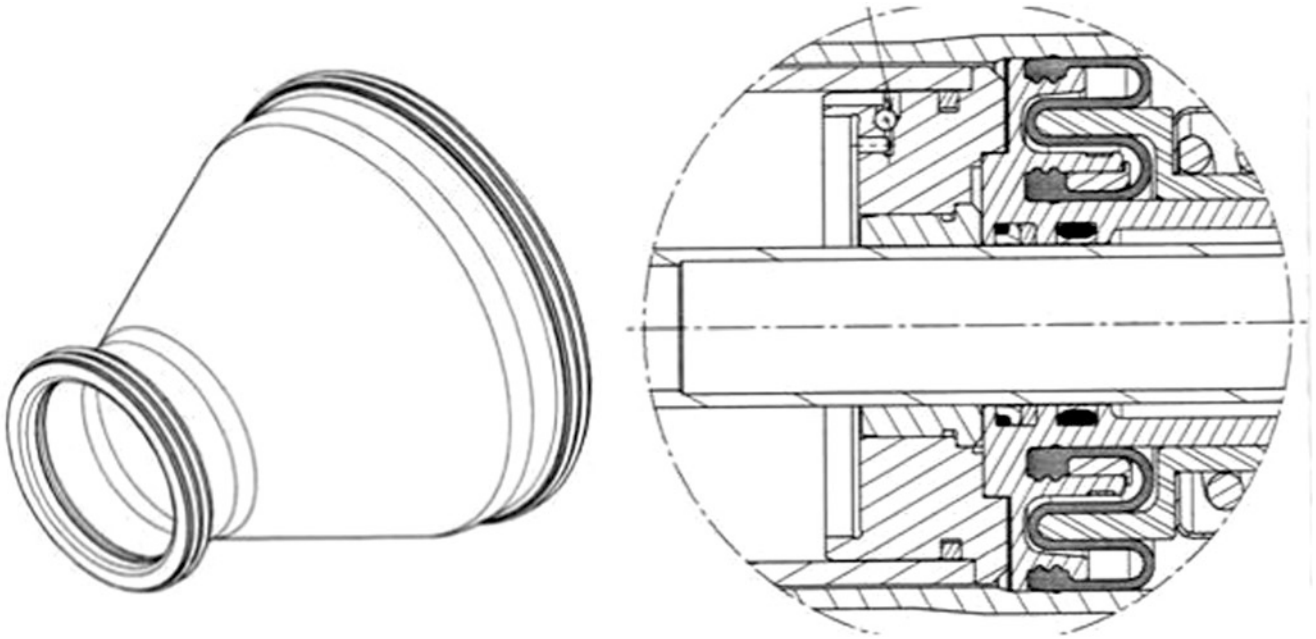

Fig. 44.1 Detail of the membrane before and after assembly

44.2 Material Characterization

Since the membrane in question, after installation, will bear in its operative life a relatively limited number loading-unloading cycles of the duration of 300 h of flight, in the simulations we attempted to reproduce as faithfully as possible the operation under non-stationary conditions, that is from the first cycle and without conditioning cycles; the characterization of this material consisted in determining not only the hyperelastic characteristic of the rubber, but also to its time-dependent response due to viscoelasticity, and its softening due to mullins effect.

44.2.1 Hyperelasticity

The characterization of the hyperelastic behavior of the virgin material (i.e. without conditioning cycles for stabilizing the mullins effect) was performed by means of different experimental tests; the main test implemented is a biaxial tension on cruciform specimen, that provides a heterogeneous distribution of deformation within the specimen; in order to obtain the constitutive coefficients from this type of test, the method of virtual fields (VFM) has been applied to deformation maps detected experimentally by DIC [1]. The identified coefficients of the third order Ogden model are shown in Table 44.1; they were excellently confirmed by conventional tensile testing (UT) and compression (UC) uniaxial, as well as equal-biaxial tension (ET) by bulge test. The stress–strain are shown in Fig. 44.2; in red and magenta are reported the analytical curves related to the coefficients obtained from VFM, in blue the experimental ones obtained from the individual tests UT, UC, ET.

The tests UT and ET were also used to identify the stress and strain at failure of rubber, summarized in Table 44.2, which will then be used with appropriate failure criteria [5] to verify the resistance of the membrane to the operating loads.

$$W = \sum_{p=1}^{N} \frac{\mu_p}{\alpha_p} \left(\lambda_1^{\alpha_p} + \lambda_2^{\alpha_p} + \lambda_3^{\alpha_p} - 3 \right)$$

Table 44.1 Ogden model coefficients

μ_1 [MPa]	+0.0006
μ_2 [MPa]	−0.6382
μ_3 [MPa]	+0.6130
α_1	+2.3240
α_2	−1.1556
α_3	+2.8690

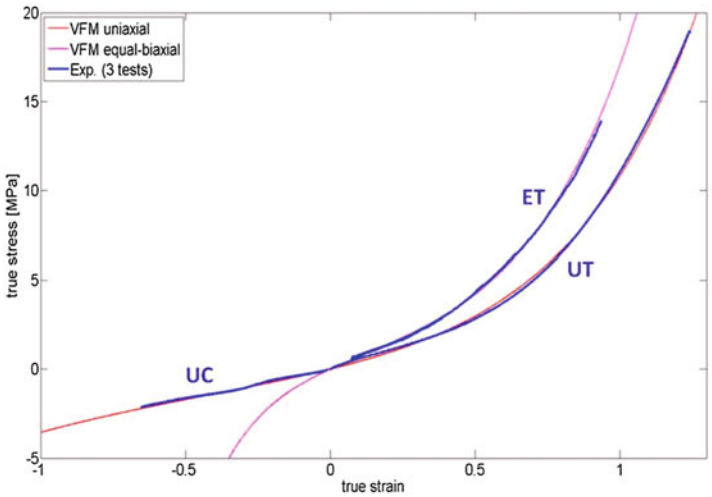

Fig. 44.2 Hyperelastic stress–strain curves

Table 44.2 Stresses and elongations at failure

	UT	ET
σ_{ut} [MPa]	25	11.5
λ_{ut}	4.02	2.35

44.2.2 Viscoelasticity

The material viscoelasticity has been highlighted as well as by cycles of hysteresis curves encountered in repeated loading-unloading test, shown in the next Sect. 44.2.3, also from creep and relaxation tests carried out at room temperature in uniaxial compression. The creep test was carried out by imposing an engineering constant stress of 5.5 MPa and measuring the deformation accumulated over time from the cylindrical specimen; the test of relaxation was carried out by imposing an engineering strain of −56 % and by measuring the required force; the duration was approximately $3{\cdot}10^5$ s for both tests.

The experimental data were used to perform the fitting of a 10 terms Prony series, with relaxation times chosen a priori and evenly spaced in the range $10^0 \div 10^7$ s (after extrapolation of the experimental curves). The experimental results are shown in Fig. 44.3 together with the values obtained numerically; one observes a correspondence almost perfect in relaxation stress, while there is a slight divergence, as one might expect using a generalized Maxwell model, in the description of the creep strain. The coefficients of the series of Prony are shown in Table 44.3.

44.2.3 Pseudo-elasticity

The characterization of the mullins effect was conducted according to the previous work [4]; a test was carried out again on a cruciform specimen repeating several loading-unloading cycles at different levels of elongation. The experimental curves of force and crosshead displacement are shown in Fig. 44.4, for both the horizontal and vertical directions.

Through the DIC and the VFM, applied to the last cycle of each series of repetitions, we calibrated the Ogden-Roxburgh model [6, 7], which is briefly summarized by the relations:

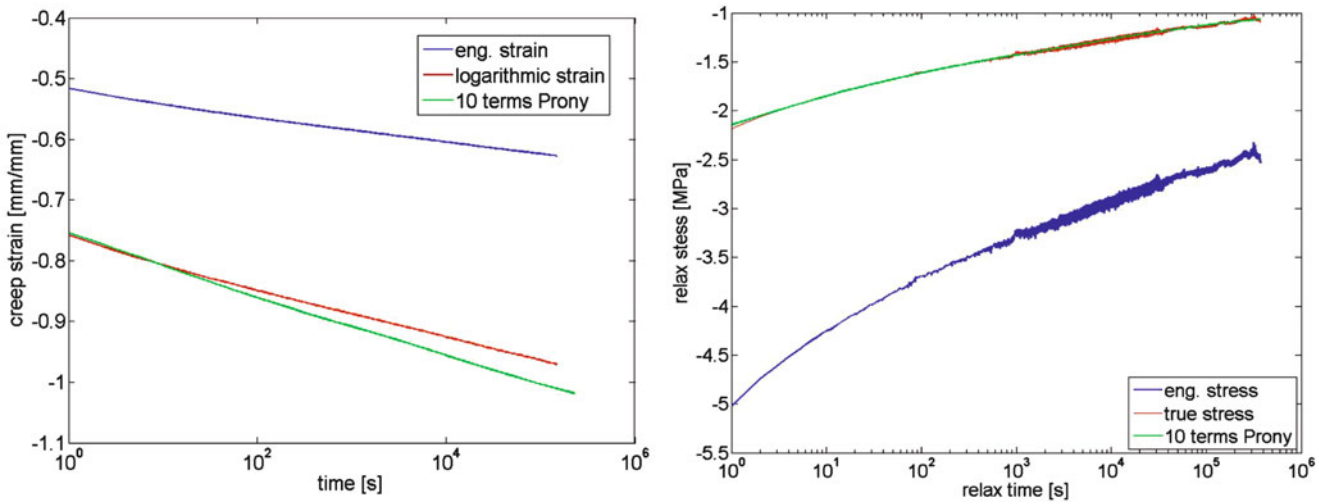

Fig. 44.3 Creep and relaxation curves

Table 44.3 Prony series coefficients

τ_i	1.00	5.62	31.6	177.8	1,000	5,623	3,1628	177,828	1E6	10E6
α_i	0.0974	0.1011	0.0776	0.0695	0.0478	0.0581	0.0464	0.0506	0.0025	0.0015

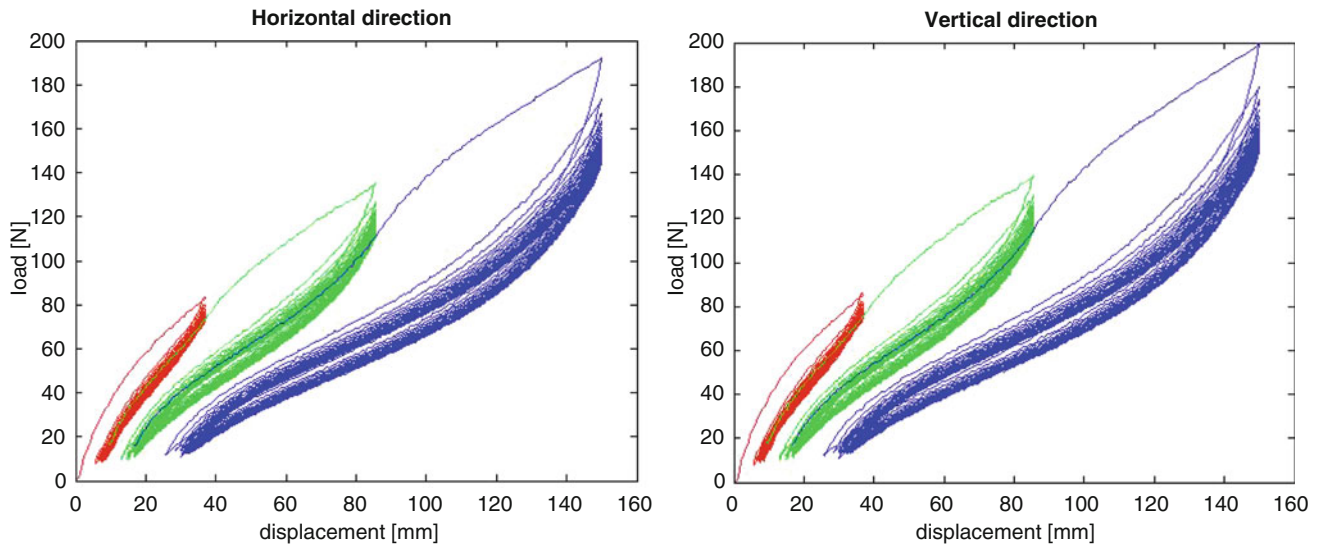

Fig. 44.4 Load–displacement curves on the two branches of the cruciform specimen

$$\sigma_s = \eta\sigma_i = \lambda_i \frac{\partial \tilde{W}}{\partial \lambda_i}$$
$$\eta = 1 - \frac{1}{r} erf\left[\frac{\tilde{W}_m}{\mu \cdot m}\left(1 - \frac{\tilde{W}}{W_m}\right)\right] \tag{44.1}$$

where σ_i e σ_s are respectively the stresses of the virgin material (hyperelastic only) and of the cycled material (with softening); m and r are material parameters, which were found to value 0.308 MPa e 2.559.

The overall results of the characterization of the material is synthesized by the curves of Fig. 44.5, where are compared the stress–strain curves obtained by cyclic tests repeated on a dumbbell specimen; the experimental curves are on the left,

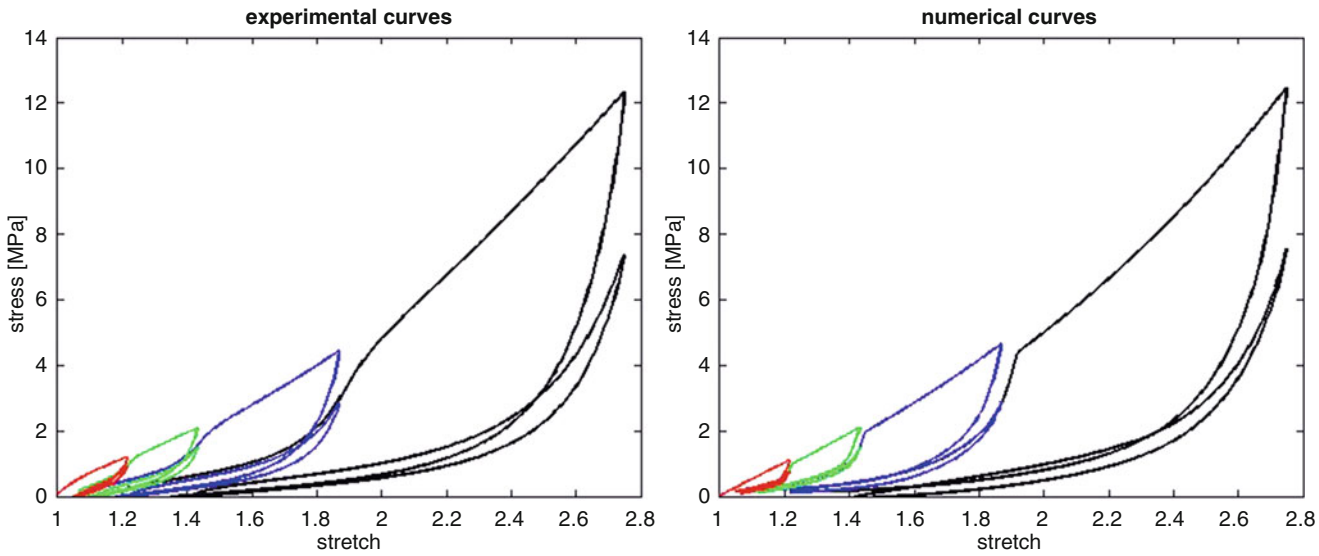

Fig. 44.5 Cyclic test on a dumbbell specimen: experimental (*left*) and numerical (*right*)

while on the right are reported the analytical curves that contemplate simultaneously all the three phenomena of hyperelasticity, viscoelasticity and pseudo-elasticity (for the analytical curves are shown only the first and last cycle of several repetitions). It is noticed the good agreement between the curves; the main difference, however, acceptable, is given by a lower amplitude of the hysteresis loop in the analytical curves.

44.3 FE Model

The elastomeric component of Fig. 44.1 was modeled within the commercial FEM code ANSYS® v. 13.0; the model was made by axisymmetric PLANE 183 elements (Fig. 44.6), with average size of 0.3 mm. The membrane has a constant thickness of 1.5 mm, except in areas of gripping and sealing where it has a thickness of 4 and 3 mm, with further grooves of 0.3 mm that allow the pressure seal through their crushing. The minimum inner radius (R_i) is 18 mm, which coincides with the mounting position in the damper, while the maximum outer radius (R_o) is 39 mm and 42 mm is the outer mounting radius (R_{om}) after the reversal, corresponding to the inner diameter of the main tube. The length (L) of the membrane before the inside-out reversal is 80 mm. The simulation is divided into several phases: (1) reversal of the membrane through 180° rotation (and translation) of the external grip portion. (2) Activation of the contacts between the inner tube and the crushing grooves, lifting of the piston (approximately 21 mm) without differential pressure. (3) Return of the piston into the initial position with insertion of the operating pressure of 3 bar on the upper face of the membrane; this condition represents the situation of the damper fully charged at the beginning of its operating life. (4) The oil consumption determines a progressive reduction of overpressure, and then the plunger is pushed upwards by the contrast spring; the piston advances then of 21 mm and the pressure on the upper face of the membrane decreases progressively up to 1.5 bar; this is the final condition of exhausted damper that needs the oil recharge. (5) Simulation of prolonged maintenance (300 h) at 3 bar with piston down. (6) Simulation of the qualification test at 7.5 bar (300 s) with piston down. (7) Simulation of numerous cycles of loading-unloading from 3 to 1.5 bar in non-stationary regime of the duration of 300 h each, with evaluation of the evolution of the strain over time to compare with ultimate values, according to the criterion of maximum deformation [5].

As explained above, in the simulations we tried to take into account all possible factors; so the resulting model is rather complex, as it included non-linearity due to large displacements, contact, hyperelasticity of the material (Ogden model of the third order), as well as viscoelasticity (11 elements Prony series) and mullins effect (two coefficients Ogden-Roxburgh).

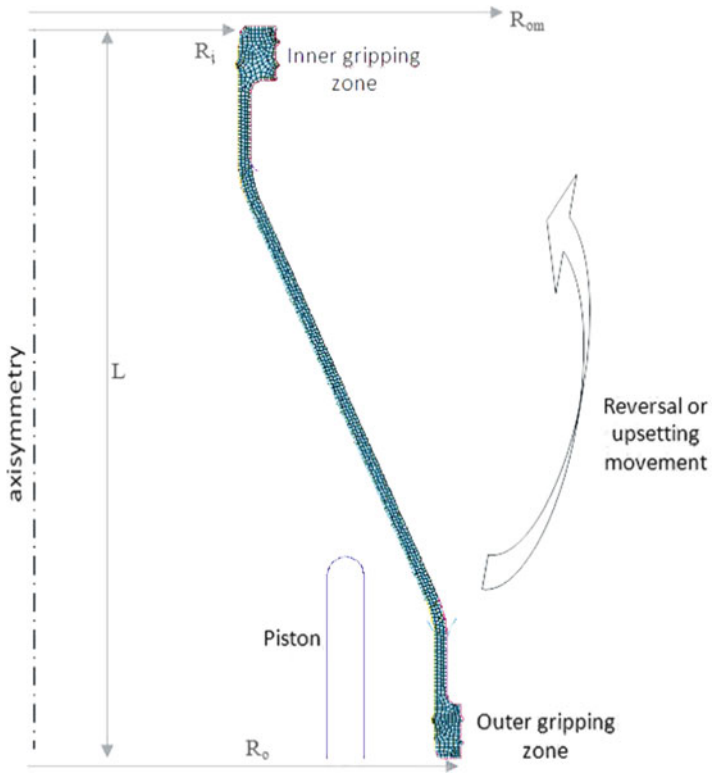

Fig. 44.6 FE model of the rubber membrane

44.4 Simulation Results and Discussion

The main results of the simulations of the different phases described in the previous paragraph are exposed below. For the sake of brevity, only the maps of maximum principal strain (ε_1) and stress (σ_1) will be shown.

It should be noted that the upsetting (phase 1), whose final deformed is shown in Fig. 44.7, has been simulated as axisymmetric, while in reality this is a process carried out manually in two opposite points of the membrane and the rest of the material is accompanied in the movement which. This approximation would be valid for a perfectly hyperelastic material, where the final stress depend only from the final state of the object and not from the history of the load, while it is not totally correct if we consider a damage phenomenon as the mullins effect; however, the logarithmic strain reached at the end of this phase is not very high for this material (0.21 max), so the eventual damage has been neglected and the axisymmetric approximation has been accepted. Figures 44.8, 44.9, and 44.10 refer instead to steps 2, 3 and 4 simulated considering only the hyperelasticity of the material; it is noted that the stresses are very small, and the maximum principal strain occurs at the inner lobe of the membrane when the pressure is 3 bar (phase 3), and the outer lobe when the plate is lifted at a lower pressure (phase 4). Anyway, these strain levels are tolerable by the material.

The time-dependent behavior of the material comes into play when one considers the evolution of the membrane subjected to the charge condition (plate lowered, as in step 3) for a prolonged period of time equal to 300 h. The deformed shape and related maps are shown in Fig. 44.11, where it is noted that the internal lobe is more pronounced with respect to Fig. 44.10, and the maximum values are increased up to 0.68 for ε_1 and up to 2.09 MPa for σ_1.

Reproducing the values of the main stretch of all the nodes calculated to stage 3 and 5, normalized with respect to the ultimate values, as shown in Fig. 44.12, it is noted that the dispersion of points widens, but without getting too close to the limit resistance, which is ideally represented by lines connecting the experimental points in ET (triangle) and UT (round).

Similarly, in Fig. 44.13 we show the normalized values of elongation for the stage 6 of the simulation, which reproduces the qualification test to be carried out on a one-off membrane sample, with an internal pressure of 7.5 bar at the initial time and after 300 s; also in this case, after the initial loading, the relaxation of the material causes the deformation to proceed over time, reaching values rather considerable, amounting to approximately 70 % of maximum elongation at break; however the application appears to be safe.

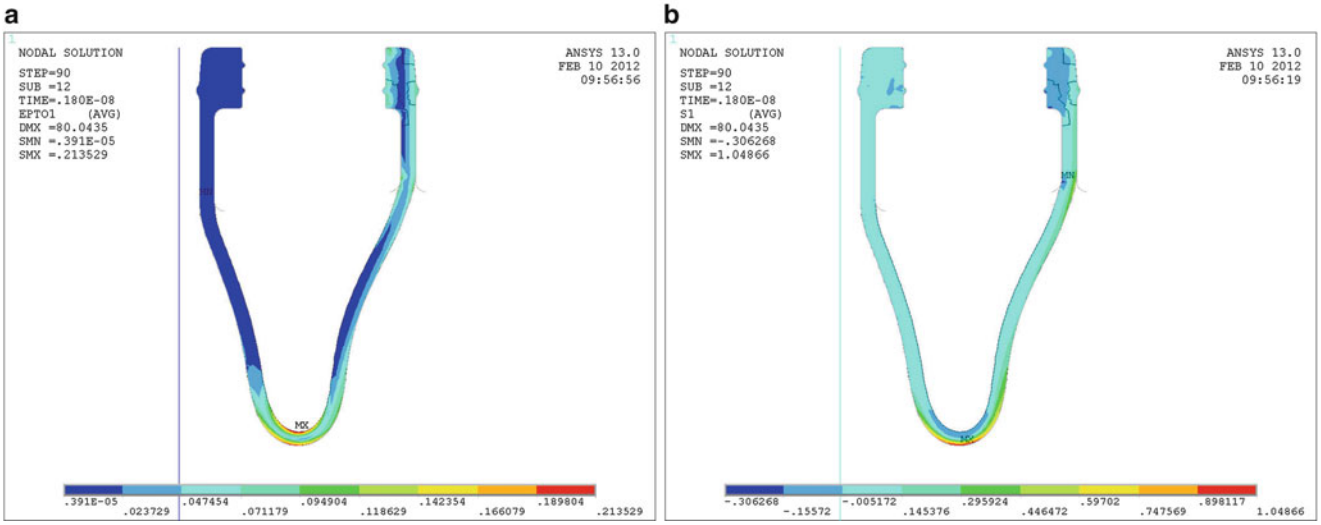

Fig. 44.7 Phase (1) distributions of maximum principal strains (*left*) and stresses (*right*)

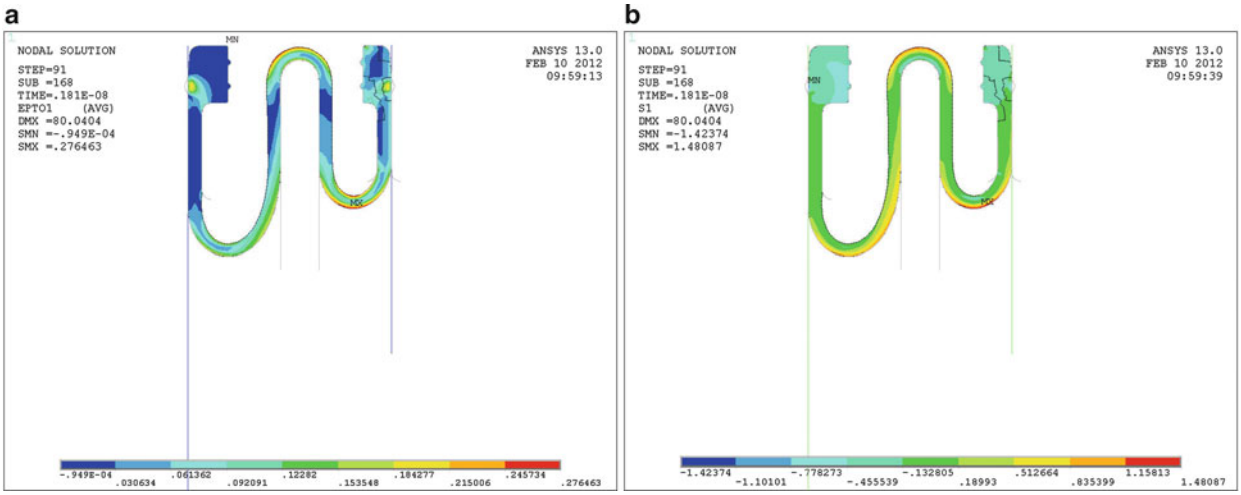

Fig. 44.8 Phase (2) distributions of maximum principal strains (*left*) and stresses (*right*)

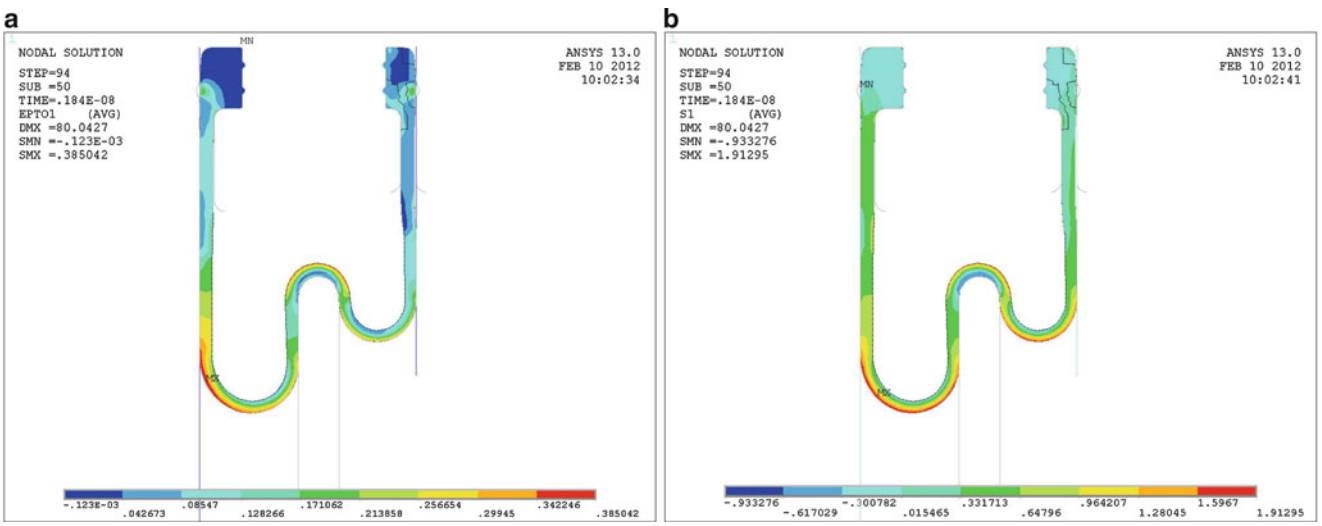

Fig. 44.9 Phase (3) distributions of maximum principal strains (*left*) and stresses (*right*)

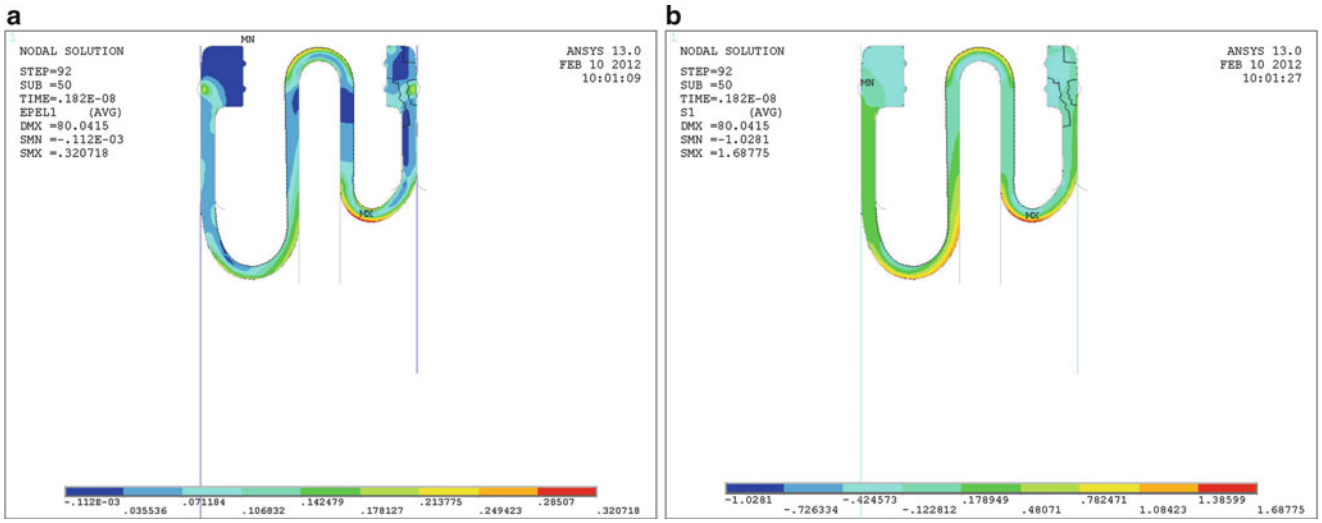

Fig. 44.10 Phase (4) distributions of maximum principal strains (*left*) and stresses (*right*)

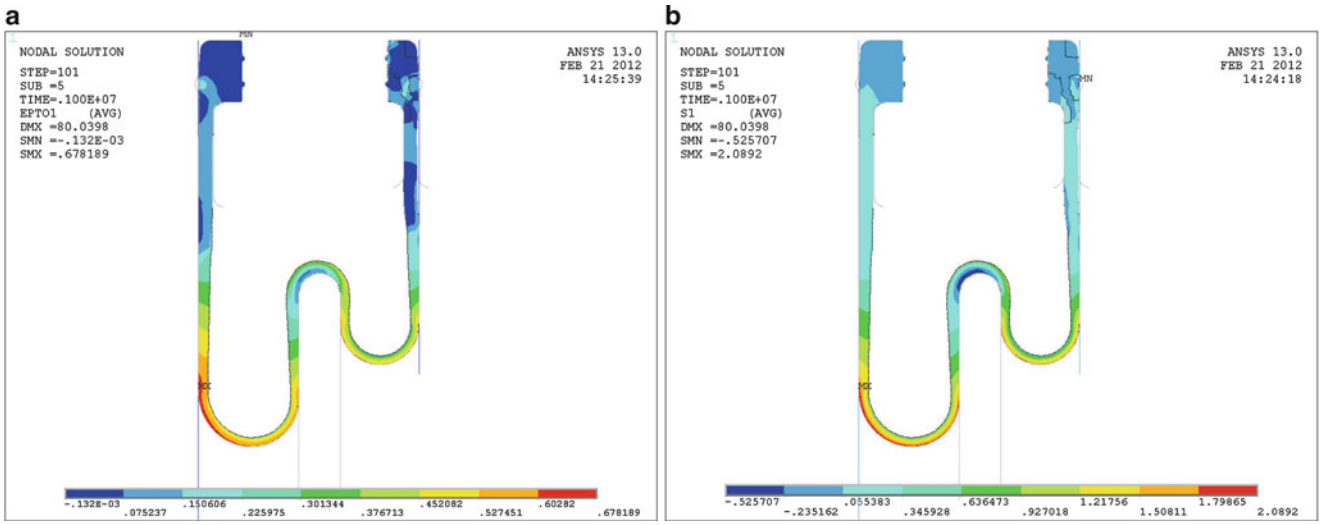

Fig. 44.11 Phase (5) distributions of maximum principal strains (*left*) and stresses (*right*)

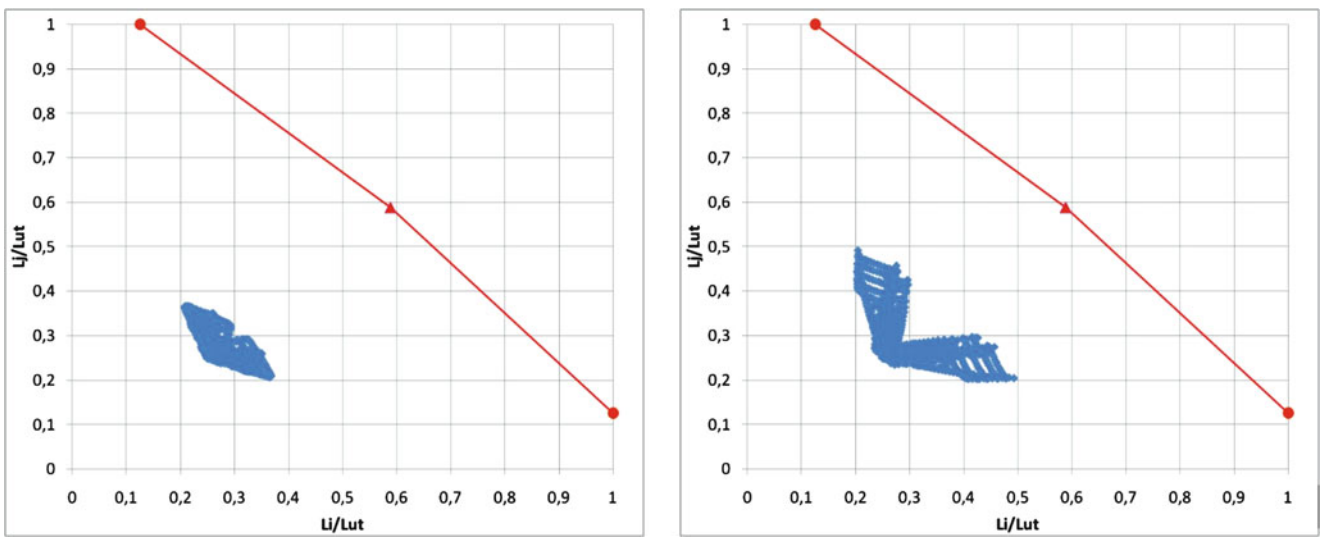

Fig. 44.12 Comparison of the principal stretches with the rupture values for phase 3 (*left*) and phase 5 (*right*)

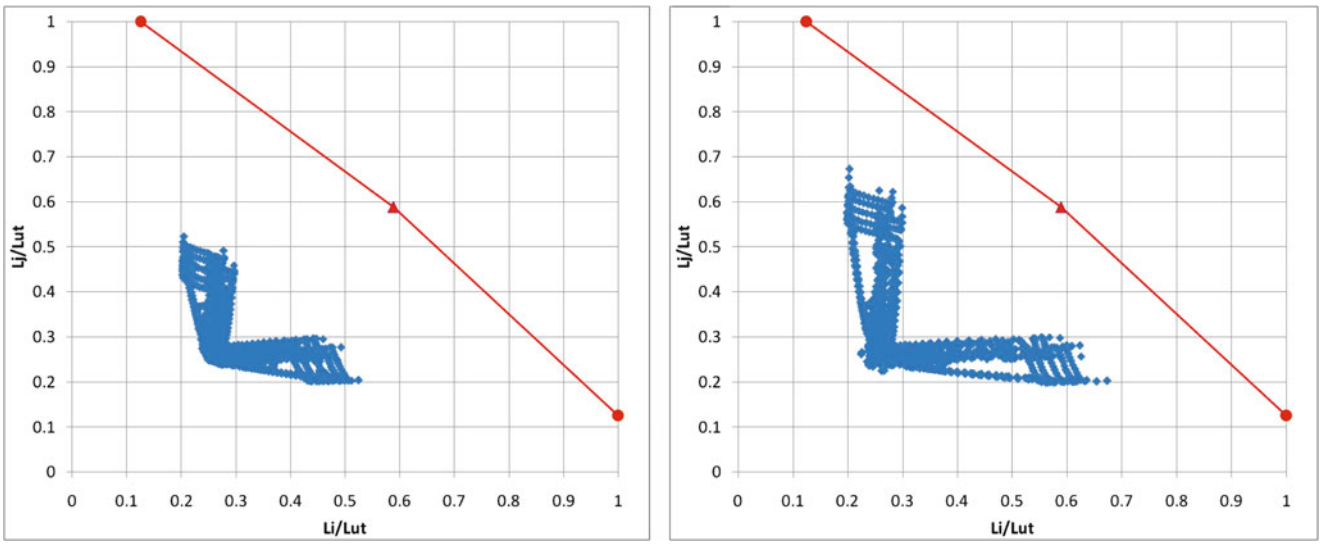

Fig. 44.13 Comparison of the principal stretches with the rupture values for phase 6, pressure 7.5 bar, at t = 0 s (*left*) and t = 300 s (*right*)

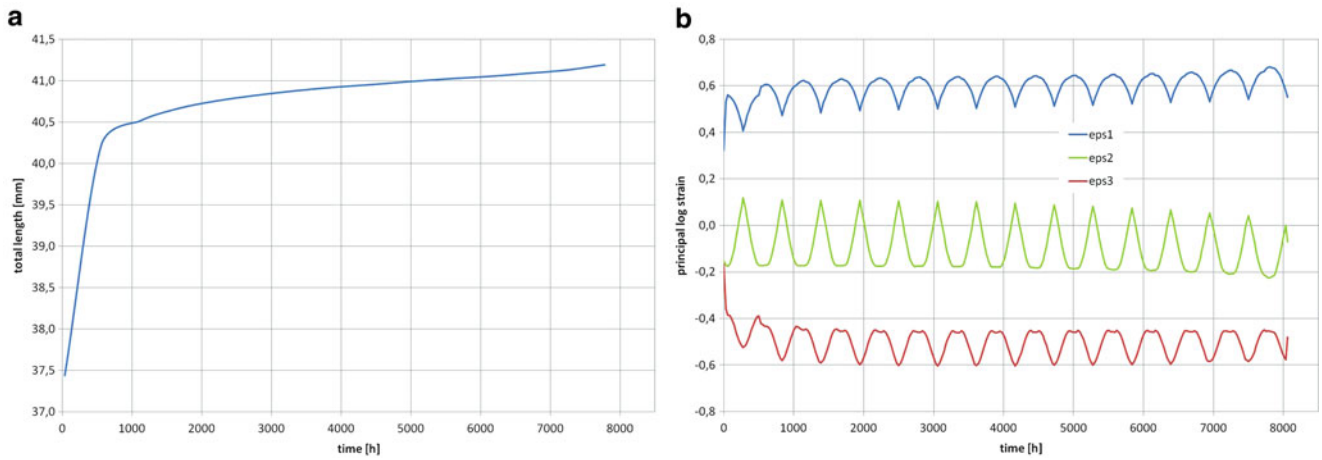

Fig. 44.14 (**a**) Envelope of maximum size over time (**b**) Principal strain over time

The last part of the study, step 7, involved the simulation of 15 cycles of pressure loading-unloading with simultaneous movement of the piston; the duration of each cycle is 300 h each. For the sake of brevity, images relating to the deformed shape are omitted, but are proposed in Fig. 44.14a, b the graphs relating to the maximum size and the maximum principal strains at the node corresponding to the maximum elongation of the membrane.

It is noted that the combined effect of material softening and viscoelasticity determine a progressive increase of axial dimensions of the membrane and an increase, cycle after cycle, of the principal strain that passes from 0.57 during the first cycle to reach nearly 0.7 in the last cycle; we note, however, a tendency towards stabilization that assures the capability of the component to withstand an even higher number of cycles with an adequate margin of safety.

44.5 Conclusions

Through the data obtained from different experimental tests, we characterized the hyperelastic, viscoelastic and pseudoelastic behavior of an elastomeric material used in an innovative device of damper for helicopter rotor. The mounting, testing and operating loads of the damper have been numerically reproduced loads of installation, by finite element

simulations; from their results, relevant but sustainable levels of deformation of the membrane have emerged. Also the evolution over time, due to material relaxation, has been investigated with the conclusion that the strain level appears to be below the limits of the material and compatible with the use within the damper.

Aknowledgement The authors would like to express their gratitude to Mecaer Aviation Group, Borgomanero (Italy), for making this work possible with the provision of cruciform and conical membranes, as well as for the qualified technical support.

References

1. Palmieri G, Chiappini G, Sasso M, Papalini S (2009) Hyperelastic materials characterization by planar tension tests and full-field strain measurement. In: SEM annual conference and exposition on experimental and applied mechanics 4:2232–2238
2. Palmieri G, Sasso M, Chiappini G, Amodio D (2011) Virtual fields method on planar tension tests for hyperelastic materials characterisation. Strain 47(2):196–209
3. Sasso M, Chiappini G, Rossi M, Palmieri G (2011) Assessment of inverse procedures for the identification of hyperelastic material parameters. Proceeding of SEM Annual conference (5): 113–139
4. Palmieri G, Sasso M, Chiappini G, Amodio D (2009) Mullins effect characterization of elastomers by multi-axial cyclic tests and optical experimental methods. Mech Mater 41(9):1059–1067
5. Amdi A, Abdelaziz MN, Hocine NA, Heuillet P, Benseddiq N (2006) A fracture criterion of rubber-like materials under plane stress conditions. Polym Test 25:994–1005
6. Ogden RW, Roxburgh DG (1999) A pseudo-elastic model for the Mullins effect in filled rubber. Proc R Soc Lond A 455:2861–2877

Chapter 45
Structural Dynamic Modification to Predict Modal Parameters of Multiple Beams

Naim Khader

Abstract An Impulse Response Function (IRF) matrix for a cantilever beam with N_o response points and N_i excitation points is obtained from simulated data. The Unified Matrix Polynomial Approach (UMPA) is employed to estimate its modal parameters. The scaled mode shapes to a unity Modal-A matrix are calculated and used to formulate a modal model for the beam. This model is used in a Structural Dynamics Modification (SDM) technique combined with the Component Mode Synthesis (CMS) to predict the modal parameters of connected beams with additional lumped masses attached to them, and with additional linear springs and dampers between the beams and between each beam and the ground. On the other hand, the impedance method is used to generate the Frequency Response Function (FRF) matrix of the two-beam system with the additional masses, springs, and dampers. The FRF matrix of the original beam, are used to synthesize the FRF matrix of the new structure. Time and frequency domain UMPA algorithms are employed to extract the modal parameters of the system. Results from both modal modeling and impedance modeling are compared with the corresponding theoretical results.

Keywords Structural dynamic modification • Modal analysis • Modal parameter estimation • Vibration • Structural dynamics

45.1 Introduction

Structural Dynamic Modification is the process of modifying the mass, stiffness or damping properties of the structure, or by adding new elements, such as vibration absorbers, to improve its dynamic behavior. Theoretical or experimental modal data or data in the form of Frequency Response Function (FRF) matrix of the original structure can be used to estimate the dynamic behavior of as many versions as required of the modified structure, with no need for extensive theoretical or experimental examination.

Excessive and resonant vibration encountered at later stages of design and development of structural systems, require structural modification to alter its dynamic characteristics, and to bring its vibration and noise to acceptable levels. Structural Dynamics Modification (SDM) has been used for a long time to achieve this objective, where modal parameters of the original structure, determined from either Finite Element Analysis (FEA) or from Experimental Modal Analysis (EMA), are used to predict the modal parameters of the modified structure. Simple modal analysis can be carried out for as many versions of the modified structure as required, using the available modal parameters of the original system, without performing extensive FEA or EMA for each version of the modified structure. This technique can be used along with the modal synthesis method to predict modal properties of an assembly of connected components, from the knowledge of their individual modal properties. SDM allows designers to visualize the effect of any intended structural modification on the dynamic behavior of the modified structure before actual implementation of this modification. Thus, SDM allows the designer of mechanical and structural systems to reduce the number of built and tested prototypes. This results in considerable saving in time, effort, and cost, which results in less expensive product, with competitive price at the market.

N. Khader (✉)
Department of Mechanical Engineering, Jordan University of Science & Technology, P. O. Box 3030, 22110 Irbid, Jordan
e-mail: nkhader@just.edu.jo

M. Rossi et al. (eds.), *Residual Stress, Thermomechanics & Infrared Imaging, Hybrid Techniques and Inverse Problems, Volume 8*, Conference Proceedings of the Society for Experimental Mechanics Series, DOI 10.1007/978-3-319-00876-9_45,

There are two approaches in the SDM technique: The direct and the inverse approaches. In the direct approach, one can predict how structural modifications affect the dynamic characteristics of the examined system, and in the inverse approach, one can predict the structural modifications, required to produce a desired change in the dynamic characteristics of the system.

In SDM, one can use the dynamic characteristics of the original system in two ways: First, properly scaled modal vectors are used to transform the system from physical space to modal space, known as modal model; Second, the Frequency Response Function (FRF) matrix of the original system are used to predict the FRF matrix of the modified structure, which are then used to estimate the modal parameters of the modified structure, known as the impedance method.

At early stages of the development of the SDM technique, a Local Eigenvalue Modification Procedure (LEMP) was used to predict the effect of adding or subtracting a point mass at one degree of freedom (dof) of the system, or adding or removing a spring or damper between two dofs of the system. Jimin He [1], discussed various methods of SDM, their implementation to real engineering structures, and outlined the main problems, encountered by SDM analyst. Avitable [2], summarized the development of SDM over the last 20 years of the twentieth century, and discussed the problems, encountered during the implementation of this technique. He presented the basic theory of SDM along with its limitations and restrictions. Nad [3] introduced the fundamental approaches and formulations of the SDM. He applied this technique to evaluate the effect of a constraining viscoelastic layer on the natural frequencies and loss factor of a cantilever beam, and the effect of initial stress in a circular disk on its natural frequencies. According to Wallak et al. [4], the local eigenvalue modification method was first used with modal data from modal test in 1978, where the eigenvalue problem was formulated in the modification space, one modification after another, where each modification employed modal data, obtained from considering the previous modification. These authors, Wallak et al., extended this method and presented what is known as simultaneous structural dynamic modification (S^2DM), where several modifications can be considered simultaneously, and the eigenvalue problem is formulated in the modal space. They validated this method later [5], by comparing results from S^2DM with those obtained from Finite Element Analysis (FEA) and modal test of a rib-stiffened plate. Sesteir [6] discussed the SDM direct method, and its application to evaluate modal parameters of a modified system, using both modal model and FRF data of the unmodified system. Kundra [7], considered SDM to predict how the dynamic behavior of a structure is affected by the introduction of mass and stiffness modification, changes in the material of the structure, as well as the effect of adding a tuned absorber to the considered structure. He presented SDM in terms of modal data as well as in terms of data in the form of FRF. Hang et al. [8], presented an analytical technique to assess the effect of distributed structural modifications, with and without additional dofs. They employed FRF of the original structure and the changes in the dynamic stiffness matrix to calculate the FRF of the modified structure. Later, the same authors [9] estimated the effect of distributed structural modifications with additional dofs, and combined the experimentally determined FRF of the original structure with the delta structural dynamic stiffness matrix of the modification to estimate FRF of the modified structure. They validated their results by comparing the obtained results from SDM with experimental and numerical results, obtained for the modified structure. Ozguven [10], presented a method to estimate the FRF of a modified structure, based on the knowledge of the FRF of the original structure and changes in the mass, stiffness, and damping matrices, introduced by the implemented structural modifications. Canbaloğlu et al. [11], presented a SDM method for modifications with additional dofs, and applied this method to a real structure by adding a stiffener beam under the wing of scaled aircraft test structure. They estimated the FRF of the modified structure from the FRF of the original structure and system matrices of the modifying structure.

This work examines a system of two beams, connected by springs and viscous dampers at selected points, with additional lumped masses. Additional points of each beam can be connected to ground by other springs and viscous dampers. Modal parameters, as well as the FRF matrices of the individual beams are used in a modal modeling and impedance modeling approaches respectively, to estimate the modal properties of the connected beams with the additional springs and dampers. The obtained results are compared with the corresponding results, obtained from a theoretical modal analysis approach.

45.2 Theoretical Analysis

A system of two uncoupled beams is considered in the presence of general viscose damping. Their Modal parameters, i.e., natural frequencies, damping ratios, and modal vectors are obtained from theoretically generated Frequency Response Function (FRF) and Impulse Response Function (IRF) matrices $[H(\omega)]_{N_o x N_i x N_f}$ and $[h(t)]_{N_o x N_i x N_f}$, respectively, where N_o and N_i are number of response and excitation points, respectively, and N_f is the number of frequency bins for FRF and number of

time samples for IRF. The Eigensystem Realization algorithm (ERA), [12], which is a first order Unified Matrix Polynomial Approach (UMPA), is employed to extract the required modal parameters of constituent uncoupled beams. The resulting modal frequencies are expressed in the diagonal matrix, and the corresponding modal vectors

$$[\psi]_{N_o x 2N} = \left[\begin{Bmatrix} \psi_1 \\ \vdots \\ \psi_{N_o} \end{Bmatrix}_1 \cdots \begin{Bmatrix} \psi_1 \\ \vdots \\ \psi_{N_o} \end{Bmatrix}_N \begin{Bmatrix} \psi_1^* \\ \vdots \\ \psi_{N_o}^* \end{Bmatrix}_1 \cdots \begin{Bmatrix} \psi_1^* \\ \vdots \\ \psi_{N_o}^* \end{Bmatrix}_N \right] \text{ are scaled to a unity Modal-A matrix.}$$

These modal parameters, as well as the FRF matrices of the uncoupled beams will be adopted for the proposed SDM, using the modal modeling and impedance modeling approaches, respectively. Note that $()^*$ means the complex conjugate of the quantity.

45.2.1 Modal Modeling

The governing equations of the free vibration of the two-beam system in discrete form are given by:

$$[M]\{\ddot{x}\} + [C]\{\dot{x}\} + [K]\{x\} = \{0\} \tag{45.1}$$

Where

$$\mathbf{M} = \begin{bmatrix} M_1 & 0 \\ 0 & M_2 \end{bmatrix}; \quad \mathbf{C} = \begin{bmatrix} C_1 & 0 \\ 0 & C_2 \end{bmatrix}; \quad \mathbf{K} = \begin{bmatrix} K_1 & 0 \\ 0 & K_2 \end{bmatrix}; \quad \text{and} \quad \mathbf{x} = \begin{Bmatrix} x_1 \\ x_2 \end{Bmatrix}$$

M_k, C_k, K_k, are $N_k x N_k$ mass, damping, and stiffness matrices of the k-th beam, k = 1 for the first beam and k = 2 for the second beam

$\{x_k\}$ is $N_k x 1$ response vector of the k-th beam

N_k, is the number of dofs of the k-th beam.

These equations can be written in state space form as:

$$[A]\{\dot{q}\} + [B]\{q\} = \{0\} \tag{45.2}$$

Where

$$[A] = \begin{bmatrix} 0 & M \\ M & C \end{bmatrix} = \begin{bmatrix} \begin{bmatrix} 0 & 0 \\ 0 & 0 \end{bmatrix} & \begin{bmatrix} M_1 & 0 \\ 0 & M_2 \end{bmatrix} \\ \begin{bmatrix} M_1 & 0 \\ 0 & M_2 \end{bmatrix} & \begin{bmatrix} C_1 & 0 \\ 0 & C_2 \end{bmatrix} \end{bmatrix}$$

$$[B] = \begin{bmatrix} -M & 0 \\ 0 & C \end{bmatrix} = \begin{bmatrix} \begin{bmatrix} -M_1 & 0 \\ 0 & -M_2 \end{bmatrix} & \begin{bmatrix} 0 & 0 \\ 0 & 0 \end{bmatrix} \\ \begin{bmatrix} 0 & 0 \\ 0 & 0 \end{bmatrix} & \begin{bmatrix} K_1 & 0 \\ 0 & K_2 \end{bmatrix} \end{bmatrix}, \text{ and } \{q\} = \begin{Bmatrix} \dot{x} \\ x \end{Bmatrix}$$

Coupling between the beams can be achieved by a set of springs and dampers, which connect selected points of the beams. Additional springs and dampers can be considered to restrict the motion of these beams by connecting these springs and dampers between each beam and the ground. Furthermore, changes in the lumped masses representing beam inertia can be considered. This results in changes in the mass, damping and stiffness matrices of the two-beam system, represented by ΔM, ΔC, and ΔK respectively, which in turn results in changes in A and B matrices, i.e., ΔA and ΔB.

$$\Delta\mathbf{M} = \begin{bmatrix} \Delta M_1 & 0 \\ 0 & \Delta M_2 \end{bmatrix},\ \Delta\mathbf{C} = \begin{bmatrix} \Delta C_{11} & \Delta C_{12} \\ \Delta C_{21} & \Delta C_{22} \end{bmatrix},\ \Delta\mathbf{K} = \begin{bmatrix} \Delta K_{11} & \Delta K_{12} \\ \Delta K_{21} & \Delta K_{22} \end{bmatrix}$$

$$[\Delta A] = \begin{bmatrix} 0 & \Delta M \\ \Delta M & \Delta C \end{bmatrix} = \begin{bmatrix} \begin{bmatrix} 0 & 0 \\ 0 & 0 \end{bmatrix} & \begin{bmatrix} \Delta M_1 & 0 \\ 0 & \Delta M_2 \end{bmatrix} \\ \begin{bmatrix} \Delta M_1 & 0 \\ 0 & \Delta M_2 \end{bmatrix} & \begin{bmatrix} \Delta C_{11} & \Delta C_{12} \\ \Delta C_{21} & \Delta C_{22} \end{bmatrix} \end{bmatrix}$$

$$[\Delta B] = \begin{bmatrix} -\Delta M & 0 \\ 0 & \Delta K \end{bmatrix} = \begin{bmatrix} \begin{bmatrix} -\Delta M_1 & 0 \\ 0 & -\Delta M_2 \end{bmatrix} & \begin{bmatrix} 0 & 0 \\ 0 & 0 \end{bmatrix} \\ \begin{bmatrix} 0 & 0 \\ 0 & 0 \end{bmatrix} & \begin{bmatrix} \Delta K_{11} & \Delta K_{12} \\ \Delta K_{21} & \Delta K_{22} \end{bmatrix} \end{bmatrix}$$

The governing equations of motion in state space form with these changes

$$[A + \Delta A]\{\dot{q}\} + [B + \Delta B]\{q\} = \{0\} \tag{45.3}$$

For the simple case of identical beams, the scaled mode shapes will be the same for both beams, and the state space vector can be expressed in terms of the scaled modes and modal coordinates as:

$$\{q\}_{(2N_{o1}+2N_{o2})x1} = [\Psi]_{(2N_{o1}+2N_{o2})x(2N_1+2N_2)}\{p\}_{(2N_1+2N_2)x1} \tag{45.4}$$

Where

$$[\Psi] = \begin{bmatrix} \begin{bmatrix} [\psi][\lambda] \\ [0] \end{bmatrix}_{(N_{o1}+N_{o2})x2N_1} & \begin{bmatrix} [0] \\ [\psi][\lambda] \end{bmatrix}_{(N_{o1}+N_{o2})x2N_2} \\ \begin{bmatrix} [\psi] \\ [0] \end{bmatrix}_{(N_{o1}+N_{o2})x2N_1} & \begin{bmatrix} [0] \\ [\psi] \end{bmatrix}_{(N_{o1}+N_{o2})x2N_2} \end{bmatrix}$$

N_1, N_2 are number of considered modes for beams 1 and 2 respectively, and factor 2 means that modal vectors and their complex conjugates are included.

N_{o1}, N_{o2} are numbers of considered response points in the IRF matrix for beams 1 and 2, respectively and the factor 2 appears due the fact that the state space vector is considered.

If Eq. 45.4 is substituted in Eq. 45.3 and the resulting equation is pre multiplied by the transpose of the transformation matrix, i.e. $[\Psi]^T$ the following eigenvalue problem is obtained,

$$\left[[I] + \left[\Delta\hat{A}\right]\right]\{\dot{p}\} + \left[[\Lambda] + \left[\Delta\hat{B}\right]\right]\{p\} = \{0\} \tag{45.5}$$

$$\left[\Delta\hat{A}\right] = [\Psi]^T[\Delta A][\Psi],\ \left[\Delta\hat{B}\right] = [\Psi]^T[\Delta B][\Psi],\ \text{and}\ [\Lambda] = \begin{bmatrix} [\lambda]_1 & [0] \\ [0] & [\lambda]_2 \end{bmatrix}$$

$[\lambda]_1$, $[\lambda]_2$ are diagonal matrices with modal frequencies of beams 1 and 2 along the diagonal.

The obtained eigenvalue problem of the modified system with coupled beams, Eq. 45.5, can be solved for the desired modal parameters.

45.2.2 Impedance Modeling

The FRF matrices $[H_1(\omega)]_{N_o x N_i x N_f}$ and $[H_2(\omega)]_{N_o x N_i x N_f}$ developed for individual beams are used to form the FRF matrix $[H(\omega)]_{(N_{o1}+N_{o2})x(N_{i1}+N_{i2})xN_f}$ of the combined system, which relates response and input spectra of the modified system as shown below:

$$\{X(\omega)\} = [H(\omega)]\{F(\omega)\} \tag{45.6}$$

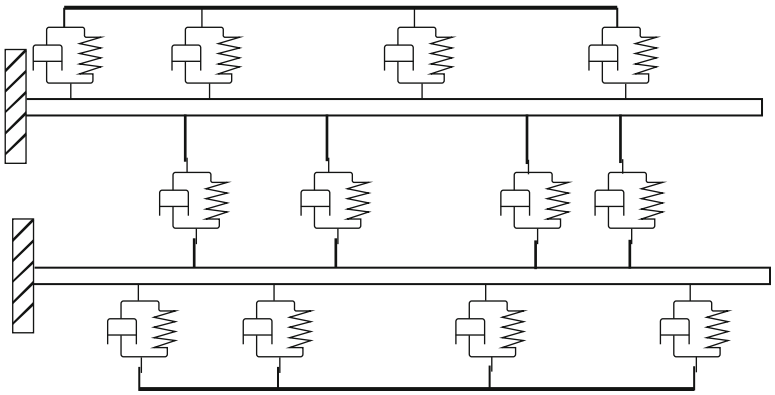

Fig. 45.1 Schematic of spring-damper connection between beams and between beams and ground

Where, (see [6], for example)

$$[H(\omega)] = [[I] + [H_o(\omega)][\Delta B]]^{-1}[H_o(\omega)] \tag{45.7}$$

$$[\Delta B(\omega)] = \left[[\Delta K] + j\omega[\Delta C] - \omega^2[\Delta M]\right] \tag{45.8}$$

$$\left[H_o(\omega)_{(N_{o1}+N_{o2})x(N_{i1}+N_{i2})xN_f}\right] = \begin{bmatrix} \left[H_o(\omega)_{N_{o1}xN_{i1}xN_f}\right] & [0] \\ [0] & \left[H_o(\omega)_{N_{o2}xN_{i2}xN_f}\right] \end{bmatrix} \tag{45.9}$$

Having the FRF matrix of the modified structure, it can be used to extract its modal parameters in the frequency domain, or the corresponding IRF matrix can be obtained by inverse Fourier Transform of the FRF matrix, which can be used with time domain modal parameter extraction algorithm, to estimate the modal parameters of the modified system.

45.2.3 Numerical Example and Results

Two identical uniform steel beams with circular cross section are considered. The beams have the same length of 0.5 m, diameter of 0.005 m, Young's modulus of 200 Gpa, and density of 7,800 kg/m^3. The FRF and IRF matrices are generated theoretically for the beams assuming 20 response and three excitation points. The first order UMPA [13], (essentially an ERA algorithm), was used to estimate the beam's modal parameters from the generated IRF matrix. The approach discussed in [14] was used to estimate the enhance impulse response function, which is then used to estimate modal scaling factors and residues in order to calculate scaled mode shapes, required for modal modeling approach. Three types of structural modifications are considered as shown in Fig. 45.1: first, each beam was connected to ground by a series of viscous dampers and springs, which is expected to result in a new set of uncoupled modes of the beams; second, the two beams were interconnected by another set of viscous dampers and springs, which results in coupling between their uncoupled modes; third, the inertia properties can be modified by changing the lumped masses, used to discretize the beams. The introduced stiffness and damping are shown in Fig. 45.1, and their values as well as the involved response points of the beams, are listed in Table 45.1.

The CMIF based on the imaginary part of the generated FRF matrices of the original beams are shown in Fig. 45.2, where the peaks indicate the existence of modes. The estimated modal vectors and modal scaling factors are employed to generate the residue matrix, which is used to estimate the desired scaled modal vectors, which are then used along with changes in A and B matrices (Eq. 45.2) to calculate $[\widehat{\Delta A}]$ and $[\widehat{\Delta B}]$. The modal parameters of the modified structure can be estimated from the eigenvalue problem described by Eq. 45.5 above, which were in agreement with the corresponding theoretical results, as will be discussed later.

On the other hand, the impedance approach was employed to calculate the FRF matrix of the modified structure $[H(\omega)]$, see Eq. 45.7 above, where the FRF matrix of the original structure $[H_o(\omega)]$, and the structural modification matrix $[\Delta B]$,

Table 45.1 Springs and dampers connecting the beams and beams with the ground

Connecting spring-damper	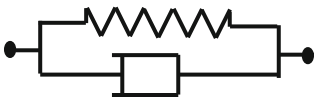	
Beam1- Response 8	k = 600 N/m; c = 600 N.S/m	Beam2- Response 2
Beam1- Response 14	K =1,800 N/m; C = 1.24 N.S/m	Beam2- Response 3
Beam1- Response 4	K = 3,350 N/m; C = 3.78 N.S/m	Beam2- Response 4
Beam1- Response 11	K = 1,250 N/m; C = 6.43 N.S/m	Beam2- Response 5
Beam1- Response 10	K = 600 N/m; C = 2.55 N.S/m	Beam2- Response 6
Beam1- Response 7	K = 2,100 N/m; C = 1.2 N.S/m	Beam2- Response 7
Beam1- Response 9	K = 2,850 N/m; C = 4.07 N.S/m	Beam2- Response 9
Beam1- Response 1	K = 500 N/m; c = 1.03 N.S/m	Ground
Beam1- Response 3	K = 1,500 N/m; c = 3.15 N.S/m	Ground
Beam1- Response 5	K = 2,500 N/m; c = 4.8 N.S/m	Ground
Beam1- Response 7	K = 1,000 N/m; c = 2.04 N.S/m	Ground
Beam1- Response 12	K = 2,000 N/m; c = 4.00 N.S/m	Ground
Beam1- Response 17	K = 1,000 N/m; c =1.94 N.S/m	Ground
Ground	K = 600 N/m; c = 1.24 N.S/m	Beam2- Response 2
Ground	K = 1,250 N/m; c = 2.63 N.S/m	Beam2- Response 4
Ground	K = 1,100 N/m; c = 2.11 N.S/m	Beam2- Response 7
Ground	K = 750 N/m; c = 1.53 N.S/m	Beam2- Response 11
Ground	K = 1,600 N/m; c = 3.2 N.S/m	Beam2- Response 18

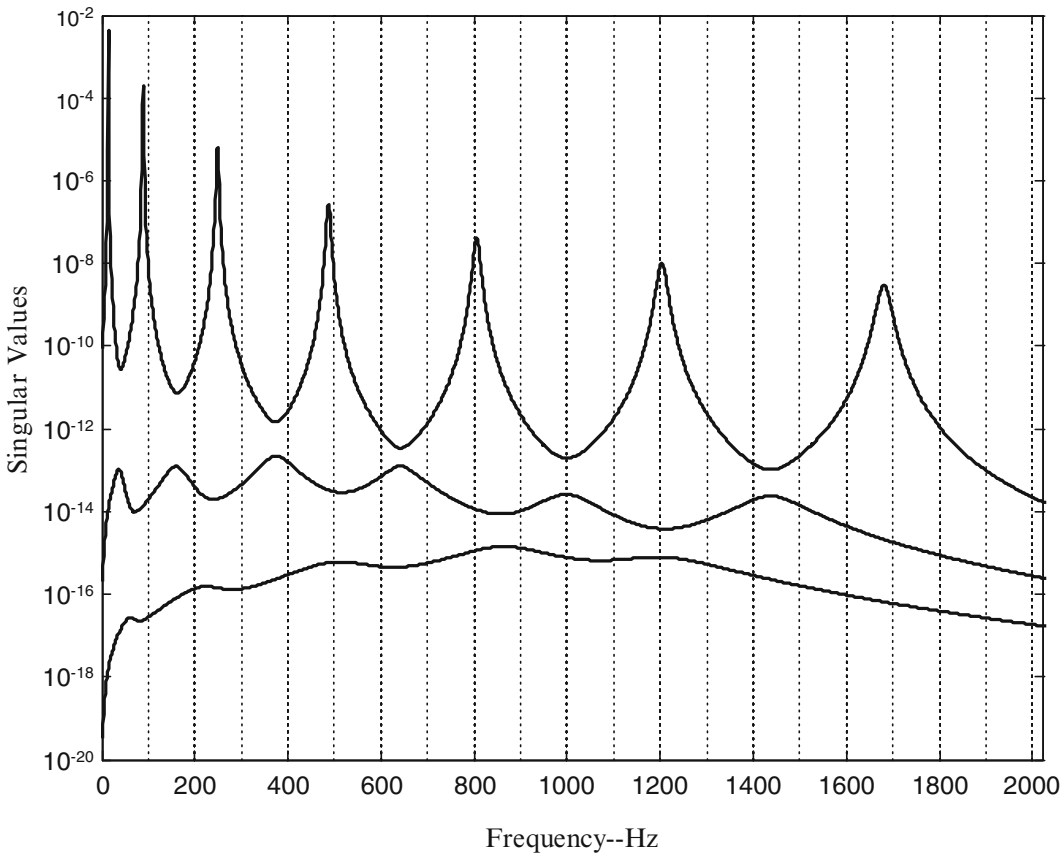

Fig. 45.2 Quad CMIF of the original beam's FRF matrix

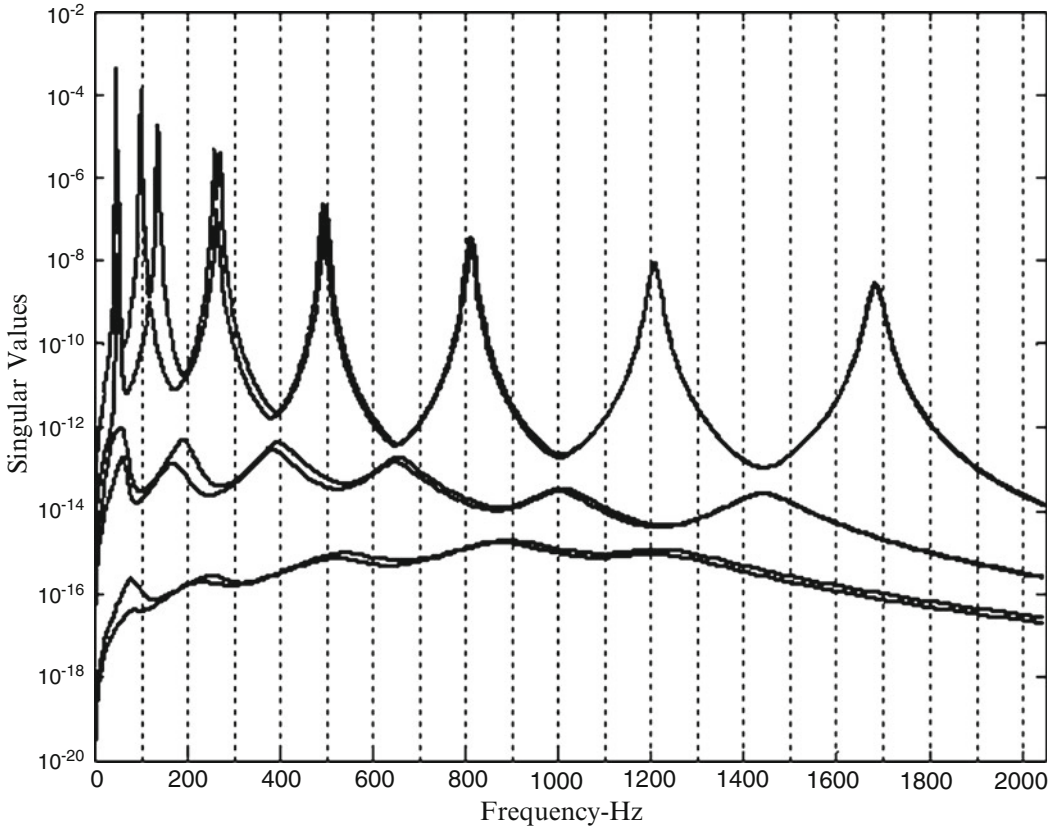

Fig. 45.3 Quad CMIF of the modified beams' FRF matrix

Eq. 45.8 above, are used to generate $[H(\omega)]$. The CMIF [15] of resulting FRF matrix is shown in Fig. 45.3. This FRF information was used in three ways to estimate the modal parameters of the modified structure; first, the Enhanced Mode Indicator Function (EMIF) [16], which is a frequency domain low order UMPA estimation algorithm, was used to estimate the modal parameters from the obtained FRF; second, a high order UMPA-based frequency domain algorithm, which uses Forsyth Orthogonal Polynomials, was used to estimate the modal parameters from the same FRF; third, the corresponding IRF was estimated via Inverse Fourier Transform and the time domain first order UMPA algorithm was used to estimate the desired modal parameters.

The obtained results from modal and impedance modeling are presented in Table 45.2 along with the corresponding results from theoretical modal analysis. The agreement between the obtained results from current work on one hand, and between these results and results from theoretical modal analysis are clear. Some of the obtained mode shapes of the two beam system are presented in Figs. 45.4, 45.5, 45.6, 45.7, and 45.8. The uncoupled two beam system has repeated frequencies because identical beams were considered. The two repeated frequencies associated with a given uncoupled mode split and result in two separate frequencies, one lower, the other is higher than the uncoupled frequency. The presented mode shapes show that the two beams move in phase at the lower frequency and out of phase at the higher frequency.

45.3 Conclusions

Modal and impedance modeling approaches are employed to predict modal parameters of a system from the modal properties and FRF matrices of its individual components, respectively. To estimate the modal parameters of the modified system, both low and high order frequency domain UMPA algorithms were used with the FRF matrix of the synthesized

Table 45.2 Modal frequencies of the two beam system in Hz, obtained by different methods

Mode number	Theoretical modal analysis	Modal modeling	Impedance modeling ERA	Impedance modeling EMIF	Impedance modeling RFP
1	46.13	46.13	46.13	46.03	46.14
2	50.74	50.74	50.74	50.70	50.74
3	100.16	100.16	100.16	100.19	100.16
4	136.49	136.49	136.49	136.53	136.50
5	258.19	258.19	258.19	258.16	258.18
6	269.15	269.15	269.15	269.08	269.13
7	491.62	491.62	491.62	491.55	491.63
8	498.55	498.55	498.55	498.44	498.56
9	807.61	807.61	807.61	807.58	807.61
10	812.72	812.72	812.72	812.68	812.72
11	1,205.40	1,205.40	1,205.40	1,205.26	1,205.40
12	1,205.84	1,205.84	1,205.84	1,205.70	1,205.84
13	1,680.98	1,680.98	1,680.98	1,680.75	1,680.98
14	1,682.94	1,682.94	1,682.94	1,682.70	1,682.94

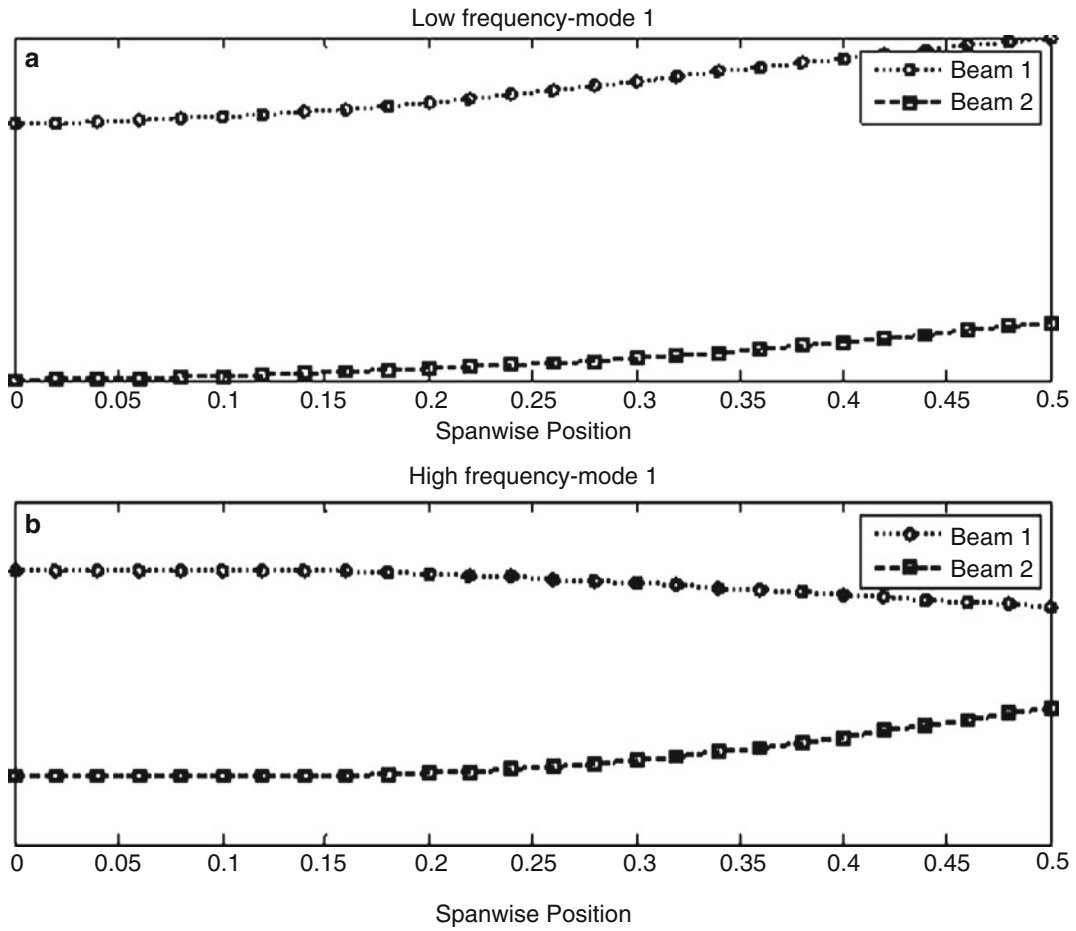

Fig 45.4 Coupled mode shapes associated with the first uncoupled beam mode

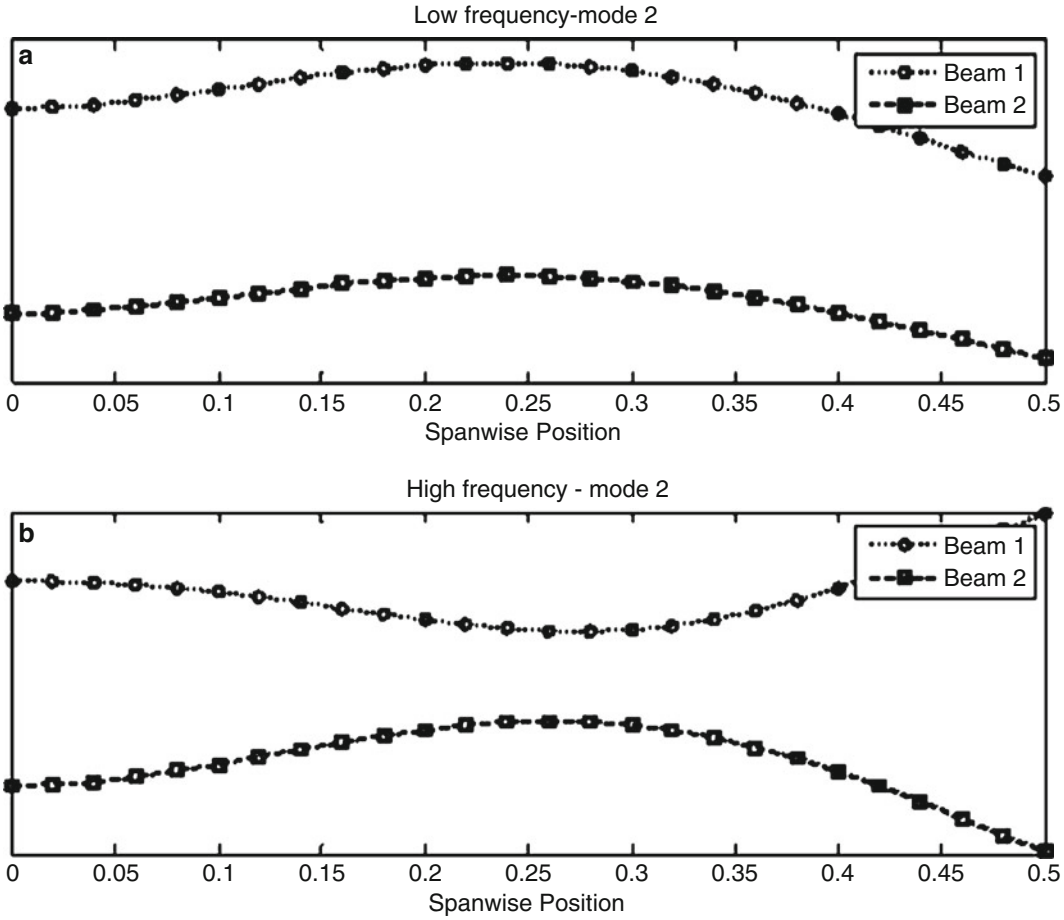

Fig. 45.5 Coupled mode shapes associated with the second uncoupled mode

structure, and a first order time domain UMPA algorithm was used with the corresponding IRF matrix. Results from the employed algorithms were in excellent agreement with theoretical results, which suggests that this procedure can be used with confidence and the next step in this direction is to employ these algorithms for actual experimental data.

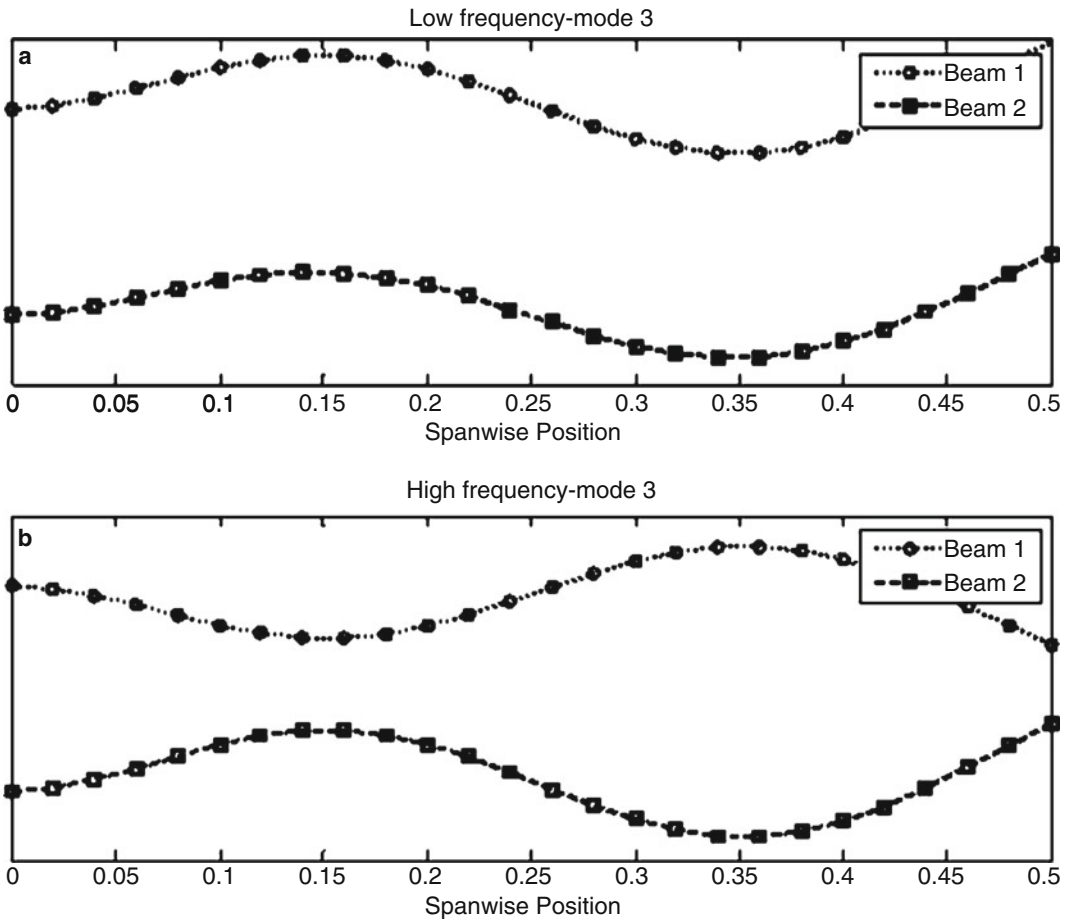

Fig. 45.6 Coupled mode shapes associated with the third uncoupled mode

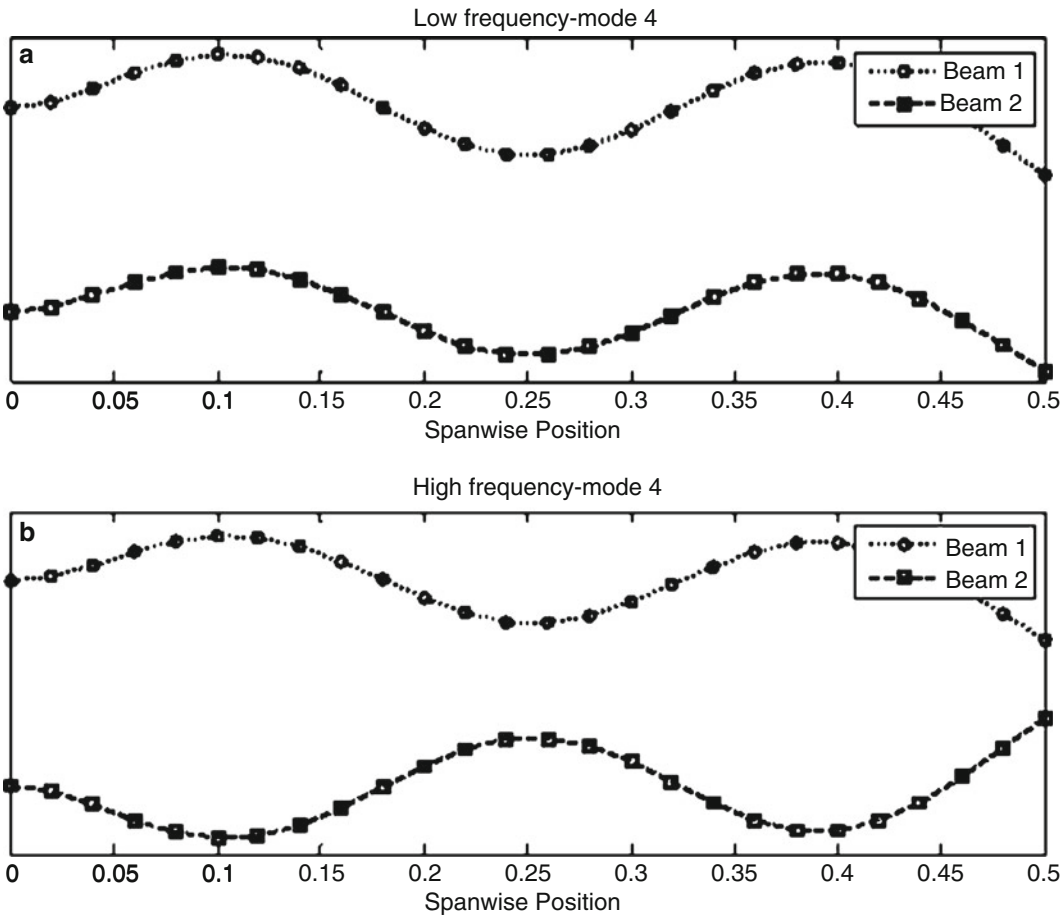

Fig. 45.7 Coupled mode shapes associated with the fourth uncoupled mode

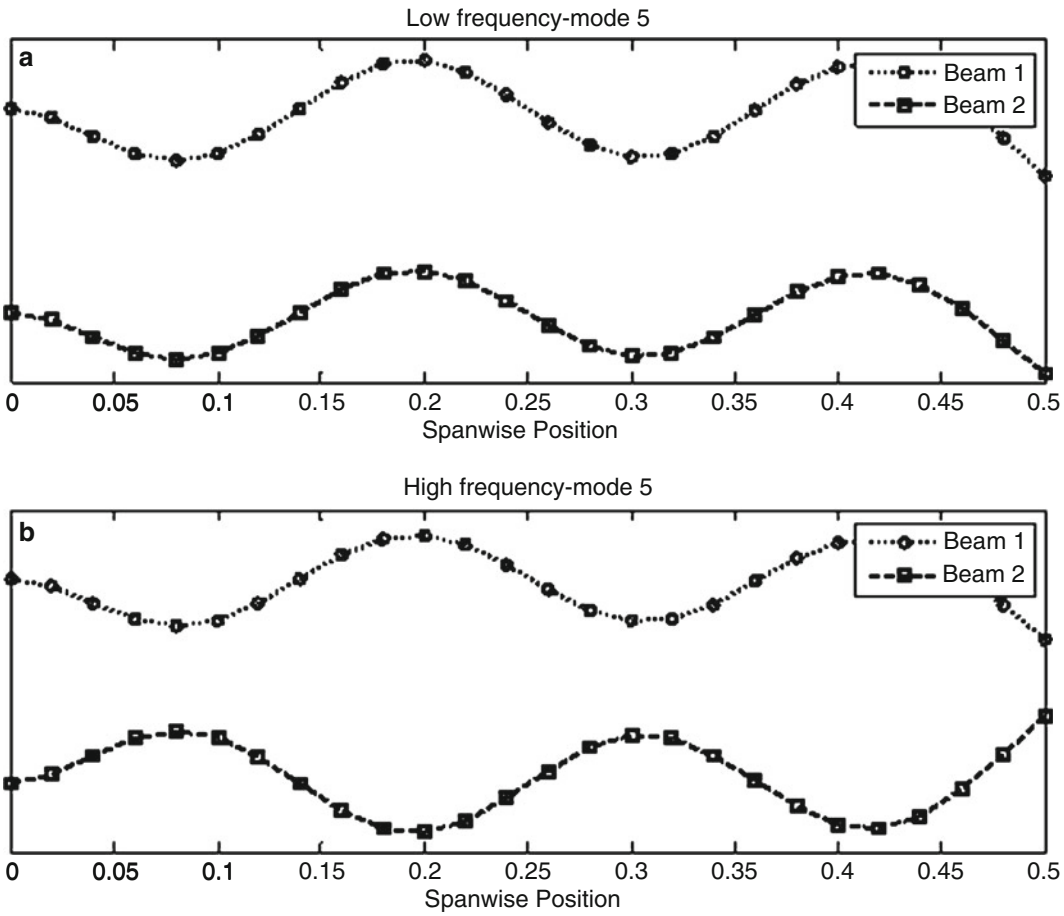

Fig. 45.8 Coupled mode shapes associated with the second uncoupled mode

Acknowledgement This work has been carried out during the author's stay at University of Cincinnati Structural Dynamics Research Lab. (UC-SDRL) while on a sabbatical leave from Jordan University of Science & Technology (JUST) The author acknowledges the financial support provided by JUST, as well as the valuable discussions with Dr. David Brown, Dr. Randal Allemang, and Dr. Allyn Phillips from UC-SDRL.

References

1. Jimin He (2001) Structural modification. Philos Trans R Soc Lond A: Math Phys Eng Sci, vol 359(1778):187–204
2. Avitabile P (2003) Twenty years of structural dynamic modification-a review. Sound Vib 37(1):14–27
3. Nad̆ M (2007) Structural dynamic modification of vibrating systems. Appl Comput Mech 1:203–214
4. Wallack P, Paul S, Mark R (1988) Simultaneous structural dynamics modification(S 2 DM). In: Proceedings of international modal analysis conference, VI, vol 2. Kissimmee
5. Wallack P, Paul S, Mark R (1989) Comparison of analytical and experimental rib stiffener modifications to a structure. In: Proceedings of international modal analysis conference, VII, vol 2. Las Vegas
6. Sestieri A (2000) Structural dynamic modification. Sadhana 25(3):247–259
7. Kundra TK (2000) Structural dynamic modifications via models. Sadhana 25(3):261–276
8. Hang H, Shankar K, Lai J (2010) Effects of distributed structural dynamic modification with additional degrees of freedom on 3D structure. Mech Syst Signal Process 24(5):1349–1368
9. Hang H, Shankar K, Lai J (2008) Prediction of the effects on dynamic response due to distributed structural modification with additional degrees of freedom. Mech Syst Signal Process 22(8):1809–1825
10. Nevzat Özgüven H (1990) Structural modifications using frequency response functions. Mech Syst Signal Process 4(1):53–63

11. Juang JN, Pappa RS (1985) An eigensystem realization algorithm for modal parameter identification and model reduction. AIAA J Guid Control Dyn 8(4):620–627
12. Canbaloğlu G, Nevzat Özgüven H (2009) Structural modifications with additional DOF-applications to real structures. In: Proceedings of the 27th international modal analysis conference, Orlando
13. Brown DL, Phillips AW, Allemang RJ (2005) A first order, extended state vector expansion approach to experimental modal parameter estimation. In: Proceedings, international modal analysis conference, Orlando, FL
14. Allemang RJ (1998) The enhanced frequency response function (eFRF): scaling and other issues. In: Proceedings, international conference on noise and vibration engineering, vol 1. Katholieke Universiteit Leuven, Belgium
15. Phillips AW, Allemang RJ (1998) The complex mode indicator function (CMIF) as a parameter estimation method. In: Proceedings, international modal analysis conference, Santa Barbara, CA
16. Allemang RJ, Brown DL (2006) A complete review of the complex mode indicator function (CMIF) with applications. In: Proceedings, international conference on noise and vibration engineering (ISMA), Katholieke Universiteit Leuven, Belgium